TMRC 2025

Digests of
The 36th Magnetic Recording Conference
- TMRC 2025 -

Tohoku University,
Sendai, Japan

28th – 30th July 2025

RIEC
Research Institute of Electrical Communication

IEEE MAGNETICS

TMRC 2025 | Chair's Welcome

It is our great pleasure to welcome you to the 36th TMRC conference, TMRC 2025, which is sponsored by the IEEE Magnetics Society. This year the conference returns to Japan for the first time since 2017, where the host will be Tohoku University in the city of Sendai.

This year's oral program consists of 41 invited talks on topics such as HAMR, heads and media, MRAM, and neuromorphic computing. Contributed work will be presented during the two poster sessions, where about 40 posters will be displayed alongside those from the invited speakers.

We would like to thank all the members of the organising committee for their hard work in helping to make TMRC a reality. The program committee members actively solicited invited talks from experts in their field. The publication co-chairs have set up the manuscript and digest submission sites and will continue to manage the review process, dealing with tardy reviewers, long after the conference is over. The publicity chair has strove to inform everyone about TMRC, whilst the local chair has arranged the food, drink and conference facilities. Any IEEE conference is inevitably accompanied by a panoply of bureaucracy and our experienced co-treasurers have been a great help in dealing with this. We also very much appreciate their contribution to managing the budget and balancing the books.

Finally, we would like to thank our sponsors for their support of TMRC. Their generous donations help to keep down registration fees and allow us to provide what we hope will be ample refreshments, and the conference dinner.

We look forward to meeting you in Sendai, and hope you enjoy the conference.

Simon Greaves

Ganping Ju

Conference Co-Chairs, TMRC 2025

TMRC 2025
Tohoku University, Sendai
28th July - 30th July, 2025

The 36th Magnetic Recording Conference will be held at Tohoku University, Sendai, Japan from 28th July to 30th July, 2025. The focus of TMRC 2025 is Solid State Magnetic Memory and Recording Technologies for >3 Tbits/in^2.

41 invited papers of the highest quality will be presented orally at the conference. Poster sessions will also be held following the oral sessions and will feature posters from the invited speakers and accepted contributed posters. Presenters of invited and contributed papers are encouraged to submit their work for publication in IEEE Transactions on Magnetics.

TMRC 2025 Organising Committee

Conference Co-Chairs

Simon Greaves
Tohoku University

Ganping Ju
Seagate Technology

Treasurers

Jan-Ulrich Thiele
Seagate Technology

Ikuya Tagawa
Tohoku Institute of Technology

Local Chair

Yoichiro Tanaka
Tohoku University

Program Co-Chairs

Stephanie Hernandez
Seagate Technology

Dmytro Apalkov
Samsung

Niranjan Natekar
Western Digital

Tazumi Nagasawa
Toshiba Corporation

Masahiko Nakayama
Kioxia

Publicity Chair

S. N. Piramanayagam
Nanyang Technological University

Poster Co-Chairs

Hirofumi Suto
NIMS

Asif Bashir
Western Digital

Tobias Maletzky
TDK

Publication Co-Chairs

Brandon Zink
NIST

Chanon Warisarn
KMITL

Local Host

Research Institute of Electrical Communication, Tohoku University

Sponsor

IEEE Magnetics Society

Platinum Sponsors

Gold Sponsors

Silver Sponsors

Local Information

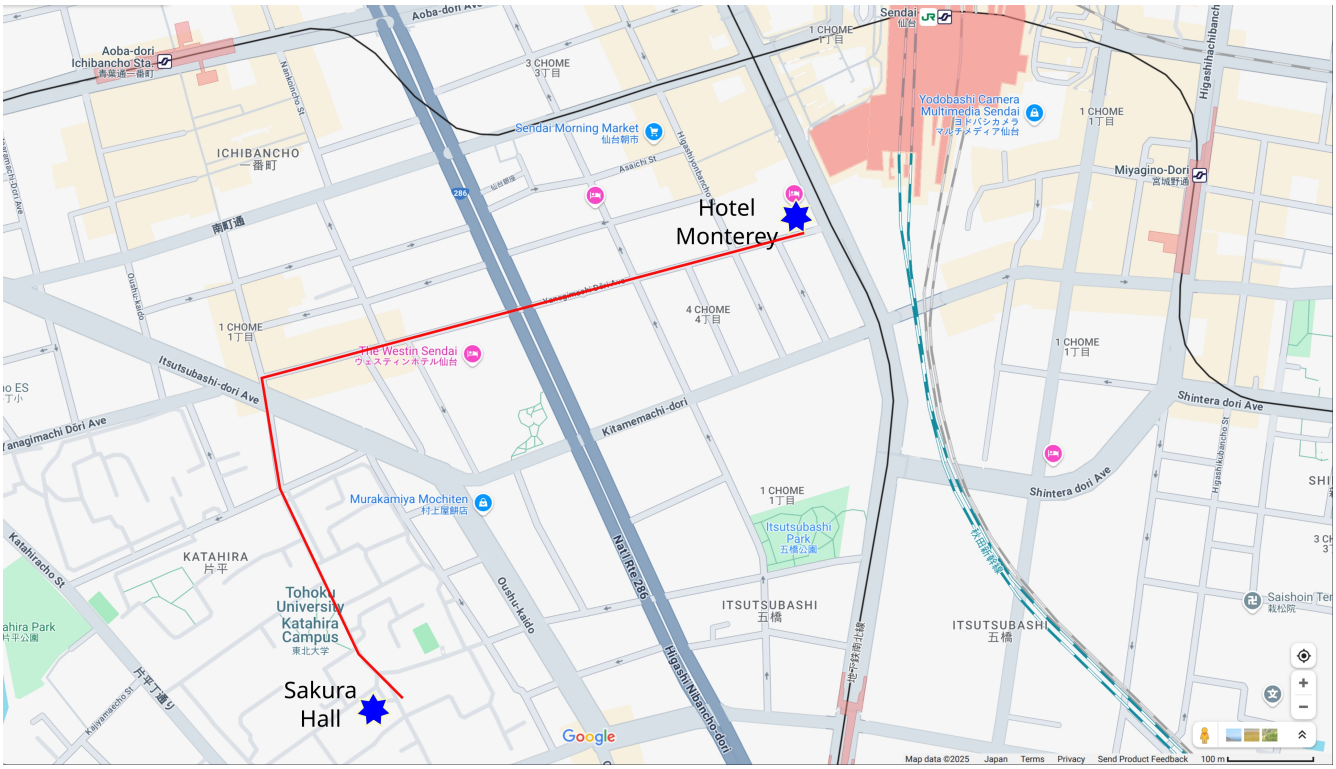

TMRC 2025 will be held at Sakura Hall on the Katahira campus of Tohoku university. It is a 15-20 minute walk from Sendai station. The conference dinner will be held at the Hotel Monterey on Tuesday 29th July. The Hotel Monterey is across the road from Sendai station.

No on-campus parking is available. The nearest subway stations are Aoba-dori Ichibancho and Itsutsubashi, although if you are staying near Sendai station it will probably be quicker to walk to the campus. A taxi from Sendai station will cost about ¥1000.

The weather in Sendai in late July is usually hot and humid. with daytime temperatures often exceeding 30˚C. Rain is common and an umbrella is recommended. Nights are warm and jackets are rarely needed.

Trains to Tokyo leave from Sendai station about three times per hour. Trains to Sendai airport run at a similar frequency.

TMRC 2025 | Schedule

Location	28th July (Monday)	29th July (Tuesday)	30th July (Wednesday)
Sakura Hall 1st floor	On-site registration 8:00 am	On-site registration 8:00 am	On-site registration 8:00 am
Sakura Hall Auditorium	Welcome Address 8:50 am Session A HAMR 9:00 am to 12:15 pm	Session C Advances Systems, Sensors and Alternative Storage 9:00 am to 12:15 pm	Session E Spintronics I: STT MRAM, New Switching Mechanism 9:00 am to 12:15 pm
	Coffee Break 10:40 am - 11:00 am	Coffee Break 10:40 am - 11:00 am	Coffee Break 10:40 am - 11:00 am
Sakura Hall 1st Floor	Lunch 12:15 pm to 1:30 pm	Lunch 12:15 pm to 1:30 pm	Lunch 12:15 pm to 1:30 pm
Sakura Hall Auditorium	Session B Heads and Media 1:30 pm to 4:45 pm	Session D Neuromorphic Computing, Devices for AI 1:30 pm to 4:45 pm	Session F Spintronics II: SOT MRAM, Racetrack Memory 1:30 pm to 4:20 pm Closing Remarks
	Coffee Break 3:10 pm - 3:30 pm	Coffee Break 3:10 pm - 3:30 pm	Coffee Break 2:45 pm - 3:05 pm
Sakura Hall 1st Floor	Session P1 Posters (Invited & Contributed) Bierstube 5:00 pm to 7:00 pm	Session P2 Posters (Invited & Contributed) 5:00 pm to 6:30 pm	
Hotel Monterey		Banquet 7:00 pm to 9:00 pm	
		Keynote 8:00 pm to 8:30 pm	

Keynote Speaker

Tuesday, 29th July, 2025, 8:00-8:30pm

Dr. Xiaodong Che
Western Digital
Chief Technology Officer

Dr. Xiaodong (Carl) Che is a widely respected leader in the data storage industry, known for his pioneering contributions to magnetic recording technologies and his commitment to advancing innovation at scale. As Senior Vice President and Chief Technology Officer at Western Digital, Dr. Che has played a key role in shaping the industry's technological direction, driving the development and deployment of storage breakthroughs such as PRML channel, PMR, Ultra-SMR and energy-assisted recording technologies.

With over three decades of experience, Dr. Che has led global engineering organizations, deepened industry–academic collaboration, and helped establish strategic technology roadmaps that have influenced the broader ecosystem. He holds more than 50 patents and has authored over 30 technical publications in the field of data storage.

Throughout his career, Dr. Che has fostered innovation through both technical achievement and organizational leadership—mentoring global teams and building frameworks that support sustainable technology development. His cross-sector collaborations with leading universities and research institutes have catalyzed advances in magnetics, AI/ML-enabled storage, and next-generation device architectures.

Dr. Che earned his Ph.D. in condensed matter physics from the University of California, San Diego, and his B.S. in physics from Fudan University. He is a Senior Member of IEEE and a founding board member of the Chinese American Information Storage Society (CAISS).

TMRC 2025 Invited Presentations

Monday 28th July, 9:00 am to 12:15 pm

Session A: Heat Assisted Magnetic Recording (HAMR)			
Session chairs: R. Victora (University of Minnesota) and M. A. Bashir (Western Digital Corporation)			
Presentation	Mon AM	Title	Speaker
A1	9:00-9:25 AM	Laser power optimization effect on jitter and write width in HAMR	C. Keener Western Digital Corporation
A2	9:25-9:50 AM	Shingled magnetic recording using HAMR technology	Y. Tomoda Toshiba
A3	9:50-10:15 AM	Thermal footprints measurements for heat assisted magnetic recording	P. O. Jubert Western Digital Corporation
A4	10:15-10:40 AM	Thermal spin-torque heat-assisted magnetic recording	S. Isogami NIMS
	10:40-11:00 AM	Break	
A5	11:00-11:25 AM	HAMR absorbing carbonaceous smear combustion kinetics in different oxygen environment	T. Trinh Western Digital Corporation
A6	11:25-11:50 AM	HAMR ADC CMR and SMR with MSMR-2R/3R gain: linear density vs. trackpitch	S. Granz Seagate
A7	11:50-12:15 PM	Measured and modeled responses for heat assisted magnetic recording up to ultra-high areal densities	R. Wood Western Digital Corporation

Monday 28th July, 1:30 pm to 4:45 pm

Session B: Heads and Media			
Session chairs: S. Hernandez (Seagate)			
Presentation	Mon PM	Title	
B1	1:30-1:55 PM	Anisotropic spin exchange modeling and Curie temperature dispersion in L10-FePt nanoparticles for HAMR media	K. Ochiai Resonac Corporation
B2	1:55-2:20 PM	The impact of in-plane grains on HAMR performance and THMap metrics	N. Natekar Western Digital Corporation
B3	2:20-2:45 PM	Phase-field study of microstructure formation of FePt-C nanogranular film for heat-assisted magnetic recording media	Y. Matsuoka NIMS
B4	2:45-3:10 PM	The computational analysis of HAMR media noise with a multilayer micromagnetic media model	L. Xu Western Digital Corporation
	3:10-3:30 PM	Break	
B5	3:30-3:55 PM	Determination of coupling state in a dual-FGL STO using injection locking	Y. Nakagawa Toshiba Corporation
B6	3:55-4:20 PM	Near field transducer reliability improvements due to media stack	M. A. Bashir Western Digital Corporation
B7	4:20-4:45 PM	An ionic liquid (IL)-based media lube for hard disc drives (HDDs)	L. Li University of Pittsburgh

TMRC 2025 Invited Presentations

Tuesday 29th July, 9:00 am to 12:15 pm

Session C: Advanced Systems, Sensors, and Alternative Storage

Session chairs: Y. Nakamura (Ehime University) and A. Kikitsu (Toshiba)

Presentation	Tue AM	Title	Speaker
C1	9:00-9:25 AM	Vector recording: advancing areal density in HAMR with innovative read head design	R. Victora University of Minnesota
C2	9:25-9:50 AM	Pushing the limits of areal density: fusing advanced channel coding, HAMR, and SMR in next-generation HDDs	J. Goode Western Digital Corporation
C3	9:50-10:15 AM	Efficient multidimensional signal processing scheme for heated-dot magnetic recording with triple-layered bit patterned media	H. Saito Kogakuin University
C4	10:15-10:40 AM	64 channel tape recording	R. Biskeborn Western Digital Corporation
	10:40-11:00 AM	Break	
C5	11:00-11:25 AM	The viability of single pass three level recording in HAMR	J. Zhu Carnegie Mellon University
C6	11:25-11:50 AM	Development of Co-Mn-Al thin films with giant anomalous Hall effect towards read head applications	M. K. Manikketh NIMS
C7	11:50-12:15 PM	Large magnetoresistance and high spin-transfer torque obtained in CPP-GMR devices with Heusler alloy electrodes through high-throughput compositional optimization	V. Barwal NIMS

Tuesday 29th July, 1:30 pm to 4:45 pm

Session D: Neuromorphic Computing, Devices for AI

Session chairs: S. N. Piramanayagam (NTU) and S. Li (Beihang University)

Presentation	Tue PM	Title	Speaker
D1	1:30-1:55 PM	Probabilistic and analog spintronic devices for energy-efficient AI hardware	S. Fukami Tohoku University
D2	1:55-2:20 PM	Scalable and energy-efficient on-device SNNs enabled by magnetic tunnel junctions	S. Li Beihang University
D3	2:20-2:45 PM	Self-regulated spintronic long short-term memory for spiking neural networks	C-H. Lai National Tsing Hua University
D4	2:45-3:10 PM	A magnetic Hopfield neural network capable of self-learning	W. Yu Fudan University
	3:10-3:30 PM	Break	
D5	3:30-3:55 PM	Spintronic foundation cells for large-scale integration	Q. Shao Hong Kong University of Science and Technology
D6	3:55-4:20 PM	Toward all-electric non-volatile intelligence in spintronic reservoir	Z. Jing National University of Singapore
D7	4:20-4:45 PM	Noise-aware training of dynamical physical neural networks of spintronic nanodevices	M. O. A. Ellis University of Sheffield

TMRC 2025 Invited Presentations

Wednesday 30th July, 9:00 am to 12:15 pm

Session E: Spintronics I - STT MRAM, New Switching Mechanisms			
Session chair: J-P. Wang (University of Minnesota)			
Presentation	Wed AM	Title	Speaker
E1	9:00-9:25 AM	Advanced magnetic tunnel junctions for voltage-controlled MRAM	S. Yuasa AIST
E2	9:25-9:50 AM	Demonstration of reliable memory operation in the world's smallest 1 Selector-1 MTJ cell	K. Sugiura Kioxia Korea
E3	9:50-10:15 AM	TEL PVD technology for spintronic devices	C-M. Park TEL US
E4	10:15-10:40 AM	Magnetic ordered alloy based free layer materials for high-speed writing of MRAM devices with high retention	M. Gottwald IBM
	10:40-11:00 AM	Break	
E5	11:00-11:25 AM	Voltage control of interfacial antiferromagnetic spins based on magnetoelectric effect	Y. Shiratsuchi Osaka University
E6	11:25-11:50 AM	Nanoelectromechanical magnetic storage and memory: a scalable, energy-efficient approach to next-generation nonvolatile storage	J. Hong UC Berkeley
E7	11:50-12:15 PM	Strain control of spintronic devices	V. Lomakin UCSD

Wednesday 30th July, 1:30 pm to 4:20 pm

Session F: Spintronics II - SOT MRAM, Racetrack Memory			
Session chair: S. Yuasa (AIST)			
Presentation	Wed PM	Title	Speaker
F1	1:30-1:55 PM	Towards field-free and ultra-low power spintronic devices: leveraging altermagnetism and orbitronics	R. Maddu Nanyang Technological University
F2	1:55-2:20 PM	From antiferromagnet to altermagnet: the controllable spin source for MRAM	C. Song Tsinghua University
F3	2:20-2:45 PM	Fully field-free spin-orbit torque switching induced by spin splitting effect in altermagnetic RuO_2	Y. Xu Nanjing University
	2:45-3:05 PM	Break	
F4	3:05-3:30 PM	Energy efficient spin-orbit-torque devices for memory and computing by new materials, new physics and voltage control	J-P. Wang University of Minnesota
F5	3:30-3:55 PM	Ultra-high efficiency of SOT-MRAMs using MTJs with strain-induced magnetic anisotropy	H. Yoda YODA-S Inc.
F6	3:55-4:20 PM	Magnetic skyrmion transport in racetracks: toward the realization of skyrmion racetrack memory	S. Yang KRISS

TMRC 2025 Poster Session 1

Poster session 1
Monday 28th July, 5:00 pm to 7:00 pm

Poster session 1 also includes posters from the invited talks of Sessions A, B, and C		
Session chair: C. Warisarn (KMITL)		
Poster	**Title**	**Presenter, affiliation**
P1-1	Three-track detection using a multi-layer perceptron for dual-layer bit-patterned magnetic recording systems	C. Warisarn King Mongkut's Institute of Technology Ladkrabang
P1-2	Layered magnetization reversal by multi-head writing in three-dimensional magnetic recording	Y. Jian Huazhong University of Science and Technology
P1-3	Interference mitigation via top-layer-assisted signal rescaling in dual-layer 3D magnetic recording	K. Luo Huazhong University of Science and Technology
P1-4	AI-based layout optimization of HDDs in full-rack heterogeneous server and storage systems	Y-J. Liao National Tsing Hua University
P1-5	Write current control based on THMap in HAMR	A. Sakoguchi Western Digital Corporation
P1-6	Improvement of dual-layer HAMR recording conditions using SMR	Y. Nakamura Ehime University
P1-7	Crystal orientation improvement by carbon addition for FePt-oxide granular films for heat assisted magnetic recording media	K. K. Tham Tanaka Kikinzoku
P1-8	Heat assisted magnetic recording (HAMR) smear characterization by using head-disk interface (HDI) sensor	W. Zhao Western Digital Corporation
P1-9	In-plane component suppression and K_u enhancement of FePt-oxide granular films by using (Pt, Ag)-C/ FePtCu-C stacked granular buffer layers	D. Miyazaki Tanaka Kikinzoku
P1-10	Experimental study on ternary recording possibility in heat assisted magnetic recording	T. Nakagawa Western Digital Corporation
P1-11	Effect of diffusion stopper layer on surface morphology of MgO underlayer of L10-FePt granular layer for HAMR	D. Isurugi Tohoku University
P1-12	Dark-laser-heating (DLH) using ultra-fast laser pulsing for mode hop mitigation in heat assisted magnetic recording (HAMR)	S. Rajauria Western Digital Corporation
P1-13	High-density L10-FePt grains on an electrically conductive (Mg,Ti)O underlayer for HAMR media	A. R. Dilipan NIMS
P1-14	Optimized multi-level heat assisted magnetic recording media with Mo spacer layer for high-capacity data storage	S. Helen NIMS
P1-15	Patterned tape head air bearing surface development	K. Kuroki Western Digital Corporation
P1-16	Magnetic properties and microstructure of FePt (BN/AlN, Ag, C) film	J-L. Tsai National Chung Hsing University
P1-17	Effect of MgTiO/Pt-BN/MgTiO underlayer on FePt-X grain size and distributions	V. Bollapragada Western Digital Corporation
P1-18	Utilizing the transversal encoder with modified PRML detection for dual-layer magnetic recording	A. Khametong King Mongkut's Institute of Technology Ladkrabang
P1-19	Inter-layer interference (ILI) suppression in dual-layer bit-patterned magnetic recording systems	N. Rueangnetr King Mongkut's Institute of Technology Ladkrabang
P1-20	A study on the fitness of GA for improving SP decoding performance	M. Nishikawa Ehime University

TMRC 2025 Poster Session 2

Poster session 2
Tuesday 29th July, 5:00 pm to 6:30 pm

Poster session 2 also includes posters from the invited talks of Sessions D, E, and F		
Session chair: H. Suto (NIMS)		
Poster	**Title**	**Presenter, affiliation**
P2-1	A high-speed and high-reliable fully digital STT-MRAM based computing-in-memory for binary neural network	Y-C. Wang Tohoku University
P2-2	Study on correlation between TMR and exchange bias in MTJs for STT-MRAM applications	S. Seo University of Ulsan
P2-3	Multi-bit magnetic memory using magnetic multilayer pillars with two-terminal structure	S. Honda Kansai University
P2-4	Ensemble learning for STT-MRAM channel detection	C. D. Nguyen FPT University
P2-5	Anisotropic exchange stiffness of perpendicularly magnetized Co/Pt multilayer thin film	W. Won NIMS
P2-6	Multi-bit magnetic memory based on a vertically magnetized pillar on two perpendicularly magnetized pinning layers	S. Honda Kansai University
P2-7	NIST SP 800-90B compliant perpendicular magnetic tunnel junction based true random number generator	Q. Jia University of Minnesota
P2-8	Topological heterostructure engineering toward advanced read head technologies for hard disk drives	Z. Wen NIMS
P2-9	Magnetization reversal cluster size under microwave field excitation	N. Kikuchi Akita University
P2-10	Impact of metal, oxide, and hybrid metal-oxide interlayers on spin-Hall effect in BiSb topological insulator and magnetic interfaces	Z. Ruixian Institute of Science Tokyo
P2-11	Optical control of RKKY coupling and perpendicular magnetic anisotropy in a synthetic antiferromagnet	J. Wu Guangdong University of Technology
P2-12	Complex magnetism, Griffiths-like phase, large spontaneous and conventional exchange bias effect in Eu2CoMnO6	A. Nayak National Institute of Technology Andhra Pradesh
P2-13	Depinning of domain walls in a notched ferromagnetic nanostrip: role of inertial and nonlinear damping effects	S. Dolui National Institute of Technology Andhra Pradesh
P2-14	Damping modification in epitaxially grown continuous L10-FePt thin films with different substrates	Y. Sasaki NIMS
P2-15	Giant bipolar unidirectional photomagnetoresistance	Y. Jiang Suzhou University of Science and Technology
P2-16	Interface design for concurrent realization of high perpendicular magnetic anisotropy and low magnetic damping in Fe/MgO	Y. N. Apriati Mie University
P2-17	Effect of excimer laser annealing on crystallization and atomic ordering of $Co_2Mn_{0.5}Fe_{0.5}Ge$ Heusler alloy thin films toward spintronic applications	H. Suto NIMS
P2-18	Proposal and micromagnetic validation of bipolar switching in voltage-controlled MRAM devices	M. Al-Mahdawi Libyan International University
P2-19	Exploring skyrmion deformation in antiferromagnetic systems: a pathway to next-generation memory devices	X. Wang Hong Kong University of Science and Technology

Laser Power Optimization Effect on Jitter and Write Width in HAMR

Chris D. Keener, Pierre-Olivier Jubert, Masato Matsubara, and Barry Stipe

Western Digital Corporation, San Jose, CA, USA, chris.keener@wdc.com

In HAMR, increasing laser power widens write erase width (WEW), reducing TPI, and reduces jitter, increasing BPI. Optimum laser power, WEW, jitter, TPI, and BPI have been modeled using the assumption of a Gaussian thermal profile. Because the laser power is adjustable, if the coefficient of the jitter term that depends on thermal gradient is improved, optimum laser power is reduced. Thus, TPI increases at the expense of BPI. TPI takes advantage of the high effective field gradient, giving HAMR its TPI advantage, lowering the bit aspect ratio. On the other hand, the portion of jitter resulting from thermal noise and grain size governs BPI. These predictions are verified in a fast measurement of the jitter contributions, which sweeps write current and laser power for each head to determine three independent jitter terms that vary with: 1) grain or cluster size, 2) T50 and DCSNR, and 3) downtrack thermal gradient.

***Index Terms*— Heat Assisted Magnetic Recording (HAMR), jitter, noise, writing process, Areal Density Capability (ADC).**

I. Introduction

JITTER strongly influences areal density in HAMR. For deeper understanding, jitter has been broken down into components [1,2]. A unique feature for HAMR is the ability to adjust laser power, so that write erase width (*WEW*) and thermal gradient are adjustable. Hence HAMR has an added degree of freedom that is not available in conventional perpendicular recording.

As laser power (*LP*) increases, *WEW* becomes wider, degrading track density (*TPI*, or tracks per inch). However, thermal gradient improves, resulting in lower jitter and improved linear density (*BPI*, or bits per inch). Jitter reaches an asymptote for high *LP* at high thermal gradient, and because *BPI* gain with increasing *LP* becomes more gradual, we can calculate *LP* for maximum *ADC* (*ADC* = *BPI* × *TPI*).

II. Approximate Model of HAMR Recording

We assume a Gaussian thermal profile for media temperature, $T - T_{amb} = \left(T_{peak} - T_{amb}\right)e^{-y^2/\sigma^2}$, where T_{peak} is the peak media temperature, T_{amb} is the ambient temperature, y is the offtrack position in nm, and σ is the 1/e width of the Gaussian in nm. This Gaussian assumption is not strictly correct, but it is a useful approximation allowing analytical solutions and an intuitive understanding of the recording physics [3]. Laser Power is proportional to laser current minus the threshold laser current above which lasing occurs. WEW is the width where the criterion $T_{peak} \geq T_w$ (writing threshold temperature for the media) is met. We define a reference WEW_{TwLC} at $LP_{Tw} = 1.21 \times LP_0$, where LP_0 is the *LP* needed to begin writing, when T_{peak}=T_w. Cross-track thermal gradient CTTG is the derivative d*T*/d*y*. Then WEW and CTTG vary with laser power as

$$WEW = \frac{2\sqrt{2}}{1.23} WEW_{TwLC} \sqrt{ln\left(\frac{LP}{LP_0}\right)} \quad (1)$$

and

$$CTTG = \frac{1.23\sqrt{2}(T_w - T_{amb})}{WEW_{TwLC}} \sqrt{ln\left(\frac{LP}{LP_0}\right)}. \quad (2)$$

As *LP* increases, both *CTTG* and *DTTG* (down track thermal gradient) improve, and we assume that *CTTG* and *DTTG* are proportional—a close approximation to the actual data.

The conventional breakdown of jitter into components [1] is

$$j = \sqrt{j_{CS}^2 + j_{SFD}^2 + j_{wth}^2 + j_{rem}^2}, \quad (3)$$

where j is total jitter, j_{wth} is noise induced by thermal fluctuations at the moment of magnetization freezing, j_{rem} is amplitude noise that is detected by the reader as jitter, j_{SFD} is related to the switching field distribution, and j_{CS} is transition position error due to the finite cluster size (previously referred to as grain size noise, although exchange coupling of grains can cause cluster size to be slightly larger than the grain size). The only term that is strongly dependent on *LP* is j_{SFD}. So for the purpose of understanding *LP* dependence, we simplify (3) as

$$j^2 = j_0^2 \left(1 + \frac{\alpha}{DTTG^2}\right), \quad (4)$$

with j_0 and α being two fitting parameters, the second term being j_{SFD}^2. Jitter asymptotes to j_0 for high *LP*.

Experimentally, we know that TPI and BPI fit well as linear functions of $1/WEW_{ADC}$ (where WEW_{ADC} is *WEW* at *LP* that is optimal for maximizing *ADC*) and jitter, respectively. The data in Fig. 1 demonstrate this linearity clearly for a sample of about 15,000 heads. Equations (5) and (6) are the fit to the data.

$$TPI = 223 - 15652/WEW_{ADC} \quad (5)$$

$$BPI = 3345 - 554j \quad (6)$$

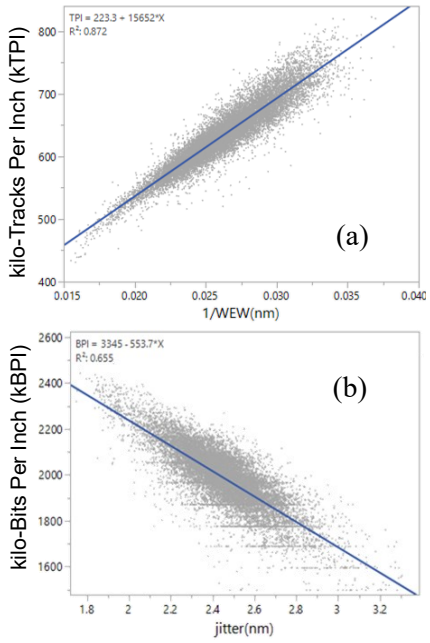

Fig. 1. (a) k*TPI* vs $1/WEW_{ADC}$, and (b) k*BPI* as a function of jitter.

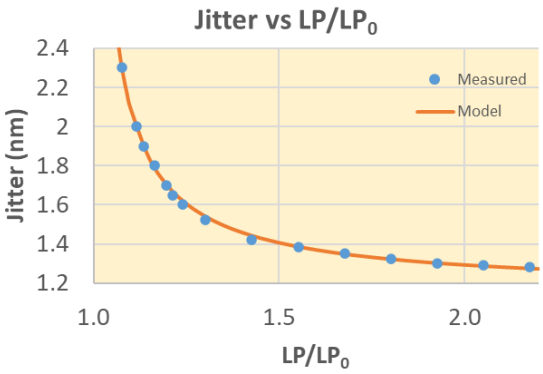

Fig. 2. Jitter vs LP/LP_0. Blue points are measured data, and the orange curve is a fit of the data to (4), with DTTG proportional to (2).

Average jitter for five heads is plotted vs *LP* and fit to (4) in Fig. 2. Note that jitter decreases steeply at low *LP* and more gradually at high *LP*. Thus at low *LP*, *BPI* rises sharply, but the increase is more gradual at high *LP*. Since *TPI* decreases monotonically with *LP*, at some laser power, the rise in *BPI* is more than offset by the loss of *TPI*. Quantitatively, there is an optimum *LP* to maximize *ADC*, and the derivative of *ADC* with respect to *LP* is zero at the maximum *ADC*:

$$\frac{\mathrm{d}ADC}{\mathrm{d}LP} = BPI\,\frac{\mathrm{d}TPI}{\mathrm{d}LP} + TPI\,\frac{\mathrm{d}BPI}{\mathrm{d}LP} = 0 \qquad (7)$$

By substitution [(5) and (6) into (7), (1) into (5), (4) into (6), and (2) into (4) with an adjustment of $\alpha' = \alpha(DTTG/CTTG)^2$ for α into (4)], we can solve for the *LP* at optimum *ADC*, as well as for *BPI* and *TPI*.

Following this line of reasoning, we find that improvements of media SFD, σ_{Tw} (standard deviation of T_w), or thermal gradient produced by the head result in *TPI* gain but little change in *BPI*, whereas improvements in j_0 (thermal, remanent, or cluster size components) result in improved *BPI* but little change in *TPI*. In other words, the bit aspect ratio (BAR) becomes lower with improved SFD or thermal gradient, but BAR increases with improvement in other jitter components.

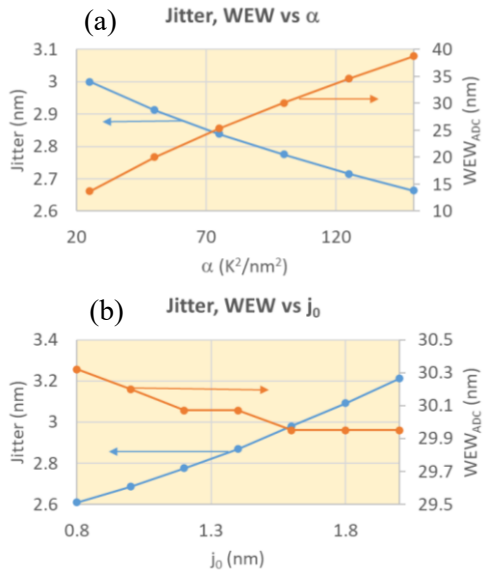

Fig. 3. Jitter (left axis) and WEW_{ADC} (right axis) vs (a) α and (b) j_0. In (b), j_{SFD} is held constant; thus $\alpha = 144/j_0^2$.

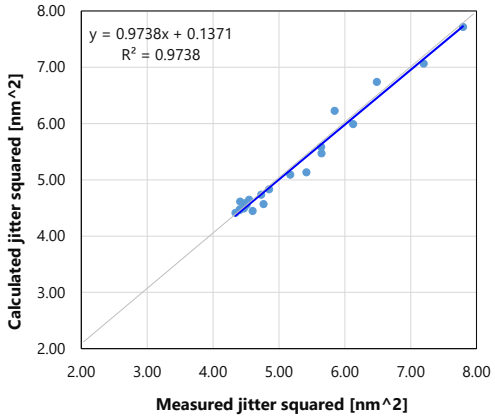

Fig. 4. Least-squares fitted j^2 from (8) vs measured j^2.

This point is illustrated in Fig. 3. Note the expanded scale of jitter in Fig. 3a and of WEW_{ADC} in Fig. 3b, corresponding to little change of these two parameters.

III. Fast Measurement of Jitter Components

We have developed a fast measurement of the breakdown of jitter into its components. Write current I_w and *LP* are swept (five I_w values between 25-105 mA, seven *LP* settings between 80% and 120% of the optimum for maximum *ADC*). Magnetic read width *MRW*, *T50*, *DTTG*, low-frequency signal-to-noise ratio *DCSNR* (in dB) are measured at each I_w and *LP*, and σ_{Tw} (from THmap [3]) at each I_w. In (8), the first term is j_{CS}^2, the second term is j_{rem}^2, and the last term is j_{SFD}^2. From a least-squares fit, parameters *CS*, γ, and β are extracted. Fig. 4 shows an excellent fit for one head as an example.

$$j^2 = \frac{CS^3}{12MRW} + \gamma\left(\frac{T50}{10^{DCSNR/20}}\right)^2 \frac{CS}{MRW} + \beta\left(\frac{\sigma_{Tw}}{DTTG}\right)^2 \frac{CS}{MRW} \qquad (8)$$

Two types of media were compared in Table 1. The jitter breakdown is the average for 8 heads that were measured on both Media A and Media B. Media A has superior j_{SFD}; therefore, we expect it to have higher *TPI*. Media B has smaller grain size and cluster size, and we expect it to have higher *BPI*. The independent *ADC* measurement confirmed these expectations.

TABLE I
Jitter Breakdown and ADC for Two Media Types

Parameter	Media A	Media B
j	1.87	1.77
j_{SFD}	1.12	1.31
j_{rem}	0.72	0.66
j_{CS}	1.31	0.98
ADC (Tb/in²)	1.274	1.270
k*TPI*	609	594
k*BPI*	2093	2138

Jitter breakdown and ADC for two media types. Media A has superior j_{SFD} and thus higher *TPI*, and Media B has smaller grain size and thus higher *BPI*.

References

[1] J. Hohlfeld *et al.*, "Improving Our Understanding of Measured Jitter (in HAMR)," *IEEE Trans. Magn.*, vol. 55, no. 3, Art. no. 3000511, pp. 1-11, 2019.

[2] C. D. Keener *et al.*, "HAMR Media Jitter Relationships and Opportunities" IEEE Trans. Magn., vol. 60, no. 5, Art. no. 3200204, pp. 1-4, 2024.

[3] P.-O. Jubert *et al.*, "Spin-stand Measurements to Extract the Switching Distributions of Heat-Assisted Magnetic-Recording Media," *IEEE Trans. Magn.*, vol. 59, no. 3, Art. no. 3200405, pp. 1-5, 2023.

Shingled Magnetic Recording Using HAMR Technology

Yusuke Tomoda[1], Jianfeng Xiao[1], Takuya Maeda[2], Kaori Kimura[1], Masaya Ohtake[1], Gaku Koizumi[1], Takao Furuhashi[1], Takuma Kido[1], and Akihiko Takeo[1]

[1]Storage Products Division, Toshiba Electronic Devices & Storage Corporation, 8 Sinsugita-cho, Isogo-ku, Yokohama-shi, Kanagawa 235-8522, Japan, yusuke.tomoda@toshiba.co.jp
[2]Corporate Laboratory, Toshiba Corporation, 1 Komukai-toshiba-cho, Saiwai-ku Kawasaki-shi, Kanagawa 212-8582, Japan, takuya1.maeda@toshiba.co.jp

Recently, two primary writing architectures have been employed in magnetic hard disk drive (HDD) storage devices: conventional magnetic recording (CMR) and shingled magnetic recording (SMR). SMR offers higher areal density capability (ADC) compared to CMR, although it compromises random write/read performance. On the other hand, two main writing process is applied to hard disk drive, which are heat assisted magnetic recording (HAMR) and flux control microwave assisted magnetic recording (FC-MAMR). This two writing process is completely different each other, but HAMR method can obtain higher ADC rather than that of MAMR technology. In this work, we compared ADC gain from CMR to SMR using FC-MAMR and HAMR drives. ADC gain is almost comparable between FC-MAMR and HAMR in our design. Therefore, we can obtain highest capacity using HAMR SMR drive.

***Index Terms*— Heat-assisted Magnetic Recording (HAMR), Microwave-assisted magnetic recording (MAMR), Perpendicular magnetic recording (PMR), Shingled magnetic recording (SMR)**

I. Introduction

HARD DISK DRIVES (HDD) achieve high areal density with various technology such as perpendicular magnetic recording[1]-[2], giant magnetoresistive junction[3]-[4], tunnel magentoresistive junction[5]-[6], shingled magnetic recording (SMR)[7]-[8], flux control microwave-assisted magnetic recording (FC-MAMR)[9] and heat-assisted magnetic recording (HAMR)[10]. The market primarily utilizes two writing schemes: conventional magnetic recording (CMR) and SMR. SMR method is suppressed random performance but higher areal density rather than CMR method. FC-MAMR and HAMR are completely different writing principle. Magnetic field between write gap and to recording media can be controlled using FC-MAMR. On the other hand, HAMR technology can control temperature of media using laser diode. FC-MAMR drives are mainly used in the latest market but HAMR is expected as higher capacity of next generation. In the following sentence, FC-MAMR will simply be referred to as MAMR.

Higher tracks per inch (TPI) is obtained from HAMR rather than MAMR architecture, because bit aspect can be defined heat spot size from laser diode. Therefore, we can obtain higher areal density capability with optimized laser conditions. In this study, we compared some SMR properties with MAMR and HAMR technology.

II. HDD Experiment

In order to investigate difference between MAMR and HAMR on SMR scheme, we compared some properties using HDD drives. HDD has 7200 rpm of rotation speed. Skew angle is around 17 deg. at outer diameter (OD) side and -17 deg. at inner diameter (ID) side, respectively. We evaluated bit error rate of write pattern both on-track and after erase at adjacent track. Then, we calculated maximum areal density capability with each condition of CMR and SMR using MAMR and HAMR drives.

III. Results and Discussion

First, we compared switching properties of SMR write direction. The switching properties were defined by comparing adjacent track interference of IDtoOD and ODtoID direction, respectively. Fig.1 shows maximum write offset value dependency on each radius position with SMR write direction using MAMR drive. In OD area, maximum write offset value of ODtoID direction is larger than that of IDtoOD direction. On the other hand, IDtoOD direction is higher than ODtoID direction in ID area. Both properties are overlapping around 9 of radius, which is defined as switching position of SMR write direction. Fig.2 shows also HAMR case. Maximum write offset dependency shows same tendency on MAMR.

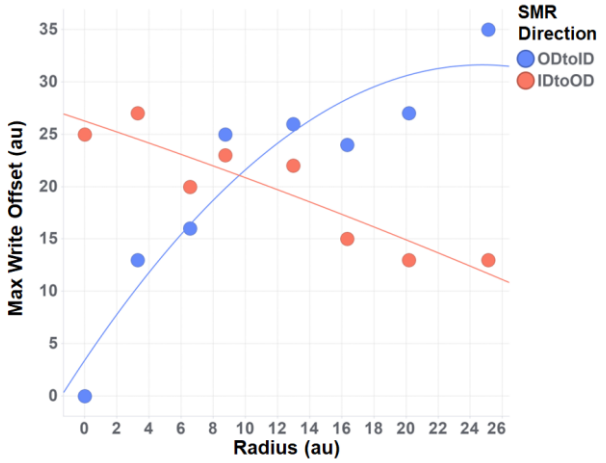

Fig. 1. Max write offset as a function of radius on MAMR drive.

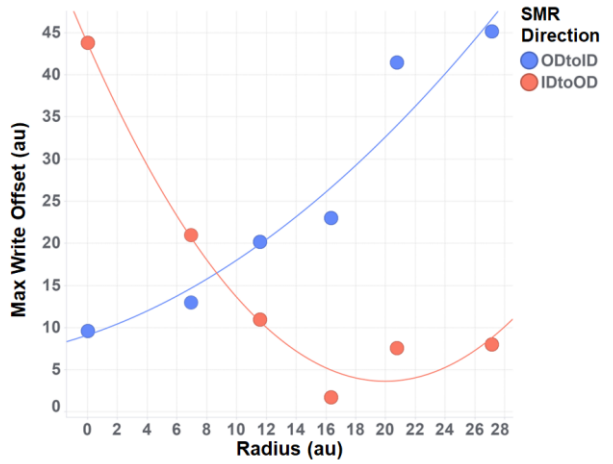

Fig. 2. Max write offset as a function of radius on HAMR drive.

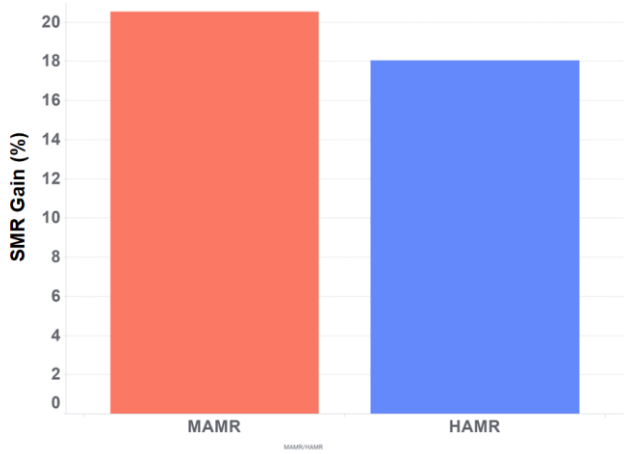

Fig. 4. Comparison of SMR gain between MAMR and HAMR drives.

Fig.3 illustrates the distribution of switching positions for MAMR and HAMR. In the case of MAMR, the average switching position is approximately 10, which corresponds closely to a skew angle of 0 degrees on the drive. of skew angle on the drive. On the other hand, switching position of HAMR drives is shifted to inner side around 9. Moreover, standard deviation of HAMR is larger than that of MAMR, which suggests that cross track thermal/magnetic field properties are almost same between OD and ID side and less dependent on skew angle.

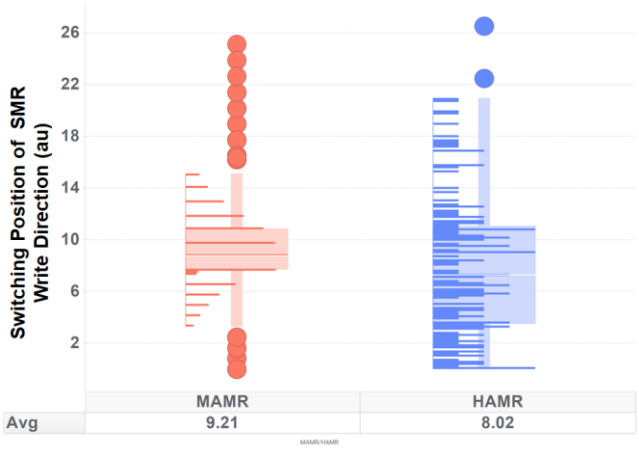

Fig. 3. Comparison of switching position between MAMR and HAMR drives.

Fig.4 shows SMR gain on MAMR and HAMR drives. SMR Gain is calculated by ratio of areal density capability of SMR to that of CMR. Around 20 % of SMR gain is obtained from MAMR drives. On the other hand, HAMR drives are about 2.5 % smaller than MAMR case. This difference is came from HAMR writer properties of less difference at track edge between both side[11]. However, around 18 % of SMR gain are obtained even HAMR drives.

IV. Conclusions

In this study, we compared some SMR properties using MAMR and HAMR drives. Since writing process is completely different both methods, several characteristics show little bit different between MAMR and HAMR. Although the SMR gain of HAMR drives is slightly lower than that of MAMR, it still achieves approximately 18%, indicating the potential for higher areal density with HAMR-based SMR. These results imply that higher areal density can be obtained with HAMR drives applying SMR method.

References

[1] S. Iwasaki and K. Takemura, "An analysis for the circular mode of magnetization in short wavelength recording," *IEEE Trans. Magn.* MAG-11 (5), pp. 1173–1175, 1975.

[2] S. Iwasaki and Y. Nakamura, "An analysis of the magnetization mode for high density magnetic recording," *IEEE Trans. Magn.* MAG-13, pp. 1272–1277, 1977.

[3] M. N. Baibich*, J. M. Broto, A. Fert, F. Nguyen Van Dau, F. Petroff, P. Etienne, G. Creuzet, A. Friederich, and J. Chazelas, "Giant Magnetoresistance of (001)Fe/(001)Cr Magnetic Superlattices," *Phys. Rev. Lett.* Vol. 61, pp. 2472-2475, 1988.

[4] J. Barnaś, A. Fuss, R. E. Camley, P. Grünberg, and W. Zinn, "Novel magnetoresistance effect in layered magnetic structures: Theory and experiment," *Phys. Rev B* Vol. 42, pp.8110-8120, 1990.

[5] T. Miyazaki and N. Tezuka, "Giant magnetic tunneling effect in Fe/Al2O3/Fe junction," *J. Magn. Magn. Mater.* Vol. 139, pp. L231-L234, 1995.

[6] J. S. Moodera, Lisa R. Kinder, Terrilyn M. Wong, and R. Meservey, "Large Magnetoresistance at Room Temperature in Ferromagnetic Thin Film Tunnel Junctions," *Phys. Rev. Lett.* Vol. 74, pp. 3273-3276, 1995.

[7] Y. Cassuto, M. A. A. Sanvido, C. Guyot, D. R. Hall, and Z. Z. Bandic., "Indirection systems for shingled-recording disk drives," *MSST Conf.* May 2010.

[8] A. Amer, D. D. E. Long, E. L. Miller, J.-F. Paris, and T. Schwarz, S.J., "Design issues for a shingled write disk system," *MMST Conf.* May 2010.

[9] N. Narita, M. Takagishi, H. Iwasaki, H. Suto, G. Koizumi, A. Takeo, and T. Maeda, "Design and Numerical Study of Flux Control Effect Dominant MAMR Head: FC Writer," *IEEE Trans. Magn*. Vol. 57, 3300205, 2021.

[10] R. E. Rottmayer, S. Batra, D. Buechel, W. A. Challener, J. Hohlfeld, Y. Kubota, L. Li, Bin Lu, C. Mihalcea, K. Mountfield, K. Pelhos, C. Peng, T. Rausch, M. A. Seigler, D. Weller, and X. Yang, "Heat-Assisted Magnetic Recording," *IEEE Trans. Magn*. Vol. 42, pp. 2417-2412, 2006.

[11] K. Schouterden, "Maximizing Areal Density," *IDEMA Symposium* Autumn 2024.

Thermal Footprint Measurements for Heat Assisted Magnetic Recording

Pierre-Olivier Jubert[1], Esmeralda Yitamben[1], Wan Kuang[1], Takuya Matsumoto[1], Barry Stipe[1] and Richard Brockie[1]

[1]Western Digital Corporation, San Jose, CA 95119, USA, Pierre-Olivier.Jubert@wdc.com

A method for characterizing the thermal footprints generated by a heat-assisted magnetic recording head (HAMR) onto an HAMR medium is presented. It uses a static tester and has the advantage over traditional recording techniques of measuring an undistorted two-dimensional image of the temperature profile, highlighting the lower temperature background created in the medium. Two-dimensional temperature profiles obtained from different near-field transducer (NFT) designs are presented that compare very well to expectations from optical/thermal modeling.

***Index Terms*— Heat-assisted magnetic recording (HAMR), static tester, near-field-transducer designs, temperature profiles.**

I. Introduction

Heat assisted magnetic recording (HAMR) is being introduced in hard disk drives to enable areal densities beyond that of enhanced perpendicular magnetic recording (e-PMR) technology [1]. HAMR recording relies on locally heating the recording layer FePt magnetic grains to temperatures just above their Curie temperature (~660K), enabling data writing into the high anisotropy medium with conventional writer fields while the grains cool. The heat spot defines the writing location and is achieved by the absorption of light confined into the medium via a near field transducer (NFT) excited by a laser and positioned at the air bearing surface of the HAMR head [2-4]. The thermal profile results from both the optical characteristics of the coupled NFT-media system and the thermal transport properties of the media. The characteristics of the thermal hot spot in the recording layer play a large role in determining the areal density capability of the media: high areal densities require high thermal gradients and narrow thermal write widths to enable good on track performance and high track density.

Partial temperature profile information is accessible from down-track and cross-track gradient measurements in hard disk drives or spin-stand testers [5]. But due to the high disk velocity (~20m/sec), direct measurement of the full two-dimensional thermal profiles is practically not accessible in these recording systems.

In this work, we present a new method that allows measuring the two-dimensional temperature map generated by an NFT into the recording layer by using pulse recording with a static tester.

II. Experimental Measurement of Thermal Footprints

The thermal footprint measurements are performed using a piezo scanning write/read tester [6-8]. This setup allows for a very accurate positioning of an HDD head over a recording medium. The head slider is in contact with the disk at an optimized tilt angle and dragged over the medium at 100 μm/s. A conventional HAMR medium that is initially thermally erased is used for the measurements.

At controlled intervals, the laser diode embedded in the HAMR head is excited with 50 nanosecond pulses. Before each laser pulse, the writer coils are energized at a set amplitude and polarity. The magnetization orientation changes in the direction of the applied field only in areas where the temperature exceeds the media writing threshold. This results in the writing of isolated head footprints into the HAMR medium. A two-dimensional readback image of the media allows to measure the extent of the write footprint.

Write footprints of alternating writer polarity are written on the medium at regular interval, typically of more than 1 μm apart. The amplitude of the laser pulse is varied sequentially from a reference value, LP_{ref}, and a second value, LP. At LP_{ref}, small footprints are formed that serve as alignment marks to average hundreds of footprints generated at the laser power LP. From each average write footprint, the footprint contour is defined as the location where the readback signal amplitude is 50% of the maximum readback signal, which corresponds to a temperature isotherm in the recording layer. At the applied field used in this experiment, T_w is 625K [9].

Thermal footprints are measured and averaged for varying laser power LP, allowing to extract the footprints boundaries or T_w isotherms for each laser power (Fig. 1). Increasing the input laser power results in progressively larger magnetic footprints. These set of T_w isotherms are tomographic projections of the temperature profile generated by the NFT in the HAMR medium. The head/medium optical/thermal system is linear, such that the change in medium temperature is directly proportional to the laser power change. The T_w isotherms at different laser power LP can be converted into a temperature contour map at a fixed laser power LP_0:

$$T\left(x_{T_w}, y_{T_w}\right)_{@LP_0} = T_{amb} + \frac{LP_0}{LP}\left(T_w\left(x_{T_w}, y_{T_w}\right)_{@LP} - T_{amb}\right)$$

Typically, we chose LP_0 corresponding to a 50 nm written track width or equivalently such that the T_w contours extend up to +/- 25 nm in the cross-track direction. The contour line measured at $2xLP_0$ is the location where the temperature is $(T_w - T_{amb})/2$ or 460 K at LP_0.

Fig. 1(a)-(b) shows two-dimensional temperature maps measured on the same recording medium using HAMR heads with two different NFT designs. The laser power LP_0 is adjusted for each case to the same 50-nm wide written track width. The first NFT design produces low temperature background that

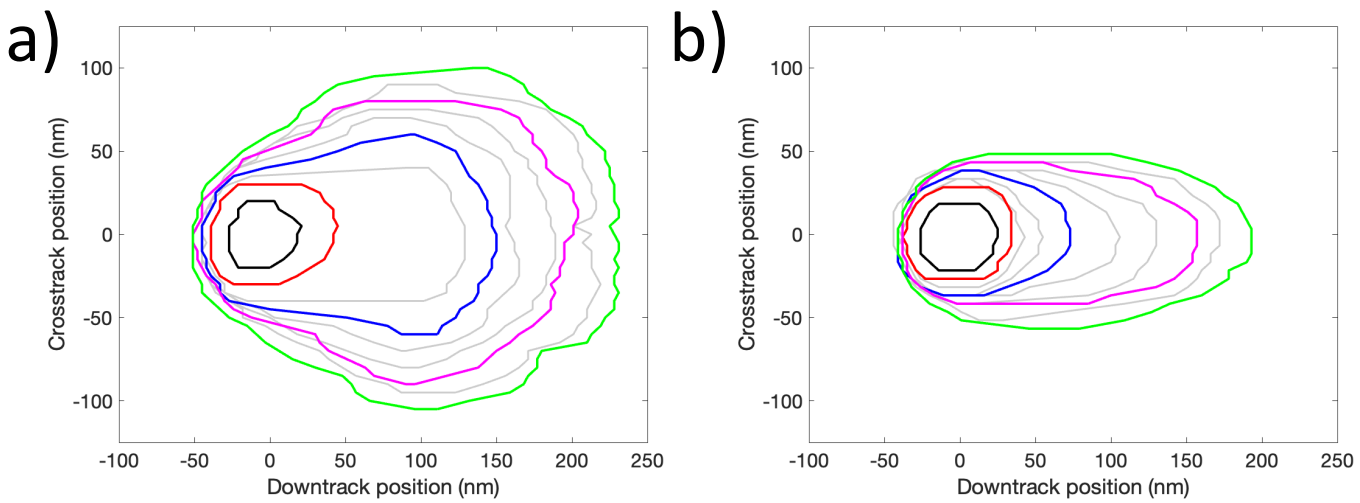

Fig. 1. Two-dimensional thermal footprints measured for HAMR heads with different NFT designs on the same HAMR medium. The temperature footprints are for a laser power that produces 50-nm wide written tracks. Color lines correspond to isotherms at (black) 625K, (red) 600K, (blue) 550K, (magenta) 500K, and (green) 475K. Grey lines are intermediate isotherms that are less than 20K apart.

extends towards the leading side of the footprint and widely cross-track. The medium is heated to 500 K at +/- 100 nm from the track center, which given typical switching temperature distributions of HAMR media [9] can lead to noticeable adjacent track erasure. The second NFT design is modified to significantly reduce the extent of the low temperatures in the cross-track direction, which lead to improved recording capability.

III. Conclusion

With the combination of slow head motion and fast laser diode pulse, the proposed method provide a means to measure an instant and non-smeared two-dimensional temperature profile that is characteristic of the NFT and medium optical and thermal designs. Thermal profiles for different combinations of NFT designs and media designs can be obtained, highlighting the low temperature background in the recording medium. These profiles can be compared to optical/thermal simulation results to validate assumptions used in the modeling, extract optical/thermal properties of the media, and more generally to reveal performance limiters in the head/medium optical and thermal designs.

References

[1] E. Roddick, M. Kief and A. Takeo, "A new Advanced Storage Research Consortium HDD Technology Roadmap," *2022 IEEE 33rd Magnetic Recording Conference (TMRC)*, Milpitas, CA, USA, 2022, pp. 1-2.

[2] M. H. Kryder, *et al*, "Heat assisted magnetic recording," Proc. IEEE, vol. 96, no. 11, pp. 1810–1835, Nov. 2008.

[3] T. Matsumoto, *et al*, "Thermally assisted magnetic recording on a bit patterned medium by using a near field optical head with a beaked metallic plate", Appl. Phys. Lett., vol. 93, pp. 031108, 2008

[4] W. A. Challener *et al.*, "Heat-assisted magnetic recording by a near-field transducer with efficient optical energy transfer," *Nature Photon.*, vol. 3, no. 4, pp. 220–224, 2009.

[5] H. J. Richter *et al*., "Direct Measurement of the Thermal Gradient in Heat Assisted Magnetic Recording," in *IEEE Transactions on Magnetics*, vol. 49, no. 10, pp. 5378-5381, Oct. 2013.

[6] A. Moser, *et al.*, "Dynamic coercivity measurements in thin film recording media using a contact write/read tester," J. Appl. Phys., vol. 85, no. 8, pp. 5018–5020, Apr. 1999.

[7] T. R. Albrecht et al., "Bit-patterned magnetic recording: Theory, media fabrication, and recording performance," IEEE Trans. Magn., vol. 51, no. 5, May 2015, Art. ID 0800342.

[8] P.-O. Jubert et al., "Probing HAMR Media Thermal Properties with Pulsed Recording" *IEEE Trans Magn*. vol. 52, n.7, pp. 3201704, July 2016.

[9] P.-O. Jubert et al., "Spin-stand measurements to extract the switching distributions of heat-assisted magnetic-recording media", *IEEE Trans. Magn.*, vol. 59, no. 3, Mar. 2023.

Thermal spin-torque heat-assisted magnetic recording

S. Isogami[1], Y. Sasaki[1], Y. Fan[2], Y. Kubota[3], J. Gadbois[2], K. Hono[1], and Y.K. Takahashi[1]

[1]National Institute for Materials Science (NIMS), Tsukuba, 305-0047, Japan
[2]Seagate Technology, Advanced Technology Development, Bloomington, MN 55435, USA
[3]Seagate Technology, Recording Media Organization, Fremont, CA 94538, USA

To achieve higher recording density with lower power consumption than the current heat-assisted magnetic recording (HAMR) for next-generation, a more efficient writing with less laser power would be indispensable. An advanced HAMR concept is developed to address such specification, and the writability has been demonstrated in multilayer media stacks comprising the core structures of antiferromagnetic MnPt and ferromagnetic FePt layers with the magnetic easy axis oriented perpendicular to the film plane. The concept is based on two distinct switching mechanisms: thermally activated (TA) and spin-transfer-torque (STT) assisted magnetization switching. The latter is driven by an out-of-plane temperature gradient (ΔT) in the MnPt/FePt multilayer which is referred as thermal spin-torque (TST) HAMR media. Pump-probe measurements reveal significant magnetic coercivity (H_c) modulation by ΔT at the local magnetization of the FePt layer. The hybrid mechanism with TA and STT can be separated by sweeping the delay time between the pump and probe laser pulses, and it is found that the STT dominates the mechanism for H_c modulation in the short delay time regime. Furthermore, the modulation of H_c of the FePt layer is demonstrated to be dependent on the magnitude and the direction of steady state ΔT. These results suggest that lower laser power consumption is achievable owing to the contribution of STT assisted switching in the TST-HAMR media.

***Index Terms*—HAMR, spin-transfer torque, pump-probe MOKE, HDD**

I. Introduction

The hard-disk-drives (HDDs) community has put tremendous efforts to develop revolutionary recording technologies to break records of recording density, providing cost efficient solutions to large volume data storage. Many research and developments have been extensively performed, for example, the material engineering of granular media[1-3] was initialized to reduce the grain diameter to increase the recording areal density.[4] The shrinking size of media grains inevitably leads to a decrease in the thermal stability. To overcome such issue, $L1_0$-ordered FePt granular media has been developed, which achieved a sufficiently high K_u value up to 7 MJ/m^3.[5,6] However, this possesses significant challenge to the conventional magnetic writer to switch FePt grains as the magnetic coercivity (H_c) of granular media increases with K_u. This is referred as *trilemma in HDDs*.

Heat-assisted magnetic recording (HAMR) has been developed as a breakthrough technology to solve the trilemma problem.[4-6] To achieve both high thermal stability and writability in the FePt granular media, laser pulses from writing heads are irradiated right before the moment of writing. The laser pulse raises the temperature of FePt grains to a level above the Curie temperature (T_c), which significantly reduces the switching barrier, enabling the writing with minimal magnetic fields required. Followed by locally field cooling the grains, the high thermal stability resumes, which stores information into FePt media. Therefore, the trilemma problem is solved by utilizing thermal energy to assist switching. And HAMR based HDDs have been shipped to data centers with a 28 TB capacity per drive in 2024, and mass production has been started. In addition, new technology such as multi-level recording in HAMR has been demonstrated to further increase data capacity in the future.[7]

Besides of further increasing recording density, it is desirable to reduce the power consumption to heat FePt grains of the media, which is one of the important factors to be considered for large volume data centers. Here, we focus on utilizing the temperature gradient (ΔT), that is inevitably formed in the HAMR media by the heating of laser pulses, as a driving force of the magnetization switching in addition to the conventional thermally activated (TA) switching. The spin-current, generated by the out-of-plane ΔT originating from the spin Seebeck effect (SSE),[8] would provide the magnetization of FePt grains with spin-transfer torques (STTs) to assist switching, therefore, it is expected that the laser power for the TA switching could be reduced. This is the new concept of magnetic recording based on the hybrid effect of STT and TA, leading to an advanced thermal spin-torque (TST)-HAMR media in the future.[9]

II. Concept of TST-HAMR

The HAMR with hybrid mechanisms of STT and TA, referred to as a TST-HAMR, could achieve both ultra-high efficiency and low power consumption. Figure 1(a) illustrates the principles of TST-HAMR, as compared to the current HAMR. Laser irradiation induces ΔT along the out-of-plane direction. With spin current generated from the antiferromagnets (AFMs) such as the MnPt layer under the FePt layer, the more efficient magnetization switching could be expected owing to the ΔT-driven STT, arising from the SSE.[8] For example, the spin momentum (σ) with -z orientation that is represented by the green allows with balls, originating from the possible uncompensated magnetic moment at the AFM/FePt interface ($M_{\mathrm{Mn}}^{\mathrm{UC.}}$), could assist the magnetization switching of the FePt layer from up-to-down, while it is not expected for the conventional system without AFM layer. Figure 1(b) depicts the energy diagram showing the bi-stable magnetic states of the FePt layer separated by an energy barrier of K_uV. The energy barrier can be suppressed by TA with uniform heating, in addition, the STT can serve as an extra driving force for magnetization switching. Figure 1(c) illustrates the expected

hysteresis loops impacts from the TA and the STT. The TA is responsible for both H_c reduction and demagnetization, while STT primarily contributes to only H_c reduction, because the SSE induced spin-angular momentum transfer can occur without charge transfer, resulting in no Joule heating or extra power consumption. Thus, demagnetization caused by elevating temperature is unrelated with STT.

AFMs have a potential to achieve more efficient spin generation driven by the ΔT.[10-13] We focus on the MnPt with the same $L1_0$ atomic order and lattice constants as the FePt, and high Néel temperature reaching 970 K.[14] These characteristics allow us to prepare the full epitaxial multilayer samples, and the AFM phase is stable regardless of the representative working temperature by laser pulses of HAMR media around 700 K. Figure 1(d) shows the crystal structure of $L1_0$-MnPt, in which the stable magnetic structure with collinear AFM is indicated by arrows. Although two possible collinear magnetic structures of MnPt were reported, with Néel vectors pointing in out-of-plane and in-plane directions,[14] the Néel vector is determined to be parallel to the out of-plane direction in the present MnPt layer by controlling its atomic composition, as revealed by the enhanced H_c of the top FePt layer.

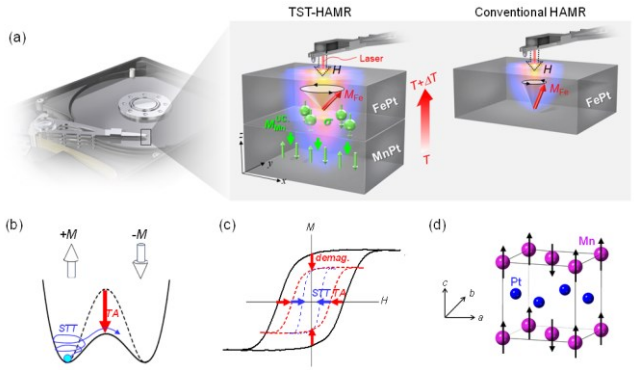

Fig. 1. (a) Concept of the thermal spin-torque heat-assisted magnetic recording (TST-MAHR) with the $L1_0$-MnPt / $L1_0$-FePt bilayer system, together with the conventional HAMR. The green arrows at the MnPt/FePt interface represent the uncompensated Mn moment ($M_{\mathrm{Mn}}^{\mathrm{UC.}}$) induced by the exchange magnetic interaction between Mn and Fe. The green arrows with balls represent the spin angular momentum (σ) that is parallel to the $M_{\mathrm{Mn}}^{\mathrm{UC.}}$. The writing field ($H$) from the HDD-dead is shown by dashed arrow. (b) Energy diagram showing the bi-stable magnetic states of FePt and its change depending on the heating by laser pulses. (c) Possible magnetic hysteresis loops of the FePt layer with temperature gradient by laser pulses. (d) Schematic illustration of $L1_0$-MnPt unit cell.

III. H_c Modulation by Laser Pulses

We verify that the MOKE hysteresis loop without pump pulse (black symbols) agrees with the magnetic hysteresis behavior measured using MPMS. In contrast, the loops are dramatically impacted by pump pulses, showing dependence on the Δt: similar signal with remarkably small H_c at $\Delta t = -1$ ps (red symbols), and remarkably small MOKE signal with large H_c at $\Delta t = +1$ ps (blue symbols), followed by the increase of MOKE signal with the decrease of H_c obtained at $\Delta t = 30$ ps (green symbols). The magnetization measured in the MOKE hysteresis at $\Delta t = -1$ ps corresponds to the magnetic states of the FePt layer at the initial state. Figure 2(b) shows the demagnetization dependence on Δt, which is determined by the ratio of MOKE signal obtained at each Δt to the value measured without pump laser. The magnetization is governed by temperature in general, so that Fig. 2(b) indicates the elevated temperature in the FePt layer. The magnetization decreases by ~75 % of initial value at $\Delta t = +1$ ps, suggesting the highest temperature in the FePt layer induced by the pump laser pulse heating. Then the magnetization starts recovery to the initial magnitude with Δt, suggesting heat dissipation from the FePt layer. It is inferred from the measurement that the magnitude of magnetization is fully recovered before the irradiation of next pump pulse.

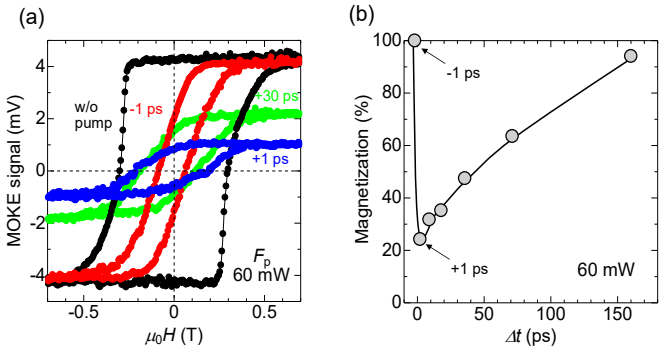

Fig. 2. (a) Magneto optical Kerr effect (MOKE) as a function of magnetic field (H) measured via pomp-probe method with different delay time (Δt) for the multilayer sample, MgO substrate//VN(10 nm)/MnPt(10 nm)/FePt(10 nm). (b) Demagnetization as a function of Δt.

Acknowledgement

This work was supported by KAKENHI Grants-in-Aid No 23K22803 from the Japan Society for the Promotion of Science (JSPS) and the JST- CREST (JPMJC22C3).

References

[1] D. Reinsel, et al., The digitization of the world from edge to core, Framingham: Int. Data Corp. 16 (2018) 1.

[2] V. Ozdemir, N. Hekim, Birth of industry 5.0: making sense of big data with artificial intelligence, “the internet of things” and next-generation technology policy, Omics J. Integr. Biol. 22 (2018) 65.

[3] G. Albuquerque, et al., HDD reader technology roadmap to an areal density of 4 Tbpsi and beyond, IEEE Trans. on Magn. 58 (2021) 1.

[4] D. Weller, et al., Review Article: fePt heat assisted magnetic recording media, J. Vac. Sci. Technol. B 34 (2016), 060801-1-10.

[5] K. Hono, et al., Heat-assisted magnetic recording media materials, MRS Bull. 43 (2018) 93–99.

[6] D. Weller, et al., L10 FePtX–Y media for heat-assisted magnetic recording, Phys. Status Solidi A 210 (2013) 1245–1260.

[7] P. Tozman, et al., Dual-layer FePt-C granular media for multi-level heat-assisted magnetic recording, Acta Mater. 271 (2024), 119869-1-8.

[8] K. Uchida, et al., Observation of the spin Seebeck effect, Nature 455 (2008) 9.

[9] S. Isogami, et al., Thermal spin-torque heat-assisted magnetic recording, Acta Materialia 286 (2025) 120743.

[10] S. Seki, et al., Thermal generation of spin current in an antiferromagnet, Phys. Rev. Lett. 115 (2015), 266601-1-5.

[11] S. Wu, et al., Antiferromagnetic spin Seebeck effect, Phys. Rev. Lett. 116 (2016), 097204-1-5.

[12] I. Gray, et al., Spin Seebeck imaging of spin-torque switching in antiferromagnetic Pt/NiO heterostructures, Phys. Rev. X 9 (2019), 041016-1-10.

[13] S. Rezende, et al., Theory of the spin Seebeck effect in antiferromagnets, Phys. Rev. B 93 (2016) 014425.

[14] R. Umetsu, et al., Magnetic and electrical properties, and mechanism of exchange bias-field of γ-phase and $L1_0$-type antiferromagnetic Mn alloys, Trans. Magn. Soc. Japan 3 (2003) 59.

HAMR Absorbing Carbonaceous Smear Combustion Kinetics in Different Oxygen Environment

Tan Trinh, Roshan Mathew Tom, Sukumar Rajauria, and Qing Dai

Western Digital Corporation, San Jose, California, USA, tan.trinh@wdc.com

Heat-assisted Magnetic Recording (HAMR) technology enables areal density scaling to meet growing storage needs. In HAMR recording, a nanometer sized spot on the media surface is heated beyond the Curie temperature (~450˚C) of the FePt layer to facilitate writing. Such high temperature causes media surface materials to accumulate on heads, leading to the formation of smear that impacts the reliability and performance of HAMR near-field transducer (NFT). In this study, kinetics of the carbonaceous absorbing smear combustion is studied as a function of oxygen concentration of the environmental gas inside the enclosed chamber. Our experimental results suggest that higher oxygen leads to a faster combustion of the absorbing smear at the interface, and can help improve NFT reliability.

***Index Terms*—Heat-assisted magnetic recording, Smear, Absorbing, Kinetics, Gas composition.**

I. Introduction

SMEAR is a key challenge to commercialize heat-assisted magnetic recording (HAMR) technology. In heat-assisted magnetic recording, a near-field transducer (NFT) on the air bearing surface of the slider is used to convert optical power from a laser diode to heat a nanometer spot on the HAMR media above the Curie temperature to facilitate writing. The local nanoscale heating spot leads to carbon overcoat and lubricant desorption and degradation that transfer to the head surface [1,2,3]. Smear in the vicinity of the near-field transducer consists of various materials with different optical and thermal properties, causing recording performance fluctuation such as track width and signal to noise ratio (SNR) variation [1,2,3,5,6]. More importantly, head smear with high extinction coefficient k that absorbs light leads to smear self-heating, thereby increasing the NFT temperature. Elevated temperature leads to NFT degradation. It is hypothesized that in N_2 condition, carbonaceous smear would accumulate on NFT area, causing self-heating, while in the presence of oxygen, such smear will be oxidized, and NFT temperature decreases as a result. In this study, kinetics of the absorbing carbonaceous smear combustion is studied as a function of oxygen concentration and humidity of the environmental gas inside the enclosed chamber.

II. Experimental Setup

Experiment is conducted using a Guzik spinstand enclosed inside an environmental chamber as shown in the Figure 1. Oxygen concentration can be controlled by tuning flow rates of the dry air and dry nitrogen gas inlet valves. Humidity inside the chamber is controlled using a bubbler with deionized water. Environmental chamber pressure is kept at the atmospheric pressure (1atm) and temperature is maintained at 25˚C. Temperature, relative humidity, and oxygen concentration inside the chamber are measured using sensors located near the head-media interface.

To monitor local NFT temperature changes, an embedded sensor is fabricated near the NFT, named NFT temperature sensor (NTS) [7]. A constant direct current of 2mA from a spinstand controller is applied to the sensor, and the voltage signal across the NTS sensor is measured using an oscilloscope. NTS sensor signal results from combined effect of laser power that couples to the NFT (or laser-induced NTS), and the corresponding local temperature increase due to smear. While laser-induced NTS stays constant at a fixed laser power, NFT temperature rise is a strong function of the smear extinction coefficient k at the head-media interface is shown in Figure 2.

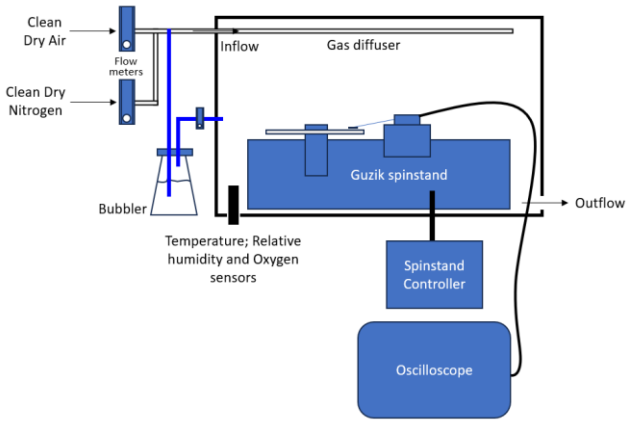

Figure 1: *Schematic of a Guzik spinstand enclosed inside an environmental chamber*

At the beginning of the experiment, the chamber was purged with dry air (20% O_2 + 80%N_2) gas. HAMR head was loaded to the MD location of the HAMR media. The head was kept flying at approximately 10nm spacing on the media surface. Laser current was optimized to target 50nm Magnetic Write Width (MWW) on the HAMR media as shown in literature [4]. After laser optimization, NTS signal was measured for 5 seconds as a baseline during HAMR writing using the optimized laser current. Then clean dry air gas was stopped, clean dry nitrogen gas was purged to the chamber until reaching <1%O_2 level inside the chamber. Following nitrogen purging, NTS signal was measured for 20 seconds continuously with the same laser current mentioned above. After continuous writing in dry nitrogen environment, both flow meters to oxygen and nitrogen are opened to reach a designated percentage of oxygen inside the chamber, ranging from 1% to 20% O_2. NTS signal

was measured for another 60 seconds. Raw NTS signals were recorded and analyzed to investigate the effects of oxygen concentration on the changes of the NTS signals.

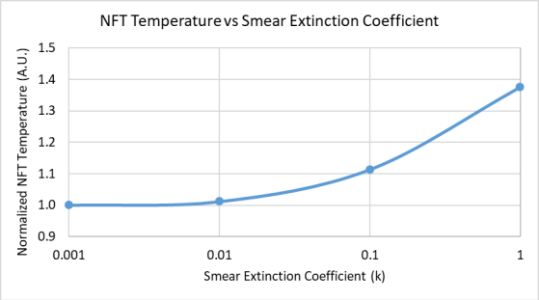

Figure 2: *NFT temperature as a function of smear extinction coefficient k*

III. EXPERIMENTAL RESULTS

After the test was completed, changes of the NTS signal (deltaNTS), was calculated by subtracting the laser-induced NTS signal, to estimate local temperature changes around the NFT caused by smear self-heating. Typical deltaNTS signals are shown in Figure 3. We observed that deltaNTS stays constant in dry air environment as shown by blue lines in Figure 3. Switching to <1%O_2 environment leads to an increase of deltaNTS signals as shown in the red lines, indicating a local temperature rise. After switching to different %O_2, the deltaNTS signals start decreasing, suggesting a decrease of the local temperature near NFT. The decrease of the deltaNTS signals is believed to be due to the removal of the absorbing smear at the head-media interface at different oxygen concentration.

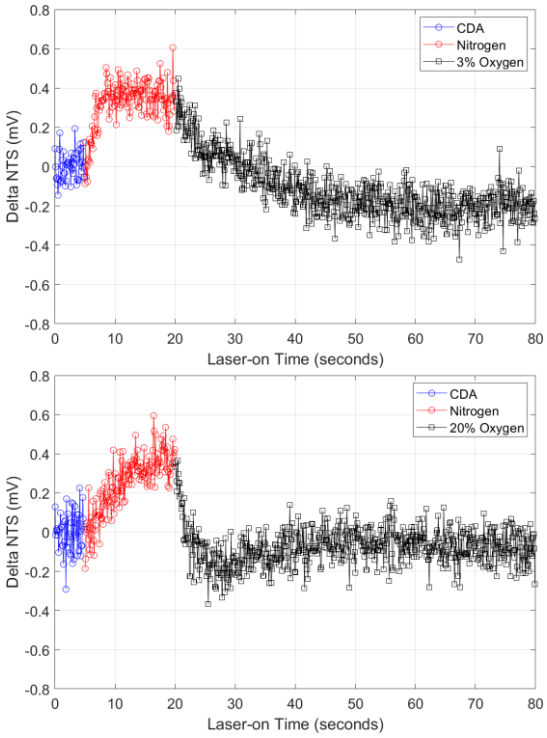

Figure 3: *DeltaNTS signals in clean dry air (CDA), nitrogen, and different oxygen concentration gas*

deltaNTS curve can be fitted using an exponential decreasing function, such as in Figure 4, to determine the time constant of the removal process of absorbing smear at the HAMR head-disk interface at different oxygen concentration, respectively. We observed that 20% oxygen leads to much faster combustion of the absorbing smear than 3% oxygen condition.

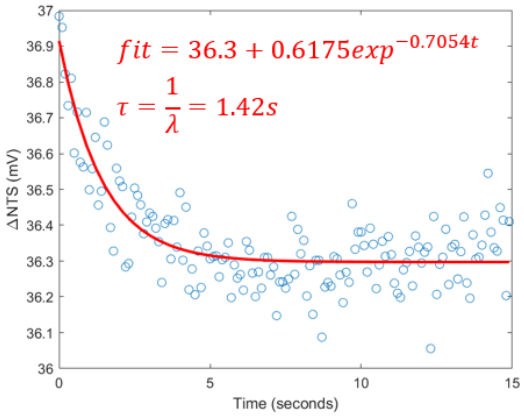

Figure 4: *Exponential decreasing function fitting for deltaNTS signal*

Our experimental results show absorbing smear combustion time constant is a strong function of oxygen percentage inside the environmental chamber in Figure 5. As oxygen percentage increases, time constant of the removal process decreases sharply, indicating a shorter duration to oxidize the absorbing smear. This finding, along with other improvements, can help with NFT lifetime improvement. Similar study was carried out on relative humidity effect which will be discussed in the full paper.

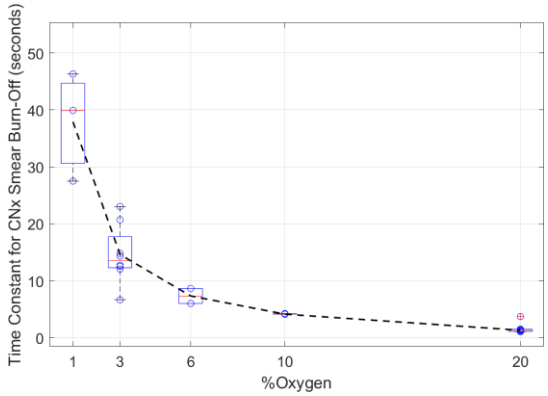

Figure 5: *Time constant to remove absorbing carbonaceous smear as a function of oxygen percentage in environmental gas composition*

REFERENCES

[1] J. D. Kiely et. al., "Write-Induced Head Contamination in Heat-Assisted Magnetic Recording*", IEEE Transactions on Magnetics*, February 2017.

[2] B. Marchon et. al., "Head-Disk Interface Materials Issues in Heat-Assisted Magnetic Recording", *IEEE Transactions on Magnetics,* March 2014.

[3] S. Xiong et. al., "Experimental Study of Material Pick Up on Heat-Assisted Magnetic Recording (HAMR) Heads*", IEEE Transactions on Magnetics*, June 2021.

[4] T. Trinh et. al., "Temperature-induced Near-field Transducer Failure in Heat-Assisted Magnetic Recording", *IEEE Transactions on Magnetics*, April 2020.

[5] R. Smith et. al., "Opto-Thermal Simulation of Metallic Smear's Impact on HAMR Technology", IEEE TMRC, August 2021.

[6] R. M. Tom et. al., "Optical Forces in Heat-Assisted Magnetic Recording Head-disk Interface", Nature Scientific Report, May 2023.

[7] S. Rajauria et. al, "Electromagnetically-shielded near-field transducer thermal sensor for Heat-assisted Magnetic Recording", US Patent US-10283145-B2.

HAMR ADC CMR and SMR with MSMR-2R/3R Gain: Linear Density vs Trackpitch

Steven Granz[1], M. Fatih Erden[1], Ganping Ju[2], Jan-Ulrich Thiele[2], Pu-Ling Lu[3], and Chris Rea[1]

[1]Seagate Technology, Bloomington, MN 55408, USA, steven.d.granz@seagate.com
[2]Seagate Technology, 47488 Kato Road, Fremont CA 94538, USA
[3]Seagate Technology, 1280 Disc Drive, Shakopee, MN 55379, USA

HAMR areal density demonstrations for both CMR and SMR are presented with MSMR, a subset of TDMR where readers are reading from a single track of interest. The MSMR gain was taken in both linear density and trackpitch. HAMR CMR tracks preferred to take the MSMR gain in linear density to maximize areal density capacity whereas HAMR SMR tracks preferred to take the MSMR gain in trackpitch. At spinstand, 3700 Gfpsi areal density demonstration, equating to over 6.5 TB/disk, has been achieved with HAMR SMR when combined with 2 Reader MSMR.

Index Terms— Heat Assisted Magnetic Recording (HAMR), Conventional Magnetic Recording (CMR), Shingled Magnetic Recording (SMR), Multiple Sensor Magnetic Recording (MSMR), Two Dimensional Magnetic Recording (TDMR), Areal Density Capacity (ADC)

I. Introduction

Heat Assisted Magnetic Recording (HAMR) has proven to be the primary successor to perpendicular magnetic recording providing continued and significant growth in areal density [1]. There are two current productized write architectures for the layout of tracks in HAMR hard disk drives: Conventional Magnetic Recording (CMR) and Shingled Magnetic Recording (SMR). In CMR, any track can be written at any time and neighboring tracks do not intentionally overlap. In SMR, the tracks are written sequentially in bands with the tracks intentionally overlap like shingles on a roof [2]. The read-back architecture Multiple Sensor Magnetic Recording (MSMR) can be combined with the two different write architectures to increase areal density [3, 4] by using two or more readers and/or multiple spins to read-back the same track. Previously, the MSMR gain was taken in linear density [4]. In this paper, we compare the areal density capability (ADC) of HAMR CMR and HAMR SMR with read-back with one reader (1R), MSMR with 2 readers (MSMR-2R) and MSMR with 3 readers (MSMR-3R) taking the MSMR gain in linear density and trackpitch.

II. Spinstand Experimental Details

We investigated the ADC for HAMR CMR and SMR with 1R, MSMR-2R and MSMR-3R on the spinstand with 6x adjacent track writes for CMR and 1x adjacent track write for SMR. The ADC demo criteria had additional margin for adjacent track interference with a tighter requirement than the ASTC areal density metric [5]. For this study, eleven integrated HAMR heads were measured on HAMR media. The HAMR heads and media were similar in design to those used in the previous study [6].

Spinstand measurements were at radius of 29 mm, skew 0° and 7200 rpm with linear velocity of ~22 m/s. Writer and reader clearances were maintained at 1 nm and compensated for changes in writer and laser protrusions. Channel areal density (Gfpsi) was measured and the channel code rate was similar to the previous studies [3-6]. The MSMR gain with 2-3 readers was calculated with multiple spin captured waveforms from the spinstand with the native HAMR reader processed by MSMR 2 and 3 reader software channel.

III. Results

The spinstand results of the MSMR-2R linear density gain and trackpitch improvement for HAMR CMR and SMR are shown in Fig. 1. For the CMR tracks, the MSMR-2R gain preferred linear density (3.9% ADC gain) to trackpitch improvement (3.1% ADC gain) to maximize ADC. For the SMR tracks, the MSMR-2R gain preferred trackpitch improvement (4.5% ADC gain) to linear density (3.7% ADC gain) to maximize ADC.

The MSMR-3R linear density gain and trackpitch improvement for HAMR CMR and SMR are shown in Fig. 2. For the CMR tracks, the MSMR-3R gain preferred linear density (5.9% ADC gain) to trackpitch improvement (4.8% ADC gain) to maximize ADC. For the SMR tracks, the MSMR-3R gain preferred trackpitch improvement (7.4% ADC gain) to linear density (6.0% ADC gain) to maximize ADC.

For both MSMR-2R and MSMR-3R, HAMR CMR tracks preferred to take the MSMR gain in linear density to maximize ADC whereas HAMR SMR tracks preferred to the MSMR gain in trackpitch. The preference for MSMR gain for linear density or trackwidth is due to the physics of CMR double sided adjacent track interference compared with SMR single sided adjacent track interference.

The ADC of HAMR CMR and SMR with 1R, MSMR-2R and MSMR-3R with the MSMR gain taken in linear density and trackpitch are shown in Fig. 3.

Spinstand high ADC demonstrations using HAMR CMR and HAMR SMR are shown in Fig. 4 and Fig. 5. The highest HAMR ADC record of 3700 Gfpsi with state-of-art HAMR heads and media are shown. The estimated capacity per disk for this ADC demonstration was 6.5 TB/disk based on expected format efficiency. This ADC demonstration used HAMR SMR with MSMR-2R gain taken in trackpitch. The spinstand demonstration represents what is possible in a recording system and that there are no fundamental physic barriers to achieving over 3500 Gfpsi or 6 TB/disk with HAMR technology.

IV. Conclusion

HAMR areal density demonstrations for both CMR and SMR are presented with MSMR. The MSMR gain was taken in both linear density and trackpitch. HAMR CMR tracks preferred to take the MSMR gain in linear density to maximize areal density capacity whereas HAMR SMR tracks preferred to take the MSMR gain in trackpitch. At spinstand, 3700 Gfpsi areal density demonstration, equating to over 6.5 TB\disk, has been achieved with HAMR SMR with MSMR-2R with MSMR gain taken in trackpitch. These experiments help to establish the intrinsic scalability of HAMR with significant and continued growth in areal density.

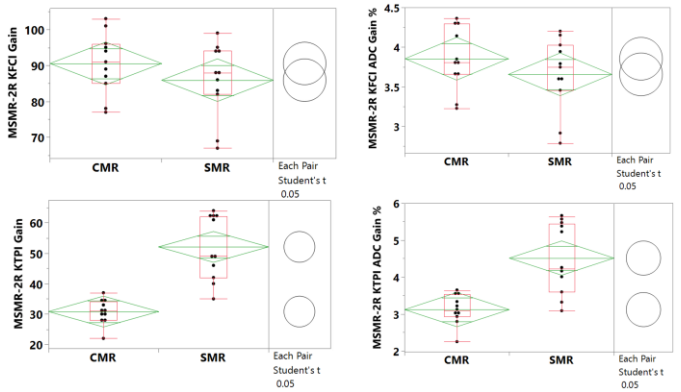

Fig. 1. Spinstand Results of the MSMR-2R Linear Density Gain and Trackpitch Improvement for HAMR CMR and SMR

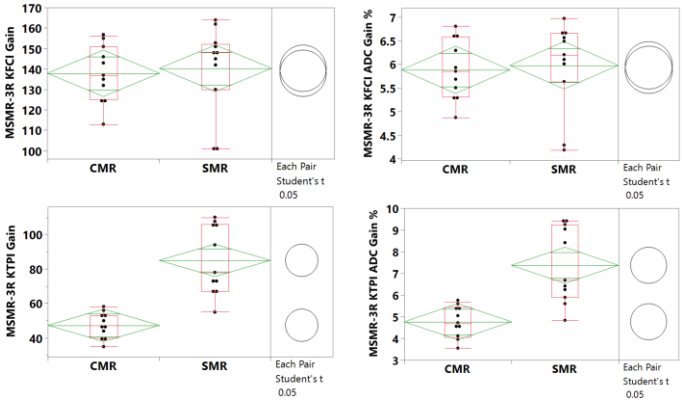

Fig. 2. Spinstand Results of the MSMR-3R Linear Density Gain and Trackpitch Improvement for HAMR CMR and SMR

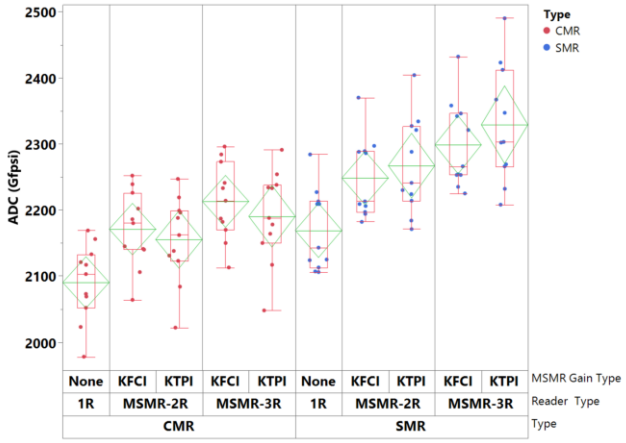

Fig. 3. Areal Density Capability of HAMR CMR and SMR with MSMR-2R and MSMR-3R Gain taken in Linear Density and Trackpitch

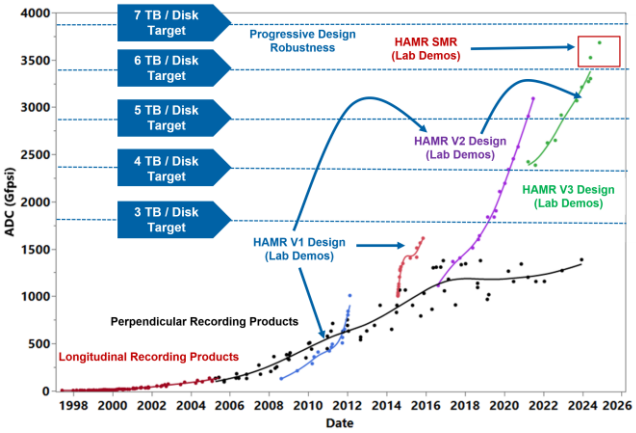

Fig. 4. Areal Density Capability over time for Seagate Longitudinal Recording Products, Perpendicular Recording Products and HAMR Spinstand Demonstrations

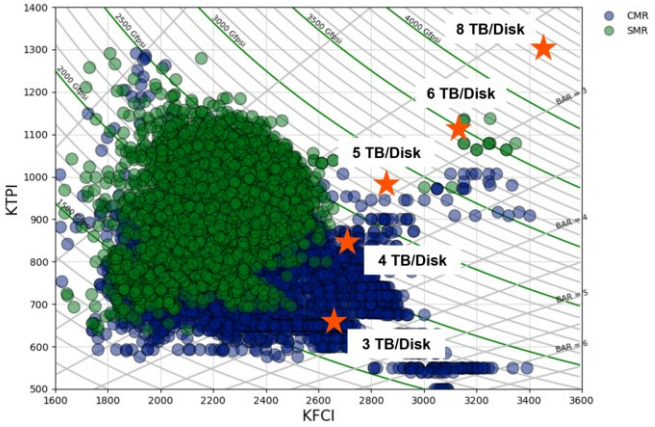

Fig. 5. HAMR Areal Density Capability Demonstrations using HAMR CMR and SMR

References

[1] M. H. Kryder, *et al.,* "Heat assisted magnetic recording," Proc. IEEE, vol. 96, no. 11, pp. 1810–1835, Nov. 2008.

[2] R.Wood, M. Williams, A. Kavcic, J. Miles "The feasibility of magnetic recording at 10 terabits per square inch on conventional media" IEEE Trans. Magn., vol. 45, no. 2, pp.917 -923 2009.

[3] C. Rea, et al. "Heat Assisted Recording: Advances in Recording Integration" IEEE Trans. Magn., vol 53, no.11, pp.1-6, 2017.

[4] S. Granz *et al.,* "Areal Density Comparison Between Conventional, Shingled, and Interlaced Heat-Assisted Magnetic Recording With Multiple Sensor Magnetic Recording," IEEE Trans. On Magn., vol. 55, no. 3, pp. 1-3, March 2019.

[5] S. Granz, *et al.,* "Definition of an Areal Density Metric for Magnetic Recording Systems", IEEE Trans. Magn., vol. 53, no. 2, Feb. 2017 (3100104).

[6] S. Hernandez, *et al.,* "High Areal Density HAMR Demonstrations" 2024 IEEE 35th Magnetic Recording Conference (TMRC), Berkeley, CA, USA, 2024, pp. 1-2.

Measured and Modeled responses for Heat Assisted Magnetic Recording up to Ultra-high Areal Densities

Roger Wood[1], Jonas Goode[2], Rick Galbraith[3], and Amirhossein Sayyafan[2]

[1]Western Digital Corporation, San Jose, California, USA, roger.wood@wdc.com
[2]Western Digital Corporation, Irvine, California, USA, jonas.goode@wdc.com, amir.sayyafan@wdc.com
[3]Western Digital Corporation, Rochester, Minnesota, USA, rick.galbraith@wdc.com

While current magnetic recording components are still far from able to support user areal densities of 10 Terabits per square inch, it is nevertheless instructive to examine the behavior of readback waveforms as such extreme densities are approached. Waveforms from a contemporary shingled Heat Assisted Magnetic Recording (HAMR) system are captured and separated into linear & nonlinear signal components, inter-track interference (ITI), signal-dependent media noise, and head/electronic noise. These are tracked and compared with modeled behavior as media areal-density (FCI x TPI) is gradually increased. The modeled signal and noise are based on the reader response being approximated as the difference of two 2D Gaussians. The model agrees quite well all the way from 1 Tbit/in^2 to 10 Tbit/in^2 At the extreme of 10 Tbit/in^2, the signal is still clearly identifiable and is well-behaved with minimal distortion. It is however completely overwhelmed by high levels of stationary media noise and, to a lesser extent, inter-track interference and then head/electronic noise.

***Index Terms*— Hard Disk Drives, Heat Assisted Magnetic Recording, Recording Channel**

I. Introduction

Areal Densities of 10 Terabits per square inch remain a very distant goal for hard disk drives (HDD). However, it is still important to explore this regime to understand the opportunities for advanced coding and detection techniques [1]. In the 2000s, there was great optimism as rapid increases in areal density occurred corresponding with the introduction of several new technologies, notably: perpendicular recording, tunnel-junction heads, and fly-height control [2,3]. But over the last decade progress has slowed [4], and today's drives ship at a little more than 1 Tbit/in^2. Recently, Heat Assisted Magnetic Recording (HAMR) has been introduced with a promise to revitalize the industry [5]. Early shipments of HDDs with HAMR are already offering significantly higher areal-densities and capacities, though some of the challenges and practical limitations of the technology are also becoming apparent [6].

In this paper we examine the behavior of signals, interference, and noise on a contemporary shingled HDD recording channel up to extreme media densities (FCI x TPI) of 10 Tbit/in^2. These measurements are matched with a simple model based on 2D Gaussian pulses. [*Note: 'media densities' refers to the product of flux-changes per inch (FCI) and tracks per inch (TPI) and certainly not to the ability to store user data at such densities.*]

II. Modelling of the readback response as the difference of two 2D Gaussians

For practical reasons, in HAMR, the soft magnetic underlayer is spaced relatively far below the recording layer [5]. It does play a role in enhancing the write field from the relatively large write head but plays no appreciable role in the readback process [7]. For this reason, the reader sensitivity function can be modeled considering the recording layer alone. In particular, it can be modeled in terms of the *difference* between magnetic charges at the top of the recording layer and ideally identical charges at the bottom of the recording layer.

Classically, the read sensitivity function would be derived starting with Lorentzian type functions or, in the frequency domain, with the corresponding exponentials [7]. Indeed, for a magnetic spacing, d, and a perpendicular media thickness, δ, the vertical field component has the rather elegant form

$$\frac{d}{(d^2+r^2)^{3/2}} - \frac{d+\delta}{((d+\delta)^2+r^2)^{3/2}} \quad \overset{FFT}{\Longleftrightarrow} \quad e^{-\kappa d} - e^{-\kappa(d+\delta)}$$

The left side represents the spatial domain with $r^2 = x^2 + y^2$ (down-track and cross-track, respectively). The right side represents the frequency domain with $\kappa^2 = k_x^2 + k_y^2$ (down-track and cross-track spatial frequencies, respectively). The 'FFT' arrow indicates a 2D Fourier transform relationship. *[Note: for clarity, all the various scaling constants have been omitted throughout the digest]*

However, the expression above does not fit the measured spectra well. The reader itself includes a finite gap-length and finite shield thicknesses and has a finite sensor-width. Also, the writing process has a finite resolution ('a-parameter') and a finite write-width with pronounced transition curvature, etc. These result in a more Gaussian-like shape [8] and so, instead, we base the analysis on the *difference of two 2D Gaussians*

$$\frac{e^{-(r/d)^2}}{d^2} - \frac{e^{-(r/(d+\delta))^2}}{(d+\delta)^2} \quad \overset{FFT}{\Longleftrightarrow} \quad e^{-(\kappa d)^2} - e^{-(\kappa(d+\delta))^2}$$

An advantage of using Gaussians is that both the time-domain and the frequency domain responses have the same Gaussian form. Furthermore, Gaussians are separable, for example, $e^{-(r/d)^2} = e^{-(x/d)^2} e^{-(y/d)^2}$. This allows us to apply a 1D Fourier transform to just the down-track direction (x-axis).

$$e^{-(kd)^2} . \frac{e^{-(y/d)^2}}{d} - e^{-(k(d+\delta))^2} . \frac{e^{-(y/(d+\delta))^2}}{d+\delta}$$

This expression describes the frequency response for an impulse of magnetization (i.e. a tiny grain with height, δ)

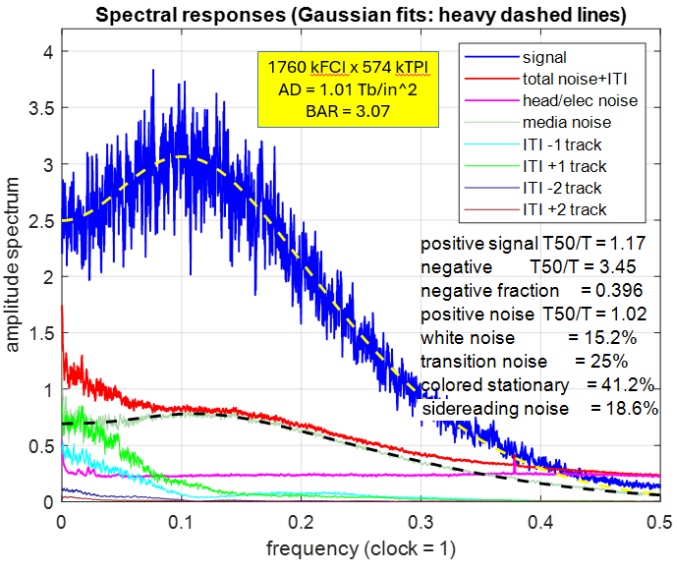

Fig. 1. Signal, interference, and noise spectra evaluated at the 1 Tb/in² base density. The heavy dashed lines are the model fits for the signal and media noise. "T50/T" is a more familiar measure that describes the width (proportional to α, β, or γ) of the corresponding 2D Gaussians.

passing under or near the reader. For a finite width written track extending from cross-track position y_1 to y_2, the integral gives

$$e^{-(kd)^2}\left[\mathrm{erf}\left(\frac{y_2}{d}\right)-\mathrm{erf}\left(\frac{y_1}{d}\right)\right]-e^{-(k(d+\delta))^2}\left[\mathrm{erf}\left(\frac{y_2}{d+\delta}\right)-\mathrm{erf}\left(\frac{y_1}{d+\delta}\right)\right]$$

With the assumption that the media noise is uncorrelated and stationary, we can also derive an expression for the media noise

$$\frac{1}{d\sqrt{2}}e^{-2(kd)^2}-\frac{2}{\sqrt{d^2+(d+\delta)^2}}e^{-k^2(d^2+(d+\delta))^2}+\frac{1}{(d+\delta)\sqrt{2}}e^{-2(k(d+\delta)^2}$$

The quantities d and δ may no longer be directly equal to the physical distances they are supposed to represent. But, as fitting parameters, they are valuable for matching to measured spectra and in observing trends as densities are pushed to the extreme.

III. Measurements and Model Fitting

Measurements are made on a contemporary HAMR HDD with shingled recording at media densities covering the range from 1 Tb/sq.in. to over 10 Tbit/in². Waveforms are captured at 10 GigaSamples/s. The subsequent filtering and synchronous bit-rate sampling operations are conducted in software before the waveforms are analyzed. The random data patterns on five consecutive shingled tracks are known. The read-back waveform is taken on the center track and is captured twice so that head/electronic noise can be easily separated.

From the waveforms and the known written data, we can determine the wanted signal response and the distortion, and also the inter-track interference (ITI) from up to two tracks on either side. By subtracting the wanted signal, the ITI responses, and the head/electronic noise from the waveform spectrum, we are left with the media noise spectrum.

We fit the signal spectrum with the following expression with four free parameters: A and α representing the amplitude and time-domain width of the positive Gaussian pulse and similarly the fractional, b, and β describe the negative Gaussian pulse

$$A\left[e^{-(k\alpha)^2}-be^{-(k\beta)^2}\right]$$

(the sinc function for random NRZ data is included separately).

The noise spectrum is modeled with two further parameters, C and γ representing amplitude and time-domain width of the effective positive Gaussian pulse characterizing the noise.

$$C\sqrt{\frac{1}{\gamma\sqrt{2}}e^{-2(k\gamma)^2}-\frac{2}{\sqrt{\gamma^2+\beta^2}}e^{-k^2(\gamma^2+\beta^2)}+\frac{1}{\beta\sqrt{2}}e^{-2(k\beta)^2}}$$

The noise differs from the signal in that it is the integral over all space and the DC response must be zero (no field from a uniform magnetized sheet). This removes one degree of freedom. We leave the noise free to assume a wider bandwidth than the signal since it does not include factors such as the writing resolution or written track-width. Accordingly, measurements show that the noise resolution, γ, is significantly narrower than the signal resolution, α. The broader negative pulse-width, β, will tend to swamp these other dimensions, however, and is assumed the same for both signal and noise.

IV. Results and Conclusions

Figure 1 shows the results of measurements at the starting density of 1 Tb/sq.in. At this low density, the wanted signal is clearly dominant. The ITI from the immediately adjacent tracks, ±1, is also seen clearly, but the ITI from tracks at ±2 is very small. Media noise dominates strongly over the ITI and head/electronics noise. As shown, the model curves fit very closely at this low density, though slightly less well at extreme densities.

As densities increase, we see the wanted signal diminish, yet it does remain well-behaved with low levels of non-linear distortion (not shown). At no point is there any abrupt degradation or failure. As expected, the side-reading noise (ITI) increases with track-density and the head/electronic noise increases with data-rate, but the main feature is the increasing media noise. By 10 Tbit/in², the media noise is very much larger than the signal or any other component and it also shows very little dependence on the presence or absence of magnetic transitions in the data. The implications of these findings are to be discussed in a companion presentation [1].

References

[1] J. Goode et al., "Toward 10 Tb/in²: Fusing Advanced Channel Coding, HAMR, and SMR in Next-Generation HDDs", TMRC 2025, Sendai, Japan, July, 2025

[2] R. Wood, "Future hard disk drive systems", JMMM Vol. 321, No. 6, pp. 555-561, 2009,

[3] R. Wood, M. Williams, A. Kavcic, J. Miles, "The feasibility of magnetic recording at 10 terabits per square inch on conventional media", IEEE Trans. Magn., Vol. 45, No. 2, pp. 917-923, Feb. 2009

[4] T. Coughlin, "We Need A Boost In HDD Areal Density!", Forbes, Sep 18, 2022

[5] T. Coughlin, "Seagate Introduces 36TB HAMR Hard Disk Drives", Jan 21, 2025,

[6] M. H. Kryder *et al*., "Heat Assisted Magnetic Recording" in *Proceedings of the IEEE*, vol. 96, no. 11, pp. 1810-1835, Nov. 2008

[7] R. Wood, D. Wilton, "Readback responses in three dimensions for multi-layered recording media configurations", IEEE Trans. Magn. Vol. 44, No. 7, June 2008

[8] B. Valcu, T. Roscamp, H. N. Bertram, "Pulse Shape, Resolution, and Signal-to-Noise Ratio in Perpendicular Recording", IEEE Trrans. Magn., Vol. 38, No. 1, pp. 288-294 Jan. 2002

Anisotropic Spin Exchange Modeling and Curie Temperature Dispersion in L10-FePt Nanoparticles for HAMR Media

Kohei Ochiai[1], Tomoyuki Tsuyama[1], Tatsushi Saito[1], Sumera Shimizu[1], Lei Zhang[2], Jin Watanabe[2], Fumito Kudo[2], Jian-Gang Zhu[3], and Yoshishige Okuno[1]

[1]Resonac Corporation, Research Center for Computational Science and Informatics, Yokohama, 221-8517, Japan, ochiai.kohei.xiqrk@resonac.com
[2]Resonac Hard Disk Corporation, Research & Development Center, Ichihara, 290-0067, Japan
[3]Data Storage Systems Center, Carnegie Mellon University, Pittsburgh, PA 15213, USA

We developed an anisotropic exchange spin model that accounts for magnetic anisotropy and evaluated the Curie temperature (T_c) dispersion due to finite size effects in L1$_0$-FePt nanoparticles. In heat-assisted magnetic recording (HAMR) media, a next-generation magnetic recording technology, high-density recording is achieved by locally heating L1$_0$-FePt nanoparticles near their T_c and rapidly cooling them. However, variations in T_c caused by differences in particle size and shape can compromise recording stability and areal density capacity, making the control of T_c dispersion critical. In this study, we constructed atomistic LLG models to explicitly incorporate the spin exchange anisotropy of L10-FePt, based on parameters determined by first-principles calculations. Using this model, we evaluated the impact of particle size on T_c dispersion. As a result, (1) the T_c dispersion critical to the performance of HAMR can be reproduced, whereas it was previously underestimated by isotropic models and (2) approximately 70% of the experimentally observed T_c dispersion can be attributed to particle size effects. This research highlights the role of exchange anisotropy in amplifying finite-size effects and underscores the importance of size control in HAMR media.

***Index Terms*— Computer simulation, Heat-assisted magnetic recording, Magnetic materials, Nanostructured materials**

I. Introduction

With the rapid growth of cloud-based infrastructure, the global data volume is soaring, presenting challenges to overcome the fundamental limitations of recording density, known as the "Magnetic Trilemma." Heat-Assisted Magnetic Recording (HAMR) has emerged as a promising next-generation technology to tackle these challenges [1,2]. HAMR achieves high-density recording by heating the magnetic particles of the storage medium to near their Curie temperature (T_c) and quickly cooling them, all while maintaining high magnetic anisotropy.

Among the candidate materials, the L10-phase FePt (L10-FePt) stands out due to its exceptionally high magnetic anisotropy constant (Ku) [3]. However, its layered structure leads to strong anisotropic exchange interactions. This results in Curie temperature dispersion caused by variations in particle size, shape, and degree of order, posing critical challenges. Such T_c dispersion causes a mismatch between the writing temperature and the actual Curie temperature of particles, ultimately reducing recording stability and the signal-to-noise ratio (SNR)[4]. Moreover, its impact on areal density capability (ADC) is well-recognized, highlighting the importance of controlling T_c dispersion in HAMR media design.

To address these issues, this study presents an atomistic-scale spin model that incorporates the intrinsic anisotropic exchange interactions of L10-FePt and conducts numerical simulations to investigate T_c dispersion stemming from realistic particle size distributions.

II. Theories and Computational Methods

In L1$_0$-FePt, alternating monolayers of Fe and Pt are stacked along the (001) axis [5]. The in-plane exchange coupling within Fe layers ($J_{//}$) is strong due to direct Fe–Fe interactions, whereas the out-of-plane exchange coupling between adjacent Fe layers ($J_\perp$) is comparatively weaker as it is mediated through Fe-Pt-Fe pathways. This pronounced exchange anisotropy is a key factor in determining magnetization reversal mechanisms and thermal spin fluctuations.

To investigate these properties, we developed an anisotropic spin model [6]. This model approximates their layered crystal structure by employing a modified simple cubic lattice that incorporates only Fe degrees of freedom. It explicitly integrates the exchange interaction anisotropy derived from first-principles calculations (DFT), particularly the anisotropy induced by the layered structure (Figure 1).

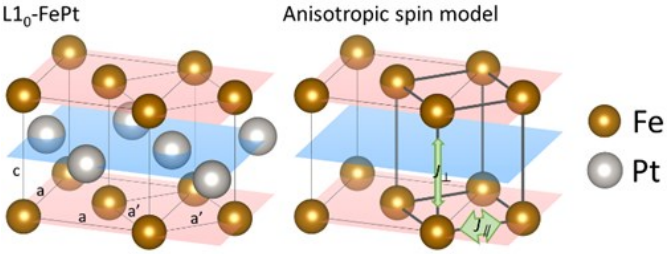

Fig. 1. Schematic diagram of the anisotropic spin model.

The Hamiltonian governing the magnetic dynamics is defined as follows:

$$H = -\frac{1}{2}\left[\sum_{\langle i,j\rangle||} J_{||}(s_i \cdot s_j) + \sum_{\langle i,j\rangle\perp} J_\perp(s_i \cdot s_j)\right] - k_u \sum_i (s_i \cdot \hat{e})^2 - \sum_i \mu_i (s_i \cdot \mathbf{B}) \quad (1)$$

Here $\Sigma\langle i,j\rangle_{//}$ and $\Sigma\langle i,j\rangle_\perp$ d denote summations over nearest-neighbor sites within the same atomic layer and between adjacent layers, respectively. The term si represents the unit

spin vector at site i, ku is the uniaxial anisotropy constant, μ_i is the magnetic moment corresponding to spin i, and B is the external magnetic field. By increasing the $J_{//}/J_{\perp}$ ratio, the model explicitly captures the differences between intralayer and interlayer couplings. Furthermore, the Metropolis Monte Carlo method [7] was employed to determine the thermal equilibrium magnetization distribution at temperature. T_c was estimated by fitting magnetization data [8].

Simulations were performed for various sizes and heights of rectangular L10-FePt nanoparticles to analyze the dependence of T_c on particle size.

III. Results and Discussions

To assess the exchange interaction anisotropy in L10-FePt, Density Functional Theory (DFT) calculations were performed using the Quantum ESPRESSO package [9]. These simulations revealed a pronounced anisotropy ratio, where the in-plane exchange $J_{//}$ is approximately 7.06 times larger than the out-of-plane exchange $J_{\perp}$. Based on these considerations, the exchange interaction parameters for the anisotropic spin model were set to $J_{//}$=10.033 J/link and $J_{\perp}$=1.422. Using these parameters, T_c of the bulk crystal was reproduced as approximately 685 K, which aligns well with experimental observations.

Using the established anisotropic spin model, we explored the size-dependent variation in T_c for three sample sets: Prototype (Legacy In-house), Current In-house, and Current External. These samples were distinguished by their differences in particle size and height distributions. The model demonstrated that the size-dependent dispersion of the Curie temperature, $\sigma T_{c,size}$, accounted for approximately 70–80% of the experimentally observed total T_c dispersion, σT_c. This finding suggests that variations in particle size and height are the primary drivers of the observed T_c distribution.

TABLE I
Measured grain sizes and Curie temperatures for several samples, and predictions of the Curie temperatures from the anisotropic spin model.

A) Measured data

Sample	Width (nm)	$\sigma_{\_Width}$ (%)	Hight (nm)	$\sigma_{\_Hight}$ (%)	T_c (K)	σT_c (%)
Prototype In-house	7.8	20	10.0	12	650	2.5
Current In-house	6.6	23	10.4	4.8	650	2.5
Current External	5.7	23	11.6	14	650	3.5

B) Predicted by anisotropic spin model

Sample	T_c (K)	$\sigma T_{c,size}$ (%)	$\sigma T_{c,size}/\sigma T_c$
Prototype In-house	638.9	1.7	0.68
Current In-house	632.3	2.0	0.80
Current External	630.1	2.5	0.71

The remaining ~30% of σT_c is likely attributed to secondary factors such as chemical ordering and lattice strain. Nonetheless, the numerical simulations effectively isolated the dominant contribution of size effects to T_c variations, providing valuable insights into controlling these dispersions for HAMR media design. By minimizing T_c dispersion through approaches such as regulating particle dimensions or refining material composition, significant advancements in recording stability and ADC could be achieved. These results underscore the practical importance of the developed atomistic spin model in optimizing next-generation magnetic storage systems.

IV. Conclusion

This study investigated the dispersion of Curie temperature (T_c) in L10-FePt nanoparticles by developing an anisotropic spin model and examining the influence of particle size distribution on Tc variability. The findings revealed that finite-size effects are responsible for approximately 70%–80% of the experimentally observed T_c c dispersion (σT_c), with particle size and height distributions identified as the main contributors.

Non-equilibrium dynamics during HAMR processes, such as rapid thermal fluctuations, significantly impact recording performance. Future research will focus on incorporating temperature- and time-dependent simulations to gain deeper insights into the transient behaviors tied to these processes.

The proposed model and its results provide actionable guidelines for minimizing Tc dispersion through optimized particle size management and material modifications, paving the way for enhanced performance in next-generation high-density storage systems.

At the conference, we will present a comprehensive simulation analysis of the nonlinear impact of particle size on Tc dispersion and look forward to discussing practical strategies for reducing σT_c by optimizing grain-size distributions.

References

[1] D. Weller and A. Moser, “Thermal effect limits in ultrahigh-density magnetic recording,” *IEEE Transactions on Magnetics* 35, 4423–4439 (1999).

[2] S. N. Piramanayagam, “Perpendicular recording media for hard disk drives,” *Journal of Applied Physics* 102, 011301 (2007).

[3] K. Hono and Y. K. Takahashi, “L10 fept granular films for heat-assisted-magnetic recording media,” *in Ultrahigh Density Magnetic Recording*, enny Stanford Publishing, 2016, pp. 246–277.

[4] J.-G. Zhu and H. Li, “Signal-to-noise ratio impact of grain-to-grain heating variation in heat assisted magnetic recording,” *Journal of Applied Physics* 115, 17B747 (2014).

[5] A. Perumal, Y. K. Takahashi, and K. Hono, “Fept-c nanogranular films for perpendicular magnetic recording,” *Journal of Applied Physics* 105, 07B732 (2009).

[6] K. Ochiai, T. Tsuyama, S. Shimizu, L. Zhang, J. Watanabe, F. Kudo, J.-G. Zhu and Y. Okuno, "Anisotropic exchange spin model to investigate the Curie temperature dispersion of L10-FePt magnetic nanoparticles." *Journal of Applied Physics* 137.18 (2025)

[7] R. F. L. Evans, W. J. Fan, P. Chureemart, T. A. Ostler, M. O. A. Ellis, and R. W. Chantrell, “Atomistic spin model simulations of magnetic nanomaterials,” *Journal of Physics: Condensed Matter* 26, 103202 (2014).

[8] N. T. Binh, S. Ruta, O. Hovorka, R. F. L. Evans, and R. W. Chantrell, “Influence of finite-size effects on the curie temperature of L10-FePt,” *Phys. Rev. B* 106, 054421 (2022).

[9] P. Giannozzi, *et al*., “Quantum espresso: a modular and open-source software project for quantum simulations of materials,” J*ournal of Physics: Condensed Matter* 21, 395502 (2009).

The impact of in-plane grains on HAMR performance and THMap metrics

Niranjan A. Natekar[1], Pierre-Olivier Jubert, Terry Olson, Alexander Goncharov, Richard Brockie and Kiwamu Tanahashi

Western Digital Corporation, San Jose, CA 95119, USA Niranjan.Natekar@wdc.com

An important source of noise in the Heat Assisted Magnetic Recording (HAMR) medium results from structural defects or magnetic defects of the FePt grains. One origin of this noise is the in-plane grains with easy axes pointing in-plane instead of out-of-plane. While the presence of these grains has been confirmed in the literature through experiments, there is a lack of understanding of how these grains can impact the HAMR performance and THMap metrics. In this modeling study, we first evaluate the impact of in-plane grains on the HAMR performance. We then model the THMap process to understand the effect of in-plane grains on magnetization mean, variance and the readback signal mean, variance. We also compare the signal, noise, low frequency SNR (LF SNR) and jitter captured through micromagnetic simulations to values obtained from an analytical DC noise model. Finally, we use analysis with correlation length for magnetization to explain the relationship of the magnetostatic interactions between grains and signal variance as a function of in-plane grains. This work establishes the performance impact of in-plane grains, the effect on specific THMap metrics and explains the relationship between the magnetostatic interactions between grains and signal variance through correlation length analysis .

Index Terms— HAMR, in-plane grains, noise, jitter, LF SNR, RTS, THMap, micromagnetic simulations, analytical model

I. Introduction

In the last two decades, efforts surrounding the Heat Assisted Magnetic Recording (HAMR) process have focused on improving the Signal to Noise Ratio [1, 2], reducing noise (jitter) [3-5] and alleviating erasure from overlapping data tracks [6, 7]. These efforts have allowed the technology to be commercialized in a 30TB drive. The next step is to ensure viability of the technology for the next couple of decades. Media noise is the most important noise source in HAMR, and a major contributor to this noise is in-plane grains. The distribution of these grains is difficult to control, and they are ubiquitous irrespective of the fabrication process parameters. This study establishes the impact of in-plane grains through HAMR micromagnetic simulations. We use the THMap methodology to calculate noise (readback signal variance) due to the in-plane grains in the absence and presence of magnetostatic interactions and compare the results to an analytical noise model. Finally, through autocovariance analysis, we explain both the behavior of the noise curve for different proportions of in-plane grains in the presence of magnetostatic interactions and the reasons why these trends deviate from the analytical noise model.

II. Micromagnetic Simulations And THMap Method

We use the micromagnetic technique described previously [8-10] to simulate discretized single layer media with magnetic grains. We've explained results from our HAMR Micromagnetic model in a digest published previously [11]. In this current work, simulations with the HAMR micromagnetic model show that in-plane grains reduce the Areal Density Capability (ADC) by 30 Gbpsi for every 1% increase of in-plane grains. The ADC loss occurs due to a reduction of the Linear Density (LD), which results from an increase in jitter, decrease in Low Frequency SNR (LFSNR), and a decrease in reader SNR. Simulations indicate that in-plane grains have almost no effect on track squeezability, and that the loss in LFSNR occurs because of the increase in noise power due to the presence of in-plane grains and impacts both the center of the bit and the transition. In addition to recording simulations, we run simulations of the THMap method [12]. First, the simulated media is initialized in a negatively saturated state by applying a high field in negative (-1) direction. This is followed by band erase at a particular temperature and an applied field (T & H respectively). The final magnetization state for each grain is then convolved with the reader sensitivity function to generate the readback signal.

III. Analytical Noise Calculation

We provide analytical expressions for the DC signal and DC noise power as a function of the proportion of in-plane grains [13] via a derived statistical model. The orientation of the grains' magnetization is described by binomial statistics. Let R be the proportion of out-of-plane grains. Of the R out-of-plane grains, a proportion p has their magnetization up and a proportion q=(1-p) have their magnetization down.

We extend the model to arbitrary reader point spread functions [13, 14] and include noise that arises from the grains' random positions. The expression for the average DC signal becomes:

$$\langle Signal \rangle = H_1 . pf . \left(M_g t_g\right) . R(2p-1) \quad (1)$$

where H_1 is the head signal sensitivity pre-factor, pf the medium packing fraction, M_g the average grain out-of-plane magnetization and t_g the grain thickness. H_1 is proportional to the integral of the reader sensitivity function ϕ (x,y).

The expression for the signal variance is:

$$var[Signal] = H_2 . pf . A_{grain} . \left(M_g t_g\right)^2 \left[\left(1+\left(\frac{S_{corr}}{S_{area}}\right)^2\right)\left(4.\ R^2 . p . (1-p) + R.(1-R) + \left(R(2p-1)\right)^2\right) - \left(R(2p-1)\right)^2\right] \quad (2)$$

where H_2 is the head noise sensitivity pre-factor, A_{grain} the average grain area, S_{corr}/S_{area} is the grains spatial correlation ratio that depends on the random granular structure of the

medium [13]. H_2 is proportional to the integral of $\phi^2(x,y)$. Details behind the derivations of equations (1) and (2) will be provided in a separate publication.

IV. THMap Results

The THMap runs are implemented using two writer fields, 250 Oe (which ensures randomization of magnetization) and 12.5 kOe (which ensures media saturation). Results are plotted for temperature $T > T_c$. Fig. 1(a) shows curves for the readback signal mean in the absence of magnetostatic interactions (MSI). For the low field, random orientation of grains leads to mean ~ 0, whereas the magnetization at the high field is dependent on proportion of in-plane grains. As the proportion of in-plane grains increases, the signal decreases linearly as per equation (1), as indicated by the red squares. The green lines are fits constructed based on equation (1) where 'H_l*M_rt' and 'p' are fitting factors. The value of 'p' for the higher field 12.5 kOe is 1, which indicates the saturation of magnetization in the direction of applied field. The value of 'p' for the low field is ~ 0.5, given the randomness in orientation for the grains in the presence of a low field at $T > T_c$.

Fig. 1(b) shows the impact of the MSI on the signal variance. Signal variance decreases when MSI are introduced (black circles to blue triangles). This is because MSI introduces anti-correlations between the magnetizations of adjacent grains. The analytical fit cannot predict the signal variance for the low field when the same fitting parameters as the high field variance fit are used with equation (2). To examine whether the impact on signal variance is purely due to the MSI (and the corresponding magnetostatic field), the magnitude of magnetostatic field is varied, and the signal variance is plotted. The impact of the field magnitude on signal variance is not linear. The comparison of the variance data with the analytical equation fit improves as the magnetostatic field magnitude is reduced. This clarifies that the mismatch between the analytical model and variance data is due to the magnetostatic field since the analytical model does not explicitly account for MSI.

V. Understanding The Impact of MSI

We employ the autocovariance function on the vertical component of the magnetization (Mz) from the micromagnetic simulations. In Fig. 2(a), we note that with stronger applied field the autocovariance function changes shape. Defining the correlation length (CL) as the zero crossing of the autocovariance function, we see that the CL changes from 8 to 3 nm when increasing the applied field from 250 Oe (blue plusses) to 12.5 kOe (red circles). Considering the CL to be equivalent to a switching unit from a noise perspective, then there are significantly more switching units to be averaged, and consequently less noise, at high field. This is consistent with the results from Fig 1 (b).

Next, we examine the effects of MSI in the context of the magnetostatic field being just another applied field. In Fig. 2(b), we note that as the MSI magnitude increases, the correlation length decreases. This makes sense given that MSI "prefer" for neighboring grains to be anti-correlated to create flux closure between them. Thus, increasing MSI means increasing anti-correlations which reduce the CL. Secondly, given that a smaller CL implies smaller switching units, more switching units to be averaged, and less noise, we can understand the trend of the 250 Oe data in Fig 2(b). The CL from the fitted curve (7.7 nm) is close to the grain pitch of the micromagnetic simulations (7.4 nm). This is reasonable since we expect the switching unit size to be roughly equal to the grain pitch if there are no fields present (except the stochastic thermal field) between the grains.

References

1) R. Ahmed, M. F. Erden, P. Krivosik, and R. H. Victora, doi: 10.1109/TMAG.2019.2935400.
2) N. A. Natekar, Z. Liu, S. Hernandez, and R. H. Victora, doi: 10.1063/1.5007072
3) J. Hohlfeld, P. Czoschke, P. Asselin, and M. Benakli, doi: 10.1109/TMAG.2018.2872758
4) N. A. Natekar and R. H. Victora, doi: 10.1109/LMAG.2020.2992221
5) C. D. Keener, B. C. Stipe, P. -O. Jubert, H. -T. Chou, L. Xu and A. Bashir, doi: 10.1109/TMAG.2023.3312043
6) C. Rea et al., doi: 10.1109/TMAG.2013.2287886.
7) N. A. Natekar and R. H. Victora, doi: 10.1109/TMAG.2020.3038805
8) N. A. Natekar, E. Roddick, and R. M. Brockie, doi: 10.1109/TMAG.2021.3122981.
9) E. Roddick, L. Xu, and R. M. Brockie, doi: 10.1109/TMAG.2020.3012941
10) L. Xu, R. M. Brockie, N. A. Natekar, and E. Roddick, doi: 10.1109/TMAG.2022.3221782.
11) N. A. Natekar, P.-O. Jubert, T. Olson, A. Goncharov, R. Brockie, and K. Tanahashi, doi: 10.1109/TMRC62973.2024.10713977
12) P.-O. Jubert et al., doi: 10.1109/TMAG.2022.3214085.
13) H. N. Bertram, M. Marrow, J. Ohno, and J. K. Wolf, doi: 10.1109/TMAG.2004.833171
14) H. N. Bertram and M. E. Schabes, doi: 10.1109/TMAG.2009.2018544.

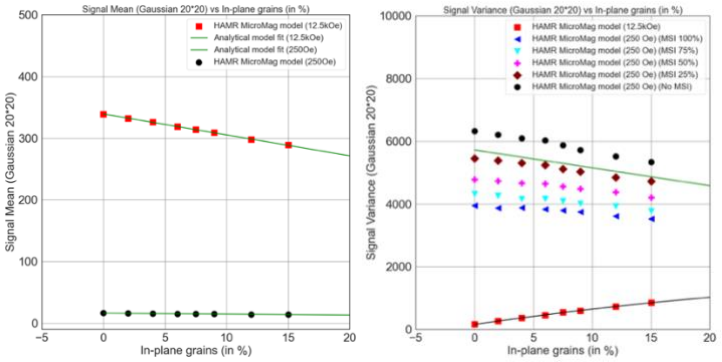

(a) (b)

Fig. 1: THMap metrics calculated from the HAMR Micromagnetic model for a Gaussian reader 20nm*20nm (a) Readback signal mean and (b) variance (for different magnetostatic fields)

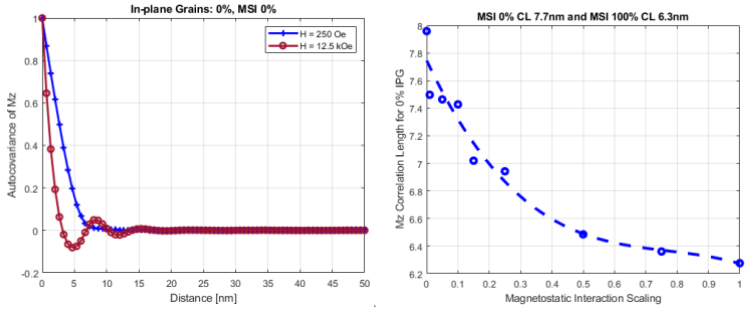

(a) (b)

Fig. 2: (a) Autocovariance of Mz for no MSI and zero in-plane grains. The correlation lengths are 8 and 3nm for the two field values (b) Correlation lengths of Mz for various strengths of MSI with no in-plane grains and a 250 Oe applied field

Phase-field study of microstructure formation of FePt-C nanogranular film for heat-assisted magnetic recording media

Yusuke Matsuoka[1], Machiko Ode[1], Taichi Abe[1], Toshiyuki Koyama[1], Yukiko K. Takahashi[1,2]

[1] National Institute for Materials Science, Tsukuba 305-0047, Japan, matsuoka.yusuke@nims.go.jp
[2] Research Institute of Electrical Communication, Tohoku University, Sendai, 980-8577, Japan

Heat-Assisted Magnetic Recording (HAMR) utilizing FePt nanogranular films holds promise for high-density data storage. Achieving target densities requires precise control of film microstructure – small, high-aspect-ratio, and uniform grains. This study employs a phase-field (PF) method to model FePt-C film evolution during sputtering. The model, validated against experimental TEM data, accurately reproduces observed island-like structures. Crucially, simulations demonstrate that elastic strain relaxation, stemming from lattice mismatch with the MgO substrate, drives island formation. This insight provides a foundation for optimizing HAMR film deposition processes and material selection.

Film deposition, Heat-assisted magnetic recording media, Microstructure, Phase-field simulation

I. Introduction

The escalating demands of the digital age are driving unprecedented growth in demand for capacity and power consumption of data center [1]-[2]. Since improving recording density of Hard Disk Drives (HDD) can be a solution for both problems, active research is underway. Heat-Assisted Magnetic Recording (HAMR), utilizing $L1_0$-ordered FePt as a magnetic medium, is a one of the candidates for the solution of these problems, offering potential for high recording density and improved power efficiency per capacity [2]. Currently, development is progressing toward a recording density of 4TB/in^2. Achieving a target density of 4 TB/in^2 requires FePt-X nanogranular films to meet multiple conditions: small grain size (<4.3 nm), high aspect ratio (>1.6), and good size uniformity (<10-15%) [2]. Current research focuses on optimizing sputtering processes and exploring novel materials for substrates and segregants to achieve these microstructural requirements. For the efficient process optimization and material exploration, it is necessary to have a precise understanding of the mechanisms of microstructural formation. While experimental investigations have yielded significant insights into the underlying mechanisms for the microstructural formation, some limitations still remain. For example, the difficulty in *in situ* observation of microstructural evolution hinders the ability of keeping track of the shape change of individual FePt grains. The impossibility of independent control of physical property of substrate/segregant makes the elucidation of the influence of each property on microstructural formation difficult. To overcome these challenges, this study employs a phase-field (PF) method [3] to model the temporal evolution of FePt-C nanogranular films during deposition. This approach allows for investigation of the interplay between material properties, deposition parameters, and resulting microstructures. The model is validated against experimental data and subsequently utilized to elucidate the key mechanisms controlling the formation of island-like FePt grains.

II. Method

This study utilizes a PF method to simulate microstructure evolution of FePt-C nanogranular film during sputtering process. The model tracks the evolution of local volume fractions (f_p) for each phase – vacuum, $L1_0$-FePt, C, and MgO – governed by following time-dependent equation incorporating diffusion and sputtering-driven atomic supply.

$$\frac{\partial f_p}{\partial t} = \nabla \cdot \left(\sum_{q=1}^{4} M_{pq} \nabla \left(\frac{\delta G_{\mathrm{sys}}}{\delta f_q} \right) \right) + B s_p \frac{\partial f_1}{\partial z} \tag{1}$$

Here, M_{pq} is the diffusion mobility, G_{sys} is the Gibbs energy of the system, B denotes the sputtering rate, and s_p is the sputtering concentration of phase p. The total Gibbs energy of the system (G_{sys}) comprises chemical, gradient, and elastic energy ($G_{\mathrm{sys}}=G_{\mathrm{chem}}+G_{\mathrm{grad}}+G_{\mathrm{elas}}$), formulated to accurately represent surface, interfacial and elastic strain energies. The elastic strain energy is calculated using phase-field micro-elasticity theory:

$$E_{\mathrm{str}} = \frac{1}{2} \int_{\mathbf{r}} C_{ijkl} (\varepsilon_{ij} - \varepsilon_{ij}^0)(\varepsilon_{kl} - \varepsilon_{kl}^0) d\mathbf{r} \tag{2}$$

Here, C_{ijkl} is the elastic constant, ε is the total strain, and ε_0 is the eigenstrain. Crucially, the model incorporates elastic strain energy calculated via a micro-mechanics approach, accounting for lattice mismatch between FePt and the MgO substrate through the inclusion of eigenstrain. Model parameters are sourced from existing literature where available, while those lacking published values were carefully calibrated to reproduce experimentally observed microstructural features. This integrated approach allows for a detailed investigation of the interplay between thermodynamic driving forces, kinetic limitations, and resulting nanogranular morphologies during film deposition.

III. Results and Discussion

A. Comparison with experimental observation

Figure 1 presents a comparison of simulated microstructures (Fig. 1a-c) and a TEM micrograph (Fig. 1d) of a 4.5 nm thick FePt-35 vol.% C film. For the simulated results, a 3D view (Fig. 1a), a cross-section along the (010) plane (Fig. 1b), and a projection along the [001] direction (Fig. 1c) are shown. In both experimental and computational results, well-separated island-like structure of FePt grains are formed. In addition, many FePt grains have rounded square shapes, and some have irregular shapes due to the coalescence of multiple FePt grains. Notably, the simulated microstructure exhibits in-plane anisotropy, with the FePt grains arranged along the [100] or [010] directions. Previous studies have demonstrated that the in-plane anisotropy of thin film microstructures is influenced by elastic anisotropy and surface energy anisotropy [4]-[5]. Given that the PF model employed in this study assumes isotropic surface and interfacial energies, the observed anisotropy is likely attributable to the elastic anisotropy of MgO and FePt.

Collectively, the simulation reproduces the key features observed in the experiment, indicating that the microstructural evolution during sputtering have been correctly modeled by proposed PF model.

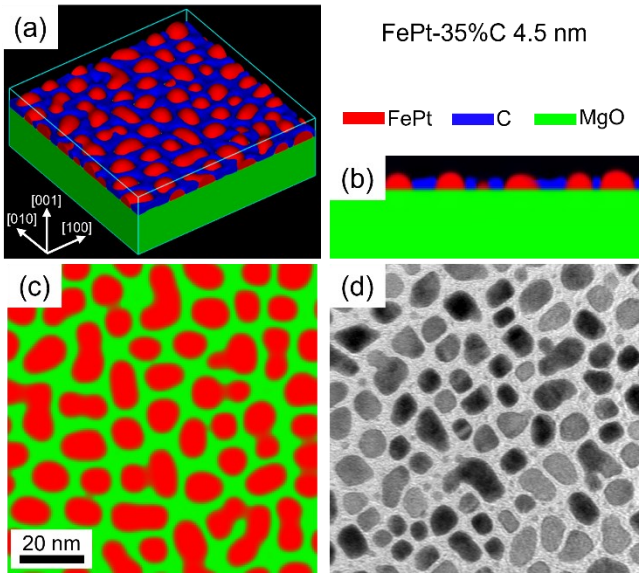

Fig. 1. The simulated (a-c) and experimentally observed (d) microstructure of FePt-35%C film with the thickness of 4.5 nm. For the simulated results, a 3D view (a), a cross-section along the (010) plane (b), and a projection along the [001] direction (c) are shown. Note that the C is not displayed in the projection view (c) for better visibility.

B. Influence of elastic energy relaxation

A key advantage of computational modeling lies in its ability to isolate and verify factors governing microstructural formation by changing parameters or conditions. Here, we investigate the influence of elastic strain energy—arising from lattice mismatch between the substrate and FePt—by performing simulations excluding its contribution.

The resulting microstructure, presented in Fig. 2, reveals the formation of a network-like structure where adjacent FePt grains connect—a morphology distinct from that observed when elastic strain energy is considered (Fig. 1). These results demonstrate that elastic strain energy is crucial for the formation of the uniform, fine, island-like microstructure. Given that phase-field simulations calculate microstructural evolution by minimizing the Gibbs energy of the system, the formation of island-like structure is considered to be driven by the relaxation of elastic strain energy.

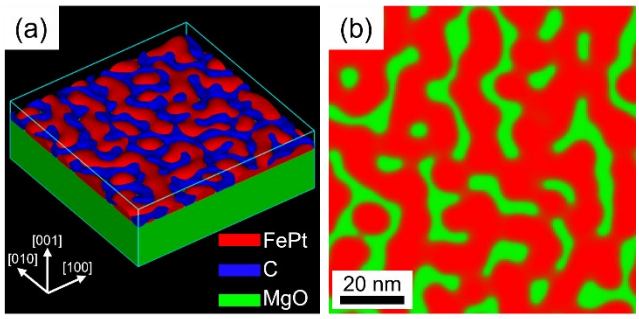

Fig. 2. A 3D view (a) and a projection along the [001] direction (b) of the microstructure of FePt-35%C film with the thickness of 4.5 nm simulated without considering elastic strain energy. Note that the C is not displayed in the projection view (b) for better visibility.

IV. Conclusion

This study modeled microstructural formation of FePt-C nanogranular films on MgO substrates during sputtering using the phase-field method. The main findings are as follows:

- The model, incorporating strain energy between the MgO substrate and the film, successfully reproduced island-like structures in the FePt-C nanogranular film.
- Relaxation of elastic strain energy plays a key role in the formation of island-like microstructure.

Based on these findings, our numerical experiment provides critical insight for the mechanisms behind the microstructural formation of FePt magnetic recording films and will be useful for future studies on process optimization and material exploration of substrate and segregant.

Acknowledgements

This work was supported by JST, CREST Grant Number JPMJCR22C3 and MEXT Program: Data Creation and Utilization-Type Material Research and Development Project Grant Number JPMXP1122715503.

References

[1] IEA, Energy and AI, Paris, 2025. https://www.iea.org/reports/energy-and-ai.

[2] D. Weller, G. Parker, O. Mosendz, E. Champion, B. Stipe, X. Wang, T. Klemmer, G. Ju, A. Ajan, A HAMR Media Technology Roadmap to an Areal Density of 4 Tb / in, 50 (2014).

[3] Y.U. Wang, Y.M. Jin, A.G. Khachaturyan, Phase field microelasticity modeling of surface instability of heteroepitaxial thin films, Acta Mater. 52 (2004) 81–92.

[4] Y. Ni, L.H. He, A.K. Soh, Three-dimensional phase field simulation for surface roughening of heteroepitaxial films with elastic anisotropy, J. Cryst. Growth. 284 (2005) 281–292.

[5] J. Deng, H. Li, K. Dong, R.W. Li, Y. Peng, G. Ju, J. Hu, G.M. Chow, J. Chen, Lattice-Mismatch-Induced Oscillatory Feature Size and Its Impact on the Physical Limitation of Grain Size, Phys. Rev. Appl. 9 (2018) 34023.

The Computational Analysis of HAMR Media Noise with a Multilayer Micromagnetic Media Model

Lei Xu, Vincent Le, Terry Olson and Kiwamu Tanahashi

Western Digital Corporation, San Jose, CA 95119 USA

Heat-assisted magnetic recording (HAMR) media noise is a critical factor in determining HAMR recording performance. In this study, we employ an exchange-coupled multilayer media model to analyze the media noise. We present a computational investigation of THMap metrics, especially the top and bottom edges of the THMap, to extract the switching distributions. We focus on the cap magnetic properties and interlayer vertical exchange coupling to evaluate their impact on the THMap metrics. We find that introducing the domain wall ("incomplete switching") into a proper location of multilayer stack reduces the media noise. In parallel, we run recording simulations to relate THMap metrics to the recording performance. These results contribute to a better understanding of future HAMR media design.

***Index Terms*— Areal Density, Heat Assisted Magnetic Recording, micromagnetic simulation**

I. Introduction

Heat-assisted magnetic recording (HAMR) is a breakthrough storage technology to increase the storage capacity in hard disk drives. It has the capability to push areal density (AD) growth beyond 5Tb/sq.in [1]. A key component of HAMR is L10-FePt medium, which consists of small grains with high magnetic anisotropy field (Hk). The medium distributions, such as the Hk and Curie temperature (Tc) distributions, are critical factors for limiting the recording performance in the writing process. Previously, several efforts have been made to mitigate the transition noise; a composite medium structure with superparamagnetic writing layer [2] and incoherently switched magnetic grains with sufficient height [3] were proposed to reduce jitter noise. Here we investigate the media noise using THmap metrics. In our exchange-coupled multilayer media model, the cap magnetic properties and interlayer vertical exchange coupling are varied to see how the media noise is affected. We present recording simulations to relate THmap metrics to recording performance.

II. HAMR Simulation Setup Description

A. Implementation & media

In this study, we introduce an exchange-coupled multilayer media with granular grains. The micromagnetic simulation method has been described previously [4]. The magnetization reversal of each sub-layer of grains is described by the stochastic Landau-Lifshitz-Bloch equation [5].

There are 6 sub-layers in our media model. The bottom 5 layers are composed of FePt ordered alloy and have the same magnetic properties. The top layer is composed of cap material. We vary cap Hk from 10 kOe to 50 kOe and interlayer exchange coupling constant from 1 erg/cm^2 to 8 erg/cm^2.

B. Thermal profiles and writer fields

In our recording simulations, we employ 2-D Gaussian thermal profiles that peak at 90% with a 10% conical background [4]. However, in THmap simulations, for simplicity, we stretch these profiles in the cross-track direction, assuming them to be uniform across the medium slab crosstrack width.

This study uses finite-element electromagnetic (FEM) simulations to calculate writer field maps. Both high (65 mA) write current and low (5 mA) write current field maps are calculated for the experimental writer design.

III. Results And discussion

A. THmap metrics

The THmap method has been developed to characterize the switching distributions at recording time scales [6]. Using DC noise simulations or measurements, a 2D map of the grains' switching probabilities are extracted as functions of both the writer fields and medium temperatures.

In this work, we focus on simulating the bottom and top edges of the map, corresponding to laser peak temperature sweeps under low and high writer currents. We calculate noise power based on the readback signal for media A and B. Their cap Tc is fixed at 1000 K, cap Hk values are 30 kOe and 10 kOe respectively, and a weak exchange coupling 2erg/cm^2 is artificially introduced between the topmost FePt layer and the other four FePt layers beneath it for medium B. As shown in Fig 1, the peak noise power of medium A (blue) at 65 mA write current is higher than at 5 mA, while for medium B (green) the peak noise power at 65 mA write current is lower than at 5 mA.

B. Noise power reduction mechanism

To understand why the two media's noise powers have different relative heights, we first vary the cap Hk and plot the noise power at 5 mA write current. Fig 2 shows that noise power decreases with the increase of cap Hk, when the laser peak temperature is at or above FePt Tc 660 K. Next, we select the media with low Hk cap (10 kOe), then vary the vertical exchange coupling strength between the topmost FePt layer and the other four FePt layers beneath it. As shown in Fig 3, near the writing temperature, noise power reduces with the decrease of interlayer vertical exchange coupling at 65 mA write current.

If the grains are fully saturated and act as macrospins, the noise power reaches maximum when 50% of the grains switch. However, if grains are partially switched or form internal

domain walls within the height of a grain (also referred to in this work as "incomplete switching"), there is a significant reduction of media noise. Such domain walls could be introduced by weak vertical exchange coupling or a hard-to-switch cap layer." In Fig 4, we plot the incomplete switching fraction as a function of temperature. When both writer field and interlayer exchange coupling are weak, the thermal fluctuation field dominates for temperatures near and above FePt Tc, which increases the probability of incomplete switching in the grains. A more interesting case is medium B under strong writer field: there is about 9% incompletely switched grains, leading to lower noise power as previously shown in Fig 1. This is because below the writing temperature of FePt, the writer field is still strong enough to switch the soft cap and generate a domain wall within FePt layers.

C. Recording Simulations

In the above discussion, we calculate only the medium DC noise power in THmap. We also explore the recording transition noise. In the following isolated track simulation, the laser peak temperature is fixed at 718K. Here we compare the calculated jitter for pure FePt, medium A and medium B in Fig 5. There is almost no improvement for medium A, while there is a large jitter noise reduction for medium B, in correlation to the reduction of the high write current noise power.

IV. Conclusions

We present THmap DC noise power calculations for various media, and transition noise calculations to check the recording performance. In medium stack design with proper cap selection and interlayer vertical exchange coupling strength modulation, incompletely switched grains are generated, and thus a medium noise reduction occurs. More results for media with various cap properties and exchange couplings will be presented in a subsequent paper to substantiate this conclusion.

References

[1] E. Roddick, et.al., doi: 10.1109/TMRC56419.2022.9918580
[2] N.A. Natekar et al., doi: 10.1063/1.5007072.
[3] Jian-gang zhu et al., doi:10.1109/TMAG.2020.3039767
[4] E. Roddick, et.al, doi: 10.1109/TMAG.2020.3012941.
[5] M Tzoufras, et.al, doi: 10.1088/1367-2630/17/10/103014.
[6] Pierre-Olivier Jubert, e.t.al, doi: 10.1109/TMAG.2022.3214085

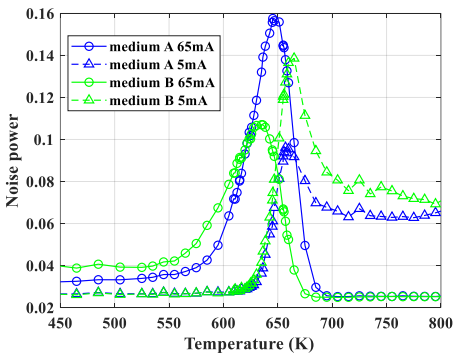

Fig. 1. Noise power as a function of laser peak temperature at the maximum write current 65 mA and at the minimum write current 5 mA.

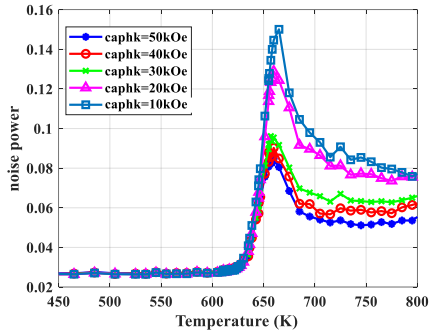

Fig. 2. Simulated noise power versus laser peak temperature at the minimum write current 5 mA. Each media has the same cap Tc 1000 K, but cap Hk varies.

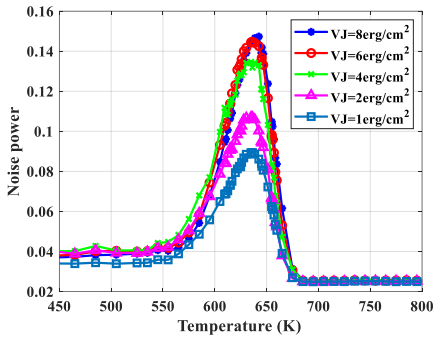

Fig. 3. Plots of noise power at maximum write current 65 mA. Interlayer vertical exchange coupling between varies.

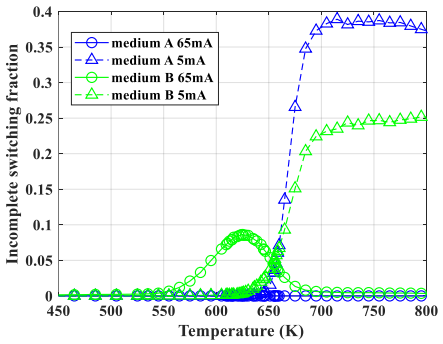

Fig. 4. Fraction of incompletely switched grains as a function of laser peak temperature for medium A and medium B.

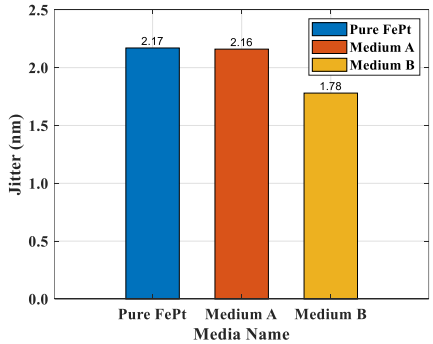

Fig. 5. Comparison of transition jitter for 3 media

Determination of coupling state in a Dual-FGL STO using injection locking

Yuji Nakagawa[1], Hirofumi Suto[2], Yuya Sakuraba[2], and Tomoyuki Maeda[1]

[1]Corporate Laboratory, Toshiba Corporation, Kawasaki 212-8582, Japan
[2]Research Center for Magnetic and Spintronic Materials, National Institute for Materials Science (NIMS), Tsukuba 305-0047, Japan
yuji4.nakagawa@toshiba.co.jp

We studied a dual-field generation layer spin-torque oscillator (dual-FGL STO) in an HDD head using a newly established analysis method based on *injection locking*. The dual-FGL STO is designed to induce the coupled oscillation of the dual-FGL for higher performance in microwave-assisted magnetic recording (MAMR). However, direct evidence of the coupled oscillation has not been obtained yet. Here, we report that injection locking, which is synchronization between STO oscillation and external microwave input, enables clear differentiation between the coupled and non-coupled oscillation state. We used a microwave magnetic field (H_{MW}) from a coplanar waveguide and observed resistance modulation only in the non-coupled oscillation state because the coupled state is insensitive to H_{MW}. These results demonstrate that the injection locking method is useful for studying spintronic devices and that the dual-FGL STO realizes the coupled oscillation state in the HDD head for MAMR.

***Index Terms*— Dual field generation layer (dual-FGL), hard disk drive (HDD), injection locking, microwave-assisted magnetic recording (MAMR), spin-torque oscillator (STO)**

I. Introduction

MICROWAVE-ASSISTED magnetic recording (MAMR) is one of the next key technologies in hard disk drives (HDDs) [1, 2]. In MAMR, a spin-torque oscillator (STO) fabricated in the write gap of an HDD head generates a microwave magnetic field, which assists magnetization switching in recording media (microwave-assisted switching, MAS). In order to maximize the recording capacity of HDDs by MAMR, the development of STO optimized for MAMR is required.

Recently, we have focused on an STO with two oscillation layers (field generation layers, FGLs) that we call dual-FGL STO [3-5]. The dual-FGL is aiming at anti-parallelly coupled oscillation of the magnetizations due to their dipolar field. With the coupled oscillation mode, the dual-FGL STO provides a focused microwave field oscillating in the media plane with smaller interaction with the main pole and trailing shield, which are the desired conditions for recording density improvement with MAMR.

In previous studies, we measured the dual-FGL STO fabricated in HDD heads [5-7]. To confirm its oscillation, we have conducted a conventional measurement, which measures the oscillation of giant magnetoresistance (GMR) caused by the oscillation of magnetization. Although we observed an oscillation peak [5], the spectrum itself did not indicate whether it originated from the coupled oscillation and could not exclude other possibilities, such as non-coupled oscillation. Only micromagnetic simulation results, which show oscillation frequency and bias current dependence consistent with the experiment, support the realization of the coupled oscillation state [5]. We also measured recording performance using the dual-FGL STO and confirmed the improvement due to the MAS effect [6, 7]. However, we have not extracted the indication of the coupled oscillation from those results. Other evidence that directly proves the coupled oscillation is desired.

In this study, we report clear differentiation between the coupled and non-coupled oscillation state using a novel analysis method based on injection locking. The analysis method has been proposed for studying oscillation states in STOs, which is applicable to HDD heads [8, 9]. By applying an external microwave magnetic field (H_{MW}) to the STO (Fig. 1a), the resistance is modulated when the STO oscillation is synchronized to the microwave field, which tells us the detailed properties of the oscillation state [9]. As we discuss later, the coupled oscillation state in the dual-FGL STO is insensitive to the external field, and no resistance modulation occurred despite the clear spectrum peak in the conventional spectrum experiment. On the contrary, when we intentionally induced a non-coupled oscillation state, which is a single oscillation of an FGL, we observed clear modulation in resistance at the same frequency as the spectrum peak. With these results, we can conclude that the coupled oscillation state is realized in the dual-FGL STO, which can be identified with the injection locking method.

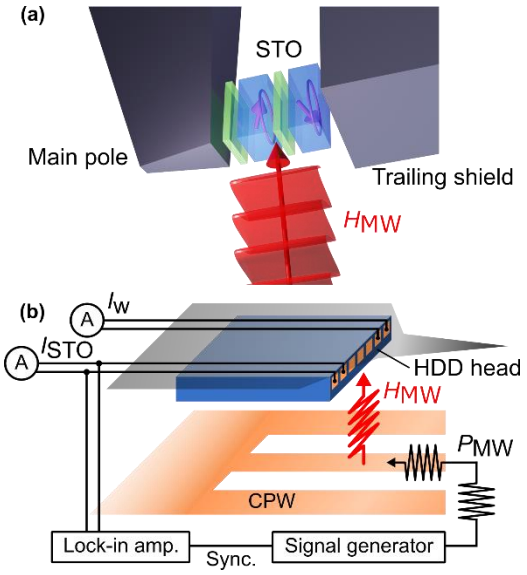

Fig. 1. Analysis method based on injection locking. Schematic figures of (a) the dual-FGL STO in the write gap and (b) experimental setup.

II. Experimental Setup

We prepared a coplanar waveguide (CPW) with a 3-μm-wide signal line, which emits H_{MW} by applying a microwave signal. The HDD head was attached to a suspension, and it was aligned at the center of the CPW. During the alignment, we applied a low-frequency (1,013 Hz) signal to the CPW and monitored the output from the reader element in the HDD head.

In the injection locking experiment (Fig. 1b), we applied coil current I_w and STO bias current I_{STO} to the HDD head. The microwave signal was generated with a 50% duty with a modulation frequency of 1 kHz. While we changed the frequency of the microwave signal (f_{MW}), we measured resistance modulation in the STO (ΔR_{STO}) synchronized to the modulation of the microwave signal.

For the conventional spectrum experiment, we employed the same setup as in the previous study [5]. We obtained the intensity of the GMR oscillation at each frequency (f_{STO}).

III. Results

Figures 2a and 2b show the results of the conventional spectrum experiment at I_{STO} = -5.0 and +3.0 mA, respectively. The positive bias (Fig. 2b) can induce the coupled oscillation for MAMR. On the other hand, using the negative bias (Fig. 2a), we can expect a single oscillation of an FGL, that is, a non-coupled oscillation state. However, the peak frequency was similar to each other. We could not distinguish the oscillation states from the conventional spectrum measurements.

Figures 2c and 2d show the results of the injection locking experiment, which is f_{MW} dependence of ΔR_{STO}, where I_{STO} = -5.0 and +3.0 mA as same as in Fig. 2a and 2b, respectively. In Fig. 2c, we observed an increase followed by a decrease of ΔR_{STO} as f_{MW} crosses the oscillation frequency in Fig. 2a, which is the injection locking signal [9]. In Fig. 2d, however, such injection locking signal was absent despite the similar spectrum peaks in Fig. 2b to Fig. 2a.

Based on these results, we successfully confirmed the coupled oscillation as the state in which we can observe a peak in the conventional spectrum experiment without the appearance of any signal in the injection locking experiment.

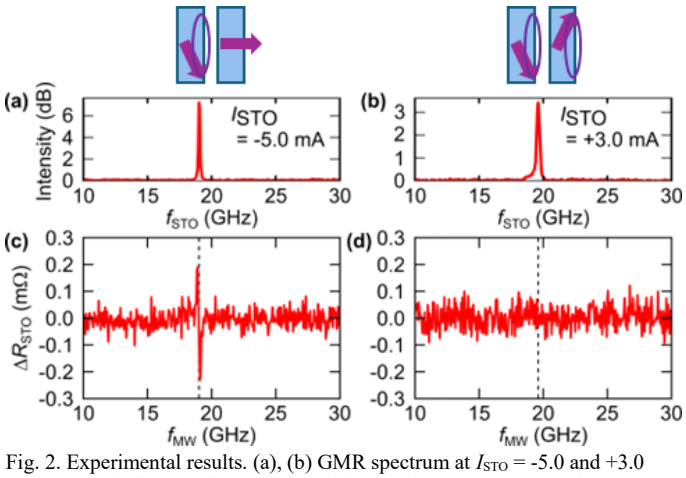

Fig. 2. Experimental results. (a), (b) GMR spectrum at I_{STO} = -5.0 and +3.0 mA, respectively. (c), (d) Injection locking results at I_{STO} = -5.0 and +3.0 mA, respectively.

IV. Discussion

The results above enable us to confirm the coupling state experimentally. Here, we discuss its mechanism by referring to the micromagnetic simulation results. As shown in Fig. 3, we reproduced the experimental results, where only the single-FGL oscillation shows injection locking.

In the locking state of the single-FGL oscillation, we confirmed that the magnetization of the FGL and H_{MW} are locked into the same phase. Therefore, there is a gain in Zeeman energy in the system, and modification of f_{STO} is preferred.

On the other hand, in the coupled oscillation state, its anti-parallel configuration of the FGL magnetizations cancels out such Zeeman energy gain. The system prefers the STO oscillation with its original frequency, and the injection locking is difficult to occur.

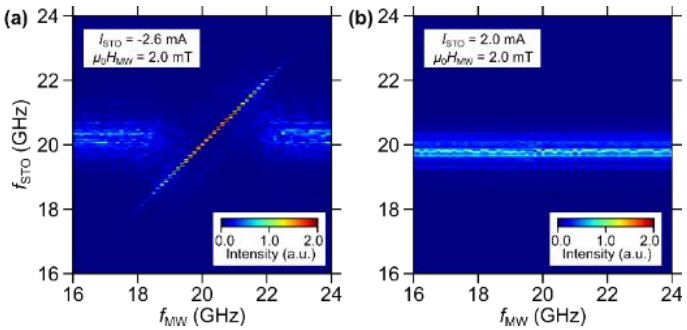

Fig. 3. Simulation results. (a), (b) Locking phenomena of f_{STO} to f_{MW} at I_{STO} = -5.0 and +3.0 mA, respectively.

V. Conclusion

With the injection locking method, we observed a clear difference between oscillation states, which is attributed to the different coupling states, and thus confirmed the coupled oscillation state in the dual-FGL STO. This method is applicable to product-level HDD heads and other spintronic devices, enabling the detection and study of their coupling states.

References

[1] J. -G. Zhu, X. Zhu, and Y. Tang, "Microwave assisted magnetic recording," *IEEE Trans. Magn.* **44**, 125-131 (2008).

[2] M. Takagishi *et al*., "Microwave assisted magnetic recording: Physics and application to hard disk drives," *J. Magn. Magn. Mater.* **563**, 169859 (2022).

[3] M. Takagishi *et al*., "Design concept of MAS effect dominant MAMR head and numerical study," *IEEE Trans. Magn.* **57**, 3300106 (2021).

[4] Y. Nakagawa *et al*., "Multiple spin injection into coupled field generation layers for low current operation of MAMR heads," *IEEE Trans. Magn.* **58**, 3201005 (2022).

[5] Y. Nakagawa *et al*., "Spin-torque oscillator with coupled out-of-plane oscillation layers for microwave-assisted magnetic recording: Experimental, analytical, and numerical studies," *Appl. Phys. Lett.* **122**, 042403 (2023).

[6] N. Narita *et al*., "Demonstration of substantial improvements in recording process with MAMR," *J. Magn. Magn. Mater.* **582**, 171011 (2023).

[7] Y. Nakagawa *et al*., "Verification and Design of Position Matching Effect in MAMR Using Dual-FGL STO," *IEEE Trans. Magn.* **60**, 3200106 (2024).

[8] H. Suto *et al*., "Analysis of an all-in-plane spin-torque oscillator using injection locking to an external microwave magnetic field," *Appl. Phys. Express* **14**, 053001 (2021).

[9] N. Asam *et al*., "Analysis method of a spin-torque oscillator using dc resistance change during injection locking to an external microwave magnetic field," *Appl. Phys. Lett.* **119**, 142405 (2021).

Near Field Transducer Reliability Improvements Due to Media Stack

Muhammad Asif Bashir[1], Pierre-Olivier Jubert[1], Yunfei Ding[1], Pradeep Senanayake[1], Yaguang Wei[1] and Alexander Goncharov[1]

[1]Western Digital Corporation, San Jose, CA, 95131, USA, asif.bashir@wdc.com

A key challenge in HAMR systems is maintaining NFT reliability, especially as enhanced performance often requires increased laser power, placing additional thermal stress on the NFT. This presents a critical performance-reliability tradeoff. In this study, we investigate fixed NFT design while media parameters changes aimed at breaking this performance-reliability dilemma. Specifically, we explore total resistance at critical interfaces, head to media spacing, recording layer optical properties, heat sink (HS) thickness, heat sink thermal conductivity, soft underlayer (SUL) thickness. Our findings demonstrate how modifications in media layer properties not only impact thermal management but also influence the magnetic field profile essential for effective grain freezing during the recording process. These insights help pave the way for achieving high HAMR performance without compromising long-term device reliability.

***Index Terms*— HAMR, NFT, plasmonic, antenna design, reliability, refractive index, extinction constant, heat sink**

I. Introduction

Heat Assisted Magnetic Recording (HAMR) is a critical technology for enabling continued areal density (AD) growth in hard disk drives (HDDs) [1]. A central component of HAMR is the laser-coupled near field transducer (NFT), which enables localized heating of the recording layer (RL) via surface plasmon excitation from light delivered through a waveguide. Localized heating depends on NFT dimensions and optical-thermal properties of the coupled head/media system [2]-[4]. During operation, the media temperature can reach close to 700K, while writing occurs during the cooling process at temperature just below the grains Curie temperature [3]. A magnetic write head, placed in close proximity to the NFT, produces a sufficiently strong magnetic field at the freezing location to define the grain orientation by the field polarity.

A key challenge in HAMR systems is maintaining NFT reliability, particularly as enhanced performance often requires increased laser power—resulting in additional thermal stress on the NFT. This presents a critical performance–reliability tradeoff. In this study, we investigate various media layer parameters to explore how this dilemma can be mitigated.

A nanobeak NFT design is employed in this study, requiring transverse magnetic (TM) mode to excite the NFT, which in turn excites a localized plasmon and strong optical near-field closer to ABS [5]. The maximum temperature of the NFT near the air bearing surface (ABS) can exceed 100–200K above room temperature, while the peak media temperature can reach approximately 400K above room temperature. This difference arises from light absorption: the NFT absorbs less light than the recording layer. In general NFT temperature increases further as we tune the media parameters to obtain higher areal density, resulting in increased laser power requirement to obtain a constant peak media temperature.

To examine these dependencies, we kept the NFT dimensions fixed while varying the media layer thicknesses, thermal conductivity, interface thermal resistance, and optical properties of the RL. An example case is shown in Figure 1, where the reference model uses standard parameters as presented in Table 1. We scaled the laser power to achieve a peak media temperature of 690 K. Note that the line scan is obtained at the trailing edge of the NFT at the center; the peak media temperature may not necessarily be at this location. Beyond the recording layer, or further away from the ABS, the temperature quickly drops. Maximum NFT temperature near the ABS can be around 525 K.

We also provide two examples of media variations. In Example 1, we demonstrate that optimized media parameters can cause the temperature beyond the RL to drop rapidly, improving both media performance and NFT reliability. In contrast, Example 2 shows that while peak media temperature is similar and media performance is enhanced, the NFT temperature is elevated—causing reliability concerns. These observations motivate a detailed exploration of media parameters to understand their impact on NFT reliability.

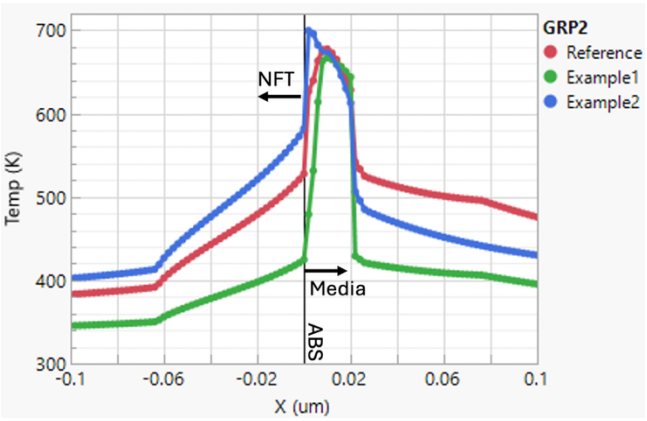

Fig. 1. Temperature as a function of distance perpendicular to ABS at trailing edge of the NFT (downtrack) at the center of the NFT (cross track). Two example line scans are plotted to compare against Reference thermal profile.

The paper is organized as follows: In section II we will provide the details of the model and variables used in the media studies while in section III we will provide some results and discussion on the results before concluding this study in section IV.

II. Model Setup

We used finite-element analysis (FEA) via commercial software [6] to calculate the optical near-field and the thermal field generated by the NFT. NFT details are taken from [5] and

applied using current state of the art NFT dimensions. The head surface includes a carbon overcoat and an air gap between the head and the media. The total head-to-media spacing is kept at constant unless varied for spacing studies. The medium consists of a medium overcoat, recording layer (RL), seed layer, heat sink, soft underlayer (SUL), and substrate. Our primary goal was to examine how critical media layer properties affect NFT reliability, so we established a baseline model with standard parameters listed in Table 1.

TABLE I
MEDIA LAYER VARIATIONS

Item	Variation
Spacing (nm)	2 - 7
RL (nm)	5 – 20
RL n	0.5 - 5
UL resistivity (m^2K/GW)	0.5 – 20
Seedt (nm)	1 – 20
HSt (nm)	10 – 150
HSk (W/mK)	10 – 100
SULt (nm)	50 – 300

III. RESULTS AND DISCUSSION

To compare NFT performance and reliability with various media parameters, we determined the required laser power to reach a fixed peak media temperature of 690 K. This enables us to relate laser power to NFT temperature, as shown in Figure 2 (a). Since writing occurs at a temperature below the curie temperature, we used the 630 K temperature contour to compare magnetic write width (MWW) in Figure 2(b), thermal downtrack gradient (DTTG) at the 630K contour line in Figure 2(c), and cross-track gradient (CTTG) at the 630K contour line in Figure 2(d). Recording layer variations in the legend correspond to those in Table 1.

We find that NFT temperature increases with laser power. However, some parameters both reduce MWW, improve DTTG and CTTG, and simultaneously decrease NFT temperature. These key parameters include spacing, underlayer resistance (ULR), and RL optical refractive index.

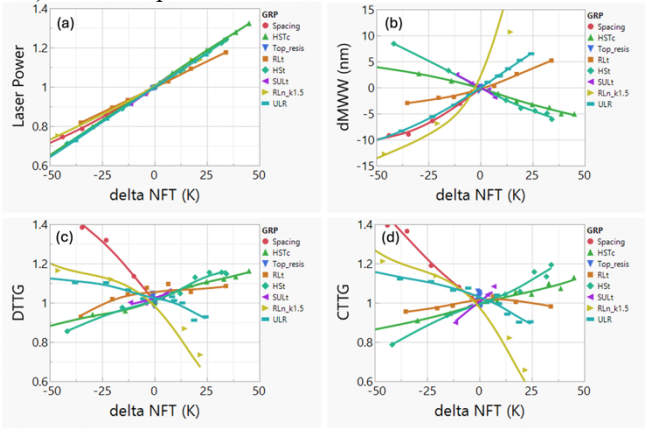

Fig. 2. Delta NFT temperature is plotted against laser power (a), delta MWW (b), normalized DTTG (c) and normalized CTTG (d). Within each graph an individual line shows the impact of varying one parameter across the range provided in table 1.

The higher interface resistance between the RL and the seed traps heat within the RL, lowering the laser power requirements and improving thermal gradients at fixed peak temperatures. Reducing spacing brings the RL closer to the NFT, which improves the system optical coupling and improves performance. A lower optical refractive index of the RL also improves the system optical coupling, providing higher absorption in the RL. Therefore, reducing the RL's refractive index significantly enhances NFT reliability and performance by reducing laser power.

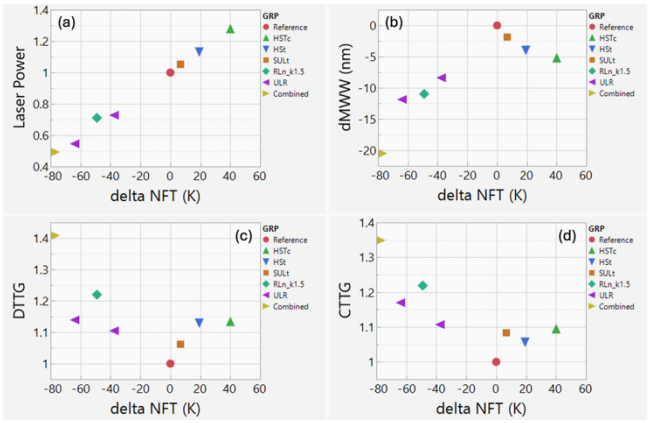

Fig. 3. Delta NFT temperature is plotted for few key cases and combined media case to show Laser Power (a), MWW reduction (b) and DTTG (c), CTTG (d) improvements.

Conversely, other parameters - such as heat sink (HS) thickness or SUL thickness or HS thermal conductivity - improve performance (smaller MWW and higher thermal gradients) at the expense of higher laser power and increased NFT temperature.

To evaluate the cumulative effects, we combined the beneficial media parameters in one configuration. Figure 3 shows that this combined media can reduce MWW by 20 nm and improve thermal gradients by 35–40%, while also lowering NFT temperature by 80 K.

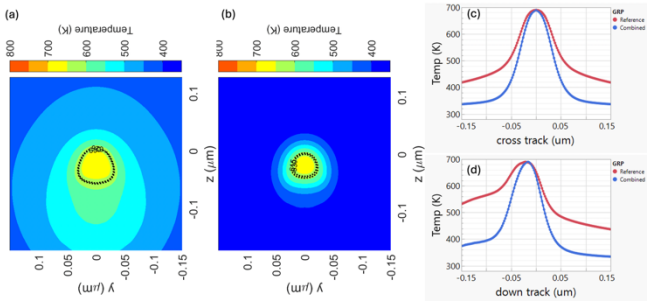

Fig. 4. Thermal maps are plotted at the center of the recording layer for Reference and Combined media cases (a), (b) respectively. Line scan along downtrack (c) and cross track (d) vs temperature for two cases is provided.

Figure 4 compares thermal maps of the Reference and the combined media, captured at the center of the recording layer. Downtrack and crosstrack line scans in Figures 4(c) and 4(d) show a clear reduction in background temperature, narrower MWW, and much improved thermal gradients in the optimized media.

IV. Conclusion

This study demonstrates that careful tuning of media layer parameters—especially recording layer optical properties and interface thermal resistance—can significantly improve both media performance and NFT reliability. These findings provide a path to break the performance–reliability dilemma in HAMR systems.

References

[1] M. Ha. Kryder et al., "Heat assisted magnetic recording", *Proc. IEEE,* vol. 96, no. 11, pp. 1810-1835, Nov. 2008.

[2] B. C. Stipe et al., "Magnetic recording at 1.5Pb m^{-2} using an integrated plasmonic antenna", *Nature Photon*, vol. 4, pp. 484-488, May 2010.

[3] P. Jubert, F. Zhong and M. K. Grobis, "Optimizing the Optical and Thermal Design of Heat-Assisted Magnetic Recording Media", *IEEE Trans. Magn*., vol. 53, no. 2, pp. 3200109, Feb. 2017.

[4] G. Ju et al., "High Density Heat-Assisted Magnetic Recording Media and Advanced Characterization—Progress and Challenges", *IEEE Trans. Magn.*, vol. 51, no. 11, pp. 3201709, Nov. 2015.

[5] T. Matsumoto, F. Akagi, M. Mochizuki, H. Miyomoto and B. Stipe "Integrated head design using a nanobeak antenna for thermally assisted magnetic recording*" Optics Express*, vol. 20, no. 17, pp. 18947-19854, August. 2012.

[6] CST Studio Suite by Dassault Systems, Paris, France

An ionic liquid (IL)-based media lube for Hard Disc Drives (HDDs)

Bingchen Wang[1,2], Alan Tirado[1], Fan Yang[1], Catherine Moran[1], Meghan Vander Woude[1], Yihan Song[1], Sofia Bai[2], Qian Guo[2], Huan Tang[2] and Lei Li [1]

[1] Department of Chemical & Petroleum Engineering, University of Pittsburgh, Pittsburgh, PA 15261, United States
[2] Recording Media Operations, Seagate Technology LLC, 47488 Kato Road, Fremont, CA 94538, United States

***Index Terms*—hard disc drive (HDD), heat-assisted magnetic recording (HAMR), ionic liquid (IL), media lube**

I. Introduction

With the continuous need for higher HDD storage capacity, reduced head-media spacing (HMS) is required. A lubricant nanofilm with lower thickness and/or higher fly clearance can provide valuable space to further reduce HMS. Meanwhile, heat-assisted magnetic recording (HAMR), which uses momentary laser heating to help increase the areal density, has been developed and identified as the next-generation HDD technology.[1] However, current state-of-the-art lubricants, i.e., perfluoropolyether (PFPE), are not thermally stable for HAMR, which is a serious concern for long-term reliability. Moreover, the minimum lubricant thickness of PFPE is limited by their polymeric nature, i.e., the radius of gyration (R_g), and difficult to be further reduced. Notably, ILs, on the other hand, are promising as the next-generation media lubricant due to their high thermal stability, nonvolatility, and small size of ion pairs. Indeed, some ILs have recently been evaluated as the candidates of media lubricant in HDDs.[14-17] However, high surface tension and low bonded ratio have been shown to be the major challenges. Here, we report our design, synthesis, and characterizations of a novel nanometer-thick IL media lubricant that contains abundant fluorinated segments and a hydroxyl functional endgroup. The testing results have demonstrated the advantage of the IL as media lubricant with respect to PFPE lubricant.

II. Results & Discussions

A. IL Synthesis & Characterizations

The chemical structure of the novel IL lube, i.e., HFIL-OH, is shown in Figure 1a. HFIL-OH are obtained through a two-step synthesis.[x] The TGA results (Figure 1b) show that the weight loss starts at ~350 °C for HFIL-OH, compared to ~150 °C for PFPE Ztetraol The higher thermal stability of HFIL-OH can be attributed to the strong electrostatic interactions between the IL ions, the aromatic cation, and the highly fluorinated structure. As shown in Figure 1c, the pendant drop testing shows that the surface tension of HFIL-OH is only ~18.2 mN/m, which is significantly lower than the surface tensions of PFPE Ztetraol and the commercially available fluorinated IL [Bmim][FAP]. The lower surface tension of the HFIL-OH can be attributed to the highly fluorinated components in the cation and anion of HFIL-OH since the low polarizability of C–F bonds results in weak intermolecular forces and consequently low surface tension.

HFIL-OH nanofilms with various thicknesses are applied on the COC of the media by dipcoating, widely used in the HDD industry, from solutions of various concentrations, and the average nanofilm thicknesses measured by ellipsometry are shown in Figure 1d. A layer of lubricant with a thickness of ~0.4-0.5 nm stays on COC for each HFIL-OH nanofilm after washing with Vertrel XF, suggesting that HFIL-OH molecules bond to the polar sites on the COC surface via hydrogen bonding, similar to the bonding of PFPEs.

The monolayer (ML) thickness of the lubricant molecules is the key parameter impacting the minimum thickness of the lubricant nanofilm. It has been established previously, when the film thickness exceeds the ML thickness, there is a sharp increase in surface roughness as dewetting occurs. Therefore, the ML thickness can be determined based on the change in the root mean square (RMS) surface roughness with the nanofilm thickness.[14,15] Figure 1e shows the AFM RMS surface roughness results for the HFIL-OH nanofilms with various thicknesses on COC, with the surface roughness results of PFPE Ztetraol as control. The ML thickness of HFIL-OH has been determined to be ~0.75 nm.

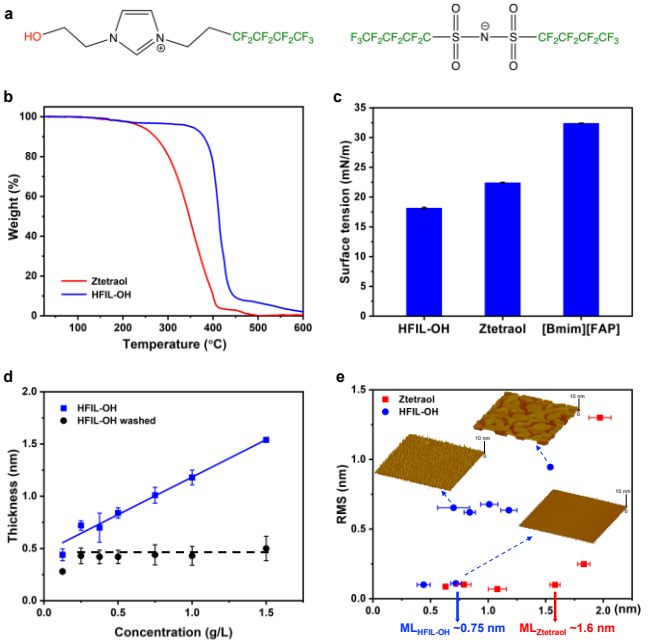

Fig. 1. Characterization of HFIL-OH. (a) Chemical structure of HFIL-OH. (b) TGA results of bulk HFIL-OH with Ztetraol as control. (c) Surface tension of HFIL-OH at RT with Ztetraol and [Bmim][FAP] as control. (d) Average thicknesses of HFIL-OH nanofilms on COC fabricated from various concentrations before and after Vertrel XF washing. (e) Surface roughness results of HFIL-OH nanofilms on COC. The insets are representative AFM images of the HFIL-OH nanofilms at the scan areas of 10 μm by 10 μm.

B. Component-level testing

The industry-level head-disk interface (HDI) tribology performances of HFIL-OH lubricant on rigid perpendicular recording magnetic disks (Figure 2a) have been tested, and the Seagate production disks with PFPE ($M_n \approx 2000$ g/mol) lubricant are used as references. The thermal stability of the thin-film HFIL-OH lubricant is examined by baking the lubricated disks at 150 °C for 2 hours. As shown in Figure 2b, HFIL-OH has significantly better thermal stability, with a 2.4% thermal loss compared with an 8.0% thermal loss for the reference disk, which is in line with the bulk TGA results. Here, the thickness of the HFIL-OH lubricant film on disk relative to that of the reference disk is determined by dividing the mean bit error rate (BER) difference between the HFIL-OH and the reference disks by the mean clearance sensitivity in the read/write-based spin-stand recording tests. The results in Figure 2c show that the tested HFIL-OH lubricant film is only ~0.35 Å thicker than that of the reference, indicating the thickness of HFIL-OH and PFPE reference are comparable. The fly clearance (i.e., touchdown height) is assessed by the spin-stand clearance tests with an embedded contact sensor to detect the head touchdown, and the results in Figure 3c indicate that HFIL-OH has a 2.0 Å higher clearance than the reference. The HFIL-OH molecules closely pack on the disk surface in ion layers because of the hydrogen bonding between COC's NH_2 groups and cations' OH groups and the strong electrostatic cation-anion association. Since the strong packing in the IL nanofilm is unlikely to be perturbed by the approaching flying head, there is a higher clearance for the head to fly closer to the media surface. In contrast, the PFPE reference lubricant has lower fly clearance, although the relative thickness is comparable to the HFIL-OH lubricant. This is because the polymeric backbone takes the random coil conformation. When the flying head approaches the media and the PFPE lubricant nanofilm, the Van der Waals force between the head and the PFPE backbone deform the flexible polymer towards the flying head, leading to lower clearance.[27] Therefore, HFIL-OH has the fly clearance advantage over PFPE, which provides valuable space to further scale down HMS. Meanwhile, the lower surface tension of HFIL-OH could also contribute to the higher fly clearance since lower surface tension results in lower head-lubricant interaction, i.e., Van der Waals force.

The friction coefficient results obtained from the pin-on-disk tests show that the HFIL-OH lubricant has a 12% higher friction than the PFPE reference, as shown in Figure 3d, indicating a slightly lower but comparable lubricity. The head burnish results (Figure 3d) based on the spin-stand tests show that the HFIL-OH lubricant has a comparable head wear performance to the reference, albeit with somewhat higher variations. Moreover, the HDI wear durability performance is assessed by the spin-stand tests, and the results in Figure 2d show that the durability performance of the HFIL-OH lubricant is slightly, i.e., 12%, worse than that of the PFPE reference. Overall, the HFIL-OH lubricant shows good tribology and durability performance.

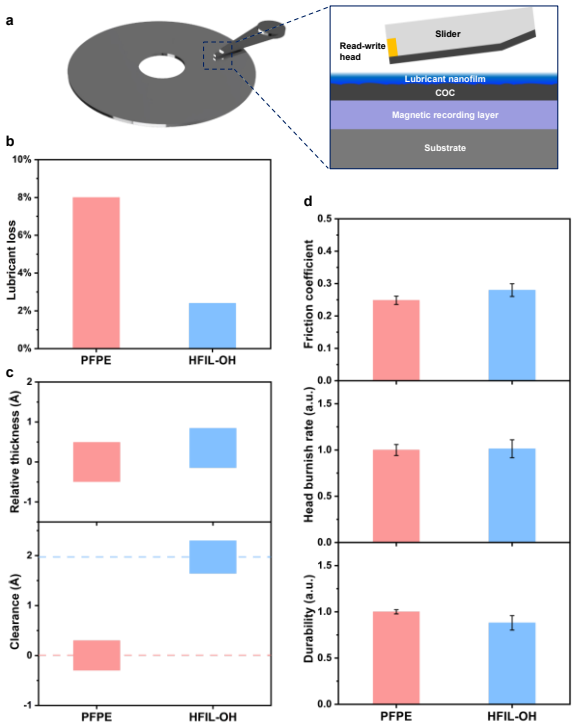

Fig. 2. Component-level testing of the HFIL-OH lubricated disks with the PFPE lubricated production disks as references. (a) HDI components. (b) On-disk lubricant loss after baking at 150 °C for 2 hours. (c) Relative lubricant film thickness measurement based on spin-stand recording tests and clearance performance based on the spin-stand clearance tests. (d) Friction coefficient results based on the pin-on-disk test, head burnish rate results based on the head wear performance tests, and HDI wear durability results based on the spin-stand tests.

C. Conclusion

In summary, a novel IL media lubricant for HDDs has been designed, synthesized, and characterized. Both lab-level and industry-level testing suggest that the IL lubricant has higher thermal stability and higher fly clearance than the state-of-the-art PFPE lubricant. Meanwhile, the IL lubricant also shows good lubricity and durability, which are comparable to the PFPE lubricant. This work has established the novel IL as the next-generation media lubricant for hard disk drives.

References

[1] Kryder MH, Gage EC, McDaniel TW, et al. Heat assisted magnetic recording. *Proceedings of the IEEE*. 2008;96(11):1810-1835.

[2] I. S. Jacobs and C. P. Bean, "Fine particles, thin films and exchange anisotropy," in *Magnetism,* vol. III, G. T. Rado and H. Suhl, Eds. New York: Academic, 1963, pp. 271-350.

[3] T. L. Gilbert, *Formulation, Foundations and Applications of the Phenomenological Theory of Ferromagnetism,* Ph.D. dissertation, Illinois Inst. Tech., Chicago, IL, 1956, unpublished.

[4] S. O. Demokritov, "Brillouin light scattering spectroscopy of magnetic nanostructures," *IEEE Trans. Magn.,*submitted for publication.

[5] E.H. Miller, "A note on reflector arrays," *IEEE Trans. Antennas Propagat.,* to be published.

[6] C.J. Kaufman, Rocky Mountain Research Laboratories, Boulder, CO, private communication, 2014.

Vector Recording: Advancing Areal Density in HAMR with Innovative Read Head Design

R. H. Victora[1], *Life Fellow IEEE,* Kamal Hosen[1], and M. F. Erden[2]

[1]Department of Electrical and Computer Engineering, University of Minnesota Twin Cities, USA.
[2]Seagate Technology, MN, USA. **Corresponding author:** victora@umn.edu

Heat-assisted magnetic recording (HAMR) enables enhanced areal density capacity (ADC) beyond that provided by perpendicular magnetic recording. However, the existing reader architecture restricts the increase in bits per inch (BPI) and tracks per inch (TPI), becuase it requires scaling down the reader dimension to read data with a smaller bit length and narrower track width. Recently, two-dimensional magnetic recording (TDMR) has shown some ability to increase the ADC of the reading process by relaxing the reader scaling, but this improvement is not sufficient to address the data storage crisis. In this paper, we propose a novel read head design to detect the magnetic field both perpendicular and parallel to the surface of the recording layer, thus resulting in higher ADC.

***Index Terms*—Reader Design, HAMR, Vector Recording, Read-Head Dimension, Areal Density.**

I. Introduction

The demand for data storage is growing exponentially over time due to modern technologies such as artificial intelligence and advanced communications. On the other hand, the hard disk drive (HDD) industry is experiencing a data storage crisis as the existing data storage architectures approach their limits in enhancing areal density capacity (ADC) [1]. In recent times, the HDD industry has shifted from perpendicular magnetic recording (PMR) to heat-assisted magnetic recording (HAMR) to meet this immense demand for data storage. In HAMR systems, ADC improvement is possible by writing smaller bits and narrower tracks. However, smaller bit length means high KBPI that demands small grain size. Narrower tracks have less need for small grain size, however, this likely demands new readback processes to be developed. The scaling of the reader width is approaching its limit [1] and a single reader is insufficient to further improve ADC. Over the years, researchers have proposed some alternative techniques as shown in Fig. 1 (b) where two written bits in two adjacent tracks result in four possible states (+ +, - -, - +, + -). In two-dimensional magnetic recording (TDMR), the readers can distinguish only three states and cannot differentiate between + - and - +. This limitation of TDMR reduces the effective ADC to $log_2(3)/log_2(4)$ = 79% of the original written ADC for a particular KTPI [2].

In this regard, Seagate has proposed a novel recording technique named "vector recording" to achieve better ADC with higher KTPI [2]. This technique consists of two readers: a conventional reader (R_c) and a vector reader (R_v), each scanning two tracks as shown in Fig. 1 (c). R_c reads the magnetic field perpendicular to the recording layer plane (R_c = T1 + T2) and is not able to distinguish magnetization conditions 3 (- +) and 4 (+ -). Therefore, to detect conditions 3 and 4 separately we have designed a vector reader (R_v) which reads magnetic field parallel to the media plane (R_v = T1 - T2) and is not capable of reading condition 1 (+ +) and 2 (- -). Now, by combining a vector reader with a conventional reader, we can successfully read four different writing states between two adjacent tracks, ensuring a 21% higher ADC than TDMR with the same KTPI and without any reduction in reader dimension. We demonstrate the compatibility of our novel reader design with existing HAMR systems and analyze its performance using micromagnetic simulations.

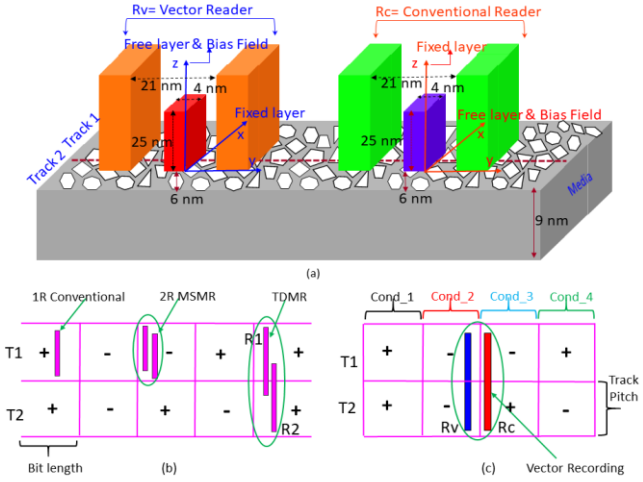

Fig. 1. (a) 3D schematic diagram of two readers with respective filed orientation. (b) Different types of read head architectures [2]. (c) Reading strategy of vector recording.

Figure 1 (a) shows the 3D schematic diagram of two readers along with their respective field orientation that we have considered in our reader simulations. For the conventional reader, we kept the fixed layer along the direction perpendicular to the media surface (along z axis) and the free layer was biased along the crosstrack direction (along x axis). For the vector reader we fixed our pinned layer along the x axis and biased the free layer along the z axis. Here the assembly moves from –y to +y direction (along down track direction) and reads perpendicular and parallel magnetic fields from the media by conventional and vector reader respectively. For the readback process we have calculated the magnetic head potential for both readers using the reciprocity theorem [3].

II. Signal-To-Noise Ratio (SNR) Analysis

We examined two distinct writing patterns in order to compare the performance of the new vector reader (R_v) with the conventional reader (R_c): same single tone (ST) on both

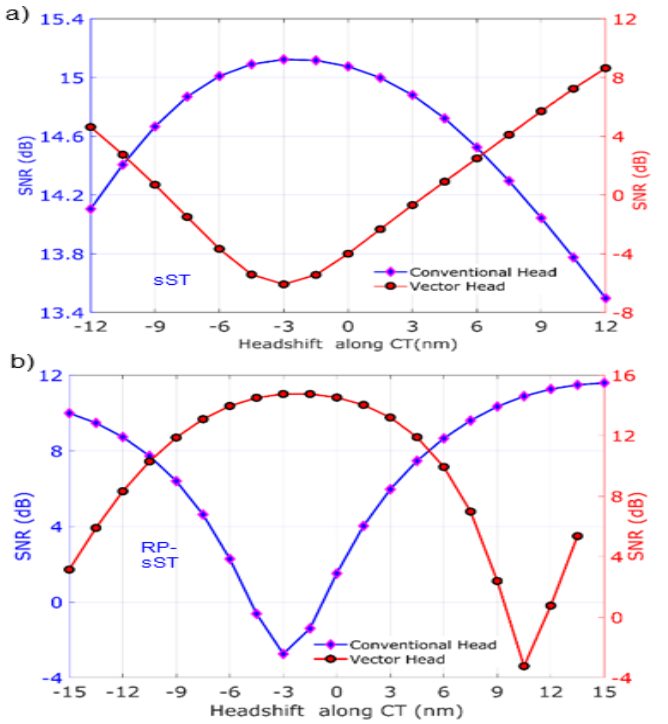

Fig. 2. SNR characteristics of conventional and vector reader at different head-shift position along cross track direction: a) sST, b) RP-sST.

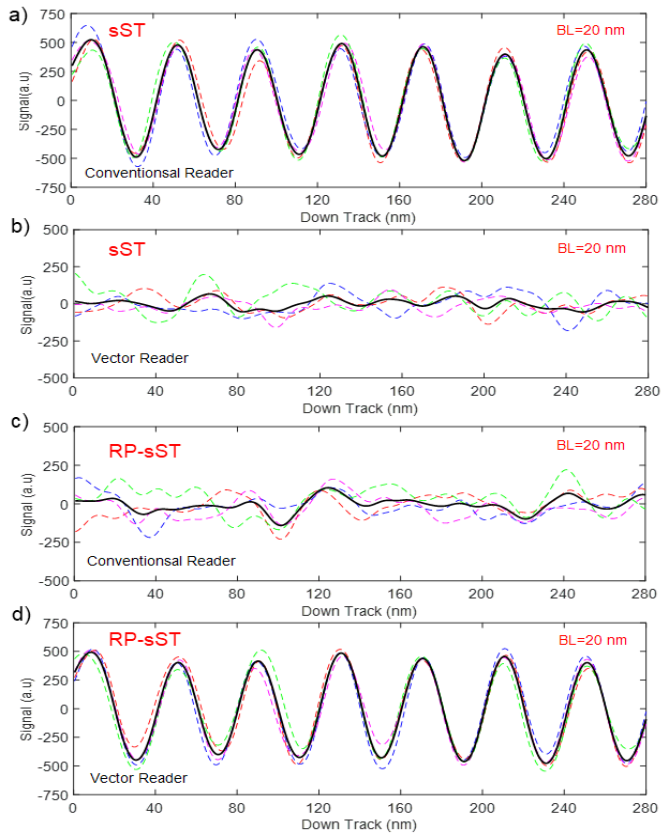

Fig. 3. Readback signals of conventional and vector reader for different single tone writing patterns at the track edge ; a) R_c with sST, b) R_v with sST, c) R_c with RP-sST, d) R_v with RP-sST.

tracks (sST) and same ST but with reverse polarity from one track to the other (RP-sST). For the sST writing pattern we first read signals using the (*Rc*), followed by the (R_v), and then calculated the SNR for both readers at different headshift positions along the cross track (CT) direction, as shown in Fig. 2 (a). From Fig. 2 (a) it is clear that the (R_c) SNR (blue line) exhibits a strong dependence on head position and provides maximum SNR around 15.2 dB at a headshift = -3 nm. As expected, only the (*Rc*) provides a strong signal because the presence of + + and - - magnetization states only produces a strong magnetic field along the perpendicular direction of the media surface. However, our newly designed (R_v) exhibits negative SNR (red line) at the track edge region as a result of the absence of + - and - + magnetization states, which would otherwise create a strong magnetic field along the parallel direction of the media surface. For the RP-sST writing pattern, we have performed the same reading technique and calculated the SNR characteristics of both (R_c) and (R_v), as shown in Fig. 2 (b). In contrast to the sST case, only the (R_v) reads a strong signal and provides the highest SNR of nearly 15 dB at headshift = -3 nm. This is because only the presence of + - and - + magnetization states creates a strong magnetic field parallel to the media plane. However, Fig. 2 (b) also shows that the SNR of R_c begins to peak up before and after the track edge region. This is because when we move R_c far from the track edge in the CT direction, it begins to read the signal from a single track, which improves the SNR.

III. Crosstalk Between Readers

The signal interference (crosstalk) between readers is a critical aspect of HAMR, given the narrower tracks and increased recording density; hence, it is essential to address this issue. We have performed readback signal analysis for both R_c and R_v with different writing patterns. The R_c and the R_v are anticipated to achieve their maximum and minimum signal power, respectively, for sST writing pattern. The readback signals of R_c and R_v along the downtrack position for sST writing pattern are shown in Fig. 3 (a)–(b). Here, the R_c provides strong readback signal as expected since only + + and - - magnetic states are available as shown in Fig. 3 (a). Conversely, the R_v is not intended to read any signals; rather, it detects weak, noisy signals as a result of the stray magnetic field that is generated by the minor lack of synchronization between two tracks as depicted in Fig. 3 (b). In the RP-sST writing pattern, Rv detects signals with optimal intensity since it only identifies the +- and -+ magnetic states, as shown in Fig. 3 (d). However, as seen in Fig. 3 (c), the R_c picks up noisy signals from the stray magnetic field produced by the small mismatch between the two tracks. In our simulation we used synchronized writing between tracks; this minor mismatch occurs mostly due to the curved transitions at the track edge region.

References

[1] R. Wood, M. Williams, A. Kavcic, and J. Miles, "The feasibility of magnetic recording at 10 terabits per square inch on conventional media," *IEEE Transactions on Magnetics*, vol. 45, no. 2, pp. 917–923, 2009.

[2] M. F. Erden, W. Eppler, S. Granz, and S. Hernandez, "Vector recording: A new read process at ultra high tpis," *presented at the IEEE TMRC Conference*, 2023.

[3] H. N. Bertram, *Theory of magnetic recording.* Cambridge University Press, 1994.

Pushing the Limits of Areal Density: Fusing Advanced Channel Coding, HAMR, and SMR in Next-Generation HDDs

Jonas Goode[1], Roger Wood[2], Rick Galbraith[3], Andreas Moser[2],
Pradhan Bellam[3], Iouri Oboukhov[3], Niranjay Ravindran[3], Amirhossein Sayyafan[1], Austin Striegel[3], and Henry Yip[1]

Western Digital Corporation, [1]Irvine, [2]San Jose, and [3]Rochester, USA · jonas.goode@wdc.com

Pushing HDD areal density to new extremes requires a fusion of cutting-edge technologies. This paper examines the interplay of advanced coding strategies, Heat-Assisted Magnetic Recording (HAMR), and Shingled Magnetic Recording (SMR), and how their integration enables substantial gains in areal density. We present a series of measured results demonstrating how jointly-optimized modulation and LDPC coding enhances performance across ePMR, HAMR, and SMR environments. Through these demonstrations, we showcase the tangible gains enabled by these technologies and outline a clear trajectory for continued areal density scaling in next-generation HDDs.

***Index Terms*— channel coding, hard disk drives, heat assisted magnetic recording, shingled magnetic recording**

I. Introduction

The relentless demand for higher storage capacity in hard disk drives (HDDs) necessitates aggressive advancements in areal density. Achieving significant gains from today's baseline requires more than incremental progress—it calls for a fusion of transformative technologies. Over the past decade, the channel coding strategies implemented in nearly all commercial HDDs have remained largely unchanged. Meanwhile, the recording physics—including ongoing use of energy-assisted Perpendicular Magnetic Recording (ePMR), as well as the emergence of Heat-Assisted Magnetic Recording (HAMR) and the increasing adoption of Shingled Magnetic Recording (SMR)—has shifted dramatically. These shifts demand a fundamental rethinking of channel coding design.

This paper presents a systematic exploration of three interdependent innovations: advanced coding strategies, HAMR, and SMR. We demonstrate how each contributes individually to areal density improvements, and more critically, how their interaction lays the foundation for a radical leap in HDD capabilities. Our combined analysis of these technologies outlines a clear path forward—one in which coordinated innovation across the full stack of read/write technologies is essential for enabling the next generation of ultra-high-density HDDs.

II. Modulation-aware coding for high-density recording

Channel coding is foundational to pushing areal density, especially as track pitch narrows and noise increases. In this section, we introduce a refined coding architecture that enhances both the modulation and Low-Density Parity-Check (LDPC) components, enabling deeper channel optimization.

One of the most persistent challenges in magnetic recording is the presence of consecutive transitions—closely spaced flux reversals—which generate particularly noisy and poorly resolved readback signals. Maximum Transition Run (MTR) codes address this by explicitly prohibiting transition runs beyond a chosen threshold (e.g., J=3), and continue to be effective in scenarios where full elimination of these high-risk patterns is achievable without excessive rate loss.

Rather than outright forbidding specific patterns or 'contexts', Mutual Information (MI) is used to shape the code toward less harmful patterns, reducing the occurrence of low-MI patterns while preserving a higher overall code rate. These codes-often implemented via constrained Markov models or arithmetic encoders-achieve a careful trade-off between pattern suppression and code rate. Figure 1 shows the MI across all 5-bit contexts for three modulation strategies: an unconstrained (uniform) code, a classic MTR (J=3) constrained code, and an MI-optimized code.

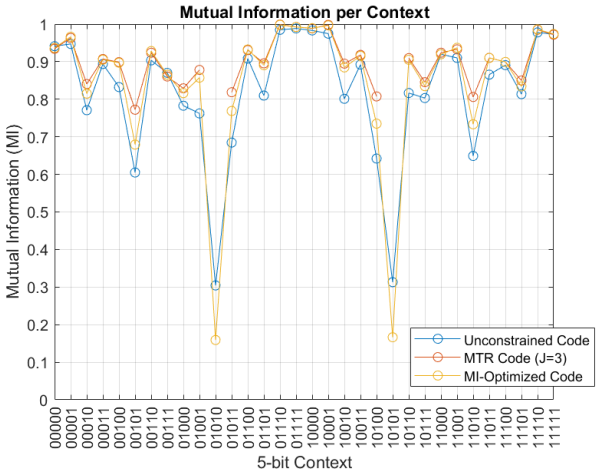

Fig. 1. Mutual information per 5-bit context for three modulation codes: Unmodulated, MTR (J=3), and MI-Optimized.

Layered on top, LDPC codes are re-optimized to account for these reshaped modulation statistics. Mutual information, a proxy for iterative decoder success, guides joint LDPC and modulation optimization [1]. Figure 2 illustrates a MI-based areal density contour. This surface serves as a map for identifying the modulation-LDPC pair that maximizes areal density for a given head/media/radius combination. The peak of the contour reflects the optimal pairing of modulation shaping and code rate, underscoring the need to co-design both elements as a function of channel conditions.

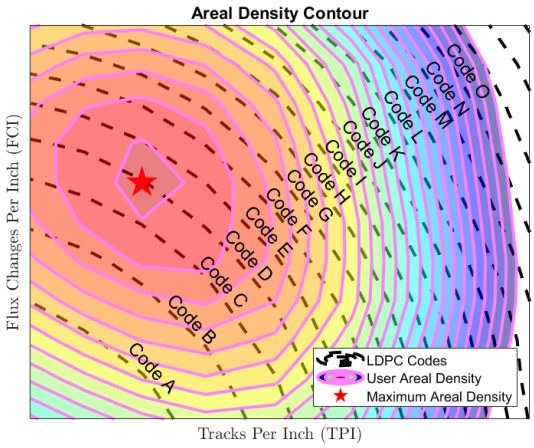

Fig. 2. Areal density contour based on mutual information. Color shows achievable density; dashed lines indicate optimized LDPC codes. Peak is found via joint modulation–LDPC optimization.

III. HAMR-DRIVEN TRACK PITCH REDUCTION AND CODING SYNERGY

HAMR enables narrower track pitch by focusing a tightly confined thermal spot on the media during writing, temporarily lowering the coercivity of high-anisotropy grains. This smaller thermal spot and sharper thermal edge gradient enable more precise magnetization switching without requiring increased write current and reduce adjacent track interference.

However, laser power must be carefully managed. While higher laser current can enhance signal quality and support higher linear densities, it also accelerates component wear. Operating at lower laser power improves reliability and extends lifetime — but also degrades SNR and increases jitter.

While HAMR alone provides areal density gains over ePMR, further improvement is enabled when the modulation and LDPC codes are optimized for the degraded channel conditions at reduced laser power. Figure 3 shows the areal density gain versus laser current. While the optimal Bits Per Inch (BPI) may decrease slightly at these lower laser powers, the associated Tracks Per Inch (TPI) gains more than compensate, yielding a net increase in areal density. This further lowers the Bit Aspect Ratio (BAR), enabling density scaling beyond ePMR.

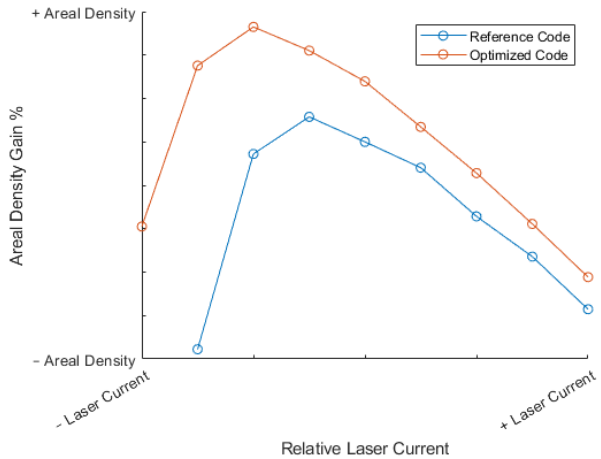

Fig. 3. Areal density and lifetime improvements via laser current reduction

IV. SHINGLED MAGNETIC RECORDING IN HIGH-TPI REGIMES

Shingled Magnetic Recording is inherently well-suited to achieving high TPI values, and its benefits are magnified when combined with advanced coding strategies and HAMR. Even in conventional ePMR environments, joint modulation and LDPC code optimization yields measurable areal density improvements, providing a viable path to extend ePMR product life at higher densities.

When these same coding optimizations are applied within ePMR SMR environments, further gains are realized. However, the most compelling opportunities arise when these techniques are paired with HAMR. With the ability to reduce track pitch via laser current control, HAMR enables significantly denser track layouts. In this regime, SMR recording further amplifies the gains achieved through optimized coding, surpassing 1 million TPI with ease.

As track pitch continues to shrink, the BAR naturally decreases, and inter-track interference (ITI) becomes a dominant noise source. In this high-ITI regime, additional areal density gains are achieved by explicitly equalizing interference from adjacent tracks. If modulation and LDPC codes are re-optimized for this interference-equalized environment, the cumulative gain is substantial — as highlighted in Figure 4, where SMR with ATE (adjacent-track equalization) delivers a total improvement of over 60% compared to the Conventional Magnetic Recording (CMR) baseline.

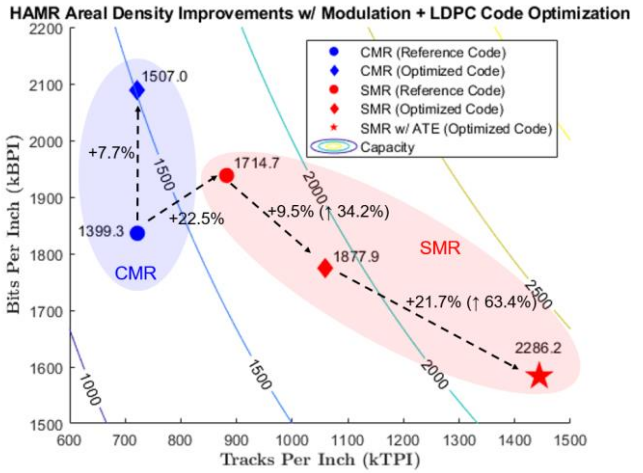

Fig. 4. Areal density achieved across HAMR CMR and SMR recording modes using reference and optimized modulation + LDPC codes. The final point reflects further gain from SMR with adjacent-track equalization (ATE). All data shown are measured under identical test conditions

These results highlight how continued gains in TPI are driving the BAR steadily closer to 1.0—a trend that opens the door to new architectural strategies for sustaining areal density growth. Together, these findings reinforce that the HDD remains a vibrant and evolving platform for innovation.

REFERENCES

[1] Galbraith, R., “Use of Mutual Information as a Channel Metric”, TMRC 2024

[2] Shannon, C.E., “A Mathematical Theory of Communication”. Bell System Technical Journal, 27, 379-423

Efficient Multidimensional Signal Processing Scheme for Heated-Dot Magnetic Recording with Triple-Layered Bit Patterned Media

Hidetoshi Saito, *Member, IEEE*, and Fumiko Akagi, *Member, IEEE*
Graduate School of Engineering, Kogakuin University, 1-24-2 Nishi-Shinjuku, Sinjuku City, Tokyo, 163-8677, Japan
h-saito@cc.kogakuin.ac.jp, fumiko.akagi@cc.kogakuin.ac.jp

This research explores a new method of multidimensional signal processing which is applicable to a heated-dot magnetic recording (HDMR) system using triple-layered bit-patterned media (BPM). For each data sequence recorded on a single track of respective layers, the proposed signal processing scheme detects each data sequence in the order of upper layer, middle layer, and lower layer. Our proposed method further expands the existing method which is applied to the signal pressing scheme using double-layered BPM. This new method is expected to be applied to a HDMR system with an effective recording density of up to 7.5 Tdpsi. The proposed HDMR system with triple-layered BPM uses two types of multiple symbol detectors and a single one-dimensional (1D) symbol detector. The effective transmission rate of the proposed HDMR system is capable of increasing three times that of the HDMR system with single-layered BPM. It is evaluated that the error rate performance of the proposed HDMR system gives a significant improvement over the conventional HDMR system with single-layered or double-layered BPM by computer simulation.

***Index Terms*—heated-dot magnetic recording, multi-layered recording, triple-layered bit-patterned media, two-dimensional generalized partial response equalization**

I. Introduction

The recently emerging combined technologies for high areal density digital magnetic recording have been introduced to attain an effective recording density of 5 Tdpsi [1]. These technologies consist of the following three elemental technologies: heated-dot magnetic recording (HDMR), double-layered magnetic recording, and multi-track recording. As a result, this combinational method using above three elemental technologies is useful for increasing the effective transmission rate of the HDMR system with double-layered bit-patterned media (BPM). However, considering the signal-to-noise ratio (SNR) of the reproducing signals generated from the recorded data in both top and bottom layers, the SNR of the reproducing signals generated from the bottom layer significantly deteriorates compared to that of the reproducing signals generated from the top layer. In other words, increasing the effective transmission rate leads to suppressing deterioration of signal quality regarding transmission using a plurality of magnetic recording media. Based on this combinational method, we propose *the two-stage signal processing scheme* as an effective signal processing technique [1], [2]. This two-stage signal processing scheme is provided with two serially connected one-dimensional (1D) multi-level log-likelihood ratio (LLR) detectors for two-track recording and detects the data sequences recorded on both top and bottom layers in turn. In this digest, we will expand the existing two-stage signal processing approach mentioned above and propose a new three-stage signal processing scheme for the HDMR system with triple-layered BPM. This HDMR system is capable of achieving an effective recording density of 7.5 Tbpsi. This proposed scheme is constituted of three-stages of 1D LLR detectors for single-track recording in cascade connection. Every recorded data sequence in each layer is detected at each stage in the order of upper layer, middle layer, and lower layer. After completing three-stage detection, the total error rate performance is evaluated.

II. Proposed HDMR System

Fig. 1 shows the block diagram of the proposed HDMR system with triple-layered BPM and the three-stage signal processing scheme. We assume the head/medium conditions and modeling with FePt granular magnetic media to achieve an areal density of 2.5 Tdpsi for each layer using micro-magnetic simulation. A raw data sequence $\{a_k\}$ is input to each encoder which generates run length limited (RLL) constraint sequences with no error correction coding $\{b^u_{i,k'}\}$, $\{b^m_{i,k'}\}$, and $\{b^\ell_{i,k'}\}$ for the down-track direction in the upper, middle, and lower layers, respectively. The notations of u, m, ℓ correspond to the upper, middle, and lower layers, respectively.. The notation of i represents the track number for the cross-track direction while k and k' represent the symbol numbers for the down-track direction. The sequences $\{b^u_{i,k'}\}$, $\{b^m_{i,k'}\}$, and $\{b^\ell_{i,k'}\}$ are transformed into the precoded sequences $\{c^u_{i,k'}\}$, $\{c^m_{i,k'}\}$, and $\{c^\ell_{i,k'}\}$, respectively.

For the readback channel, the readback signal of BPM is represented by the evaluated two-dimensional (2D) pulse response obtained by the defined BPM model. The readback signal waveform $\{r_{i,k'}\}$ is given by as follows. $r_{i,k'} = r^u_{i,k'} + r^m_{i,k'} + r^\ell_{i,k'} + n_{i,k'}$, where the noise sequence $\{n_{i,k'}\}$ is added at the reading point and $n_{i,k'}$ is additive white Gaussian noise (AWGN) with zero mean and variance σ_n. The reproducing waveforms corresponding to the recording sequences readback by the reading head are input into the equalizer which consists of a 2D low-pass filter (LPF) and the 2D transversal filter (TVF). Equalization is performed so that the overall characteristic between the input of the recording head and the output of each equalizer is equal to the aimed 2D generalized partial response (GPR) targets $\boldsymbol{g}_t$. The equalizer output sequence $\{y^j_{k'}\}$ is obtained which sums equalizer output sequences from trios of upper, mididle, and lower dots. Tap-gain coefficients in the 2D TVF are evaluated by minimizing the expectation of the mean square error $E(\{e^j_{i,k'}\})$, where

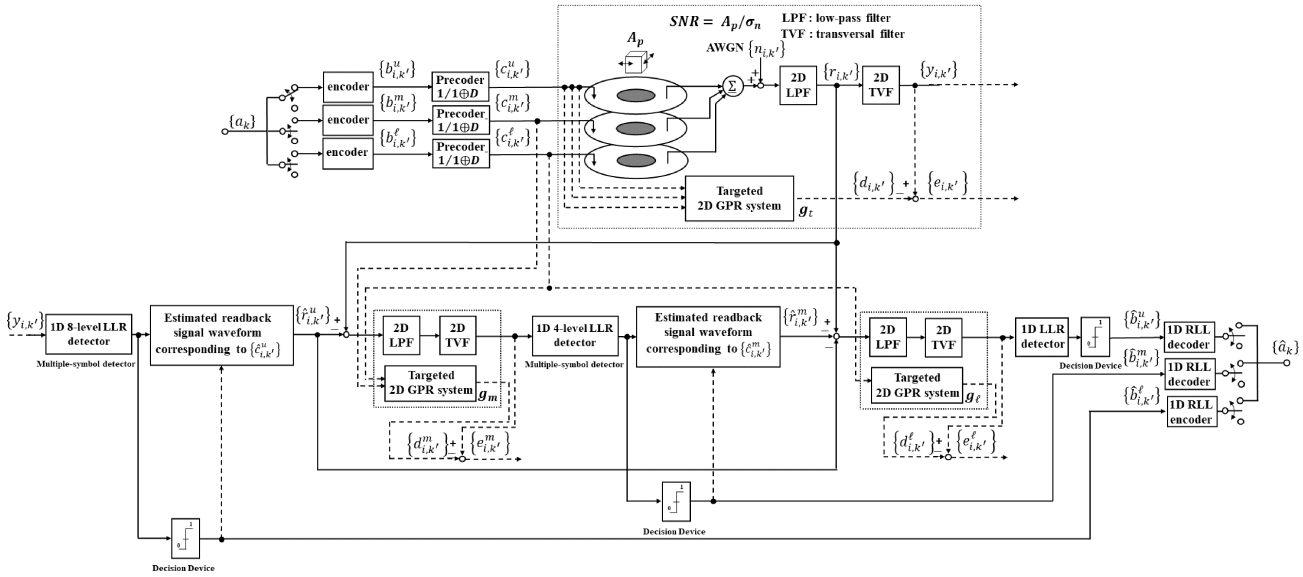

Fig. 1. The block diagram of the proposed HDMR system with triple-layered BPM.

the sequence $\{e^j_{i,k'}\}$ is the equalized error sequence between the ideal GPR target output sequence $\{d^j_{i,k'}\}$ and the sequence $\{y^j_{i,k'}\}$. The SNR at the reading point is defined as the ratio of the normalized peak amplitude A_p and the noise power of AWGN.

In the decoding process, the sequence $\{y^j_{i,k'}\}$ is detected by respective 1D LLR detectors during the decoding process of each stage. The estimated sequence $\{\hat{c}^u_{i,k'}\}$ is given as the first detector outputs. From the sequence $\{\hat{c}^u_{i,k'}\}$, we generate the replicated readback signal waveform $\{\hat{r}^u_{i,k'}\}$ corresponding to the sequence $\{\hat{c}^u_{i,k'}\}$. Using this first replicated waveform $\{\hat{r}^u_{i,k'}\}$, we can obtain the second replicated waveform $\{\hat{r}^m_{i,k'}\}$ as the difference waveform between the waveforms $\{r_{i,k'}\}$ and $\{\hat{r}^u_{i,k'}\}$. The replicated waveform $\{\hat{r}^m_{i,k'}\}$ is input into 2D TVF and equalized to generate the aimed 2D GPR re-equalized sequence and the second 1D LLR detector gives the estimated sequence $\{\hat{b}^m_{i,k'}\}$ from this re-equalized sequence. Moreover, using the second replicated waveform $\{\hat{r}^m_{i,k'}\}$, we can obtain the third replicated waveform $\{\hat{r}^\ell_{i,k'}\}$ as the difference waveform between the waveform $\{r_{i,k'}\}$ and the synthetic waveform created by combining two replicated waveforms $\{\hat{r}^u_{i,k'}\}$, $\{\hat{r}^m_{i,k'}\}$. The sequences $\{\hat{b}^u_{i,k'}\}$, $\{\hat{b}^m_{i,k'}\}$, and $\{\hat{b}^\ell_{i,k'}\}$ are decoded by respective RLL decoders. After demodulation, we get the estimated input sequence $\{\hat{a}_k\}$. The bit error rate (BER) performance is evaluated by computer simulation between the sequences $\{a_k\}$ and $\{\hat{a}_k\}$.

III. Error Rate Performance Evaluations

Fig. 2 shows the BER performances for several three-stage schemes for HDMR systems. These signal processing schemes use the same 64/65 (0,8) RLL coding scheme. In Fig. 2, the symbol of ◯ shows the BER performance of the proposed three-stage signal processing scheme with the triple-layered BPM. This three-stage signal processing scheme has three different 1D LLR detectors to detect recording sequences recorded in the upper, middle, and lower layers.

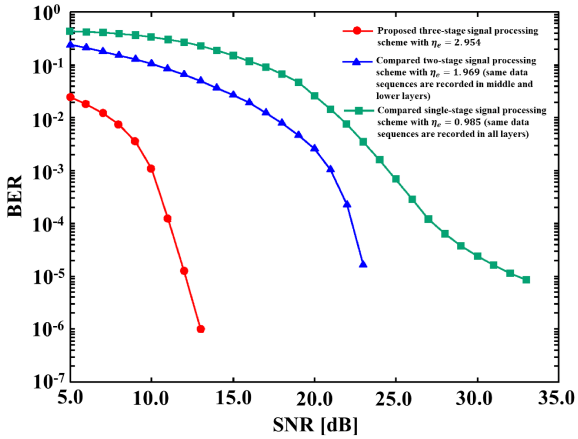

Fig. 2. BER performances of several three-stage signal processing schemes.

The proposed three-stage signal processing scheme has *the effective transmission rate* η_e = 2.954. The symbols of △ and □ show the BER performances of the compared two-stage and single-stage signal processing scheme with triple-layered BPM, respectively. These two compared schemes have the rate η_e = 1.969 and 0.985. Compared to these schemes, it is found that increasing the rate η_e leads to remarkably improve the error rate performance of the HDMR system.

IV. Conclusion

In this research, we propose a three-stage signal processing scheme for a HDMR system with triple-layered BPM. The simulation result shows that our proposed signal processing scheme is useful for improving the error rate performance of the HDMR system with triple-layered BPM.

References

[1] H. Saito, *IEEE Trans. Magn.*, vol. 59, no. 3, 3000810, Mar. 2023.
[2] H. Saito and F. Akagi, *IEEE Trans. Magn.*, vol. 61, no. 4, 3100210, Apr. 2025.

Head for 64 Channel Tape Recording

Robert G. Biskeborn, David J. Seagle and Trevor Olson

Western Digital Corporation, San Jose, CA 95119, USA, robert.biskeborn@wdc.com

Linear magnetic tape systems have taken many forms over the past 73 years. An important example is the transition from open tape reels to ½" tape cartridges beginning in the 80's. In 2000, tape drives built to the new "Linear Tape Open" (LTO) specification launched. Cartridges held 0.1TB, and tape heads had 8 concurrently operable write/read channels, supporting a data rate of 20MB/sec. LTO is now in its 10th generation, with cartridges holding 30TB, and heads having 32 concurrently operable channels, supporting a data rate of 400MB/sec. The 2024 INSIC Tape Technology Roadmap anticipates continued sustained capacity growth, a doubling to 64 active channels and a data rate of more than 800MB/sec, in a small number of years. This talk discusses head design challenges and concludes with an outlook for a future head and drive.

***Index Terms*—Linear tape recording, multi-channel recording heads, tape dimensional stability, magnetostatic crosstalk**

I. Introduction

MODERN tape libraries may house up to several thousand ½" tape cartridges and store over 100PB. Data access is handled by robots that retrieve the cartridges and hand them off to any available drives. After a tape is queued, it is wound onto the drive take-up reel at high speed, e.g., 10 or more m/s, to its starting location. Data can then be written (appended) or read at up to the drive's maximum data rate, host permitting, e.g. 400MB/s for the "Linear Tape Open" (LTO) 10th generation tape drive. This is more than 1.4x higher than the maximum data rate of a modern HDD at its OD, and unlike HDD, which is nearly 2x slower at its ID, does not diminish as the medium fills. Tape drives achieve this data rate despite having significantly lower head-to-medium velocity of ~2-6m/s, vs approximately a 33.5m/s maximum velocity for a 7200rpm HDD, and lower linear density, as will be discussed.

II. Multiple Active Channels

A. Background

That tape has inherently lower single channel data rate stems from the fact that tape media is particulate, unlike HDD, which transitioned to sputtered media 40 years ago. Accordingly, tape magnetic coating is both thicker (~50nm) and rougher than disk coating and has significantly larger magnetic "grains" (particles). Furthermore, tape is contact recording, so the head elements, particularly sensitive magneto-resistive read sensors, must be recessed after lapping, e.g., by ion-milling; and the tape bearing surfaces must be provided with relatively thick dielectric protective coatings. Today, effective magnetic spacing for tape is roughly 35-45nm [1], compared to less than 2-3nm for HDD. Thus, linear density (bits/um) for tape is more than 10x lower than it is for disk. So, today as in the past, tape drives rely on deployment of multiple, concurrently active transducing elements to achieve target data rates.

B. LTO format

The first LTO drives, which launched in 2000 (with a cartridge capacity of 100GB), had 8 concurrently operating write/read channels supporting a data rate of 20MB/s. The array of write/read channels was flanked by timing-based servo (TBS) readers at each end and spanned slightly less than ¼ of the ½" tape width. Five servo tracks divides the tape into 4 equal regions called "data bands," each being 2859um wide. The consortium anticipated that the number of active channels in the drive would need to increase every few generations to maintain drive performance [2]. Further, it envisioned that, if possible, each new generation would support up to twice the capacity of the previous generation and would also support writing tapes from the previous one, and reading tapes from the previous two, generations. Accordingly, the pitch between legacy channels is fixed, and channel count increases twofold when more are needed. The net is that the pitch between legacy and new channels drops precisely 2x. The width of the servo tracks on tape may change but their centerline spacing does not. Finally, ASIC design constraints mandate design choices compatible with doubling.

TABLE I
Tape Drive Parameters

gen	year	channels	capacity (TB)	data rate (MB/s)	hours to fill	one-way wraps	tape length (m)	linear density (bits/um)	tracks
1	2000	8	0.1	20	1.38	48	609	4.88	384
2	2003	8	0.2	40	1.38	64	609	7.40	512
3	2005	16	0.4	80	1.38	44	680	9.64	704
4	2007	16	0.8	120	1.85	56	820	13.25	896
5	2010	16	1.5	140	3.17	80	846	15.14	1280
6	2012	16	2.5	160	4.33	136	846	15.14	2176
7	2015	32	6	300	5.55	112	960	19.09	3584
8	2017	32	12	360	9.27	208	960	20.67	6656
9	2021	32	18	400	12.50	280	1035	21.46	8960
10	2025	32	30	400	20.83	462	1035	21.65	14784

Table 1 shows that in 2005, the number of active channels increased from 8 to 16 for the 3rd generation drive, and again in 2014 from 16 to 32 for the 7th generation drive. In both cases, elements were added between the legacy elements. Pitch between was 333um for the 1st generation and is currently 83.35um. Increasing the number of channels, results in fewer

one-way "wraps" needed to fill the tape, thus minimizing wear and tear of the tape, head and the drive, and addressing the time needed to fill the tape (capacity/data rate). It also helps to enable data rate growth while keeping tape speed below ~6.5m/s. The strategy of increasing channels by doubling also enables preserving the tape 4-data band format. However, it is to be noted that the 32-channel 10th generation drive does not support backward read or write compatibility due to a modification of the head-tape interface.

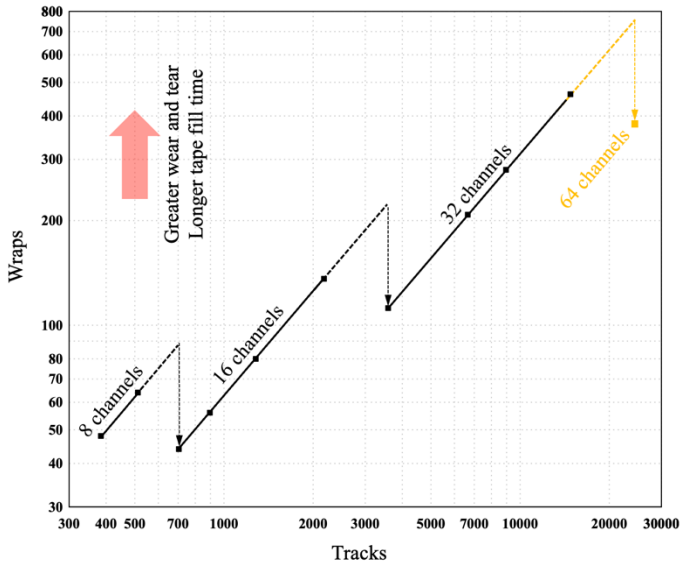

Fig. 1. Number of wraps versus tracks for the 10 tape generations shown in the table. Note that Wraps = Tracks / Channels. The 64 channels data point is anticipated based on the historical trend, which is driven by need to minimize wear and tear, tape fill time and tape velocity.

C. *Transition details*

First generation LTO heads from IBM deployed 8 write and 8 read elements in an alternating side-by-side arrangement (as opposed to piggyback). In that configuration, each element in the array is on a half pitch of 166.5um. Thus, there was no need to change transducer pitch for the transition to 16 channels. For that, single elements were replaced by piggy-back reader-writer pairs. However, this did bring a substantial increase in wiring complexity. The transition to 32 channels presented new challenges, as it meant adding elements where there were none. And making these piggyback pairs would have resulted in very congested I/O, as well as creating other problems. A decision was made to build the writers and readers on separate wafers. This resulted in 32-channel tape heads having 3 modules (2 writers and a central reader) as described in [3].

III. 64 Channels Strategies

Doubling the number of channels again, from 32 to 64, presents even greater challenges. The question of whether backward compatibility is required is beyond the present scope, and so the authors will explore two basic strategies that they believe potentially support backward compatibility to LTO10.

The first of these is to adopt the 32-channel strategy, namely insert recording elements between the existing elements, thus reducing the element pitch to 83.25 / 2 = 41.625um. This is shown with the current 32-channel head in the top and middle schematic drawings of Fig. 2. For this, the write transducer yoke and coils (presently a 2-layer 14 turn design), would require a major redesign to fit in half the space. A concern is writer-to-writer magnetostatic crosstalk, a phenomenon that was investigated and shown to degrade channel performance [4]. Whether or not the yoke can be designed such that crosstalk is acceptable depends on design details beyond the scope of this digest.

Fig. 2. Two approaches that address the transition to 64 active channels. In the "Squeezed 64 channels," all transducers are in the same span as in the 32-chsnnles head. In the "Dual 32-channels," the 32-channel array is duplicated, and the two span two (of 4) data bands.

A second strategy takes a very different approach. This is shown in the lower drawing of Fig. 2. Here, rather than squeezing the elements to fit into the existing 32-channel head span, the current 32-channel element array is duplicated and re-centered, thus creating a pair of arrays that share the central servo reader(s). This preserves element pitch and transducer dimensions. But it also doubles the span between outermost servo reader(s), potentially affecting alignment between head and recorded tracks due to a phenomenon called Tape Dimensional Stability (TDS). One method [5] for dealing with linear TDS is based on making small changes to a nominally tilted head to align projected head span with the tape. However, linear compensation does not address mis-registration due to non-linear distortion (head and/or tape) which could potentially impact achievable capacity. Presumably, misregistration can be dealt with via mechanical engineering principles, which is preferable to having to face fundamental principles of physics, e.g., magnetostatic crosstalk.

IV. Outlook

The dual 32-channel head records data over a twofold wider (6mm) region than a squeezed 64-channels configuration, thus enabling ECC to better deal with non-functioning read elements. For comparison, in HDD ECC is confined to a 50nm wide region. With non-linear TDS remediation, a 128 channels head comprised of two dual-32 channel arrays may be possible.

References

[1] INSIC International Magnetic Tape Storage Technology Roadmap 2024, White Paper, 2024
[2] lto.org/roadmap
[3] R. G. Biskeborn, "Head and interface for high areal density tape recording," IEEE Transactions on Magnetics, vol. 48, no. 11, Nov. 2012.
[4] R. G. Biskeborn, P. Hergert, and P. O. Jubert, "Crosstalk between write transducers," IEEE Transactions on Magnetics, vol. 44, no. 11, Nov. 2008.
[5] John S. Judge and Robert A. Johnson, "Method of reading recorded information from a magnetic tape that compensates for track pitch change," US Patent 6,141,174, Quantum Corporation, Oct. 2000.

The Viability of Single Pass Three Level Recording in HAMR

Jian-Gang (Jimmy) Zhu[1], *Fellow, IEEE*

[1]Data Storage Systems Center, Electrical and Computer Engineering, Carnegie Mellon University, USA, jzhu@cmu.edu

The atomic structure of a highly ordered FePt $L1_0$ grain provides the possibility for domain wall trapping sites within the grain. Near zero magnetic moment grains at recorded transition centers would yield a significant reduction of transition jitter noise, enabling high track density capability. This characteristic property would also enable single pass three level recording for which a zero magnetization state can be created with zero recording head field. The zero moment grains in the zero magnetization-level bit yields significant medium noise reduction and making the three-level recording potentially viable.

***Index Terms*—HAMR, Magnetic Recording, HDD, FePt, L10 grain, three-level recording.**

I. Introduction

FePt $L1_0$ granular thin film as the media for heat assisted magnetic recording (HAMR) has some very important characteristics [1]. In specific, an ordered $L1_0$ FePt grain consists of Fe and Pt atomic monolayers alternating along grain height perpendicular to the thin film plane. For a pure Pt monolayer, the exchange coupling between the two adjacent Fe monolayers would depend on the induced spin polarization of the Pt atoms. If the two Fe monolayers are magnetized in parallel, the Pt atoms would be spin polarized, consequently mediating ferromagnetic exchange coupling between the two Fe monolayers. If the two Fe monolayers happen to be oppositely magnetized, the Pt atoms in between would not be polarized, leading to zero exchange coupling between the Fe monolayers. In such case, the two oppositely magnetized Fe monolayers can be stable and the Pt layer effectively becomes a domain wall trapping site. If the order parameter of the FePt grain is not sufficiently high, a Pt monolayer could contain significant number of Fe atoms, yielding direct exchange coupling between the Fe monolayers. However, if the order parameter is a near unity, wall trapping site could form on a highly pure Pt monolayer.

The domain wall trapping sites within a FePt $L1_0$ grain in HAMR media can lead to formation of zero moment grains at recorded transition centers and the existence of zero moment grains at center of recorded transitions significantly reduces transition noise [2]. In this study, we investigate the viability of single-pass three-level recording for media with and without the wall trapping sites within the grains in FePt $L1_0$ HAMR media. With each bit-interval having three choices of magnetization levels $(+1, 0, -1)$, the linear density increases by 50%.

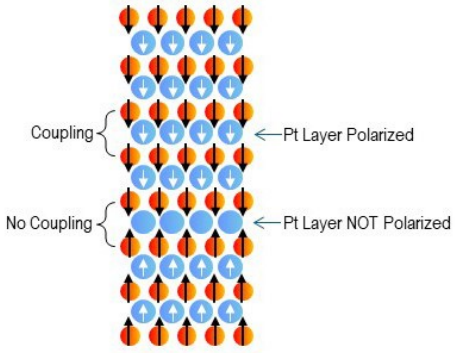

Fig. 1 Illustration of the proposed exchange coupling mechanism between adjacent Fe atomic monolayers in a perfectly L10 ordering with orange circles for Fe atoms and light blue for Pt atoms.

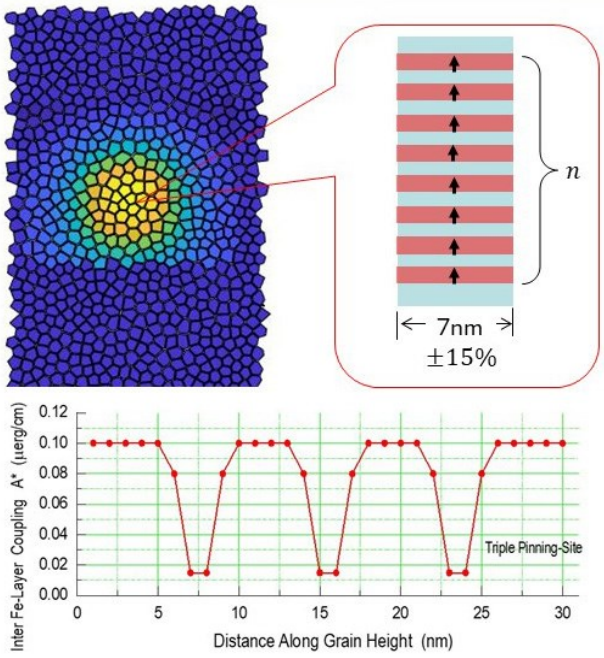

Fig. 2. Micromagnetic model setup for simulating heat-assisted magnetic recording process. A grain comprises of 32 Fe monolayers, with each monolayer represented by a macro-spin. A reduction of interlayer exchange coupling models a possible domain wall trapping site.

II. Modeling of $L1_0$ FePt Granular Media

The detailed recording model has been introduced in previous publications [2][3]. For the work presented here in specific, grain size follows a gaussian distribution of $\sigma = 15\%$ and mean $\overline{D} = 7nm$. Grain Curie temperature distribution has a of $\sigma = 15\%$ and a mean $\overline{T_C} = 660\ K$. Recording processes are simulated using a generic NFT with peak temperature of the recording thermal profile is $T_{peak} = 780K$ and resulting curved transitions are studied. In addition, a straight cross-track front thermal profile is also created by extend the track center temperature uniformly across recording track for noise analysis.

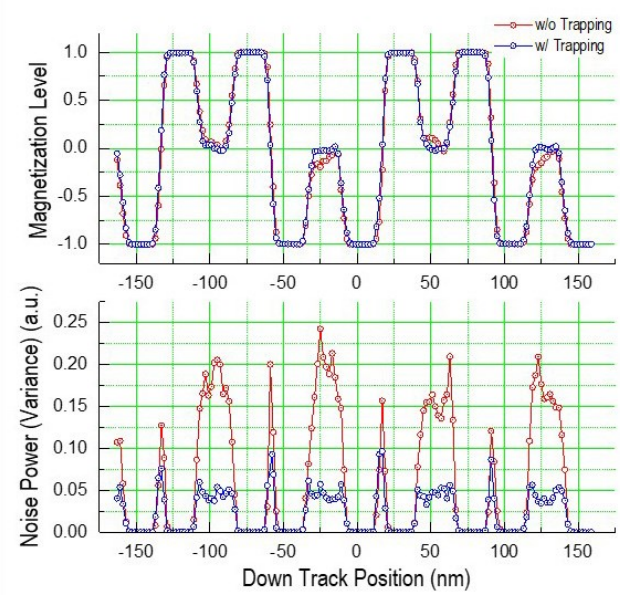

Fig. 3. Calculated three-level recording transition proffile mean (upper) and variance (lower) for media grains with (blue) and without (red) wall trapping sites within each grain. Straight cross-track thermal profile is assumed. 100 recording processes on different granular realizations are used for the statistics.

III. Results and Discussions

Single-pass three-level recording processes are simulated with zero-level state created by zero recording head field. Figure 3 shows three-level recording results at a bit-length of $B = 25nm$. The identical recording process is repeated 100 times on different realizations of the Voronoi granular structure. The upper graph in the figure shows the statistical mean of the transition profiles for media grains with (blue) and without (red) wall trapping centers. For the case of media grains with wall trapping centers, the mean magnetization level for the "zero" state in between the two "1"s is well defined, and the medium noise power (variance) is substantially lower than that of the case without wall trapping sites in the medium grains. Figure 4 shows the recorded magnetization patterns corresponding to the results shown in Fig. 3. For the medium of grains with wall

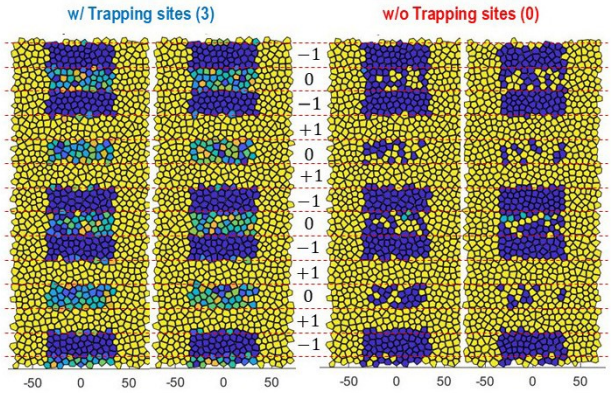

Fig. 4. Three-level recording granular magnetic momennt patterns for media grains with zero trapping site (left two) and three per grain (right two). The bit length is B=25nm.

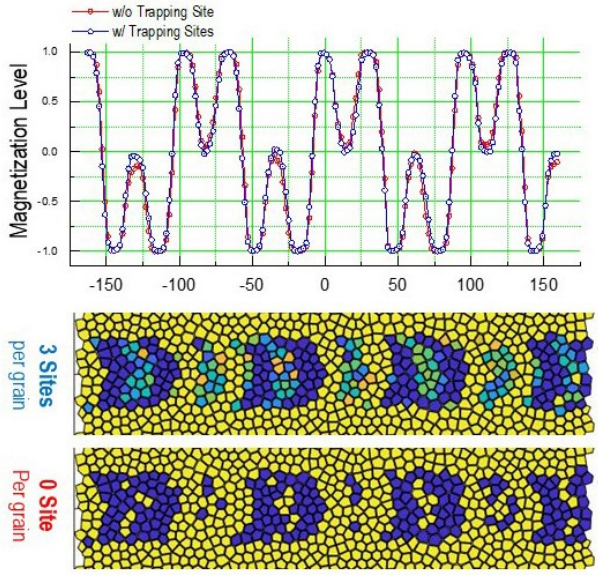

Fig 5. Three-level recording simulation with bit length B=16nm and a thermal profile by a generic lollipop NFT which result in curved transition fronts. Two cases shown here: a medium of grains with wall trapping sites (blue) and that grains without wall trapping sites (red). The read track width is 20nm.

trapping sites, the state of zero magnetization level is formed by zero moment grains (indicated by light blue color) whereas for the media of grains without wall trapping site, the zero magnetization state is formed by a combination of positive and negatively magnetized single domain grains in the perpendicular direction. The zero moment grains in the zero magnetization state created absent of head field is the key for the low medium noise level.

Figure 5 shows the three-level recording with the thermal profile of a generic near field transducer (NFT) which results in curved transition fronts. The bit length is B=16nm. For the "0"-state, always sandwiched in between two "1"s in this case, the magnetization level is zero for the media of grains with trapping sites whereas magnetization deviates away from zero for the media without trapping site.

In conclusion, single-pass three-level recording should be viable if FePt grains can achieve sufficiently high $L1_0$ ordering so that wall trapping sites can be formed in FePt grains. It should be mentioned that trapping sites could also be artificially engineered [4][5].

References

[1] G. Ju *et al*., "Heat Assisted Magnetic Recording – Next Generation Mass Storage Technology," *2018 IEEE International Magnetics Conference*, Singapore, 2018, pp. 1-1, doi: 10.1109/INTMAG.2018.8508092.

[2] J.-G. Zhu and Y. Yan, "Incoherent Magnetic Switching of $L1_0$ FePt Grains," *IEEE Trans. Magn.,* vol.57, No.3, 3200809 (2021)

[3] J.-G. Zhu, *et al*, "The Enabling Mechanism for High Track Density in HAMR," *IEEE Trans. Magn*., vol. 61 (4), 3000509 (2025).

[4] T.Y. Chang, et al, "Zero-State Insert Dual Layer HAMR Media Recording," *IEEE Trans. Magn.* Vol. 59, 3200107 (2022).

[5] P. Tozman, *et al*, "Dual-layer FePt-C granular media for multi-level heat-assisted magnetic recording," *Acta Materialia*, vol. 271, 119869 (2024)

Development of Co-Mn-Al thin films with giant anomalous Hall effect towards read head applications

Murali Krishnan M[1], Ryo Toyama[1], Tomoya Nakatani[1], Hirofumi Suto[1], Suwannaharn Nattamon[1], Taisuke Sasaki[1] and Yuya Sakuraba[1]

[1]Research Center for Magnetic and Spintronic Materials, National Institute for Materials Science, 1-2-1, Sengen, Tsukuba, Ibaraki 305-0047, Japan. manikketh.muralikrishnan@nims.go.jp

Recent advancements in magnetic recording densities have led to a growing demand for a new read head technologies achieving sufficient SNR in a small sensor size. Anomalous Hall effect (AHE) sensors can be a suitable candidate for the next generation read heads. In this work we explore the composition dependence of AHE in Co-Mn-Al (CMA) Heusler alloys for a wide range of compositions within a small deposition area. For this, we employed a high-throughput technique based on composition gradient films fabricated by combinatorial sputtering. The AHE results from this two-dimensional (2D) composition-spread film provided a critical range of Co, Mn and Al compositions within which one can yield the best AHE properties. This experiment demonstrated that Al-rich off-stoichiometric compositions provided higher anomalous Hall resistivity (ρ_{yx}) than the stoichiometric one. In order to have a detailed material investigation and to study the post-annealing temperature (T_A) dependence, uniform films with composition based on the above results were prepared. The highest ever reported value of ρ_{yx} (~ 30 μΩ·cm) for films post-annealed at 500 °C has been achieved on a Si/SiO$_x$ substrate. The results show that CMA Heusler alloys are potential candidates for application in AHE based reader devices.

***Index Terms*—Anomalous Hall effect, magnetic read-head, Heusler alloys, combinatorial sputtering, composition-spread films.**

I. Introduction

THE ever-increasing demand for higher areal density in hard disk drives (HDDs) necessitates the development of advanced magnetic sensor materials for read head devices with improved reading resolutions and signal-to-noise ratio [1]. AHE-based reader devises have been identified as promising candidates for the next-generation read head technologies due to their high linearity, larger dynamic range, high output voltage, and predicted low noise level [2]. A schematic diagram showing an AHE-reader for reading the magnetization information from magnetic bits is shown in Fig. 1a. The schematic of currently used TMR reader and a proposed structure for AHE reader are shown in Fig. 1c and 1d. The AHE reader has a simpler structure with a single sensing layer. Thicker sensing layers can be used within the allowable gap space, unlike the free layers in TMR readers. This increased thickness helps suppress magnetization noise caused by thermal fluctuations, which is a major issue in miniaturized readers. In [2] the output voltages for AHE-based sensing layer (SL) and a TMR-free layer (FL) in response to an external field (analogous to a media field from magnetic bits) is estimated based on micromagnetic simulations (see Fig. 1b). The output voltage in the case of TMR is clearly assymetric in comparison to AHE. Higher linearity and improved dynamic range is also attained for AHE based SL. The requirement of materials with large AHE, from an application viewpoint to overcome the issues such as bias current shunting and output voltage leakage is also pointed out in this work. A giant room-temperature AHE with ρ_{yx} of 36.9 μΩ·cm has been reported in bulk single crystal Co_2MnAl [3]. For epitaxial Co_2MnAl thin films deposited by combinatorial sputtering, ρ_{yx} up to ~22 μΩ.cm has been reported [4].

It is known that one of the dominant mechanisms for large AHE arises from the electronic band structure of the material, particularly, the presence of large Berry curvature near the Fermi level [5]. As the position of the Fermi level is sensitive to changes in stoichiometry, composition variation is expected to have a significant effect on the AHE properties. However, a comprehensive study on the effect of composition on ρ_{yx} for polycrystalline CMA films is lacking. Therefore, in this work, we studied the composition dependence of AHE in CMA by using a high-throughput technique based on combinatorial sputtering.

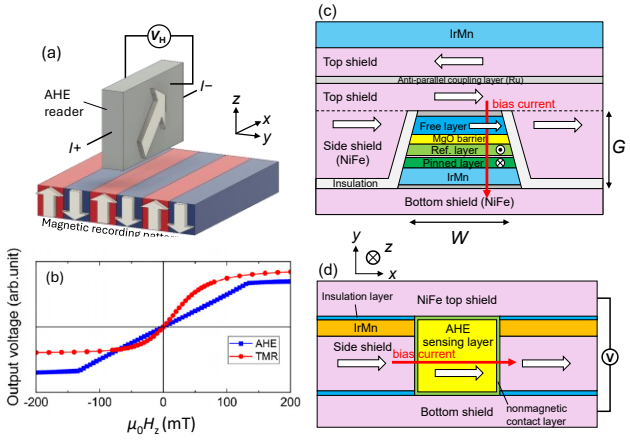

Fig. 1. (a) Schematic of an AHE reader. (b) comparison of output voltage for AHE and TMR readers. (c) Schematic of the existing TMR reader structure (d) Proposed AHE reader structure. *W* is reader width, and *G* is read gap. The white arrows in the shields and free (sensing) layer indicate the magnetization directions of the layers. (Data from [2])

II. Experimental Methodology

A. Composition-spread films

Two-dimensional (2D) composition-spread thin films of CMA were fabricated on 10 × 10 mm^2 thermally oxidized Si (Si/SiO$_x$) substrates using a combinatorial sputtering system (CMS-A6250X2, Comet, Inc.). The deposition was performed at room temperature and an Argon gas pressure of 0.6 Pa. As shown in Fig. 1a, composition-spread region forms a triangular area with the three vertices designed to have compositions of $Co_{62}Mn_{16}Al_{22}$, $Co_{42}Mn_{16}Al_{42}$ and $Co_{42}Mn_{36}Al_{22}$. The deposition was carried out by co-sputtering from Co, Mn and Al targets. Initially, uniform layers of Co, Mn and Al of thickness 0.17 nm,

0.074 nm and 0.142 nm, respectively, are deposited, and subsequently, wedge-shaped layers with thickness varying from 0 to 0.114 nm are deposited sequentially for each of the elements. After depositing a wedge for each element, the substrate was rotated by 120° before the wedge deposition of the subsequent layer. The deposition cycle of uniform and wedge layers is repeated for 60 times to form a total thickness of ~25 nm in the triangle region. The deposited films are then in-situ post-annealed at 500 °C for 30 minutes. A Ta capping of 3 nm was deposited after the film is cooled down to room temperature.

Hall-bar devices of length and width 80 and 20 μm, respectively, were fabricated on the 2D composition-spread film for AHE measurements. Because of the small dimensions, the composition gradient within the individual Hall-bar devices is negligibly small. AHE and longitudinal resistivity (ρ_{xx}) measurements are conducted using a Physical Property Measurement System (VersaLab, Quantum Design).

The compositions of individual Hall-bar devices were measured for selected devices using electron probe microanalysis (EPMA) . The composition for the rest of the devices were estimated by interpolating from the measured composition values. A slight deviation from the designed composition values was observed, and EPMA-based values are used in the following part.

B. Uniform films

Uniform films of CMA with a thickness of 30 nm were fabricated by co-sputtering from $Co_{66}Mn_{34}$ and Al targets. The films are capped with a 3 nm SiO_2 layer. Ex-situ post-annealing of the deposited films was performed at 500 °C for 1 h. The composition measurement was conducted by X-ray fluorescence spectroscopy (XRF) using a quantitative analysis method, which was calibrated using standard Co-Mn-Al films whose compositions were premeasured by inductively coupled plasma mass spectrometry.

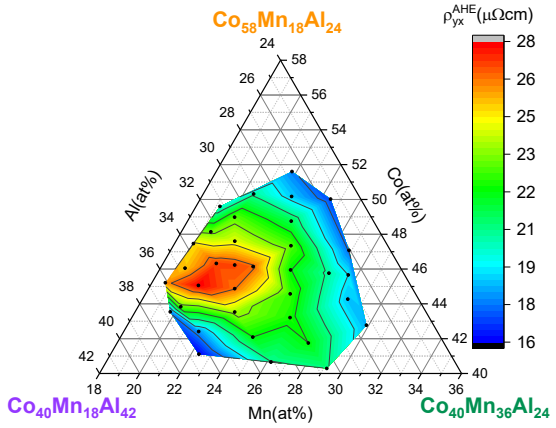

Fig. 2. Ternary contour plot showing the variation of ρ_{yx} with Co-Mn-Al composition.

III. Results

Figure 2 shows the AHE results for the 2D composition-spread film. The ternary contour plot depicts the variation of ρ_{yx} with CMA composition, based on the data obtained from 35 Hall-bar devices (black dots). A clear compositional dependence of ρ_{yx} can be seen. For a composition close to the stoichiometric one ($Co_{50}Mn_{24.5}Al_{25.5}$), ρ_{yx} was ~17 μΩ·cm, which is consistent with the previously reported value [6].

The ρ_{yx} values over 26 μΩ·cm, represented by the red region in Fig. 2, were obtained for off-stoichiometric Al-rich compositions with the highest value of ~27.7 μΩ·cm achieved at $Co_{45.1}Mn_{20.4}Al_{34.5}$. Scanning transmission electron microscopy (STEM) observation of a device with composition $Co_{46.3}Mn_{20.7}Al_{33}$ and a high ρ_{yx} (26.9 μΩ·cm) showed that the film had a polycrystalline structure with *B*2 atomic ordering.

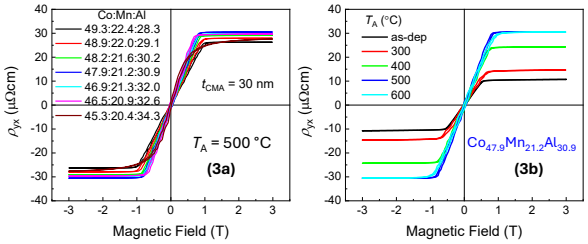

Fig. 3. (a) AHE behavior for uniform-CMA films with varying compositions. (b) ρ_{yx} dependence on post-annealing temperature for $Co_{47.9}Mn_{21.2}Al_{30.9}$.

AHE results for uniform CMA films annealed at T_A = 500 °C with varying Al concentrations from 28.3 to 34.3 at.% is shown in Fig. 3a. The saturation field, which represents the saturation magnetization due to demagnetization field, decreases with increasing Al. The highest ρ_{yx} of 30.4 μΩ·cm is obtained for $Co_{47.9}Mn_{21.2}Al_{30.9}$. The annealing temperature dependence of this film exhibits a monotonic increase in ρ_{yx} up to T_A = 500 °C and showed no improvement in ρ_{yx} with increasing T_A.

IV. Conclusion

In conclusion, we have employed a high-throughput combinatorial sputtering technique to explore the composition dependence of the anomalous Hall effect (AHE) in CMA. Based on this result, uniform films with the highest ever reported value of ρ_{yx} of 30.4 μΩ·cm were achieved for $Co_{47.9}Mn_{21.2}Al_{30.9}$ on polycrystalline substrates. Such high values, along with linear response and large dynamic range, are advantageous for applications in magnetic reader devices. The temperature dependence of these films was also studied.

References

[1] G. Albuquerque; S. Hernandez; M. T. Kief; D. Mauri; L. Wang, "HDD Reader Technology Roadmap to an Areal Density of 4 Tbpsi and Beyond," *IEEE Trans. Magn.*, vol. 58, 3100410, 2022.

[2] T. Nakatani, P. D. Kulkarni, H. Suto, K. Masuda, H. Iwasaki, and Y. Sakuraba, "Perspective on nanoscale magnetic sensors using giant anomalous Hall effect in topological magnetic materials for read head application in magnetic recording", Appl. Phys. Lett., vol. 124, 070501, 2024.

[3] P. Li, J. Koo, W. Ning, J. Li, L. Miao, L. Min, Y. Zhu, Y. Wang, N. Alem, C.-X. Liu, Z. Mao, and B. Yan, "Giant room temperature anomalous Hall effect and tunable topology in a ferromagnetic topological semimetal Co_2MnAl" Nat. Commun. 11, 3476, 2020.

[4] R. Modak, K. Goto, S. Ueda, Y. Miura, K. Uchida and Y. Sakuraba, "Combinatorial tuning of electronic structure and thermoelectric properties in Co2MnAl1−xSix Weyl semimetals", APL Mater. 9, 031105, 2021.

[5] D. Xiao, M. Chang, and Q. Niu, "Berry phase effects on electronic properties", Rev. Mod. Phys. 82, 1959, 2010.

[6] Y. Sakuraba, K. Hyodo, A. Sakuma, and S. Mitani, "Giant anomalous Nernst effect in the Co2MnAl1−xSix Heusler alloy induced by Fermi level tuning and atomic ordering", Phys. Rev. B 101, 134407, 2020

Large magnetoresistance and high spin-transfer torque obtained in CPP-GMR devices with Heusler alloy electrodes through high-throughput compositional optimization

Vineet Barwal, Hirofumi Suto, Ryo Toyama, Kodchakorn Simalaotao, Taisuke Sasaki, Yoshio Miura, and Yuya Sakuraba

Research Center for Magnetic and Spintronic Materials, National Institute for Materials Science (NIMS), Tsukuba, 305-0047, Japan

Half-metallic Heusler alloys having high spin polarization are crucial for future high-density hard disk drives and energy-efficient memory technologies, as they enhance spin-transfer torque (STT) and magnetoresistance (MR) in spintronic devices. While compositional tuning improves performance, conventional methods for optimizing composition are time-consuming. To address this, we developed a high-throughput compositional optimization method using combinatorial sputtering, microfabrication, and automated measurements, enabling efficient exploration of MR and STT responses in current-perpendicular-to-plane giant magnetoresistance devices. Focusing on $Co_2Mn_xFe_{1-x}Ge$ Heusler alloys, we observed a composition-dependent MR with the maximum of MR ratio ~ 38% in the Mn-rich region of $x = 0.85$ at 250°C annealing. The MR ratio further increased to ~ 45% at 350°C annealing along with high STT efficiency (~ 0.6) over a broad composition range ($0.2 \leq x \leq 0.7$). These results represent record-high MR values for all-metal CPP-GMR devices, achieved at relatively low annealing temperatures (250°C-350°C).

***Index Terms*—Spintronics, Heusler alloys, Giant magnetoresistance, Spin transfer torque**

I. Introduction

Giant magnetoresistance (GMR) and spin-transfer torque (STT) effects are technologically significant and serve as the operating principle in magnetoresistive random access memory [1], hard-disk-drive (HDD) read heads [2], spin-torque oscillators [3], and other spintronic devices. Enhancing device performance relies on materials with high spin polarization(P). Among these, half-metallic Heusler alloys are the promising candidates owing to their high P and high Curie temperature.

Compositional tuning of Heusler thin films used as ferromagnetic (FM) electrodes in current-perpendicular-to-plane giant magnetoresistance (CPP-GMR) devices is carried out to enhance the device performance[4]–[6]. Traditionally, this involves depositing and fabricating devices for each selected composition, a process that is both time- and resource-consuming. The combinatorial sputtering can break through the limitation by enabling efficient and systematic investigation of a wide range of material compositions on a single library sample [7], [8]. We recently developed a high throughput composition optimization method to achieve large magnetoresistance (MR) and high STT in CPP-GMR devices incorporating composition-gradient Co_xFe_{1-x} ($0 \leq x \leq 1$) as FM electrodes [4].

Here, we report the large MR ratio and high STT efficiency in CPP-GMR devices containing epitaxial $Co_2Mn_xFe_{1-x}Ge$ ($0 \leq x \leq 1$) Heusler alloy thin films achieved through the high throughput and detailed composition optimization method. $Co_2Mn_xFe_{1-x}Ge$ (CMFG), a mixture of the intermetallic compounds, Co_2MnGe (CMG) and Co_2FeGe (CFG), is expected to exhibit strong chemical ordering behavior at low-temperature annealing[9]. Such alloys exhibit a strong driving force for chemical ordering from a disordered state in thin-film form. High atomic ordering in Heusler alloys is critical for achieving high P, thereby enhancing device performance. For several potential applications such as the read head of HDDs, high atomic order in Heusler film is required to be obtained at lower process temperature below 350°C [2]. CMFG is particularly well suited for such applications.

II. Experimental Details

Epitaxial thin film stacks incorporating CMFG composition-gradient layers were deposited on 2×2 cm^2 MgO (001) substrate using combinatorial sputtering system. Figure 1 (a) shows the combinatorial sputtering process. Two types of CPP-GMR sample stacks, shown in figure 1(b), were prepared. The Type-I sample consisted of a CPP-GMR stack with both magnetic layers being $Co_2Mn_xFe_{1-x}Ge$, used to evaluate the MR output of the devices. The Type-II sample was comprised of CPP-GMR stack with magnetic layers being $Co_2Mn_xFe_{1-x}Ge$ and $Ni_{80}Fe_{20}$, used for STT measurement. The red arrows in figure 1(b) indicate the layer after which in-situ post annealing was done. The top 8 nm Ru cap layer was deposited after cooling down the sample to room temperature. CPP-GMR devices were fabricated for the Type-I and Type-II samples' stacks for the MR and STT measurements.

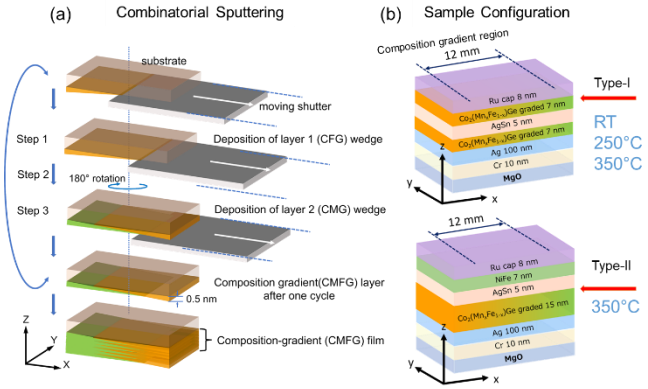

Fig. 1. Schematic showing combinatorial sputtering process. Sample configuration for the Type-I and Type-II sample structures with arrows indicating temperature and layer after which in-situ annealing was done.

III. Results and Discussion

A. X-ray Diffraction

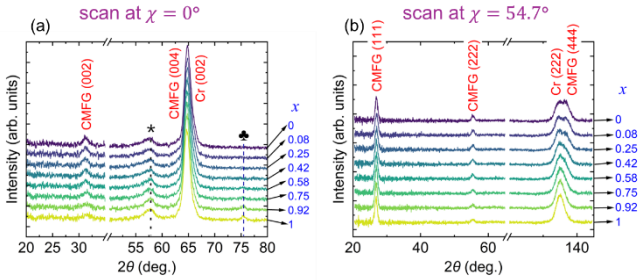

Fig. 2. θ-2θ XRD profiles for the 350ºC annealed Type-I sample along (a) (002) and (b) (111) plane. The * symbol marks the peak position for the Ru 102 plane and ♣ marks the peak position for the hcp $Co_{1.75}Ge$ 004, or fcc Co 220, or hcp Co 110 planes.

The XRD measurements were conducted at several positions with different compositions on the Type-I samples. The atomic ordering was found to increase with annealing temperature. Figure 2(a) and 2(b) shows the XRD scans at $\chi = 0°$ and $\chi = 54.7°$, respectively, for the 350ºC annealed Type-I sample. The presence of a 111 superlattice diffraction peaks in the 350°C annealed sample indicates the presence of $L2_1$ ordered phase (atomic order between (Fe, Mn) and Ge sites.

B. Magnetoresistance and spin tranfer torque

Figure 3(a) shows the change in intrinsic MR ratio with Mn content for the CPP-GMR devices from the Type-I sample. In the as-deposited sample, the MR ratio exhibited gradual change with Mn content. The CFG side showed lower MR ratio ~ 2.5% and the CMG side showed slightly higher MR ratio ~ 5%. The CPP-GMR devices fabricated from the stacks annealed at 250°C exhibit clear composition dependence of MR with a maximum MR ratio ~ 38 % in the Mn-rich region of $x = 0.85$. The MR ratio was further enhanced with increasing annealing temperature to 350°C and we observed maximum MR ratio close to ~ 45% over a broad composition range $0.2 \leq x \leq 0.7$. An overall improvement in MR ratio with increasing annealing temperature can be attributed to the enhanced atomic order with increasing annealing temperature.

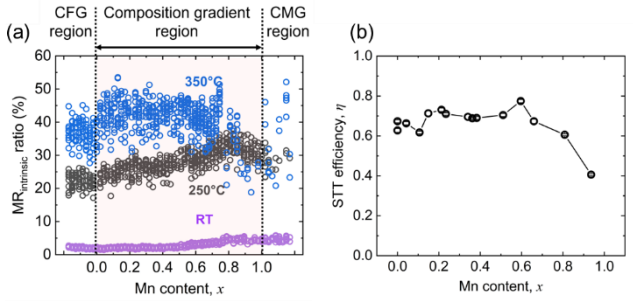

Fig. 3. Change in (a) intrinsic magnetoresistance (MR) ratio and (b) STT efficiency with Mn content for the Type-I and Type-II CPP-GMR sample stack , respectively.

We performed the STT induced magnetization reversal measurements to evaluate the composition dependent STT efficiency for the 350°C annealedType-II sample using devices with circular pillar geometry having designed diameter of 80 nm. Figure 3(b) shows the change in STT efficiency parameter (η) of CPP-GMR devices with Mn content for the Type-II sample. The η exhibits high value ~ 0.6 across the composition range $0 \leq x \leq 0.8$, decline slightly with value reaching close to 0.3 towards the Mn rich ($x = 0.9$) composition. The high value of η indicates high spin polarization in epitaxially grown CMFG Heusler thin films over a broad composition range.

IV. Conclusion

We fabricated high performance CPP-GMR devices from the GMR stacks containing composition-gradient $Co_2Mn_xFe_{1-x}Ge$ ($0 \leq x \leq 1$) film by high throughput and detailed composition optimization method. The combinatorially sputtered composition-gradient film and local measurements enabled efficient compositional optimization at fine composition interval. The CPP-GMR devices fabricated for the 250°C annelaed sample exhibit clear composition dependence of MR with a maximum of MR ratio ~ 38 % in the Mn-rich region of $x = 0.85$. The MR ratio was further enhanced with increasing annealing temperature to 350°C and we observed maximum MR ratio close to ~ 45% (ΔRA ~ 8 mΩ μm^2) along with high STT efficiency ~ 0.6 over a broad composition range $0.2 \leq x \leq 0.7$. We achieved record high MR for the all-metal CPP-GMR devices at low annealing temperature of 250°C by the present composition optimization method. The results provide comprehensive guidance on the composition optimization to obtain large MR ratio and high STT efficiency in the CPP-GMR devices using $Co_2Mn_xFe_{1-x}Ge$ at lower process temperature.

References

[1] S. Bhatti, R. Sbiaa, A. Hirohata, H. Ohno, S. Fukami, and S. N. Piramanayagam, "Spintronics based random access memory: a review," *Mater. Today*, vol. 20, no. 9, pp. 530–548, Nov. 2017.

[2] T. Nakatani, Z. Gao, and K. Hono, "Read sensor technology for ultrahigh density magnetic recording," *MRS Bull.*, vol. 43, no. 2, pp. 106–111, Feb. 2018.

[3] S. I. Klselev *et al.*, "Microwave oscillations of a nanomagnet driven by a spin-polarized current," *Nature*, vol. 425, no. 6956, pp. 380–383, 2003.

[4] Y. Sakuraba *et al.*, "Extensive study of giant magnetoresistance properties in half-metallic Co2(Fe,Mn)Si-based devices," *Appl. Phys. Lett.*, vol. 101, no. 25, p. 252408, Dec. 2012.

[5] M. Inoue *et al.*, "Influence of off-stoichiometry on magnetoresistance characteristics of Co2MnSi/Ag-based current-perpendicular-to-plane spin valves," *Appl. Phys. Lett.*, vol. 111, no. 8, p. 082403, 2017.

[6] S. Li *et al.*, "Large enhancement of bulk spin polarization by suppressing CoMn anti-sites in Co2Mn(Ge0.75Ga0.25) Heusler alloy thin film," *Appl. Phys. Lett.*, vol. 108, no. 12, p. 122404, 2016.

[7] A. Frisk *et al.*, "Magnetic and structural characterization of CoFeZr thin films grown by combinatorial sputtering," *Phys. Rev. Mater.*, vol. 3, no. 7, p. 074403, Jul. 2019.

[8] H. Masuda *et al.*, "Large spin-Hall effect in non-equilibrium binary copper alloys beyond the solubility limit," *Commun. Mater.*, vol. 1, no. 1, p. 75, Oct. 2020.

[9] T. Nakatani, S. Li, Y. Sakuraba, T. Furubayashi, and K. Hono, "Advanced CPP-GMR Spin-Valve Sensors for Narrow Reader Applications," *IEEE Trans. Magn.*, vol. 54, no. 2, p. 3300211, Feb. 2018.

Probabilistic and Analog Spintronic Devices for Energy-Efficient AI Hardware

Shunsuke Fukami[1,2,3,4,5], *Member, IEEE*

[1] Research Institute of Electrical Communication, Tohoku Univ., Sendai 980-8577 Japan
[2] Center for Science and Innovation in Spintronics, Tohoku Univ., Sendai 980-8577 Japan
[3] Center for Innovative Integrated Electronic Systems, Tohoku Univ., Sendai 980-8572 Japan
[4] Center for Science and Innovation in Spintronics, Tohoku Univ., Sendai 980-8577 Japan
[5] Inamori Research Institute for Science, Kyoto, 600-8411 Japan
s-fukami@riec.tohoku.ac.jp

Energy-efficient computing hardware is highly demanded in future information societies. Here I review recent progress of spintronics research for use in unconventional computing hardware that are promising for energy-efficient computation. Spintronics devices have attractive unexplored attributes such as probabilistic or analog functionalities. I first show a probabilistic bit and computer made of a stochastic magnetic tunnel junction device. A constructed rudimentary probabilistic computer can efficiently address combinatorial optimization, machine learning, quantum simulation, and Bayesian inference that conventional computers require large energy to execute. I also present a three-terminal analog spin-orbit torque driven device that can store the weight of neural networks and hence function as an artificial synapse. Proof-of-concept demonstration of reservoir computing is described, where the analog spin-orbit torque devices are used to store the weight of the output layer.

***Index Terms*—Probabilistic Computing, Magnetic tunnel junction, Artificial synapse, Reservoir Computing**

Conventional computers, based on a principle of Turing machine, von Neumann architecture, and complementary metal-oxide-semiconductor (CMOS) circuits, have evolved into sophisticated machines for half a century and are an indispensable platform of today's information societies. Nevertheless, there remain several computational tasks categorized into difficult classes of problem, that the classical computers are hard to address. This leads to an increasing interest in unconventional computing paradigms, in which one employs hardware with new operation principles, architecture, circuits and devices that are, for example, inspired by information processing in brain or physical phenomena [1-5]. This demand is of particular importance for edge devices in the coming internet-of-things (IoT) era, because real-time processing with limited energy is a critical requirement in IoT applications.

Spintronics is a promising field for the unconventional computing paradigm. In spintronics, one can design a device to store the information in a nonvolatile manner and yet can virtually unlimitedly switch it in a nano or subnano-second timescale. In addition, spintronics devices have compatibility with the integration process and operation voltage of standard CMOS circuits. These properties show promise for being a key building block in low-power integrated circuits [6]. Moreover, spintronics devices possess various intriguing attributes such as stochasticity and analog-memory functionality, and effective utilization of these properties is expected to pave the pathway toward the unconventional computing paradigm [7]. In this talk, I describe the following two approaches for the unconventional computing hardware based on spintronics devices, which are promising for energy-efficient computing hardware.

I first show a probabilistic bit and computer made of a stochastic magnetic tunnel junction device. A constructed rudimentary probabilistic computer can efficiently address combinatorial optimization [8], machine learning [9], quantum simulation [10], and Bayesian inference [11]. I delve into the physics of the stochastic magnetic tunnel junction elucidating the time-domain and time-averaged properties [12-17]. I also discuss the advanced design of the s-MTJs [18-21] tailored for reliable, large-scale probabilistic computers.

Second, I present a three-terminal analog spin-orbit torque driven device that can store the weight of neural networks and hence function as an artificial synapse. I discuss material and device technologies to realize artificial synapses made of antiferromagnet-ferromagnet bilayer system that is operated by the spin-orbit torque [22-25]. Proof-of-concept demonstration of reservoir computing is described, where the analog spin-orbit torque devices are used to store the weight of the output layer [26].

These studies on probabilistic computers and stochastic magnetic tunnel junctions are carried out in collaboration with H. Ohno, S. Kanai, W. A. Borders, K. Hayakawa, K. Kobayashi, R. Ota, H. Kaneko, S. Datta, K. Y. Camsari, whereas those on analog spin-orbit torque devices and reservoir computers are carried out in collaboration with H. Ohno, S. Kanai, A. Lagarrigue, K. V. D. Zoysa, S. Varaganti, S. Moriya, S. Sato, Y. Horio. The studies were partly supported by JST-CREST JPMJCR19K3, JST-AdCORP JPMJKB2305, JST-ASPIRE JPMJAP2322, MEXT X-NICS JPJ011438, JSPS Kakenhi (24H00039 and 24H02235) and RIEC Cooperative Research Projects.

References

[1] R. P. Feynman, "Simulating physics with computers," International Journal of Theoretical Physics, vol. 21, pp. 467-488, 1982.

[2] P. A. Merolla, J. V. Arthur, R. Alvarez-Icaza, A. S. Cassidy, J. Sawada, F. Akopyan, et al., "A million spiking-neuron integrated circuit with a scalable communication network and interface," Science, vol. 345, pp. 668-673, 2014.

[3] N. P. Jouppi, C. Young, N. Patil, D. Patterson, G. Agrawal, R. Bajwa, et al., "In-datacenter performance analysis of a tensor processing unit," in 2017 ACM/IEEE 44th Annual International Symposium on Computer Architecture (ISCA), 2017, pp. 1-12.

[4] M. Davies, N. Srinivasa, T. Lin, G. Chinya, Y. Cao, S. H. Choday, et al., "Loihi: A Neuromorphic Manycore Processor with On-Chip Learning," IEEE Micro, vol. 38, pp. 82-99, 2018.

[5] M. Prezioso, F. Merrikh-Bayat, B. D. Hoskins, G. C. Adam, K. K. Likharev, and D. B. Strukov, "Training and operation of an integrated neuromorphic network based on metal-oxide memristors," Nature, vol. 521, pp. 61-64, 2015.

[6] H. Ohno, T. Endoh, T. Hanyu, N. Kasai, and S. Ikeda, "Magnetic tunnel junction for nonvolatile CMOS logic," in 2010 International Electron Devices Meeting, 2010, p. 9.4.1.

[7] J. Grollier, D. Querlioz, K. Y. Camsari, K. Everschor-Sitte, S. Fukami, and M. D. Stiles, "Neuromorphic spintronics," Nature Electronics 3, 360–370 (2020).

[8] W. A. Borders, A. Z. Pervaiz, S. Fukami, K. Y. Camsari, H. Ohno, and S. Datta, "Integer factorization using stochastic magnetic tunnel junctions," Nature 573, 390-393 (2019).

[9] J. Kaiser, W. A. Borders, K. Y. Camsari, S. Fukami, H. Ohno, and S. Datta, "Hardware-Aware In Situ Learning Based on Stochastic Magnetic Tunnel Junctions," Physical Review Applied 17, 014016(1)-(12) (2022).

[10] A. Grimaldi, K. Selcuk, N. A. Aadit, K. Kobayashi, Q. Cao, S. Chowdhury, G. Finocchio, S. Kanai, H. Ohno, S. Fukami and K. Y. Camsari, "Experimental evaluation of simulated quantum annealing with MTJ-augmented p-bits," 68th Annual IEEE International Electron Devices Meeting (IEDM2022), San Francisco, USA + Online, 2022/12/03-2022/12/07.

[11] N. S. Singh, S. Niazi, S. Chowdhury, K. Selcuk, H. Kaneko, K. Kobayashi, S. Kanai, H. Ohno, S. Fukami, K. Camsari, "Hardware Demonstration of Feedforward Stochastic Neural Networks with Fast MTJ-based pbits," 69th Annual IEEE International Electron Devices Meeting (IEDM 2023), San Francisco, CA, USA, 2023/12/09-2023/12/13.

[12] K. Hayakawa, S. Kanai, T. Funatsu, J. Igarashi, B. Jinnai, W. A. Borders, H. Ohno, and S. Fukami, "Nanosecond Random Telegraph Noise in In-Plane Magnetic Tunnel Junctions," Physical Review Letters 126, 117202 (2021).

[13] S. Kanai, K. Hayakawa, H. Ohno, and S. Fukami, "Theory of relaxation time of stochastic nanomagnets," Physical Review B 103, 094423 (2021).

[14] K. Kobayashi, W. A. Borders, S. Kanai, K. Hayakawa, H. Ohno, and S. Fukami, "Sigmoidal curves of stochastic magnetic tunnel junctions with perpendicular easy axis," Applied Physics Letters 119, 132406(1)-(5) (2021).

[15] T. Funatsu, S. Kanai, J. Ieda, S. Fukami, and H. Ohno, "Local bifurcation with spin-transfer torque in superparamagnetic tunnel junctions," Nature Communications 13, 4079(1)-(8) (2022).

[16] H. Kaneko, R. Ota, K. Kobayashi, S. Kanai, M. Elyasi, G. E. W. Bauer, H. Ohno, and S. Fukami, "Temperature dependence of the properties of stochastic magnetic tunnel junction with perpendicular magnetization," Applied Physics Express 17, 053001(1)-(4) (2024).

[17] M. Elyasi, S. Kanai, H. Ohno, S. Fukami, and G.E.W. Bauer, "Effect of nonlinear magnon interactions on stochastic magnetization switching," Physical Review B 110, 094433(1)-(11) (2024).

[18] K. Y. Camsari, M. M. Torunbalci, W. A. Borders, H. Ohno, and S. Fukami, "Double-Free-Layer Magnetic Tunnel Junctions for Probabilistic Bits," Physical Review Applied 15, 044049(1)-(10) (2021).

[19] K. Kobayashi, K. Hayakawa, J. Igarashi, W. A. Borders, S. Kanai, H. Ohno and S. Fukami, "External-Field-Robust Stochastic Magnetic Tunnel Junctions Using a Free Layer with Synthetic Antiferromagnetic Coupling," Physical Review Applied 18, 054085(1)-(9) (2022).

[20] K. Selcuk, S. Kanai, R. Ota, H. Ohno, S. Fukami, and K. Y. Camsari, "Double-free-layer stochastic magnetic tunnel junctions with synthetic antiferromagnets," Physical Review Applied 21, 054002(1)-(12) (2024).

[21] R. Ota, K. Kobayashi, K. Hayakawa, S. Kanai, K. Y. Çamsarı, H. Ohno, and S. Fukami, "Voltage-insensitive stochastic magnetic tunnel junctions with double free layers," Applied Physics Letters 125, 022406(1)-(6) (2024).

[22] S. Fukami, C. Zhang, S. DuttaGupta, A. Kurenkov, and H. Ohno, "Magnetization switching by spin-orbit torque in an antiferromagnet-ferromagnet bilayer system," Nature Mater., vol. 15, pp. 535-41, 2016.

[23] A. Kurenkov, C. Zhang, S. DuttaGupta, S. Fukami, and H. Ohno, "Device-size dependence of field-free spin-orbit torque induced magnetization switching in antiferromagnet/ferromagnet structures," Appl. Phys. Lett., vol. 110, 092410, 2017.

[24] S. Fukami and H. Ohno, "Magnetization switching schemes for nanoscale three-terminal spintronics devices," Jpn. J. Appl. Phys., vol. 56, 0802A1, 2017.

[25] A. Kurenkov, S. DuttaGupta, C. Zhang, S. Fukami, Y. Horio, and H. Ohno, "Artificial Neuron and Synapse Realized in an Antiferromagnet/Ferromagnet Heterostructure Using Dynamics of Spin–Orbit Torque Switching," Advanced Materials, vol. 31, p. 1900636, 2019.

[26] S. Moriya, Y. Iida, A. Lagarrigue, K. V. D. Zoysa, M. Ishikawa, H. Yamamoto, S. Fukami, and S. Sato, “Event-Driven Inference with Spiking Neural Networks Enhanced by Non-Volatile Analogue Spin-orbit Torque Devices,” 2025 IEEE International Symposium on Circuits and Systems, Presentation no. 2562 (2025).

Scalable and Energy-Efficient On-Device SNNs Enabled by Magnetic Tunnel Junctions

Sai Li[1], Ziyi Teng[1], Shuncheng Jia[2], Zhaohao Wang[1], Kaihua Cao[3], Hongchao Zhang[3], Hongxi Liu[3], Tielin Zhang[2],Weisheng Zhao[1] *Fellow, IEEE*

[1]National Key Laboratorycof Spintronics, School of Integrated Circuit Science and Engineering, Beihang University, Beijing, 100191, China
[2]Research Center for Brain-inspired Intelligence, Institute of Automation, Chinese Academy of Sciences (CASIA), Beijing 100190, China
[3]Truth Memory Corporation, Beijing 100088, China

To address the critical need for efficient, biologically-inspired neuromorphic chip exhibiting flexible learning and robustness against noise and catastrophic forgetting, We present a neuromorphic computing engine that leverages the intrinsic stochasticity and fast switching characteristics of spin-orbit torque magnetic tunnel junctions (SOT-MTJs). Its architecture innovatively integrates multi-port SOT switching to implement a 9-type spike-timing-dependent plasticity (STDP) rule, enhanced by meta-learning, while achieving excitation-inhibition balance of the spiking neural networks (SNNs) via sparsity-aware input encoding. This integrated approach effectively realizes key functions of flexible synaptic plasticity and selective neuronal activation. The results demonstrate over 96% classification accuracy on both MNIST and TIDigits datasets. Crucially, it showcases robust continuous learning capabilities by sequentially training all 10 MNIST classes in a single pass, thereby substantially reducing catastrophic forgetting with minimal computational overhead. This work demonstrates that MTJs can enable on-device SNNs, paving the way for the development of scalable and energy-efficient neuromorphic computing chips.

***Index Terms*—Spintronic Devices, Neuromorphic Computing, Synaptic Plasticity, Continuous Learning**

I. Introduction

The remarkable capability of the human brain is to continuously learn from dynamic environments, where different regions such as the occipital and temporal lobes govern distinct cognitive modalities and are modulated by various neurotransmitters (Figure 1a). Excitatory and inhibitory neurons coexist within each region, with inhibitory neurons blocking neurotransmission to help maintain network stability. Higher-order learning is further regulated by metaplasticity, a neuromodulation-driven mechanism that dynamically tunes the threshold and polarity of synaptic plasticity in response to environmental context. Key among these are two mechanisms: neuronal selection, which allows the brain to focus on relevant information, and synaptic modulation, which underpins learning and memory (Figure 1b). Specifically, neuronal selection are achieved through a delicate Excitation-Inhibition (E-I) balance, which dictates whether neurons fire intensively, sparsely, or remain silent in response to inputs (Figure 1c) [1]. On the other hand, neuromodulatory mechanisms—particularly those involving dopamine—adjust synaptic efficacy beyond classical Hebbian rules [2]. These effects, known as metaplasticity, regulate the amplitude, polarity, and temporal dynamics of long-term potentiation (LTP) and depression (LTD), which can manifest as 9 distinct forms of STDP (Figure 1d) [3].

However, existing neuromorphic hardware often supports only simplified functionalities, hindering the realization of complex learning mechanisms on energy-efficient chips [4]. To overcome this limitation, we introduce a novel neuromorphic engine (Figure 1(e)) leveraging the intrinsic stochasticity and rapid switching characteristics of SOT-MTJs [5]. This engine employs multi-port SOT switching to directly implement both neuronal selection and synaptic modulation within on-device SNNs for learning via weight updates and controlling neuron spiking rates.

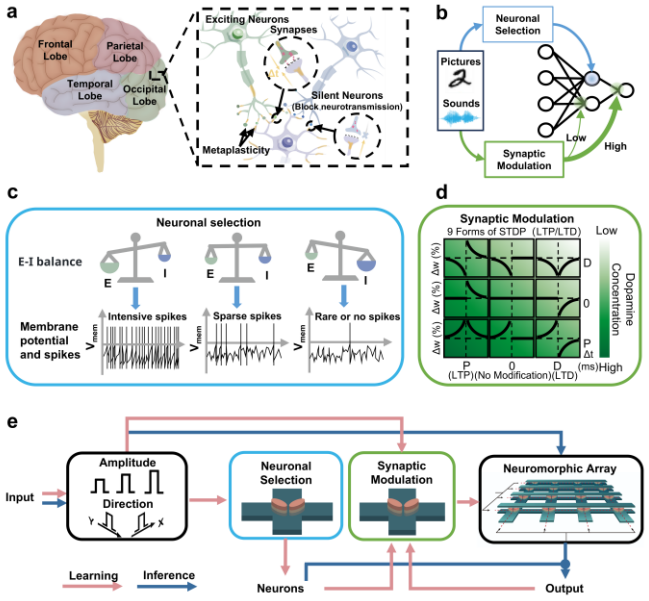

Fig. 1. Biologically inspired architecture and its SOT-MTJ implementation. (a) Brain regions and fundamental neural components (excitatory/silent neurons, synapses, metaplasticity). (b) Schematic of selective information processing in a SNN, where input stimuli (e.g., images, audio) are handled by neuron populations based on neuronal selection and synaptic modulation. (c) Neuronal selection via E-I balance, controlling spike rates. (d) Synaptic modulation is governed by dopamine-dependent metaplasticity, enabling dynamic combinations of LTP and LTD and realizing nine distinct STDP learning rules. (e) Architecture of the proposed neuromorphic engine using SOT-MTJs, integrating neuronal selection and synaptic modulation blocks within a neuromorphic array for input processing, learning, and inference.

II. Methods

We fabricated an in-plane type-Y SOT-MTJ pair, whose multilayer stack and device layout are illustrated in Fig. 2a. The four-terminal structure features a heavy-metal cross acting as the SOT current channels, with two MTJs patterned on its orthogonal arms, yielding a 90°tilt between their easy axes. Current-induced switching was examined with the circuit shown in Fig. 2b. Applying current along the X-direction induces synchronous switching of the two MTJs, whereas Y-direction excitation causes them to switch anti-synchronously. This inherent capability to toggle between correlated and anti-correlated states provides the hardware basis for the synaptic functions discussed subsequently.

Given that SOT devices offer highly reproducible, pulse-controlled switching, we focused on their single-pulse response rather than pursuing conventional multi-level conductances. Using the previously determined threshold voltages as a guide, rectangular voltage pulses of varying amplitude were applied to the SOT-MTJs at room temperature without external magnetic field. For the measurements shown in Fig. 2c, the pulse amplitude was swept from –3.94 V to –3.66 V in 0.02 V steps. The switching probability was calculated as $P_{SW} = N_{flip}/N_{tot}$ and plotted against pulse amplitude, where each probability was measured 50 times. Therefore, we could obtain sigmoid fits of the switching probability curve under different SOT currents. Repeating the protocol for the opposite polarity and for the left/right MTJ produces four characteristic curves (AP to P and P to AP for both junctions), which form the quantitative basis for the pulse-based synaptic modes.

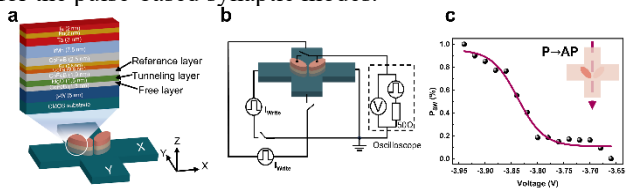

Fig. 2. Structure, measurement set-up, and single-pulse switching statistics of the SOT-MTJ. (a) Multilayer stack and geometry of the four-terminal device. (b) Electrical measurement setup used for SOT switching. (c) Probability switching characterization for the left MTJ under –Y excitation.

III. Result

Exploiting the direction-dependent switching of the two MTJs—synchronous under ±Y excitation and anti-synchronous under ±X excitation—the SOT-MTJ pair implements 9-type STDP rules. A local selector chooses which junction is monitored, while the sign of its conductance change, ΔG, defines long-term potentiation (LTP, $\Delta G > 0$, $\Delta W = +1$) or depression (LTD, $\Delta G < 0$, $\Delta W = -1$); the weight remains unchanged when no switch occurs.

For instance, when a pre-synaptic pulse($-Y$) followed by a post-synaptic pulse($+Y$) the left MTJ switches from AP to P, generating a LTP mode ($\Delta t > 0$); reversing the Y direction order, it produces a LTD mode ($\Delta t < 0$). Selecting the right MTJ could invert these updates because its SOT Y-polarity is opposite. Currents along $\pm X$ drive the two MTJs synchronously, giving pure LTD (DD), no change (00) or pure LTP (PP), irrespective of Δt. Formally, the update obeys $\Delta W = f_{local} \times LTP/LTD$.

Neuronal selection is implemented by the same stochastic response. A sigmoid switching curve $G(\cdot)$ of the SOT-MTJ pair is used to generate a Mask. When the device is in the AP state, Mask ≠ 0 and the leaky-integrate-and-fire (LIF) neuron behaves normally (“Fire”); when it is in the P state, Mask = 0 and the neuron is silenced even if its membrane potential reaches threshold (“don’t Fire”).

We simulated these synaptic-modulation and neuron-selection schemes in a pulse-based spiking neural network. The resulting accuracy reached 96.51 % on MNIST and 96.54 % on TIDigits. Furthermore, the architecture demonstrates effective continuous learning capability by sequentially training on all 10 MNIST classes without iteration, significantly reducing catastrophic forgetting while maintaining low computational overhead.

References

[1] J. Liang, Z. Yang, and C. Zhou, “Excitation–Inhibition Balance, Neural Criticality, and Activities in Neuronal Circuits,” *The Neuroscientist*, vol. 31, no. 1, pp. 31–46, Feb. 2025.

[2] G. Bi and M. Poo, “Synaptic modification by correlated activity: Hebb’s postulate revisited,” *Annu. Rev. Neurosci.*, vol. 24, pp. 139–166, Mar. 2001.

[3] S. B. Flagel, J. J. Clark, T. E. Robinson, L. Mayo, A. Czuj, I. Willuhn, C. A. Akers, S. M. Clinton, PE. M. Phillips, and H. Akil, “A selective role for dopamine in stimulus-reward learning,” *Nature*, vol. 469, no. 7328, pp. 53–57, Jan. 2011.

[4] D. Kudithipudi, C. Schuman, and S. Furber, “Neuromorphic computing at scale,” *Nature*, vol. 637, no. 8047, pp. 801–812, Jan. 2025.

[5] Z. Guo, J. Yin, Y. Bai, D. Zhu, K. Shi, G. Wang, K. Cao, and W. Zhao, “Spintronics for energy-efficient computing: An overview and outlook,” *Proc. IEEE*, vol. 109, no. 8, pp. 1398–1416, Aug. 2021.

Self-regulated spintronic long short-term memory for spiking neural networks

Rudis Ismael Salinas Padilla[1], and Chih-Huang Lai[1,2]

[1]Department of Materials Science and Engineering, National Tsing Hua University, Hsinchu 300044, Taiwan,
[2]College of Semiconductor Research, National Tsing Hua University, Hsinchu 300044, Taiwan, chlai@mx.nthu.edu.tw

As predictive technologies like real-time language processing, autonomous control, and edge artificial intelligence (AI) continue to expand, the demand for energy-efficient computation has intensified. Spiking neural networks (SNNs) offer a biologically inspired and low-power alternative to conventional AI models, yet their implementation is hindered by the difficulty of reproducing complex temporal dynamics in hardware. A particularly important function is long- and short-term memory handling, essential for tasks involving sequential data. In this work, we demonstrate a spin-orbit torque (SOT)-driven magnetization switching mechanism in the antiferromagnet(AFM)/ferromagnet(FM) heterostructures that mimics leaky neuronal behavior. The device exploits the interplay between SOT and persistent thermally induced spin currents, resulting in post-current pulse magnetization relaxation and controlled temporal decay. While the SOT pulse induces deterministic switching, the thermally generated spin current persists beyond the pulse, exerting a delayed torque on the magnetization. This post-pulse thermal action gives rise to gradual magnetic state evolution, effectively emulating leaky-integrate characteristics. Such a dynamic forms the physical basis of Long Short-Term Memory (LSTM) functionality in spintronic devices, where magnetization decay and memory retention can be tuned through current amplitude and pulse width. This study presents a hardware-efficient, biomimetic approach for neuromorphic computing and paves the way for spintronic architectures capable of real-time, in-memory sequential information processing.

***Index Terms*—Long short-term memory, Magnetic domain walls, Spiking neural networks, Spin-orbit torque.**

I. Introduction

The implementation of neuromorphic functionalities in solid-state devices is increasingly sought to meet the demands of low-power, real-time data processing. While spintronic platforms have shown promise due to their non-volatility and fast switching, most demonstrations remain limited to binary or fixed multistate behaviors. These constraints hinder their application in hardware mimicking the adaptive, time-dependent characteristics of biological systems [1].

In this work, we report a distinct magnetization dynamic in the perpendicularly magnetized antiferromagnet/ferromagnet (AFM/FM) heterostructures, where a leaky, gradual relaxation of the magnetic state occurs following the removal of a spin-orbit torque (SOT) pulse. This behavior arises from the interplay between electrical and thermal spin currents at the AFM/FM interface. Notably, the thermally generated spin current persists after the current pulse ends, driving a delayed torque that gradually restores the magnetization, a process analogous to the leaky integrate-and-fire mechanism in biological neural systems [2]-[3].

This built-in relaxation provides a physical basis for implementing time-dependent computation, crucial for tasks involving memory and temporal correlation. As a result, spintronic devices exhibiting these leaky dynamics offer a promising route toward hardware-efficient emulation of long short-term memory (LSTM) behavior in spiking neural networks (SNNs) [4]. The ability to harness intrinsic physical processes to encode temporal information represents a significant advance for future computing technologies [5]. It opens the door to energy-efficient, compact, and scalable hardware systems capable of learning, forgetting, and adapting in real time—hallmarks of biological intelligence and essential for next-generation artificial intelligence platforms.

II. Results and Discussion

The magnetization dynamics of the AFM/FM heterostructure were investigated using a sequence of current-induced SOT switching pulses and time-resolved anomalous Hall voltage (V_{AHE}) measurements. Fig. 1(a) shows the evolution of V_{AHE} as a function of pulse current amplitude (I_p). As I_p increases, the system transitions from a stable initial state to a fully switched magnetic configuration, with the intermediate states revealing a smooth, non-binary response.

This indicates a multilevel magnetization profile modulated by the applied current. The inset highlights the measurement scheme, where each state is probed 500 ms after the end of the current pulse, capturing the system's response beyond the direct excitation window.

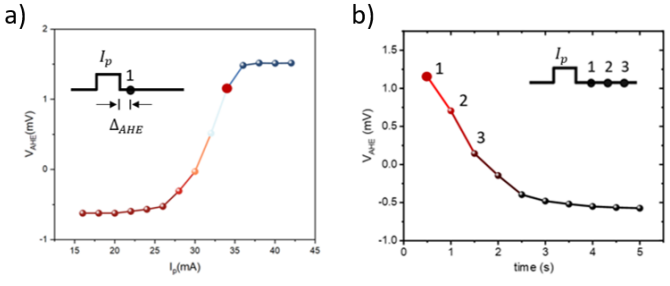

Fig. 1. (a) Anomalous Hall voltage (V_{AHE}) as a function of pulse current amplitude (I_p), showing a smooth transition of magnetic states. (b) Temporal evolution of V_{AHE} for a selected intermediate state, showing a gradual decay over a few seconds. The persistent change is attributed to a thermally driven spin current that continues to influence magnetization after the pulse, emulating leaky neural behavior.

More importantly, as shown in Figure 1b, the temporal evolution of these intermediate magnetization states exhibits an evident post-pulse decay over a few seconds. This behavior arises from the persistent thermal spin currents generated at the AFM/FM interface, which continue to exert torque after the electrical excitation ends. The decay trajectory, following a smooth relaxation curve, mirrors the leaky integration behavior of biological neurons, confirming that the device retains a fading memory of past stimuli. The inset schematic illustrates the temporal reading of each state, underscoring the device's capacity for encoding time-dependent information.

This intrinsic leaky dynamic not only allows for analog multistate behavior but also introduces programmability via pulse amplitude and duration, enabling flexible control over memory decay rates, a critical functionality for neuromorphic operations such as sequence processing or state-based learning. Figure 2 expands upon the device's time-dependent behavior by demonstrating synaptic plasticity through a train of current pulses applied to the device. The anomalous Hall output exhibits distinct temporal evolution depending on the stimulation pattern. Repeated pulses lead to a progressive increase in the resistance state, mimicking long-term potentiation (LTP). In contrast, isolated or sparse pulses result in a gradual relaxation, analogous to long-term depression (LTD). More importantly, the device also exhibits features of short-term plasticity (STP) and short-term depression (STD), where brief or subthreshold pulse sequences induce transient resistance changes that decay back to baseline without consolidation.

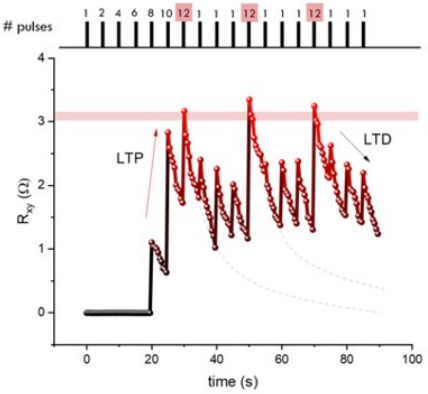

Fig. 2. AHE evolution under sequential current pulse stimulation, showing synaptic-like plasticity. Pulse trains (top) lead to long-term potentiation (LTP), while isolated pulses result in long-term depression (LTD). The system exhibits history-dependent resistance modulation, enabling physical emulation of learning and forgetting dynamics in spintronic devices.

This combination of transient and cumulative magnetization dynamics captures the fundamental ingredients for LSTM behavior: integration, selective memory retention, and controllable forgetting, all realized through intrinsic device physics without complex peripheral circuitry. The capability to realize both history-dependent integration and activity-driven plasticity demonstrates the potential of AFM-enhanced spintronic devices for constructing compact, low-power modules capable of learning, forgetting, and adapting over time, key features for real-time neuromorphic computing platforms.

III. Conclusions

In summary, we demonstrate a spintronic device that harnesses the interplay of electrical and thermal spin currents to generate post-pulse leaky magnetization dynamics. This behavior enables the emulation of biologically inspired temporal processes and provides a hardware-efficient path toward implementing neuromorphic functions such as LSTM in SNN architectures. The observed gradual decay and multistate encoding offer an unprecedented opportunity to develop spin-based systems capable of sequential learning and real-time information processing. These findings mark a step forward in integrating antiferromagnetic materials into neuromorphic in-memory computing platforms, expanding the design space for future intelligent devices.

References

[1] Lanza M, Pazos S, Aguirre F, et al. The growing memristor industry. Nature. 2025 Apr;640(8059):613-622.

[2] Abbott LF. Lapicque's introduction of the integrate-and-fire model neuron (1907). Brain Research Bulletin. 1999;50(5-6):303-304.

[3] Hodgkin AL, Huxley AF. A quantitative description of membrane current and its application to conduction and excitation in nerve. J Physiol. 1952 Aug;117(4):500-44.

[4] Hochreiter S, Schmidhuber J. Long short-term memory. Neural Comput. 1997 Nov 15;9(8):1735-80.

[5] Wright LG, Onodera T, Stein MM, et al. Deep physical neural networks trained with backpropagation. Nature. 2022 Jan;601(7894):549-555.

A magnetic Hopfield neural network capable of self-learning

Chang Niu, Huanyu Zhang, Chuanlong Xu, Wenjie Hu, Yunzhuo Wu, Yu Wu, Yadi Wang, Tong Wu, Yi Zhu, Yinyan Zhu, Wenbin Wang, Yizheng Wu, Lifeng Yin, Jiang Xiao, Weichao Yu*, Hangwen Guo*, Jian Shen*

State Key Laboratory of Surface Physics and Institute for Nanoelectronic Devices and Quantum Computing, Fudan University, Shanghai 200433, China

Physical neural networks (PNN) using physical materials and devices to mimic synapses and neurons offer an energy-efficient way to implement artificial neural networks. Yet, training PNN is difficult and heavily relies on external computing resources. An emerging concept, "physical self-learning," uses intrinsic physical parameters as trainable weights. Here, a real spintronic system mimicking Hopfield neural networks (HNN) is demonstrated, where unsupervised learning is intrinsically performed via the evolution of the physical process. Using a magnetic texture–defined conductance matrix as trainable weights, it is shown that under external voltage inputs, the conductance matrix naturally evolves and adapts Oja's learning algorithm in a gradient descent manner. The self-learning HNN is scalable and can achieve associative memories on patterns with high similarities. Fast spin dynamics and reconfigurability of magnetic textures offer a platform toward efficient autonomous training directly in materials.

***Index Terms*—associative memory, Hopfield neural network, magnetic textures, self-learning, spintronics**

I. Introduction

Machine learning relies increasingly on energy-intensive artificial neural networks (ANNs). Physical neural networks (PNNs) emulate neural function using real materials—spintronics, memristors, optics, and more—to achieve energy efficiency beyond silicon processors. However, most experimental PNNs, especially for training, depend extensively on external computers, limiting their practical advantage.

A central challenge is realizing **physical self-learning**: mapping trainable weights directly to intrinsic, tunable material parameters, so training occurs through natural evolution following physical laws—mimicking biological learning. If such evolution adapts modern learning rules (e.g., gradient descent), autonomous material-based training becomes possible.

The Hopfield neural network (HNN) is a classic model for associative memory. It is widely implemented in various physical forms, but typically uses only simple Hebbian/outer-product rules, limiting capacity to highly orthogonal patterns and requiring off-chip weight calculation.

This work reports a spintronic realization of a **magnetic HNN with intrinsic gradient descent**. Synaptic weights are mapped to a conductance matrix defined by the configuration of magnetic textures in a Permalloy (Py) film. Voltage training pulses applied to gold electrodes induce Oersted fields, reshaping these textures and evolving the network according to Oja's rule—a more powerful, convergent learning strategy—entirely through physical dynamics.

II. Device and Physical Learning Mechanism

Device Architecture and Measurement. The core device consists of three layers: a bottom Py (Fe80Ni20) film, insulating Al_2O_3, and top Au (gold) patterned into four electrodes (neurons). Voltage pulses applied to Au encode binary input patterns; these pulses generate in-plane currents and corresponding Oersted fields, modulating local magnetization in the underlying Py.

Conductance between each node pair (G_{ij}) forms a

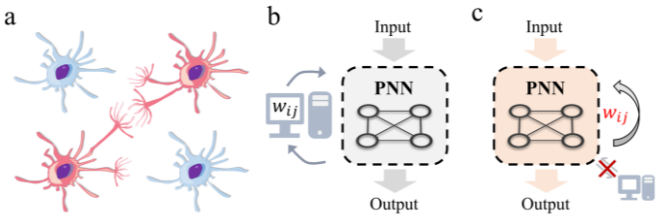

Figure 1 Concept of physical self-learning . a) Biological neural network learns by itself where activated neurons intend to strengthen their connection. b) Physical Neural Networks (PNNs) whose internal learning parameters w_{ij} are determined via external computation and updated in the physical system. c) PNNs with self-learning capability, whose learning parameters are determined and updated in an autonomous way according to inherent physical dynamics without interference of external computation.

symmetric matrix mapped to HNN weights. The evolution of Gij under pulse input is tracked via the anisotropic magnetoresistance (AMR) effect: the local resistance of Py depends on the angle between electrical current and magnetization, measurable with small probe currents.

Intrinsic Gradient Descent Learning. Upon repeated voltage pulse training, the conductance matrix elements G_{ij} evolve in a manner described by:

$$G_{ij}(t) - G_{ij}(t-1) = \eta \left[V_i^{\mathrm{Au}} V_j^{\mathrm{Au}} - 2\alpha_{ij} \left(G_{ij}(t-1) - G_{ij}^{\mathrm{avg}} \right) \right], \quad (1)$$

where η is the evolution speed, α_{ij} an effective learning rate determined by voltage differences, and G_{ij}^{avg} a constraint average.

This evolution is mathematically equivalent to Oja's rule, a well-known modification to Hebbian learning that ensures weight normalization and stability. The key physical insight: the network's energy minimization under external driving directly implements gradient descent on a cost function, with purely local updates and no need for software supervision.

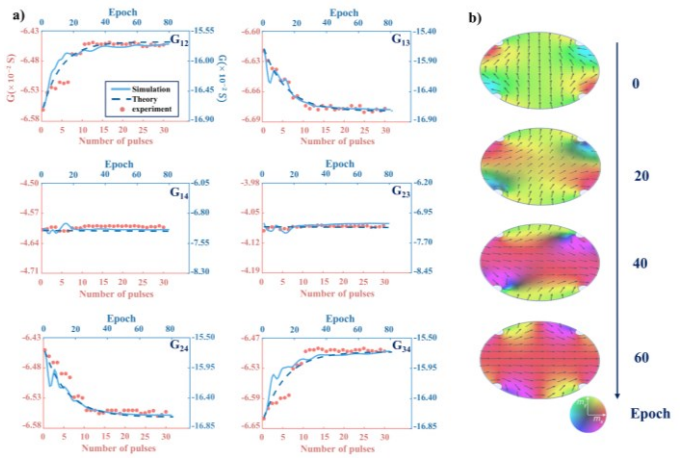

Figure 2 Intrinsic gradient descent learning. a) Evolution of conductance matrix G_{ij} when the voltage pattern is switched from initial "+ − + −" to "+ + − −" under "+ + − −" voltage pulses in the Au layer. The experiment, simulation and theory curves are plotted respectively where the matrix evolution is equivalent to the Oja's learning rule for unsupervised learning. b) Snapshots of corresponding evolution of spin textures from simulation.

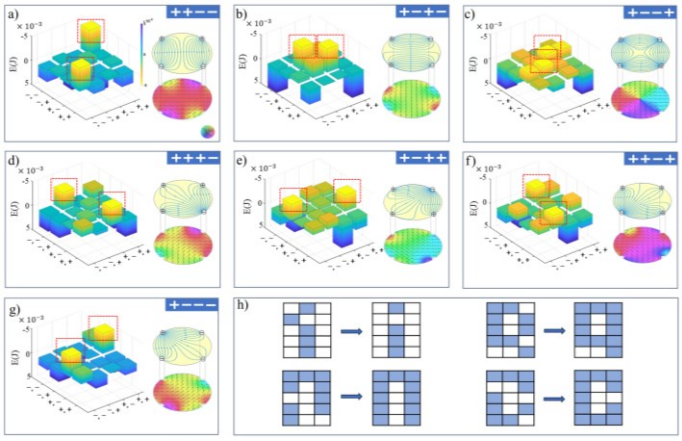

Figure 3 Examination of the magnetic HNN. a) The effective energy diagram (left) and corresponding current and spin texture distribution (right) for the trained pattern "+ + − −". The effective energy E is minimal for the trail state "+ + − −" or equivalent "− − + +" as marked by red dashed box. b)-g) Results for other six trained patterns. h) Associated memory. When a distorted letter is fed to the network, the correct letter can be recalled during inference. Four letters (i, n, q, c) are demonstrated respectively.

III. ASSOCIATIVE MEMORY PERFORMANCE & SCALABILITY

Experimental Demonstration and Inference. The 4-node system enables seven independent binary patterns. For each, training proceeds via pulse input; the conductance matrix converges, mapping the network attractor to the desired pattern as confirmed by energy minimization and recurrent inference, even with noisy/distorted inputs. The trained device robustly recalls correct patterns via iterative updates, matching Hopfield energy criteria.

Scalability and Advanced Application. Micromagnetic simulation of a scaled-up device (e.g., 35 nodes) shows robust associative memory for complex, low-orthogonality patterns (e.g., recognition of similar letters), achieving up to 97% recall accuracy—substantially outperforming the standard outer-product rule (approx. 33%). The self-learning approach is inherently parallel: multi-node training occurs simultaneously as magnetic textures evolve, offering fast operation limited only by the nanosecond-scale spin dynamics.

Additionally, the programmable magnetic network supports Boolean logic functions (e.g., AND, OR, NAND, NOR) with stability and reconfigurability—key steps towards neuromorphic computing.

IV. DISCUSSION AND CONCLUSION

This demonstration establishes that tunable magnetic textures in spintronic devices can implement powerful, autonomous training rules for neural networks, with:

1. nanosecond-scale, parallel, and energy-efficient training;
2. robust, nonvolatile storage and reconfigurability;
3. effective recall of similar patterns exceeding previous physical HNNs.

Future improvements include signal amplification using giant magnetoresistance (GMR) and extension to more complex networks (e.g., deep networks, Boltzmann machines), potentially realizing fully neuromorphic, material-driven learning hardware.

REFERENCES

[1] W. Yu, J. Xiao, G. E. W. Bauer, "Hopfield neural network in magnetic textures with intrinsic Hebbian learning," Phys. Rev. B 104, L180405 (2021).
[2] C. Niu et al., "A self-learning magnetic Hopfield neural network with intrinsic gradient descent adaption," Proceedings of the National Academy of Sciences of the United States of America, 121 (51) e2416294121 (2024).
[3] W. Yu, H. Guo, J. Xiao, J. Shen, "Physical neural networks with self-learning capabilities," SCIENCE CHINA Physics, Mechanics & Astronomy, Volume 67, Issue 8: 287501 (2024).
[4] J. Grollier et al., Neuromorphic spintronics. Nat. Electron. 3, 360 (2020).
[5] M. A. Zidan, J. P. Strachan, W. D. Lu, The future of electronics based on memristive systems. Nat. Electron. 1, 22–29 (2018).
[6] S. G. Hu et al., Associative memory realized by a reconfigurable memristive Hopfield neural network. Nat. Commun. 6, 7522 (2015).
[7] Q. Xia, J. J. Yang, Memristive crossbar arrays for brain-inspired computing. Nat. Mater. 18, 309 (2019).
[8] J. J. Hopfield, Neural networks and physical systems with emergent collective computational abilities. Proc. Natl. Acad. Sci. U.S.A. 79, 2554–2558 (1982).
[9] F. Cai, Power-efficient combinatorial optimization using intrinsic noise in memristor Hopfield neural networks. Nat. Electron. 3, 409 (2020).
[10] E. Oja, Simplified neuron model as a principal component analyzer. J. Math. Biol. 15, 267–273 (1982).

Spintronic foundation cells for large-scale integration

Zhihua Xiao[1,2*], Yaoru Hou[1,2], and Qiming Shao[1,2#], *Senior Member, IEEE*

[1]Department of Electronic and Computer Engineering, HKUST, Hong Kong, China, *zxiaoam@connect.ust.hk
[2]ACCESS – AI Chip Center for Emerging Smart Systems, InnoHK Centers, Hong Kong, China, #eeqshao@ust.hk

As Moore's law reaches its practical limits and computing paradigms become increasingly complex, there is a growing demand for innovative device technologies. However, completely replacing complementary metal-oxide-semiconductor (CMOS) technology is not considered feasible in the foreseeable future. In this paper, we present how a promising emerging technology, spintronic devices, can be integrated with CMOS to function as foundational building blocks for scalable memory and computing systems.

***Index Terms*—Spintronics, CMOS, Neuromorphic Computing**

I. Introduction

Recent advancements in intelligent systems have transformed the computing paradigm by reshaping both computational architectures and resource demands. The traditional Von Neumann architecture and CMOS technology, which underpinned information processing during the 20th century, now face significant challenges such as the memory wall and intrinsic physical limitations. These issues have spurred interest in novel memory technologies and alternative computing paradigms that address modern system demands.

Emerging memory technologies promise to overcome the limitations of conventional architectures by addressing performance bottlenecks and reducing latency. New memory modalities—including phase-change memory, resistive random-access memory (RAM), and magnetic RAM—offer substantially lower latency and nonvolatility compared to traditional DRAM, thereby reducing CPU idle times and enhancing throughput. Advances in non-volatile memory improve energy efficiency by lowering power consumption for data retention and enable integration of persistent storage within computing systems. Moreover, these technologies support high-bandwidth memory architectures that boost data transfer rates and parallelism, facilitating rapid bulk data movement and improved processing efficiency. Collectively, such innovations provide scalable, high-performance solutions tailored to the needs of modern applications and big data analytics.

Alternative computing paradigms, including neuromorphic, probabilistic, and quantum computing, also rely on emerging device technologies for enhanced efficiency. Notably, spintronic devices—exploiting electron spin in addition to charge—offer novel functionalities and dynamic behaviors. In the past two decades, spintronic mechanisms have evolved from spin-transfer torque (STT) to spin–orbit torque (SOT) and voltage-controlled magnetic anisotropy (VCMA). The fabrication of these devices now incorporates advanced materials such as antiferromagnetic, topological, and two-dimensional (2D) substances. Research into these new physical phenomena and device architectures is continuously driving improvements in overall computing performance [1].

Integrating spintronic devices into large-scale architectures necessitates compatibility with CMOS technology[2].

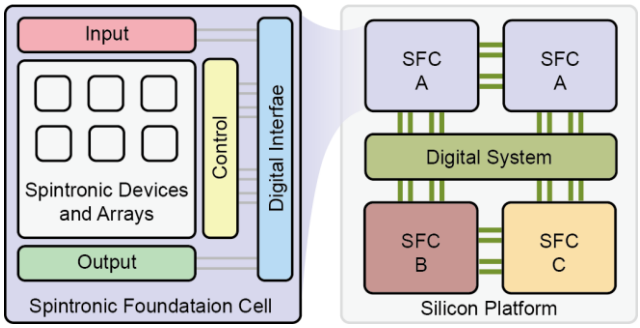

Fig. 1. Schematic diagram of a spintronic foundational cell. The scalable system consists of multiple spintronic foundational cells of various types, which are interconnected via digital interfaces.

Conventional CMOS logic relies on integrating fundamental cells such as logic gates, and these principles remain vital as emerging technologies develop. Novel devices and mechanisms must form foundational cells that interface seamlessly with CMOS or similar scalable architectures. To this end, spintronic foundational cells (SFCs) are designed to integrate key components—such as memory or crossbar arrays and probabilistic bits—with CMOS peripheral circuits for device control. Digital interfaces in these cells facilitate interaction among spintronic modules and existing digital circuits (Fig. 1).

In this work, we present design examples of spintronic foundational cells specifically tailored for scalable memory and computing systems, highlighting their potential to meet the challenges posed by next-generation intelligent systems.

II. Memory Foundation Cell with Quantum Materials

The schematic of foundation cell of SOT-MRAM is shown in Fig. 2a, in which the memory unit is the SOT-magnetic tunnel junction (MTJ) (Fig. 2b). To improve energy efficiency of SOT-MRAM, promising routes include increasing SOT efficiency and removing external field [3]. We report an all–van der Waals heterostructure integrating a type-II Weyl semimetal (Fig. 2c), $TaIrTe_4$, with an above-room-temperature ferromagnet, Fe_3GaTe_2, that enables robust field–free magnetization switching via an unconventional SOT [4]. The reduced crystal symmetry at the $TaIrTe_4$ surface produces a significant out–of–plane spin polarization and thus induces energy-efficient field-free switching when current is applied along its a–axis (Fig. 2d). The field-free switching polarity maintains until an in–plane

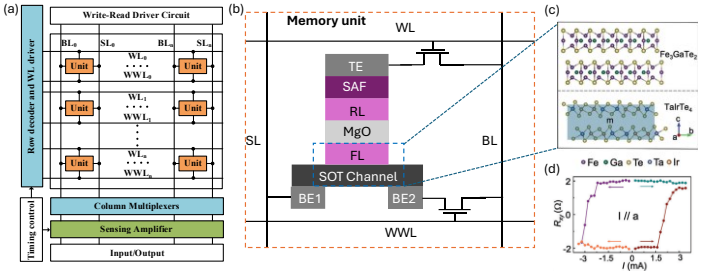

Fig. 2. (a) Schematic of the foundation cell of SOT-MRAM. (b) Schematic of the memory unit of SOT-MTJ. (c) Schematic of $TaIrTe_4$ and Fe_3GaTe_2. (d) Field-free SOT switching when the current is applied along the a-axis of $TaIrTe_4$.

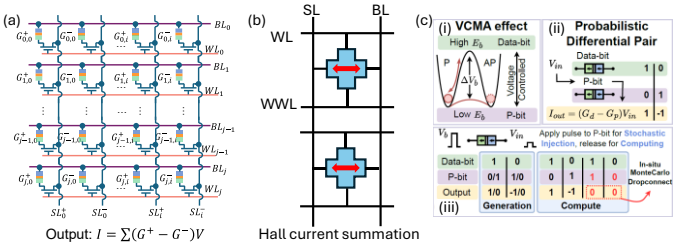

Fig. 3. (a) Schematic of an AiMC crossbar array. (b) Schematic of two Hall bar devices for realizing Hall current summation. (c) Schematics of (i) data bit, p-bit and (ii) their differential pair based on VCMA-MTJs. (iii) Possible outputs of the probabilistic differential pair for weight and dropconnect. (a)

magnetic field of 252 mT is applied. Macrospin simulations incorporating thermal fluctuations corroborate that larger spin canting angles reduce the required switching currents and improve stability. This robust, energy–efficient switching and high magnetic field resilience highlight the $TaIrTe_4/Fe_3GaTe_2$ heterostructure's potential for non–volatile memory and scalable spintronic applications.

III. Analog in Memory Computing Foundation Cells

Memristors have emerged as promising devices for efficient multiply-accumulate (MAC) operations in crossbar array-based foundation cells (Fig. 3a)—a capability that is critical for advancing analog in-memory computing (AiMC). However, device and circuit variations inherent in memristors can compromise the accuracy of analog computations. To construct a scalable AiMC system, it is essential to address and leverage these variations. Traditionally, on-chip training has been used to mitigate such issues; however, this approach is challenging for memristors due to their limited endurance.

In our recent study[5], [6], we introduce a hardware–software co-design framework that employs MTJ-based off-chip calibration for AiMC, achieving software-level accuracy without the overhead associated with expensive on-chip training. Experimentally, our results demonstrate that MTJ devices exhibit ultralow cycle-to-cycle variations, a finding validated through tests on over one million mass-produced devices. On the software side, the high degree of hardware uniformity enables us to develop an off-chip training strategy that fine-tunes deep neural network parameters, resulting in highly precise AiMC inference. This approach allows the system to be scaled by replicating multiple identical AiMC spintronic foundation cells, without being limited by device variations.

Furthermore, implementing AiMC under cryogenic temperatures can enhance performance and energy efficiency in computation-intensive environments, particularly in applications such as quantum control[7]. Magnetic topological insulators (MTIs) offer a promising path toward reliable AiMC by facilitating the summation of the anomalous Hall current[8], enabled by their large anomalous Hall resistance range and high noise-to-signal ratio (Fig. 3b).

In addition to stable memory states, probabilistic bits (p-bits) can be constructed using MTJs [9]. Conventionally, the generation and computation of random bits are separated by sample and transfer operations between analog and digital systems. We propose to use the dual feature – stable data bit and p-bit – of MTJs to realize an in-memory probabilistic computing scheme (Fig. 3c) [10]. We use probabilistic differential pairs to construct a Monte Carlo dropconnect Bayesian neural network to directly calculate the stochastic differential equations for image generation.

IV. Acknowledgements

These works are partially supported by ACCESS – AI Chip Center for Emerging Smart Systems, the InnoHK initiative of the Innovation and Technology Commission of the Hong Kong Special Administrative Region Government, ITC ITSP seed program (ITS/153/22), and RGC Theme-based Research Scheme (T46-705/23-R).

References

[1] Q. Shao, Z. Wang, Y. Zhou, S. Fukami, D. Querlioz, and L. O. Chua, "Spintronic memristors for computing," *npj Spintron.*, vol. 3, no. 1, p. 16, May 2025, doi: 10.1038/s44306-025-00078-z.

[2] Q. Shao, K. Garello, and J. Tang, "Spintronic foundation cells for large-scale integration," *Nat. Rev. Electr. Eng.*, Oct. 2024, doi: 10.1038/s44287-024-00106-w.

[3] Q. Shao *et al.*, "Roadmap of Spin-Orbit Torques," *IEEE Trans. Magn.*, vol. 57, no. 7, pp. 1–1, 2021, doi: 10.1109/TMAG.2021.3078583.

[4] Y. Zhang *et al.*, "Robust Field-Free Switching Using Large Unconventional Spin-Orbit Torque in an All-Van der Waals Heterostructure," *Adv. Mater.*, 2024, doi: 10.1002/adma.202406464.

[5] Z. Xiao, V. B. Naik, J. H. Lim, Y. Hou, Z. Wang, and Q. Shao, "Adapting magnetoresistive memory devices for accurate and on-chip-training-free in-memory computing," *Sci. Adv.*, vol. 10, no. 38, Sep. 2024, doi: 10.1126/sciadv.adp3710.

[6] Z. Xiao *et al.*, "Device Variation-Aware Adaptive Quantization for MRAM-based Accurate In-Memory Computing Without On-chip Training," *Tech. Dig. - Int. Electron Devices Meet. IEDM*, vol. 2022-Decem, pp. 1051–1054, 2022, doi: 10.1109/IEDM45625.2022.10019482.

[7] Y. Liu *et al.*, "Cryogenic in-memory computing using magnetic topological insulators," *Nat. Mater.*, Jan. 2025, doi: 10.1038/s41563-024-02088-4.

[8] K. Qian *et al.*, "Cryogenic In-Memory Computing Circuits with Giant Anomalous Hall Current in Magnetic Topological Insulators for Quantum Control," *Int. Electron Devices Meet.*, 2024.

[9] S. Chowdhury *et al.*, "A Full-Stack View of Probabilistic Computing With p-Bits: Devices, Architectures, and Algorithms," *IEEE J. Explor. Solid-State Comput. Devices Circuits*, vol. 9, no. 1, pp. 1–11, 2023, doi: 10.1109/JXCDC.2023.3256981.

[10] Z. Xiao *et al.*, "In-Memory Neural Stochastic Differential Equations with Probabilistic Differential Pair Achieved by In-situ P-bit using CMOS Integrated Voltage-Controlled Magnetic Tunnel Junctions," *Tech. Dig. - Int. Electron Devices Meet. IEDM*, 2024, doi: 10.1109/IEDM50854.2024.10873318.

Toward All-Electric Non-volatile Intelligence in Spintronic Reservoir

Jing Zhou[1], Jikang Xu[2], Lisen Huang[1], Sherry Lee Koon Yap[1], Shaohai Chen[1], Xiaobing Yan[2], *Senior Member, IEEE,* and Sze Ter Lim[1]

[1]Institute of Materials Research and Engineering, Agency for Science, Technology and Research (A*STAR), 2 Fusionopolis Way, Innovis #08-03, Singapore 138634, Republic of Singapore, zhou_jing@imre.a-star.edu.sg; lim_sze_ter@imre.a-star.edu.sg

[2]Key Laboratory of Brain-like Neuromorphic Devices and Systems of Hebei Province, Key Laboratory of Optoelectronic Information Materials of Hebei Province, Hebei University, Baoding 071002, China, yanxiaobing@ime.ac.cn

Integrating physical dynamics with computational models is gaining traction for boosting neural network efficiency. Physical reservoir computing leverages the intrinsic dynamics of materials for temporal processing but faces challenges in constructing efficient reservoirs. Here, we move beyond delay-based designs by harnessing spatiotemporal transformations in all-electric, non-volatile spintronic devices. By triggering devices with varied pulse widths, we emulate neurons and build a compact reservoir with strong non-linearity and dense interconnectivity. Despite using only 14 physical nodes, our system achieves a 0.903 recognition rate on handwritten digits and a 0.076 error rate in Mackey-Glass prediction, validated on a proof-of-concept PCB.

***Index Terms*—Reservoir Computing, Nonvolatile Memory, Hall Effect Devices, Spin Valves.**

I. Introduction

The recurrent neural network (RNN) is a special framework of artificial intelligence (AI) designed for temporal data processing, which has broad applications in physics, biology and finance. RNN suffers from the haunting problem of exploding (or vanishing) gradient during training, to which the conventional approaches, such as long short-term memory and backpropagation through time, remain inefficient. Reservoir computing (RC) emerges as an improved RNN paradigm[1]. It is featured by an input-driven reservoir of high-dimensional data space and a memoryless readout layer. Only the readout layer is trained, making RC particularly suitable for the edge AI, where resources are constrained. Recent advances leverage physical processes to implement RC with analog responses of hardware – known as physical RC (PRC) – including mechanical, photonic and electronic systems[2, 3]. However, conventional PRC approaches rely on delay-based volatile reservoirs, enforcing a pulse-train-like input stream with a narrow bandwidth, limiting AI task performance. Here, for the first time, we provide an approach to construct non-volatile PRC using all-electric spintronic devices, completely separating input timescale from task timescale[4]. Our physical reservoir is realized on a customized printed circuit board (PCB) to mimic on-chip training. It exhibits excellent performance in benchmark classification and prediction tasks while lowering energy consumption by 99.6% compared to software implementation.

II. Methods and Approaches

A. Fading Memoroy

A mathematical precondition of reservoir computing is fading memory, which requires the future readout of reservoir to depend on past inputs and this dependence weakens over time. We demonstrate this property with Hall bars made of perpendicularly magnetized ferromagnetic layer, which can be switched by SOT without external magnetic field[5]. Fig. 1(a) shows SOT-induced Hall resistance (R_H) changes when 6 voltage pulse trains are applied. Note that only the third pulse (N_p = 3) has a different pulse amplitude (V_p) and the remaining V_p are the same for each pulse across the 6 trains. Clearly, the R_H response begins to diverge at N_p = 3 and eventually converge at N_p = 7, thus phenomenologically showing fading memory. We attribute this behaviour to the path dependence of domain evolution in magnetic hysteresis. That is, as long as the magnetization is not fully switched, its future trajectory depends on both the history of its past states and the sequence of electrical inputs.

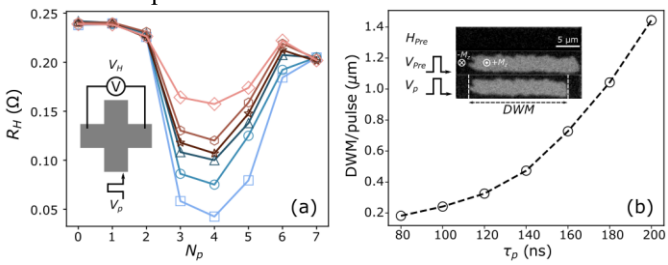

Fig. 1. Fading memory and non-linearity. (a) Variation of Hall resistance by 6 pulse trains with a different pulse amplitude only at the 3rd pulse. (b) Dependence of domain wall motion (DWM) per pulse on pulse width (τ_p).

B. Non-linearity

A working reservoir also requires non-linear dynamics. We study the SOT-driven domain evolution in a 5-μm microstrip using magneto-optic Kerr effect (MOKE) microscopy. The initial state is created using the same preset field (H_{pre}) and voltage (V_{pre}) for measurement. Then we count the total number of a fixed voltage pulse required to switch all $+M_z$ domains to $-M_z$. The extracted average domain wall motion (DWM) per pulse is shown in Fig. 1(b), which is unambiguously non-linear in different pulse widths (τ_p). Since R_H is proportional to $\pm M_z$, we expect R_H-τ_p to be non-linear as well.

C. Network and circuits

The physical reservoir is constructed in a three-step process as illustrated in Fig. 2(a). First, the input u_n is converted to a pulse train of fixed amplitude with the magnitude of u_n linearly mapped to τ_p. Second, the same u_n is mapped to different τ_p intervals – defined as the dynamic range (DR) – to generate distinct neurons. Finally, multiple neuron responses are stacked to generate a high-dimensional reservoir matrix X, followed by a standard readout using ridge regression (W_{out} is output weight matrix). We develop peripheral circuit on a customized PCB to support parallel processing. In Fig. 2(b), a total of 14 Hall bars

– as devices under test (DUT) – of highly homogeneous device properties are connected such that different neurons can be generated simultaneously, ensuring a high processing speed. The PCB is connected to a computer vias the USB port, and Python is used to run training algorithm and process data.

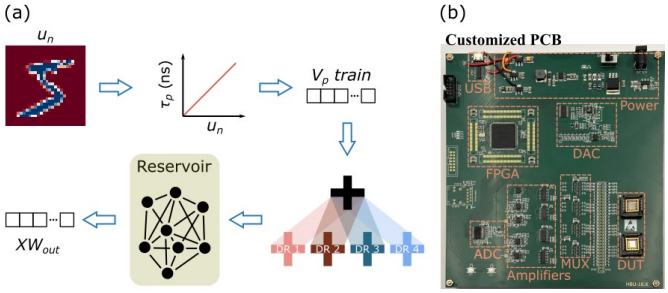

Fig. 2. Reservoir structure. (a) Construction of a physical reservoir from analog responses of Hall bars. (b) Customized PCB.

III. Performance

A. Classification

We first test our approach with a benchmark AI task – MNIST written digit recognition. We use the first 20,000 training samples from the database as our data pool then perform 10-fold cross validation. Fig. 3(a) shows the confusion matrix of a single trial with 20000 samples (N_s = 20k), achieving a high testing accuracy (A_{test}) of 0.903. Notably, our reservoir is making human-like mistakes since it confuses '5' with '3' and '9' with '4'. In Fig. 3(b), when we gradually increase the sample population, the training accuracy (A_{train}) decreases but A_{test} increases. This is because the reservoir can capture the features of a small dataset, but a sufficiently big dataset is required for generalization. The best performance achieved at N_s = 20000 are A_{train} = 0.916±0.001 and A_{test} = 0.880±0.001.

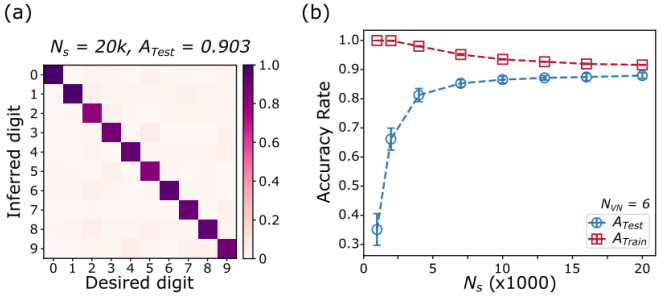

Fig. 3. Written digit classification. (a) Confusion matrix of a single trial. (b) Ttraining (A_{train}) and testing accuracy (A_{test}) from 10-fold cross validation.

B. Prediction

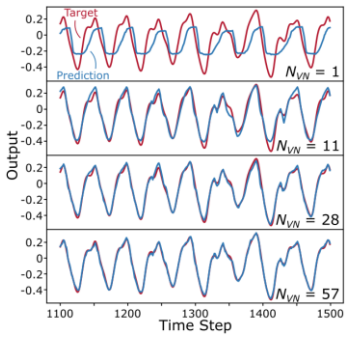

Fig. 4. Mackey-Glass chaotic time series prediction.

We also performed Mackey-Glass chaotic time series prediction, which is a specific benchmark task for RNN. We flush the first 100 data points and train the next 1000 data points to predict the 400 points after. Fig. 4 shows the effect of increasing the number of neurons (N_{VN}) on reservoir performance. When N_{VN} = 1, the prediction only captures the major frequency of the data, producing large discrepancies and phase difference. As N_{VN} increases, the discrepancies between prediction and target rapidly decreases, eventually producing highly superimposed traces at N_{VN} = 57. The normalized root mean square error achieved is 0.076, which is among the lowest.

C. Evaluation

We evaluate our physical reservoir by benchmarking its energy consumption against software implementation of RC in Table I. Our systems has a 99.6% and 94.8% of energy saving compared with a CPU implementation using state-of-the-art echo state network and feed forward neural network (FNN), respectively. We attribute this to the much less matrix multiplication in our system and operating energy of devices.

TABLE I. COMPARISON OF RC

Method	Network	Energy/sample	Energy/task
Spintronic memristor + CPU	RC	Device:1.16 µJ CPU: 0.212 mJ Total: 0.213 mJ	Device: 23.1 mJ CPU: 4.25 J Total: 4.27 J
CPU	RC	51.0 mJ	1.02 kJ
CPU	FNN	4.07 mJ	285 J

D. Scaling

We have successfully integrated the field-free strategy in our Hall bar with SOT-MTJ, which has a cell diameter of 240 nm, an endurance larger than 10^{12} and 100% switching probability at 10 ns[6]. The proposed domain-based reservoir construction strategy can be adapted to MTJ arrays where individual MTJ – being single-domain – switches on a probabilistic basis. The collective readout of MTJ arrays will be used in the place of R_H.

IV. Conclusion

We have demonstrated a non-volatile physical reservoir using non-linear dynamics of magnetic domains. The proposed method shows excellent AI task performance, and is scalable and adaptable to other nonvolatile memristors.

References

[1] M. Lukoševičius and H. Jaeger, "Reservoir computing approaches to recurrent neural network training," *Computer Science Review,* vol. 3, no. 3, pp. 127-149, 2009.

[2] X. Liang, J. Tang, Y. Zhong, B. Gao, H. Qian, and H. Wu, "Physical reservoir computing with emerging electronics," *Nature Electronics,* vol. 7, no. 3, pp. 193-206, 2024.

[3] H. Jaeger, B. Noheda, and W. G. van der Wiel, "Toward a formal theory for computing machines made out of whatever physics offers," *Nature Communications,* vol. 14, no. 1, p. 4911, 2023.

[4] J. Zhou *et al.*, "Harnessing spatiotemporal transformation in magnetic domains for nonvolatile physical reservoir computing," *Science Advances,* vol. 11, no. 2, p. eadr5262, 2025.

[5] J. Zhou *et al.*, "Chiral Interlayer Exchange Coupling for Asymmetric Domain Wall Propagation in Field-Free Magnetization Switching," *ACS Nano,* vol. 17, no. 10, pp. 9049-9058, 2023.

[6] J. Zhou *et al.*, "Synergizing intrinsic symmetry breaking with spin–orbit torques for field-free perpendicular magnetic tunnel junction," *APL Materials,* vol. 12, no. 8, 2024.

Noise-Aware Training of Dynamical Physical Neural Networks of Spintronic Nanodevices

Luca Manneschi[1], Ian T. Vidamour[1], Kilian D. Stenning[2], Charles Swindells[1], Guru Venkat[1], David Griffin[3], Lai Gui[2], Daanish Sonawala[2], Denis Donskikh[2], Dana Hariga[1], Elisa Donati[4], Susan Stepney[3], Will R. Branford[2], Jack C. Gartside[2], Thomas J. Hayward[1], Matthew O. A. Ellis[1] and Eleni Vasilaki[1]
[1]The University of Sheffield, Sheffield, S1 4DP, United Kingdom
[2]Blackett Laboratory, Imperial College London, London SW7 2AZ, United Kingdom
[3]University of York, Heslington, York, YO10 5DD, United Kingdom
[4]Institute of Neuroinformatics, University of Zurich and ETHZ, Zurich, Switzerland

Spintronic nano-devices hold significant promise for energy-efficient neuromorphic computing, thanks to their non-volatility, efficient control methods, and complex non-linear dynamics. However, their inherent noise and stochasticity can often hinder performance and necessitate off-chip training. This talk introduces a framework for constructing dynamical physical neural networks (PNNs) from spintronic nano-devices, specifically for temporal tasks, using differentiable digital twins. By incorporating noise directly into the training process via data-driven stochastic models, this approach captures the devices' variability, enabling rapid prototyping, off-device training, and informed network design. Noise-aware training significantly improves transferability to hardware, outperforming deterministic models in tasks such as smart prosthetic gesture prediction, while also requiring fewer experimental measurements than alternative methods. This work highlights how the noisy nature of spintronic systems can be harnessed as a valuable asset for unconventional computing.

***Index Terms*—Physical Neural Networks, Neuromorphic Computing, Spintronics.**

I. Introduction

SPINTRONIC devices hold significant promise as physical substrates for neuromorphic computing, thanks to their non-volatile and non-linear behaviour, with potential for low-energy control [1], [2]. When interconnected into physical neural networks (PNNs), these devices can exhibit complex emergent behaviours that go beyond the principles of reservoir computing, offering potential for richer computational capabilities directly within the hardware—an approach especially relevant for edge computing tasks.

In conventional artificial neural networks, the connection weights between neurons are optimised by directly calculating the error gradient via backpropagation. In physical systems, however, measuring gradients directly is often inefficient or impractical due to a lack of accurate models, the presence of noise, variability, and device-specific limitations. As a result, training is commonly performed using alternative methods that estimate gradients indirectly—often by simulating the device's behaviour in software while grounding the training methodologies in experimental data wherever feasible. Examples include Physics-Aware Training (PAT) [3] which uses a digital twin of the physical system to compute approximate gradients, but so far it has primarily been demonstrated on static, feed-forward tasks such as image classification.

Notably, many physical systems naturally exhibit temporal dynamics, which may be particularly advantageous for solving tasks such as signal transformation, time-series forecasting, or classification of long-term dependencies, but these capabilities remain largely under-explored in current techniques. In this work, we present an approach that extends the PAT methodology to address such tasks while crucially accounting for the stochastic variability in device responses, enabling robust learning and deployment.

II. Noise-aware training of physical neural networks

In physical systems their inherent stochasticity and noise can be detrimental, especially when the connection weights are trained off-device. To avoid this 'simulation-reality gap', we present an approach based around the creation of stochastic digital twins that are trained to model the device responses and provide a analogue for training off-device using powerful gradient-based approaches. This approach leverages advanced machine learning models based on stochastic differential equations (SDEs) [4] to create device responses that mimic experimental measurements with similar noise distributions. This allows for off-device training using backpropagation-through-time (BPTT) to learn the interconnection weights between devices to effectively solve a temporal task. Since the off-device training observes realistic noisy device responses, the learning process is able to account for this and create a more robust solution. This means when the interconnection weights are transferred to the real devices for testing, there is minimal drop in performance. An overview of this process if shown in Fig. 1 for a PNN comprised of nanomagnetic ring array.

III. Results

The first stage of this approach involves training models that replicate the responses of target nanomagnetic systems. In this work, we use neural stochastic differential equations (SDEs) [4], which employ a small deep neural network to learn functions for both the deterministic and stochastic time derivatives.

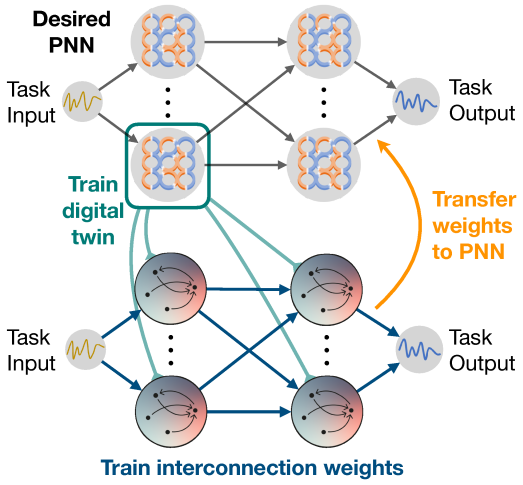

Fig. 1. Offline training loop for physical neural networks. First, a stochastic digital twin based on a neural-SDE is trained on individual spintronic devices to allow offline training using backpropagation-through-time. The interconnection weights are then trained in simulation using realistic responses generated by the model. Finally, the optimised weights are transferred to the experimental system for inference.

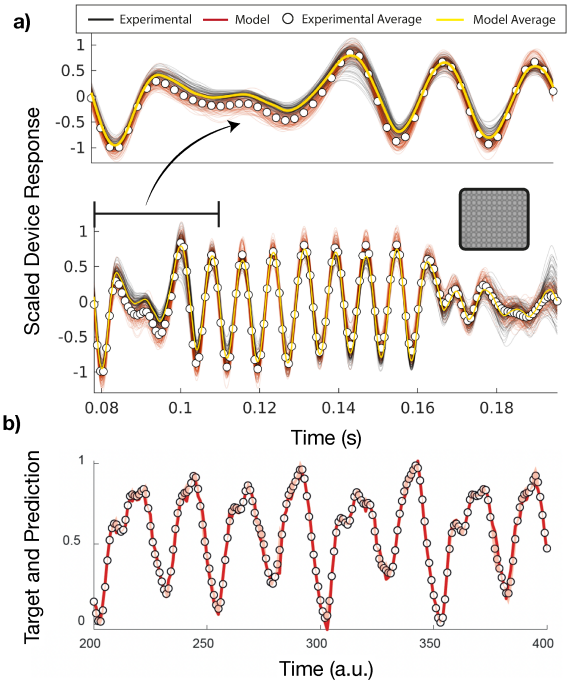

Fig. 2. Results of a) training a neural-SDE to predict the dynamics of a nanomagnetic ring array response, and b) testing of the physical neural network to forward predict the Mackey-Glass task.

This method was applied to two candidate spintronic nanodevices: a nanomagnetic ring array (NRA) [5] and artificial spin vortex ice (ASVI) [6], both of which have previously been investigated for neuromorphic computing. Figure 2(a) shows the model's predicted device response for the NRA device under a given driving magnetic field. Repetitions of the same field sequence produce different trajectories due to device stochasticity, and our trained model successfully captures this behaviour. This approach yields a noisy output that reflects the inherent variability of the physical system and may assist in identifying parameter regimes during the optimisation process that avoid large noise fluctuations.

An example of this is shown in Fig. 2(b). The task uses the chaotic Mackey-Glass time series as a benchmark for regression performance, requiring the system to forecast five steps ahead—a standard challenge in neuromorphic spintronic systems [7]. In this result, we train a three-layer neural network using the device models in simulation. The optimised connection weights are then transferred to the experimental system, where a single device is time-multiplexed to emulate multiple devices. In this case, we observe a mean squared error approximately an order of magnitude lower than existing results in the literature [7]. Furthermore, we apply this methodology to a temporal classification task based on handwritten digits, where a two-layer PNN achieves comparable improvements. In both cases, incorporating stochastic effects is crucial for the successful transfer of weights to the physical network.

In summary, we have proposed a framework for training physical neural networks composed of spintronic devices using stochastic models. These models provide noisy predictions of device dynamics under input signals, enabling simulated optimisation of the connectivity that can then be transferred to the physical system with minimal loss of accuracy. This approach is general and can be applied across a range of neuromorphic systems.

Acknowledgements

The authors gratefully acknowledge funding from the EPSRC (Projects No. EP/V006339/1, EP/V006029/1, EP/W524335/1, EP/Y003276/1 and EP/S009647/1), The Eric and Wendy Schmidt Fellowship Program, Horizon 2020 FET-Open (Agreement No 861618), and the Royal Academy of Engineering.

References

[1] J. Grollier, D. Querlioz, K. Camsari, K. Everschor-Sitte, S. Fukami, and M. D. Stiles, "Neuromorphic spintronics," *Nature electronics*, vol. 3, no. 7, pp. 360–370, 2020.

[2] D. A. Allwood, M. O. Ellis, D. Griffin, T. J. Hayward, L. Manneschi, M. F. Musameh, S. O'Keefe, S. Stepney, C. Swindells, M. A. Trefzer *et al.*, "A perspective on physical reservoir computing with nanomagnetic devices," *Applied Physics Letters*, vol. 122, no. 4, 2023.

[3] L. G. Wright, T. Onodera, M. M. Stein, T. Wang, D. T. Schachter, Z. Hu, and P. L. McMahon, "Deep physical neural networks trained with backpropagation," *Nature*, vol. 601, no. 7894, pp. 549–555, 2022.

[4] P. Kidger, J. Foster, X. Li, and T. J. Lyons, "Neural sdes as infinite-dimensional gans," in *International conference on machine learning*. PMLR, 2021, pp. 5453–5463.

[5] R. W. Dawidek, T. J. Hayward, I. T. Vidamour, T. Broomhall, G. Venkat, M. Al Mamoori, A. Mullen, S. J. Kyle, P. Fry, N.-J. Steinke, J. Cooper, F. Maccherozzi, S. S. Dhesi, L. Aballe, M. Foerster, J. Prat, E. Vasilaki, M. O. A. Ellis, and D. A. Allwood, "Dynamically-Driven Emergence in a Nanomagnetic System," *Advanced Functional Materials*, vol. 31, no. 8, 2021.

[6] J. C. Gartside, K. D. Stenning, A. Vanstone, H. H. Holder, D. M. Arroo, T. Dion, F. Caravelli, H. Kurebayashi, and W. R. Branford, "Reconfigurable training and reservoir computing in an artificial spin-vortex ice via spin-wave fingerprinting," *Nature Nanotechnology*, vol. 17, no. 5, pp. 460–469, 2022.

[7] K. D. Stenning, J. C. Gartside, L. Manneschi, C. T. Cheung, T. Chen, A. Vanstone, J. Love, H. Holder, F. Caravelli, H. Kurebayashi *et al.*, "Neuromorphic overparameterisation and few-shot learning in multilayer physical neural networks," *Nature Communications*, vol. 15, no. 1, p. 7377, 2024.

Advanced magnetic tunnel junctions for voltage-controlled MRAM

Shinji Yuasa[1], Takayuki Nozaki[1], Tatsuya Yamamoto[1], Tomohiro Nozaki[1], Hiroyasu Nakayama[1], Tomohiro Ichinose[1], Junyeon Kim[1], Sumito Tsunegi[1], Shingo Tamaru[1], Kay Yakushiji[1], Hitoshi Kubota[1]

[1]National Institute of Advanced Industrial Science and Technology (AIST), Tsukuba, 305-8568, Japan, yuasa-s@aist.go.jp

Voltage-controlled (VC) – MRAM based on the voltage-controlled magnetic anisotropy (VCMA) effect and dynamic switching is expected to be an ultimate writing technology with ultra-low power consumption. Magnetic tunnel junctions (MTJs) for VC-MRAM need to have high magnetoresistance (MR) ratio, large perpendicular magnetic anisotropy (PMA) and high VCMA ecoefficiency. To develop such MTJs, we developed a novel sputtering deposition process at cryogenic temperatures. By means of the cryogenic temperature deposition, we fabricated high-quality free layers with ultrathin CoFeB and boron-free ferromagnetic materials on MgO or Fe-doped MgO tunnel barrier.

***Index Terms*— Magnetic tunnel junction, Tunneling magnetoresistance, Perpendicular magnetic anisotropy**

I. Introduction

Giant tunnel magnetoresistance (TMR) effect in MgO-based magnetic tunnel junctions (MTJs) is the key technology in magnetoresistive random-access memory (MRAM). Among several types of magnetoresistive random-access memory (MRAM), spin-transfer-torque (STT) – MRAM has been extensively studied and already commercialized as embedded non-volatile memory for system LSI. For MRAM to replace high-speed memory such as SRAM, however, MRAM needs to have higher speed and lower energy consumption for writing. One of the candidates for such advanced MRAM is voltage-controlled (VC) – MRAM based on voltage-induced dynamic switching, which is expected to be an ultimate writing technology with ultra-low power consumption [1]. For practical VC-MRAM, magnetic tunnel junctions (MTJs) need to have high magnetoresistance (MR) ratio, large perpendicular magnetic anisotropy (PMA) and high voltage control of magnetic anisotropy (VCMA) coefficient. We also need to suppress write errors of the dynamic switching. High-density VC-MRAM requires MTJs to have PMA > 0.5 mJ/m^2 and VCMA coefficient > 300 fJ/Vm.

II. New materials and processes for VC-MRAM

To establish basic technologies for VC-MRAM, we developed advanced MTJs with new materials. By using new free-layer materials such as Ir-doped Fe(-Co) and hybrid tunnel barrier, we have achieved VCMA > 300 fJ/Vm and PMA > 0.5–1 mJ/m^2 [2-4], which almost satisfy the requirements for VC-MRAM.

It is also important to fabricate high-quality ultrathin free layer on MgO(001) tunnel barrier. However, an ultrathin free layer grown on MgO(001) tends to be low quality due to the poor wettability of ferromagnetic layer on MgO surface. To overcome this difficulty, we developed a novel sputtering deposition process at cryogenic temperature [5-6]. CoFeB/MgO/CoFeB MTJ films were deposited on 300 mm Si wafers by using an advanced sputtering system shown in Fig. 1. The top CoFeB free layers were deposited at 100 K. The cryogenic temperature deposition improves the quality of CoFeB/MgO interface, resulting in a thinner dead layer, higher MR ratio, larger PMA and VCMA, and lower damping constant. Moreover, Fe-doping into MgO tunnel barrier was found to be effective for further improving the quality of free layer and thus the voltage-induced switching properties [7-8]. These properties are favorable not only for VC-MRAM but also for STT-MRAM.

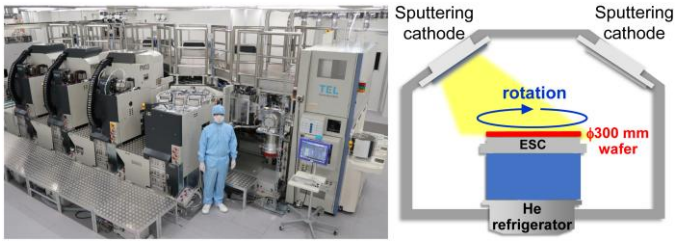

Fig. 1. Manufacturing-type sputtering deposition system (left) and schematic illustration of sputtering deposition chamber with wafer cooling stage (right).

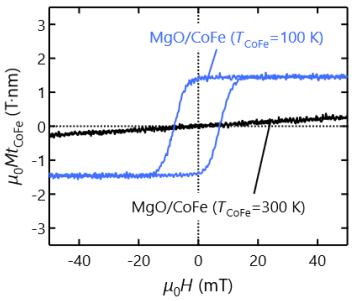

Fig. 2. Magnetization curves of an ultrathin Co-Fe layer deposited on MgO at 300 or 100 K.

By using the cryogenic temperature deposition technique, we have also prepared high-quality free layers without boron [9-10]. It should be noted that the sputtering deposition of ultrathin Co-Fe layer on oxide tunnel barrier is more difficult than the deposition on CoFeB because the wettability of Co-Fe on MgO is poorer than that of CoFeB. By means of the cryogenic temperature deposition process, we fabricated uniform ultrathin Co-Fe top free layer with sharp interfaces, resulting in better perpendicular magnetic anisotropy compared with the case of room temperature deposition (Fig. 2). The cryogenic temperature deposition of Co-Fe on the Fe-doped MgO tunnel barrier further improved the MTJ properties, providing a high

potential of boron-free ferromagnetic materials [10]. In the talk, we will also discuss write errors of voltage-induced dynamic switching.

ACKNOWLEDGEMENTS

This study was partly based on the results obtained from a project, JPNP16007, subsidized by the New Energy and Industrial Technology Development Organization (NEDO).

REFERENCES

[1] T. Nozaki *et al*., Micromachines, vol. 10, 327 (2019).
[2] T. Nozaki *et al*., APL Mater., vol. 10, 081103 (2022).
[3] T. Nozaki *et al*., NPG Asia Mater., vol. 14, 5 (2022).
[4] T. Nozaki *et al*., Appl. Phys. Lett., vol. 121, 172401 (2022).
[5] T. Ichinose *et al*., ACS Appl. Electr. Mater., vol. 5, 2178 (2023).
[6] A. Sugihara *et al*., Appl. Phys. Express, vol. 16, 023003 (2023).
[7] T. Yamamoto *et al*., Acta Materialia, vol. 267, 119749 (2024).
[8] T. Yamamoto *et al*., Phys. Rev. Appl., vol. 21, 054008 (2024).
[9] T .Yamamoto *et al*., Phys. Rev. Appl., vol. 19, 024020 (2023).
[10] T. Ichinose *et al*., arXiv:2504.07350.

Demonstration of reliable memory operation in the world's smallest 1 Selector-1 MTJ cell

Kuniaki Sugiura[1], Hisanori Aikawa[1], Jeonghwan Song[2], Toshihiko Nagase[1], Soo Man Seo[2], Yuich Ito[1], Tae Jung Ha[2], Kenichi Yoshino[1], Bo Kyung Jung[2], Tadaaki Oikawa[1], Ku Youl Jung[2], Su Jin Chae[2], Bum Su Kim[2], Min Chul Shin[2], Dong Keun Kim[2],Tae Ho Kim[2], Kosuke Hatsuda[3], Katsuhiko Hoya[3], Soo Gil Kim[2], Jae Yun Yi[2], and Seon Yong Cha[2]

[1] Kioxia Korea Corporation, Seoul, 06620, Korea, toshihiko.nagase@kioxia.com
[2] SK hynix Inc., Icheon, 17336, Korea
[3] Kioxia Corporation, Yokohama-shi, 247-8585, Japan

We demonstrate 1 Selector-1 MTJ (1S1M) cell operation in the world's highest-density 64 Gb cross-point STT-MRAM chips. We have achieved Half Pitch (HP) of 20.5 nm and MTJ Critical Dimension (CD) of 20 nm using As doped SiO2 selector and perpendicularly magnetized MTJ (p-MTJ). A novel read scheme utilizing transient behavior of selector along with the low capacitance circuitry enables us to overcome MTJ read disturbance which typically occurs when the selector turns on in scaled 1S1M cells.

***Index Terms*—MRAM, Selector, Crosspoint architecture, Read disturbance**

I. Introduction

NOVEL applications such as AI and big data processing are driving the growth of an enormous market. To further accelerate this growth, the long-awaited arrival of storage-class memory (SCM) with high performance and high bit density is essential. STT-MRAM (Spin Transfer Torque Magnetic Random Access Memory) is a promising candidate for next-generation non-volatile memory. We previously presented 4 Gb STT-MRAM with $9F^2$ 1 transistor-1 MTJ cells in 2016 [1]. However, transistors as three-terminal select devices pose challenges for increasing bit density due to their poor drivability for write operation and the complexity of contact plug layout. Recently, 1 selector-1 MTJ (1S1M) cell, comprising two-terminal select device and MTJ has been proposed to shrink cell size toward $4F^2$ [2-4]. Although low read disturbance was demonstrated in relatively large MTJ CD of 60 nm for high-density embedded memory [4], shrinking MTJ with maintaining low disturbance remains to be done.

In this work, we demonstrate 1S1M cell operation in the world's highest-density 64 Gb cross-point STT-MRAM chips [5]. We have achieved HP of 20.5 nm and MTJ CD of 20 nm using As doped SiO2 selector and perpendicularly magnetized MTJ (p-MTJ). A novel read scheme utilizing transient behavior of selector along with the low capacitance circuitry enables us to overcome MTJ read disturbance which typically occurs when the selector turns on in scaled 1S1M cells.

II. Structure of 1S1M Cells

Figure 1 shows the cross-sectional TEM images of 64 Gb cross-point MRAM test chip. To minimize the chip size, CMOS circuitry is integrated underneath 1S1M cell array. The CMOS circuitry contains row and column select switches (SW), a write driver (W/D) and a sense amplifier (S/A).

The cell array consists of word-line (WL), bit-line (BL) and 1S1M cells with HP of 20.5 nm. The 1S1M cells have As-doped SiO2 selector and p-MTJ. 4K (2K) cells are connected to BL (WL). At every cross point, 1S1M cell is sandwiched between BL and WL to make up an 8 Mb MAT. Finally, the world's smallest cell, measuring 0.001681 um^2, has been achieved with $4F^2$ design. The key features of the test chip are summarized in Table 1.

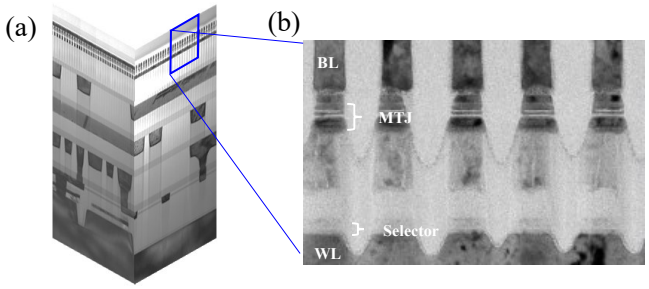

Fig. 1. 64 Gb cross-pint MRAM architecture. (a) Cross sectional TEM image. (b) 1S1M array [5].

TABLE I
Key Features of the Test Chip [5]

Item	Specification
Tech node	20.5 nm
Density	64 Gb
MAT size	4096-Rows and 2048-Columns
Read speed	6~10 nsec
Write speed	15~30 nsec

III. MTJ Characteristics

The resistance-field (R-H) curve and write error rate (WER) of typical 20 nm MTJ with HP 20.5 nm are shown in Figure 2(a) and (b), respectively. For comparison, the data of previous HP 22.5 nm MTJ [2] are also included. From self-fluctuation of magnetic coercivity (H_c), thermal stability factor (Δ) is estimated to be greater than 60 at 90℃. Despite extensive modifications to the MTJ and its fabrication process, MTJ data retention and WER have been maintained while reducing HP from 22.5 nm to 20.5 nm.

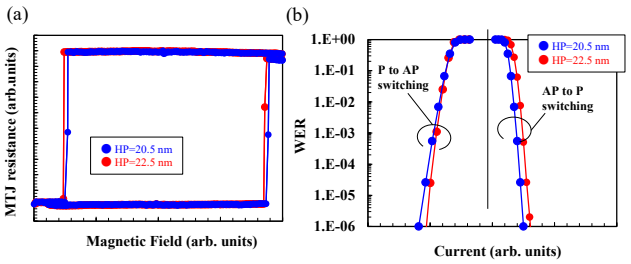

Fig. 2. Typical MTJ properties of HP 20.5 nm (blue dot) and 22.5nm (red dot). (a) R-H curve of a single MTJ device. (b) Write Error Rate (WER) at write pulse duration of 15 nsec [5].

IV. 1S1M Cell Operation

Reducing read disturbance is one of the most critical challenges in high-density 1S1M architecture. As MTJ CD shrinks, read current must be reduced to suppress unintentional writing, known as read disturbance. However, the selector holding current, which is necessary to prevent selector on/off oscillation, is typically much higher than the required read current, especially in scaled 1S1M cells. Additionally, the large spike current generated during selector turn-on operation further excerbates read disturbance. To address this issue, a novel read scheme utilizing transient behavior of selectors along with the low capacitance circuitry has been implemented in our test chip. The circuitry is pre-charged before selector turn-on, and the release of a spike current in a short duration right after the turn-on is utilized for read operation.

Figure 3 shows the simulated time evolution of the cell current from selector turn-on to turn-off. In high-cap mode, where the circuitry has a large capacitance component, a large amount of charge flows, leading to severe read disturbance. Conversely, in low-cap mode, the capacitance component is minimized, making the cell current decay faster to effectively suppress read disturbance. Figure 4(a) shows the external field response of readout signal for a typical 1S1M cell. In high-cap mode, only AP state can be maintained at zero magnetic field due to large cell current at reading operation, whereas bi-stable state of AP and P can be read in low-cap mode. Figure 4(b) shows the read disturbance test by monitoring 1S1M readout signal under cyclic read stress. No read disturbance was observed at least up to 1E6 read cycle in low-cap mode.

Finally, cyclic read/write operation was tested for a typical 1S1M cell as shown in Figure 5. The extrapolated read/write error rate reaches approximately -5σ (<1E-6), demonstrating the effectiveness of the novel read scheme with low-cap mode in suppressing read disturbance.

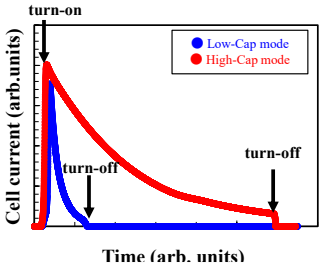

Fig. 3. Simulation results of cell current evolution from selector turn-on to turn-off, on low capacitance circuitry (blue line) and high capacitance circuitry (red line) [5].

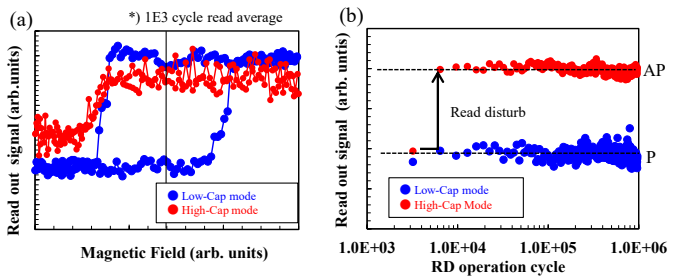

Fig. 4. (a) External magnetic field response of 1S1M cell, on low capacitance circuitry (blue dots) and high capacitance circuitry (red dots). (b) The result of read disturbance test by applying cycling read-only stress [5].

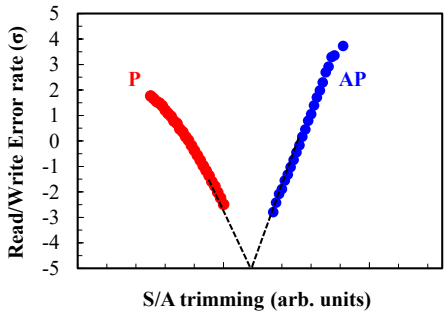

Fig. 5. Cyclic read/write operation test result for a typical 1S1M cell. Test sequence is up to 1E3 cycle consecutive "Reset (0/1) > Read > Write (1/0) > Read" operation at each S/A trimming condition. The extrapolated read/write error rate reaches around -5σ (<1E-6) [5].

V. Conclusion

We have successfully achieved the world's smallest 1S1M cell, measuring 0.001681 um^2, by incorporating optimized material design and fabrication process technologies. Furthermore, reliable 1S1M read/write operation with error rate of <1E-6 has been demonstrated. To achieve this low error rate, the novel read scheme utilizing transient behavior of selector along with the low capacitance circuitry plays a critical role in reducing read disturbance, which remains one of the most essential technical challenges for cross-point 1S1M architecture. We believe our work represents a significant leap toward high-density, high-performance, and highly reliable cross-point MRAM for SCM applications.

References

[1] S.-W. Chung et al., "4Gbit density STT-MRAM using perpendicular MTJ realized with compact cell structure" *IEDM Tech. Digest,* pp.659-662, 2016.

[2] S.M. Seo et al., "First demonstration of full integration and characterization of 4F2 1S1M cells with 45 nm of pitch and 20 nm of MTJ size", *IEDM Tech. Digest*, pp.218-221, 2022.

[3] H. Yang et al., "Threshold Switching Selector and 1S1R Integration Development for 3D Cross-point STT-MRAM", *IEDM Tech. Digest*, pp.836-839, 2017.

[4] E. Ambrosi et al., "Low voltage (<1.8 V) and high endurance (>1M) 1-Selector/1-STT-MRAM with ultra-low (1 ppb) read disturb for high density embedded memory arrays", *IEDM Tech. Digest*, 21-5, 2023.

[5] H. Aikawa et al., "Reliable memory operation with low read disturb rate in the world smallest 1Selector-1MTJ Cell for 64 Gb cross-point MRAM," *IEDM Tech. Digest*, 20-1, 2024.

TEL PVD Technology for the Spintronics Devices

Chang-Man Park[1], Kanto Nakamura[2], Atsushi Gomi[2], Koji Maeda[2], Noel Abarra[2], Hiroaki Chihaya[2]
Yasushi Kodashima[2], Naoki Watanabe[2], Qin Fei[2], Ono Kazunaga[2], Atsushi Shimada[2], Tetsuya Miyashita[2], Toru Kato[3], Hiroki Nakagawa[4], Toshiyuki Ikebuchi[4], Hideomi Satoh[4], Akihisa Sekiguchi[4]

[1]Tokyo Electron U.S. Holdings, Inc. 2859 Bayview Drive, Fremont, CA 94538, USA, chang-man.park@us.tel.com,
[2]Tokyo Electron Technology Solution (TTS), [3]Tokyo Electron America (TEA), [4]Tokyo Electron Ltd. (TEL)

This talk will give you an overview of Tokyo Electron Ltd.'s PVD technology for the spintronics technology devices such as MgO tunnel barrier based MTJ process. It will introduce general concept of MTJ PVD module technology to fabricate sophisticated MTJ multilayer thin film. And the talk will share the latest performance of p-MTJ for STT-MRAM, ultra-low RA in-plane MTJ for HDD read sensor and lastly high RA TMR MTJ for the magnetic sensor application. And will briefly touch about the future roadmap for the mass production up to SOT MRAM

***Index Terms*—PVD, Magnetic Tunnel Junction, STT-MRAM, Tunneling Magneto Resistance, SOT-MRAM**

I. Introduction

The field of spintronics is rapidly evolving, ushering in a new era of memory technologies such as STT-MRAM**,** HDD**,** and TMR magnetic sensors**.** These innovative devices are poised to replace conventional solutions due to their superior performance, including enhanced speed**,** accuracy, reduced power consumption, and improved thermal stability.

However, the widespread adoption of STT-MRAM, HDD, and TMR devices hinges on overcoming key manufacturing hurdles, particularly in physical vapor deposition (PVD)**.** This talk will delve into the crucial role of TEL PVD tools in fabricating these advanced spintronic devices, highlighting how TEL's technology enables the precise material properties essential for their optimal function. Figure 1 shows how the MgO MTJ's RA decreasing by the STT-MRAM node size as well as the HDD AD (Areal Density) increases.

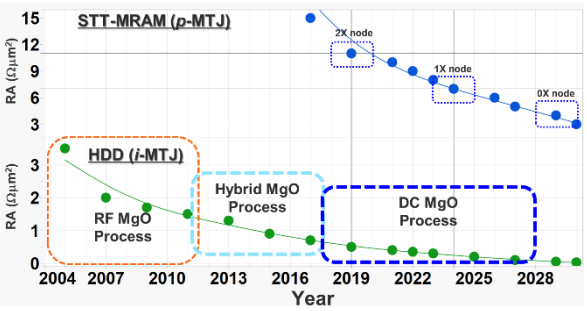

Fig. 1. RA requirement for the STT-MRAM node and HDD AD

II. p-MTJ for STT-MRAM Application

The landscape of embedded memory is undergoing a significant transformation, driven by the advent of perpendicularly magnetized CoFeB (p-MTJ) with an MgO tunnel barrier. This innovative technology, pioneered by IBM and Tohoku University, is propelling 22nm embedded STT-MRAM devices to the forefront, positioning them as a compelling replacement for eFlash in a wide array of microcontroller (MCU) and Internet of Things (IoT) applications. This shift is particularly impactful within 300 mm wafer-based semiconductor foundries.

The fabrication of these advanced p-MTJ devices primarily leverages multi-chamber Physical Vapor Deposition (PVD) technology. A critical aspect of this process is the highly specialized MgO growing technique, where TEL have developed industry-proven modules and technologies, ensuring the consistent and reliable production of these high-performance memory components.

This convergence of materials innovation and advanced manufacturing processes is enabling the widespread adoption of STT-MRAM, promising enhanced performance, lower power consumption, and improved scalability for next-generation embedded systems in 1x node and up to the SOT-MRAM era. As a result, TEL MTJ PVD is already being used far beyond the SOT-MRAM of the magnetic memory R&D area.

III. Ultra-Low RA i-MTJ for Hard Disk Drive Read Sensor Application

The demand for high areal density per cost in the Hard Disk Drive (HDD) industry is experiencing a significant resurgence, driven by the growth of edge computing and nearline storage solutions. This renewed demand has accelerated the reduction of the resistance-area product (RA) in magnetic read sensors, specifically the in-plane magnetic tunnel junction (i-MTJ), at a pace far exceeding what was seen 20 years ago when the first MgO tunnel barrier i-MTJs were introduced.

The evolution of read sensor design and integration has moved beyond basic configurations, making the process repeatability and cost of ownership of PVD (Physical Vapor Deposition) tools for ultra-low RA i-MTJs critical business considerations. In response to these challenges, TEL has achieved a world-first record in ultra-low RA with high Tunnel Magnetoresistance (TMR) using its 8-inch MTJ PVD tool, which is now in mass production for HDD read sensor processes. This continuous improvement process (CIP) in existing modules enables areal densities capable of reaching 2 Tb/in^2 with technologies like Heat-Assisted Magnetic Recording (HAMR) and beyond, pushing the boundaries of HDD technology.

IV. TMR MAGNETIC SENSOR APPLICATION

The rapid advancements in visual intelligence (VI), electric vehicles (EVs), and autonomous control (spanning robotics, transportation, logistics, and delivery) have created a surprising surge in demand for high-performance, low-power system-on-chip (SoC) integrated Tunnel Magnetoresistance (TMR) sensors. Similar to other Magnetic Tunnel Junction (MTJ) device industries, the TMR magnetic sensor sector faces the crucial challenge of cost reduction and achieving a favorable Cost of Ownership (CoO). To expand the market and its roadmap, increasing wafer size and optimizing tool utilization are essential, alongside continuous technological assessment. V.Interestingly, despite this push, the TMR magnetic sensor PVD (Physical Vapor Deposition) market is still in its early stages, with a less aggressive Compound Annual Growth Rate (CAGR). This means there's currently no immediate urgency for high-throughput PVD solutions with excellent CoO, making it a space to watch for long-term developments.

Given TEL MTJ PVD's established success in both STT-MRAM semiconductor foundries and the production of ultra-low RA (resistance-area product) HDD (Hard Disk Drive) read sensors with high TMR ratios, we are particularly interested in this application. Our goal is to provide omparable or superior technology and manufacturability for the long term, all while maintaining a focus on superior Cost of Ownership (CoO) and Cost of Consumables (CoC).

Lastly figure 2 is showing the overall TEL BKM p/i-MTJ performance of RA vs. TMR which can cover wide capability by unique TEL MgO and PVD technology

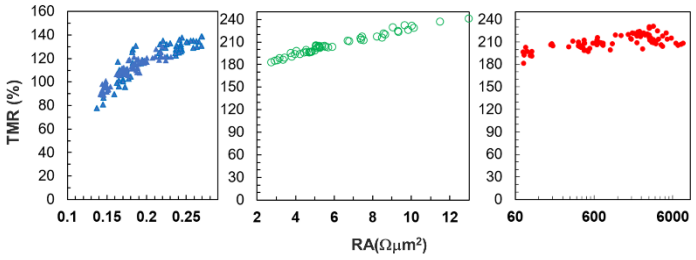

Fig. 2. TEL BKM i/p-MTJ performance for HDD, STT-MRAM and TMR magnetic sensor applications

Conclusion

After more than a decade of working closely with customers in spintronics semiconductor foundries and Hard Disk Drive (HDD) mass production, we've identified the critical requirements for contributing to cutting-edge technology and robust products. We dedicate our daily efforts to these key areas:

High-Quality MTJ Deposition

It's essential to achieve consistent Resistance-Area (RA) product, a high Tunnel Magnetoresistance (TMR) ratio, and optimal magnetic properties. This consistency must be maintained from the initial R&D phase all the way through to high-volume production.

Flexibility in MTJ Stacks

Our systems need the flexibility to deposit material stacks for both in-plane and perpendicular Magnetic Tunnel Junctions (MTJs). This adaptability, along with the ability to handle varying RA values, is crucial for accommodating future technological advancements in the field.

High Throughput and Consistency

Finally, enabling high-volume manufacturing demands both high throughput and exceptional consistency. This means ensuring uniform deposition across wafers and maintaining stable tool performance over extended periods.

REFERENCES

[1] D. C. Worledge *et al*., "Switching distributions and write reliability of perpendicular spin torque MRAM," *2010 International Electron Devices Meeting*, 2010, pp. 12.5.1-12.5.4

[2] Ikeda, S. *et al.*, "A perpendicular-anisotropy CoFeB–MgO magnetic tunnel junction" in *Nature Mater* **9,** 721–724 (2010)

[3] YOLE Intelligence, "Magnetic Sensors 2024", Market & Technology Report

Magnetic Ordered Alloy based Free Layer materials for high-speed writing of MRAM devices with high retention

M. G. Gottwald, G. Hu, P. L. Trouilloud, L. Rehm, C. Safranski, G. Kim, S. L. Brown, J. Bruley, C. D'Emic, H. Jung, J. Kim, C. Lavoie, J. Lee, J. Liang, M. Robbins, J. Z. Sun, P. Hashemi, and D. C. Worledge

IBM-Samsung MRAM Alliance, IBM TJ Watson Research Center, Yorktown Heights, New York
E-mail: mgottwa@us.ibm.com

In this study we are discussing new materials options for STT-MRAM free layer materials beyond CoFeB films with perpendicular interface anisotropy. We demonstrate the growth and integration of low moment and high bulk perpendicular magnetic anisotropy ordered alloy films on CMOS wafers. Novel device properties such as high retention (E_b > 80k_BT), high device coercivity (H_c>8kOe) and reliable switching down to 2ns write times are obtained simultaneously.

***Index Terms*— High retention MRAM, High perpendicular magnetic anisotropy, Ordered magnetic alloy, STT-MRAM**

I. Introduction

Perpendicular anisotropy for STT-MRAM free layer materials has typically been relying on the CoFeB|MgO interface anisotropies [1, 2]. More recently, shape anisotropies through the use of high aspect ratios between film thickness and device diameter have been explored [3,4] or combinations of interface and shape anisotropies. Both approaches, CoFeB|MgO interface anisotropy dependent and shape anisotropy dependent device designs provide a significant challenge for the reconciliation of fast write times and high retention. Fast and reliably writing devices (<10ns, below 1E-6 write error rate (WER) floor) have typically shown low retention barriers of E_b<60k_BT. When focusing on high retention devices (E_b>80k_BT) using prior free layer designs and materials options reliable and fast writing could not be shown. Here, we present an STT-MRAM free layer material that relies on bulk magnetocrystalline anisotropy as a source of anisotropy. Unlike in prior work [5] using ordered L10 alloys with high M_s of about 850kA/m we are using materials with about 4 times lower magnetization of around 200kA/m. Using these new low moment high perpendicular bulk anisotropy materials allows for simultaneous achievement of high retention and fast and reliable writing.

II. Materials Growth and Characterization:

Achieving high crystalline ordering is crucial for high perpendicular bulk anisotropy low magnetization materials [6]. We achieve high crystalline ordering through control of growth and annealing conditions using commercially available PVD tools. Blanket film analysis is done on films grown on Si/SiO_2 substrate wafers. Device structures are integrated from magnetic tunnel junction films integrated in back-end-of line metal levels of CMOS wafers. The ordered alloy materials system appears amorphous as grown based on X-ray diffraction experiments (Fig. 1a). Subsequent annealing at temperatures above about ≥ 300°C crystalizes the alloy in its ordered phase and desired (001) texture (Fig. 1a and 1b). A perpendicular moment corresponding to an M_s of about 200kA/m can be measured by VSM once the sample has been exposed to temperatures above its crystallization temperatures (Fig. 1c). The perpendicular anisotropy field of such annealed alloy was found to be larger than 30 kOe [7]. High resolution TEM images using the High Angle Annular Dark Field method with Z contrast show excellent crystallinity of the magnetic ordered alloys with the expected ordering of different atomic layers (Fig. 1d).

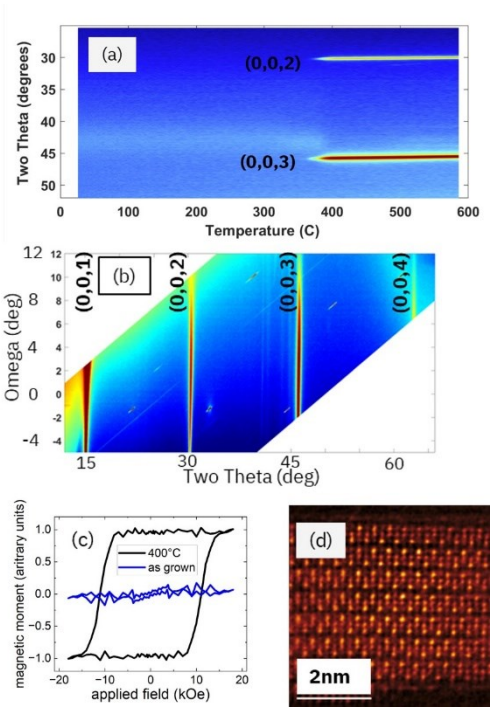

Fig. 1: Blanket film analysis of ordered alloy film. The ordered alloy film thickness is about 15nm and deposited in between 2 MgO layers of about 1nm thickness on an amorphous seed on a Si/SiO_2 wafer. (a) 2θ X-ray diffraction intensity as a function of temperature (ramped at 3°C/s). (b) ω-2θ X-ray diffraction intensity after temperature ramp up to 600°C. (c) Perpendicular VSM loop of as grown film vs annealed at 400°C for 60 minutes. (d) High Angle Annular Dark Field Image with Z contrast of the ordered alloy showing the arrangement of the atoms in the crystalline lattice. Figure reprinted from [7] with permission (CC-BY-NC 6042791244981).

III. Device Integration and Performance

Magnetic tunnel junction stacks using high perpendicular bulk anisotropy ordered alloy materials were deposited on CMOS wafers and integrated into 4kb STT-MRAM arrays. Device sizes for given arrays are controlled through lithography and etch processes. Properties for a device with about 39 nm CD are shown in Fig. 2.

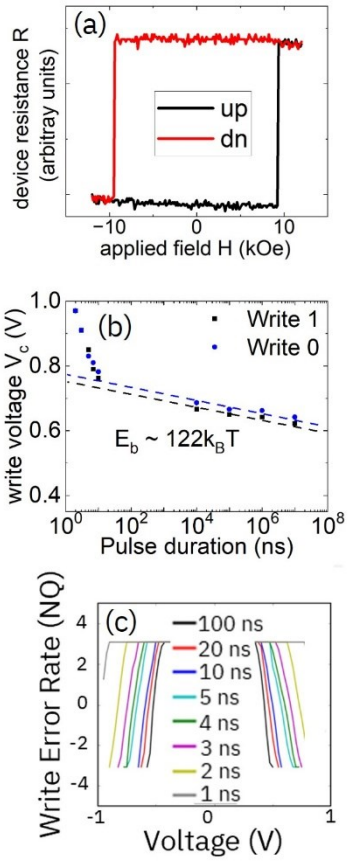

Fig. 2: Single device data example (a) hysteresis loop R-H for 39nm device (b) pulse-width-dependence for V_c for the same device as in (a). (c) WER example for single device: pulse width from 100ns to 1ns. Figures reprinted from [7] with permission (CC-BY-NC 6042791244981).

Fig. 2a demonstrates the high coercive fields of more than 8kOe that can be achieved by using low moment high perpendicular bulk anisotropy materials as free layer. The high coercivity is consistent with a measured retention barrier E_b of about 122k_BT which is well above typical application needs of 40-80 k_BT. It is expected that retention of the ordered alloy free layer can be controlled via the free layer material thickness while maintain the same high perpendicular anisotropy field. It was further shown that these high coercivity fields, H_c, and anisotropy fields, H_K, of the material make the devices particularly field insensitive compared to typical CoFeB|MgO interface anisotropy based devices [7]. Fig. 2c represents the typical pulse width dependence of the write voltage of such high anisotropy low moment material devices by looking at shallow write error rate (WER) slopes. Switching down to 2ns pulse width is shown. Deeper WER floors have been demonstrated elsewhere [7].

IV. Conclusion

Unique novel STT-MRAM device behavior allowing the extension of the application space of STT-MRAM was demonstrated. Low moment, high anisotropy, ordered-alloy based free layers allow addressing some limitation of CoFeB based free layer devices in terms of high retention and fast write times. Further work on tunneling magneto-resistance (TMR) and write voltages and currents should allow extending the application space of STT-MRAM towards new applications requiring fast writing and high retention.

V. Acknowledgements

We gratefully acknowledge the staff of the Microelectronics Research Laboratory at the IBM T. J. Watson Research Center for technical support, and the MRAM Research Group at the IBM Almaden Research Center for scientific discussions. Part of the research described in this paper was performed at the Canadian Light Source, a national research facility of the University of Saskatchewan, which is supported by the Canada Foundation for Innovation (CFI), the Natural Sciences and Engineering Research Council (NSERC), the Canadian Institutes of Health Research (CIHR), the Government of Saskatchewan, and the University of Saskatchewan.

References

[1] G. Hu et al., "Spin-transfer torque MRAM with reliable 2 ns writing for last level cache applications," 2019 IEEE International Electron Devices Meeting (IEDM), San Francisco, CA, USA, 2019, pp. 2.6.1-2.6.4, https://doi:10.1109/IEDM19573.2019.8993604.

[2] D. C. Worledge and G. Hu, Spin-transfer torque magnetoresistive random access memory technology status and future directions, Nature Reviews Electr. Eng. 1, 730–747 (2024). https://doi.org/10.1038/s44287-024-00111-z

[3] Perrissin, N.; Lequeux, S.; Strelkov, N.; Chavent, A.; Vila, L.; Buda-Prejbeanu, L. D.; Auffret, S.; Sousa, R. C.; Prejbeanu, I. L.; Dieny, B. A highly thermally stable sub-20 nm magnetic random-access memory based on perpendicular shape anisotropy. Nanoscale 2018, 10, 12187, https://doi.org/10.1039/C8NR01365A

[4] B. Jinnai et al., "High-Performance Shape-Anisotropy Magnetic Tunnel Junctions down to 2.3 nm," 2020 IEEE International Electron Devices Meeting (IEDM), San Francisco, CA, USA, 2020, pp. 24.6.1-24.6.4, https://doi:10.1109/IEDM13553.2020.9371972. B. Jinnai, J. Igarashi, T. Shinoda, K. Watanabe, S. Fukami and H. Ohno, "Fast Switching Down to 3.5 ns in Sub-5-nm Magnetic Tunnel Junctions Achieved by Engineering Relaxation Time," 2021 IEEE International Electron Devices Meeting (IEDM), San Francisco, CA, USA, 2021, pp. 1-4, https://doi:10.1109/IEDM19574.2021.9720509

[5] T. Kishi et al., Proc. IEDM Tech. Dig. 1 (2008).

[6] Jeong, J., Ferrante, Y., Faleev, S. et al. Termination layer compensated tunnelling magnetoresistance in ferrimagnetic Heusler compounds with high perpendicular magnetic anisotropy. Nat Commun 7, 10276 (2016). https://doi.org/10.1038/ncomms10276

[7] M. G. Gottwald et al., "First Demonstration of High Retention Energy Barriers and 2 ns Switching, Using Magnetic Ordered-Alloy-Based STT MRAM Devices," 2024 IEEE Symposium on VLSI Technology and Circuits (VLSI Technology and Circuits), Honolulu, HI, USA, 2024, pp. 1-2, https://doi:10.1109/VLSITechnologyandCir46783.2024.10631319

Voltage control of interfacial antiferromagnetic spins based on magnetoelectric effect

Yu Shiratsuchi[1,2,3] and Kentaro Toyoki[1,2,3]

[1]Graduate School of Engineering, The University of Osaka, Osaka, 565-0871, Japan, shiratsuchi@mat.eng.osaka-u.ac.jp
[2]Institute for Open and Transdisciplinary Research Initiatives, The University of Osaka, Osaka, 565-0871, Japan
[3]Center for Spintronics Research Network, The University of Osaka, Osaka, 560-8531, Japan

Efficient manipulation of antiferromagnetic (AFM) state is desirable for advanced spintronic devices with fast operation and robustness against the magnetic field perturbation. Using the magnetoelectric Cr_2O_3 epitaxial film, we demonstrate the giant voltage modulation of the antiferromagnetic spin reversal. We obtained the significant modulation efficiency of the switching field, $\Delta\mu_0 H_{SW}/\Delta V$ ($\Delta\mu_0 H_{SW}/\Delta E$), −500 mT/V (−4.80 T·nm/V) in maximum. We also found that the stable spin direction was determined depending on the sign of the electric and magnetic field product, yielding the checkerboard-like assignment of the spin state in the *E*-*H* plane. Our findings not only advance the voltage-based insulating AFM spintronics but also provide the basis of the device function such as a deterministic logic operation by means of the field combination.

***Index Terms*—Antiferromagnetic materials, Hall effect, Magnetoelectric (ME) effect**

I. Introduction

Voltage control of magnetism has attracted much attention as the energy efficient spin manipulation principle as well as a benefit from CMOS compatibility. However, since the voltage (the electric field E) is not directly coupled with the magnetic moment, the elaborate method is required to couple them. So far, two distinct physical phenomena underlying this coupling have been attempted: Voltage-controlled magnetic anisotropy (VCMA) effect [1] and magnetoelectric (ME) effect [2]. The VCMA effect is defined as a change in the magnetic anisotropy energy density by E, and it typically occurs at a metallic magnetic layer/nonmagnetic insulator interface. Since the VCMA effect reduces the energy barrier and does not change the symmetry of the energy landscape of magnetic anisotropy, the finally obtained magnetization state is not deterministic [3].

The ME effect is an alternative principle which couples the magnetic moment and the voltage (or E). The ME effect is defined as the induction of the net magnetization M by E or the induction of the dielectric polarization P by the magnetic field H, expressed as

$$M_i = \alpha_{ij} E_j \,,\; P_i = \alpha'_{ij} H_j \qquad (1)$$

where α_{ij} and α'_{ij} are ME coefficient ($i, j = x, y, z$). The non-zero α_{ij}, i.e., the emergence of the finite ME effect is involved by the crystal structure with the broken spatial inversion symmetry. The E-induced magnetization via eq. (1) can obtain the Zeeman energy gain as in the ordinal ferromagnetic (FM) materials. Therefore, the combination of E and H in the ME materials switches the spin state in a deterministic way.

Another significance to use the ME effect is that some ME materials exhibit the antiferromagnetic (AFM) order. Although no net magnetization in the AFM materials hinders controlling its spin state by conventional techniques, the ME-based mechanism would be a solution. Using Cr_2O_3, prototypical ME-AFM material, we have been investigating the ME-based spin manipulation [4,5]. In this digest, we summarize our progress on the ME-based control of AFM spin state.

II. Detection of Interfacial AFM spins

As described above, the ME feature involves the specific crystal structure with the broken special inversion symmetry. At the surface/interface, the structural inversion symmetry is inherently broken. The symmetry-arguments [6] predict the emergence of the sizable spin density at the surface in conjunction with the ME effect, called the surface magnetization or the boundary magnetization coupled with the bulk AFM order parameter (the Néel vector). By utilizing the interface-sensitive principle, we can detect the surface magnetization, consequently the orientation of the Néel vector. We employed spin-dependent transport at the nonmagnetic heavy metal/magnetic insulator interface such as $Pt(111)/Cr_2O_3(0001)$. Since the electric conductivity is relied on the Pt layer, we can access the interfacial AFM (Cr) spin state separated from the bulk site.

Figure 1 shows the R_{xy} as a function of magnetic field for $Pt(111)/Cr_2O_3(0001)/Pt(111)$ film with the 8-nm thick Cr_2O_3. [4] According to the magnetocrystalline anisotropy, the magnetic easy axis should be perpendicular to the film due to the magnetocrystalline anisotropy; The field direction was normal to the film plane, i.e. along the c-axis of Cr_2O_3. The R_{xy}-H curve shows the rectangular hysteresis below 250 K, resembling the magnetization curve along the easy axis. The emergence of hysteresis is due to the enhanced contribution of the surface magnetization by reducing the Cr_2O_3 thickness. The hysteresis in the R_{xy}-H curve becomes absent for the Cr_2O_3 film thicker than 40 nm wherein the bulk AFM nature is dominant and consequently, the energy gain by the Zeeman effect is insufficient to switch the surface magnetization. We confirmed that the interfacial Cr spin reversal occurred using the soft X-ray magnetic circular dichroism. Notably, no appreciable signal was detected by the conventional magnetization measurements, which supports that Cr_2O_3 maintains the antiferromagnetic nature in whole film for all studied films.

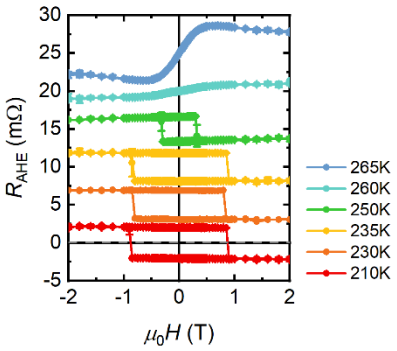

Fig.1 Series of R_{xy}-H curves measured at various temperatures [4].

III. Voltage-control of AFM spin reversal field

Advancing the results shown in Section II., we measured the R_{xy}-H curves upon applying the gate voltage V_G. Figure 2(a) shows the R_{xy}-H curves with $V_G = 0$ and ±0.3 V for the film with 8-nm thick Cr_2O_3 [5]. The switching field H_{SW} is modulated by V_G; the $\mu_0 H_{SW}$ value was changed from 680 mT at $V_G = -0.3$ V to 550 mT at $V_G = +0.3$ V. As plotted in Fig. 2(b), the switching field monotonically decreases with increasing V_G. The linear fitting gives the modulation efficiency $\Delta\mu_0 H_{SW}/\Delta V_G$ ($\Delta\mu_0 H_{SW}/\Delta E$) as −180 mT/V (−1.4 T·nm/V). The temperature dependence of the modulation efficiency revealed that the highest efficiency reached −500 mT/V (−4.8 T·nm/V) which is about 50 times larger than the FM counterpart based on the VCMA mechanism. Based on this feature, the V_G-induced spin reversal under the constant magnetic field was also possible. In this switching protocol, the leakage current (the current density) at the switching condition about 1.2 nA (1.5 A/m^2) was achieved, about 9 orders lower than the current based mechanism such as the spin-orbit torque.

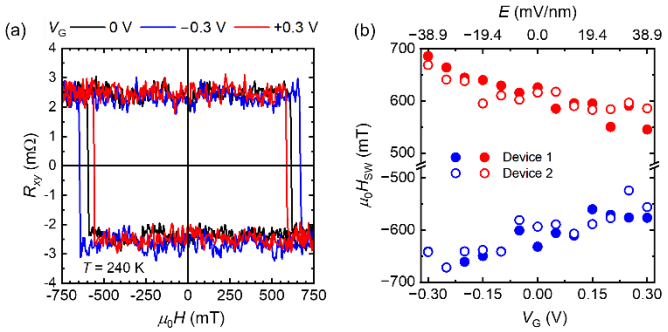

Fig. 2 (a) R_{xy}-H curve under V_G and (b) V_G dependence of switching field [5].

At $V_G = 0$, the thick Cr_2O_3 film did not show hysteresis. Since the Zeeman energy gain is proportional to EH, the thick Cr_2O_3 film would show similar hysteresis under the finite V_G. Figure 3(a) shows the R_{xy}-H curves at $V_G = +4.0$ V. Despite the absence of hysteresis at $V_G = 0$ V (black curve), the rectangular hysteresis emerged by the V_G application. Interestingly, when the negative V_G was applied (blue curve), the polarity of hysteresis is reversed. This polarity change is relevant to the difference in magnetic moments that couples with the magnetic field and that are responsible for the AHE. As long as the driving force of the spin reversal is Zeeman energy, the magnetic field responsiveness relies on the net magnetization. Thus, net magnetization defined by eq. (1) becomes parallel to the magnetic field in the saturated state. In contrast, AHE is relevant to surface magnetization coupled with the AFM order parameter and consequently, α. Therefore, the surface magnetization can be opposite to the magnetic field direction depending on E and H. In Fig. 3(c), the sign of R_{xy} was mapped in the E-H plane. Symbols represent the switching field at each E. The sign of R_{xy} in the saturated region is assigned in each four quadrants in a checkerboard manner. Each region is separated by two sets of hyperbolas with the positive/negative α. The inner region is the bi-stable regime corresponding to the inside of hysteresis shown in Figs. 1 and 2. In the functional viewpoints, when the map is intercepted along the horizontal axis, the E-sweep with the constant H would also switch the spin state, which would make this feature more fascinating, and it will be tackled in near future.

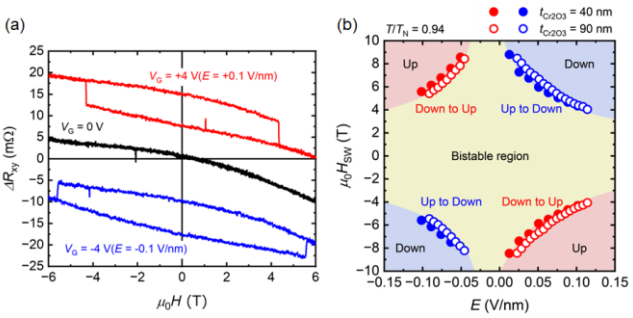

Fig. 3 (a) R_{xy}-H curve under $V_G = 0, \pm 4$ V, and (b) Map of spin state in E-H plane [5].

IV. Conclusions

We demonstrated voltage-based AFM spin manipulation by taking advantage of the surface magnetization relevant to the ME effect. The ME driven mechanism yields the quite high modulation efficiency exceeding hundred mT/V (a few T·nm/V). Besides, utilizing the sign change of ME coefficient, the novel functionality, e.g., the four quadrants assignment of spin state in E-H plane was demonstrated. The demonstration shown here will open a avenue on the voltage-driven AFM spintronics.

References

[1] T. Maruyama *et al*., "Large voltage-induced magnetic anisotropy change in a few atomic layers of iron," *Nature Nanotech.* vol. 4, pp. 158-1161, Jan. 2010.

[2] D. N. Astrov, "The magnetoelectric effect in antiferromagnets," *J. Exptl. Theoret. Phys. (U.S.S.R),* vol. 11., pp.708-709, Sep. 1960.

[3] Y. Shiota *et al*., "Induction of coherent magnetization switching in a few atomic layers of FeCo using voltage pulses," *Nature Mater.* vol. 11, pp. 39-43, Nov. 2012.

[4] K. Ujimoto *et al*., "Direct observation of antiferromagnetic domains and field induced reversal in Pt/Cr_2O_3/Pt epitaxial trilayers," *Appl. Phys. Lett.* vol. 123, pp. 022407 (7 pp), Jul. 2023.

[5] K. Ujimoto *et al*., "Giant gate modulation of antiferromagnetic spin reversal by the magnetoelectric effect," NPG Asia Mater. vol. 16, pp. 20 (11 pp), Arl. 2024.

[6] K. D. Belashchenko, "Equilibrium Magnetization at the Boundary of a Magnetoelectric Antiferromagnet," Phys. Rev. Lett. vol. 105, pp. 147204 (4 pp), Oct. 2010.

Nanoelectromechanical Magnetic Storage and Memory: A Scalable, Energy-Efficient Approach to Next-Generation Nonvolatile Storage

Chuncheng Wang[1] and Jeongmin Hong[1,2]

[1]School of Sciences, Hubei University of Technology, Wuhan, 430068, China, jehong@hbut.edu.cn
[2]Department of Physics, University of California, Berkeley, CA 94720, USA, jehong@berkeley.edu

Increasing the recording density of magnetic hard disk drives (HDDs) and demands high-anisotropy media to ensure thermal stability. However, conventional scaling faces fundamental limits because generating sufficiently strong magnetic fields for writing becomes impractical, even as technologies like heat-assisted (HAMR) and microwave-assisted magnetic recording (MAMR) seek to address this challenge. Here, we demonstrate an alternative approach using spin-transfer torque (STT) to manipulate tunneling spin-polarized currents—rather than magnetic fields—between a nanoscale magnetic probe and the recording media. Writing is achieved by injecting spin-polarized electrons from the probe into the media via the STT effect, while reading leverages the tunneling magnetoresistance (TMR) effect between the probe and media layers. This STT-based recording method overcomes magnetic field limitations for both writing and reading, enabling energy-efficient, ultrahigh-density recording for next-generation nonvolatile storage.

***Index Terms*—Spin Transfer Torque, Probe Switching, Magnetic Memory, Magnetic Storage**

I. Introduction

ACHIEVING higher areal densities in magnetic recording requires writing into high-anisotropy media to maintain thermal stability, yet scaling is fundamentally limited by the challenge of generating sufficiently strong magnetic fields for writing. Beyond increased energy demands, magnetic field-based writing inherently restricts spatial and temporal resolution. This study explores spin-transfer torque (STT) as a strategy to overcome these limitations by replacing magnetic fields with spin-polarized tunneling currents. Specifically, a magnetic nanoprobe positioned in close proximity to the recording media injects spin-polarized electrons to locally switch the media's magnetization through the STT effect.

To ensure effective spin-transfer, maintaining an extremely small probe-to-media separation—ideally within ~1 nm—is critical for adequate local spin accumulation. This target is practically achievable, given current HDD technologies already achieve fly heights as low as 4 nm across the entire disk surface using advanced tribology and servo control. Nanoprobe devices with sub-10 nm features have previously demonstrated exceptional spintronic properties, including significantly reduced STT switching currents. In this work, the nanoprobe writes to perpendicular magnetic media via STT, while reading is performed by measuring the tunneling magnetoresistance (TMR) effect, which distinguishes local magnetization directions through small tunneling currents between the probe and media layers.

II. Results and Discussion

Both the nanoprobe and the recording media were fabricated using CoFeB-based perpendicular magnetic films. The key difference was that the probe's anisotropy field was engineered to be higher—by adjusting the thickness of the CoFeB and MgO layers—so that the probe's magnetization could serve as a stable reference orientation. A programmable point contact mounted on a scanning probe microscopy (SPM) system enabled high-sensitivity transport measurements. By applying a constant current, the probe was brought into contact mode with the recording media using a nanoscale piezoelectric manipulator. A "tunneling contact" was established once the tunneling current exceeded a threshold, indicating a separation below 3 Å.

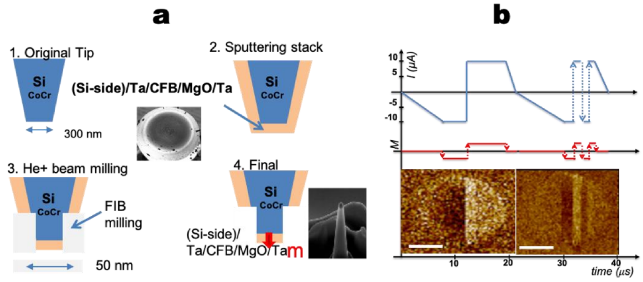

Fig. 1 (a) Fabrication of a probe writer. recording system. (b) Writing with spin polarized currents through the STT effect as confirmed through MFM imaging. The scale bar is 50 *nm*.

To fabricate the nanoscale magnetic probe structure, state-of-the-art helium-ion focused ion beam (He-FIB) trimming was performed, as illustrated in Fig. 1(a). CoFeB thin-film stacks were deposited onto pristine silicon probes and milled using an Orion NanoFab system with helium and neon ion beams to isolate the active region. This fabrication approach has been validated in prior studies to avoid detrimental ion implantation effects.

Figure 1(b) shows the writing process using spin-polarized currents via the STT effect. The top graph presents the time-dependent sequence of the applied spin-polarized current. Simultaneously, the magnetic state of the media was imaged using magnetic force microscopy (MFM), with the bottom row showing the resulting MFM images and the middle row illustrating the corresponding magnetization directions. A clear correlation was observed between the programmed current sequence and the magnetization state in the media. Magnetization switching consistently occurred whenever the applied current exceeded the STT switching threshold, directly

confirming local magnetization reversal in the media by spin-polarized currents injected from the nanoprobe.

III. Conclusion

This work demonstrates that spin-transfer torque (STT) magnetic recording offers a promising pathway for next-generation ultrahigh-density data storage. By replacing magnetic fields with spin-polarized currents for writing and tunneling magnetoresistance (TMR) for reading, this approach drastically reduces writing energy while overcoming fundamental scaling limitations of conventional magnetic recording. Moreover, the elimination of external magnetic fields simplifies the potential integration of three-dimensional (3D) stacks of magnetic bits into nonvolatile memory devices.

Looking ahead, this technology could be extended to record and read information in next-generation magnetic media based on antiferromagnetic (AFM) materials. Because AFM media lack stray fields and exhibit significantly higher spin exchange energies compared to the anisotropy energies of traditional ferromagnets, they offer the potential for processing information at unprecedented densities and data rates, with bits encoded in the AFM order parameter (the Néel vector).

References

[1] M. Tsoi et al., “Excitation of a magnetic multilayer by an electric current,” Phys. Rev. Lett., vol. 80, pp. 4281–4284, Apr. 1998.

[2] P.-J. Hsu et al., “Electric-field-driven switching of individual magnetic skyrmions,” Nat. Nanotechnol., vol. 12, pp. 123–126, Jan. 2017.

[3] J. Hong et al., “Energy-efficient spin-transfer torque magnetization reversal in sub-10-nm magnetic tunneling junction point contacts,” J. Nanopart. Res., vol. 15, Art. no. 1599, Apr. 2013.

Strain control of spintronic devices

Egor Savostin[1], Jiawei Duan[1], and Vitaliy Lomakin[1], *Fellow, IEEE*

[1]Center for Memory and Recording Research and Department of Electrical and Computer Engineering, University of California, San Diego, California 92093, USA, vlomakin@ucsd.edu

This work presents a theoretical and numerical study of strain-controlled magnetic and spintronic devices. A finite-element micromagnetic framework is introduced that self-consistently incorporates magnetoelastic coupling together with strain-induced Dzyaloshinskii-Moriya interactions. The influence of mechanical strain on both static and dynamic magnetic configurations is characterised. Results reveal that the interplay between magnetoelastic energy and SIDMI modifies the characteristics of spin-transfer-torque oscillators, enhancing individual device tunability and enabling robust phase locking across oscillator arrays. These findings provide design guidelines for next-generation, mechanically reconfigurable spintronic devices.

***Index Terms*—Micromagnetics, strain, spintronics, magnetoelastics.**

I. SINTRODUCTION

SPINTRONICS and straintronics are envisioned to play important roles in a set of applications, such as high-density data storage, wave computing, neuromorphic computing and related applications in emerging electronics platforms [1-3]. These platforms demand a comprehensive understanding of nonlinear dynamics of spatially inhomogeneous magnetization states.

Strain and the magnetization can be coupled in multiple ways, including magnetoelastic interactions (MEI) via magnetostriction and inverse magnetostriction as well as via strain induced Dzyaloshinskii-Moriya interactions (SIDMI). Such coupling allows controlling static and dynamic magnetization and elastic properties of materials and devices.

Here, we present a study demonstrating how strain can be used to control static and dynamic magnetization states by means of MEI and SIDMI. We show how SIDMI affects static states as well as the dynamics of breathing magnetic skyrmions. We also discuss how MEI can be used to couple spin transfer torque oscillators (STOs).

II. FORMULATION

We consider multi-physics modeling of MEI and SIDMI [1]. We use the Landau-Lifshitz-Gilbert equation (LLGE) for magnetization. The effective magnetic field includes the inverse magnetostriction component to describe MEI as well as SIDIM component. SDIM is a modified interfacial DMI, which is anisotropic with respect to the in-plane directions because of an indirect exchange between neighboring spins mediated by an impurity with a large spin-orbit coupling on heavy metal – ferromagnet interfaces. Elastic statics and dynamics is affected by the magnetization states via the magnetostriction effect as and SIDMI. As a result, hybrid behavior is obtained that can be used to control the functionality of nanomagnetic devices.

The formulation was implemented via a finite element method framework as a part of the FastMag simulator [4]. The micromagnetic component uses first-order nodal tetrahedral or hexahedral elements. The elastic component uses second-order tetrahedral or first-order hexahedral elements. The equations are solved concurrently. At each time step the LLGE and elastic solutions are obtained using implicit second-order time evolution. Their self-consistency is achieved via an iterative process. The approach allows for accounting for a two-way coupling between magnetization and elastic behaviors.

III. STATIC AND DYNAMIC BEHAVIOR

A. Static magnetization states

We start by showing how the magnetization states in a thin film can be controlled by a static strain. Figure 1 presents phase diagrams of magnetic textures that emerge in thin CoFe films as a function of anisotropic in-plane strain, defined by the relation $\varepsilon_{xx} = -2.7\varepsilon_{yy}$, and film thickness d, for the parameter K_e=10, which quantifies the strength of strain-dependent Dzyaloshinskii–Moriya interaction (DMI). The diagrams reveal how the interplay between elastic strain and film thickness influences the stability of various magnetic phases through modulation of interfacial DMI. The system supports a broad range of magnetic textures including ferromagnetic (FM) order at low strain, X-stripe and Y-stripe phases at negative and positive strain respectively, and a prominent central region of coexisting helical and skyrmion states. A distinct out-of-plane magnetized phase appears at high tensile strain and low thickness, while the helical and skyrmion region persists in a narrower strain range. These results highlight the critical role of strain-controlled DMI in tuning magnetic order in CoFe thin films, offering a route to engineer complex spin textures through mechanical means. The insets show representative spin textures for stripe and skyrmion configurations.

B. Breathing skyrmions

Figure 2 illustrates the nonlinear response of a magnetic system by presenting the ratio of the second harmonic to the first harmonic magnitude under varying driving amplitudes and frequencies. Panel (a) demonstrates how this harmonic ratio evolves with increasing strain amplitude (ε_{zz}) for two cases: with and without strain-induced SIDMI, denoted by $\eta = 0.5$ (red) and $\eta = 0$ (blue), respectively. A striking enhancement is observed at a driving frequency of 1.75 GHz (half the system's primary resonance), where the second harmonic magnitude reaches approximately 80% of the first harmonic for a minute strain of just 0.02%. This represents over a 400% increase

compared to the system without SIDMI, highlighting the strong nonlinear behavior.

Panel (b) shows the second-to-first harmonic ratio as a function of driving frequency for a fixed amplitude. The red points (η = 0.5) exhibit significantly stronger second harmonic generation in the low-frequency range, particularly near subharmonic resonances. Even at high frequencies (10–20 GHz), the presence of SIDMI maintains a noticeable nonlinear response, with second harmonic components accounting for about 3–5% of the primary response—still roughly 30 times higher than in the absence of SIDMI, where the second harmonic contribution is nearly negligible (~0.1%).

Insets in both panels provide supporting spectral data and comparative amplitude ratios, reinforcing the role of SIDMI in enhancing harmonic generation in a broad frequency range.

C. Coupled oscillators

Figure 3 shows the spatial distribution of the strain field generated by two spin-torque oscillators (STOs) embedded in a 3 nm-thick ferromagnetic film. The oscillators, with labeled average magnetization vectors $\mathbf{m}_1$ and $\mathbf{m}_2$, are separated by approximately 2 microns. The color map represents the strain component induced by magnetoelastic interactions, with localized patterns centered around each oscillator, indicating the generation of propagating elastic waves. The magnetization dynamics of each STTO acts as a source of elastic waves due to the magnetoelastic coupling. These waves mediate long-range interactions between the oscillators, effectively coupling them over micron-scale distances—well beyond the ~1 μm limit typically imposed by exchange and dipolar (demagnetization) interactions. Importantly, this coupling is bidirectional: while magnetization dynamics emit strain waves (direct magnetostriction), the strain field, in turn, modifies the local magnetic state via the inverse magnetostrictive effect. This mutual feedback enables efficient synchronization or interaction of distant oscillators via the elastic channel. The visualization emphasizes the non-local nature of this coupling mechanism, offering a pathway to design densely packed, elastically interconnected STO arrays without relying on short-range magnetic interactions.

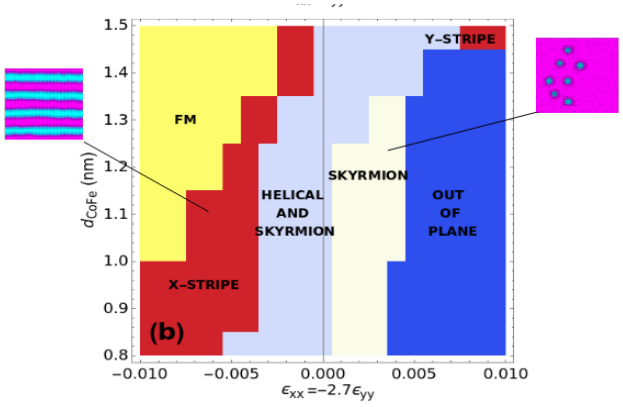

Fig. 1. Phase diagram of static magnetization states controlled by SIDMI.

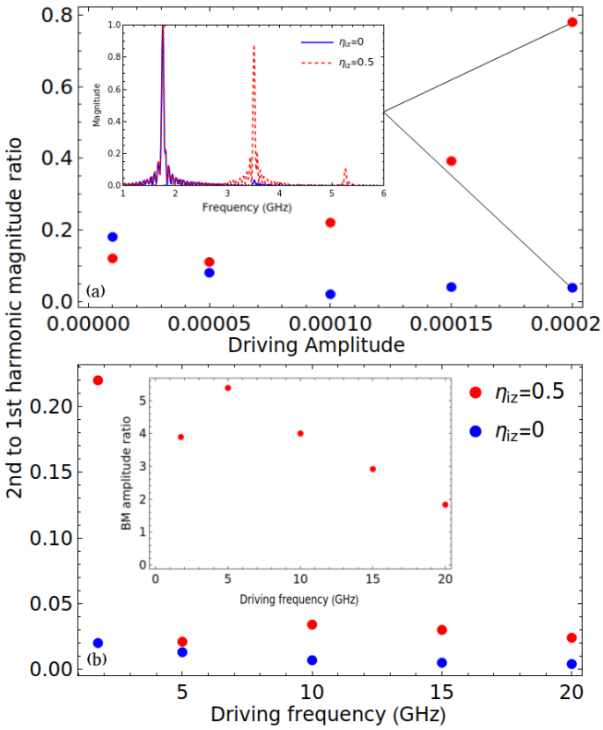

Fig. 2. The ratios between the magnitudes of the n = 2 to n = 1 harmonics as a function of the elastic wave amplitude of (a) 1.75 GHz and (b) 0.01 % of deformations. The inset in Fig. 4(b) shows the ratio of the real-space BM amplitudes for ηiz = 0.5 (with SIDMI) and ηiz = 0(without SIDMI)..

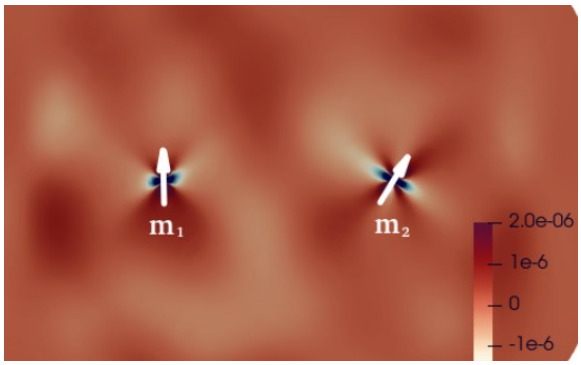

Fig. 3. Synchronization of STOs by means of elastic waves.

References

[1] E. Savostin and V. Lomakin, "Giant phonon–skyrmion interaction mediated by strain-induced Dzyaloshinskii–Moriya interaction," *Phys. Rev. B*, vol. 110, p. 064423, 2024.

[2] C. Kittel, "Interaction of spin waves and ultrasonic waves in ferromagnetic crystals," *Phys. Rev.*, vol. 110, pp. 836–841, Apr. 1958.

[3] N. S. Gusev, A. V. Sadovnikov, S. A. Nikitov, M. V. Sapozhnikov, and O. G. Udalov, "Manipulation of the Dzyaloshinskii–Moriya interaction in Co/Pt multilayers with strain," *Phys. Rev. Lett.*, vol. 124, p. 157202, Apr. 2020.

[4] R. Chang, S. Li, M. Lubarda, B. Livshitz, V. Lomakin, "FastMag: Fast micromagnetic simulator for complex magnetic structures," *J. Appl. Phys.*, vol. 109, p. 07D358, 2011.

Towards Field-Free and Ultra-Low Power Spintronic Devices: Leveraging Altermagnetism and Orbitronics

Ramu Maddu[1], Badsha Sekh[1], Hasibur Rahaman[1], Subhakanta Das[1], Pinkesh Kumar Mishra[1], Bilal Jamshed[1], Sabpreet Bhatti[1], and S.N. Piramanayagam[1]

[1]School of Physical and Mathematical Sciences, Nanyang Technological University, 21 Nanyang Link, Singapore 637371

Current-induced spin-orbit torque (SOT) offers a promising approach for achieving energy-efficient magnetization switching in advanced spintronic devices. However, the technological advancements have been hindered by two key challenges: the requirement of an external in-plane magnetic field for deterministic switching and the need for high switching current density. To address these issues, we have been concurrently investigating two emerging mechanisms: Spin Splitting Effect (SSE) in altermagnets and Orbital Hall Effect (OHE) in light metals. In one study, we explored the potential of a newly emerged altermagnetic material (RuO_2) in combination with a heavy metal (Pt) to achieve both field-free and low-power switching concurrently. We leveraged σ_Z in RuO_2 for field-free switching (FFS) via the SSE and enhanced SOT efficiency by utilizing σ_Y in Pt through spin Hall effect (SHE). A maximized FFS of 82% was observed at an optimized t_{Pt} = 1.5 nm for an applied current density, $J = 2.56 \times 10^{11}$ A/m^2 (36 % lower than reported) at a crystal angle of $\Theta = 90°$ with respect to the [101] axis. In another study, we investigated Ru/Pt/Co heterostructure, where we utilized combined effects of OHE in Ru and SHE in Pt, to enhance SOT efficiency and reduce the threshold current density. We observed 1.7 times enhancement in SOT efficiently, with an additional 2.5 times improvement upon inserting a seed layer (NiW), compared to a Pt/Co reference sample. We are further interlinking both SSE and OHE to achieve ultra-low power field-free magnetization switching in a single heterostructure. This talk will provide an overview of these two phenomena and their potential use for spin-based devices.

***Index Terms*—Altermagnet, spin-splitting effect, orbital Hall effect, field-free switching, spin-orbit torque.**

I. Introduction

The advancement of emerging spintronic devices relies on the ability to control their magnetization in a reliable and energy-efficient manner. Over the last decade, SOT has emerged as an efficient approach for ultra-fast magnetization switching in heavy metal (HM)/ferromagnetic (FM) heterostructures. In the SOT mechanism, a charge current is converted into a spin current in the HM layer via SHE [1]. The generated spin current then flows orthogonally to the charge current and exerts a torque on the adjacent FM layer. Over the past few years, SOT driven magnetization switching in perpendicular magnetized devices has been widely investigated, but an external in-plane magnetic field is commonly needed for deterministic switching.

Various techniques, such as utilizing interlayer coupling, exchange coupling, structural asymmetry, and tilted magnetic anisotropy, have been proposed to achieve FFS. However, these techniques are not industry friendly due to large current requirement and complex device structures. Recently, a new class of magnetic materials called altermagnets have emerged that combine the benefits of both ferromagnetic and antiferromagnetic materials. In this class of materials, RuO_2 has been found to exhibit σ_Z spin polarization, owing to its SSE. Both theoretical and experimental studies have shown that the spin-polarization tends to align with Neel vector along [001] axis, regardless of the direction of applied current. As such, by tilting the Neel vector through a specific crystal growth, the direction of spin polarization can be controlled, enable the generation of σ_Z spin current and hence the FFS. Bose et al. demonstrated that RuO_2 deposited on TiO_2 substrates of different orientation can result in perpendicular, in-plane, and canted vector with respect to the surface normal to the unit cell. Karube et al. investigated the role of σ_Z for FFS in RuO_2/Ru/Co heterostructure by utilizing tilted spin polarization. They observed FFS efficiency of 75% at $J \approx 3.5 \times 10^{11}$ A/m², achieved through the SSE in RuO_2. Therefore, further improvements in FFS efficiency are required to meet the demands of energy-efficient, next-generation spintronic devices.

Besides this, another challenge hindering the development of SOT-based perpendicular magnetized device is the large current density for magnetization switching. Two independent studies reported the highest spin Hall angle (SHA) values of 0.62 and 0.64 for tungsten (W) in W/CoFeB/MgO heterostructures as a single-layered HM material. To further enhance SOT switching efficiency, various approaches have been explored, including ion implantation, self-induced SOT from ferromagnetic materials, alloying of heavy metal materials, and multilayered HM structures. However, many of these techniques are not suitable for large-scale production. Therefore, sustained research efforts are required to make SOT-based devices more efficient and viable for commercial applications.

Recent theoretical calculations showed that the OHE in certain materials with weak SOC can have higher orbital Hall conductivity (OHC) than spin Hall conductivity (SHC) of mostly used elements in the field of spintronics. However, the orbital current generated from OHE cannot directly interact with local magnetization of magnetic materials. Instead, OHE needs an intermediate material with strong SOC to convert I_{OH} to I_{SH}. Therefore, we need two materials with weak SOC and strong SOC to fully utilize the potential of OHE. It has been demonstrated that materials with strong SOC can exhibit large

Corresponding Author: S.N. Piramanayagam (Email: prem@ntu.edu.sg)

SHE. Hence, by choosing right combination of materials to form a heterostructure, it is possible to synergistically harness both OHE and SHE to obtain giant SOT efficiency.

In this talk, we will provide an overview of these two emerging phenomena: SSE and OHE. By combining SSE from RuO_2 and SHE from Pt, we achieved 36% reduction in the switching current density, and a 82% enhancement in the FFS as switching percentage. In another study, we explored combined effects of OHE in Ru and SHE in Pt and obtained giant enhancement in SOT efficiency.

II. Results and Discussions

A. Enhanced Field-Free switching via σ_Z Spin Polarization

RuO_2 is an altermagnetic metallic oxide with a rutile-type crystal structure. Fig. 1 (a) shows the crystal structure of RuO_2 unit cell, where antiferromagnetically coupled Ru atoms surrounded by octahedrally coordinated oxygen atoms. We deposited RuO_2(101) layer epitaxially on a single crystal Al_2O_3 ($1\bar{1}02$) substrate using DC/RF sputtering. The crystallinity of RuO_2 (101) has been confirmed by XRD measurement (Fig. 1(b)). Later, we deposited Pt(1.2, 1.5, 1.7 and 2 nm)/Co(1 nm)/Ru(2 nm) films and investigated switching dynamics.

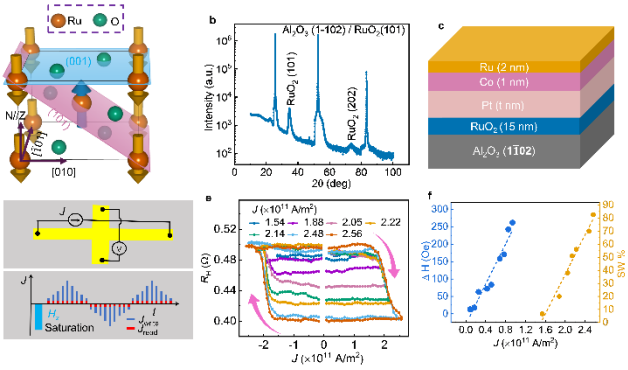

Fig. 1 (a) Crystal structure of RuO_2 unit cell. (b) Gonio scan (θ-2θ) showing crystallinity of sputtered RuO_2 film. (c) Schematic of stack structure. (d) Experimental schematic for SOT-driven switching. (e) R_H vs J switching loops at various ranges of J. (f) Variation of ΔH and SW% as a function of different applied J.

Based on the results of magnetic hysteresis loop-shift measurements, we first investigated SOT-driven switching experiments on Hall bar devices with t_{Pt} = 1.5 nm. Fig. 1(d) illustrates experimental schematic and protocol of the measurements. Initially, we saturated the device to a positive magnetization state and swept pulse currents in absence of external in-plane magnetic field, along a 90° angle with respect to RuO_2 [101] and measured the AHE signal. Fig. 1 (e) shows switching loops over the entire applied range of J values without any external in-plane field, confirming the presence of FFS. Fig. 1(f) shows SW% increases with increasing J, probably due to enhancement of both SHE and SSE. We have attained a maximum SW% of 82 at J = 2.56 × 10^{11} A/m^2, The SW% is higher compared to reported values of 70 and J is also 36% lower compared to reported values for RuO_2 only as a spin source [2].

B. Giant SOT via leveraging both OHE and SHE

In another study, we achieved an enhancement in the SOT efficiency and reduction in the switching current density by utilizing combined effects of SHE and OHE. We deposited sample stacks of S1: Ta(1)/Ru(4)/Pt(1.5)/Co(1.1)/Ru(2) and S2:Ta(1)/NiW(2)/Ru(4)/Pt(1.5)/Co(1.1)/Ru(2) using DC magnetron sputtering (Fig. 2(a)). Here, bottom Ru layer has strong orbital Hall conductivity and generates an I_{OH} [3]. The generated I_{OH} then converts into spin current upon traverses through an intermediate Pt layer due to its strong spin-orbit coupling as depicted in Fig. 2(b). Additionally, Pt itself generates I_S. Hence, combining both I_{OH} and I_s can lead to a giant SOT efficiency.

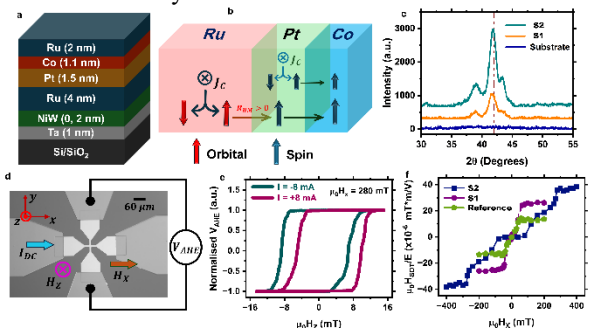

Fig. 1(a) Schematic of stack structures. (b) Schematic representation of spin and orbital torque generation in Ru/Pt/Co heterostructure. (c) XRD plot of bare substrate and samples with Ru as OHL deposited below Pt layer. (d) Schematic of loop-shift measurement setup. (e) Shift in the hysteresis loops for sample S2 by applying a DC of ±8 mA in the presence of an in-plane field of $\mu_0 H_X$. (f) Comparison of the slope $\mu_0 H_{SOT}/E$ as a function of $\mu_0 H_X$.

We characterized damping-like torque efficiency ξ_{DL}^{E} using current induced loop shift measurements on Hall bar devices to quantify the effective field. For this experiment, we applied a constant DC while varying an out-of-plane magnetic field and recorded R_H vs H_z loop. As shown in Fig. 2(c), +8 mA (-8 mA) DC produces a significant shift in the hysteresis loop. This shift can be attributed to the effective field arises from both spin and orbital Hall effects. Further, we calculated H_{SOT}/E as a function of H_x, where E is the electric applied to the device. As shown in Fig. 2(e), we observed 1.9-fold enhancement by utilizing the OHE of Ru and a 2.7-fold enhancement by improved OHE of Ru using NiW seed layer.

Conclusions

We investigated both the SSE and OHE in two separate studies to address the issues of in-plane field requirement and high-power needed for switching. In one study, We leveraged σ_Z in RuO_2 to achieve FFS via SSE and enhanced SOT efficiency by utilizing σ_Y in Pt through SHE. In another study, we utilized the combined effects of OHE in Ru and SHE in Pt, to enhance SOT efficiency and reduce threshold current density.

References

[1] Liu et al., Current-Induced Switching of Perpendicularly Magnetized Magnetic Layers Using Spin Torque from the Spin Hall Effect. Phys. Rev. Lett. 109, 096602 (2012).

[2] B. Sekh et al., E Enhanced Field-Free Perpendicular Magnetization Switching via spin splitting torque in Altermagnetic RuO_2-based Hetero-structures, arXiv:2501.12593 (2025).

[3] D. Go et al., Intrinsic Spin and Orbital Hall Effect from Orbital Texture, Phys. Rev. Lett. 121, 086602 (2018).

Corresponding Author: S.N. Piramanayagam (Email: prem@ntu.edu.sg)

From antiferromagnet to altermagnet: the controllabe spin source for MRAM

Cheng Song[1], Shixuan Liang[1], Hua Bai[1], Feng Pan[1], Aitian Chen[2] and Xixiang Zhang[2]

[1]Key Laboratory of Advanced Materials, School of Materials Science and Engineering, Tsinghua University, Beijing 100084, China, songcheng@mail.tsinghua.edu.cn
[2]Physical Science and Engineering Division, King Abdullah University of Science and Technology, Thuwal 23955, Saudi Arabia, aitian.chen@kaust.edu.sa; xixiang.zhang@kaust.edu.sa

The generation of the spin current is fundamental to spin-orbit torque and the development of corresponding magnetic random access memory (MRAM). Compared with the conventional spin Hall effect (SHE), Neél vector-dependent spin current generation offers enhanced controllability for MRAM applications. By harnessing the out-of-plane spin polarization (σ_z) from antiferromagnetic SHE in Mn_2Au, we achieve field-free SOT switching of perpendicular magnetic tunnel junctions (pMTJs), enabling fully electrical writing and reading. For a non-relativistic counterpart, we utilized spin splitting torque in altermagnet RuO_2, and also demonstrate a σ_z-enabled pMTJ, where spin polarization is aligned with the Neél vector. These three-terminal pMTJs operate at room temperature with a tunnel magnetoresistance ratio over 60%, lower critical current density, and faster, more efficient switching than conventional in-plane devices. These findings advance the application of unconventional spin current and support the development of high-density, low-power magnetic memory technologies.

***Index Terms*—antiferromagnet, altermagnet, magnetic tunnel junction, spin source**

I. Introduction

THE generation of spin current is fundamental to spin-orbit torque (SOT), which enables higher endurance, higher switching speeds and lower energy consumption in magnetic random access memory (MRAM). Conventional spin Hall effect (SHE) is widely employed to generate spin current capable of inducing magnetization switching in adjacent ferromagnetic layers. However, in systems with perpendicular magnetic anisotropy, the orthogonality between the perpendicular magnetization and the in-plane spin polarization (σ_y) necessitates an external in-plane magnetic field to break the symmetry and achieve deterministic switching. This requirement poses a significant challenge for high-density memory applications. A promising strategy to overcome this limitation is the introduction of an out-of-plane spin polarization (σ_z), which emerges in spin sources with low crystal[1] or magnetic symmetry, including ferromagnets, antiferromagnets[2] and altermagnets[3], [4].

In this work, we utilize both the antiferromagnet Mn_2Au[5] and the altermagnet RuO_2 as spin sources to demonstrate σ_z-enabled three-terminal functional perpendicular magnetic tunnel junctions (pMTJs) with fully electrical writing and reading. Our devices exhibit a room-temperature tunnel magnetoresistance ratio exceeding 60%, along with a reduced critical current density and ultrafast, more efficient switching of perpendicular magnetization compared to conventional in-plane devices. Our findings advance the practical applications of unconventional spin polarization and pave the way for embedded memory and edge computing as the future magnetic memory.

II. Generation of Unconventional Spin Polarization

In Mn_2Au (Fig. 1a), the magnetic sublattices exhibit local broken inversion symmetry. As shown in Fig. 1b, the emergence of σ_z depends on the alignment between the Néel vector **n** and the applied current **J**—σ_z appears only when **J** has a component parallel to **n**. In this case, carrier spins (aligned with **n**) are rotated out of plane by the spin-orbit field $\mathbf{H_{so}}$ (purple arrows), which arises from the local symmetry breaking. Because both the carrier spins and $\mathbf{H_{so}}$ are antiparallel between sublattices, a net σ_z is generated. Additionally, Mn_2Au also produces σ_y via the conventional SHE. Both σ_z and σ_y flow along the z-axis and exert unconventional spin-orbit torques on the adjacent ferromagnetic layer.

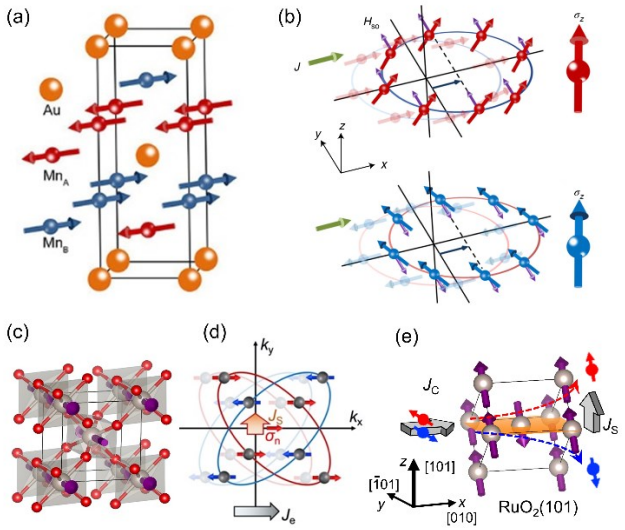

Fig. 1. Schemic of generating unconventional spin polarization in Mn_2Au and RuO_2.

In RuO_2, magnetic Ru atoms sit at the center of stretched octahedra formed by surrounding O atoms (Fig. 1c). Octahedra from opposite sublattices are related by rotational symmetry, generating alternating crystal potentials that lead to anisotropic magnetization densities and spin-split Fermi contours at $k_z = 0$. Due to this anisotropic spin band splitting, applying an charge current J_e along the [010] axis shifts the Fermi contours, generating a transverse spin current J_s polarized along the Néel

vector, as shown in Fig. 1d[6]. For (101)-oriented RuO_2 films, a charge current along [010] induces a transverse, time-reversal-odd spin current along [100], with both the current and spin polarization containing out-of-plane components. As illustrated in Fig. 1e, this results in a σ_z spin current flowing along the *z*-axis, with spin polarization aligned with the Néel vector ([001]).

III. Electrical Control of Perpendicular MTJs

The schematic and optical images of the σ_z-enabled pMTJs are illustrated in Fig. 2a and 2b, respectively. Above the spin source channel, the device stack consists of a CoFeB free layer, an MgO barrier, and a CoFeB reference layer (the perpendicularly magnetized synthetic antiferromagnetic Co/Pt multilayers used to pin the reference layer are not shown). A Mo buffer layer is inserted beneath the free layer to enhance its perpendicular magnetic anisotropy and to facilitate efficient spin current transmission, owing to Mo's relatively long spin diffusion length.

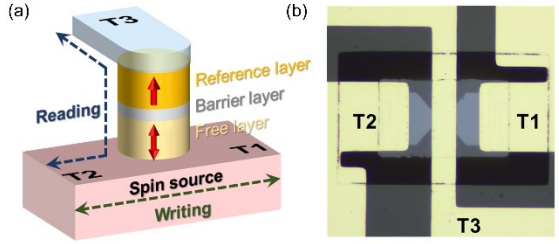

Fig. 2. Reading and writing in the σ_z-based pMTJs.

A current applied between Terminal 1 (T1) and Terminal 2 (T2) flows through the spin source channel (writing path, indicated by the green dashed double arrow), generating both conventional spin torque via the SHE and *z*-polarized spin torque via antiferromagnetic SHE in Mn_2Au (or spin splitting torque in RuO_2). This enables deterministic switching of the free layer's perpendicular magnetization without an external magnetic field, completing the writing operation in the MTJ. Subsequently, a reading current of 1 μA is applied between Terminal 3 (T3) and Terminal 2 (T2) to measure the tunnel magnetoresistance (TMR). Thus, the MTJ supports fully electrical writing and reading, enabling low-power SOT-MRAM operation.

The electrical performance of the Mn_2Au-based MTJ is characterized by TMR, defined as $(R_{ap}-R_p)/R_p \times 100\%$, where R_{ap} and R_p are the resistances in the antiparallel and parallel configurations respectively. After applying a magnetic field of +0.15 T, the minor loop was measured as shown in Fig. 2a, indicating a TMR of 66%. We then demonstrate field-free SOT switching in the SOT-MTJ cell by sweeping the current from positive to negative and back. Using a parallel circuit model, the critical current density in Mn_2Au is estimated at 5.6×10^6 A/cm^2, an order of magnitude lower than conventional heavy-metal-based MTJs. Notably, the high- and low-resistance states in Fig. 3b match those in Fig. 3a, confirming fully electrical SOT switching without an external field. Under an applied in-plane magnetic field, deterministic switching is also observed with opposite polarity at –10 mT and +10 mT, as shown in Fig. 3c.

RuO_2-based pMTJ was characterized similarly. We demonstrate all-electrical control of pMTJ using RuO_2 writing channel along the [010] axis. Fig. 2d shows the minor loop of tunnel resistance versus $\mu_0 H_z$ for this device. When an applied field $\mu_0 H_x$ of ±10 mT, current pulses induce magnetization switching of the free layer, causing TMR changes (Fig. 2f). More importantly, deterministic switching driven by current pulses was achieved without any external field $\mu_0 H_x$ as shown in Fig. 2e, with the critical switching current density is below 1×10^7 A/cm^2.

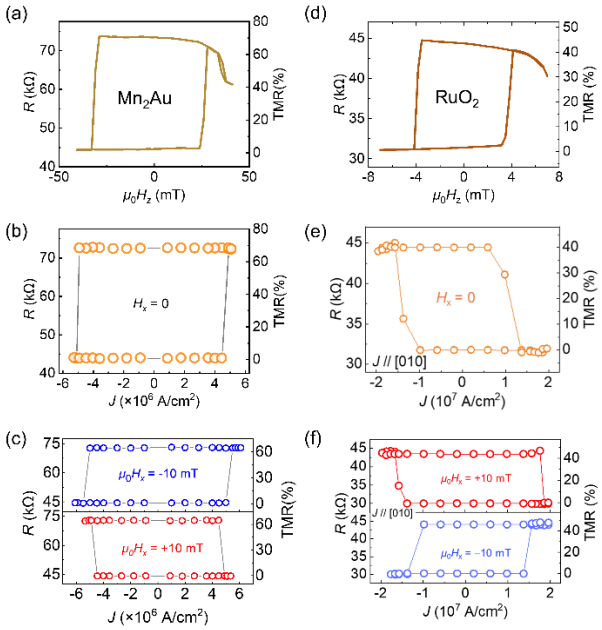

Fig. 3. Reading and writing in the σ_z-based pMTJs.

References

[1] D. MacNeill, G. M. Stiehl, M. H. D. Guimaraes, R. A. Buhrman, J. Park, and D. C. Ralph, "Control of spin-orbit torques through crystal symmetry in WTe2/ferromagnet bilayers," *Nat. Phys.*, vol. 13, no. 3, pp. 300-+, 2017, doi: 10.1038/NPHYS3933.

[2] X. Chen *et al.*, "Observation of the antiferromagnetic spin Hall effect," *Nat. Mater.*, vol. 20, no. 6, pp. 800–804, 2021, doi: 10.1038/s41563-021-00946-z.

[3] C. Song *et al.*, "Altermagnets as a new class of functional materials," *Nat. Rev. Mater.*, 2025, doi: 10.1038/s41578-025-00779-1.

[4] Z. Zhou *et al.*, "Manipulation of the altermagnetic order in CrSb via crystal symmetry," *Nature*, vol. 638, no. March 2024, 2025, doi: 10.1038/s41586-024-08436-3.

[5] S. Liang *et al.*, "Field-Free Perpendicular Magnetic Memory Driven by Out-of-Plane Spin-Orbit Torques," *Adv. Funct. Mater.*, vol. 2417731, pp. 1–8, 2024, doi: 10.1002/adfm.202417731.

[6] H. Bai *et al.*, "Observation of Spin Splitting Torque in a Collinear Antiferromagnet RuO2," *Phys. Rev. Lett.*, vol. 128, no. 19, p. 197202, 2022, doi: 10.1103/PhysRevLett.128.197202.

Fully Field-Free Spin-Orbit Torque Switching Induced by Spin Splitting Effect in Altermagnetic RuO_2

Zhuoyi Li[1], Zhe Zhang[1], Xianyang Lu[1], Yongbing Xu[1, 2]*,

[1]*National Key Laboratory of Spintronics, Nanjing University, Suzhou 215163, China, ybxu@*nju.edu.cn
[2]*York-Nanjing International Center for Spintronics, School of Physics, Engineering and Technology, University of York, York YO10 5DD, UK*

Altermagnetism, a newly identified class of magnetism blending characteristics of both ferromagnetism and antiferromagnetism, is emerging as a compelling frontier in spintronics. This work report a groundbreaking discovery of robust, 100% field-free spin-orbit torque (SOT) switching in a RuO_2 (101)/Co/Pt/Co/Pt/Ta structure. The spin currents, induced by the in-plane charge current, are found to flow along the [100] axis with the spin polarization direction aligned parallel to the Néel vector. These z-polarized spins generate an out-of-plane anti-damping torque, enabling deterministic switching of the Co/Pt layer without the necessity of an external magnetic field. This study highlights the potential of RuO_2 as a powerful spin current generator, opening new avenues for advancing spin-torque switching technologies and other cutting-edge spintronic devices.

***Index Terms*— Altermagnetism; SOT Effect; Spin Current.**

A novel class of magnetism, which exhibits characteristics of both ferromagnetism and antiferromagnetism, has recently been identified. This new phenomenon, predicted to occur in over 200 materials, has been termed "altermagnetism"[1,2]. Materials such as ruthenium dioxide (RuO2) could exhibit this dual nature, combining the stable, fast spin-flipping properties of antiferromagnets with the distinct spin states of ferromagnets. Unlike conventional magnetic materials where electron spins align with the atomic orientation in the crystal lattice, in altermagnets, spin arrows can rotate independently of the atoms. Previously considered a paramagnet, RuO_2 has been shown to exhibit itinerant antiferromagnetism, with a Néel temperature above 300 K and the Néel vector aligned along the [001] axis [3]. Recent theoretical work has suggested that the collinear antiferromagnet RuO_2 might generate strong electric-field-induced spin currents with spin orientation roughly aligned along the Néel vector. RuO_2 crystallizes in the rutile structure with the P42/mnm space group, where ruthenium atoms are situated in the centers of stretched oxygen octahedrons [4]. This octahedral crystal field results in an anisotropic electronic structure and elliptical Fermi surfaces at kz = 04. The 90° rotation of Ru atoms in opposite magnetic sublattices, surrounded by directionally distinct oxygen octahedrons, leads to anisotropic spin band splitting in momentum space, making RuO_2 an efficient spin splitter [5]. In this work, we propose a RuO_2 (101)/Co/Pt/Co/Pt/Ta structure for efficient and robust field-free SOT switching with perpendicular magnetization. The z-polarized spins from the (101)-oriented RuO_2 layer are found to generate an out-of-plane anti-damping torque, enabling deterministic switching of the Co/Pt layer without the necessity of an external magnetic field. And it has been observed to have a clear dependence on the direction of J_C. The sample demonstrates an optimal switching ratio nearly 100% at an applied in-plane field H_x = 0 Oe, when JC flows along the $[01\bar{0}]$ axis. Notably, the ASSE dominates the spin current, especially when the applied current aligns with the [010] direction (θ = 90°). In this configuration, the spin polarization component σ_z creates a substantial field-like effective field. This interplay highlights the crucial role of σ_z in enhancing spin-torque efficiency, thereby elucidating the mechanics of spin flow modulation within this crystalline context.

I. Sample Preparations

All the samples were grown on Al_2O_3 $(1\bar{1}02)$ substrates using a magnetron sputtering system. The layer sequence RuO_2 (15 nm)/Co (0.5 nm)/Pt (1 nm)/Co (0.5 nm)/Pt (1 nm)/Ta (2 nm) was deposited from bottom to top, as shown in Fig. 1a. The (101)-oriented RuO_2 generates spin current with out-of-plane spin polarization. The spin current (J_S) flowing along the [100] axis, induced by the charge current (J_C) along the $[0\,\bar{1}\,0]$ axis.The spin polarization direction (σ) for J_S is approximately aligned parallel to the Néel vector ([001] axis). High-quality RuO_2 (101) films were grown on single-crystal Al_2O_3 $(1\bar{1}02)$ substrates by introducing O_2 gas into an Ar base gas during film growth in our magnetron sputtering system. To achieve defect-free, high-quality RuO_2 epitaxial films that can exhibit excellent ASSE, we optimized the growth conditions of the films and identified the optimal oxygen flow rate and growth temperature. During the film growth process, a 50 standard cubic centimeter per minute (sccm) Ar gas flow was introduced, while the O_2 flow rate was controlled at 10 sccm. A pure ruthenium target was used, with the Radio Frequency (RF) power set at 50 W. The substrate temperature was fixed at 500 ℃ during deposition. More details on the optimization process are presented in Supplementary Information. As shown in Fig. 1c, the clear and sharp RHEED pattern for the 15 nm RuO_2 (101) film indicates that the film exhibits good crystallinity with a flat, well-ordered surface. XRD measurements of a 50 nm RuO_2 film, shown in Fig. 1d, reveal clear and sharp RuO_2 (101) and RuO_2 (202) peaks, confirming the good (101) orientation of our RuO_2 films. Raman spectroscopy analysis, shown in Fig. 1e, indicates three Raman active modes for the RuO_2 (101) film: E_g, A_{1g} and B_{2g} modes. High-resolution cross-sectional scanning transmission electron microscopy (HRTEM) was conducted on the RuO_2 (101)/Co/Pt/Co/Pt structure, as shown in Fig. 1f. The

results demonstrate the high-quality layered growth of the multilayer thin film structure.

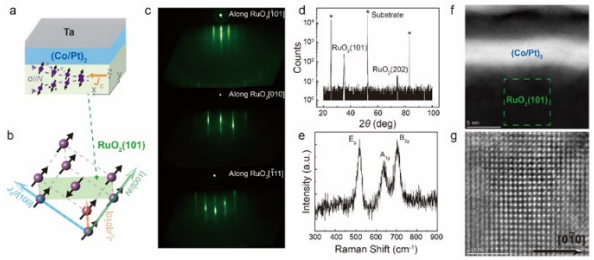

Fig. 1. a, Schematic representation of our sample. The spin polarization direction (σ) for the spin current (J_S) is aligned parallel to the Néel vector ([001] axis). **b,** The schematic illustrates J_S flowing along the [100] axis induced by the charge current (J_C) along the [$0\bar{1}0$] axis. The RuO_2 (101) crystal plane is highlighted by the green shading. **c,** Reflection high-energy electron diffraction (RHEED) patterns of a 15 nm RuO_2 (101) film grown on the Al_2O_3 ($1\bar{1}02$) substrate. **d,** θ-2θ scan x-ray diffraction (XRD) spectrum of a 50 nm thick RuO_2 (101) film grown on the Al_2O_3 ($1\bar{1}02$) substrate. Peaks from the substrate are marked with *. **e,** Raman spectra of a 50 nm thick RuO_2 (101) film grown on the Al_2O_3 ($1\bar{1}02$) substrate, showing three active modes: E_g, A_{1g} and B_{2g} modes. **f,** High-resolution HAADF image of the cross-section of RuO_2 (101)/$(Co/Pt)_2$/Ta and **g,** RuO_2 (101) film.

II. Results and Discussions

We investigate the current induced field-free SOT switching behavior. Fig. 2a and Fig. 2b present schematic diagrams illustrating the generation of spin current via ASSE in the (101)-oriented RuO_2 film, along with the Hall device used for the experiments. Fig. 2c compares the anomalous Hall effect (AHE) measurement curves at different θ, all of which exhibit good perpendicular magnetic anisotropy (PMA) with coercive fields around 300 Oe. To achieve SOT switching, we swept a pulsed direct current and measured the Hall resistance change of the Hall bar. Fig. 2d-f display the current-induced SOT magnetization switching loops in RuO_2/Co/Pt/Co/Pt at different in-plane external fields (H_{ext}) from + 400 Oe to - 400 Oe at θ values of 90°, 45°, and 0°, respectively, with H_{ext} aligned parallel to the direction of the applied current (I_{pulse}). In conventional structures [6,7], no switching loop occurs at zero magnetic field, necessitating H_{ext} to break the rotational symmetry of the spin torque. Remarkably, at θ = 90°, where the current flows along the x-axis ([010] crystal direction), SOT switching has been achieved without H_{ext}, with a switching ratio approaching 100% ($R_{SOT}/R_{AHE} = 1$, where R_{SOT} and R_{AHE} denote the Hall resistance responses to SOT and magnetic field variations, respectively), as shown in Fig. 2d. Similarly, in Fig. 2e, field-free SOT switching is observed at θ = 45°, with a switching ratio of approximately 85%, while no magnetization switching occurs at θ = 0° (Fig. 2f).

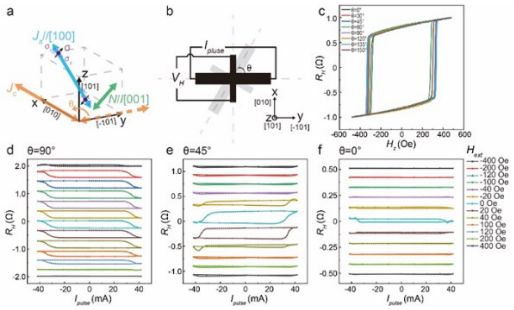

Fig. 2. a, Schematic diagram illustrating the generation of spin current via ASSE in the (101)-oriented RuO_2 film. **b,** The Hall device used for the experiments. θ represents the angle between the current direction and the y-axis. **c,** Anomalous Hall effect (AHE) loops for diffenent values of θ. **d-f,** Corresponding current-induced magnetization switching behaviors observed in Co/Pt multilayers at θ = 90°, 45° and 0°.

III. Conclusion

We have demonstrated the full 100% SOT switching in the RuO_2 (101)/Co/Pt/Co/Pt/Ta structure where any possible pinning effects in the Co/Pt/Co/Pt multi-layers are eliminated due to the reduced formation of AFM domains associated with the high-quality growth of the single crystal RuO_2 (101) layer achieved by a well-controlled magnetron sputtering growth process. Our research further reveals that (101)-oriented RuO_2 films effectively generate spin currents with an out-of-plane spin polarization component σ_z, driven by the altermagnetic spin splitting effect (ASSE). The controllability of spin polarization and the high efficiency of out-of-plane spin current generation position RuO_2 as a standout candidate for next-generation spintronic devices.

References

[1] Šmejkal, L., Sinova, J. & Jungwirth, T. Emerging Research Landscape of Altermagnetism. *Phys. Rev. X* **12** (2022).

[2] Šmejkal, L., Sinova, J. & Jungwirth, T. Beyond Conventional Ferromagnetism and Antiferromagnetism: A Phase with Nonrelativistic Spin and Crystal Rotation Symmetry. *Phys. Rev. X* **12** (2022)..

[3] Berlijn, T. et al. Itinerant Antiferromagnetism in RuO2. Phys. Rev. Lett. 118, 077201 (2017).

[4] .Mattheiss, L. F. Electronic structure of RuO2, OsO2, and IrO2. *Phys. Rev. B* **13**, 2433 (1976).

[5] Bai, H. *et al.* Observation of Spin Splitting Torque in a Collinear Antiferromagnet RuO2. *Phys. Rev. Lett.* **128**, 197202 (2022)

[6] Kong, W. J. *et al.* Spin-orbit torque switching in a T-type magnetic configuration with current orthogonal to easy axes. *Nat. Commun.* **10**, 233 (2019)..

[7] Liu, L., Lee, O. J., Gudmundsen, T. J., Ralph, D. C. & Buhrman, R. A. Current-induced switching of perpendicularly magnetized magnetic layers using spin torque from the spin Hall effect. *Phys. Rev. Lett.* **109**, 096602 (2012).

Energy-Efficient Spin-Orbit-Torque Devices for Memory and Computing by New Materials, New Physics and Voltage Control

Jian-Ping Wang[1]*, Yifei Yang[1], Yu-Chia Chen[1], Seungjun Lee[1], Qi Jia[1], Tony Low[1], Onri Benally[1], Brahmdutta Dixit[1], Duarte Sousa[1], Thomas Peterson[1], Deyuan Lyu[1], Michael Odlyzko[2], Javier Garcia-Barriocanal[2], Guichuan Yu[2], Greg Haugstad[2], Yihong Fan[1], Yu-Han Huang[1], Zach Cresswell[3], Shuang Liang[3], Brandon Zink[1]

[1]Department of Electrical and Computer Engineering, University of Minnesota, Minneapolis, MN 55455, USA
[2]Characterization Facility, University of Minnesota, Minneapolis, MN 55455, USA
[3]Department of Chemical Engineering and Materials Science, University of Minnesota, Minneapolis, MN 55455,USA

Energy-efficiency has long been the bottleneck for the implementation of spin-orbit torque (SOT)-based memory and computing devices. To address this, we have proposed and demonstrated Ni_4W as a novel and energy efficient SOT material. Epitaxial Ni_4W thin films were successfully grown using magnetron sputtering, yielding a high damping-like SOT efficiency of 0.73 and a Z-spin SOT efficiency of 0.02. Efficient field-free switching was demonstrated using the multi-directional spins [1]. To enhance the voltage-controlled magnetic anisotropy (VCMA), we have also proposed and demonstrated a tri-layer SOT stack structure through a working function engineering, inducing electron depletion in the PMA CoFeB/MgO system with a VCMA coefficient of -100.8 fJ/V-m [2]-[3]. Field-free switching with optimized performance was demonstrated. We have also demonstrated that voltage-controlled exchange coupling (VCEC) induces a directional exchange field that persists under nanosecond voltage pulses in a perpendicular magnetic tunnel junction (pMTJ). We will report a latest result that VCEC assisted by VCMA enables magnetization switching within 87.5 ps with 50% switching probability and 100 ps with 94% switching probability, respectively [4]. These advancements pave the way for next-generation spintronic applications.

***Index Terms*—Magnetoresistive RAM, Spintronics, Spin-orbit torque, Voltage-controlled device**

I. Introduction

Spin-orbit torque (SOT) is a promising mechanism for the efficient manipulation of magnetization, offering lower power consumption, higher endurance, and faster switching speeds compared to the traditional spin-transfer torque (STT). However, challenges such as the high write current requirement and the need for field-free switching of magnets with perpendicular magnetic anisotropy (PMA) remain key limitations to broader adoption.

To address these challenges, several approaches have been proposed. Unconventional SOT materials have been discovered that intrinsically break symmetry and enable field-free switching [5]. These materials also exhibit significantly higher energy efficiency for switching PMA magnets compared to conventional sources such as heavy metals and topological insulators, owing to the generation of Z-polarized spin currents.

The electron-depletion voltage-controlled magnetic anisotropy (VCMA) effect presents another promising strategy to reduce energy consumption during SOT-induced switching. By integrating VCMA with field-free SOT mechanisms, highly efficient switching can be achieved. To further minimize power requirements, voltage-controlled exchange coupling (VCEC) is combined with VCMA, enabling ultrafast magnetization switching. In this study, we demonstrate switching within 87.5 ps with a 50% probability, highlighting the potential of this voltage-driven approach for energy-efficient spintronic applications.

* Email: jpwang@umn.edu

II. Unconventional SOT in Ni_4W

Although unconventional SOT materials present promising results for the spin source, the SOT efficiency of these materials is not ideal, typically below 0.1. Through a thorough search of the material database with over thousands of materials, we have first identified Ni_4W (211) as an unconventional SOT material that allows unconventional spins, as shown in the inset of Fig. 1. Symmetry analysis and density-functional theory were used to confirm the existence of X-, Y-, Z-spins, providing the theoretical support to our proposal. To experimentally demonstrate the properties, we have grown epitaxial thin films of Ni_4W (211), with outstanding crystalline quality. The full width at half maximum was below 0.1° for Ni_4W films with thicknesses ranging from 5 nm to 30 nm.

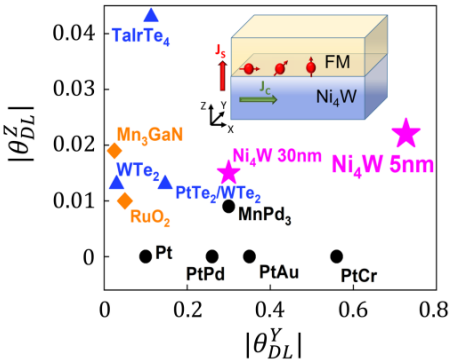

Fig. 1. Summary of SOT efficiencies of Ni_4W and other state-of-the-art materials. The inset shows the generation of spins along all X, Y, Z directions [1].

Second harmonic Hall measurements were used to characterize the SOT efficiency of Ni_4W. A large conventional

SOT efficiency (θ_{DL}^{Y}) of 0.3 was observed at room temperature in the bulk Ni_4W. Notably, a larger θ_{DL}^{Y} of 0.73 was found in W / Ni_4W(5 nm), which is attributed to additional interfacial or extrinsic effects. The unconventional Z-spin efficiency (θ_{DL}^{Z}) of 0.02 was also observed. The SOT efficiencies Ni_4W are among the largest compared to state-of-the-art materials, as summarized in Fig. 1. Field-free switching of a PMA magnet was demonstrated using the multi-directional spins of Ni_4W, and the switching current density is almost 40% less than Pt, which is a commonly used SOT material.

III. Electron-Depletion-Based VCMA Enhancement

The limited efficiency of the VCMA coefficient remains a key challenge for practical implementation of the VCMA strategy in real-world applications. To overcome this limitation, first-principles calculations have predicted the intrinsic distribution of magnetic anisotropy energy (MAE) as a function of excess electron number [6]. An enhanced VCMA coefficient was observed with decreasing excess electron concentration at the Fe/MgO interface. Our previous study utilizing Ta/Pd/Ta underlayers indicated that a significantly higher underlayer work function is required due to the insufficient VCMA enhancement [7].

To experimentally reduce the excess electron density, high work function PtW and W/Pt/W underlayers were investigated in the PMA CoFeB/MgO system. As illustrated in Fig. 1(a), Pt has a work function of 5.7 eV, which is considerably higher than that of CoFeB (~4.6 eV). Under thermal equilibrium, electrons in CoFeB are more likely to transfer into the higher work function underlayers, as shown in Fig. 1(b). The anomalous Hall effect was employed to extract the VCMA coefficients under various gate bias conditions. As shown in Fig. 1(c), the VCMA coefficients for PtW and W/Pt/W samples are –70.7 and –100.8 fJ/(V·m), respectively. In addition, field-free spin–orbit torque (SOT) switching was demonstrated in the W/Pt/W trilayer structure, which features opposite spin Hall angles in its constituent layers.

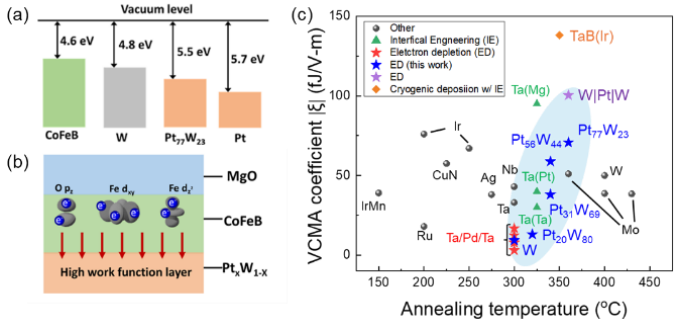

Fig.2.(a) Energy band diagrams of CoFeB with W, $Pt_{77}W_{23}$, and Pt underlayers under flat-band conditions. (b) Eectron depletion at the CoFeB/MgO interface in thermal equilibrium with high work function underlayers. (c) VCMA coefficients in CoFeB/MgO structures vs underlayers. [2,3]

IV. Combination of VCEC and VCMA

VCEC theoretically serves as a mechanism capable of achieving bipolar deterministic switching of a magnetically coupled layer [8]. This is realized by modulating spin scattering at the FM/NM/FM (ferromagnetic material / nonmagnetic material / ferromagnetic material) interface by introducing a boundary barrier [9]. The concept was subsequently integrated into MTJ structures, manifesting as a voltage-controlled analog of the traditional STT effect [9]. Notably, the associated critical current density is one to two orders of magnitude lower than that of conventional STT mechanisms [4],[9].

We examined the influence of voltage pulse width on the switching probability under a constant magnetic field. A pulse generator with a fixed 5 V output (~10 V across the MTJ) and sub-100 ps pulse capability was employed. After each pulse, the resistance was measured to confirm the switching event. This configuration achieved 50% switching probability within 87.5 ps (Fig. 3), accompanied by a 40 ps rise time, highlighting an exceptionally short incubation period [10].

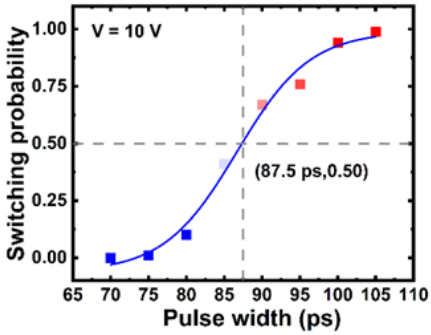

Fig. 3. The switching probability as a function of pulse width, measured under a constant 10 V pulse applied by a high-speed pulse generator capable of delivering sub-100 ps pulses, with each data point averaged over 100 trials [10].

References

[1] Y. Yang, et al. J.P. Wang, "Large spin-orbit torque with multi-directional spin components in Ni_4W," *Adv. Mat.*, 2416763, 2025

[2] Y.-C. Chen, et al. J.P. Wang, "Enhanced voltage-controlled magnetic anisotropy and field-free magnetization switching achieved with high work function and opposite spin Hall angles in W/Pt/W SOT tri-layers," *Adv. Funct. Mat.*, vol. 35, no. 10, p. 2416570, 2025.

[3] Y.-C. Chen, et al. J.P. Wang, "Large and tunable electron-depletion-based voltage-controlled magnetic anisotropy in the CoFeB/MgO system via work-function-engineered Pt_xW_{1-x} underlayers," *ACS Nano*, vol. 19, no. 16, pp. 15953, 2025.

[4] Q. Jia, et al. J.P. Wang, "Energy efficient stochastic signal manipulation in superparamagnetic tunnel junctions via voltage-controlled exchange coupling," *Nano Lett.*, vol. 25, no. 23, p.9181, 2025

[5] D. MacNeill, et al., "Control of spin–orbit torques through crystal symmetry in WTe_2/ferromagnet bilayers," *Nat. Phys*, vol. 13, no. 3, pp. 300, 2017.

[6] Zhang, Jia, et al. "Model of orbital populations for voltage-controlled magnetic anisotropy in transition-metal thin films," *Physical Review B,* vol. 96, pp. 014435, 2017.

[7] Thomas J. Peterson, et al. J.P. Wang "Enhancement of voltage controlled magnetic anisotropy (VCMA) through electron depletion," *Journal of Applied Physics,* vol. 131, pp. 153904, 2022.

[8] P. Bruno, "Theory of interlayer magnetic coupling," *Physical Review B,* vol. 52, no. 1, pp. 411, 1995.

[9] D. Zhang et al. J.P. Wang, "Bipolar electric-field switching of perpendicular magnetic tunnel junctions through voltage-controlled exchange coupling," *Nano Letters,* vol. 22, no. 2, pp. 622, 2022.

[10] Q. Jia, et al. J.P. Wang, "Ultrafast and Directional Magnetization Control via Voltage-Controlled Exchange Coupling," submitted for publication.

Ultra-high Efficiency of SOT-MRAMs using MTJs with Strain-induced Magnetic Anisotropy

Hiroaki Yoda, Taisuke Yoda, Yuichi Ohsawa, Yuichi Yamazaki, and Tomomi Yoda

YODA-S, Inc., Tsukuba, Ibaraki 305-0047, Japan, hi.yoda@yoda-s.com

To break through the limits of conventional MRAMs, MTJs with strain-induced magnetic anisotropy (SIMA-MTJs) were proposed as SOT-MRAM cells and proved to be superior to STT-MRAM with perpendicular magnetic anisotropy. This talk reviews the performances including TMR and write-efficiency compared with those of STT-MRAMs.

***Index Terms*—MRAM, SOT, Strain, Write-efficiency, TMR**

I. Introduction

STT-MRAMs using MTJs with perpendicular magnetic anisotropy (PMA-MTJs) have been commercialized mainly for embedded Flash-memory replacement where nonvolatility matters. However, the inherent trade-off relationship between critical switching-current (I_{csw}) and nonvolatility has been a big obstacle to be applied for working memory replacements where power consumption in active mode matters.

In order to break the trade-off relationships, MTJs with strain-induced magnetic anisotropy (SIMA-MTJs) were proposed as SOT-MRAM cells [1]. In this talk, the write-efficiency and other performances are reviewed by comparing with those of STT-MRAMs.

II. MTJ Materials and Structure of MTJs with SIMA

Fig.1 shows the schematic drawing and the cross-sectional TEM image of a SIMA-MTJ.

The materials and the structure were the same as those of conventional MTJs with in-plane magnetic anisotropy. Ta-based spin-Hall electrode (SHE) was deposited as the underlayer of the MTJs. CoFeB with magneto-striction constant of about 4E-5 was used as the storage-layer. MTJ stack was etched by ion-beam into MTJ elements with aspect-ratio of 1 to 2. Anisotropic strain was produced in order for the MTJs to have SIMA by the same concept reported before [1].

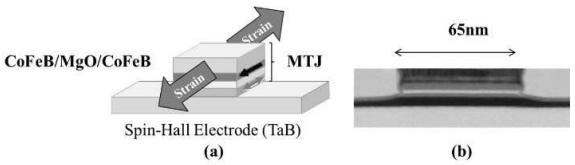

Fig. 1. (a) Structure and materials and (b) cross-sectional TEM image of SIMA-MTJ.

III. TMR and Nonvolatility of MTJs with SIMA

Reading speed also matters for working memory replacement. However, 150-200% TMR of PMA-MTJs are not enough for the application. The main reason for the limited TMR is due to limited thickness of the storage-layer or insertion of non-magnetic layer in the storage-layer.

A. Tunneling magneto-resistance(TMR)

There is no thickness limit for the storage-layer of SIMA-MTJs as far as the I_{csw} can be kept small enough for CMOS transistors to be able to supply.

Fig.2(a) shows a hysteresis curve of a patterned SIMA-MTJ with 1.9nm thick storage-layer and 61nm×104nm in size. Over 300% TMR was obtained[2].

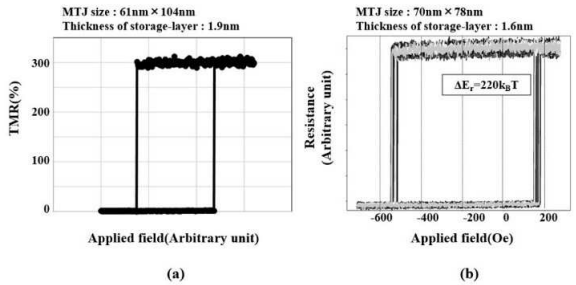

Fig. 2. 300% TMR ratio and the result of repeated hysteresis measurement of SIMA-MTJ

B. Nonvolatility

Retention energy ΔE_r was estimated by fitting the switching probability data obtained from repeated resistance-vs-applied magnetic field measurement (RH curves) with the Sharrock's formula [3].

Fig.2(b) shows the repeated R-H curves for a patterned SIMA-MTJ. The MTJ element has large retention energy, ΔE_r, of 220k_BT. Almost all the energy is thought to come from SIMA.

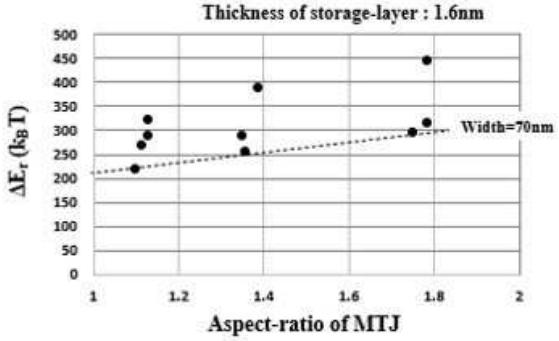

Fig. 3. Aspect-ratio dependence of ΔE_r of SIMA-MTJs.

Fig.3 shows the aspect-ration dependence of ΔE_r. The dotted extrapolation lines shows that MTJ elements with aspect-ratio of 1 would have large ΔE_r of larger than 200 k_BT. This is a proof of the existence of SIMA.

IV. SCALABILITY OF NONVOLATILITY(RETENTION ENERGY)

Fig.4 shows the scalability of SIMA-MTJ's retention energy .

The dotted extrapolation lines suggest that even with small size of 20nm, ΔE_r can be as large as 100k_BT to secure 10 years nonvolatility.

The retention energy of SIMA-MTJs is proportional to the width of the MTJs as observed by Fig.4, while that of PMA-MTJs is proportional to the area of the MTJs. Because of this, the retention energy of SIMA-MTJs decrease slower as its size gets smaller than that of PMA-MTJs does. SIMA-MTJs have better scalability in terms of nonvolatility.

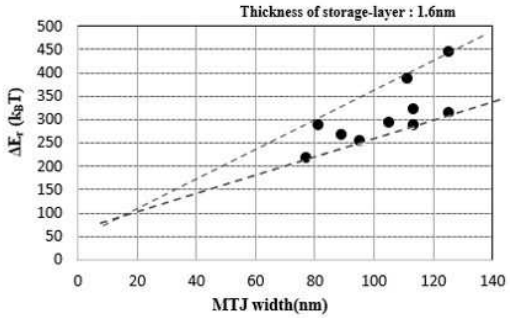

Fig. 4. Scalability of nonvolatility of SIMA-MTJ.

V. WRITE-EFFICIENCY OF SIMA-MTJS

Here, write-efficiency is defined as $\Delta E_r/I_{csw}$ with write-current pulse width of 10ns.

Fig.5 shows MTJ length dependence of the SOT write-efficiencies of SIMA-MTJs in comparison with those of STT-writing in PMA-MTJs. The smaller the length, the higher the efficiencies for both cases.

For SOT-writing in SIMA-MTJs, very high efficiency of 4.1 k_BT / μA was obtained for MTJs even with large size compared with that for the PMA-MTJs.

At the same size, the efficiency of SIMA-MTJs is about 4 times of those of PMA-MTJs.

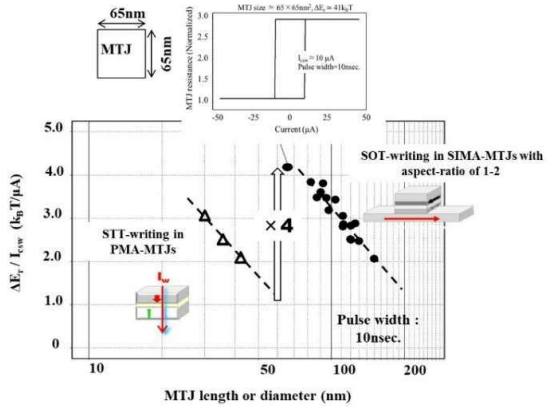

Fig.5. Write-efficiencies and the scalabilities of STT-writing PMA-MTJ and SOT-writing SIMA-MTJ[4] .

VI. TMR AND WRITE EFFICIENCY IMPROVEMENT TRENDS

Fig.6 shows TMR improvement trend and write-efficiency improvement trend[5].

After the proposal of PMA-MTJs for STT-MRAM with CoFeB/MgO/CoFeB based material in 2005-2008, both TMR and write-efficiency were improved to reach TMR of 200% and write-efficiency of 1k_BT/μA, respectively, in 2008-2010[6].[7],[8].

However, after that there had been almost no improvement reported for about 13-15 years. The development of STT-MRAM technologies seems to reach a deadlock.

In 2023, large TMR of 300% and very high write-efficiency of 4.1 k_BT/μA were reported with SOT-MRAM using SIMA-MTJs[2],[4].

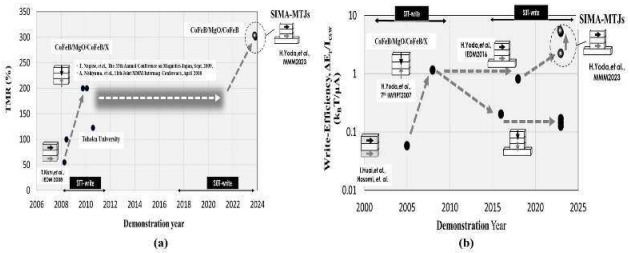

Fig. 6. Improvement history of MRAM. (a) TMR trend, (b) write-efficiency trend[5].

VII. SUMMARY

Development of SOT-MRAM with SIMA-MTJs was reviewed. The technology has proved much higher write-efficiency and larger TMR than those of PMA-MTJs used in commercialized STT-MRAM.

SOT-MRAM with SIMA-MTJs broke through the trade-off relationships between critical switching-current and nonvolatility to be a promising candidate for cache memory applications of nonvolatile memory.

REFERENCES

[1] H. Yoda, K. Yakushiji, and A. Fukushima, Digests of VLSI-TSA 2022.
[2] H. Yoda, S. Araki, Y. Ohsawa, T. Yoda, Y. Yamazaki, T. Kishi, and T. Yoda, IEEE Transactions on Magnetics, doi: 10.1109/TMAG.2024.
[3] M. P. Sharrock, "Time dependence of switching fields in magnetic recording media," *J. Appl. Phys.*, 76, pp. 6413-6418 (1994)
[4] H. Yoda, Y. Ohsawa, T. Kishi, Y. Yamazaki, T. Yoda, and T. Yoda, AIP Advances 14, 025327 (2024).
[5] H.Yoda, T. Yoda, Y. Ohsawa, Y. Yamazaki, and T. Yoda, Digests of IcAUMS 2025.
[6] M. Nakayama, T. Kai, N. Shimomura, *et. al.*, J. Appl. Phys. 103, 07A710 (2008).
[7] T. Kishi, H. Yoda, T. Kai, *et. al.*, Technical Digest of IEDM 2008, 12.6.
[8] K. Nishiyama, *et. al.*, 11th Joint MMM-Intermag Conference 2010 Digest (2010).

Magnetic skyrmion transport in racetracks: toward the realization of skyrmion racetrack memory

Seungmo Yang[1], Kyoung-Woong Moon[1], and Chanyong Hwang[1]

[1]Quantum Technology Institute, Korea Research Institute of Standards and Science, Daejeon, 34113, Republic of Korea, justin.yang@kriss.re.kr

Magnetic skyrmions offer promising potential for next-generation memory and logic devices due to their nanoscale size, stability, and efficient electrical manipulation. In this work, we demonstrate the three fundamental operations required for skyrmion racetrack memory: individual skyrmion generation, deletion, and current-driven transport. In a robust skyrmion hosting material, skyrmions are nucleated and annihilated via vertical voltage pulses applied through a GdOx layer that locally modulates magnetic states by forming conductive filaments. We further verify skyrmion deletion through negative pulses. By combining these capabilities with in-plane spin-orbit torque-induced motion, we realize a three-terminal device architecture capable of executing binary operations. As a proof of concept, we encode the bit sequence "1101," demonstrating complete racetrack memory functionality. These results pave the way for electrically programmable, skyrmion-based memory technologies.

***Index Terms*—Magnetic skyrmion, Racetrack memory, Spintronics**

I. Introduction

Since their first experimental observation [1, 2], magnetic skyrmions, topologically protected spin in real space, have attracted significant attention due to their distinct topological features, including the skyrmion Hall effect [3, 4], the topological Hall effect, and their robustness against defects [5]. Beyond their fundamental scientific interest, a wide range of skyrmions-based devices have been proposed, spanning from skyrmion racetrack memories [6] to neuromorphic computing units [7]. In this work, we introduce the key operation techniques to realize skyrmion racetrack memories. These include skyrmion generation at designated positions, electrically-driven skyrmion transport. Using this, we further present the proof-of-concept experiments of skyrmion racetrack memory devices.

II. Skyrmion Generation and Deletion

As skyrmion hosting materials, we employ multilayer stacks of MgO (1 nm)/Ta (0.08 nm)/CoFeB (1.3 nm)/W (5 nm)/TaO_x (2 nm) deposited on Si/SiO_2 substrates, where the CoFeB layer is a ferromagnetic layer, the W layer serves as a source of both spin-orbit torque (SOT), and Dzyaloshinskii-Moriya Interaction (DMI), the MgO layer induces Perpendicular Magnetic Anisotropy (PMA), and the ultrathin Ta dusting layer is introduced to precisely modulate the strength of PMA because the PMA here originates from the interface between the CoFeB/MgO layers. At zero magnetic field, this system exhibits a half-filled stripe domain pattern with a width of 2.4 μm. However, applying a +z-axis magnetic field of 4.3 Oe breaks the symmetry along the z-axis, expanding the +z domains whereas the –z domains shrink, as described in Fig. 1c. Note that under a +z magnetic field of 4.3 Oe, the skyrmion state becomes the global ground state, whereas the stripe domain state transitions into a local energy minimum state. However, skyrmions are not spontaneously formed because external perturbation, such as thermal energy, is not sufficient to overcome the barrier between the stripe domain state, skyrmion state, and uniform state.

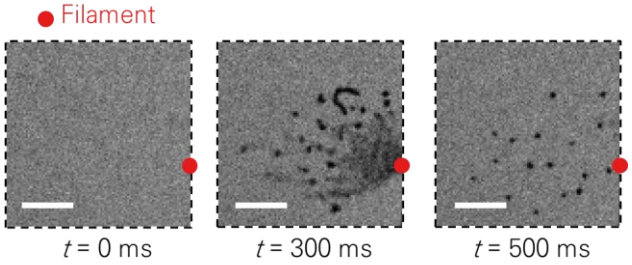

Fig. 1. Isolated skyrmion generation via vertical current injection.

Therefore, in order to generate an isolated skyrmion at a desired position, we adopt an alternative approach by introducing an additional source of external perturbations. A GdO_x (2 nm)/Pt (2 nm) layers are selectively deposited on the magnetic stacks using magnetron sputtering. Upon applying a sufficient voltage pulse across the GdO_x/Pt layers, dielectric breakdown occurs, resulting in the formation of a localized conductive filament. Subsequently, as shown in Fig. 1, the initial state is prepared as a uniformly magnetized configuration along the +z direction by applying a z-axis magnetic field of 4.3 Oe. When a voltage pulse (V_v) is applied, localized magnetization reversal is induced near the conductive filament (marked by the red dot in Fig. 1), resulting in the generation of several isolated skyrmions.

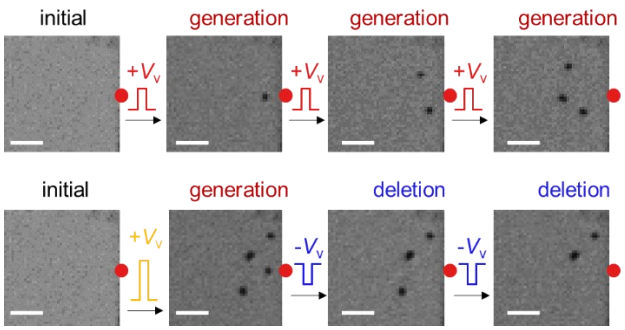

Fig. 2. Successive generation and deletion of isolated magnetic skyrmions

One isolated skyrmion can be also generated by applying an appropriately tuned V_v pulse of 1.0 V. This allows for the controlled accumulation of skyrmions through the sequential applications of a pulse train. To experimentally confirm this accumulation process, we began from a uniformly magnetized initial state (Fig. 2). The application of a single 1.0 V V_v pulse resulted in the formation of an individual skyrmion. Repeating the same pulse led to the creation of an additional skyrmion, and further pulses continued to nucleate skyrmions, each slightly displacing the previously generated ones due to SOT.

Conversely, applying a negative voltage V_v pulse drives and in-plane current toward the location of the conductive filament, effectively pulling in and annihilating nearby domain walls and skyrmions. This mechanism serves as a functional means of skyrmion deletion. For instance, when four skyrmions were generated using a 1.3 V V_v pulse, the subsequent application of -1.0 V removed one skyrmion. Repeated applications of -1.0 V V_v pulses continued to eliminate skyrmions one by one, eventually return to the initial state (Fig. 2).

III. Skyrmion Transport in Racetrack

A. Fert et al. [6] proposed introduced the concept of skyrmion racetrack memory, where digital information is represented by the presence or absence of magnetic skyrmions. In such a scheme, writing and erasing data require precise control over the generation and deletion of individual skyrmions, while data shifting corresponds to the controlled displacement of skyrmion positions. Building on our experimental demonstrations of skyrmion generation, deletion, and motion, we present a proof-of-concept implementation of all three essential operations within a three-terminal device structure that incorporates both vertical and in-plane current injection pathways.

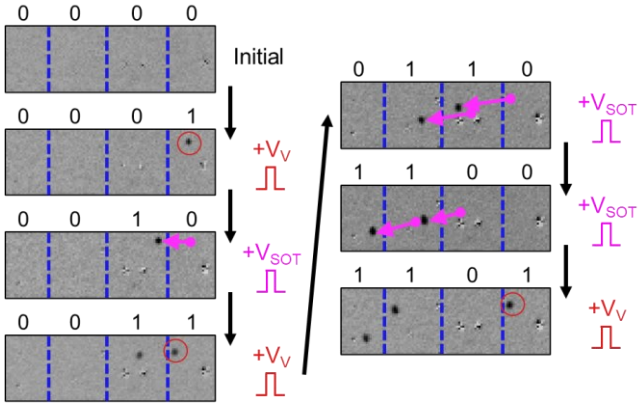

Fig. 3. Operation of the skyrmion racetrack memory.

As a demonstration, we encoded the binary number 1101, which corresponds to the decimal number 13. The process begins with a uniformly magnetized +z state, divided into four segments as indicated by blue dashed lines in Fig. 3. To write the first '1' in the rightmost bit position, a skyrmion is generated via a positive V_v pulse, resulting in the state (0001). A subsequent shift operation to the left is executed using a positive V_{SOT} pulse, after which another skyrmion is written to the rightmost bit, yielding (0011). Two additional shift operations are then applied, moving both skyrmions two bits to the left while preserving their relative spacing. Finally, a third skyrmion is generated in the rightmost bit, completing the target bit sequence (1101), equivalent to the binary representation of decimal 13 [8].

References

[1] U. K. Rößler, A. N. Bogdanov, and C. Pfleiderer, "Spontaneous skyrmion ground states in magnetic metals" *Nature, 442,* 797-801, 2006.

[2] S. Mühlbauer, B. Binz, F. Jonietz, C. Pfleiderer, A. Rosch, A. Neubauer, R. Georgii, and P. Böni, "Skyrmion Lattice in a Chiral Magnet" *Science*, 323, 915-919, 2009.

[3] U W. Jiang, X. Zhang, G. Yu, W. Zhang, X. Wang, M. Benjamin Jungfleisch, John E. Pearson, X. Cheng, O. Heinonen, K. L. Wang, Y. Zhou, A. Hoffmann, and Suzanne G. E. te Velthuis, "Direct observation of the skyrmion Hall effect" *Nat. Phys., 13,* 162-169, 2017.

[4] K. Litzius, I. Lemesh, B. Krüger, P. Bassirian, L. Caretta, K. Richter, F. Büttner, K. Sato, O. A. Tretiakov, J. Förster, R. M. Reeve, M. Weigand, I. Bykova, H. Stoll, G. Schütz, G. S. D. Beach, and M. Kläui, "Skyrmion Hall effect revealed by direct time-resolved X-ray microscopy" *Nat. Phys. 13,* 170-175, 2017.

[5] N. Nagaosa, and Y. Tokura, "Topological properties and dynamics of magnetic skyrmions" *Nat. Nanotech., 8,* 899-911, 2013.

[6] A. Fert, V. Cros, J. Sampaio, "Skyrmions on the track" *Nat. Nanotech, 8,* 152-156, 2013.

[7] K. M. Song, J.-S. Jeong, B. Pan, X. Zhang, J. Xia, S. Cha, T.-E. Park, K. Kim, S. Finizio, J. Raabe, J. Chang, Y. Zhou, W. Zhao, W. Kang, H. Ju, and S. Woo, "Skyrmion-based artificial synapses for neuromorphic computing" *Nat. Electron., 3,* 148-155, 2020.

[8] S. Yang, K.-W. Moon, T.-S. Ju, C. Kim, H.-J. Kim, J. Kim, B. X. Tran, J.-I. Hong, and C. Hwang, "Electrical Generation and Deletion of Magnetic Skyrmion-Bubbles via Vertical Current Injection" *Adv. Mater., 33,* 2104406, 2021.

Three-Track Detection Using a Multi-Layer Perceptron for Dual-Layer Bit-Patterned Magnetic Recording Systems

Santi Koonkarnkhai[1], *Member, IEEE*, Siriphon Plotchu[1], Warunee Martnok[1], Natthakan Rueangnetr[2], Sathapath Kilaso[3], Piya Kovintavewat[1], *Senior Member, IEEE*, and Chanon Warisarn[2], *Member, IEEE*
[1]Faculty of Science and Technology, Nakhon Pathom Rajabhat University, Nakhon Pathom, Thailand
[2]School of Integrated Innovation Technology, King Mongkut's Institute of Technology Ladkrabang, Bangkok, Thailand
[3]College of Innovation and Management, Suan Sunandha Rajabhat University, Bangkok, Thailand

This paper proposes a multi-layer perceptron (MLP)-based three-track detection method for dual-layer bit-patterned magnetic recording systems. Three architectures are explored: one MLP for three tracks, two MLPs for upper and lower layers, and three individual MLPs per track. Simulation results show that all MLP-based methods outperform conventional partial response maximum likelihood detection, especially under high areal density and complex interference. Among them, the two-MLP system achieves the best bit-error rate performance by effectively separating detection tasks across layers.

***Index Terms*—Dual-layer magnetic recording, multi-layer perceptron, multi-track detection, three dimensional interference**

I. Introduction

TRADITIONALLY, hard disk drives use single-layer magnetic recording. Recent studies, however, have proposed dual-layer magnetic recording (DLMR) systems to significantly increase areal density (AD), potentially reaching 10 Tb/in^2, as targeted by the Advanced Storage Research Consortium (ASRC) [1]. Designing the writing, reading, and signal processing systems for DLMR encounters major challenges due to increased complexity and data density if compared to a single-layer magnetic recording system.

One of the main challenges that DLMR faces the three dimensional (3D) interference, consisting of inter-symbol interference (ISI), inter-track interference (ITI), and inter-layer interference (ILI). If these interferences are not effectively managed, they can result in a high error rate during a data detection process. In addition to the 3D interference, DLMR also encounters other unwanted issues, such as track misregistration (TMR) and media noise.

Several studies have addressed the interference mitigation in DLMR. Luo *et al.* [2] combined PRML detection with a neural network (NN) to manage bit-cell misalignment. Given that the interference often exhibits nonlinear characteristics, NNs have been applied effectively, including iterative decoding approaches proposed by Jeong and Lee [3] and ITI mitigation by Koonkarnkhai *et al.* [4].

This paper introduces a multi-layer perceptron (MLP)-based 2-head 3-track (2H3T) detection method for a dual-layer BPMR system, whose objectives are to develop MLP architectures capable of detecting data across three tracks.

II. A Channel Model for Dual-Layer BPMR

Fig. 2 shows a dual-layer BPMR system employing 2H3T detection, where $\{a_{j,k}\} \in \{\pm 1\}$ is a binary user bit sequence of the j-th track at k-th bit. Note that if j is an odd number, it refers to a track in the 1-st recording layer, whereas if j is an even number, it refers to a track in the 2-nd recording layer.

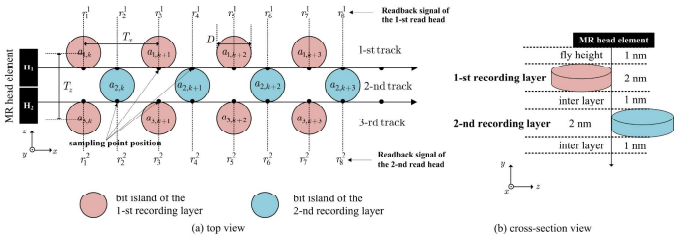

Fig. 1. The geometry of dual-layer BPMR medium, (a) top view and (b) cross-section view under the total AD of 4.0 Tb/in^2.

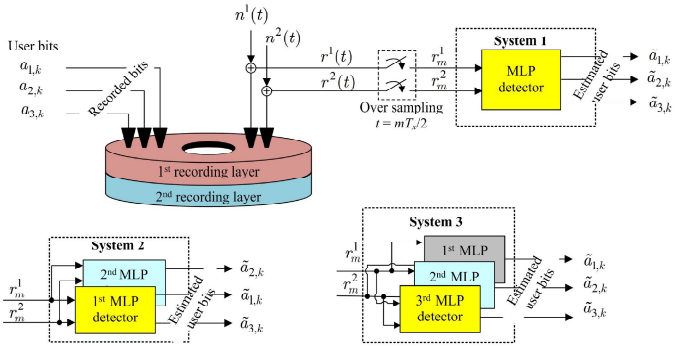

Fig. 2. A dual-layer BPMR system with the proposed MLP-based 2H3T detection methods.

This paper assumes that each recording layer has a thickness of 2 nm, and the isolation layer separating the two recording layers has a thickness of 1 nm, as depicted in Fig. 1(b). Each readback signal can be modeled as the output of two dimensional convolution between the magnetization of the bit-patterned medium and the read head sensitivity response. Thus, the readback signal of the q-th read head where $q \in \{1, 2\}$ can be expressed as

$$r^q(x,t) = \sum_{l=q}^{q+1} \iint_S m_l(\xi,\eta)\, h_l(x-\xi, t-\eta)\, d\xi\, d\eta + n^q(t), \quad (1)$$

where $m_j(\xi, \eta)$ denotes the magnetization at position (ξ, η) in the down- and cross-track directions of the j-th track, $h_j(x, z)$ represents the read head sensitivity response of the j-th track, and $n^q(t)$ is additive white Gaussian noise of the q-th read head with with two-sided power spectral density $N_0/2$.

At the conventional receiver, the readback signal $r^q(t)$ are oversampled a time $t = mT_x/2$ to obtain the sequence $\{r^q_m\}$. The sampled sequences $\{r^q_m\}$ are then fed to 1D equalizers and the 2D Viterbi detectors to obtain the estimated input bit sequences $\{\tilde{a}_{j,k}\}$, according to the PRML technique [5]. Nonetheless, in the presence of ultra-high ADs and multi-dimensional interference, PRML cannot perform reliably. Consequently, this paper proposes using an MLP-based detection approach to replace traditional PRML detection, aiming to improve data detection accuracy under more complex conditions.

III. Proposed MLP-Based Detection

Fig. 2 shows three proposed MLP-based data detection architectures. Specifically, System 1 uses a single MLP to detect all three tracks simultaneously; System 2 employs two MLPs, with the first detecting two upper-layer tracks and the second detecting the lower-layer track; and System 3 uses three independent MLPs, each dedicated to a single track.

All MLPs are configured with identical parameters, comprising one input layer and five hidden layers. Additionally, System 1 uses one MLP with three output nodes to detect all tracks simultaneously. System 2 employs two MLPs: one with two outputs for the upper tracks and another with one for the lower track. System 3 uses three separate MLPs, each dedicated to detecting a single track. All systems leverage inter-track correlation learning to improve detection performance.

All systems are trained using the Adam optimizer with a learning rate of 0.001 on 1000 4096-bit sectors without TMR or media noise to assess baseline performance under ideal condition. Extensive simulation searches identify that the optimal MLP architecture composes of five hidden layers with 128, 64, 32, 16, and 8 nodes, respectively, and utilizes the hyperbolic tangent activation function for best performance. Also, an input layer with 8 nodes provides the highest detection accuracy and system efficiency (data not shown).

IV. Simulation Result

This paper defines a signal-to-noise ratio as SNR $= 10\log_{10}\left(A^2/\sigma^2\right)$ in dB, where $A = 1$ is the normalized peak amplitude of the readback signal, and σ^2 represents the noise power. A performance comparison is conducted among different systems at an AD of 4 Tb/in^2, including the three proposed systems as shown in Fig. 2 and the conventional system, which utilizes a PRML-based detection scheme consisting of a 7-tap 1D equalizer and a 2D Viterbi detector.

Fig. 3 compares the performance of different systems. It is apparent that all proposed systems are superior to the conventional approach in terms of bit error rate (BER). Specifically, System 2 demonstrates the best performance, followed by System 3 and System 1, respectively. This may be attributed to System 2's ability to effectively separate data detection across two recording layers. Specifically, the first MLP processes

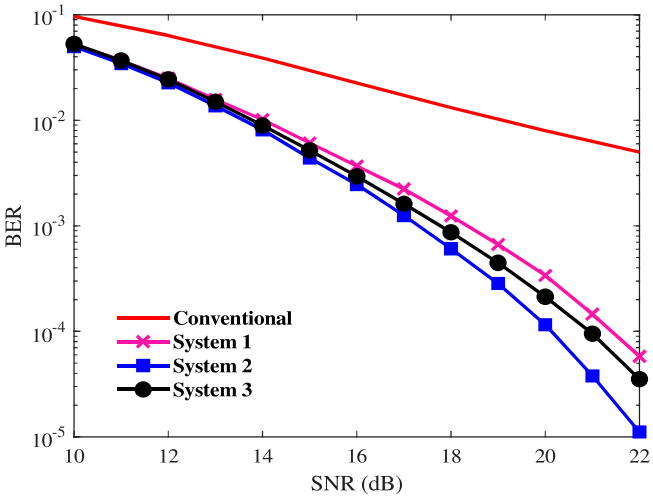

Fig. 3. Performance comparison for different systems.

data from the two upper tracks, which carry stronger signals, while the second MLP handles data from the lower layer. This separation reduces data complexity, improves learning accuracy, and enables the model to better capture the distinct characteristics of each layer. In contrast, System 1 employs a single MLP for all three tracks, which increases the likelihood of errors, whereas System 3 assigns a separate MLP to each track, which is more susceptible to overfitting.

V. Conclusion

This paper proposes an MLP-based three-track detection approach for dual-layer BPMR systems. Three architectures are evaluated, namely, a single MLP for all tracks, two MLPs for the upper and lower layers, and three separate MLPs for each track. Simulation results demonstrate that all MLP-based systems significantly outperform the conventional PRML detection, with the two-MLP architecture achieving the lowest BER by effectively partitioning the detection tasks between the layers.

Acknowledgments

This project is funded by School of Integrated Innovative Technology (SiiTEC), grant number 2568-02-10-003, King Mongkut's Institute of Technology Ladkrabang, Thailand.

References

[1] E. Roddick, M. Kief, and A. Takeo, "A new advanced storage research consortium HDD technology roadmap," in *Proc. of IEEE 33rd Magn. Recording Conf. (TMRC)*, Milpitas, CA, USA, Aug. 2022, pp. 1-2.

[2] K. Luo, Y. Liao, K. Zhang, Y. Jian, S. Wang, J. Chen, and P. Lu,"On the impact of interlayer misalignment for dual-layer data detection in three dimensional magnetic recording," *J. Magn. Magn. Mater.,* vol. 610, pp. 172522, Nov. 2024.

[3] S. Jeong and J. Lee. "Iterative signal detection scheme using multilayer perceptron for a bit-patterned media recording system," *Appl. Sci.,* vol. 10, no. 10, 2020.

[4] S. Koonkarnkhai, P. Kovintavewat, and C. Warisarn, "An MLP-based ITI suppression method for multi-head multi-track bit-patterned magnetic recording," *IEEE Trans. Magn.,* 2025. doi:10.1109/TMAG.2025.3542387

[5] J. Moon and W. Zeng, "Equalization for maximum likelihood detector," *IEEE Trans. Magn.,* vol. 31, no. 2, pp. 1083 – 1088, Mar. 1995.

Layered Magnetization Reversal by Multi-Head Writing in Three-Dimensional Magnetic Recording

Yugen Jian[1,2], *Graduate Student Member, IEEE*, Ke Luo[1], Jincai Chen[1,3,4], and Xuanyao Fong[2], *Member, IEEE*
[1]Wuhan National Laboratory for Optoelectronics, Huazhong University of Science and Technology, Wuhan 430074, China, jcchen@hust.edu.cn
[2]Department of Electrical and Computer Engineering, National University of Singapore, Singapore 117583, Singapore
[3]School of Computer of Science and Technology, Huazhong University of Science and Technology, Wuhan 430074, China
[4]Key Laboratory of Information Storage System, Engineering Research Center of Data Storage Systems and Technology, Ministry of Education of China, Wuhan 430074, China

Three-dimensional magnetic recording (3DMR) is a highly promising approach to achieving ultra-large data storage capacity in hard disk drives. One of the greatest challenges for 3DMR lies in performing sequential and correct writing of bits into the multi-layer recording medium. In this work, we propose a multi-head writing architecture with graded heat-assisted recording, and validate it in a dual-layer 3DMR system with FePt-based thin films via micromagnetic simulation. Our results reveal the layered magnetization reversal mechanism of the medium, ultimately attaining appreciable medium signal-to-noise ratio (SNR) for each layer. In particular, an optimal head-to-head distance is identified as the one that maximizes the medium SNR, which can support 3DMR scaling to more recording layers.

***Index Terms*—Heat-assisted magnetic recording (HAMR), three-dimensional magnetic recording (3DMR).**

I. INTRODUCTION

MASS-CAPACITY hard disk drives (HDDs) continue to be one sustainable and reliable choice to meet the escalating demand for large-scale data storage. Three-dimensional magnetic recording (3DMR), which utilizes more than one layer of recording medium, has been considered a very promising approach capable of surpassing the capacities of existing HDD products [1]. The implementation of 3DMR is facing a number of challenges [2] and the most critical of these is how to write bits sequentially and correctly to the multi-layer recording medium. In this work, we propose a multi-head writing architecture that features graded heat-assisted recording for 3DMR. Through micromagnetic modeling and simulation, we examined the architecture in a system with dual-layer FePt-based thin films. The magnetization reversal dynamics of top- and bottom-layer grains during the multi-head writing process were elucidated. Discussions on the performance of our proposed architecture were conducted, with the results demonstrating its superiority for the future realization of robust 3DMR.

II. MULTI-HEAD HEAT-ASSISTED RECORDING

To enable independent writing on either recording layer in 3DMR, it is imperative that they possess distinct anisotropy fields and can be magnetized under different physical conditions. Heat-assisted magnetic recording (HAMR) with graded temperatures has been reported as a feasible way to realize 3DMR [3]. Adjusting the laser's focal depth and power to match the position and Curie temperature of each recording layer thus allows for separated writing in 3DMR.

Here we propose a multi-head writing architecture for 3DMR, leveraging multi-pass writing with graded HAMR to sequentially write data into the multi-layer recording medium. Fig. 1(a) gives a schematic diagram of the architecture. Overall, the multi-head writing process begins from the bottom layer and progresses upward, layer by layer, as the medium moves. Each head corresponds to the respective layer, i.e., head i operates on layer i at the i-th pass writing ($i = 1, 2, \cdots, N$). Writing temperature T_{wi} and writing field $\vec{H}_{wi}$ produced by head i are determined by the structural position and physical properties of layer i, and will be either preset or controlled by the write current.

The writing fields can be independent from one another, while the writing temperatures need to satisfy the conditions:

$$\begin{cases} T_{w1} > T_{w2} > \cdots > T_{wN} \\ T_{wi} = T_{Ci} + \delta T_i \quad (i = 1, 2, \cdots, N) \end{cases} \tag{1}$$

T_{wi} and T_{Ci} are the writing and Curie temperatures of head/layer i, respectively. δT_i is a small positive value that represents T_{wi} is slightly higher than T_{Ci}. It is essential to hold such a temperature gradient to ensure that data previously written remains unaffected in the onward process.

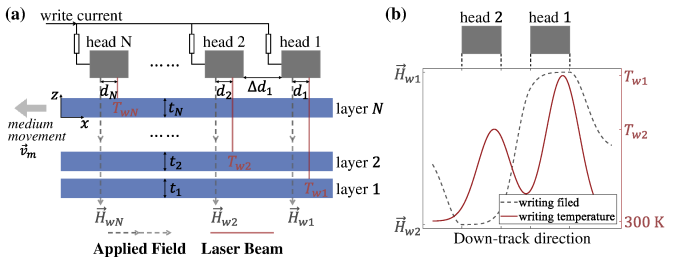

Fig. 1. (a) Schematic diagram of the multi-head writing architecture with graded heat-assisted recording for 3DMR. (b) Examples of down-track profiles of writing temperature T_w (red solid line) and writing field $\vec{H}_w$ (gray dashed line) produced by head 1 and head 2.

We have developed a micromagnetic model to simulate the multi-head writing process by solving the Landau-Lifshitz-Bloch (LLB) equation on MARS [4]. The writing temperature of each head follows a Gaussian distribution, and the writing field is considered constant within the head area, while the stray field outside the head is Gaussian distributed (as shown in Fig. 1(b)). For the recording medium, FePt-based thin film with Voronoi grains and nonmagnetic grain boundaries is modeled. In our following examination, we primarily focus on the case of $N = 2$, i.e., dual-layer 3DMR with dual-head writing. Key parameters and settings will be provided in the future full manuscript.

III. LAYERED MAGNETIZATION REVERSAL DYNAMICS

To investigate the dynamical process of layered magnetization reversal in 3DMR, the dual-head writing of consecutive transitions (square-wave binary sequence for both heads) on the dual-layer medium was simulated. The temporal evolution of layered magnetization reversal during the multi-head writing process can be divided into four stages, as shown in Fig. 2:

1) The medium was firstly heated to the higher writing temperature, of which $T_{w1} > T_{C1} > T_{C2}$, and the coercivity of both the top and bottom layers was rapidly reduced. The grains transitioned from ferromagnetic to paramagnetic ($m_z \to 0$) as the temperature rose.
2) As the head moved forward, the grains regained their ferromagnetic state while cooling, and the magnetization was reversed under the effect of the writing field. At this point, the bits corresponding to the top and bottom layers switched from "1" to "0".
3) The second-pass writing began, and the medium was heated to the lower writing temperature, of which $T_{C1} > T_{w2} > T_{C2}$. Consequently, only the magnetization of the top-layer grain would be erased. The coercivity and magnetization of the bottom-layer grain decreased as the temperature rose but did not meet the writable condition, thus the bottom-layer grain would remain in the state achieved after the first-pass writing.
4) Finally, the magnetization of the top-layer grain was reversed by the writing field, while the bottom-layer grain remained unaffected and returned to its previous state. The medium would reach equilibrium at room temperature, with data "1" and "0" separately stored in the corresponding bits of the top and bottom layers.

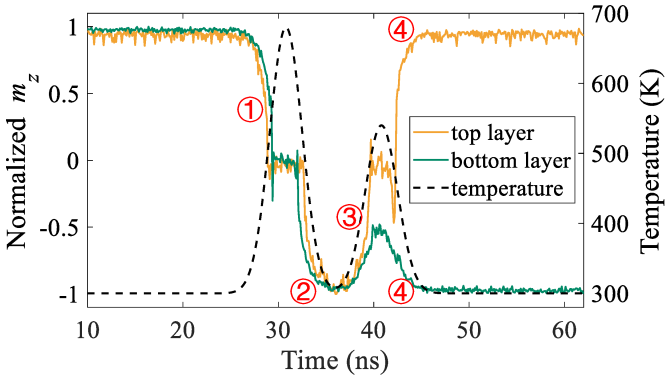

Fig. 2. Temporal evolution of the magnetization reversal of grains from the top (yellow line) and bottom (green line) layers during the multi-head writing process, which is discussed in stages ①-④. The dashed line represents the variation of the grain's temperature over time.

IV. MEDIUM SIGNAL-TO-NOISE RATIO

In the multi-head writing architecture, the distance between adjacent heads Δd emerges as an additional factor that impacts the performance of 3DMR system. Hence, we repeated the writing simulations with varying Δd, and calculated the medium signal-to-noise ratio (SNR) in each configuration.

The results of medium SNRs are shown in Fig. 3 with very interesting trends. To begin with, as the head-to-head distance Δd grows from zero, the medium SNR will gradually improve for both layers. When Δd continues to increase, the medium SNR experiences a slight decline before leveling off, which is more pronounced for the bottom layer. This suggests the existence of an optimal distance Δd_{opt}, at which the medium SNR reaches its maximum, opening up the potential for expanding to more recording layers and a larger multi-head array in 3DMR.

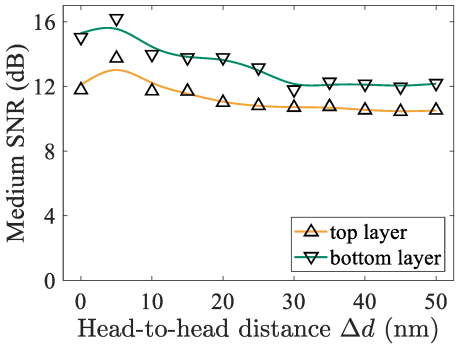

Fig. 3. The medium SNR versus the head-to-head distance Δd for the top (yellow lines) and bottom (green lines) layers.

ACKNOWLEDGEMENT

This work was supported by the National Natural Science Foundation of China under Grant 62272178 and the Fundamental Research Funds for the Central Universities under Grant YCJJ20242107. Yugen Jian would like to thank the support from the China Scholarship Council under Grant 202306160094.

REFERENCES

[1] E. Roddick, M. Kief, and A. Takeo, "A new Advanced Storage Research Consortium HDD Technology Roadmap," in *2022 IEEE 33rd Magnetic Recording Conference (TMRC)*, 2022, pp. 1–2.
[2] S. Greaves, "Three-dimensional magnetic recording," *J. Magn. Magn. Mater.*, vol. 588, p. 171343, 2023.
[3] P. Tozman, S. Isogami, I. Suzuki, A. Bolyachkin, H. Sepehri-Amin, S. Greaves, H. Suto, Y. Sasaki, T. Chang, Y. Kubota, P. Steiner, P. Huang, K. Hono, and Y. Takahashi, "Dual-layer FePt-C granular media for multi-level heat-assisted magnetic recording," *Acta Mater.*, vol. 271, p. 119869, 2024.
[4] S. Rannala, A. Meo, S. Ruta, W. Pantasri, R. Chantrell, P. Chureemart, and J. Chureemart, "Models of advanced recording systems: A multi-timescale micromagnetic code for granular thin film magnetic recording systems," *Comput. Phys. Commun.*, vol. 279, p. 108462, 2022.

Interference Mitigation via Top-Layer-Assisted Signal Rescaling in Dual-Layer 3D Magnetic Recording

Ke Luo[1,3], Ziqian Liu[2,3], Yuqian Zhao[2,3], Yugen Jian[1,3], Simon Greaves[4*], Jincai Chen[1,3*], and Ping Lu[2,3]
[1]Wuhan National Laboratory for Optoelectronics, Huazhong University of Science & Technology, 430074, China
[2]School of Computer Science & Technology, Huazhong University of Science and Technology, 430074, China
[3]Key Laboratory of Information Storage System, Engineering Research Center of Data Storage Systems & Technology, Ministry of Education of China, Huazhong University of Science & Technology, 430074, China
[4] Research Institute of Electrical Communication (RIEC), Tohoku University, Sendai 980-8577, Japan
Corresponding author: Simon Greaves (simon@riec.tohoku.ac.jp), Jincai Chen (jcchen@hust.edu.cn).

ThreeDimensional magnetic recording (3DMR) technologies, such as threeDimensional heat-assisted magnetic recording (3D HAMR) and threeDimensional bit-patterned magnetic recording (3D BPMR), enhance areal density by stacking multiple recording layers and leveraging heat-assisted writing to encode multi-bit data through vertically combined magnetization states. Current 3DMR systems primarily employ dual-layer media (also termed dual-layer magnetic recording), where the readback signal from a single head comprises superimposed responses from a top layer and a bottom layer, introducing severe threeDimensional interference—including inter-symbol interference (ISI), inter-track interference (ITI), and inter-layer interference (ILI). To improve bottom-layer detection reliability in 3DMR, this paper proposes a scaling-based signal extraction method that refines the bottom-layer signal using detected top-layer data. This approach enables efficient oneDimensional detection while significantly reducing the bottom-layer bit error rate (BER). Compared to the previously proposed dual-layer PRML detection, the method maintains the same top-layer BER while achieving a 80% reduction in the bottom-layer BER under the areal density of 3.3 Tbpsi. Moreover, it demonstrates superior bottom-layer detection performance across areal densities ranging from 1 to 4.5 Tbpsi per layer (2–9 Tbpsi for dual-layer systems).

Index Terms—**3D magnetic recording, inter-layer interference, signal extraction, bottom-layer detection**

I. Introduction

THE growing demand for storage capacity has driven magnetic recording from conventional 2D systems toward threeDimensional architectures. Notably, threeDimensional heat-assisted magnetic recording (3D HAMR) and 3D bit-patterned magnetic recording (3D BPMR) stack multiple layers and encode data using vertically combined magnetization states, enabling higher areal densities (ADs). Dual-layer magnetic recording (DLMR) is currently the most practical implementation of 3DMR. However, transitioning to 3D recording introduces challenges in signal acquisition and detection. One major issue is weak far-field sensitivity: the increased head-media spacing (HMS) causes bottom-layer signal to be overshadowed by top-layer signal. Although tunneling magnetoresistive (TMR) heads are used, signal attenuation remains significant. Another challenge is severe 3D interference, including inter-symbol (ISI), inter-track (ITI), and inter-layer interference (ILI).

To mitigate these issues, prior works have explored layer-selective sensing using spin-torque oscillators (STOs) [1], Curie-temperature-tuned dual-layer media from Seagate, and asymmetric bit geometries to improve state distinguishability [2]. Iterative detection algorithms, such as Turbo equalization for dual-layer BPMR [3], have also been proposed.

Our previous study modeled dual-layer 3DMR under inter-layer misalignment and showed that neural network-based reconstruction improves bottom-layer detection, though at a high computational cost. Since bottom-layer signals are more affected by interference, low-cost and effective detection methods are needed. Existing strategies fall into two categories:

- Mutual layer-assisted detection (exploiting inter-layer correlations),
- Layer-separated detection (processing each layer independently).

In this paper, we propose a scaling method that enhances the bottom-layer signal using detected top-layer data, enabling independent 1D detection. Compared to traditional dual-layer partial response maximum likelihood (PRML), the proposed method maintains top-layer BER while reducing bottom-layer BER across 1–4.5 Tbpsi per layer (2–9 Tbpsi total).

II. Experimental Setup

In this study, we adopt the same experimental parameters and reader structure as described in [4]. The bit length (BL) and track pitch (TP) are identically configured for both layers, with values ranging from 12 nm to 25 nm. This configuration ensures consistent linear and track densities across experiments. We focus on the detection performance of the bottom layer, assuming perfect interlayer alignment.

III. Double-Layer Data Detection

We employ the previously proposed dual-layer PRML detection as our benchmark, which jointly detects data from both recording layers in a 3D magnetic recording system. It utilizes a 2D finite impulse response (FIR) equalizer to mitigate ISI and ITI, followed by a Viterbi detector that operates on a combined target response. To account for the varying signal sensitivities between layers, weighted contributions from the top and bottom layers are incorporated during maximum likelihood sequence detection.

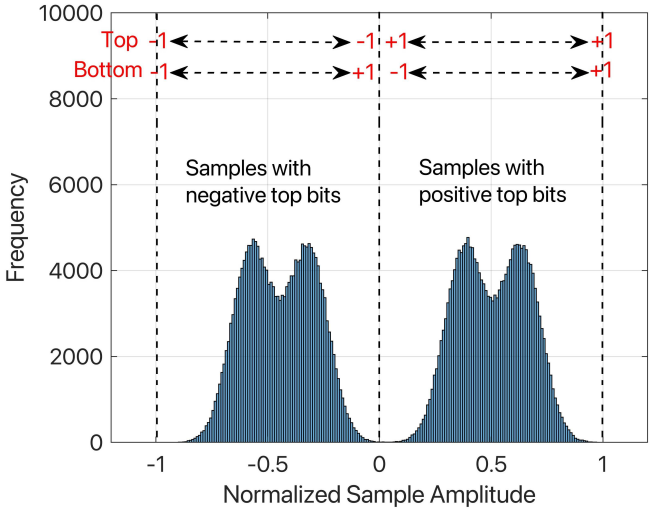

Fig. 1. Amplitude distribution of readback samples (BL=18 nm and SNR=16 dB).

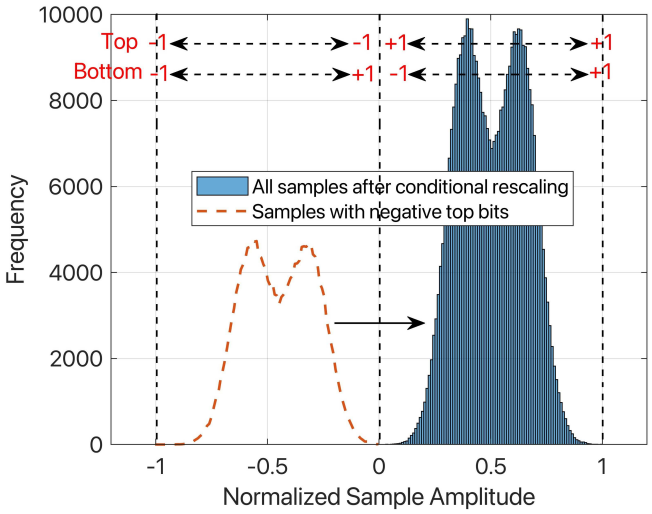

Fig. 2. The amplitude distribution of readback samples (BL=18 nm and SNR=16 dB): rescaled samples with negative top bits and original samples with positive top bits.

To enhance the reliability of bottom-layer detection, we propose independent layer processing. As illustrated in Fig. 1, the dual-layer readback signal exhibits an approximately symmetric amplitude distribution. The well-separated distributions on both sides indicate minimal interference on the top layer. In this figure, samples with negative-polarity top-layer bits "-1" predominantly occupy the left region, while samples with positive-polarity top-layer bits "$+1$" are located on the right. However, the bimodal distribution on each side overlaps between the two peaks, resulting in significant interference on the bottom layer. We apply 2D FIR equalization and 1D detection, followed by conditional amplitude rescaling. In this process, we transform samples with negative top bits into the normalized range of $[0, 1]$, while preserving the original amplitudes of samples with positive top bits. The resulting composite distribution, illustrated in Fig. 2, combines the rescaled negative-top samples with the unprocessed positive-top ones. Another 2D FIR equalizer and detector are then

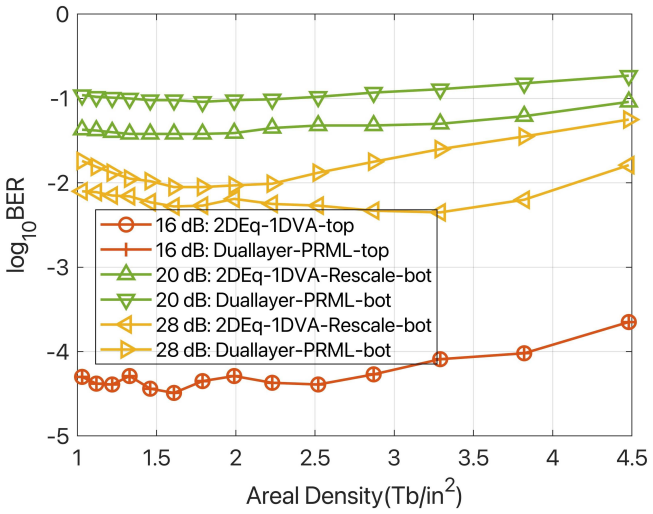

Fig. 3. BER performance comparison: proposed conditional rescaling, 1D PRML vs. dual-layer PRML across 1–4.5 Tbpsi/layer areal densities.

applied to the composite samples. The coefficients of the 2D equalizers and the partial response targets $[\alpha, 1, \beta]$ are obtained using the minimum mean square error algorithm. We utilize these targets to construct a trellis for double-layer detection. The orange dashed curve represents the distribution of samples with negative top bits. After conditional rescaling, the distribution of all samples becomes sharper. The rescaling process can be viewed as a cancellation of the top-layer component.

We evaluate the BER performance as a function of ADs ranging from 1–4.5 Tbpsi/layer that corresponds to bit lengths between 12 nm and 25 nm, as shown in Fig. 3. For top-layer detection, a 1D Viterbi detector achieves the same BER performance as dual-layer PRML detection at a SNR of 16 dB. The BER performance on the top layer, despite the low SNR of 16 dB, is superior to that on the bottom layer under higher SNRs across all ADs. Although the BER increases with higher ADs, the bottom-layer BER, after rescaling the samples with negative bits, demonstrates improved performance compared to dual-layer PRML detection. Specifically, the bottom-layer BER after conditional rescaling at an AD of 3.3 Tbpsi/layer is reduced by 80 % compared with the performance of dual-layer PRML detection.

References

[1] H. Suto, T. Nagasawa, K. Kudo, K. Mizushima, and R. Sato, "Nanoscale layer-selective readout of magnetization direction from a magnetic multilayer using a spin-torque oscillator," *Nanotechnology*, vol. 25, no. 24, p. 245501, May 2014.

[2] P. Tozman, S. Isogami, I. Suzuki, A. Bolyachkin, H. Sepehri-Amin, S. Greaves, H. Suto, Y. Sasaki, T. Chang, Y. Kubota, P. Steiner, P. Huang, K. Hono, and Y. Takahashi, "Dual-layer fept-c granular media for multi-level heat-assisted magnetic recording," *Acta Materialia*, vol. 271, p. 119869, Jun. 2024.

[3] A. Khametong, S. J. Greaves, and C. Warisarn, "Mutual soft-information improvement techniques for lower layer performance improvement in double-layered magnetic recording systems," *IEEE Transactions on Magnetics*, pp. 1–1, 2025.

[4] K. Luo, Y. Liao, K. Zhang, Y. Jian, S. Wang, J. Chen, and P. Lu, "On the impact of interlayer misalignment for dual-layer data detection in three dimensional magnetic recording," *Journal of Magnetism and Magnetic Materials*, vol. 610, p. 172522, Nov. 2024.

AI-Based Layout Optimization of HDDs in Full-Rack Heterogeneous Server and Storage Systems

Yi-Ju Liao [1], Jen-Yuan Chang [2], *Senior Member, IEEE*

[1, 2] Department of Power Mechanical Engineering, National Tsing Hua University, Hsinchu, Taiwan

Heterogeneous rack systems combining servers, storage arrays, and switches are common in modern data centers, yet hard disk drives (HDDs) within such configurations face performance degradation from complex structural and airflow-induced vibrations. This work proposes a slot-based, machine learning framework to predict HDD degradation risk and guide layout optimization. Each rack slot is characterized by a feature vector comprising modal frequency, local stiffness, airflow excitation, and vibrational coupling, estimated via representative simulations. Decision tree and neural network models are trained to predict IOPS degradation based on these descriptors. A reference configuration—switches at the top, servers in the middle, storage at the bottom—is used to demonstrate rack-level risk mapping. The framework supports explainability through SHAP analysis and enables layout recommendations that reduce slot-level exposure to high-risk conditions. The proposed method is modular, generalizable across rack designs, and suitable for deployment-oriented optimization of HDD placement strategies.

***Index Terms*—Data center reliability, hard disk drives, machine learning, vibration analysis**

I. Introduction

The increasing heterogeneity of data center rack systems—comprising co-located servers, storage arrays, and switch modules—poses new challenges to mechanical stability and long-term hard disk drive (HDD) reliability. While prior studies have investigated HDD failure under isolated conditions or uniform enclosures, real-world deployments often exhibit complex physical interactions due to structural discontinuities, varying airflow patterns, and device-specific mounting configurations [1]. These factors result in spatially nonuniform vibrational and thermal environments that can significantly degrade HDD input/output operations per second (IOPS) performance. However, current industry practices lack a predictive framework capable of modeling such position-dependent degradation and guiding layout optimization at the full-rack level. To address this gap, we propose a slot-based predictive framework that combines structural and thermal simulation with machine learning techniques to assess HDD degradation risk and support layout-aware planning. Each slot in the rack is abstracted into a physical feature vector describing its modal response, airflow exposure, local mounting conditions, and proximity-based coupling effects. These features are derived from representative finite element and airflow models of heterogeneous full-rack configurations. Supervised learning models—specifically decision trees and artificial neural networks—are then trained to predict IOPS degradation at the slot level. The resulting framework supports SHAP-based model interpretability, enabling identification of high-risk regions and informing placement strategies that align with rack design constraints. This paper introduces the proposed methodology, demonstrates its application on a reference configuration, and outlines future directions for integrating interpretable slot-level risk analysis into rack-level design workflows.

II. System Modeling

In the proposed framework, the heterogeneous rack comprising switches, servers, and storage modules—is abstracted into a set of discrete slots, each of which is represented by a feature vector encoding its physical and environmental characteristics [4]. This slot-level abstraction enables the modeling of complex interdependencies between device types, airflow dynamics, and structural responses within the rack.

Each slot is described by a set of features that include: (1) modal frequency, obtained from simplified structural simulations or vendor specifications; (2) local stiffness, which accounts for tray design and mounting conditions; (3) airflow velocity, derived from computational fluid dynamics (CFD) simulations or empirical fan profiles; (4) proximity-based coupling intensity, modeling vibrational energy transmission from adjacent slots; and (5) device type, a categorical indicator (e.g., HDD, server, switch, or empty). These features form a structured dataset with each row corresponding to a slot and each column to a physical parameter. This dataset serves as input to supervised learning models trained to predict slot-level IOPS degradation risks. A schematic of this modeling approach is shown in **Fig. 1**.

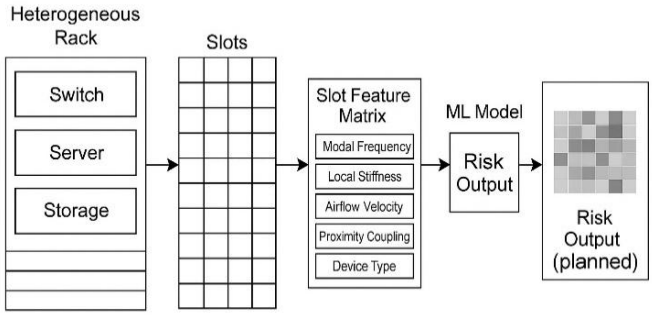

Fig. 1. Slot-based degradation modeling and explainable learning framework

III. Macine Learning Architecture

A supervised learning framework is employed to predict slot-specific hard disk drive (HDD) performance degradation using

physical and environmental descriptors derived from rack-level modeling. Each rack configuration is transformed into a structured feature matrix, where each row corresponds to a logical slot and each column represents a characteristic such as modal frequency, airflow velocity, local stiffness, vibrational coupling intensity, or device type. For storage enclosures housing multiple HDDs, each drive is individually abstracted into a separate logical slot. Intra-enclosure effects such as shared airflow conditions or structural coupling are reflected through common feature values across these slots, enabling the model to preserve localized distinctions while maintaining global coherence. This abstraction permits flexible modeling of mixed server–storage systems and supports evaluation of layout variations without requiring device-specific knowledge.

The predictive framework employs decision trees (DTs) for interpretability and artificial neural networks (ANNs) for capturing nonlinear interactions across slot-level features. Training data are generated through a combination of representative simulations and hypothetical rack configurations, ensuring generalizability across diverse deployment scenarios. The model output is a degradation risk score associated with each HDD slot, corresponding to predicted IOPS loss under specific vibrational and thermal conditions. To support interpretability, a SHAP-based feature attribution module is planned, enabling identification of dominant physical drivers of degradation across the slot population. While this component is under development, its intended integration highlights the extensibility of the framework for deployment-aware and layout-sensitive design optimization [2] [3].

Each slot's predicted degradation risk score is modeled as a function of its physical and environmental characteristics. The risk score R_i for slot i is computed as a weighted sum of feature contributions:

$$R_i = \beta_1 f_{modal,i} + \beta_2 v_{air,i} + \beta_3 k_{stiff,i} + \beta_4 c_{couple,i} + \beta_5 d_{type,i} \quad (1)$$

Where $f_{modal,i}$ is the first-mode frequency, $v_{air,i}$ is the local airflow velocity, $k_{stiff,i}$ is the slot stiffness, $c_{couple,i}$ is the coupling intensity from adjacent slots, and $d_{type,i}$ denotes the device type (e.g., HDD, server, or switch). The coefficients β_j are learned by the regression model. Equation (1) is used both as a conceptual formulation and as the basis for SHAP-based feature attribution in model interpretation.

TABLE I
SLOT-LEVEL FEATURE DESCRIPTIONS

Feature Name	Unit	Description
Modal Frequency	Hz	First mode frequency of the slot structure
Airflow Velocity	m/s	Estimated airflow affecting the slot
Local Stiffness	N/m	Tray stiffness or mounting-induced compliance
Coupling Intensity	–	Vibrational influence from adjacent slots
Device Type	Categorical	Type of device installed (Storage, Server, Switch, Empty)

IV. Preliminary Evaluation and Deployment Plan

The proposed framework is designed to support early-stage evaluation through simulated slot configurations and hypothetical rack layouts. In the initial phase, training data will be generated using synthesized modal and thermal descriptors representative of typical server–storage deployments. A limited matrix of 48–96 slots will be constructed to emulate vibration-sensitive regions, and corresponding IOPS degradation scores will be estimated using simplified mapping functions based on modal alignment thresholds and airflow-induced excitation levels.

Model training will begin with decision trees to establish interpretable rule sets, followed by artificial neural networks to capture complex dependencies. Initial SHAP analysis will be applied to assess feature contributions across slots, and risk maps will be visualized to support slot-level performance assessment. This workflow will enable deployment-focused layout evaluations without reliance on proprietary device data. Results from this preliminary phase will be showcased at the poster session, with ongoing work focused on expanding dataset diversity and integrating optimization modules.

V. Conclusion

This work introduces a slot-based machine learning framework for predicting HDD performance degradation across heterogeneous rack systems. The proposed modeling approach enables configuration-level flexibility, modular scalability, and integration with explainability techniques. Future work will focus on extending the framework to support real-time layout optimization and system-wide deployment scenarios.

References

[1] J. H. L. Hansen, W. Song, and T. Zhang, "Vibration-induced performance degradation of hard disk drives in data centers," *IEEE Trans. Magn.*, vol. 53, no. 11, pp. 1–7, Nov. 2017.

[2] A. Shrikumar, P. Greenside, and A. Kundaje, "Learning important features through propagating activation differences," *Proc. 34th Int. Conf. Mach. Learn.*, vol. 70, pp. 3145–3153, 2017.

[3] S. Lundberg and S.-I. Lee, "A unified approach to interpreting model predictions," in *Advances in Neural Information Processing Systems*, vol. 30, pp. 4765–4774, 2017.

[4] T. Kim and B. Karp, "The impact of airflow and rack layout on hard drive reliability in high-density servers," *Proc. ASME InterPACK*, pp. 1–8, 2019.

[5] D. Silver, J. Barto, and R. S. Sutton, *Reinforcement Learning: An Introduction*, 2nd ed. Cambridge, MA: MIT Press, 2018, pp. 145–150.

Write current control based on THMap in HAMR

Aiko Sakoguchi[1,2], Jay Lee[3]

[1]Western Digital Technologies GK, Fujisawa, 252-0888, Japan
[2]Graduate School of Science and Technology, University of Tsukuba, Tsukuba, 305-8577, Japan
[3]Western Digital Technologies, Irvine, CA 92612, USA

Both laser and write currents have large impact on write-ability, areal density capability (ADC), and reliability in heat assisted magnetic recording (HAMR). We utilized THMap for two objectives, to obtain laser and write currents condition which saturates magnetization switching of grains, and to calculate write current dependence of write temperature (T_w). ADC was maximized at higher laser and write currents than those to saturate magnetization switching. It indicates that laser and write currents for magnetization saturation are requirements to maximize ADC. To achieve both maximization of ADC and reliability, we considered an approach to reducing laser current with increased write current. From the comparison of two different design heads, write current dependence of T_w was well matched to that of magnetic write width. The approach to keep high ADC with reduced laser current and increased write current succeeded with the head which could reduce T_w by increase of write current.

***Index Terms*—heat assisted magnetic recording (HAMR), laser current, write current, THMap.**

I. Introduction

In heat assisted magnetic recording (HAMR) of hard disk drives (HDDs), heat power and magnetic field strength are adjusted by laser and write currents, respectively, with the aim of maximizing areal density capability (ADC) and reducing write stress for reliability [1]-[3], which contradict each other. High probability of magnetization switching with sufficient laser and write currents is required to obtain good bit error rate [4]. However, the relation between probability of magnetization switching and ADC is still unknown. In the point of view of reliability, increase of head temperature is a dominant factor of write quality degradation in long-run test [5]. The reduction of laser current is crucial to reliability of HAMR. First, we discussed laser and write currents dependence of ADC and its relation to saturate magnetization switching probability. Next, write current dependence of write temperature (T_w) was discussed to explore the approach to reducing laser current with increasing write current.

II. Experimental Method

All measurements were conducted using HAMR drives in temperature controlled chamber at 35 °C. We used THMap [6] to evaluate magnetization switching probability of media grains as a function laser and write currents. THMap measured noise power after reversed DC write, which is assumed to be related to the magnetization switching probability.

To compare with THMap, ADC of conventional magnetic recording (CMR) system was measured under multiple laser and write currents conditions. In the measurement, we used the industry standard method [7] with 6 times write in each adjacent track, and track density (TPI) was relaxed by 10 % from track pitch which satisfies 50 % sector failure rate.

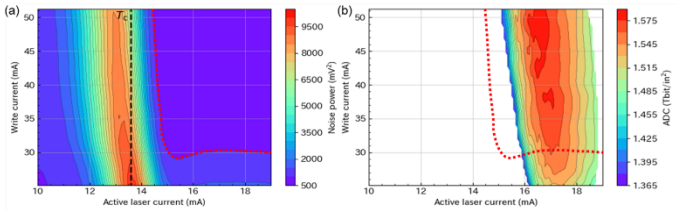

Fig. 1. (a) A THMap, noise power as a function of active laser current which is laser current above lasing threshold, and write current. Region boundary of noise power saturation is shown in red dotted line. Active laser current 13.6 mA corresponds to T_c where noise power reached peak under minimum write current, 1.8 mA. (b) A 2-D ADC map. The region boundary from (a) is shown in red dotted line.

III. Results and Discussion

Fig. 1 (a) shows a THMap. We considered that media temperature reached Curie temperature (T_c) at active laser current 13.6 mA where noise power was maximized under minimum write current, 1.8 mA. Media temperature needs to be higher than T_c to reach the saturation region, whose boundary is shown in red dashed line, because actual T_c for each grain has distribution. As well as the temperature requirement, saturation recording requires sufficiently high write current, approximately 30mA in Fig.1 (b), in order to overcome thermal agitation [8]. Fig.1 (b) shows a 2-D map of ADC as a function of active laser and write currents. Additionally, the same region boundary of noise power saturation is overlayed in red dashed line. Higher laser current than the boundary condition is required to maximize ADC. On the other hand, maximum ADC along laser current-axis almost saturated within the saturation region, and dropped if write current is below the boundary condition. In Fig.1 (b), overshoot amplitude of write current (OSA) and its duration were set to 50.8 mA and 268 psec, respectively. In addition to the condition shown in Fig.1 (b) with OSA 50.8 mA, ADC was measured with multiple OSA conditions from 42.3 mA to 93.1 mA. In all OSA conditions, ADC was maximized with higher write current than that of noise power saturation. It suggests that laser and write currents

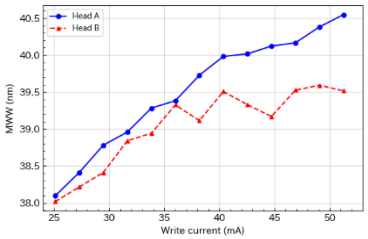

Fig. 2. Write current dependences of MWW for two head designs. Fixed active laser current 18.4 mA, and 15.3 mA were selected where MWW is around 38 nm at write current 25 mA, respectively.

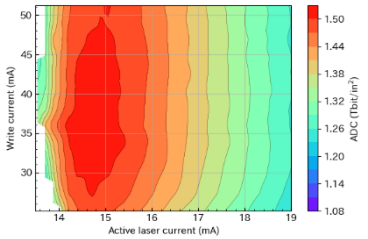

Fig. 3. A 2-D ADC map of head B. Compared with Fig.1 (b), it is less sensitive to write current.

for noise power saturation could be utilized as a necessary condition to maximize ADC. From the point of view of reliability, Fig. 1(b) also suggests the approach to reducing laser current while maintaining high ADC by increased write current.

Fig. 2 shows write current dependence of magnetic write width (MWW) under fixed laser current. Two heads with different designs, head A and head B, were tested. Head A was utilized in Fig. 1. MWW of head A increased monotonically with increase of write current. On the other hands, MWW of head B saturated at write current 40 mA. It means that write current of head B above 40 mA could not modulate TPI. Fig. 3 shows a 2-D ADC map of head B. While ADC highly depended on laser current, ADC modulation by write current was relatively small. It means that head B could not reduce laser current to keep high ADC. Fig. 4 shows write current dependence of T_w calculated from THMap [6]. T_w of head A decreased with increased write current. In contrast, head B showed saturation of T_w decrease around write current 40 mA. Since media temperature is maximized under near field transducer (NFT) and decreases toward cross track direction, decrease of T_w expands write width with fixed laser current. T_w decrease by write current increase in Fig. 4 represented MWW modulation by write current well.

IV. Summary

Laser current and write current sensitivities of noise power in THMap, and of ADC were discussed. To maximize ADC, noise saturation in THMap is required, however it is not sufficient condition, especially for laser current selection. More importantly, increasing write current can reduce T_w, and widen MWW, and consequently similar ADC can be achieved in lower laser current, which must gain reliability. The amount of such an effect depended on head design.

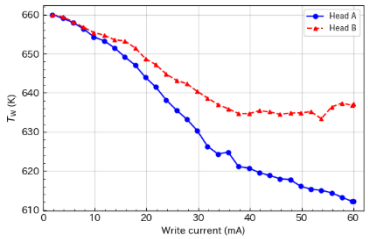

Fig. 4. Write current dependences of T_w calculated from THMap for two head designs. In T_w calculation, we assumed that T_c is 660 K.

References

[1] C. Rea, *et al*., "HAMR performance and integration challenges," *IEEE Trans. Magn*., vol. 50, no. 3, pp. 62-66, Mar. 2014.

[2] N. A. Natekar, E. Roddick and R. M. Brockie, "Interplay of the Thermal and Magnetic Fields in HAMR," *IEEE Trans. Magn*., vol. 58, no. 4, pp. 1-8, April 2022, Art no. 3101208.

[3] S. Grans, C. Rea, G. Ju, P. Czoschke, and S. Hernandez, "Heat Assisted Magnetic Recording Areal Density Dependence on Writer Current for Conventional and Shingled Magnetic Recording," *The 34th Magnetic Recording Conference (TMRC). IEEE*, 2023.

[4] A. Sakoguchi, J. Zhang, N. Ito and J. Lee, "Use of THMap for write performance characterization in HAMR," *IEEE Trans. Magn*., to be published.

[5] T. D. Trinh, S. Rajauria, R. Smith, E. Schreck, Q. Dai and F. E. Talke, "Temperature-Induced Near-Field Transducer Failure in Heat-Assisted Magnetic Recording," *IEEE Trans. Magn.,* vol. 56, no. 6, pp. 1-4, June 2020, Art no. 3300304.

[6] P. -O. Jubert, *et al*., "Spin-stand measurements to extract the switching distributions of heat-assisted magnetic-recording media," *IEEE Trans. Magn*., vol. 59, no. 3, pp.1-5, Mar. 2023.

[7] S. D. Granz, *et al*., "Definition of an Areal Density Metric for Magnetic Recording Systems," *IEEE Trans. Magn*., vol. 53, no. 2, pp. 1-4, Feb. 2017, Art no. 3100104.

[8] Y. Qin and J. -G. Zhu, "Impact of Magnetic Medium Grain Height in Heat-Assisted Magnetic Recording," *IEEE Magn. Lett.*, vol. 10, pp. 1-5, 2019, Art no. 6502305.

Improvement of Dual-Layer HAMR Recording Conditions Using SMR

Yasuaki Nakamura[1], Madoka Nishikawa[1], Simon John Greaves[2], Yasushi Kanai[3], and Yoshihiro Okamoto[1]

[1]Graduate School of Science and Engineering, Ehime University, Matsuyama 790-8577, Japan, {nakamura.yasuaki.mj, nishikawa.nadoka.vi, okamoto.yoshihiro.mj}@ehime-u.ac.jp
[2]RIEC, Tohoku University, Sendai, 980-8577, Japan, greaves.simon.john.a4@tohoku.ac.jp
[3]Deptment of Engineering, Niigata Institute of Technology, Kashiwazaki, 945-1106, Japan, kanai@iee.niit.ac.jp

Three-dimensional heat-assisted magnetic recording (3D-HAMR) with dual recording layer (DL-HAMR) aims to achieve high areal density using two conventional recording layers over one disk surface and simultaneous MR head reading. However, in conventional magnetic recording (CMR)-based DL-HAMR, the track width on the bottom layer becomes narrow due to the track width limit on the top recording layer, and the track on the top layer is also limited so as not to erase the information on the bottom layer. To address these issues, this study introduces shingled magnetic recording (SMR) into the DL-HAMR system. A simulation using a FePt granular medium with dual-layer structure was conducted. A two-pass write process with a Gaussian heat source was used, and the magnetization patterns were evaluated. SMR provided patterns close to the ideal track width for both layers. Furthermore, the medium signal-to-noise ratio (SNR) was measured, yielding 10.3 dB for CMR and 14.2 dB for SMR. The results show that the application of SMR improved the recording condition of DL-HAMR compared to the CMR method, and the medium SNR increased by approximately 4 dB.

***Index Terms*—Three-dimensional magnetic recording, Heat-assisted magnetic recording, Shingled magnetic recording, Magnetization pattern.**

I. Introduction

THREE-DIMENSIONAL (3D) magnetic recording is garnering considerable attention as a next-generation magnetic recording method to achieve high areal recording density by utilizing two recording layers on one surface and magneto-resistive (MR) head reading [1]. Heat-assisted magnetic recording with dual recording layer (DL-HAMR), which incorporates HAMR, has been proposed as a promising approach to realize 3D magnetic recording [2]. However, the leakage magnetic field from the bottom (second) recording layer, which is farther from the MR head, is weaker than that from the top (first) recording layer, resulting in a smaller amplitude of the reproduced waveform [3]. Furthermore, in DL-HAMR using conventional magnetic recording (CMR), which requires a guard band, the track widths of both recording layers must remain within the track pitch, making it difficult to maintain wide enough track widths on both layers. Therefore, we propose introducing shingled magnetic recording (SMR) [4] into the DL-HAMR system to mitigate the reduction in track width.

II. DL-HAMR Read/Write Channel Model

We simulate a granular medium with non-magnetic grain boundaries employing a discrete Voronoi model [5]. We assume FePt granular medium [2] for the recording layer of the DL-HAMR. The parameters of average grain size, standard deviation of grain size, and average non-magnetic grain boundary are set to 6 nm, 1 nm, and 1 nm, respectively. We assume that each grain has the first and second layers, and the dual recording layer is constructed on one surface of the disk by the grains. Here, the channel bit length and the track pitch are set to 12 and 26 nm, respectively. Thus, the areal recording density of each layer is 2 Tbits/inch^2, and the total areal recording density results in 4 Tbits/inch^2. The head-media structure for DL-HAMR was: Read/Write head / 5 nm Air / 4 nm first recording layer / 1nm Isolation layer / 8 nm second recording layer / Soft-under layer (SUL) [3].

The coercivities of both recording layers are assumed to be 40 kOe at 0 K, and Curie temperatures of the first and second recording layers are also assumed to be $T_{c1} = 520$ K and $T_{c2} = 620$ K, respectively. Moreover, the Curie temperatures of each recording layer fluctuate with a standard deviation of 10 K. The temperature dependence of the media coercivity was calculated using a Curie-Weiss model [6].

In the writing process, we apply the two-pass write method and use the write head field distribution by the split main poles [6]. The heat source is installed between the split main poles. The heat distribution of the medium assumes a two-dimensional Gaussian distribution [3], where the standard deviations in the down-track and cross-track directions are σ_{hx} and σ_{hy}, respectively. Furthermore, we also assume the maximum temperatures in the first and second recording layers to be T_{max1} and T_{max2}. The coercivity of the magnetic grains in the medium was reduced below the write head field strength by heating, and the grains were magnetized in the direction of the writing field according to a recording sequence. The first recording layer was recorded after the second recording layer.

In the reading process, the reproduced waveforms for each layer were obtained by convolving the magnetization pattern with the MR head sensitivity function [3] for each recording layer. Finally, the simultaneous reading waveform was obtained by linearly adding the reproduced waveforms from the first and second recording layers, assuming no MR non-linearity.

III. Magnetization Pattern

Figure 1 shows the CMR magnetization pattern recorded from left to right on the third track. (a) and (b) show the magnetization patterns for the first and second recording layers, respectively. The yellow lines represent the ideal bit boundaries,

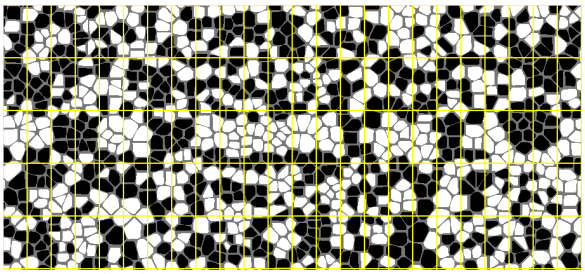

(a) First recording layer.

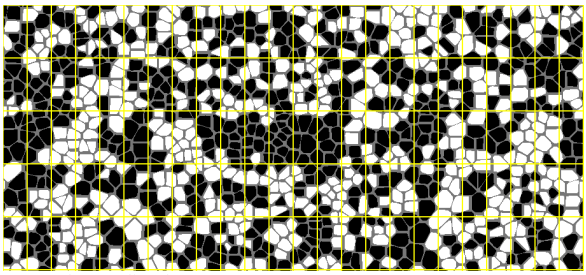

(b) Second recording layer.

Fig. 1. Magnetization patterns for CMR ($\sigma_{hx} = 6$ nm, $\sigma_{hy} = 12$ nm, $T_{max1} = 570$ K, $T_{max2} = 730$ K).

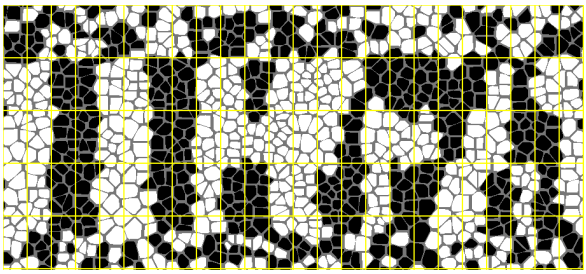

(a) First recording layer.

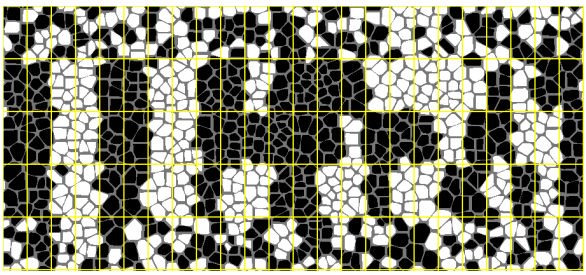

(b) Second recording layer.

Fig. 2. Magnetization patterns for SMR ($\sigma_{hx} = 6$ nm, $\sigma_{hy} = 22$ nm, $T_{max1} = 570$ K, $T_{max2} = 670$ K).

where the white and black polygons represent magnetic grains for the recorded data "0" and "1", respectively. The heat source properties are set to $\sigma_{hx} = 6$ nm, $\sigma_{hy} = 12$ nm, $T_{max1} = 570$ K, and $T_{max2} = 730$ K. In addition, opposite recording patterns are used for the first and second recording layers. As can be seen from the figures, the track width of the second recording layer is approximately equal to the ideal track width. However, on the first recording layer, information to be written on the first layer is not recorded near the track boundaries, and magnetization from the second recording layer remains in those regions.

Figure 2 shows the SMR magnetization pattern across three tracks, representing an SMR data set. The recording direction for all tracks is from left to right, as in the CMR case. In SMR, the second, third, and fourth tracks from the top are recorded sequentially in that order. The heat source properties are the same as in Fig. 1, except $\sigma_{hy} = 22$ nm and $T_{max2} = 670$ K. Also, the recorded data in the third track is the same as that in Fig. 1. As can be seen from the figures, by applying SMR, magnetization patterns nearly identical to those with the ideal track width are obtained for both recording layers. Therefore, the medium signal-to-noise ratio (SNR_M) was measured by comparing the dual-layer simultaneous reproduced waveform from an ideal recording medium divided into rectangles with that from a granular medium. The results were SNR_M= 10.3 dB for CMR and SNR_M = 14.2 dB for SMR, indicating that the adoption of SMR resulted in an SNR improvement of approximately 4 dB.

IV. Conclusion

We have proposed introduction SMR into the DL-HAMR system to mitigate the reduction in track width. The results show that the application of SMR improved the recording condition of DL-HAMR compared to the CMR method, and the medium SNR was increased by approximately 4 dB.

Acknowledgements

This work was supported by JST, CREST Grant Number JPMJCR22C3, Japan and the Advanced Storage Research Consortium (ASRC), Japan.

References

[1] S. J. Greaves, Y. Kanai, and H. Muraoka, "Multiple layer microwave-assisted magnetic recording," *IEEE Trans. Magn.*, vol.53, no.2, 3000510, Feb. 2017.

[2] P. Tozman, S. Isogami, I. Suzuki, A. Bolyachkin, H. Sepehri-Amin, S. J. Greaves, H. Suto, Y. Sasaki, T. Y. Chang, Y. Kubota, P. Steiner, P. W. Huang, K. Hono, and Y. K. Takahashi, "Dual-layer FePt-C granular media for multi-level heat-assisted magnetic recording," *Acta Materialia*, vol.271, 119869, June 2024.

[3] Y. Nakamura, M. Nishikawa, S. J. Greaves, Y. Kanai, and Y. Okamoto, "A study on HAMR read/write channel models for double layer magnetic recording," *Jpn. J. Appl. Phys.*, vol.63, no.8, 08SP11, Aug. 2024.

[4] S. J. Greaves, Y. Kanai, and H. Muraoka, "Shingled Recording for 2–3 Tbit/in^2," *IEEE Trans. Magn.*, vol.45, no.10, pp.3823-3829, Oct. 2009.

[5] M. Yamashita, Y. Okamoto, Y. Nakamura, H. Osawa, S. J. Greaves. and H. Muraoka, "Performance evaluation of neuro-ITI canceller using a modified writing process for TDMR," *IEICE Trans. Electron.*, vol.E96-C, no.12, pp.1504-1507, Dec. 2013.

[6] S. J. Greaves, R. Itagaki, and Y. Kanai, "A model for predicting transition curvature in heat-assisted magnetic recording," *IEEE Trans. Magn.*, vol.55, no.7, 3001506, July 2019.

Crystal orientation improvement by carbon addition for FePt-oxide granular films for heat assisted magnetic recording media

Kim Kong Tham[1], Ryosuke Kushibiki[1], Daiki Miyazaki[1], Shin Saito[2]

[1]TANAKA PRECIOUS METAL TECHNOLOGIES Co., Ltd, Tsukuba 300-4247, Japan, tham@ml.tanaka.co.jp
[2] Department of Electronic Engineering, Graduate School of Engineering, Tohoku University, Sendai 980-8579, Japan

Investigation of magnetic properties and nanostructure of FePt granular films with oxide grain boundary material (GBM) substituted by carbon is reported. Similar tendency to FePt-oxide granular films, saturation magnetization in FePt-oxide-carbon granular films also varies almost linearly against volume averaged melting point (T_m^{ave}) of the GBM. The values of perpendicular magnetic anisotropy and degree of order of $L1_0$-FePt phase for all FePt-oxide-carbon granular films varies to be closer to those of FePt-carbon granular films with values larger than 9×10^6 erg/cm^3 and 0.75, respectively, when oxide is partially substituted with carbon. Furthermore, the amount of magnetic grain with *c*-axis parallel to the film plane in FePt-oxide-carbon granular films is significantly reduced than that of FePt-oxide granular films.

***Index Terms*— FePt-oxide-carbon, granular film, melting point, c-axis parallel to the film plane, grain size, heat assisted magnetic recording.**

I. Introduction

HEAT ASSISTED MAGNETIC RECORDING (HAMR) is expected to replace perpendicular magnetic recording (PMR) for the next generation magnetic recording technology. For the HAMR media, $L1_0$ type FePt thin film is an attractive material due to its high magnetocrystalline anisotropy of 5×10^7 erg/cm^3 at room temperature. In-order-to realize FePt thin film as the HAMR medium, it is necessary to solve some issues, such as the formation of a granular structure with fine columnar magnetic grains, high c-axis orientation, and high degree of order. Regarding the achievement of these requirements, many studies of adding grain boundary materials (GBMs), such as C [1-2], TiO_2 [3], Ta_2O_5 [4], GeO_2 [5], Al_2O_3 [6], Nb_2O_5 [7], Cr_2O_3 [8], SiO_2 [9], and B_2O_3 [10] into the FePt thin film to isolate the magnetic grains and reduce intergranular exchange coupling have been conducted. According to our previous report, saturation magnetization (M_s) of the granular film depends on the melting point of the GBMs that M_s of the granular film shows the degree of phase separation between metal magnetic grains and amorphous non-magnetic GBM [10]. The granular films with C GBM show the characteristic of relatively low M_s, which suggests insufficient phase separation and high degree of grain-to-grain separation. When granular films with C and oxide GBMs were compared, it was found that the granular films with some oxides GBM show higher degree of phase separation than that of with C GBM. However, there is a drawback in nanostructure of the granular films with oxide GBM, which has larger amount of in-plane component compared to the films with C GBM. Therefore, to promote the grains isolation while maintaining high degree of phase separation and less in-plane component of FePt granular film with oxide GBM, we have carried out an experiment of partially substituting oxide with C GBM in granular films and evaluated the magnetic properties and nanostructure.

II. Experiments

All samples were prepared using RF/DC magnetron sputtering (Canon Anelva C3010-P7-UHV; 7-chamber configuration with single-side film fabrication, each process can be carried out in an independent chamber separated with gate valve). The in-line sputtering equipment is almost the same model as that for the mass production of PMR media. The stacking structure of the samples is amorphous glass substrate (0.635 mm thick)/ $Co_{60}W_{40}$ (Ar gas pressure: 0.6 Pa, film thickness: 80 nm, substrate temperature: RT)/ MgO (4 Pa, 5 nm, RT)/ Magnetic layer (8 Pa, 5 nm, 550 °C)/C (0.6 Pa, 7 nm, RT). The magnetic layer was deposited at sputtering power of 0.5 W/cm^2. $Fe_{50}Pt_{50}$–15vol% oxide–15vol% C sintered targets were used for the magnetic layer. For comparison, the samples prepared with $Fe_{50}Pt_{50}$–30vol% oxide sintered targets were also fabricated. *M-H* loops were measured by using a vibrating sample magnetometer equipped with a SQUID detector (Quantum Design, MPMS3) at the maximum applied field of 70 kOe. Torque curves were measured by using a physical property measurement system with a torque magnetometer option (Quantum Design, PPMS) with the maximum applied field of 90 kOe [11]. Crystal structure was examined using out-of-plane and in-plane X-ray diffraction (XRD) measurements with Cu Kα radiation at wavelength of 1.542 Å (Rigaku, SmartLab; 9 kW/ parallel beam configuration/ 2D detector). Nanostructure of the films was observed by transmission electron microscopy (TEM) with an acceleration voltage of 300 kV.

III. Results And Discussion

Fig. 1 shows dependence of (a) M_s and (b) $K_{u\perp}$ of FePt-oxide-C granular films on the volume averaged melting point (T_m^{ave}). M_s and $K_{u\perp}$ are derived from the gradient plot of total magnetization and perpendicular magnetic anisotropy of the granular film against the film thickness from 2 to 10 nm, respectively. Dotted lines in the figures represent the values of

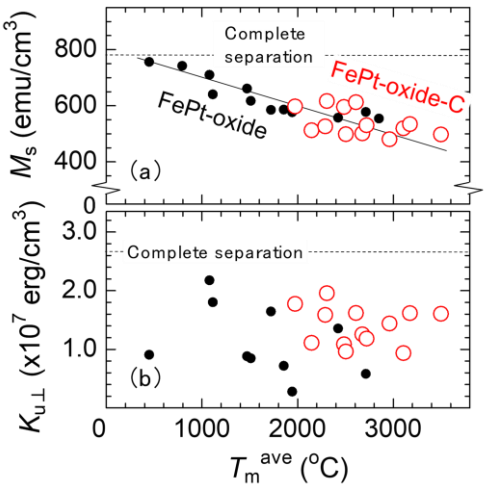

Fig. 1 Dependence of (a) M_s and (b) $K_{u\perp}$ of FePt-oxide-C granular films on the volume averaged melting point (T_m^{ave}).

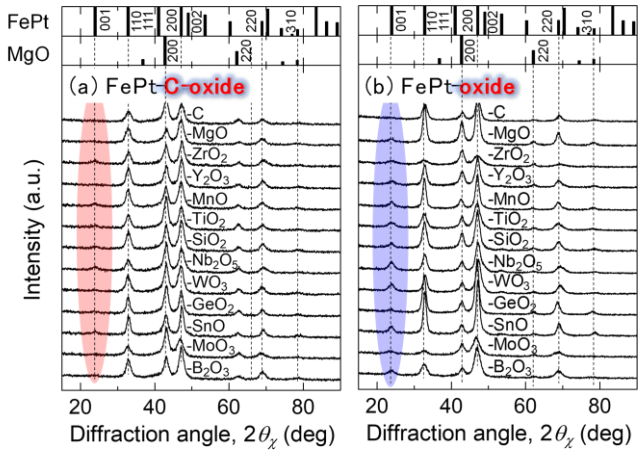

Fig. 2 In-plane XRD profiles for (a) FePt-oxide-C and (b) FePt-oxide granular films.

M_s and $K_{u\perp}$ of complete separation calculated from magnetic parameters of FePt films described in the previous results [12], assuming 70 vol% FePt and 30 vol% GBMs are completely separated, where there is no element decomposes from the GBMs and dissolves into the FePt magnetic grains. Here, Tmave is the volume averaged melting point of oxide and carbon GBMs. M_s and $K_{u\perp}$ of granular films of both oxide-C and oxide GBMs are still lower compared to those of granular films with complete separation. M_s of FePt-oxide-C granular films shows similar tendency with that of FePt-oxide granular films which varies almost linearly against T_m^{ave} [10]. When T_m^{ave} is varied from around 2000 to 3500 °C, M_s of FePt-oxide-C granular films changes from around 600 to 530 emu/cm^3. On the other hand, there is no strong correlation observed between $K_{u\perp}$ and T_m^{ave}. The value of $K_{u\perp}$ for all FePt-oxide granular films is enhanced to be larger than 9×10^6 erg/cm^3 when oxide is partially substituted by C.

Fig. 2 shows in-plane XRD profiles for (a) FePt-oxide-C and (b) FePt-oxide granular films. For both granular films, at Bragg angles of around 33°, 47°, and 69°, the (110), (200), and (220) diffractions of the L1$_0$-FePt phase are observed, respectively, which reveals that the FePt magnetic grains have *c*-plane sheet texture. Focusing at the Bragg angle of around 24°, the integral intensity of (001) diffraction of the L1$_0$-FePt phase in the FePt-oxide-C granular films is smaller compared to that of FePt-oxide granular films, which indicates that FePt-oxide-C granular films has less magnetic grains with *c*-axis parallel to the film plane than that of FePt-oxide granular films.

IV. Conclusion

The combination of oxide with C is effective to promote the grain isolation, while maintaining high degree of phase separation and small amount of in-plane component.

References

[1] J. S. Chen, B. C. Lim, J. F. Hu, B. Liu, G. M. Chow, and G. Ju, *Appl. Phys. Lett*., **91**, 132506 (2007).

[2] A. Perumal, Y. K. Takahashi, and K. Hono, *J. Appl. Phys*., **105**, 07B732 (2009).

[3] Y. F. Ding, J. S. Chen, B. C. Lim, J. F. Hu, B. Liu, and G. Ju, *Appl. Phys. Lett.*, **93**, 032506 (2008)..

[4] B. C. Lim, J. S. Chen, J. F. Hu, P. W. Lwin, Y. F. Ding, K. M. Cher, and B. Liu, *J. Appl. Phys.*, **105**, 07A730 (2009).

[5] T. Ono, T. Moriya, M. Hatayama, K. Tsumura, N. Kikuchi, S. Okamoto, O. Kitakami, and T. Shimatsu, *Appl. Phys. Lett.*, **110**, 022402 (2017).

[6] J. Bai, Z. Yang, F. Wei, M. Matsumoto, and A. Morisako, *J. Magn. Magn. Mater*., **257**, 132 (2003).

[7] T. Shiroyama, T. Abe, Y. Takahashi, and K. Hono, *IEEE Trans. Magn.*, **49**, 3616 (2013).

[8] T. Shiroyama, B. S. D. Ch. S. Varaprasad, Y. K. Takahashi, and K. Hono, *IEEE Trans. Magn.*, **50**, 3202404 (2014).

[9] E. Yang and D. E. Laughlin, *J. Appl. Phys.*, **104**, 023904 (2008).

[10] T. Saito, K. K. Tham, R. Kushibiki, T. Ogawa, and S. Saito, *Jpn. J. Appl. Phys.*, **59**, 045501 (2020).

[11] T. Saito, K. K. Tham, R. Kushibiki, T. Ogawa, and S. Saito, *IEEE Trans. Magn.*, **57**, 3200505 (2021).

[12] R. Kushibiki, K. K. Tham, S. Hinata, and S. Saito, *AIP Adv.*, **8**, 056512 (2017).

Heat Assisted Magnetic Recording (HAMR) Smear Characterization by Using Head-Disk Interface (HDI) Sensor

Wangzhen Zhao[1], Yukio Kato[1], Yuichi Aoki[1] and Qing Dai[2]

[1] Advanced Materials & Technologies, Western Digital Corporation, Fujisawa 252-0888, Japan
[2] Advanced Materials & Technologies, Western Digital Corporation, San Jose, CA 95119 USA

HAMR is considered to have the potential for achieving the areal densities beyond 4 Tb/in², although smear issues require greater attention. This work presents an experimental study conducted on a spinstand to characterize the accumulated smear at the head-disk interface (HDI) using a thermal proximity sensor integrated into the head. The smear on the head can be detected by changes in touchdown power (TDP) with the HDI sensor, while the acoustic emission (AE) sensor shows almost no response to the smear. It is confirmed that the accumulated smear height detected by the HDI sensor increases proportionally with increasing writing clearance. This indicates that more smear tends to be generated in HDI with greater spacing. Additionally, the hardness of the smear can also be characterized by observing the changes in smear height during multiple touchdown (TD) measurements.

***Index Terms*—Heat-assisted Magnetic Recording (HAMR), Head-disk Interface (HDI), Thermal Proximity Sensor, Smear**

I. Introduction

Heat-assisted magnetic recording (HAMR) is a technology with potential for realizing the areal density beyond 4 Tb/in^2 [1]. The HAMR heating process utilizes a laser to momentarily heat the recording grains, thereby lowering their magnetic coercivity and making them easier to write. This process can enable HAMR media to utilize smaller, more thermally stable recording grains [2]. However, the heating process will cause the lubricant to desorb and possibly decompose from the disk, condensing on the head [3]. The high temperature may also cause other contaminants to accumulate on heads. These accumulated matters, also known as smear, causes HDI issues and challenges the reliability of HAMR [4], [5]. Some types of smears can disrupt laser delivery efficiency, resulting in a higher NFT temperature, which may ultimately lead to poorer NFT lifetime [6], [7]. Some smear may cause flyability issues, potentially leading to a head-disk crash [8]. Therefore, the detection and characterization of smear are crucial for HAMR.

In this study, an experimental investigation was conducted on a spinstand. Touchdown (TD) experiments monitored by an HDI sensor, supported by an Acoustic Emission (AE) sensor, were introduced. The HDI sensor is a thermal proximity sensor, and its resistance change during TD can be used to detect the smear. We compared the response of the HDI thermal sensor in TD measurements before and after smear accumulation on the head to understand its effect. Finally, we conducted TD experiments on various media designs, and two of the results are presented, along with discussions on the understanding of smear characteristics.

II. Experiment Setup

The schematic diagram of the HAMR HDI setup used in this component test work is shown in Fig. 1. The disk rotates at an angular velocity of 7200 rpm, with the head embedded in the trailing edge of the slider. The components, which include a heater, laser diode, waveguide, near-field transducer (NFT), writer main pole, and HDI thermal sensor, are illustrated in the diagram. The TD measurement is conducted by increasing the power applied to the heater, which ultimately leads to head-disk contact. The power during this contact is referred to as TD power (TDP), while the power required to withdraw the head from the TD point is known as backoff (BO). The HDI thermal sensor, located near the NFT and writer, can be utilized to monitor the thermal profile during TD. Additionally, an AE sensor was used as an indicator of head-disk contact, and the TD operation was stopped at that power. The AE sensor was positioned near the end of the slider suspension (not depicted in the diagram).

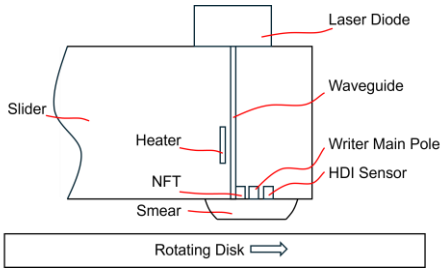

Fig. 1. The schematic diagram of the HAMR HDI (not to scale) with the smear prepared.

One should note that smear was prepared using continuous laser-on writing, which is called aging, as the laser is guided by an optical waveguide from the laser diode to the NFT. The same measured magnetic write width (MWW) of 51 nm with write clearance of 3 nm was used in the following experiments as the unified test condition. Although in some cases, laser power (LP) was increased to accelerate the aging, while laser-induced protrusion was compensated by the heater as well as the pre-optimized standard LP.

III. Experimental Results and Discussion

The TD results before and after aging on Media A were monitored by the HDI thermal sensor and plotted in Fig. 2 (a), with the aging condition of LP at 150% for 10 minutes. During aging, the slider was swept over the disk at a target radius of 27.5 mm, resulting in a velocity of ~20 m/s. The TD profile

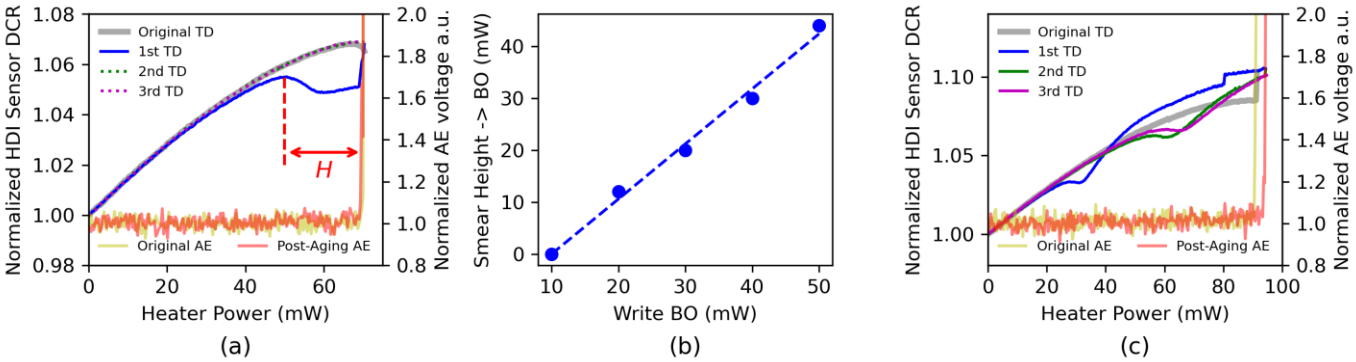

Fig. 2 (a) The normalized resistance of the HDI thermal sensor and the signal from the AE sensor during TD on Media A. (b) The bending BO, understood to correspond to smear height, as a function of the write BO. (c) The normalized resistance of the HDI sensor and the signal from the AE sensor during TD on Media B.

before aging was plotted as the gray curve. By increasing the heater power, the resistance of the HDI thermal sensor increased due to the rise in temperature at the head. The slope of the resistance curve decreased as it approached the disk, and even a negative slope was observed, which is attributed to the cooling effect with the heat transfer towards the media. In general, a further increase in heater power will lead to an abrupt increase in resistance of the HDI sensor, like the gray curve shown in Fig. 2 (c), which is caused by frictional heat with contact. However, since we used the AE signal (yellow curve) as the indicator, some of the friction contact responses from the HDI thermal sensor were not observed. At the point the AE signal reached a specific level, the heater power was referred to as the AE TDP.

When we perform aging first, however, the 1st TD exhibited different behavior: a bending of the resistance curve, understood as a significant cooling effect, was observed at lower heater power than without pre-aging. When the bending starts, the power applied to the heater is denoted as "an HDI thermal sensor TDP". This cooling effect indicates that the smear bridged the head and disk from that moment, leading to additional heat transfer from the head to the disk. By comparing the TDP of the 1st HDI thermal sensor and the post-aging AE, a difference of approximately 20 mW was observed. Since the thermal expansion efficiency of the heater will not be discussed, we regard this differential power as the smear height in the following discussion. Moreover, the bending of the curves was not observed after the 2nd and the 3rd TD, indicating the smear was removed after the 1st TD. In addition, the AE TDP of post-aging TD was nearly identical to the original, suggesting that the AE sensor is insensitive to smear during TD measurement.

We also conducted the TD experiments by adjusting the BO setting during the aging. The increase in BO during aging was anticipated to allow more smear to accumulate and fill the gap in the head disk interface. By employing the previously introduced method, the increase in smear height was confirmed when the write clearance was increased, as shown in Fig. 2(b). Consequently, the HDI thermal sensor is effectively tracking varying amounts of smear.

To gain a deeper understanding of HDI thermal sensor behavior in smear characterization, we conducted additional experiments on various media designs. Across the experiment results, a different behavior was observed in Media B. The TD behavior on Media B is depicted in Fig. 2(c). The early cooling effect of the 1st TD HDI thermal sensor resistance curve indicated the smear accumulated, as expected. However, the HDI thermal sensor curve did not recover during the 2nd and 3rd TDs, indicating that the smear was not fully mitigated by the TDs. The conclusion based on the response of the HDI sensor is that a harder smear is accumulated in the HDI during aging on Media B. Moreover, the post-aging AE TDP also changed, indicating that the solid-solid contact property of the head and disk was changed during aging, which may lead to a head-disk interaction in HDD operation.

IV. Summary

We studied the effect of HAMR smear on the HDI thermal sensor response during the TD experiment. The accumulated smear on the head will lead to an early cooling effect, which can be used to estimate the smear height. In addition, we confirmed the smear height dependence on BO in aging using the HDI sensor. A larger BO will lead to more smear generation. Finally, the HDI sensor-monitored TD process can characterize the smear hardness, which is expected to be utilized to estimate the possibility of head-disk interaction.

References

[1] D. Weller *et al.*, "A HAMR media technology roadmap to an areal density of 4 Tb/in2," *IEEE Trans Magn*, vol. 50, no. 1, Jan. 2014.
[2] M. H. Kryder *et al.*, "Heat assisted magnetic recording," *Proceedings of the IEEE*, vol. 96, no. 11, pp. 1810–1835, 2008.
[3] Q. Cheng and D. B. Bogy, "Experimental study of smear formation and removal in heat-assisted magnetic recording," *Tribol Int*, vol. 165, Jan. 2022.
[4] J. D. Kiely, P. M. Jones, and J. Hoehn, "Materials challenges for the heat-assisted magnetic recording head-disk interface," *MRS Bull*, vol. 43, no. 2, pp. 119–124, Feb. 2018.
[5] S. Xiong, N. Wang, R. Smith, D. Li, E. Schreck, and Q. Dai, "Material Transfer Inside Head Disk Interface for Heat Assisted Magnetic Recording," *Tribol Lett*, vol. 65, no. 2, Jun. 2017.
[6] J. D. Kiely *et al.*, "Write-Induced Head Contamination in Heat-Assisted Magnetic Recording," *IEEE Trans Magn*, vol. 53, no. 2, Feb. 2017.
[7] T. D. Trinh, S. Rajauria, R. Smith, E. Schreck, Q. Dai, and F. E. Talke, "Temperature-Induced Near-Field Transducer Failure in Heat-Assisted Magnetic Recording," *IEEE Trans Magn*, vol. 56, no. 6, Jun. 2020.
[8] Raman V, Gillis D, and Wolter R., "Flyability Failures Due to Organic Siloxanes at the Head/Disk Interface," J Tribol, 122 (2), pp. 444–449, Apr. 2000.

In-plane component suppression and K_u enhancement of FePt-oxide granular films by using (Pt, Ag)-C/ FePtCu-C stacked granular buffer layers

Daiki Miyazaki[1], Kim Kong Tham[1], Shin Saito[2]

[1]TANAKA PRECIOUS METAL TECHNOLOGIES Co., Ltd, Tsukuba 300-4247, Japan, tham@ml.tanaka.co.jp
[2] Department of Electronic Engineering, Graduate School of Engineering, Tohoku University, Sendai 980-8579, Japan

Investigation of nanostructure and magnetic properties of the granular films deposited on stacked buffer layers (BLs) of Pt-C/ FePtCu-C and Ag-C/ FePtCu-C are reported. By optimizing the thickness of Pt-C/ FePtCu-C and Ag-C/ FePtCu-C BLs, maximum K_u of 2.7×10^7 and 2.2×10^7 erg/cm^3, respectively, can be obtained. In addition, the amount of magnetic grain with c-axes parallel to the film plane of those granular films is suppressed. Furthermore, FePt grain size of the granular film deposited on Ag-C/ FePtCu-C BLs is smaller than that of deposited on Pt-C/ FePtCu-C BLs.

***Index Terms*— granular films, stacked buffer layers, melting, c-axis parallel to the film plane, FePt grain size**

I. Introduction

To ensure that hard disk drive (HDD) remains competitive in the data storage, recently a new design of magnetic recording technology, heat assisted magnetic recording (HAMR) has been launched into the market to replace currently commercialized perpendicular magnetic recording. The L10 type FePt phase which has high uniaxial magneto-crystalline anisotropy energy, K_u of 5.0×10^7 erg/cm^3 at room temperature is a promising material for the HAMR medium. Regarding nanostructure of the medium, a granular structure with fine columnar and isolated magnetic grains, small angular distribution of c-axis, and high degree of order are desirable, however, these goals are still unaccomplished. Based on our previous study in K_u of FePt granular film, there is a disorder portion at the initial growth region which deteriorate K_u [1-2]. Many studies on adding various grain boundary materials, such as carbon [3-4], SiO_2 [5], TiO_2 [6], and B_2O_3 [7] into FePt thin films are still unable to obtain a satisfactory result so that other approach, such as the utilization of a buffer layer (BL) in between the FePt-oxide granular film and the MgO underlayer is conducted [8]. According to our previous results, C and FePtCu-C BL [9] show large magnetic grains and high K_u. On the other hand, Pt-C BL [10] shows small magnetic grains and low K_u. Therefore, to satisfy both requirements we have investigated stacked BL. In this paper, we report the evaluation results of the nanostructure and magnetic properties of the granular films with stacked BLs, which consist of FePtCu-C deposited on Pt-C BL and FePtCu-C deposited on Ag-C BL.

II. Experiments

All samples were prepared using RF/DC magnetron sputtering (Canon Anelva C3010-P7-UHV; 7-chamber configuration with single-side film fabrication, each process can be carried out in an independent chamber separated with gate valve). The in-line sputtering equipment is almost the same model as that for the mass production of PMR media. The stacking structure of the samples is amorphous glass substrate (0.635 mm thick)/ $Co_{60}W_{40}$ (Ar gas pressure: 0.6 Pa, film thickness: 80 nm, substrate temperature: RT)/ MgO (4 Pa, 5 nm, RT)/ Pt-50vol%C or Ag-50vol%C BL (0.6 Pa, 0.2 or 0.6 nm, RT)/ $Fe_{35}Pt_{35}Cu_{30}$-30vol%C BL (8 Pa, 0 – 2.0 nm, RT)/ Magnetic layer (8 Pa, 5 nm, 550 °C)/C (0.6 Pa, 7 nm, RT). Pt-50vol%C or Ag-50vol%C BL was used as the seed layer, and $Fe_{35}Pt_{35}Cu_{30}$-30vol%C BL was used as the ordring layer. $Fe_{50}Pt_{50}$–30vol% B_2O_3 sintered targets were used for the magnetic layer. *M-H* loops were measured by using a vibrating sample magnetometer equipped with a SQUID detector (Quantum Design, MPMS3) at the maximum applied field of 70 kOe. Torque curves were measured by using a physical property measurement system with a torque magnetometer option (Quantum Design, PPMS) with the maximum applied field of 90 kOe [11]. Crystal structure was examined using out-of-plane and in-plane X-ray diffraction (XRD) measurements with Cu Kα radiation at wavelength of 1.542 Å (Rigaku, SmartLab; 9 kW/ parallel beam configuration/ 2D detector). Nanostructure of the films was observed by transmission electron microscopy (TEM) with an acceleration voltage of 300 kV.

III. Results And Discussion

Fig. 1 shows dependence of M_s and K_u of Pt-C or Ag-C/FePtCu-C/ FePt-B_2O_3 granular film in stacked BL on FePtCu-C BL thickness. When FePtCu-C thickness is varied from 0 to 0.6 nm, M_s increases from 690 to 810 emu/cm^3. For thickness more than 0.6 nm of M_s shows no obvious change. When FePtCu-C deposited on Pt-C BL, maximum K_u of 2.7×10^7 erg/cm^3 is obtain at FePtCu-C and Pt-C thickness of 1.2 and 0.2 nm, respectively. When FePtCu-C deposited on Ag-C BL, maximum K_u of 2.2×10^7 erg/cm^3 is obtain at FePtCu-C and Ag-C thickness of 0.4 and 0.6 nm, respectively.

Fig. 2 shows in-plane XRD profiles of Pt-C or Ag-C/FePtCu-C/ FePt-B_2O_3 granular films. For both granular films, at Bragg angles of around 33°, 47°, and 69°, the (110), (200), and (220) diffractions of the $L1_0$-FePt phase are observed, respectively, which reveals that the FePt magnetic grains have *c*-plane sheet

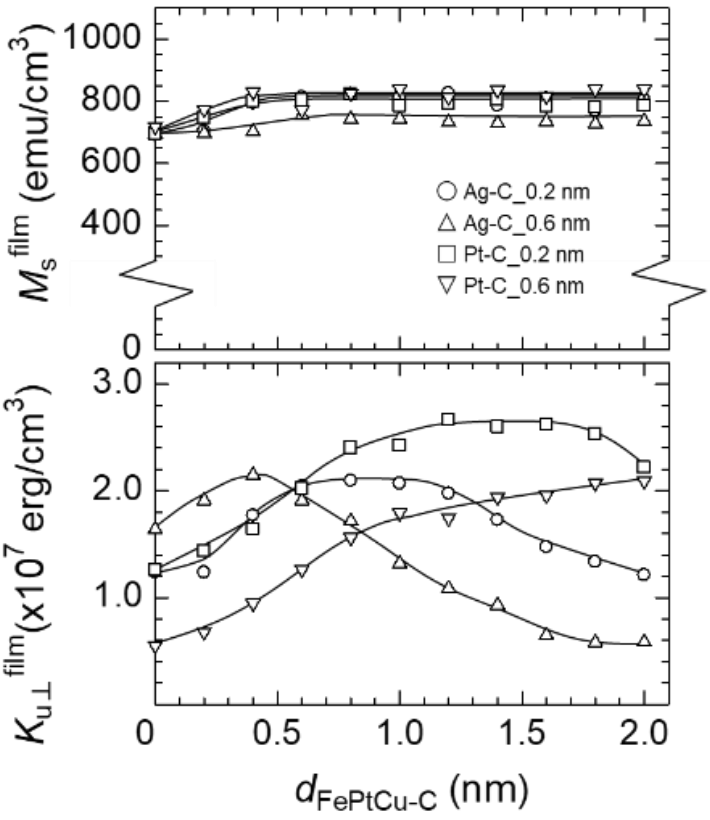

Fig. 1 Dependence of M_s and K_u of Pt-C or Ag-C/FePtCu-C/ FePt-B_2O_3 granular films.

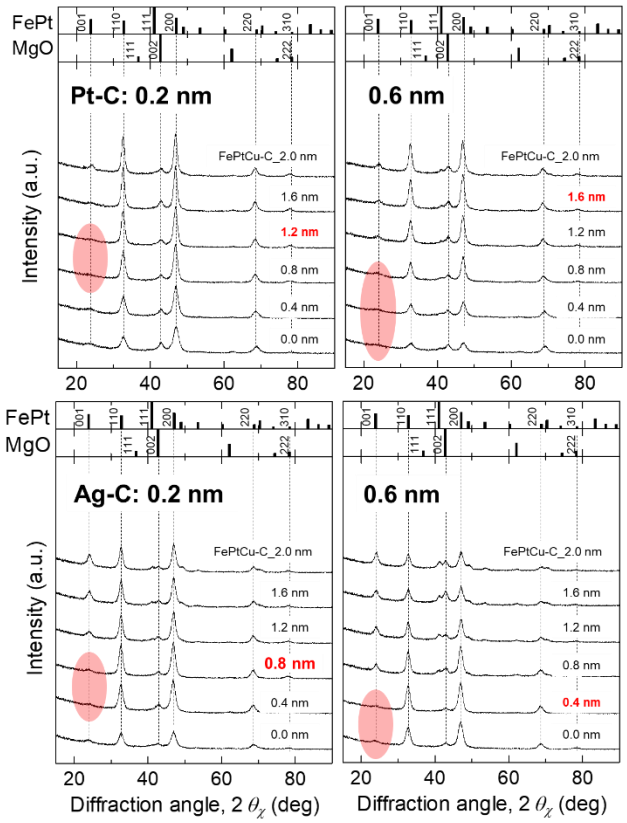

Fig. 2 In-plane XRD profiles for Pt-C or Ag-C/FePtCu-C/ FePt-B_2O_3 granular films.

texture. Focusing at the Bragg angle of around 24°, the integral intensity of (001) diffraction of FePt-B_2O_3 using FePtCu-C/Pt-C or Ag-C BL stacked buffer layer is small.

IV. Conclusion

Stacking FePtCu-C layer as the barrier layer on (Pt, Ag)-C buffer layer to prevent diffusion of BL elements results in low in-plane component, high Ku.

References

[1] T. Saito, K. K. Tham, R. Kushibiki, T. Ogawa, and S. Saito, AIP Advances, **11**, 015310 (2021).
[2] D. Isurugi, Saito, T., Tham, K.K., Ogawa, T., Tanaka, Y., Greaves, S.J., and Saito, S., *IEEE Trans. Magn*., **59**, 3201304 (2023).
[3] J. S. Chen, B. C. Lim, J. F. Hu, B. Liu, G. M. Chow, and G. Ju, Appl. Phys. Lett., **91**, 132506 (2007).
[4] A. Perumal, Y. K. Takahashi, and K. Hono, J. Appl. Phys., **105**, 07B732 (2009).
[5] E. Yang and D. E. Laughlin, J. Appl. Phys., **104**, 023904 (2008).
[6] Y. F. Ding, J. S. Chen, B. C. Lim, J. F. Hu, B. Liu, and G. Ju, Appl. Phys. Lett., **93**, 032506 (2008)..
[7] T. Saito, K. K. Tham, R. Kushibiki, T. Ogawa, and S. Saito, Jpn. J. Appl. Phys., **59**, 045501 (2020).
[8] K. K. Tham, R. Kushibiki, T. Ogawa, and S. Saito, AIP Advances, **14**, 025102 (2024).
[9] K. K. Tham, D. Miyazaki, and S. Saito, IEEE Trans. Magn., 3553632 (2025).
[10] K. K. Tham, D. Miyazaki and S. Saito, J. Sci. Adv. Mater. Devices, **10**, 100808 (2025).

Experimental study on ternary recording possibility in Heat Assisted Magnetic Recording

Takeshi Nakagawa

Western Digital Technologies GK, Fujisawa, 252-0888, Japan, takeshi.nakagawa@wdc.com

Ternary recording possibility in Heat Assisted Magnetic Recording (HAMR) [1] is studied in this prsentation. By heating the medium without applying a magnetic field in HAMR, an AC erase-like magnetization state is formed on the medium. By regarding this erase state as a new signal level of "0", ternary recording is expected to be realized in HAMR. By using prototype HAMR Hard Disk Drive (HDD), waveform observation and overwrite capability evaluation are performed as an initial feasibility study.

***Index Terms* — HAMR, magnetic recording, ternary recording**

I. Introduction

In conventional magnetic recording, direction of the magnetization on the recording medium has been used for storing information. Upward magnetization means "+1" and downward one means "-1", for example in perpendicular magnetic recording. Writing process switches these two states by applying a magnetic field corresponding to "+1" / "-1" from write head.

In HAMR, higher coercivity material is used in recording layer in the medium. Therefore, not only applying a magnetic field but heating the medium is necessary to lower effective coercivity in writing process. On the other hand, by heating the medium without applying a magnetic field, an AC erase-like magnetization state will be formed on the medium. This AC erase-like state can be regarded as a new signal level of "0" in addition to conventional signal level "+1" and "-1". This means that "ternary recording" is expected to be realized in HAMR.

Some experiments using prototype HAMR HDD were performed as an initial feasility study.

II. Experiment setup/flow

- Prototype HAMR HDD, 1head, 1location
- Datarate: 2087Mbps
- Measurement flow:
  1. To write specific pattern (*) onto specific location as an old data with normal HAMR condition.
  2. To read at the location and to get waveform of condition #1.
  3. To over-write the same location with special condition, which is heating the medium without applying a magnetic field (**).
  4. To read at the location and to get waveform of condition #3.
  5. Waveform analysis (#2 and #4)

*: 1T - 16T tone pattern and 127-bit Pseudo Random Bit Sequence (PRBS) pattern are used.
**: set write current to minimum(2mA) of the preamp spec.

III. Results and Considerations

A. Waveform observation:

Figure 1 shows waveform from "16T pattern writing" and "Heating only". As shown in this figure, "+1" and "-1" level can be seen in "16T pattern writing" portion in bottom lefthand side. In bottom righthand side of the figure, it is observed that "Heating only" forms signal level "0".

We'd like to evaluate overwrite capability of "Heating" as next step.

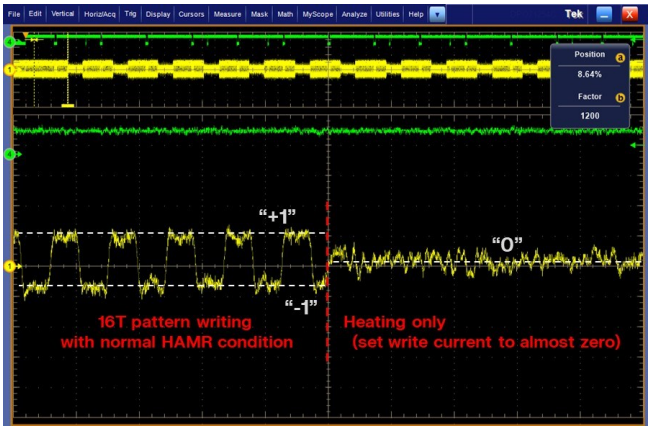

Fig. 1. Waveform (screen capture of digital oscilloscope)
Bottom lefthand side: 16T pattern writing with normal HAMR condition. Bottom righthand side: Heating only.

B. Overwrite capability:

As described in section II, we took waveforms from two situations. One is just after writing specific pattern (#1 and #2). The other is just after heating the same location (#3 and #4). By analyzing and comparing these two waveforms, we can know how much the heating can erase original pattern (~old data), which is overwrite capability of the heating.

i. Periodic tone pattern case:

Figure 2 is the chart for explanation on overwrite capability evaluation. In this case, periodic tone pattern is used as an old data. Top and middle of the figure is waveform of 16T tone pattern and after heating respectively. Bottom is frequency domain plot of each waveform.

The Difference between two plots (orange and blue) around "Normalized frequency" = 1 in horizontal axis means the overwrite capability of this example. Taking similar data for not only 16T pattern case, but 12T, 8T, 6T, 4T, 3T, 2T and 1T pattern cases, then plot these intensity data on the graph with the horizontal axis as tone pattern length is Figure 3.

As seen in Figure 3, overwrite capability is about 60~100dB in range of 1T to 16T. This means that by heating, the intensity of the old data has decreased to $1/10^6 \sim 1/10^{10}$ in signal power.

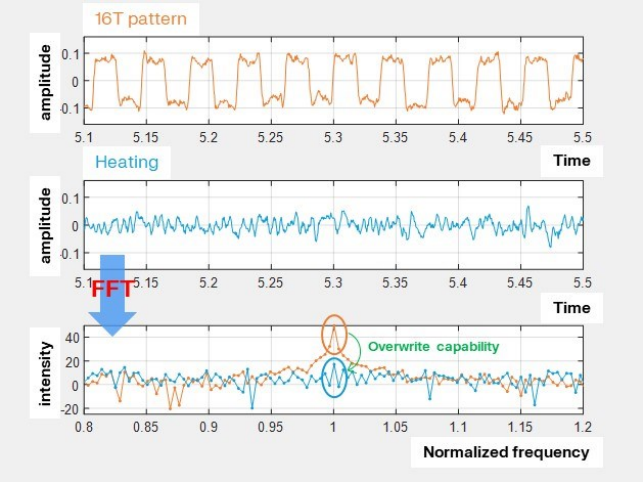

Fig. 2. Explanation of overwrite capability evaluation,
Top: Waveform from periodic 16T pattern, Middle: Waveform from after heating, Bottom: Frequency domain plot of the waveforms above.

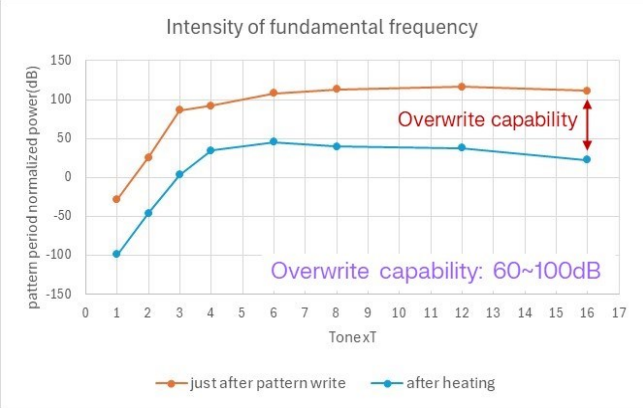

Fig. 3. Overwrite capability result

ii. Periodic 127-bit PRBS pattern case:

Figure 4 shows overwrite capability evaluation in another way. In this case, periodic 127-bit PRBS pattern is used as an old data. Top and middle of the figure is waveform of periodic 127-bit PRBS pattern and after heating respectively. Bottom is auto-correlation plot of each waveform.

As seen in auto-correlation plots, there are periodic peaks observed in orange plot which is from 127-bit PRBS pattern case. On the other hand, no periodic peak is observed in blue plot coming from after heating. That means by heating, periodic property in the old data has been erased enough.

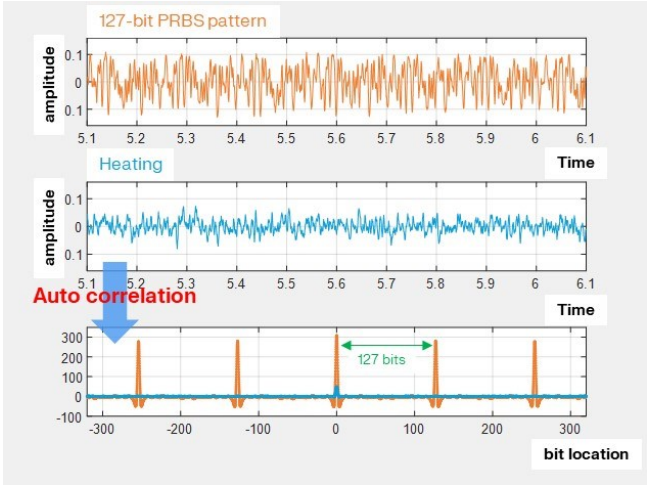

Fig. 4. Overwrite capability evaluation by 127-bit PRBS pattern,
Top: Waveform from periodic 127-bit PRBS pattern, Middle: Waveform from after heating, Bottom: Auto-correlation plot of the waveforms above.

IV. Conclusion

Some experiments have been performed to realize ternary recording in HAMR as an initial feasibility study. And, it has been experimentally confirmed that …

i. "Heating" can create new signal level "0" in addition to conventional signal level "+1" and "-1".
ii. "Heating" can overwrite an old data enough.

References

[1] R. E. Rottmayer et al., "Heat-Assisted Magnetic Recording," in IEEE Transactions on Magnetics, vol. 42, no. 10, pp. 2417-2421, Oct. 2006.

Effect of Diffusion Stopper Layer on Surface Morphology of MgO Underlayer of $L1_0$-FePt Granular layer for HAMR

Daiki Isurugi, Feng Chenming, Akihiro Shimizu, Shintaro Hinata, Tomoyuki Ogawa, and Shin Saito

Department of Electronic Engineering, Graduate School of Engineering, Tohoku University,
6–6–05, Aoba, Aramaki, Aoba–ku, Sendai 980–8579, Japan, daiki.isurugi.a1@tohoku.ac.jp

Due to the highly oriented (001) sheet texture of $L1_0$-FePt grains in HAMR media, a heteroepitaxial sputtered multilayer consisting of amorphous alloy/ (001)-bcc alloy/ (001)-fcc MgO is used as the underlayer. However diffusion of the amorphous elements into the grain boundaries of the bcc layer causes nucleation of the bcc grains with preferred orientation of (110) plane, which brings nodule-like abnormal growth of MgO with (111) sheet texture. In this study, we investigated the effect of inserting a diffusion stopper layer (DSL) to prevent the forming of nodules, and found that by thickening a 0- 5 nm DSL, nodule density was reduced 200/μm^2 to 28/μm^2 while maintaining the MgO underlayer with (002) sheet texture.

***Index Terms*— Magnetic recording, HAMR, $L1_0$–FePt, MgO**

I. Introduction

As traditional perpendicular magnetic recording faces limitations in achieving higher areal densities, HAMR leverages localized laser heating to reduce coercivity in the recording layer, enabling efficient data writing [1]. The media structure is consisted of amorphous/ (001)bcc-alloy/ (001)fcc-MgO/ $L1_0$-FePt granular layer is used as the underlayer. However, critical challenges persist in material and structural control. Key issues include the formation of nodular structures on the MgO underlayer surface, caused by diffusion of amorphous-layer elements constituents from grain boundaries during deposition [2- 6]. In this study, we investigated the effect of inserting a diffusion stopper layer to prevent diffusion of the elements constituting the amorphous layer into the bcc layer.

II. Results and Discussion

A. Mechanism of forming nodule structure [2]

The mechanism of forming nodule structure was confirmed. Fig. 1 shows the AFM topography image of the MgO(5) / CrMn(30) / CoW(50) film with area of 500 x 500 nm square when CrMn layer was deposited at 305 °C. It can be confirmed that there are two characteristic surface structures. One is a network-shaped upheaval structure with a height of 2 nm, a width of 10 nm and an interval of 30 nm observed throughout the sample, and the other is a nodule structure with a height of 3 nm and a width of several tens nm. This study focused on the nodule structure.

In order to investigate the formation factor of the nodule structure, a structural analysis in the direction of the film thickness near the structure was carried out using cross-sectional TEM analysis. Fig. 2 shows cross-sectional BF-STEM image around the nodule for a MgO(5) / CrMn(30) / $Co_{60}W_{40}$ film. The CrMn grain has a nodule structure at the lower part of the site where the nodule structure of the MgO layer surface was observed. Lattice spacing of the surrounding CrMn layer were investigated and it was found that the film surface and the (110) plane were parallel to each other at the nodule forming portion and the (002) plane was parallel at portions where there are no nodules. Figure 3 (a) shows the STEM-HAADF image of the same field of view, and (b), (c), and (d) show the EDX mapping images by the characteristic X-rays of Co, Cr and Mn, respectively. According to the HAADF image, a white contrast portion in the CrMn layer is observed in a stripe shape in the film thickness direction avoiding the nodule structure. According to the EDX image, it can be seen that existence of Co corresponds to the white portion of the HAADF image. From the above results, it was found that the nodule portion on the surface of the MgO layer corresponds to the (110) oriented CrMn grain which is different orientation from the other portion in the CrMn layer, and it is suggested that the nodule is due to the (110) oriented CrMn grain generated at the grain boundary of (002) oriented CrMn grains in the growth process. The reason for the surface roughness is presumed to be caused by different growth rate of the CrMn according to the crystal orientation.

Finally, from the above results, we consider the formation origin of nodule structure. When the amorphous elements and Mn diffuse from the grain boundary of CrMn layer, in some of grain boundaries, (110) oriented CrMn grains which have different crystal orientations are generated in the upper layer of the CrMn layer, and a nodule structure is formed on the surface of the CrMn layer. It is considered that MgO layer grow so as to cover this portion, and a nodule structure is formed on the surface of the MgO layer.

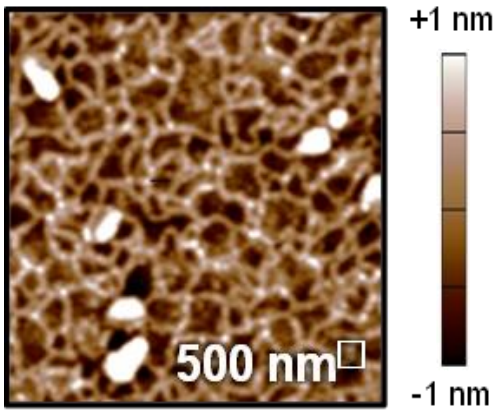

Fig. 1 AFM topography image of a MgO/ CrMn/ $Co_{60}W_{40}$ film at T_{sub}^{CrMn} of 305 °C.

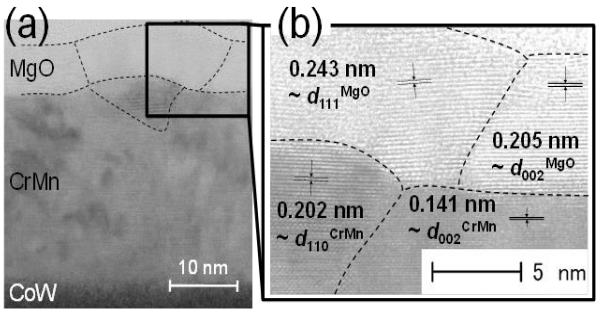

Fig. 2 Cross sectional BF-STEM image around nodule structure for a MgO/ CrMn/ $Co_{60}W_{40}$ film at T_{sub}^{CrMn} of 305 °C.

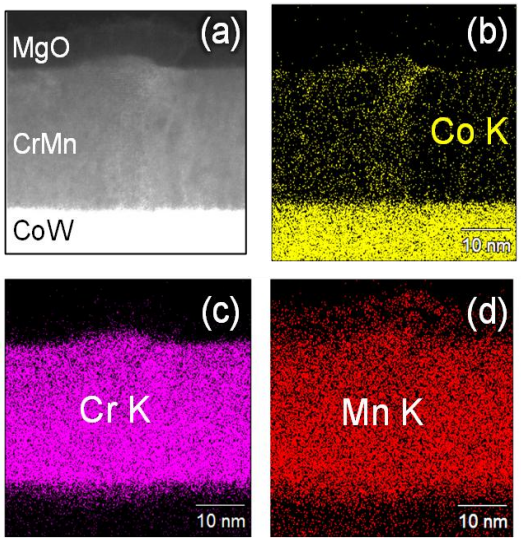

Fig. 3 (a) Cross sectional STEM-HAADF image and (b), (c), (d) -EDX maps of Co, Cr, and Mn around nodule structure for a MgO/ CrMn/ $Co_{60}W_{40}$ film at T_{sub}^{CrMn} of 305 °C.

B. *Effect of inserting a diffusion stopper layer*

Based on the consideration of the previous chapter, the dependence of the nodule occurrence number on MgO diffusion stopper layer (DSL) thickness was investigated. This chapter investigates strategies to enhance the crystal orientation and surface morphology of MgO thin films heteroepitaxially grown on orientation control layer (OCL) with diffusion stopper layer (DSL), aiming to optimize the FePt granular recording layer in Heat-Assisted Magnetic Recording (HAMR) media. Fig. 4 shows the stacking structure used in this experiment. As the DSL, MgO was deposited in a thickness of 1-5 nm.

Figure 5 shows AFM images of MgO surface structure and relationship between nodule density and DSL thickness. It shows even a 1 nm MgO DSL significantly suppresses nodule formation. By integrating a 0- 5 nm DSL, nodule density was reduced 200/μm^2 to 28/μm^2. From the above, it can be considered that the MgO diffusion stopper layer decreases the diffusion of amorphous constituent elements.

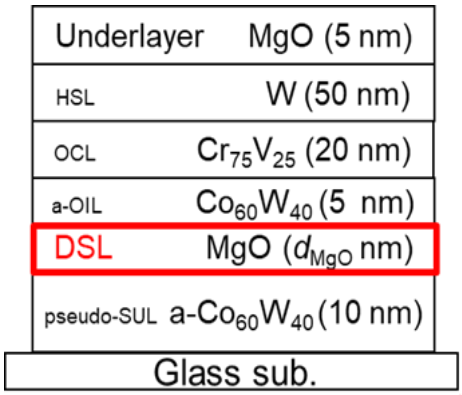

Fig. 4 The stacking structure used in this experiment.

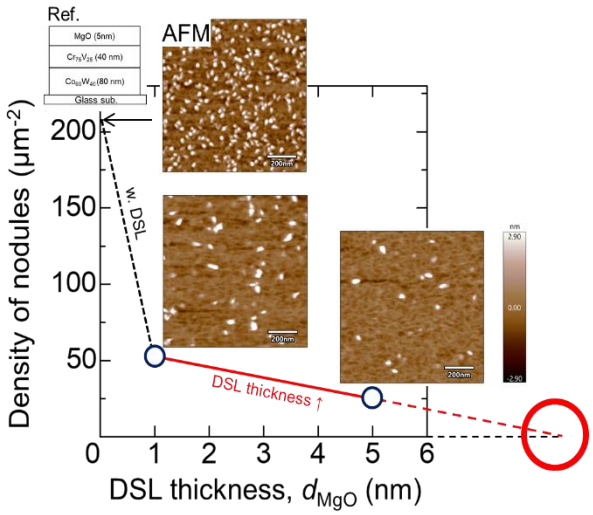

Fig. 5 AFM images of MgO surface structure and relationship between nodule density and DSL thickness.

REFERENCES

[1] A. Chernyshov, T Le, B. Livshitz, O. Mryasov, C. Miller, R. Acharya, D. Treves, "Measurement of Curie temperature distribution relevant to heat assisted magnetic recording," *J. Appl. Phys.*, **117**, 17D111 (2015).

[2] A. Shimizu, S-J. Jeon, S. Hinata, S. Jo, and S. Saito, "The Network-Shaped Upheaval Structure in (002) Textured MgO layer for $L1_0$ FePt-Based Granular Media with Columnar Nanostructure", *IEEE Trans. Magn.*, **55**, 3200208 (2019).

[3] A. Shimizu, S. Hinata, S. Jo, and S. Saito, "Proposal of network-shaped upheaval structure using grain boundary diffusion in underlayer for $L1_0$ FePt-based granular media with columnar nanostructure", *T. Magn. Soc. Jpn.* (Special Issues), **3**, 7 (2019).

[4] S. Hinata, S. Jo, and S. Saito, „"Surface structure of MgO underlayer with Ti diffusion for (002) oriented $L1_0$ FePt based heat assisted magnetic recording media", *AIP Adv.*, **8**, 056515 (2018).

[5] S-J. Jeon, S. Hinata, and S. Saito, "Amorphous Cr-Ti Texture-inducing Layer Underlying (002) Textured bcc-Cr alloy Seed Layer for FePt-C based Heat-assisted Magnetic Recording Media", *J. Magn. Soc.* **21**, 35 (2016).

[6] S-J. Jeon, S. Hinata, S. Saito and M. Takahashi, "Highly (002) textured large grain bcc $Cr_{80}Mn_{20}$ seed layer on $Cr_{50}Ti_{50}$ amorphous layer for FePt-C granular film", *J. Appl. Phys.*, **117**, 17A924 (2015).

'Dark-Laser-Heating (DLH)' using ultra-fast laser pulsing for mode hop mitigation in Heat assisted magnetic recording (HAMR)

Sukumar Rajauria,* John Contreras, Rehan Zakai, Mehdi Habibollahzadeh, Dongying Li, and Xinzhi Xing
Western Digital Company, Recording Sub System Staging and Research, San Jose, CA 95119 USA.
(Dated: May 22, 2025)

Laser diode is an integral component in heat assisted magnetic recording (HAMR) technology. Achieving a stable laser power during HAMR operation is extremely challenging and has been a key gating item in achieving high performance and storage from HAMR HDDs. The laser power variation is mostly attributed to the change in opertaing mode of laser diode, namely the mode hop, due to change in temperature. Here, we demonstrate a novel approach of 'Dark Laser Heating (DLH)' based on utilising the turn-on delay of laser diode by applying ultra-fast (few nanoseconds) laser current pulses to pre heat and manage its temperature change during normal forward bias used in HAMR writing process. In sub-nanosecond operation, the laser-diode do not emit optical light but the thermal response is fully efficient to pre-heat the laser diode to match the temperature of the laser diode in HAMR operation and suppress the laser power variations arising from mode hopping.

Hard disk drives (HDDs) have been the workhorse in cloud data centers, where the volume of data doubles every two years, pushing hard drives to achieve high capacity and even higher areal density. Heat assisted magnetic recording (HAMR) is the upcoming magnetic data storage technology used in hard drives which has surpassed areal densities beyond the limits of conventional perpendicular magnetic recording (PMR). HAMR write process requires both the magnetic field and thermal assist from the write head to periodically switch the magnetization on granular magnetic medium with very high magnetic anisotropy. Magnetic medium is locally heated to above its Curie temperature (Tc), around 400-450 C, to reduce coercivity of the magnetic medium. The localized heating of the magnetic medium is accomplished by a laser diode in conjunction with a near field transducer (NFT) embedded in the write head, which produces a hot spot with a size of few tens of nanometers on the recording medium. Individual bits are written in the down-track direction as the magnetic medium disk spins over the HAMR write head.

A laser diode is an integral component of HAMR head. High fidelity HAMR recording system requires laser diode to provide a stable and a reliable optical power during data writing process. Achieving a stable laser power during HAMR operation is extremely challenging and has been a key gating item in achieving high performance and storage from HAMR HDDs. The laser power variation is mostly attributed to the change of its temperature especially at the start of HAMR writing. In the past, we demonstrated a unique approach of Dark Laser Heating (DLH) based on reverse bias to preheat laser diode to manage its temperature change during normal forward bias used in HAMR writing process. The reverse bias increases the laser diode's temperature without any optical response. It was found that matching the laser diode temperature between pre-heat and actual HAMR writing condition suppresses mode hop, leading to a stable HAMR writing condition.

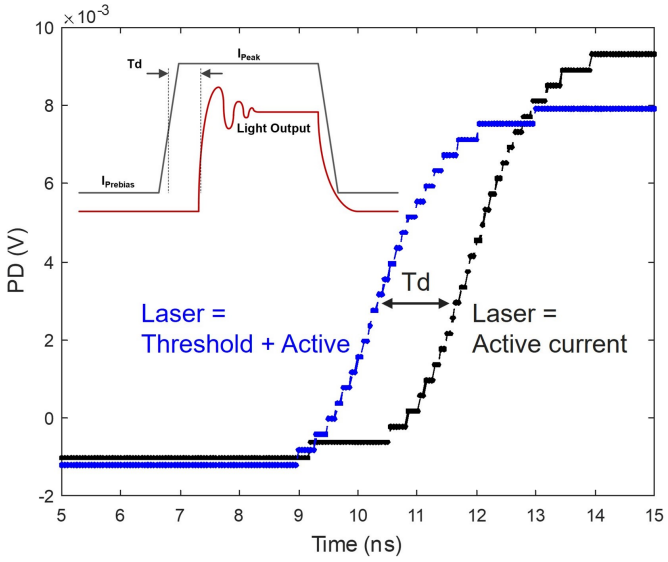

FIG. 1. Main: Photo-diode (PD) response of the laser diode when laser pre-bias is set at 0mA (black) and at laser threshold (blue). Inset shows the schematic of injection current and optical reponse of laser diode.

In this work, we propose and experimentally demonstrate a novel approach of Dark Laser Heating (DLH) in the forward bias, utilizing the turn-on delay of laser diode. By applying ultra-fast (GHz) current pulses, this method preheats the laser diode and manages its temperature changes during normal forward bias applied in HAMR writing process. It is well studied that laser diodes have a "turn-on-delay" which refers to the time for the laser to transition from a non-lasing state to a lasing state after current is applied. Here, we show that during turn-on delay the electrical Joule dissipation inside laser diode is fully efficient and leads to increase in its

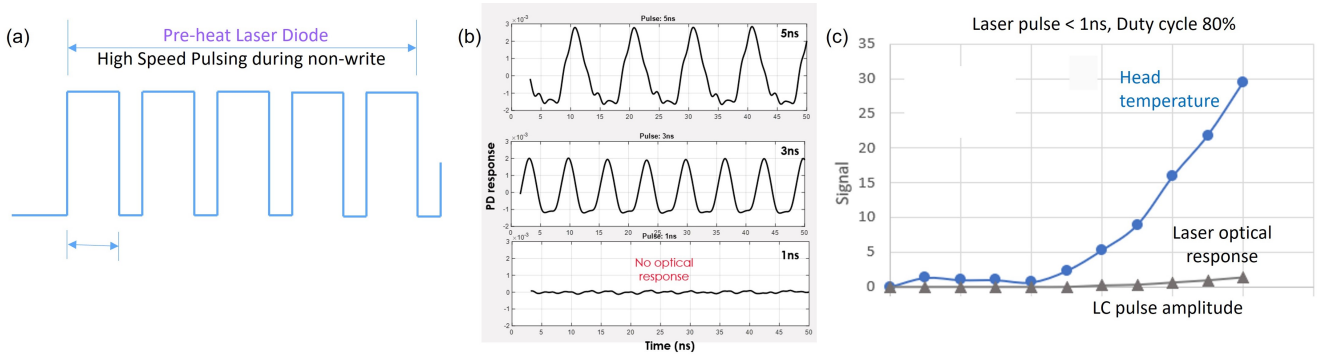

FIG. 2. (a) Current pulse profile to pre-heat the laser diode. (b) Optical response of laser diode (Photo-diode) as a function of time for different turn-on pulse width. (c) Shows the average temperature rise (blue) of the slider and optical response (black) from photo-diode as a function of applied laser current for train of short pulses (<1ns).

temperature. Furthermore, we utilize the accumulated heat from the turn-on delay to pre-heat the laser diode, matching its operational temperature during HAMR operation and suppressing the laser power variations arising from mode hopping.

When the laser current is switched on at t=0, transitioning from I=I_{off} (below the laser threshold) to I=I_{on} (above the threshold) as shown in inset of Figure 1, the carrier density will steadily increase from its below threshold value until the threshold carrier density n_{to} is reached. The turn-on delay, T_d, is primarily governed by carrier lifetime τ_e as follows:

$$T_d = \tau_e ln \frac{I_{on} - I_{off}}{I_{on} - I_{to}} \quad (1)$$

Where I_{to} is the threshold current. Interestingly, both carrier lifetime τ_e and turn-on delay time T_d are on the order of several nanoseconds. For high-fidelity application like HAMR recording, the turn-on delay is avoided by setting laser pre-bias above laser threshold. Figure 1 shows the high-speed photo-diode response for single laser current pulse. Blue line shows the response with pre-bias current set as laser threshold current and Black line shows the response with no pre-bias current. Photo-diode response for laser pulse with no pre-bias current is delayed by about 1 ns. This clearly exemplifies the role of laser pre-bias current in turn-on delay response of the laser diode. Further, we apply the train of high-speed ultra-short laser current pulses to the laser diode (as shown in Figure 2(a)) and simultaneously measure the optical response of laser diode and temperature rise of the head. Figure 2(b) shows the optical response for different pulse width of the laser diode. For laser pulse shorter than 1ns no optical response is measured. Figure 2(c) shows the average temperature rise of the slider and optical response from photo diode as a function of applied laser current. It is to note, for train of short pulses (<1ns) no optical response is observed but laser diode fully dissipate heat in the slider leading to increase laser diode temperature.

In the following, we use the high-speed pulsing of laser diode to pre heat the laser diode to its steady state temperature before doing the HAMR write operation in forward bias (as shown in Figure 3(a)). In absence of pre-heating the laser diode, the Joule dissipation leads to an increase in laser diode temperature resulting in changes in laser optical power due to laser mode hopping. Pre-heating the laser diode using the high-speed laser diode pulses brings it closer to HAMR write steady state temperature. We further verified the usefulness of high-speed laser diode pulsing to pre-heat the laser diode in the HAMR operating condition. Figure 3(b) shows the measured phase of written magnetic signal across the single track of HAMR writing with and without preheating the laser diode using the high-speed laser diode pulsing. With no pre-heating (Blue line), the phase varies significantly, which is attributed to the temperature increase leading to the laser power variation from mode hop. For Red line, the laser diode is pre-heated using the high-speed laser pulses before actual HAMR operation. Here, the phase of the written signal remains stable for the full track. This behavior clearly exemplifies the role of pre-heating to stablize laser diode temperature leading to the stable laser power during HAMR writing.

In conclusion, we have demonstrated a novel approach using the high-speed laser pulsing to preheat the laser diode. The high-speed laser pulses increase the laser diode temperature with no optical response. We have used the train of high-speed laser current pulses to pre-heat the laser diode to different laser diode temperature. It is found that matching the laser diode temperature between pre-heat and actual HAMR writing condition suppresses mode hop, leading to a stable HAMR writing condition.

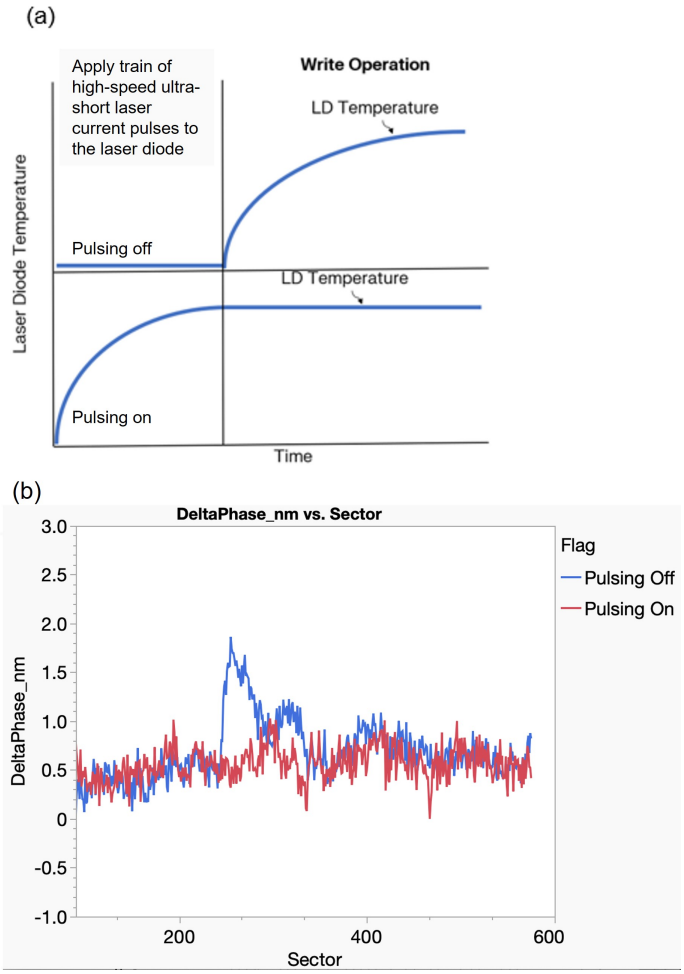

FIG. 3. (a) Cartoon showing the pre-heating the laser diode using the train of high-speed ultra-short laser current pulses to the laser diode before using the laser diode in the usual forward bias operation. (b) Measured phase of written magnetic signal across the single track of HAMR writing with and without preheating the laser diode using the high-speed laser diode pulsing.

* email: sukumar.rajauria@wdc.com

[1] K. Konnerth, and C. Lanza Delay between current pulse and light emission of a Gallium Arsenide injection laser. *Applied Physics Letters* **4**, 120-121 (1964).

[2] K. Petermann "Intensity-Modulation Charateristics of Laser Diodes" in Laser Diode modulation and noise. *Kluwer Academic Publishers*, 1998.

[3] Nagaatsu Ogasawara, Ryoichi Ito, Masahiro Kato, and Yohshitaba Takahashi Mode switching in injection lasers induced by temperature variation and optical feedback *Japanese Journal of Applied Physics* **22**, 1684-1690 (1983).

[4] Sukumar Rajauria, Erhard Schreck, Mehdi Habibollahzadeh, Dongying Li, Qing Dai, and Xiaokun Chew Active Control of Laser Diode Temperature to Mitigate Mode Hop in Heat Assisted Magnetic Recording (HAMR). *2024 IEEE 35th Magnetic Recording Conference (TMRC)*, 1-3 (2024).

[5] Erhard Schreck and Sukumar Rajauria Temperature control of a laser diode by applying reverse bias in a data storage device configured for heat-assisted magnetic recording. *US Patent*, 12,198,737 (2025).

[6] John Contreras, Sukumar Rajauria, Rehan Zakai, Joey Poss, and Xinzhi Xing Dark laser heating by positive pulse biasing in heat assisted magnetic recording. *US Patent*, 12,125,509 (2024).

High-density $L1_0$-FePt grains on an electrically conductive (Mg,Ti)O underlayer for HAMR media.

A. R. Dilipan[1,2], H. Sepehri-Amin[1,2], and I. Suzuki[1], Y. K. Takahashi[1,2,3]

[1]National Institute for Materials Science, Tsukuba 305-0047, Japan.
[2]Graduate School of Science and Technology, University of Tsukuba, Tsukuba 305-8577, Japan.
[3]Research Institute of Electrical Communications, Tohoku University, Sendai, Japan.

Achieving high-density recording media composed of small, columnar and well separated $L1_0$-FePt grain is essential for high storage capacity heat-assisted magnetic recording (HAMR) media. A suitable segregant and an efficient underlayer is utmost important factor for obtaining a high-density recording media. We investigated the growth of $L1_0$-FePt granular films on with C and BN segregants on MgO substrate with and without a (Mg,Ti)O underlayer. FePt-C grown on (Mg,Ti)O shows larger grain size of ~11.1 nm with lower grain-density 4.8 Tgrains/in^2, whereas FePt-BN show smaller grains of ~6.6 nm with about two-fold increase in grain density of 9.0 Tgrains/in^2. Microstructural analysis shows the enrichment of Ti and N at interface of FePt-BN and (Mg,Ti)O, resulting in smaller and columnar grains. These findings elucidate that the FePt-BN is an optimal choice for achieving fine-grained and high-density recording media on electrically conductive (Mg,Ti)O underlayer.

Index Terms— $L1_0$-FePt, underlayer, segregant, high-density recording media, HAMR

I. Introduction

Heat-assisted magnetic recording (HAMR) is a promising technology that has enabled large data storage capacity or areal recording density (ARD) of hard disk drives beyond 4 Tb/in^2 [1]. Chemically ordered $L1_0$ FePt has been used as a HAMR media due to their high magnetic anisotropy constant (Ku) of 6.6 MJ/m^3 [2]. An ideal microstructure with grain size <4.3 nm, a pitch distance (center-to-center distance) < 5.3 nm, and columnar grains with an aspect ratio (h/D) > 1.5, along with high (001) texture, is necessary to achieve high ARD [3]. The microstructure of the FePt-X media is primely controlled by segreant materials, underlayer and sputtering condition used for fabricating the media. Here 'X' is the segregant that act as an intergranular phase, which helps in granular microstructure and isolation of grains. Among various segregants used [4], carbon shows promising results in achieving small and well isolated grains, when deposited on MgO underlayer or substrate. However, they form spherical-shaped FePt grains and does not result in columnar grains. Recently, boron nitride as a segregant has been demonstrated to show smaller grains when compared to FePt-C [5]. In the aspect of underlayer, MgO as a substrate and as an underlayer has proven to show epitaxial growth of FePt-X grains. However, the MgO underlayer requires a longer deposition time due to their electrically insulating nature and the need for RF sputtering. An alternate is to use electrically conductive $(MgTi)_xO$ with a crystal structure and lattice parameters comparable to MgO. In previous studies, FePt-C deposited in $(MgTi)_xO$ always resulted in larger grains with irregular grain morphology [6]. In the present work, we investigated the microstructure, interface, and magnetic properties of epitaxially grown FePt-X (X= C and BN) on MgO substrate and $(Mg,Ti)_xO$ underlayer.

II. Experimental

6 nm-thick FePt-C 40 vol.% and FePt-BN 25 vol.% (hereinafter, FePt-C and FePt-BN) layers were deposited individually on MgO substrate and (Mg,Ti)O underlayer (MTO) using an ultra-high vacuum co-sputtering system with a base pressure of ~10^{-7} Pa. The MTO underlayer was grown on the MgO substrate to obtain epitaxial growth of the FePt film. Before deposition of the films, the MgO (001) single crystalline substrate was prepared by cleaning with ethanol and acetone, and thermally flushed at 650°C for 1 h. MTO underlayer of 5 nm thickness was deposited on a single crystalline MgO (001) substrate at 600°C.

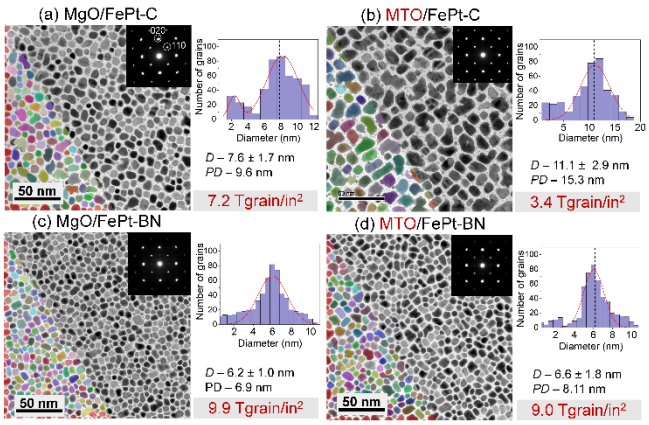

Fig. 1. Plane-view BF-TEM images, overlay color maps, grain size distribution histogram, and their SAED pattern (inset) of (a) MgO/FePt-C, (b) MTO/FePt-C (c) MgO/FePt-BN and, (d) MTO/FePt-BN.

The best deposition parameters were adopted for fabricating FePt-C and FePt-BN layers. The FePt-C 40 vol.% layer was deposited by co-sputtering FePt and C targets separately at the substrate temperature of 600°C, whereas the FePt-BN was sputtered with a composite target of FePt-25 vol.% BN with the assistance of Ar + N_2 gas flow at 700°C. Finally, a carbon capping layer of 5 nm was deposited at room temperature to avoid surface damage to the FePt-C and FePt-BN media layers. The volume fraction of FePt and segregants in the media layer was estimated using the pre-measured sputtering deposition rate. Transmission electron microscopy (TEM) coupled with energy

dispersive X-ray spectroscopy (EDS) was performed using TITAN G2 80-200 TEM and Spectra Ultra S/TEM 30-300 (Thermo Fisher Scientific).

III. Plane-view Microstructural Analysis

Figure 1 shows the plane-view bright field (BF)-TEM images, overlay color map and grain size distribution histograms of all the samples. The MgO/FePt-C (Figure 1a) shows an average grain size (D) of 7.6 ± 1.7 nm, with a pitch distance (PD) of 9.6 nm with a relatively high grain density of 7.2 Tgrain/in^2. Whereas, the MTO/FePt-C (Figure 1b) shows larger grains of of 11.1 ± 2.9 nm, and PD of 15.3 nm, resulting in a decreased grain density of 4.8 Tgrain/in^2. This observation aligns with the earlier studies on the FePt-C grown on polycrystalline substrates as reported elsewhere [6]. The larger grain size and agglomerated microstructure in FePt-C on MTO can be due to the higher surface free energy (SFE) of the MTO underlayer. The high SFE increases the wettability, which induces grain growth responsible for coarser FePt grains on MTO. The microstructure of FePt-BN on the MTO underlayer is retained with smaller and well-separated grains, similar to those grown on MgO (Figure 1c and 1d). The overall grain size of FePt-BN irrespective of the underlayer is smaller than that of FePt-C, with a D value of 6.2 ± 1.0 nm for MgO/FePt-BN and 6.6 ± 1.8 nm for MTO/FePt-BN. The smaller grain size of FePt-BN demonstrates a high grain density exceeding 9.0 Tgrain/in^2, significantly higher than FePt-C films. Although MTO possesses higher surface free energy than MgO, the use of BN segregant is advantageous in mitigating the coarsening of the grains. The reduced grain size and high grain density in FePt-BN films grown on MTO demonstrate the efficacy of this combination, which can be developed as an optimal recording media.

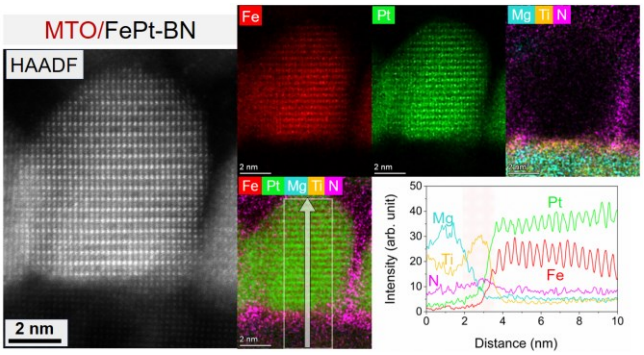

Fig. 2. Cross-sectional HAADF-STEM along with the STEM-EDS elemental maps and composition line profile of constituent elements of MTO/FePt-BN.

IV. Cross-sectional Microstructural Analysis

In order to understand the contributions to the smaller grains and growth mechanism, a detailed cross-sectional elemental analysis is conducted. Figure 2 shows the High-angle annular dark field (HAADF) Scanning-TEM images, corresponding the EDS elemental maps, and line profile analysis of the single grain corresponding to MTO/FePt-BN. From the HAADF-STEM image, a periodic dark and bright contrast is observed, representing a high $L1_0$ ordering of FePt grain. According to the EDS maps and corresponding composition line profiles, the segregation of Ti on the surface of MTO is observed with no diffusion of Ti into the FePt grains. Interestingly, N encapsulates the FePt-grains, with a noticeable N enrichment at the MTO and FePt-BN interface. This could be attributed to the reactive sputtering of FePt-BN media layer, where a mixture of Ar+N_2 was used as a sputtering gas. Due to the nitrogen flow during the main layer deposition, there is a high possibility of nitriding at the surface of the MTO underlayer. As a result, the composition of the MTO underlayer at its surface is altered to be in the combination of (Ti,N)-rich composition, which is favorable for smaller grain size with high grain density.

V. Conclusion

In conclusion, this study presents a comprehensive investigation of the microstructure, magnetic properties, and interface of the FePt-C and FePt-BN granular films deposited on MgO substrate and (Mg,Ti)O (MTO) underlayer. The plane-view microstructural analysis revealed that the MgO/FePt-C film have smaller grains with high grain density, whereas the MTO/FePt-C film displayed larger grains with coarsened grains with low grain density. Interestingly, FePt-BN on MTO show smaller grain size with two-fold higher grain density compared to MTO/FePt-C. Overall, incorporating BN as a segregant for $L1_0$ FePt, one can easily achieve a desirable microstructure with smaller grains and high grain density on an electrically conductive MTO underlayers, suitable for high storage capacity HAMR media.

VI. Acknowledgement

The authors thank T. Hiroto, T. Anzaki, Y. Mori, D. Ogawa, A. Nakama, and A. Tsuru (National Institute for Materials Science) for their contribution in conducting experiments. The authors acknowledge N. Kulesh for developing the TEM data segmentation and deep learning methods software. This work was supported in part by the JST CREST program (Grant No. JPMJC22C3) and MEXT program “Data Creation and Utilization-Type Material Research and Development Project” (Grant No. JPMXP1122715503).

References

[1] G. Varvaro, F. Casoli, Ultra-High-Density Magnetic Recording: Storage Materials and Media Designs, Pan Stanford Publishing, Florida, 2016.

[2] T. Ono, N. Kikuchi, S. Okamoto, O. Kitakami, T. Shimatsu, Novel torque magnetometry for uniaxial anisotropy constants of thin films and its application to FePt granular thin films, Appl. Phys. Express. 11 (2018) 033002

[3] D. Weller, G. Parker, O. Mosendz, A. Lyberatos, D. Mitin, N.Y. Safonova, M. Albrecht, Review Article: FePt heat assisted magnetic recording media, J. Vac. Sci. Technol. B, 34 (2016) 060801.

[4] D. Granz, K. Barmak, M.H. Kryder, Granular L10 FePt: X (X= Ag, B, C, SiOx, TaOx) thin films for heat assisted magnetic recording, Eur. Phys. J. B. 86 (2013) 1-7.

[5] C. Xu, B.S.D.C.S. Varaprasad, D.E. Laughlin, J.G. Zhu, Bias sputtering of granular L10-FePt films with hexagonal boron nitride grain boundaries, Sci. Rep. 13 (2023) 11087.

[6] B.S.D.C.S. Varaprasad, Y.K. Takahashi, A. Ajan, K. Hono, Electrically conductive (Mg0.2Ti0.8)O underlayer to grow FePt-based perpendicular recording media on glass substrates, J. Appl. Phys. 113 (2013) 203907.

Optimized Multi-Level Heat Assisted Magnetic Recording Media with Mo spacer layer for High - Capacity Data Storage

S. Helen[1,2*], A. R. Dilipan[1], D. Ogawa[1], Y. Sasaki[1], S. Kasai[1], Y. K. Takahashi[1,2,3*]

[1]National Institute for Materials science, Tsukuba 305-0047, Japan
[2] Graduate School of Science and Technology, University of Tsukuba, Tsukuba 305-8577, Japan
[3] RIEC, Tohoku University, Sendai, Japan

Multi-level Heat Assisted Magnetic Recording (HAMR) is a novel approach for HAMR technology for increasing the storage capacity of Hard Disc Drives (HDDs) with an aim to reach 4Tbit/in^2 areal recording density. This concept was first realized with dual layer FePt media with Ru as the spacer layer material. In this work, we optimize the microstructure and magnetic properties of dual layer FePt media with Molybdenum spacer layer material, thereby understanding the parameters to be considered while choosing a spacer layer material for 3D-HAMR media. The Mo spacer layer showed novel flat interface which is beneficial for the top layer ordered growth. This flatness effect was investigated and realized that both lattice misfits' strain at the interface between the two materials (FePt and Mo) and thermal energy was accountable for such rarity. Further refinement was also demonstrated by inserting an insertion layer (MgO or MgTiON) between spacer layer and top layer such that the diffusion of spacer layer material to the top FePt could be reduced thus enhancing the ordering of the top layer.

***Index Terms*—Multi level Heat Assisted Magnetic Recording, HAMR, areal recording density, dual layer FePt, 3D-HAMR, spacer layer, insertion layer, tri-layer.**

I. Introduction

The creation and usage of new digital information is taking place every moment, leading to the need for more reliable yet affordable storage solutions. An enhancement in the data storage density of Hard Disc Drives (HDD), which serves as the major storage unit in data centers, is paramount [1]. The conventional perpendicular magnetic recording (PMR) system has a limitation of maximum 1Tbit/in^2. Therefore, a new technology of magnetic recording with assistance of external energy such as heat [2] or microwave was proposed [3]. Thus, Heat Assisted magnetic recording was developed with $L1_0$ FePt, a high magneto crystalline anisotropy ferromagnetic material [4]. To attain an areal density of 4Tbit/in^2, an ideal grain size of 4.3 nm with a good $L1_0$ ordering is essential [5,7]. However, even with various non-magnetic matrixes like C, h-BN, the maximum reduction in grain size was up to 5 nm [6,7]. For further enhancement in magnetic recording density, instead of stacking a greater number of platters in one HDD and thereby increasing energy consumption, a cleantech approach of increasing the recording layers on the same platter is put forward. This concept which relies on HAMR technology is known as multi-level HAMR media, in which two magnetic recording layers are separated by a non-magnetic breaking layer, also known as spacer layer. The first experimental realization of 3D-HAMR was FePt/Ru/FePt tri- layer, however, this media faced some challenges like the presence of in-plane variants, lack of top layer $L1_0$ ordering at the initial growth of around 1nm and presence of few disorders at the top grain [8]. These issues could be due to less lattice misfit strain, as large misfit induces misfit strain that can enhance ordering and [001] texture. Thus, Molybdenum, a non-magnetic material with a lattice misfit of 18.4% and very less diffusion chances by checking the phase diagram of Fe-Mo and Pt-Mo, was considered in this work as spacer layer material.

II. Methodology

All the samples were synthesized by ultra-high vacuum magnetron sputtering on a single crystalline (001) MgO substrate at a base pressure of around 10^{-7}Pa. The tri-layer was composed of FePt-40vol%C/Mo-40vol%C/FePt-40vol%C with a 5nm carbon coating at room temperature under Ar pressure of 0.478Pa. Here, molybdenum acts as a breaking layer between the ferromagnetic FePt layers. The structural analysis was carried out by the Rigaku Smart Lab X-Ray Diffraction (XRD) machine and the degree of $L1_0$ ordering (or order parameter, S) was calculated from the integrated intensities of the superlattice (I_{001}) and fundamental peaks (I_{002}), using the equation, $S = \alpha (I_{001}/ I_{002})^{1/2}$ and $\alpha = 0.85$. The microstructure of the films was studied by Titan G2 80- 200 transmission electron microscopy (TEM) in both in-plane and cross-sectional view. The samples were prepared by polishing and chemical etching for the in-plane view. The average grain diameter and areal density were determined using deep learning models [9]. By lift-out technique with focused ion beam (FEI Helios Nanolab 650), the ultra-thin cross-sectional samples were fabricated. In order to understand the composition of the films, energy dispersive X- ray spectroscopy (EDS) was performed with FEI Super-X EDX detector and analyzed by velox software and the magnetic measurements were carried out by thin film MPMS3 (Quantum Design) up to a field of 7T.

III. Results and Discussions

1.Microstructure and magnetic properties of FePt-C /Mo-C/FePt-C

After the initial optimization, a film of FePt-40vol%C (3.5nm, 600°C)/ Mo-40vol%C (2nm, 600°C)/ FePt-40vol%C (3.5nm, 600°C) was synthesized. Having a very high order parameter of 0.96 and the coercive field of 2.05T, this sample shows not only granular microstructure with a grain diameter of 8.6nm, but the cross-sectional TEM view shows a flatness at the interface between the bottom and spacer layer. Flattening at the interface can promote a good growth of spacer layer and ordered top layer over it. In this sample, both top and bottom layer shows $L1_0$ ordering, however from the EDS analysis it is found that Mo is getting diffused into the top layer around 1nm.

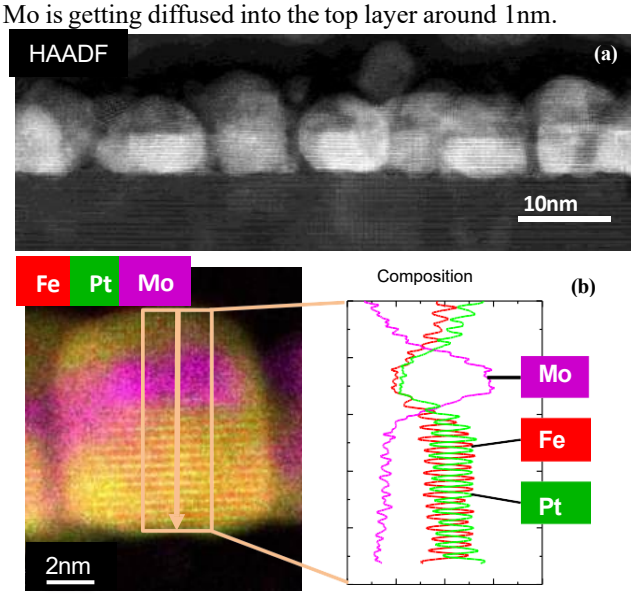

Fig 1. (a) HAADF image, and (b) EDS map with line scan of FePt-40vol%C (3.5nm,600°C)/ Mo-40vol%C (2nm, 600°C)/ FePt-40vol%C(3.5nm,600°C)

2.Flatness at the interface of FePt and Mo

The flattening at the interface was investigated, by preparing four different films as follows:

Sample A: FePt-40vol%C (3.5nm, 600°C)
Sample B: FePt-40vol%C (3.5nm,600°C)/ Mo-40vol%C (2nm, RT)
Sample C: FePt-40vol%C (3.5nm, 600°C)/ Mo-40vol%C (2nm, 500°C)
Sample D: FePt-40vol%C (3.5nm,600°C)/ Mo-40vol%C (2nm, RT)/ 500°C annealed.

The sample A FePt-40vol%C deposited at 600°C on MgO substrate with carbon segregant. It provided good $L1_0$ ordering and a granular microstructure with a spherical cross-sectional structure. The sample B consists of Mo deposited at room temperature on top of FePt grains. The motivation behind this deposition was to check if the lattice misfit between FePt and Mo alone could be responsible for the flattening of the interface. However, from the cross-sectional image of this sample, the flattening at the interface was not evident. Further, sample C was deposited with Mo at an elevated temperature of 500°C to understand the role of temperature along with lattice misfit strain. As expected, the grains had flattening at the interface, but the Mo at high temperature diffuses into the FePt grains slightly, thereby reducing the ordering. Later, the final sample, D was prepared with an aim to retain flatness while reducing the diffusion such that ordering will be reserved. Here, on FePt-40vol%C at 600°C, Mo was deposited at room temperature and the as-deposited film was annealed at 500°C for 5 minutes. Surprisingly, in this film flattening at the interface without any diffusion of spacer layer material into FePt grain was visible. Thus, concluded that not only the lattice mismatch strain, but thermal energy is also responsible for the flatness at the interface. The HAADF view of all samples is given in fig. 2.

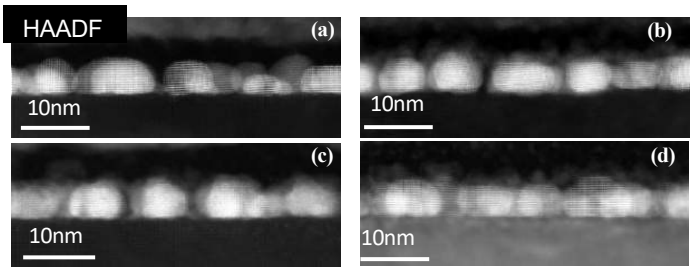

Fig. 2. HAADF image of (1) FePt-40vol%C (3.5nm,600°C), (2) FePt-40vol%C(3.5nm,600°C)/ Mo-40vol%C (2nm, RT), (3) FePt-40vol%C (3.5nm,600°C)/Mo-40vol%C (2nm,500°C), and (4) FePt-40vol%C (3.5nm,600°C)/ Mo- 40vol%C (2nm, RT)/ 500°C annealed.

IV. Conclusion

To improve the recording capacity of HDD, 3D-HAMR with Mo spacer layer has been studied. Interesting observation of flatness at the interface was investigated and concluded that large lattice misfit and thermal energy was responsible for this.

V. Acknowledgement

This work was supported by CREST.

References

[1] Albuquerque, Goncalo, et al. "Hdd reader technology roadmap to an areal density of 4 tbpsi and beyond." *IEEE Transactions on Magnetics* 58.2 (2021): 1-10.
[2] Kryder, Mark H., et al. "Heat assisted magnetic recording." *Proceedings of the IEEE* 96.11 (2008): 1810-1835.
[3] Takagishi, Masayuki, et al. "Microwave assisted magnetic recording: Physics and application to hard disk drives." *Journal of Magnetism and Magnetic Materials* 563 (2022): 169859.
[4] Hono, K., et al. "Heat-assisted magnetic recording media materials." *MRS Bulletin* 43.2 (2018): 93-99.
[5] Varaprasad, BSD Ch S., Y. K. Takahashi, and K. Hono. "Microstructure control of L1 0-ordered FePt granular film for heat-assisted magnetic recording (HAMR) media." *JOM* 65 (2013): 853-861.
[6] Xu, Chengchao, et al. "Bias sputtering of granular L10-FePt films with hexagonal boron nitride grain boundaries." *Scientific Reports* 13.1 (2023): 11087.
[7] Pandey, H., et al. "Structure optimization of FePt–C nanogranular films for heat-assisted magnetic recording media." *IEEE Transactions on Magnetics* 52.2 (2015): 1-8.
[8] Tozman, P., et al. "Dual-layer FePt-C granular media for multi-level heat-assisted magnetic recording." *Acta Materialia* 271 (2024): 119869.
[9] Kulesh, Nikita, et al. "Data-driven optimization of FePt heat-assisted magnetic recording media accelerated by deep learning TEM image segmentation." *Acta Materialia* 255 (2023): 119039.

Patterned Tape Head Air Bearing Surface Development

Oscar Ruiz[1], Eduardo Torres[1] , Kenji Kuroki[2], Yoshu Isobe[2]

[1]Western Digital Corp, San Jose, USA
[2]Western Digital Corp, Fujisawa, Japan

Unlike modern hard disk drives, magnetic tape heads operate in continuous contact with the tape media to maintain the low head-to-media spacing required for reliable magnetic recording. This contact, however, generates significant friction forces—on the order of 50 mN—which induce tape vibration and readback signal jitter. To mitigate these effects, a patterned air bearing surface (ABS) design was proposed. Design parameters for the etched steps were derived through modeling that incorporated tape mechanics, surface roughness, and Reynolds lubrication theory. The steps, fabricated via ion milling following photolithography, were placed in non-active regions of the head—areas not containing read/write elements. Experimental results from 1,000 km tape runs demonstrated a 70% reduction in friction.

***Index Terms*—magnetic recording, tape technology, air bearing, friction reduction**

I. Introduction

In magnetic tape recording systems, a tensioned tape passes at constant velocity over a stationary recording head. A slight tilt, known as the wrap angle, introduces a contact pressure that ensures head-media engagement. Figure 1 illustrates the overall system configuration. Data is written on narrow tracks, and a servo mechanism keeps the head aligned with the target track. The relative motion induces air bearing pressure, influencing contact forces between the head and tape. Friction arises from both contact pressure and viscous shear, leading to vibrations in both longitudinal and transverse directions. These vibrations degrade signal quality and limit storage capacity. In this paper, we present a method to reduce friction by introducing a patterned tape bearing surface (TBS).

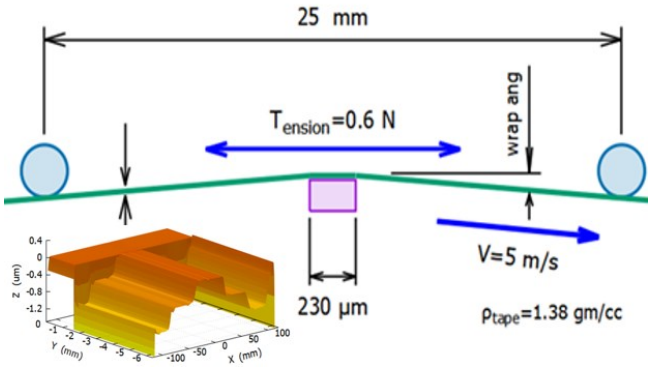

Fig. 1. Overall tape configuration and patterned tape bearing surface

II. Background

Previous studies have characterized the tape-head interaction as fundamentally contact-based due to the high surface roughness of magnetic tapes [1]. The tape itself comprises a polymeric substrate with a magnetic coating and a thin lubrication layer, lacking the carbon overcoat typically found in disk media. The magnetic elements on the head are located within a 3 mm wide central "active band" of the 22.5 mm wide head. The surrounding regions are magnetically inactive. To reduce overall friction, we targeted an increase in tape-head clearance in the inactive bands while preserving contact within the active band to ensure recording fidelity. Optimized etched steps were introduced at the leading edges of the inactive bands [2][3]. These steps generate localized air pressure that lifts the tape above the surface roughness, reducing contact. In contrast, the active band maintains contact to support consistent recording. Etched cavities have been tried [9].

III. Head Fabrication

The tape heads were fabricated using an AlTiC substrate, on which magnetic read/write elements were constructed. Each tape row includes a TBS and two arrays comprising 33 read and write transducers, respectively. A closure, also made from AlTiC, is bonded atop the read/write array to protect the transducers.

The TBS pattern was defined through a mask design that generated four photomask patterns. These were transferred onto a photosensitive resist layer using an optical lithography system. A set of rows were assembled and bonded to a stainless steel carrier to maximize process efficiency. The carrier was mounted on a vacuum spindle, and liquid photoresist was dispensed and spin-coated to achieve desired thickness. This process was repeated to obtain a final thickness target. TBS required two layers and eight exposure passes. Ion milling was then used to transfer the pattern into the substrate. Two step etching process were applied to fabricate TBS on figure 1.

IV. SIMULATION

A steady state numerical model was developed to simulate the coupled interaction between the tape, air bearing pressure and surface roughness. The model equations are:

Tape Equation: describes the out-of-plane deformation w of the tape with bending stiffness D, tension T, velocity V, under air bearing pressure P and contact pressure Pc [8].

$$\nabla^4 w + (\rho V^2 - T)\nabla^2 w = P + P_c \quad (1)$$

Reynolds Equation: models the compressible air film pressure P between the tape and head. The clearance is H, the velocity is Λ, and Q denotes pressure flow, derived from the Boltzmann equation at any clearance [4].

$$\nabla(PQH^3\nabla P - \Lambda PH) = 0 \quad (2)$$

Contact Pressure Model: characterizes tape-head interface compliance using a generalized power function with constants c1 and c2, the clearance is h. Alternatively, the classic contact Greenwood-Williamson model [7] can be used.

$$P_c/P_o = (h/c_1)^{1/c_2} \quad (3)$$

The tape and head domains were discretized with a smooth nonuniform Sobolev-norm based finite difference grid [5]. The grid smoothness ensures second order accuracy and low condition number. Detailed feature resolution was attained with 60K variables. The coupling of equations introduced nonlinearity, and the system exhibited bifurcation behavior under certain conditions, leading to multiple stable solutions. A dedicated iterative solver with super-linear convergence was developed to handle the nonlinearity and resolve the hysteresis loops that emerged during parameter sweeps.

The friction force arising from the friction and viscous shear at the tape and head interface was evaluated with the numerical model. The tape deformation, clearance and contact and air bearing pressures were also obtained. The friction results from the product of the contact force and the friction coefficient, assumed 0.5, plus the viscous shear force of the air bearing.

V. EXPERIMENTAL DATA & DISCUSSION

Figure 2 compares friction force versus wrap angle for a step-etched ABS and a standard LTO-9 reader head with no etching. At 0.5° wrap angle—corresponding to normal operating conditions—the reference head exhibited a friction force of approximately 20 mN, while the step-etched head showed a reduced force of 7 mN. Across the full range of wrap angles, the etched head consistently demonstrated lower friction. A localized friction increase at 0.7° may be attributed to the etched edge acting as a skiving surface under high wrap conditions. Low friction and friction jump angle are nicely modeled.

Friction as a function of tape velocity was also measured at a fixed 0.5° wrap angle. (Fig.3) The step-etched ABS maintained low friction from 0.5 to 6 m/s, satisfying operational velocity requirements for LTO systems.

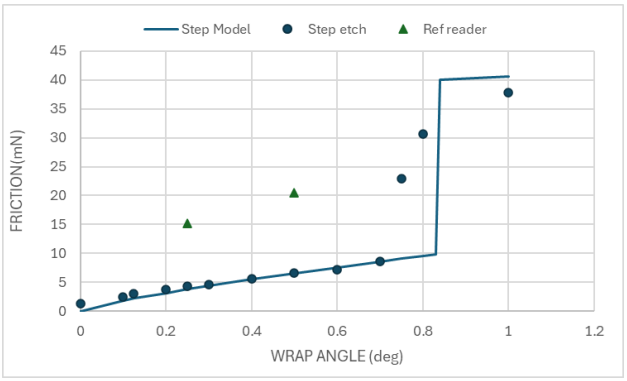

Fig. 2. Friction force as a function of wrap angle, at 5 m/s.

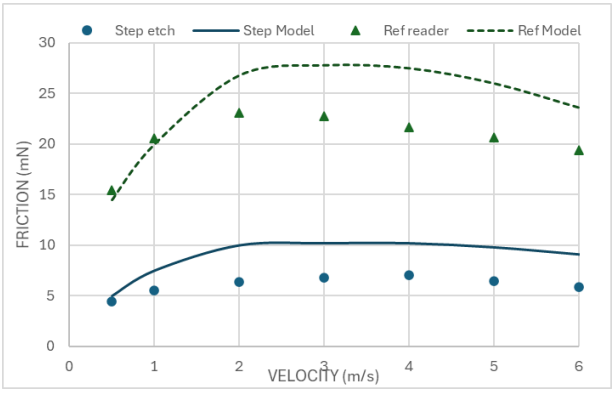

Fig. 3. Friction force as a function of tape velocity, at 0.5 deg wrap angle.

The modeling predicts velocity dependence of friction for step etch head and reference head quantitative well. It will be utilized for further design optimization to reduce friction for future tape heads.

VI. REFERENCES

[1] S. Müftü and D. J. Kaiser, *"Measurements and Theoretical Predictions of Head-Tape spacing Over a Flat-Head"* Tribol. Int., vol. 33, May 2000, pp. 415–430.

[2] O.Ruiz, Western Digital, San Jose, CA, "ABS Optimization Code", 2010

[3] M. Robert, F. Hendriks, *"Gas Optimization and Homogenization of an Externally Pressurized Air Bearing"*, Trib. Trans, v. 33, 1990, pp 41-47

[4] S. Fukui, R. Kaneko, *"Analysis of Ultra-Thin Gas Film Lubrication Based on Linearized Boltzmann Equation: First Report—Derivation of a Generalized Lubrication Equation Including Thermal Creep Flow", ASME J. Tribol.*, 110, pp. 253-261, 1988

[5] O. Ruiz, Western Digital, San Jose, CA, private communication, 2022.

[6] M. Suk, O. Ruiz, D. Gillis "*Load/unload Systems with Multiple Flying Height States" J. Tribol*, 126 (2), pp. 367-371, Apr. 2004.

[7] J. Greenwood, J. Williamson, "*Contact of Nominally Flat Surfaces*", Proc. Roy. Soc., London, 1966, 300-319

[8] J. Scheidl, Y. Vetyukov, "*Review and Perspectives in Applied Mechanics of Axially Moving Flexible Structures*" Acta Mech 234, 2023, pp. 1331-1364.

[9] J. Engelen, V. Jonnalagadda, S. Furrer, H. Rothuizen, M. Lantz, *"Tape-Head with Sub-Ambient Air Pressure Cavities"* IEEE Trans. Magn. v 52, 11, Nov 2016

Magnetic properties and microstructure of FePt (BN/AlN, Ag, C) film

Jai-Lin Tsai*, Cheng-Yu Tsai, Mau-Tin Lin, Yi-Yuan Huang, Hsin-Hau Huang
Department of Materials Science and Engineering, National Chung Hsing University, Taichung 40227, Taiwan,
tsaijl@dragon.nchu.edu.tw

The FePt (BN/AlN, Ag, C) and FePt (BN, Ag, C) films illustrate close ordering degrees (0.84), which means the hard $L1_0$ FePt phase is almost equal in both films. The FePt (BN/AlN, Ag, C) film has a higher c-axis alignment, evidenced in the lower rocking width in (001)/(002) (=3.94°/2.5°) diffraction peaks. The more c-axis anisotropic crystal grains also respond to the higher nucleation field, magneto-crystalline anisotropy, and lower hard-/easy-axis remanence ratio than the reference sample. The FePt (BN, Ag, C) film presents large perpendicular magnetic anisotropy and out-of-plane coercivity (31.7 kOe). Still, the disordered fcc FePt contributed to the in-plane magnetization and wider hard-axis hysteresis loop. However, the out-of-plane coercivity is much smaller in the FePt (BN/AlN, Ag, C) film (16.7 kOe) due to the formation of soft magnetic FeB grains and the hard- and soft-magnetic phases are exchange-coupled, which enhances the magnetic remanence and saturation magnetization. From microstructure image mapping, AlN segregated at the grains boundaries, but part of Al was presented in the FePt lattice and was supposed to initiate the formation of FeB due to high atomic diffusivity at high deposition temperature.

***Index Terms*—perpendicular magnetic anisotropy, out-of-plane coercivity, exchange-coupled grains.**

I. Introduction

In conventional CoCrPt-oxides based media, the non-magnetic exchange control layer was used to adjust the interlayer and lateral grain interaction in the magnetic layer which has gradient perpendicular magnetic anisotropy (PMA) to increase the signal-to-noise ratio. The ordered FePt-based media with gradient PMA is also required for heat-assisted magnetic recording (HAMR) media to control the read/write physical-related parameters. The compositional variation in the $L1_0$-FePt layer can change the ordering degree and magneto-crystalline anisotropy (K_u) intrinsically, and the grains-isolated materials (segregants) can also influence the magnetic properties extrinsically [1].

From microstructure and surface roughness, segregants are required to form a granular structure in which $L1_0$ FePt grains are in the matrix and amorphous BN, and carbon are in the grain boundaries. Here, BN is mechanically hard to grow the FePt columnar grains. However, the lower deposition rate causes inclined and interrupted columnar grains with different grain aspect ratios. The AlN nitride has much higher thermal conductivity and lower electric resistivity, which were doped to replace half of the BN in FePt (BN, Ag, C) film, obtaining different magnetic properties and microstructure. For segregants in HAMR media, the higher thermal conductivity is not beneficial for the thermal insulating boundary during thermal writing, and lower electric resistivity is better for the sputtering process to avoid particles. This study will extensively discuss the magnetic properties and microstructure of the FePt (BN/AlN, Ag, C) film and reference sample.

II. Experimental

The FePt (BN, Ag, C) and FePt (BN/AlN, Ag, C) thin films were prepared on the MgO (100) single-crystal substrate by direct current (DC) magnetron sputtering. The thin film deposition system was designed to have a pre-chamber which was used to transfer the substrate from the atmosphere end by load-lock feedthrough to keep the high vacuum pressure in the main main-chambers which installed four sputtering cathodes (AJA, A320, MA, USA), including gas line and lamp heated substrate holder (OSRAM, 1000W). The composite targets FePt(BN, Ag, C) (reference composition) and FePt(BN/AlN, Ag, C) with two-inch-diameter were manufactured and used. In this study, half BN was replaced by AlN and compared the AlN replacement effects on magnetic properties and microstructure. Further, the MgO (100) single crystal was chosed to provide the stable baseline for the epitaxial growth of (001) textured FePt film. The MgO (100) substrate (HF-Kejing, 10x10x0.5mm) was heated at 470 °C (real sample surface temperature after calibration) for dry cleaning and then the magnetic layers with thickness of 15 nm were sputtered under an Ar working pressure of 10 mTorr at the same temperature by the composite targets. The deposition rate of FePt (BN, Ag, C) (15nm) and FePt (BN/AlN, Ag, C) (15nm) was 0.069 nm/s and 0.005 nm/s, respectively.

The crystal structure was measured using standard X-ray diffraction (XRD) (BRUKER, D8 Discover). The magnetization curves with in-plane and out-of-plane measured hysteresis loops were performed with a superconducting quantum interference device (SQUID) magnetometer (MPMS-XL). The sample microstructure was observed using transmission electron microscopy (TEM, JEOL JEM-2010).

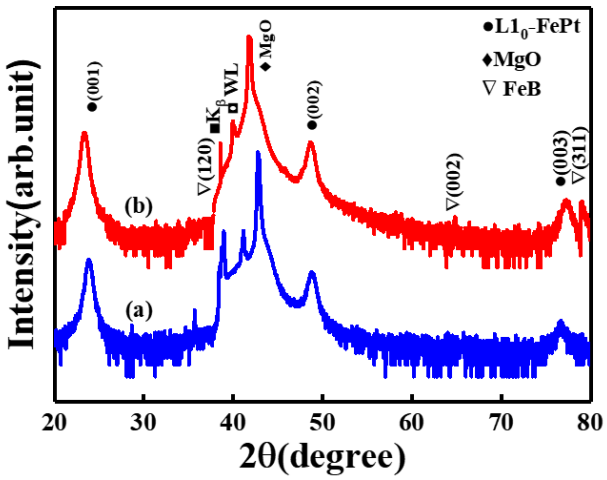

Fig. 1. XRD pattern of (a) FePt (BN, Ag, C) and (b) FePt (BN/AlN, Ag, C) films

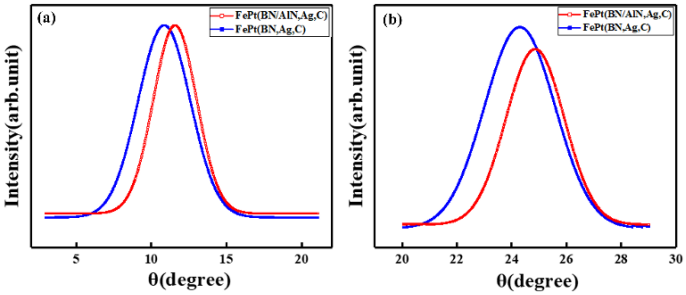

Fig. 2 Rocking curves of $L1_0$ FePt (a) (001), and (b) (002) diffraction peaks for FePt (BN, Ag, C) and FePt (BN/AlN, Ag, C) films

III. Results and Discussion

Figure 1 shows the x-ray diffraction (XRD) patterns of the FePt (BN, Ag, C) and FePt (BN/AlN, Ag, C) films presented by the log scale. The ordered FePt superlattice peaks presented by (001) and (003) and fundamental diffraction peaks presented by (002) were all indexed, and the MgO (002) peak from single crystal substrate and Cu K_β radiation (~38°) and tungsten (W) filament signal (~41°) from x-ray source tube were all observed apparently. For the soft magnetic phase, the disordered face-centered cubic (fcc) FePt (200) peak was almost neglected, and the FeB (120), (002) and (311) peaks were indexed in FePt(BN/AlN, Ag, C) film in Fig. 1(b). Figure 2 illustrates the $L1_0$-FePt (001)/(002) rocking curves, and the rocking width (full width of half maximum, FWHM, $\Delta\theta_{50}$) are 4.09°/3.03° and 3.94°/ 2.50° for reference film and FePt (BN/AlN, Ag, C) film, respectively, and the crystallinity and c-axis alignment of later is better. Due to the strong $L1_0$ FePt [001] texture, both films show high perpendicular magnetic anisotropy, with high perpendicular magnetization along the c-axis (out-of-plane) and low remanence in the film plane in Fig. 3. The FePt (BN/AlN, Ag, C) film shows a higher nucleation field (-5.67 > -2.53 kOe), magnetocrystalline anisotropy (1.84×10^7 >1.74×10^7 erg/cm^3), lower in-plane H_c (1.3<4.5 kOe) and hard-/easy-axis remanence ratio (0.073<0.121) than the reference sample. However, the FePt (BN/AlN, Ag, C) shows much lower out-of-plane H_c than the reference sample (16.7<31.7 kOe) and higher saturation magnetization (M_s, 544>502 emu/cm^3) and magnetic remanence (M_r, 479>462 emu/cm^3) due to the exchange-coupled hard-/soft-magnetic $L1_0$ FePt/FeB grains.

For the plane-view TEM images observed in bright field mode illustrated in Fig. 4, the reference and FePt(BN/AlN, Ag, C) films presented a typical granular microstructure where the core FePt grains were surrounded by the grain boundary materials (C, BN, AlN). These magnetic grain sizes have gauss

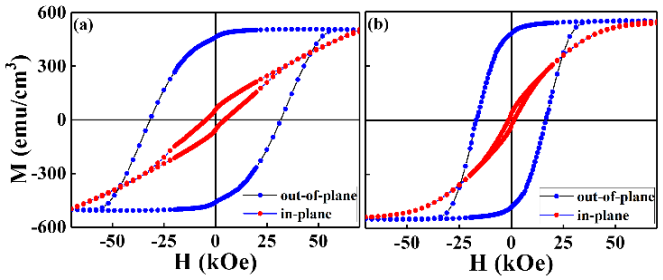

Fig. 3 Magnetic hysteresis loops measured out-of-plane and in-plane for (a) FePt (BN, Ag, C) and FePt (BN/AlN, Ag, C) films

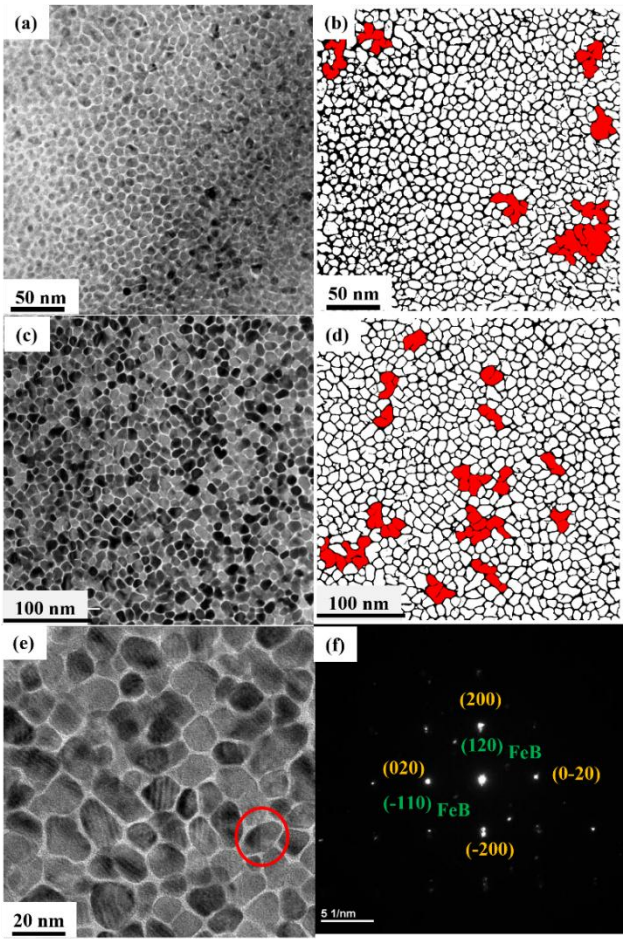

Fig. 4 The plane-view bright-field TEM images of (a) FePt(BN, Ag, C) film, (b) image segmentation of (a), (c) FePt(BN/AlN, Ag, C) film, (d) image segmentation of (c), (e) image with L10FePt-FeB grains (circle area), (f) nano-beam diffraction of circle area

distribution with average grains size <D> of 8.15 nm, and 10.8 nm, respectively, estimated by programming counting 823, and 867 grains. The distributed grains size was calculated by the standard deviation (σ) divided by the average grains size <D> with the values of 37.5 % and 33.7%. The averages of large numbers of grains were estimated by using the segmentation of TEM in-plane grains images, which was produced by the neuro network-like deep learning trained model (U-net). The highlighted grains belong to the interconnected L10 FePt grains in the reference sample and are supposed to be the FeB/L10 FePt exchange coupled grains in the FePt(BN/AlN, Ag, C) film, which has larger red areas.

To prove the FeB/$L1_0$ FePt) exchange-coupled grains, the nanobeam diffraction was performed on different grains in Fig. 5, and despite the $L1_0$ FePt {200} plane, the FeB (120) and (110) planes were also indexed in the nanobeam diffraction pattern in (b). Further, the negative formation energy (-0.38 eV/atom) of FeB also explained the formation tendency from thermodynamics.

References

[1] Jai-Lin Tsai*, Jhih-Hong Lin, Tsung-Yi Chen , Yu-Chun Lin , Li-Xiang Liu, Ming-Wei Hsieh, Jyun-you Chen, "Segregation effects of doped VN and ZrN on magnetic and microstructural characteristics of FePt-based films", Thin. Solid. Films 798, 140376-1-11 (2024).

Effect of MgTiO/ Pt-BN/ MgTiO underlayer on FePt-X grain size and distributions

Ajay Tiwari, Varaprasad Bollapragada, Huaixun Huyan, Nan Tang, Iwao Okamoto, and Ajan Antony, Mrugesh Desai, Ram Acharya

Western Digital Corporation, San Jose, California, 95119, USA,
vara.bollapragada@wdc.com

Thin films of highly ordered, tall $L1_0$-FePt with a small grain pitch distance are crucial to the development of heat-assisted magnetic recording (HAMR) media, a key technology in future data storage solutions. Recently, MgTiO and MgTiON is widely used as underlayer for FePt-X magnetic media, which plays crucial role in attaining a correct texture for magnetic media. In this paper we will discuss how the MgTiO/Pt-BN/MgTiO layer influences the microstructure of FePt magnetic layer as well as the texture.

I. Introduction

Heat-assisted magnetic recording (HAMR) technology has emerged as a promising solution for achieving higher data storage densities. A critical aspect of HAMR media design is the optimization of granular film structures to exhibit high grain aspect ratios (h/D > 1.5) and to maintain thermal stability up to approximately 600°C. Among potential materials, ordered $L1_0$-FePt has garnered significant attention due to its high magnetocrystalline anisotropy, which presents a desirable temperature dependence near its Curie transition. Ensuring a high signal-to-noise ratio (SNR) in HAMR applications which requires tall FePt grains, making the selection of a suitable grain boundary material (GBM) essential for attaining aspect ratios exceeding h/D = 1.5. Various amorphous GBMs, including carbon (C), TiO_2, SiO_2, and Cr_2Ox, have been explored to facilitate columnar growth, successfully pushing $L1_0$-FePt grain aspect ratios to approximately 2 [1, 2, and 3]. However, these materials often introduce challenges such as degraded FePt ordering, insufficient thermal stability, or suboptimal in-plane microstructures. Recently, FePt media incorporating boron nitride (BN) has demonstrated high aspect ratios (h/D ≈ 2.5) while maintaining strong thermal stability [4], positioning it as a promising candidate for HAMR media. This paper examines the structural and thermal properties of FePt-X on MTO underlayer and their potential for enhancing HAMR media performance.

II. Experimental

In this study, two FePt-based media stack configurations were deposited using an Anelva sputtering system: (1) glass substrate/buffer layer/seed layer/heat sink layer/MgTiO (MTO)/FePt-X and (2) glass substrate/buffer layer/seed layer/heat sink layer/MTO/Pt-BN(t)/MTO/FePt-X. The thickness of the inserted Pt-BN layer varied from 0 to 2 nm, allowing direct comparison with a control sample. Structural characterization was performed using standard X-ray diffraction (XRD) with a Copper-Kα source to analyze the film texture and order parameter. The microstructure of the samples was evaluated by in-plane and cross sectional transmission electron microscopy (TEM) imaging by using FEI Ticnai 200. Various analytical techniques including bright-field TEM (BF-TEM), high-resolution TEM (HR-TEM), and scanning TEM-high angle annular dark field (STEM-HAADF) were used . The grain size and grain center-to-center pitch distances were analyzed using the in-plane STEM-HAADF images using NIMS image processing analysis software [5]. The magnetic moment (M) vs. field (H) curves of the film samples were measured with a polar Kerr method.

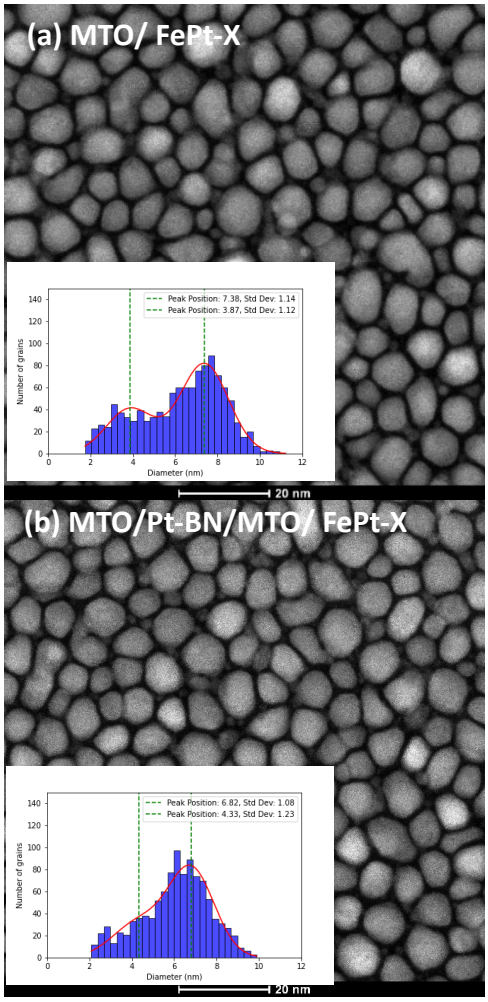

Fig 1. a) HR-STEM micrograph of MTO/FePt-X and b) HR-STEM micrograph of MTO/ Pt-BN/FePt-X (with grain size distributions

III. DISCUSSION

Plan view STEM micrograph shown in Fig. 1 (a) is the sample with MTO/ FePt-X (11 nm), While Fig. 1 (b) shows the MTO/Pt-BN/ MTO FePt-X (11nm). All the samples showed well isolated FePt grains surrounded by segregant. All the films showed a single-layer structure from cross sectional view. The cross-section shows columnar 11 nm tall grains which is showed in Fig 2. Fig. 2 shows the cross-sectional view of (a) is the sample with MTO/ FePt-X (11 nm), While (b) shows the MTO/Pt-BN/ MTO FePt-X (11nm). There are no secondary grains are observed, suggesting that these films have aspect ratio 1.5 and 1.6 respectively. In the case of MTO underlayer we have observed two distinct peaks at 7.3 and 3.8nm in the grain size distribution whereas in the case of MTO/ Pt-BN/ MTO case one prominent peak at 6.83 nm. It suggests the nucleation behavior on the Pt-BN inserted underlayer is very different from control sample. We will discuss in detail how Pt-BN layer insertion modified the underlayer using elemental mapping from TEM analysis and XRD.

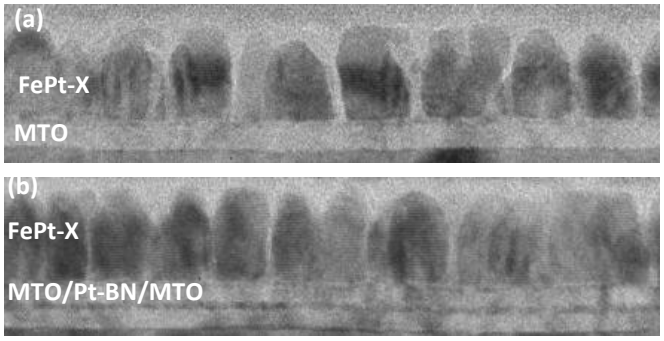

Fig 2. a) BF-TEM micrograph of MTO/FePt-X and b) BF-TEM micrograph of MTO/ Pt-BN/FePt-X

REFERENCES

[1] Y. Kubota et al., "Heat-Assisted Magnetic Recording's Extensibility to High Linear and Areal Density," IEEE Transactions on Magnetics, vol. 54, no. 11, Nov. 2018 (2018).

[2] A. Perumal, Y.K. Takahashi, K. Hono, "$L1_0$ FePt-C Nanogranular Perpendicular Anisotropy Films with Narrow Size Distribution", Appl. Phys. Express 1 101301 (2008).

[3] B. S. D. C. S. Varaprasad, M Chen, YK Takahashi, K Hono "Ordered FePt-Based Perpendicular Magnetic Recording Media for Magnetic Recording" IEEE transactions on magnetics 49 (2), 718-722 (2013)

[4] C. Xu, B. Zhou, T. Du, B.S.D.C.S. Varaprasad, D.E. Laughlin, J.-G. Zhu, Understanding the growth of high-aspect-ratio grains in granular L10-FePt thin-film magnetic media, APL Materials. 10 (2022).

[5] N. Kulesh, A. Bolyachkin, I. Suzuki, Y.K. Takahashi, H. Sepehri-Amin, K. Hono, Data-driven optimization of FePt heat-assisted magnetic recording media accelerated by deep learning TEM image segmentation, Acta Mater. 255, 119039 (2023)

Utilizing the Transversal Encoder with Modified PRML Detection for Dual-Layer Magnetic Recording

Anawin Khametong[1], Simon J. Greaves[2], and Chanon Warisarn[1]

[1]School of Integrated Innovative Technology, King Mongkut's Institute of Technology Ladkrabang, Bangkok 10520, Thailand
[2]Research Institute of Electrical Communication (RIEC), Tohoku University, Sendai 980-8577, Japan

Dual-layer magnetic recording, which contains two discrete recording layers, can support very high data densities compared to current technologies. However, this technology has to contest with inter-layer interference (ILI), which significantly affects the accuracy of data signal detection. Therefore, this work presents a signal processing technique in which written tracks in the lower layer are wider than those in the upper layer. In addition, we developed a transversal coder to reduce the impact of ILI and increase detection efficiency. A comparative evaluation of the bit error rate (BER) and signal-to-noise ratio between the proposed systems and a conventional recording system showed that our proposed systems can provide significantly lower BER.

***Index Terms*— 3D magnetic recording, interlayer interference, modified Viterbi detector.**

I. Introduction

To manage massive amounts of data efficiently, high-density storage devices are essential. Technologies like two-dimensional magnetic recording [1], heat-assisted magnetic recording [2], and microwave-assisted magnetic recording [3] have been implemented to surpass the superparamagnetic limitations of conventional recording technology. Dual-layer magnetic recording (DLMR) [4] is also an ultra-high-density recording technology, in which a second recording layer is added to increase capacity, but faces the problem of inter-layer interference (ILI). Therefore, advanced signal processing is needed to mitigate ILI and improve data estimation accuracy. While partial response maximum likelihood (PRML) [5] is widely used in magnetic recording systems, conventional implementations are inadequate for handling ILI. Developing improved interference reduction/suppression techniques, specialized encoding schemes, and enhanced decoding capabilities are therefore crucial. This research presents a dual-layer magnetic recording structure with wider tracks on the lower layer, combining 1D PRML processing with transversal coding that maps bit relationships between layers to specific signal magnitudes (+2, −2, 0). Using this proposed media structure leads to efficient mitigation of ILI through modified Trellis detection, which is designed according to the encoding scheme. Bit error rate (BER) measurements across various signal-to-noise ratio (SNR) levels confirm that our system significantly outperforms conventional single-layer magnetic recording systems.

II. Media Structure

DLMR technology is developed by stacking recording layers, with each layer designed using a discrete Voronoi model [6] to achieve realism. This study examines the impacts of transition noise and three-dimensional interference. This includes inter-symbol interference (ISI) and inter-track interference (ITI) within each recording layer, as well as inter-layer interference (ILI) between the magnetic recording layers. Fig. 1 illustrates the structure of the dual-layer magnetic recording media. Fig. 1(a) shows a top view where the lower recording layer has wider tracks than the upper recording layer, while the track in the upper recording layer is offset to the center of the lower recording layer track. Both recording layers have adjacent tracks, with the read head positioned at the center of both recording layer tracks. Fig. 1(b) depicts the offset between transitions in the two recording layers, which was half the bit length (BL) in the down-track direction, with BL in both recording layers set at 22 nm. Fig. 1(c) shows that the track pitch (TP) of RL2 was 14.75 nm, while RL1 had a TP twice that of RL2 at 29.5 nm, resulting in areal densities of 1 Tb/in² and 2 Tb/in² for RL1 and RL2, respectively.

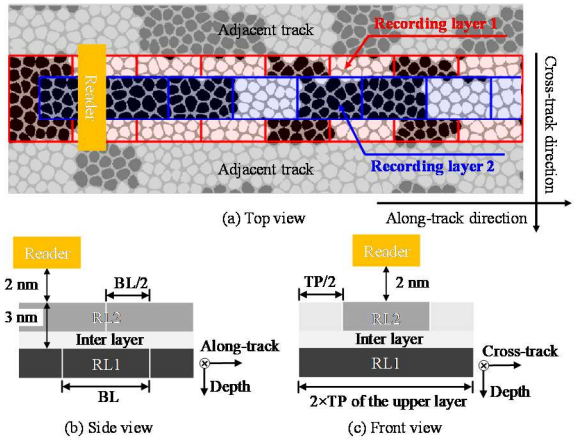

Fig. 1. Structure of dual-layer magnetic recording media in (a) top, (b) side, and (c) front views, respectively.

III. Signal Processing

A. Partial response maximum likelihood detection

Fig. 2(a) shows the channel model of the DLMR system. The process begins with recording user bits, $a_k^{(2)}$ and $a_k^{(1)}$, onto the upper and lower recording layers, respectively, under perfect writing. Subsequently, the one-dimensional partial response maximum likelihood (1-D PRML) detection system, comprising a 1-D equalizer and a 1-D detector, such as the 1-D Viterbi algorithm, is used for signal processing. The process starts by receiving the continuous-time signal, r_t, which passes through a low-pass filter before the sampling process.

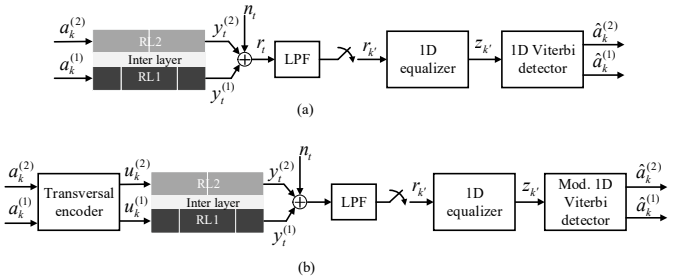

Fig. 2. Schematic of signal processing channels for dual-layer magnetic recording (a) 1D PRML and (b) transversal encoder with modified 1D PRML.

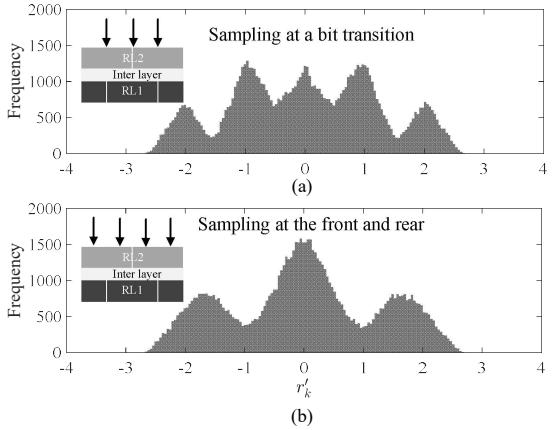

Fig. 3. Sampling position and distribution of readback signal data samples under SNR = 14 dB where (a) the sampling point begins at position BL/2 and (b) the sampling point is at position BL/4.

The discrete-time signal, r_k , is obtained using the oversampling technique at a rate of BL/2. We first consider the case of the sampling point at the bit transition, as shown in Fig. 3(a). Data from both recording layers is converted into a discrete data signal sequence, which can be classified into five groups. This signal-processing approach corresponds to partial response class 2 (PR2) with coefficients [1 2 1]. Therefore, the 1D equalizer and 1D detector can be designed to match PR2 to detect data from both the upper and lower recording layers within the same data sequence. However, this processing method cannot effectively reduce the effects of ILI.

B. Transversal encoder with modified PRML detection

As noted above, 1D PRML cannot efficiently process signals due to ILI. We, therefore, present a transversal encoder approach combined with modified PRML detection, as shown in Fig. 2(b). The user bits are sent through the traversal encoder before being recorded in the media. For user bits $a_k^{(2)}$ (upper layer) and $a_k^{(1)}$ (lower layer) at position k, the encoding follows specific rules: when $a_k^{(2)}$ is '+1' and if we need to record '+1' at position k-1 in the lower layer, the upper layer bit must be '+1', yielding a combined signal of '+2'. If position k-1 has '−1,' the upper bit must be '−1,' resulting in '−2.' However, if position k has '−1' status, the upper bit must be opposite to the previous lower layer state, yielding '0.' During reading, signals of '+2' or '−2' are decoded as '+1' bits, while '0' is decoded as '−1'. The signal is also oversampled at BL/2 rate, where the starting point is at BL/4 or the front and rear half, creating the pattern shown in Fig. 3(b). Though signals are distributed into three groups due to various interference types and noise, a 1D equalizer and detector can be designed explicitly for these encoded data. Then, using a modified trellis diagram that aligns with the data distribution can significantly improve the detection accuracy.

IV. Simulation Result and Conclusion

We compared our proposed systems with a single-layer (SL) magnetic recording system with TP and BL of 18 nm and 12 nm, yielding an areal density of 3 Tb/in^2 using 1D PRML processing. Performance evaluation involved comparing BER at various SNRs. The proposed systems include DL-1D PRML and DL-Trans-w-Mod. 1D PRML. These were compared with an SL system SL-1D PRML, as shown in Fig. 4. The results demonstrate that our proposed 1D PRML systems significantly outperformed conventional systems. Furthermore, the dual-layer system with transversal encoding and modified PRML achieved BER as low as 10^{-4}. Therefore, we can summarize that using a dual-layer approach with wider tracks in the lower recording layer combined with 1D PRML signal processing is possible. Moreover, transversal encoding and modified PRML detection can effectively mitigate the effects of ILI.

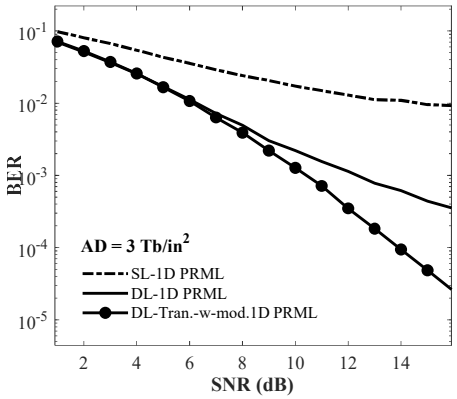

Fig. 4. BER performance comparison as a function of SNR for various recording systems.

Acknowledgments

This project is funded by School of Integrated Innovative Technology, grant number 2568-02-10-003, King Mongkut's Institute of Technology Ladkrabang, Thailand.

References

[1] R. H. Victora et al., "Two-dimensional magnetic recording at 10 Tbits/in^2," in IEEE Trans. Magn., vol. 48, no. 5, pp. 1697-1703, May 2012.
[2] R. E. Rottmayer et al., "Heat-assisted magnetic recording," in IEEE Trans. Magn., vol. 42, no. 10, pp. 2417-2421, Oct. 2006.
[3] J. -G. Zhu, X. Zhu, and Y. Tang, "Microwave-assisted magnetic recording," in IEEE Trans. Magn., vol. 44, no. 1, pp. 125-131, Jan. 2008.
[4] Y. Nakamura et al., "A study of three-dimensional equalization for reproducing a double-layer magnetic recording medium," in IEEE Trans. Magn., vol. 58, no. 8, pp. 1-4, Aug. 2022, Art no. 3101804.
[5] J. Moon and W. Zeng, "Equalization for maximum likelihood detectors," in IEEE Trans. Magn., vol. 31, no. 2, pp. 1083-1088, Mar. 1995.
[6] M. Yamashita et al., "Read/write channel modeling and two-dimensional neural network equalization for two-dimensional magnetic recording," in IEEE Trans. Magn., vol. 47, no. 10, pp. 3558-3561, Oct. 2011.

Inter-Layer Interference (ILI) Suppression in Dual-Layer Bit-Patterned Magnetic Recording Systems

Natthakan Rueangnetr[1], Santi Koonkarnkhai[2], Simon John Greaves[3], and Chanon Warisarn[1]

[1]School of Integrated Innovative Technology, King Mongkut's Institute of Technology Ladkrabang, Bangkok, Thailand
[2]Faculty of Science and Technology, Nakhon Pathom Rajabhat University, Nakhon Pathom, Thailand
[3]Research Institute of Electrical Communication (RIEC), Tohoku University, Sendai 980-8577, Japan

Dual-layer bit-patterned magnetic recording (DL-BPMR) systems are promising for achieving higher areal densities. However, they face significant challenges, including inter-symbol interference (ISI), inter-track interference (ITI), and inter-layer interference (ILI). To address these issues, this work proposes integrating a sum-soft-information (SSI) technique and an ITI suppression method to enhance detection reliability. The SSI technique is initially used to improve the reliability of the log-likelihood ratio for the bottom layer signal by leveraging the mutual information derived from a staggered array reader configuration. The enhanced data sequence from the bottom layer is subsequently utilized to suppress ILI by applying a weighting before it is subtracted from the top layer readback signals. Simulation results demonstrate that the proposed method significantly improves bit error rate (BER) performance compared to conventional single-layer and dual-layer BPMR systems, particularly at a user density of 4.0 Tb/in^2, making it a promising approach for next-generation high-density magnetic recording.

***Index Terms*—Dual-layer bit-patterned magnetic recording, Sum soft-information, Interlayer interference suppression**

I. Introduction

To achieve ultra-high areal density (AD) in bit-patterned magnetic recording (BPMR), reducing bit island and track spacing is necessary, but this leads to increased inter-symbol interference (ISI) and inter-track interference (ITI), which degrades detection performance. To overcome these limitations, dual-layer BPMR (DL-BPMR) has been introduced by stacking two magnetic layers on a single platter, potentially doubling the AD up to 10 Tb/in^2 [1-2]. Each layer independently stores data using arrays of magnetic islands, enabling three-dimensional data recording. However, simultaneous reading of both layers introduces a new challenge—inter-layer interference (ILI)—caused by magnetic field interactions between the layers. While advanced detection techniques like one-dimensional (1D) and two-dimensional (2D) partial response maximum likelihood (PRML) [3-4] have been used to mitigate ISI and ITI, they are insufficient to suppress ILI, especially at higher densities.

To address this issue, this study proposes a sum-soft-information (SSI) technique to enhance the reliability of the bottom layer data by aggregating log-likelihood ratios (LLRs) information from adjacent tracks through an optimized array reader configuration. This setup not only improves the effectiveness of the bottom layer detection but also reduces ITI and ILI in the upper layers by positioning the read heads closer together to increase the relationship of the mutual information, as illustrated in Fig. 1. Once the bottom layer data is refined using the SSI method, it is then fedback to subtract interference from the top layer readback signals, thereby improving the overall system performance.

Simulation results demonstrate that the proposed approach significantly outperforms both conventional single-layer BPMR (SL-BPMR) and standard DL-BPMR systems, particularly at a user density of 4.0 Tb/in^2 (2.0 Tb/in^2 per layer), confirming its effectiveness for high-density magnetic recording.

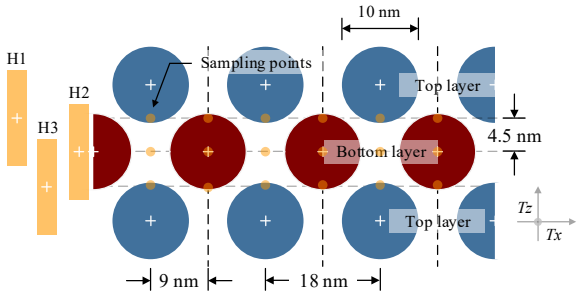

Fig. 1. Illustration of the bit-island arrangement in both top and bottom layers, sampling points, and the array reader's placement.

II. Proposed Systems

This study presents a DL-BPMR system where bit islands are arranged in a regular grid across two layers, with the top layer islands staggered relative to the bottom layer, achieving a total areal density of 4.0 Tb/in^2, as illustrated in Fig. 1. Consider the DL-BPMR channel model in Fig. 2, binary input data sequences, $a_{m,k}$ of the m-th track and the k-th bit, $m \in \{1,2,3\}$, are recorded onto media where the odd and even data sequences are recorded onto the top and bottom layers, respectively. An array of three read-heads consisting of H1, H2, and H3 are used to retrieve all three data tracks simultaneously. The middle head is positioned at the track center of the bottom layer. At the same time, the centers of the adjacent heads are placed between the bottom and top layer tracks to reduce ITI and ILI effects and enhance mutual information correlation of the bottom layer.

Three readback signals are immediately retrieved and oversampled at a sampling period $T_x/2$, as shown in Fig. 1, where T_x is the bit pitch. Path-A, the discrete-time data sequences, $r_{1,k}$, $r_{2,k}$, and $r_{3,k}$ are first sent through the 1D equalizers and 1D soft-output Viterbi algorithm (SOVA) detectors to generate soft-output LLRs of the first to the third tracks, $\lambda_{1,k}$, $\lambda_{2,k}$, and $\lambda_{3,k}$, respectively.

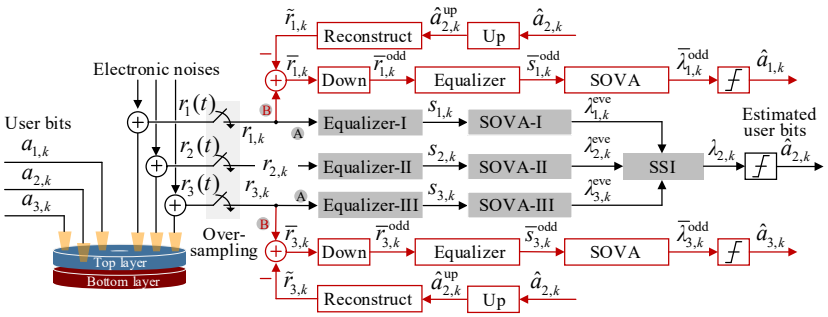

Fig. 2. The proposed dual-layer BPMR channel model incorporates the SSI technique and the reproduced readback signal.

However, only the LLRs in the even position of all three SOVAs, i.e., $\lambda_{1,k}^{\text{eve}}$, $\lambda_{2,k}^{\text{eve}}$, and $\lambda_{3,k}^{\text{eve}}$, which are the mutual information of the bottom layer, are sent to SSI to estimate the highest LLR reliability of the bottom layer using the following equation:

$$\lambda_{2,k} = \lambda_{1,k}^{\text{eve}} + \lambda_{2,k}^{\text{eve}} + \lambda_{3,k}^{\text{eve}}. \quad (1)$$

This LLR is then passed to the threshold detector to produce the estimated user bits of the bottom layer, $\hat{a}_{2,k}$. Note that even if all three SOVAs can generate all possible LLRs in odd and even positions, information from the odd positions will be disregarded. After obtaining the estimated user bits of the bottom layer, consider Path-B; the estimated user sequence will be inserted with zeroes at the odd position to have the upsample sequence, $\hat{a}_{2,k}^{\text{up}}$. The reconstructed data sequences of the first and the third tracks can be generated from the following equations:

$$\tilde{r}_{1,k} = \mathbf{h}_1 * \hat{a}_{2,k}^{\text{up}} \text{ and } \tilde{r}_{3,k} = \mathbf{h}_3 * \hat{a}_{2,k}^{\text{up}}, \quad (2)$$

respectively, where $\mathbf{h}_1$ and $\mathbf{h}_3$ are the channel coefficients related to the positions of the first and the third read heads. These two reconstructed data sequences are then subtracted from the mixed data sequence through the following equations:

$$\overline{r}_{1,k} = r_{1,k} - \alpha\tilde{r}_{2,k} \text{ and } \overline{r}_{3,k} = r_{3,k} - \alpha\tilde{r}_{2,k}, \quad (3)$$

where α is a weighting factor. These sequences are then downsampled again by deleting the data samples at the even positions. This gives us the estimated raw data sequences of the top layer, i.e., $\overline{r}_{1,k}^{\text{odd}}$ and $\overline{r}_{3,k}^{\text{odd}}$. Finally, the predesigned 1D PRML detectors can be applied to process the top layer's estimated raw data sequences for better BER performance.

III. Simulation Results

Fig. 3 illustrates the BER performance of the various recording systems as a function of SNR at a total areal density of 4.0 Tb/in^2. Here, SL-1D PRML represents the single layer media operated under conventional 1D PRML. DL-top/bot-H1-3 represents the dual media layer where the top and bottom layers are read using H1 to H3, respectively. This system operates similarly to our proposed system but has no SSI or ILI suppression techniques. DL-bot-H2-SSI is the system that uses only the SSI technique to improve the performance of the bottom layer. DL-top-H1-3-ILI-sup represents our proposed system in adopting SSI and ILI suppression techniques. As shown in Fig. 3, the single layer system did not perform well due to the severity of ITI and ISI at high areal density. The conventional DL-BPMR can provide better BER than a single-layer system. Both top layer tracks also yield better BER than the middle track, which is the bottom layer. This is not surprising: since the bottom layer is farther from the read head we obtained a poor readback signal. However, we can improve the BER by utilizing the SSI technique, which can reduce the BER by an order of magnitude at higher SNR. Moreover, at BER=10^{-4}, the BER performance of the top layer can be improved by more than 1.5 dB over the system without the proposed ILI suppression technique. These results reveal that our proposed system is well-suited for high-density magnetic recording.

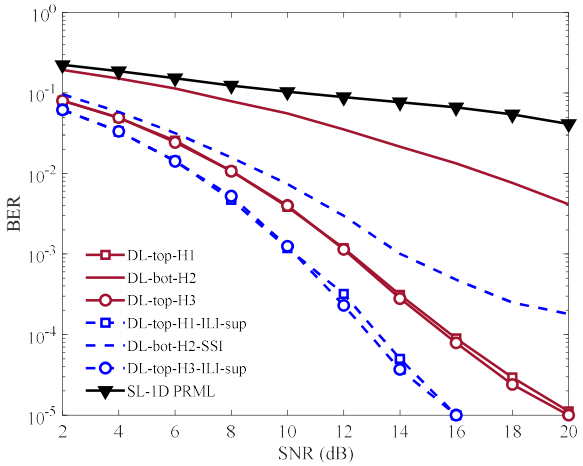

Fig. 3. Comparison of BER performance of SL- and DL-BPMR systems.

Acknowledgments

This work is supported by King Mongkut's Institute of Technology Ladkrabang [KREF046705], Thailand.

References

[1] S. J. Greaves and Y. Kanai, "Three dimensional magnetic recording," 2023 IEEE 34th Magnetic Recording Conference (TMRC), Minneapolis, MN, USA, 2023, pp. 1-2.

[2] A. Khametong and C. Warisarn, "A study of iterative signal processing schemes for double-layered bit-patterned recording," IEEE Trans. on Magn., doi: 10.1109/TMAG.2024.3402184.

[3] P. Kovintavewat et al., "Generalized partial response targets for perpendicular recording with jitter noise," IEEE Trans. Magn., vol. 38, no. 5, pp. 2340–2342, Sept. 2002.

[4] S. Karakulak, P. H. Siegel, J. K. Wolf and H. N. Bertram, "Joint-track equalization and detection for bit patterned media recording," in IEEE Trans. on Magn., vol. 46, no. 9, pp. 3639-3647, Sept. 2010.

A Study on the Fitness of GA for Improving SP Decoding Performance

Madoka Nishikawa[1], Yasuaki Nakamura[1], Yasushi Kanai[2], and Yoshihiro Okamoto[1]

[1] Graduate School of Science and Engineering, Ehime University, Matsuyama, 790-8577, Japan {nishikawa.madoka.vi, nakamura.yasuaki.mj, okamoto.yoshihiro.mj}@ehime-u.ac.jp
[2] Department of Engineering, Niigata Institute of Technology, Kashiwazaki, 945-1195, Japan, kanai@iee.niit.ac.jp

We study low-density parity-check (LDPC) coding and iterative decoding methods for shingled magnetic recording (SMR) in ultra-high-density hard disk drives (HDDs). Previously, we applied a neural network to evaluate the log-likelihood ratios (LLRs) related to row operations in the sum-product (SP) decoder for LDPC code. Then, we updated the LLR considering the influence of noise depending on the recording pattern by providing the LLRs for the decoding target and its adjacent bits to the neural network in SP decoding. Furthermore, we explored the optimal parameters to update the LLRs by applying the genetic algorithm (GA). In this study, to explore more optimal update parameters, we propose the fitness to enhance the accuracy of selecting the LLR to be updated and the number of update targets. Then, we aim to improve the performance of SP decoding based on the GA results. As a result, applying the proposed fitness to GA remains in high selection accuracy and increases the number of updating targets in SP decoding. Also, it achieves error-free performance with fewer iterations of turbo equalization compared to the conventional fitness.

***Index Terms*— Genetic algorithm (GA), low-density parity-check (LDPC) code, neural network, shingled magnetic recording (SMR), sum-product (SP) decoding.**

I. Introduction

In recent years, the explosive increase in data volume has required even higher-density hard disk drives (HDDs). Therefore, we are focusing on the shingled magnetic recording (SMR) [1], which enhances perpendicular magnetic recording (PMR), and developing signal processing methods. We studied the performance improvement of low-density parity-check (LDPC) coding and iterative decoding methods in SMR [2]. In the SMR, due to narrow tracks, signal processing methods are required to reduce the influence of inter-track interference (ITI) and signal-dependent noise like transition jitter. We have achieved the reduction of the effects of ITI by applying a two-dimensional finite impulse response (TD-FIR) filter [3]. Also, to consider the influence of signal-dependent noise, we proposed the sum-product (SP) decoder in which a neural network evaluates the log-likelihood ratio (LLR) related to row operations using the LLRs of the decoding target bit and its adjacent bits and updates the LLR based on the neural network outputs [4]. Furthermore, we showed that a genetic algorithm (GA) is useful to explore updating parameters such as the thresholds and weights in the neural network.

In this study, to explore more optimal update parameters, we propose the fitness to enhance the selection accuracy of the LLR to be updated and the number of update targets. Then, we aim to improve the performance of SP decoding based on the GA results.

II. Read/Write System

Figure 1 shows the block diagram of the SMR read/write (R/W) system with the LDPC coding and iterative decoding. The system assumes the areal recording density of 4 Tbit/inch^2. The R/W consists of the granular media and heads with R/W sensitivity function shown in [5]. In addition, the system noise defined by signal-to-noise ratio (SNR) is added at the reading point as assuming the electrical noise due to the head amplifier and read head, and is defined by $\mathrm{SNR}_S = 20\log_{10}(A/\sigma_s)$ [dB],

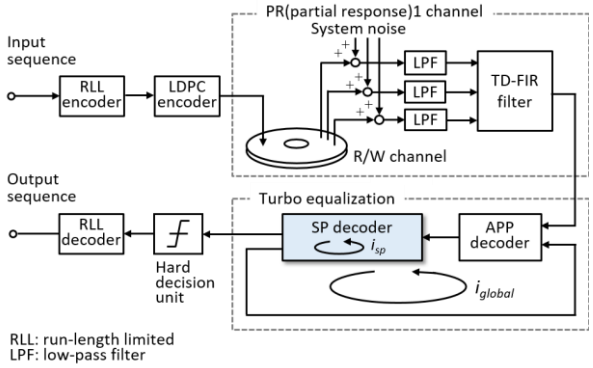

Fig. 1 The block diagram of SMR R/W system with the LDPC coding and iterative decoding.

where A is the positive saturation level of the waveform reproduced from an isolated magnetic transition and σ_s is the root-mean-square (RMS) value of the system noise in the bandwidth of the the channel bit rate f_c. The turbo equalization works between an a posteriori probability (APP) decoder and an SP decoder iteratively, where i_{sp} stands for the maximum number of iterations in the SP decoder, and i_{global} stands for the turbo equalization. Then, the bit error rate (BER) is obtained by comparing the input sequence with the output sequence.

III. Simplification of Neural Network by HGA

The SP decoding performs based on a parity check matrix and consists of row operations, parity checks, iterative decoding checks, column operations, extrinsic value operations, and posterior value operations. In this study, we employ an LDPC code defined by the parity check matrix with a code length of 4,096 bytes, a column weight of 3, and a row weight of 30, so the SP decoder calculates 3 LLR sequences. Similar to [4], we focus on $\ln \gamma_k^n$, the LLR related to the row operation. γ_k^n denotes the transition probability from the previous point to the current point on the trellis diagram [6]. Figure 2 shows the relationship between the parity check matrix and the neural network configuration. Here, for simplicity, a case is illustrated in which the code length is 12, the column weight is 3, and the

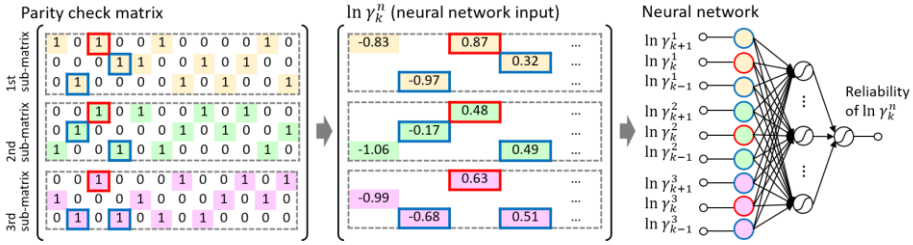

Fig. 2 Relationship between the parity check matrix and the neural network configuration.

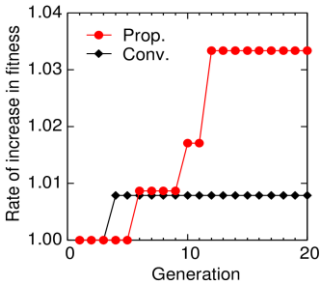

Fig. 3 Rate of increase in fitness.

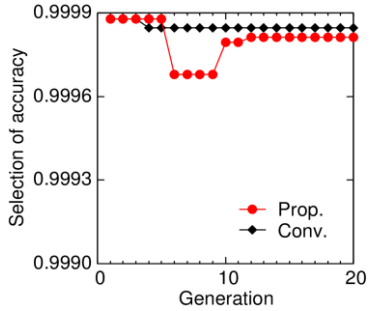

Fig. 4 Selection accuracy of the LLR to be updated.

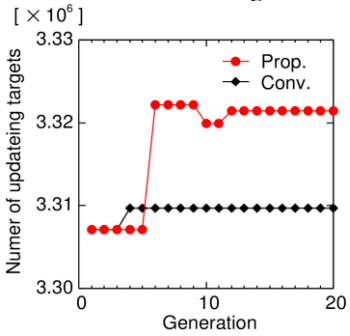

Fig. 5 Number of updating targets.

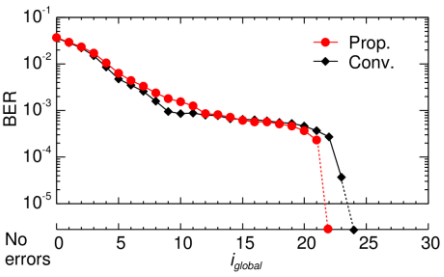

Fig. 6 BER performance for i_{global}.

row weight of 4. The neural network calculates the reliability of ln γ_k^n using the ln γ_{k-1}^n, ln γ_k^n, and ln γ_{k+1}^n. Furthermore, we apply the following parameters $TH_{\gamma m}$ and $W_{\gamma m}$ ($m = 0$ to 3) for updating ln γ_n according to decoding patterns provided the hard decision of reliability of ln γ_k^n. Here, m is the decoding pattern number. The decoding patterns in the cases of m = 0, 1, 2, and 3 correspond to "000" or "111", "001" or "110", "011" or "100", and "010" or "101", respectively. When the reliability, ln γ_k^n is greater than $TH_{\gamma m}$ or smaller than $(1 - TH_{\gamma m})$, it is multiplied by $W_{\gamma m}$. In the proposed GA, the fitness of the l-th individual on the δ-th generation is defined by $f_{\delta l} = -\log_{10}\left(N_{te}^{\delta l}/N_t^{\delta l}\right) - C_{\delta l}\log_{10}\left(1 - N_t^{\delta l}/N_{all}^{\delta l}\right)$. $N_t^{\delta l}$ and $N_{te}^{\delta l}$ are the number of updated targets and the number of update errors, respectively. $N_{all}^{\delta l}$ is the total number of LLRs in row operations. $C_{\delta l}$ is the coefficient that determines the degree to which the number of updates is reflected. We arrange $TH_{\gamma m}$, $W_{\gamma m}$, and $C_{\delta l}$ in one dimension as one chromosome and perform the selection, crossover, and mutation [4]. However, the individuals with the highest fitness are left by applying the elitist preserving selection. We also employ the GA to efficiently explore the optimal weights to enhance the LLRs in column operations and extrinsic information [7].

IV. Performance Evaluation and Conclusion

Now, we compare the performance of the best individuals obtained by the GA. Figure 3 shows the rate of increase in fitness relative to the first generation. Figures 4 and 5 show the selection accuracy of the LLR to be updated and the number of updating targets for generations, respectively. We set i_{sp}= 20, i_{global} = 20, and SNR_S = 21.0 dB. The mark of the red circle indicates the case of the proposed fitness in this study. The mark of the black diamond indicates the case of conventional fitness in [4]. From Fig. 3, the rate of increase in the proposed fitness is greater than the conventional one after the 6th generation. From Figs. 4 and 5, the update accuracy of the proposed fitness is slightly lower than the conventional one, but the overall selection accuracy remains high. On the other hand, the number of updating targets in the proposed fitness remains higher than that in the conventional one after the 6th generation. Figure 6 shows the BER performance for i_{global}. We set i_{sp}= 20 and SNR_S = 21.0 dB. The marks are the same as the previous figures. From Fig. 6, the proposed fitness achieves error-free performance at fewer i_{global} compared to the conventional fitness. From the above, when we employ the GA, setting the fitness to enhance the selection accuracy of the LLR to be updated and the number of updating targets is useful for improving SP decoding performance.

Acknowledgment

This work was supported by the Advanced Storage Research Consortium (ASRC), Japan, and Grants-in-Aid for Scientific Research (No. 22K14259), Japan.

References

[1] R. Wood et al., "The feasibility of magnetic recording at 10 terabits per square inch on conventional media," *IEEE Trans. Magn.*, vol. 45, no. 2, pp. 917–923, Feb. 2009.

[2] R. G. Gallager, "Low-density parity-check codes," *IRE Trans. Inform. Theory*, vol. 8, pp. 21–28, Jan. 1962.

[3] Y. Nakamura et al., "Suppression of ITI by array head reading and 2D-equalization," *AIP Advances*, vol. 7, no. 5, pp. 056509-1–056509-5, Feb. 2017.

[4] M. Nishikawa et al., "Improvement of SP decoding considering the influence of recording patterns by neural network," *IEEE Trans. Magn.*, vol. 60, no. 9, 3100405, Sept. 2024.

[5] Y. Nakamura et al., "Suppression of ITI by array head reading and 2D-equalization," *AIP Advances*, vol. 7, no. 5, pp. 056509-1–056509-5, Feb. 2017.

[6] P. Robertson et al., "A comparison of optimal and sub-optimal MAP decoding algorithms operating in the log domain", *Proc. IEEE Int. Conf. Commun* (*ICC 1995*), pp.1009–1013, Seattle, USA, June 1995.

[7] M. Nishikawa et al., "A study on applying GA for performance improvement of SP decoder in SMR," *AIP Advances*, vol. 15, 035004, Mar. 2025.

A High-speed and High-reliable Fully Digital STT-MRAM Based Computing-in-Memory for Binary Neural Network

Yongcheng Wang[1], Tao Li[2], Li Zhang[2], and Tetsuo Endoh[1,2], *Fellow, IEEE*

[1]School of Engineering, Tohoku University, Sendai, 980-8577, Japan, wang.yongcheng.p7@dc.tohoku.ac.jp
[2]Center for Innovative Integrated Systems, Sendai, 980-0845, Japan, tetsuo.endoh.b8@tohoku.ac.jp

This work proposes a novel STT-MRAM based Computing-in-Memory (CiM) cell architecture for binary neural network that addresses the reliability limitations inherent in prior analog STT-MRAM CiM designs, which suffer from low resistance and limited tunnel magnetoresistance (TMR) in magnetic tunnel junctions (MTJs). The proposed CiM technique introduces key enhancements: (1) accelerated computation via a differential-type memory configuration; (2) improved tolerance to TMR variation through a fully digital scheme that decouples storage and computation (3) reduced power consumption owing to the high-speed computing that makes longer no power standby durations. With SPICE simulations, it is shown that the novel CiM brings over a 50% reduction in computation latency, enhanced robustness to TMR fluctuations, and a 26.2% decrease in computation power consumption at a supply voltage of 1.2 V.

***Index Terms*— Computing-in-memory (CiM), spin-transfer torque magnetic random access memory (STT-MRAM), high-speed and high-reliable, low-power, binary neural network (BNN).**

I. Introduction

Spin-torque-transfer magnetic random access memory (STT-MRAM) has advantages of low power, high endurance, etc., that considered as an ideal candidate for computing-in-memory (CiM). Existing STT-MRAM based CiM architectures predominantly employ analog multiply-accumulate operations using the intrinsic characteristics of magnetic tunnel junctions (MTJs) [1]-[3]. However, these analog designs are challenged in terms of reliability and readout latency due to the low TMR of MTJs [2]. In contrast, a digital CiM design introduced in [4] utilizes a counter-based accumulation mechanism, improving computational accuracy by avoiding current-sum or capacitor-sum methods. However, the method proposed in [4] still employs an analog computing approach for the multiplication operation, which suffers from the same issue reported in [2].

To overcome these constraints, the proposed work introduces a fully digital STT-MRAM based CiM cell for binary neural network (BNN) applications. This architecture achieves complete digitalization in both multiplication and accumulation, thereby significantly enhancing computation reliability, latency and thus a power reduction.

II. Proposed STT-MRAM based digital CiM architecture

The proposed CiM cell structure, shown in Fig. 1, comprises seven NMOS transistors and two MTJs. The upper sub-circuit adopts a 4-transistor-2-MTJ differential-type STT-MRAM configuration [5], while the lower portion incorporates an XNOR logic circuit tailored for BNN operations. Transistors M5 and M6 implement the XNOR logic, and M7 functions as an output switch. During idle states, the output node (OUT) is precharged to V_{DD} using an external and shared switch.

For BNN processing, weight data are written into the MTJs via BL/BLB lines. During standby periods, the power line (PL) is power gated to minimize leakage. Upon activation, the PL restores stored weight data from the MTJs to the internal nodes Q and QB, which govern M5 and M6. The activation inputs IN and INB subsequently determine the state of OUT, which either remains high or discharges, representing logical '1' or '0', respectively.

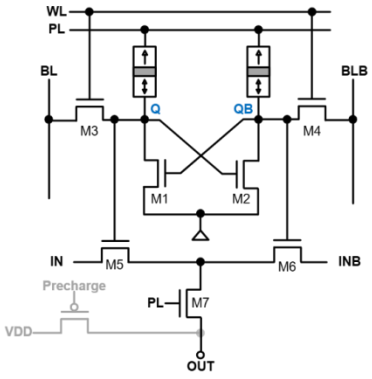

Q/QB	IN/INB	OUT
0/1	0/1	1
0/1	1/0	0
1/0	0/1	0
1/0	1/0	1

Fig. 1. Proposed CiM cell structure and the XNOR operand table.

III. Evaluation and benchmarking

The proposed CiM cell was designed using a 55 nm CMOS technology. For comparative analysis, a reference circuit from [4] was replicated using the same CMOS model parameters. An MTJ model characterized by a nominal TMR of 122% and an ambient temperature of 25 ℃. All simulations were conducted using the NS-SPICE simulator. To emulate parasitic effects in memory arrays, a 1 pF capacitor was added to the proposed cell and the reproduced cell.

Simulation results at 1 V supply voltage are shown in Fig. 2. When computing a logic '1', the output voltage remains at V_{DD}, whereas for a logic '0', it discharges from a V_{DD} to 0, and thus for a logic '0' computation, a threshold voltage is needed to be defined. In [4], the logic '1' is defined as when the output voltage is 150mV larger than the reference voltage. Following the definition in [4], a logic '0' is interpreted as an output voltage below 250 mV (with a MOSFET threshold voltage V_{th} of 0.4 V), with the primary delay metric determined by the discharge behavior. According to this, the latency and reliability of this work and [4] are mostly influenced by the logic '0' and logic '1' computation respectively.

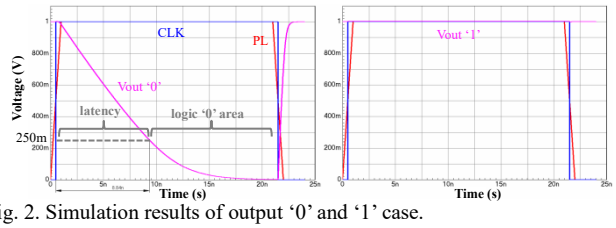

Fig. 2. Simulation results of output '0' and '1' case.

Figure 3 compares the XNOR computation delay of the proposed design and the reference method in [4] based on simulation results. The delay is measured by the time taken for the output voltage to reach the defined threshold, as described earlier. As the supply voltage varies from 1V to 1.2V, the proposed design consistently achieves shorter computation delays compared to the reference, with reductions exceeding 50% across all tested voltages. This demonstrates the high computation speed of the proposed CiM cell.

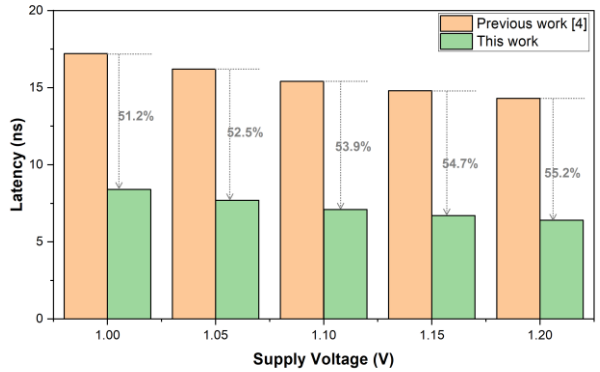

Fig. 3. Computation latency of this work and reference method under different supply voltages.

Figure 4 compares the output voltage variations under different TMR values for the proposed cell and the reference method in [4]. It shows that the proposed cell maintains a nearly constant output voltage as TMR varies from 50% to 500%, while the reference method has a voltage drop by 0.42V when TMR decreases from 500% to 50%. This observation indicates that the proposed structure exhibits enhanced stability against TMR variations. This robustness originates from the fact that the MTJ resistance does not directly affect the XNOR computation process, thereby significantly reducing the circuit's sensitivity to MTJ parameter fluctuations and enhancing its compatibility with a wide range of MTJ devices.

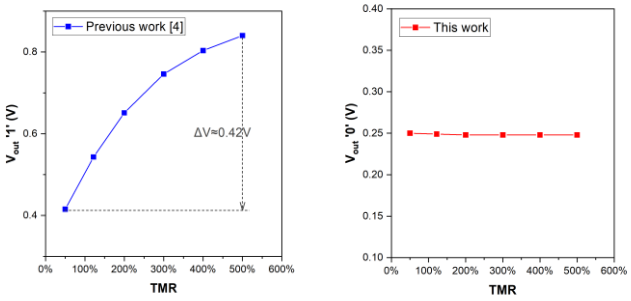

Fig. 4. Output voltages of this work and reference method under different TMR.

Figure 5 compares the computation power consumption of the proposed design and the reference method under supply voltages ranging from 1 V to 1.2 V. It is important to note that although the two designs exhibit different computation delays, the comparison uses a fixed switching duration for both. In the proposed design, the power line (PL) is turned off immediately after computation to eliminate static power consumption.

The comparison is based on the average power consumption across both logic '1' and logic '0' output cases. The results show that the proposed design consistently consumes less power than the reference. At the nominal supply voltage of 1.2V for 55 nm process technology, the proposed design achieves a 26.2% reduction in power consumption compared to the reference method.

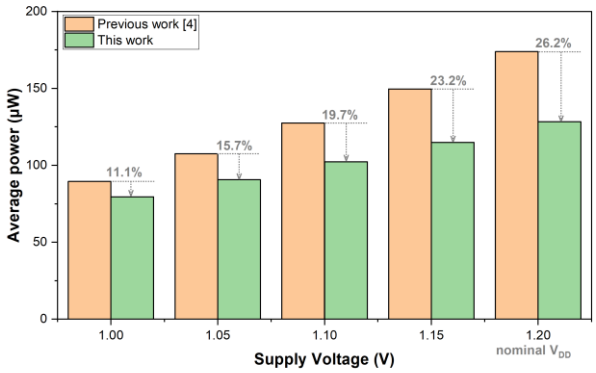

Fig. 5. Power consumption of this work and reference method under different supply voltages.

IV. CONCLUSIONS

A novel STT-MRAM based fully digital CiM architecture has been proposed. Through a state-of-the-art comparison with SPICE simulation, the proposed and designed CiM demonstrates over 50% reduction in computation latency, enhanced tolerance to TMR variation, and 26.2% power reduction at a 1.2V supply voltage. These advantages underscore its suitability for energy-efficient and high-speed and high-reliability BNN accelerators.

V. ACKNOWLEDGES

This work was supported by MEXT Initiative to Establish Next-generation Novel Integrated Circuits Centers (X-NICS) Grant Number JPJ011438 and JST SPRING, Grant Number JPMJSP2114.

REFERENCES

[1] Jung, S., Lee, H., Myung, S. et al. A crossbar array of magnetoresistive memory devices for in-memory computing. Nature 601, 211–216 (2022).

[2] H. Cai et al., "Proposal of Analog In-Memory Computing With Magnified Tunnel Magnetoresistance Ratio and Universal STT-MRAM Cell," in IEEE Transactions on Circuits and Systems I: Regular Papers, vol. 69, no. 4, pp. 1519-1531, April 2022.

[3] T. -N. Pham, Q. -K. Trinh, I. -J. Chang and M. Alioto, "STT-BNN: A Novel STT-MRAM In-Memory Computing Macro for Binary Neural Networks," in IEEE Journal on Emerging and Selected Topics in Circuits and Systems, vol. 12, no. 2, pp. 569-579, June 2022.

[4] T. Na, "Ternary Output Binary Neural Network With Zero-Skipping for MRAM-Based Digital In-Memory Computing," in IEEE Transactions on Circuits and Systems II: Express Briefs, vol. 70, no. 7, pp. 2655-2659, July 2023.

[5] T. Ohsawa et al., "A 1 Mb Nonvolatile Embedded Memory Using 4T2MTJ Cell With 32 b Fine-Grained Power Gating Scheme," in IEEE Journal of Solid-State Circuits, vol. 48, no. 6, pp. 1511-1520, June 2013.

Study on Correlation between TMR and Exchange Bias in MTJs for STT-MRAM Applications

Seongbin Seo[1], Geunwoo Kim[2], Phuoc Cao Van[3], Jae-hyeon An[3], Jong-Ryul Jeong[3], Byong-Guk Park[2], and Sanghoon Kim[1*]

[1]Department of Physics and EHSRC, University of Ulsan, Ulsan 44610, Republic of Korea
[2]Department of Materials Science and Engineering, Korea Advanced Institute of Science and Technology, Daejeon 34141, Republic of Korea
[3]Department of Materials Science and Engineering, Graduate School of Energy Science and Technology, Chungnam National University, Daejeon 34134, South Korea
* Correspondence to sanghoon.kim@ulsan.ac.kr

To evaluate the thermal robustness of spin-transfer torque magnetoresistive random-access memory (STT-MRAM), we measured the temperature dependence of magnetization in an in-plane IrMn/CoFeB/MgO/CoFeB heterostructure as it cooled from 300 K to 10 K. Over this range, the exchange bias field at the IrMn/CoFeB interface increased significantly, from 239 Oe to 439 Oe, while the coercivities of the pinned and free CoFeB layers rose from 20 Oe to 179 Oe and from 20 Oe to 99 Oe, respectively. From the strong temperature dependence of exchange bias, we estimate the Néel temperature of IrMn and confirme that exchange bias is a critical parameter governing the thermal stability of magnetic tunnel junctions (MTJs). This quantitative evaluation provides key design guidelines for developing thermally reliable exchange-biased MTJs in future STT-MRAM applications.

***Index Terms*—Thermal robustness, exchange bias, Néel temperature, magnetic tunnel junction (MTJ)**

I. Introduction

Thermal stability is a key determinant of speed, retention, and endurance in both volatile and non-volatile memory technologies. [1]-[3] As electronic systems increasingly operate under extreme environmental conditions, particularly in automotive applications, ensuring device-level robustness has become essential. [3]-[4] Spin-transfer torque magnetoresistive random-access memories (STT-MRAMs), a leading candidate for next-generation memory, has attracted significant attention due to its non-volatility, high speed, and low power consumption, and exhibits thermal reliability that meets automotive memory standards across the −40 °C to +150 °C range. [4]-[5] However, how thermal robustness affects the operation of STT-MRAM, particularly in terms of both intrinsic and extrinsic factors, remains insufficiently understood. The fundamental unit of STT-MRAM is the magnetic tunnel junction (MTJ), whose thermal robustness directly affects magnetization switching and spin-dependent transport phenomena, including tunneling magnetoresistance (TMR) and exchange bias. [6] Therefore, evaluating the thermal stability of MTJs at the device level is necessary for understanding and controlling temperature-induced degradation in these transport properties.

In this study, we investigated the temperature dependence of TMR in a NiFe/IrMn/CoFeB/MgO/CoFeB MTJ structure. The TMR measured at each temperature was analyzed by comparing the contributions of spin-independent tunneling, direct elastic tunneling, and magnon-assisted inelastic excitations. The temperature dependence of the exchange bias field was also used to estimate the Néel temperature at the device level. In addition, size-dependent simulations using MuMax3 were conducted to examine the influence of extrinsic factors, and the variation in magnetization with respect to junction size was observed under various temperature conditions. This study proposes an analytical approach to explain how thermal stability affects the operation of STT-MRAM by simultaneously considering both intrinsic and extrinsic factors.

II. Experimental Procedures and Results

The heterostructure investigated in this study consisted of $Ni_{81}Fe_{19}$ (1 nm) / $Ir_{25}Mn_{75}$ (15 nm) / $Co_{32}Fe_{48}B_{20}$ (5 nm) / MgO (1.5 nm) / $Co_{32}Fe_{48}B_{20}$ (2 nm), capped with a ruthenium layer, as illustrated in Figure 1(a). All films were deposited at room temperature by magnetron sputtering onto Si/SiO_x (200 nm) substrates under a base pressure below 3.0×10^{-8} Torr. During deposition, an in-plane magnetic field of 15 mT was applied to induce uniaxial magnetic anisotropy in the CoFeB layers. The metal layers were deposited using DC sputtering at 30 W with a working pressure of 3 mTorr, while the MgO barrier was deposited via RF sputtering at 75 W and 10 mTorr. To enhance the exchange bias at the IrMn/CoFeB interface, a thin NiFe underlayer was inserted beneath the IrMn layer. Following film deposition, bottom electrodes with a dumbbell-shaped geometry (10 μm width) were defined by photolithography and Ar^+ ion milling. The MgO barrier and top electrode were subsequently etched, and a 70 nm-thick SiO_x isolation layer was deposited in situ to electrically separate the top and bottom electrodes. MTJ pillars with a diameter of 5 μm were then patterned. Finally, a Cr (5 nm)/Au (100 nm) bilayer was deposited, and the top electrodes were completed by a standard lift-off process. The devices were annealed in vacuum at 350 °C for 40 minutes under a magnetic field of 100 mT to establish exchange coupling at the IrMn/CoFeB interface. This field strength is sufficient to fully saturate the magnetization of the CoFeB layer. The tunneling resistance was measured at room temperature using a four-point probe configuration with a

constant bias current of 10 nA, while sweeping the in-plane magnetic field in Figure 1(b). We also confirm that the TMR of the MTJ strongly depends on the temperature above 300K from 50.12% to 37.06%.

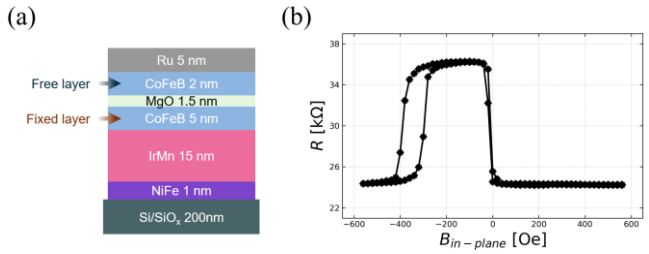

Fig. 1. (a) Cross-sectional schematic of the Ru-capped MTJ stack: 200 nm Si/SiO_x substrate / 1 nm NiFe / 15 nm IrMn / 5 nm CoFeB / 1.5 nm MgO / 2 nm CoFeB / 5 nm Ru. (b) TMR curve measured at room temperature using a four-point probe with a 10 nA bias current as a function of in-plane magnetic field.

The temperature dependence of magnetization behavior in the NiFe/IrMn/CoFeB/MgO/CoFeB heterostructure was examined by measuring in-plane hysteresis loops using the vibrating sample magnetometer (VSM) module of an magnetic property measurement system (MPMS) at temperatures from 300 K to 10 K in 50 K intervals, as shown in Figure 2. From the power-law with a critical exponent (β) model [7], we could get the Néel temperature (T_N) of the IrMn, 434 K in the MTJ.

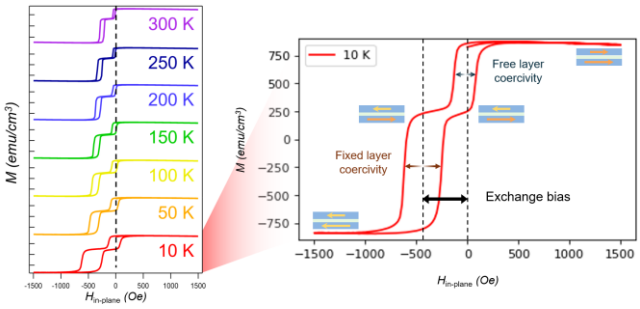

Fig. 2. VSM hysteresis loops of the IrMn/CoFeB/MgO/CoFeB heterostructure measured along the easy axis from 300 K to 10 K in 50 K intervals. The red curve represents the loop measured at 10 K, showing the coercivity fields of the free and fixed layers. The black dashed line indicates the center of the free and fixed layer loop. The black arrow denotes the exchange bias field.

From the two-measured parameters, we finally find the linear correlation between TMR and exchange bias of TMJs.

III. Conclusion

In this study, we experimentally investigated the temperature-dependent magnetic properties of an exchange-biased IrMn/CoFeB/MgO/CoFeB heterostructure. As the temperature decreased from 300 K to 10 K, the exchange bias field increased significantly, accompanied by enhanced coercivity in both the fixed and free layers, with a larger increase observed in the fixed layer. Based on these results, the Néel temperature of IrMn and thermal stability factors were quantitatively evaluated. These findings provide a useful framework for assessing the thermal reliability of lateral MTJ devices intended for memory applications in extreme environments. Future work will focus on analyzing the temperature dependence of the exchange bias field and tunneling resistance in individual MTJ cells to deepen the understanding of intrinsic and extrinsic thermal effects on STT-MRAM operation.

References

[1] G. W. Burr et al., "Phase change memory technology," *Journal of Vacuum Science & Technology B*, vol. 28, no. 2, pp. 223–262, Mar. 2010.

[2] A. Pritam, R. Gupta, and P. C. Mondal, "Recent advances in inorganic oxides-based resistive random-access memory devices," *arXiv preprint arXiv:2205.05537*, May 2022.

[3] E. Garzón et al., "Adjusting Thermal Stability in Double-Barrier MTJ for Energy Improvement in Cryogenic STT-MRAMs," *arXiv preprint arXiv:2204.09395*, Apr. 2022.

[4] J. M. Iwata-Harms, G. Jan, H. Liu, S. Serrano-Guisan, J. Zhu, L. Thomas, R.-Y. Tong, V. Sundar, and P.-K. Wang, "High-temperature thermal stability driven by magnetization dilution in CoFeB free layers for spin-transfer-torque magnetic random access memory," *Scientific Reports,* vol. 8, Art. no. 14409, Sep. 2018.

[5] K. Zeissler, "STT-MRAM that works at high temperatures," *Nature Electronics,* vol. 6, p. 180, 2023.

[6] I. N. Krivorotov et al., "Temperature dependence of spin-transfer-induced switching of nanomagnets," *Physical Review Letters,* vol. 93, Art. no. 166603, 2004.

[7] T. V. A. Nguyen, Y. Shiratsuchi, S. Yonemura, T. Shibata, and R. Nakatani, "Energy condition of isothermal magnetoelectric switching of perpendicular exchange bias in Pt/Co/Au/Cr_2O_3/Pt stacked film," *J. Appl. Phys.,* vol. 124, no. 23, no. 233902, Dec. 2018.

Multi-bit magnetic memory using magnetic multilayer pillars with two-terminal structure

Syuta Honda[1,2] and Yoshiaki Sonobe[3], *Senior Member, IEEE*

[1]Department of Pure and Applied Physics, Kansai University, Suita 564-8680, Japan, shonda@kansai-u.ac.jp
[2]Center for Spintronics Research Network, Osaka University, Toyonaka 560-8531, Japan
[3]Research Organization for Nano & Life Innovation, Waseda University, Tokyo 162-0041, Japan, yoshiakisonobe7@gmail.com

We investigate magnetization control in a magnetic multilayer pillar on an in-plane magnetized layer using micromagnetic simulations. The multilayer pillar consists of alternating layers possessing or lacking perpendicular magnetic anisotropy. When the bottom layer of the pillar has no perpendicular anisotropy, the magnetization of the pillar bottom is reversed by the spin injection from the in-plane magnetized layer and the spin-polarized current flowing through the pillar. This leads to the formation of a new domain and an accompanying domain wall which generates a new bit pattern. The domain wall is moved by the current. When a pulse current is applied, the magnetization reversal is suppressed, and the domain wall movement is induced. By adjusting the timing of the application of the constant and pulsed currents, magnetic states corresponding to various bit patterns can be realized in the pillar. This multi-bit memory structure operates with only two terminals, and a circuit using multiple pillars is proposed.

***Index Terms*— Magnetic memory, Nonvolatile memory, Spintronics, Numerical simulation**

I. Introduction

Multi-bit memory devices based on domain wall (DW) motion in vertically aligned ferromagnetic nanopillars have been proposed as a promising candidate for high-density memory applications [1]. The DW is moved by a spin-transfer torque (STT) induced by a spin-polarized current (SPC) flowing through the pillar. The magnetization direction in the pillar is read out by a magnetic tunnel junction (MTJ) located at one end of the pillar. A key challenge in realizing such multi-bit memory devices is controlling the magnetization at the opposite end of the pillar.

Micromagnetic simulations of a permalloy pillar have demonstrated a viable writing mechanism. In a structure, an in-plane magnetized layer (IL) is positioned beneath the pillar, and applying a unidirectional current from the top of the pillar through the in-plane layer enables control of the magnetization within the pillar [2]. The number of interconnects is the same as that in the STT-MRAM and fewer than those needed for the spin-orbit-torque (SOT)-MRAM.

In the pillar where the magnetization is aligned along the pillar due to shape anisotropy, the distance between multiple DWs formed within the pillar becomes large, requiring a longer pillar length to store even a single bit of information [2]. In contrast, pillars with perpendicular magnetic anisotropy (PMA) can produce narrower DW spacing, hence, switching the magnetization of the pillar end requires a large SPC [3].

As an alternative pillar structure, magnetic pillars composed of multilayer films of different magnetic materials have been proposed to reduce the DW spacing through DW pinning effects arising from the layered structure [1]. This approach shortens the pillar length required to store a single bit. However, DW writing in such multilayer pillars has not yet been demonstrated. Recent studies have reported that magnetic pillars composed of CoPt multilayers with tunable perpendicular anisotropy can now be fabricated by controlling their composition [4].

In this study, we perform micromagnetic simulations to investigate whether magnetization writing can be achieved and to characterize the behavior of multilayer magnetic pillars under unidirectional current injection control schemes. The goal is to explore the feasibility of applying current-driven control methods with unidirectional current flow to more practical multilayer structures with perpendicular anisotropy.

II. Model and Methods

We considered a cylindrical ferromagnetic pillar with a length of 150 nm along the z-direction and a diameter of 20 nm. The pillar comprised alternating magnetic layers with and without perpendicular magnetic anisotropy (PMA), each with a thickness of 5 nm, forming a multilayer structure. A 5-nm thick IL without PMA was attached to the bottom of the pillar. The magnetization pin layer for the MTJ at the top of the pillar was omitted. The structure was discretized into cubic cells of 1.0 nm³. The magnetization dynamics of each cell were calculated using the Landau-Lifshitz-Gilbert (LLG) equation including the STT term [2].

The layers with PMA had a perpendicular magnetic anisotropy energy density K_u of 1.0 MJ/m³, a saturation magnetization M_s of 600 kA/m, and an exchange stiffness constant A of 10 pJ/m. The other layers had K_u of 0.0, M_s of 200 kA/m and A of 2.5 pJ/m. The exchange coupling between the pillar and the IL was set to zero. The direction of the SPC was from the top to the bottom of the pillar. In other words, the direction of the electron flow was from the IL to the top of the pillar. The conversion between the spin current and the SPC was calculated assuming a spin polarizability P of 1.0. As the initial condition in the pillar, a magnetized state along the $-z$-direction was set and then relaxed. The magnetization of the IL was aligned predominantly in-plane due to shape anisotropy. Although we refer to this layer as the IL, its magnetization often pointed obliquely from the in-plane direction, owing to the influence of SPC and dipole-dipole interactions with the pillar.

III. Results and Discussions

We simulated the magnetization control in the pillar whose lower end is composed of 0-K_u layer as shown in Fig. 1(a). The SPC of 5×10^{11} A/m² was applied through the pillar from $t = 0$ to 3.1 ns. Figure 1 depicts the positions of the DWs in the pillar. First, the magnetization at the bottom of the pillar canted due to the spin injection from the IL (Fig. 1(c)), and then the magnetization at the bottom of the pillar was reversed and a DW was formed at 0.6 ns (Fig. 1(d)). Subsequently, the DW moved upward due to the SPC. In addition, a second DW was formed at approximately 1.2 ns, followed by a third at 1.9 ns and a fourth at 2.6 ns. Each DW continued to move upward (Fig. 1(e)). Then, at 2.9 ns, the first DW reached the top of the pillar and disappeared. At this point, the magnetization pattern consisted of four alternating up and down domains, corresponding to a bit pattern "1010." During the SPC application, the magnetization in the IL underwent canting in different directions. When the SPC was stopped at 3.1 ns, the DW motion ceased, and four DWs stabilized at z = 38 nm, 88 nm, and 127 nm. All these positions were the 0-K_u layers. These results show the successful DW writing in the magnetic multilayer pillar.

Next, we aimed to reproduce a bit pattern in which identical bits appeared in sequence. We created the bit pattern 1001 from the initial pattern 0000. A pulsed SPC was applied after 1.6 ns, in which the SPC was periodically turned on and off with an interval of 0.25 ns, as shown in Fig. 2(a). While the steady SPC was flowing, the magnetization was reversed twice at the bottom of the pillar. As a result, two DWs were formed by 1.6 ns, as shown in Fig. 2(b), (c). At this juncture, the SPC was switched to pulsed SPC with 0.25 ns intervals. When the SPC was turned off, the magnetization at the bottom of the pillar returned to its original direction before the reversal was completed, and the DWs stabilized in the nearby 0-Ku layers (Fig. 2(d)). By repeatedly switching the SPC on and off, only the DWs moved, resulting in the elongation of the domains at the bottom of the pillar. At 2.8 ns, the SPC was switched back to a steady flow, leading to magnetization reversal in the bottom region of the pillar (Fig. 2(e)). When the SPC was turned off at 3.8 ns, the magnetization stabilized into the bit pattern 1001 (Fig. 2(f)). These results demonstrate that the use of pulsed SPC allows for flexible and arbitrary bit pattern formation.

An example of a circuit composed of multiple pillar structures is shown in Fig. 3. As the magnetization state of each pillar can be controlled with just two terminals, it is possible to operate the memory using a circuit in which each pillar is paired with a single control transistor. This suggests that multi-bit memory devices can be controlled using the same number of interconnects as a single-bit STT-MRAM.

Meanwhile, when the bottom layer of the pillar was the layer with K_u = 1.0 MJ/m³, DW writing did not occur, even when an SPC of 1.0×10^{13} A/m² was applied. This indicates that, in multilayer pillar magnetic memory devices, the placement of the 0-Ku layer at the bottom of the pillar, where domains are written, is advantageous because it facilitates DW formation. Compared to our previous study using a permalloy pillar, which achieved 3 bits per 250-nm long [2], the multilayer pillar realized a higher density.

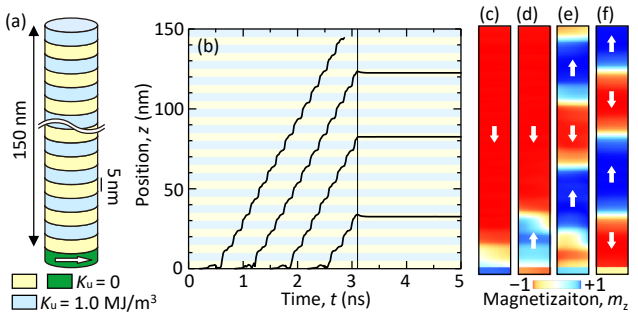

Fig. 1. Continuous and stepwise formation of DWs in the pillar, with the 0-K_u layer (yellow) placed on the IL (green). (a) Structure of the multilayer pillar. (b) DW positions and magnetic configurations at (c) 0.5 ns, (d) 1.0 ns, (e) 2.8 ns, and (f) 5.0 ns. The boundary between the pillar and the IL is z = 0. The white arrows in (c)-(d) indicate the direction of magnetization.

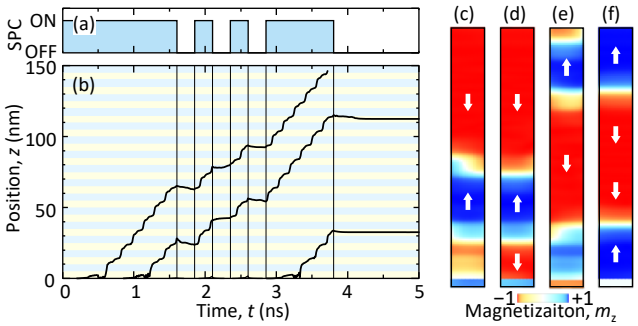

Fig. 2. Formation of the bit pattern 1001 using pulsed SPC. (a) The timing diagram of the applied SPC. (b) DW positions in the pillar. The magnetic structure of the pillar and the IL at t = (c) 1.6 ns, (d) 1.8 ns, (e) 3.7 ns, and (f) 5.0 ns.

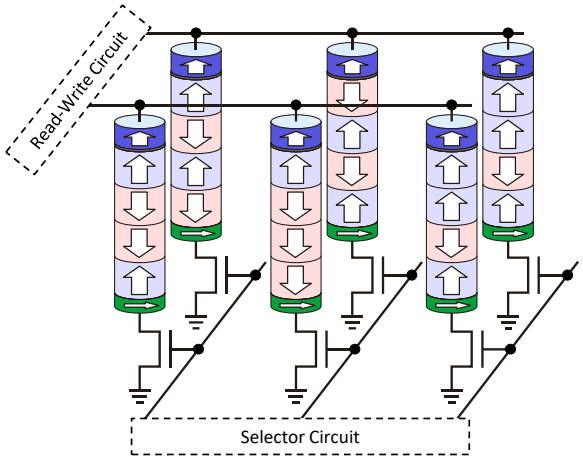

Fig. 3. Circuit comprising six pillars with individual selector transistors.

References

[1] Y. M. Hung, T. Li, R. Hisatomi, Y. Shiota, T. Moriyama, and T. Ono, "Low Current Driven Vertical Domain Wall Motion Memory with an Artificial Ferromagnet," *J. Magn. Soc. Jpn*., vol. 45, pp. 6-11, (2021).

[2] S. Honda and Y. Sonobe, "Single current control of magnetization in vertical high-aspect-ratio nanopillars on in-plane magnetization layers," *J. Phys. D: Appl. Phys*., vol. 57, pp. 325002, (2024).

[3] S. Honda and Y. Sonobe, "Spin-orbit torque assisted magnetization reversal of 100 nm-long vertical pillar," *J. Phys. D: Appl. Phys*., vol. 55, pp. 395001, (2022).

[4] R. Kawana, N. Oguchi, D. Oshima, M. Yoshida, T. Sugiura, M. Saito, T. Homma, T. Kato, T. Ono, M. Shima, and K. Yamada, "Artificial control of layer thickness in Co-Pt alloy multilayer nanowires fabricated by dual-bath electrodeposition in nanoporous polycarbonate membranes," *Appl. Phys. Express*, vol. 18 pp. 033002, (2025).

Ensemble Learning for STT-MRAM Channel Detection

Chi Dinh Nguyen[1] and Thao Thu Nguyen[2]

[1]Faculty of Computing Fundamentals, FPT University, Ha Noi 13113, Viet Nam, chind3@fe.edu.vn*
[2]Faculty of Mathematics, Hanoi National University of Education, Ha Noi 13113, Viet Nam, thaont_k681028@stu.hnue.edu.vn

We propose a stacking-based ensemble detector for STT-MRAM that combines deep neural networks (base learners) with a meta-model to fuse their outputs. Simulation results demonstrate that, even without error-correction coding, the ensemble detector achieves up to two orders of magnitude lower bit error rate (BER) compared to a conventional threshold detector and maintains graceful degradation as noise and offset severity increase. When combined with an error-correcting modulation code, the proposed approach further reduces BER under the severe effects of unknown offsets. These findings highlight the potential of stacking-based ensemble learning to enhance the reliability of next-generation nonvolatile memories substantially.

***Index Terms*—Nonvolatile RAM, ensemble learning, spin-torque transfer magnetic random access memory (STT-MRAM), neural network, asymmetric write error rate.**

I. Introduction

SPIN-TRANSFER torque magnetic random-access memory (STT-MRAM), which utilizes spin-polarized currents to manipulate the magnetization states of magnetic tunnel junctions (MTJs), is widely regarded as a leading candidate for next-generation nonvolatile memory (NVM) technologies [1]. Despite its significant advantages, the path toward widespread adoption of STT-MRAM is accompanied by several technical challenges. Notably, STT-MRAM is subject to two critical technical challenges: asymmetric write error (AWE) and unknown offsets [1, 2]. To mitigate the impact of such offsets, conventional approaches include the design of offset-cancellation sensing circuits that autonomously compensate for systematic deviations during readout [3]. In addition, advanced modulation codes and channel detection techniques have been explored to suppress offset-induced errors and overcome AWE [4 – 7]. More recently, neural network-based models have been proposed to estimate and correct readout offsets dynamically, demonstrating improvements in both the accuracy and robustness of STT-MRAM systems [5].

II. STT-MRAM Cascaded Channel Model

An STT-MRAM cell comprises two fundamental components: a magnetic tunnel junction (MTJ) and an nMOS transistor. The MTJ is composed of a reference layer, a free layer, and an ultrathin tunneling oxide barrier. The bit is encoded by the magnetization direction of the free layer; that is, if the free layer is parallel to the reference layer, the MTJ is in a low resistance state (representing bit '0'), and conversely (representing bit '1').

In this study, we adopt the STT-RAM cascaded channel model proposed by Cai and Immink [2] to simulate the error behavior of the STT-MRAM channel. Let P_1, P_0, and P_r denote the write error rate for 0 → 1 switching, the write error rate for 1 → 0 switching, and the read disturb error rate, respectively. The writing process is modeled as a binary asymmetric channel (BAC). The read disturb phenomenon is modeled as a **Z**-channel, while the read decision errors are modeled using a Gaussian Mixture Channel (GMC). In this model, the low resistance state R_0 is represented by a Gaussian distribution with its mean and standard derivation of μ_0 and σ_0, while the high resistance state R_1 follows a Gaussian distribution characterized by μ_1 and σ_1. For the effect of system offsets, we assume a resistance offset arising due to elevated operating temperatures. The offset, which only occurs with the high resistance state R_1, is regarded as a Gaussian distribution with $\mathcal{N}(\mu_{ofs}, \sigma_{ofs}^2)$.

III. Proposed Stacking-Based Ensemble Learning

Ensemble learning [6] is a machine learning paradigm in which multiple base models are trained, and their predictions are aggregated to enhance generalization and robustness compared to any individual model. In this study, we propose a stacking ensemble framework with three distinct base learners; Multi-Layer Perceptron (MLP), Convolutional Neural Network (CNN), and Long Short-Term Memory (LSTM). MLP learns complex nonlinear mappings from noisy voltage samples to bit probabilities; CNN (with Conv1D) captures localized spatial error patterns; and LSTM models temporal dependencies in readout sequences to detect time-dependent faults. The stacking procedure in this study is structured as follows.

The MLP, CNN, and LSTM models are independently trained on raw input sequences derived from the STT-MRAM channel. The outputs (predicted probabilities) from all three base models are concatenated to form a combined feature vector. The meta-model is then trained using the stacked predictions from the base models as input, learning to combine them to yield the final decision on each bit. Fig. 1 illustrates the proposed model for STT-MRAM channel. Accordingly, the stacking ensemble learning model can be represented as follows. Each base model receives the input as a vector $\boldsymbol{r} \in \mathbb{R}^{\boldsymbol{n}}$ (where n is the bit sequence length) and outputs a prediction $\hat{\boldsymbol{y}}_m \in \mathbb{R}^{\boldsymbol{n}}$ where $m \in \{MLP, CNN, LSTM\}$. Predictions from base models can be represented as follows,

$$\hat{\boldsymbol{y}}_{MLP} = f_{MLP}(\boldsymbol{r}, \theta_{MLP})$$
$$\hat{\boldsymbol{y}}_{CNN} = f_{CNN}(\boldsymbol{r}, \theta_{CNN})$$
$$\hat{\boldsymbol{y}}_{LSTM} = f_{LSTM}(\boldsymbol{x}, \theta_{LSTM})$$

where f_{MLP}, f_{CNN}, and f_{LSTM} are functions learned from the training process of MLP, CNN, and LSTM models; θ_{MLP}, θ_{CNN},

θ_{LSTM} are the corresponding parameters of each model. The predictions from the base models are concatenated to form a new (combined) feature vector $\boldsymbol{z} = [\hat{\boldsymbol{y}}_{MLP}; \hat{\boldsymbol{y}}_{CNN}; \hat{\boldsymbol{y}}_{LSTM}]^T \in \mathbb{R}^{3n}$. The vector $\boldsymbol{z}$ contains aggregated information from the predictions of the MLP, CNN, and LSTM. The meta model is a neural network that receives $\boldsymbol{z}$ as input and learns how to combine the predictions from the base models to produce the final prediction. The meta model can be expressed by,

$$\hat{\boldsymbol{c}} = f_{meta}\left(\begin{bmatrix} f_{MLP}(\boldsymbol{r}, \theta_{MLP}) \\ f_{CNN}(\boldsymbol{r}, \theta_{CNN}) \\ f_{LSTM}(\boldsymbol{x}, \theta_{LSTM}) \end{bmatrix}, \theta_{meta}\right) \quad (1)$$

where f_{meta} is function learned from the training process, and θ_{meta} is the corresponding parameters of the meta model.

IV. Simulation Results and Discussion

The experimental parameters utilized in this study for simulating the STT-MRAM cell are adopted from [2]. Specifically, the mean resistance values of the two states are set as $\mu_0 = 1\ k\Omega$ and $\mu_1 = 2\ k\Omega$, respectively. The severity of read decision errors can be systematically controlled by adjusting the ratio σ_0/μ_0 (hence σ_1/μ_1). For write errors, we assume a fixed write error probability of $P_1 = 2 \times 10^{-4}$. To model offset effects, a Gaussian distribution with $\mu_{ofs} = -0.2\ k\Omega$ and $\sigma_{ofs}/\mu_1 = 7\%$ is setup for the simulation.

We first evaluate the performance of the proposed model on the raw data without coding. In Fig. 2a, it can be easily observed that the ensemble learning (EL) detector already achieves a BER on the order of 10^{-4}, whereas the threshold detector is near 10^{-2}, a two-order-of-magnitude improvement, at the read errors $\sigma_0/\mu_0 = 3\%$. This demonstrates that the EL detector not only reduces baseline error but also degrades much more gracefully as the read-decision errors raise.

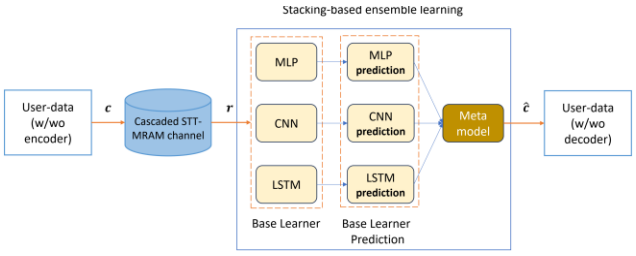

Fig. 1. Proposed model.

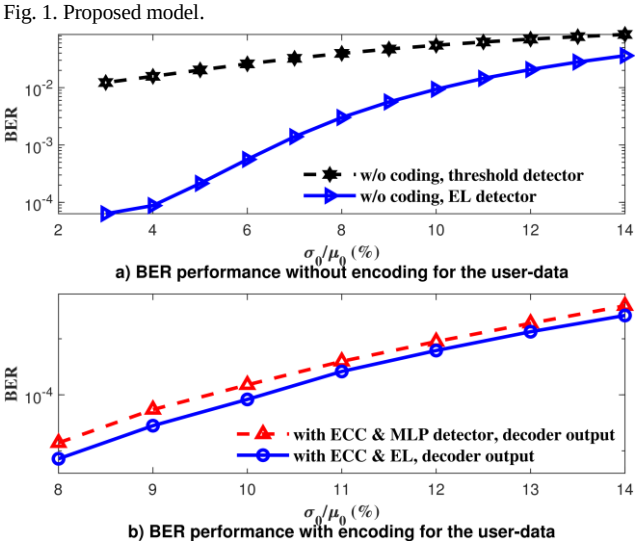

Fig. 2. BER performance for the proposed model.

In addition, we validated the proposed detection scheme under a scenario where the user signal is encoded using an error correction modulation code designed with a minimum Hamming distance (d_{min}) of 3, enabling single-bit error correction. The 4/9-rate code used in this study is constructed following the theoretical framework outlined in [7], where the selected codewords satisfy the $d_{min} = 3$. As illustrated in Fig. 2b, the inclusion of this code notably enhances system performance, especially under high-offset and noisy conditions, further reinforcing the effectiveness of the proposed stacking-based ensemble detection scheme. Both curves in Fig. 2b show significantly improved BER compared to Fig. 2a. At $\sigma_0/\mu_0 = 8\%$, the EL detector achieves a BER of roughly 10^{-5} versus 3×10^{-5} for the MLP detector. As the level of the read errors increases to 14%, both schemes converge toward BER of 10^{-3}, but the EL detector maintains a consistent gap of approximately 2×10^{-4} in absolute BER. As a result, when combined with ECC, the EL detector further enhances decoding performance over an MLP-only approach, yielding lower BER across the entire noise range.

V. Conclusion

We have shown that a stacking ensemble of MLP, CNN, and LSTM base learners, guided by a meta-model, can effectively mitigate both write-asymmetry and unknown offset challenges in STT-MRAM. The proposed detector outperforms single-model and threshold-based approaches by up to two orders of magnitude in uncoded BER and demonstrates superior robustness under high noise and offset conditions. Integration with a lightweight error-correcting modulation code further enhances performance, achieving consistently low BER values around 10^{-5} at 8% read error levels.

References

[1] C. Worledge *et al.*, "STT-MRAM - Status and Outlook," in *Proc. IEEE 33rd Magn. Recording Conf. (TMRC)*, Aug. 2022, doi: 10.1109/TMRC56419.2022.9918607.

[2] K. Cai and K. A. Schouhamer Immink, "Cascaded channel model, analysis, and hybrid decoding for spin-torque transfer magnetic random access memory," *IEEE Trans. Magn.*, vol. 53, no. 11, Nov. 2017, Art. no. 8204311.

[3] T. Na, S. H. Kang, and S.-O. Jung, "STT-MRAM sensing: A review," *IEEE Trans. Circuits Syst. II, Exp. Briefs*, vol. 68, no. 1, pp. 12–18, Jan. 2021.

[4] C. D. Nguyen and J. Lee, "Improving SOVA output using extrinsic informations for bit patterned media recording," in *Proc. IEEE Int. Conf. Consum. Electron.*, Jan. 2015.

[5] Z. Mei, K. Cai, and X. Zhong, "Neural network-based dynamic threshold detection for non-volatile memories," in *Proc. IEEE Int. Conf. Commun. (ICC)*, May 2019.

[6] Gautam Kunapuli, *Ensemble Methods for Machine Learning*, Manning, 2023.

[7] C. D. Nguyen, "On the design of 7/9-rate sparse code for spin-torque transfer magnetic random access memory," *IEEE Access*, vol. 9, pp. 164562–164569, 2021.

Anisotropic Exchange Stiffness of Perpendicularly Magnetized Co/Pt multilayer thin film

Woonjae Won[1], Yuta Sasaki[1], Nobuaki Kikuchi[2], Genta Egawa[3], Keisuke Masuda[1], Yukiko K. Takahashi[1,4], and Hirofumi Suto[1]

[1]Research Center for Magnetic and Spintronic Materials, NIMS, Tsukuba, Ibaraki 305-0047, Japan, WON.Woonjae@nims.go.jp
[2]Department of Mathematical Science and Electrical-Electronic-Computer Engineering, Graduate School of Engineering Science, Akita University, Akita, Akita 010-8502, Japan
[3]Department of Materials Science, Graduate School of Engineering Science, Akita University, Akita, Akita 010-8502, Japan
[4]Research Institute of Electrical Communication (RIEC), Tohoku University, Sendai, Miyagi 980-8577, Japan

Three-dimensional (3D) recording technologies are crucial to achieve higher recording density and faster reading/writing speeds than current magnetic recording technologies. To achieve them, magnetic materials with strong perpendicular magnetic anisotropy (PMA), such as $L1_0$-FePt and Co/Pt multilayers, have been extensively studied. Magnetic domain structure along the vertical direction is expected in 3D recording, therefore, a quantitative understanding of the out-of-plane (OOP) exchange stiffness constant ($A_{ex,OOP}$) is promising. Recent reports suggest that these materials exhibit anisotropy in exchange stiffness (A_{ex}), which influences the domain wall width, owing to the alteration of two different materials in their structure. However, estimating $A_{ex,OOP}$ for the PMA materials is technically difficult because of its high precession frequency. In this paper, we propose a promising approach for the observation of PSSW in PMA materials using all-optical time-resolved magneto-optical Kerr effect (AO-TRMOKE) and demonstrate how to extract $A_{ex,OOP}$ from this analysis. Furthermore, we provide the first experimental evidence of the anisotropy of A_{ex} in magnetic materials with PMA.

***Index Terms*—Exchange stiffness, Anisotropy, Co/Pt multilayer, All-optical time-resolved magneto-optic Kerr effect (AO-TRMOKE)**

I. Introduction

IN LINE with the exponentially growing datasphere, increasing the reading/writing speed, storage density, and low power consumption of memory devices have emerged as important research issues over the past several decades [1-2]. To solve this problem, domain wall (DW) racetrack memory [3-5] and heat-assisted magnetic recording (HAMR) [6-7] have been studied as memory devices that can replace currently widely used memory devices such as hard disk drive (HDD), solid-state drive (SSD), and dynamic random-access memory (DRAM).

A central area of interest for next-generation memory devices is the use of magnetic materials with strong perpendicular magnetic anisotropy (PMA). Among these, various multilayer structures [8] and L10-FePt [9] have been the subject of extensive study.

Recent studies suggest that these materials exhibit anisotropic exchange stiffness (A_{ex}) due to their layered structures [10]. A_{ex}, in conjunction with the magnetic anisotropy energy density (K_u), determines domain wall (DW) length [4]. Since K_u is already a well-known factor in optimizing magnetic memory performance, understanding A_{ex} is equally important.

Traditionally, A_{ex} in the out-of-plane (OOP) direction ($A_{ex,OOP}$) for materials with negligible or in-plane anisotropy has been evaluated through the observation of perpendicular standing spin wave (PSSW) using ferromagnetic resonance (FMR) [11]. However, in materials with strong PMA, the PSSW resonance frequencies shift into the sub-THz range, making FMR-based analysis impractical.

In this study, we report the first observation of PSSW in Co/Pt multilayers using an all-optical time-resolved magneto-optic Kerr effect (AO-TRMOKE) technique. Our results provide the first experimental confirmation of significant anisotropy in A_{ex} for this material system.

II. Sample Preparation and Magnetic Property

For this purpose, we prepared a Co/Pt multilayer thin film, as illustrated in Fig. 1(a). To verify the presence of PMA, we performed a vibrating sample magnetometer (VSM) measurement, with the results shown in Fig. 1(b) and its inset. A clear hysteresis loop was observed in the OOP direction, confirming that the film exhibits PMA. Specifically, magnetization saturated below 1 T in the OOP direction, while more than 1 T was required for saturation in the in-plane (IP) direction. After confirming PMA, we used AO-TRMOKE system to observe the magnetization precession of the film.

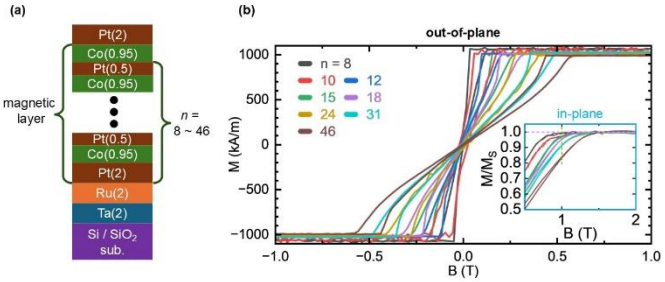

Fig. 1. (a) Structure of the Co/Pt multilayer film. (b) Magnetization (M) of various n with respect to the magnetic field (B) of out-of-plane direction. The inset shows M-B curve of in-plane (IP) direction.

III. Results

A. Estimation of $A_{ex,OOP}$

Figures 2(a) and 2(b) show the raw time-domain data and its fast Fourier transform (FFT) spectrum, respectively, for the magnetization precession of the Co/Pt multilayer with n = 15, measured by AO-TRMOKE under a magnetic field of B = 1.7 T and θ_B = 40°. The dominant peak at approximately f = 55 GHz corresponds to the fundamental resonance frequency of uniform magnon precession and is denoted as $f_0(B)$.

In addition to $f_0(B)$, two higher-frequency peaks were observed and carefully tracked while varying the strength of B. The results are presented in Fig. 2(c). One of these peaks, labeled $f_1(B)$, shows a magnetic field dependence similar to $f_0(B)$, indicating that it originates from a higher-order PSSW mode.

We quantitatively analyzed $f_0(B)$ and $f_1(B)$ based on the theoretical model described in Ref. [11-12] and extracted the out-of-plane exchange stiffness $A_{ex,OOP}$ for samples with n = 12, 15, and 18. The results were 12.5 ± 0.5, 11.9 ± 0.3, and 13.4 ± 1.2 pJ/m, respectively, 25% smaller than the $A_{ex,OOP}$ calculated through BLS in CoPt alloy with in-plane magnetic anisotropy [16].

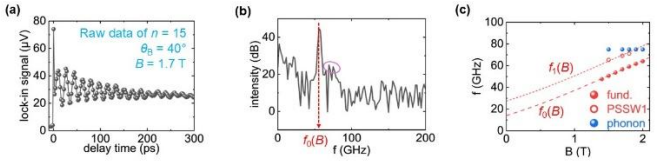

Fig. 2. (a) Raw time-domain data for the magnetization precession of the multilayer with n = 15 under B = 1.7 T and θ_B = 40°. (b) Fast Fourier transform (FFT) result of the Fig. 2(a). (c) Magnetization as a function of applied field.

B. Estimation of $A_{ex,IP}$

References [13-14] describe the method to estimate the exchange stiffness in the in-plane ($A_{ex,IP}$) direction using stripe-patterned magnetic domains. Referring them, we investigated the magnetic domains of multilayers with various thicknesses.

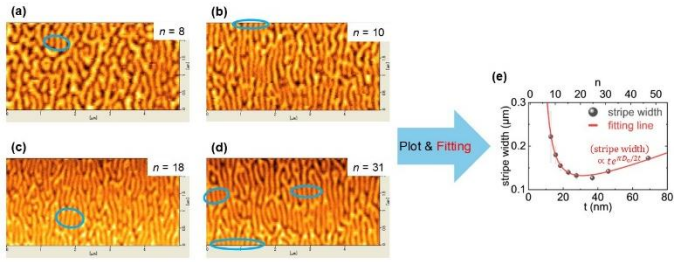

Fig. 3. (a)-(d) Magnetic domain with n = 8, 10, 18, and 31, respectively, with stripe pattern. We extracted the width of the stripe in the blue circle. (e) Thickness (t) or n dependence of the stripe width.

Figures 3(a)-(d) show the magnetic domains with stripe patterns for samples with n = 8, 10, 18, and 31, respectively. The width of the stripes was measured and plotted against the sample thickness in Fig. 3(e). By fitting the data (black symbols) to the theoretical model (red line), we extracted the dipolar length (D_0). The best-fit value of D_0 was found to be 19.80 ± 0.06 nm, which gave an exchange stiffness $A_{ex,IP}$ = 62.93 ± 8.13 pJ/m. This value is in good agreement with known values for pure cobalt within the experimental error [15].

IV. Conclusions

We successfully observed PSSW in Co/Pt multilayers, which exhibit high resonance frequencies owing to their strong PMA. This observation enabled the determination of $A_{ex,OOP}$. The extracted $A_{ex,OOP}$ remained consistent across varying film thicknesses and revealed an exchange anisotropy approximately five times smaller than its $A_{ex,IP}$. A theoretical investigation into these findings is planned for future work.

References

[1] G. Albuquerque, S. Hernandez, M. T. Kief, D. Manuri, and L. Wang, "HDD Reader Technology Roadmap to an Areal Density of 4 Tbpsi and Beyond", *IEEE Trans. Magn.* **58**, 3100410 (2022)

[2] D. R. J. G. J. Rydning, J. Reinsel, and J. Gantz, "The digitization of the world from edge to core", *Framingham: International Data Corporation* **16**, 1-28 (2018)

[3] Parkin, S. S. P., Hayashi, M. & Thomas, L. "Magnetic domain-wall racetrack memory". *Science* **320**, 190–194 (2008).

[4] Y. M. Hung, T. Li, R. Hisatomi, Y. Shiota, T. Moriyama, and T. Ono, "Low Current Driven Vertical Domain Wall Motion Memory with an Artificial Ferromagnet", *J. Magn. Soc. Jpn.* **45**, 6-11 (2021)

[5] S. Parkin, "Racetrack Memory: a high capacity, high performance, non-volatile spintronic memory," 2022 IEEE International Memory Workshop (IMW), Dresden, Germany, 2022, pp. 1-4

[6] X. Wang, K. Gao, H. Zhou, A. Itagi, M. Seigler, and E. Gage, "HAMR Recording Limitations and Extendibility", *IEEE Trans. Magn,* **49**. 686-692 (2013)

[7] D. Weller, G. Parker, O. Mosendz, A. Lyberatos, D. Mitin, N. Y. Safonova, and M. Albrecht, "Review Article: FePt heat assisted magnetic recording media", *J. Vac. Sci. Technol. B* **34**, 060801 (2016)

[8] T. Koyama, *et al.*, "Current-induced magnetic domain wall motion below intrinsic threshold triggered by Walker breakdown", *Nat. Nanotech.* **7**, 635–639 (2012)

[9] T. Seki, K. Utsumiya, Y. Nozaki, H. Imamura, and K. Takanashi. "Spin wave-assisted reduction in switching field of highly coercive iron-platinum magnets", *Nat. Commun.* **4**, 1726 (2013)

[10] A. Sakuma, "Evaluation of the Exchange Stiffness Constants of Itinerant Magnets at Finite Temperatures from the First-Principles Calculations", *J. Phys. Soc. Jpn.* **93**, 054705 (2024)

[11] H. J. Waring, Y. Li, N. A. B. Johansson, C. Moutafis, I. J. Vera-Marun, and T. Thomson, "Exchange stiffness constant determination using multiple-mode FMR perpendicular standing spin waves", *J. Appl. Phys.* **133**, 063901 (2023)

[12] P. D. Bentley, Y. Sasaki, I. Suzuki, S. Isogami, Y. K. Takahashi, and H. Suto, "Development of $L1_0$-ordered FePt with low damping and large perpendicular magnetic anisotropy by engineering the nanostructure", *Appl. Phys. Lett.* **126**, 022404 (2025)

[13] S. Okamoto, N. Kikuchi, O. Kitakami, T. Miyazaki, and Y. Shimada, "Chemical-order-dependent magnetic anisotropy and exchange stiffness constant of FePt (001) epitaxial films", *Phys. Rev. B* **66**, 024413 (2002)

[14] B. Kaplan and G. A. Gehring, "The domain structure in ultrathin magnetic films", *J. Magn. Magn. Mater.* **128**, 111-116 (1993)

[15] M. D. Kuz'min, K. P. Skokov, L. V. B. Diop, I. A. Radulov, and O. Gutfleisch, *Eur. Phys. J. Plus* **135**, 301 (2020)

[16] A. Murayama, M. Miyamura, K. Nishiyama, K. Miyata, and Y. Oka, "Brillouin spectroscopy of spin waves in sputtered CoPt alloy films and Co/Pt/Co multilayered films", *J. Appl. Phys.* **69**, 5661-5663 (1991)

Multi-bit magnetic memory based on a vertically magnetized pillar on two perpendicularly magnetized pinning layers

Syuta Honda[1,2], Hiroyoshi Itoh[1,2], and Yoshiaki Sonobe[3], *Senior Member, IEEE*

[1]Department of Pure and Applied Physics, Kansai University, Suita 564-8680, Japan, shonda@kansai-u.ac.jp
[2]Center for Spintronics Research Network, Osaka University, Toyonaka 560-8531, Japan, hitoh@kansai-u.ac.jp
[3]Research Organization for Nano & Life Innovation, Waseda University, Tokyo 162-0041, Japan, yoshiakisonobe7@gmail.com

We propose a novel multi-bit magnetic memory structure based on a vertically magnetized pillar placed on two perpendicularly magnetized pinning layers. The magnetization in the pillar is controlled by a spin-polarized current flowing from the pillar into one of the two pinning layers, and its behavior is investigated using micromagnetic simulations. The two pinning layers are magnetized in opposite directions. Depending on the magnetization direction at the bottom of the pillar, a domain wall is formed between the pillar and one of the pinning layers. When a spin-polarized current flows through this domain wall, it expands into the pillar, resulting in reversal of the magnetization at the pillar's bottom. By selecting the pinning layer through which the spin-polarized current flows, domain wall motion can be selectively induced to either reverse or preserve the magnetization direction. This enables control over the magnetization configuration within the pillar, which represents the bit pattern of the stored information. The simulation confirms that two bits of information can be written into a single pillar. This multi-bit memory structure operates with three terminals, and a circuit comprising several such pillars is also proposed.

***Index Terms*— Magnetic memory, Nonvolatile memory, Spintronics, Numerical simulation**

I. Introduction

Vertically magnetized multi-domain nanopillars have attracted attention as promising structures for realizing high-density multi-bit memory devices [1]. In such structures, domain wall (DW) motion is induced by spin-transfer torque (STT) generated by a spin-polarized current (SPC) flowing through the pillar. By shifting domains upward via DW motion, their magnetization directions can be sequentially detected using a magnetic tunnel junction (MTJ) placed at the top of the pillar. One of the major challenges in realizing this type of memory is the reliable control of magnetization at the bottom end of the pillar.

Several structures have been proposed to address this issue. In these designs, magnetization is controlled by passing SPC through the pillar while injecting transverse spins into its bottom end [2]. However, magnetization control using this method has not yet been demonstrated experimentally. Developing an alternative technique for achieving reliable control of pillar magnetization is therefore a critical step.

In this study, we propose a new method that controls pillar magnetization using only current-induced DW motion. The effectiveness of the proposed method is verified through micromagnetic simulations.

II. Proposed Structure

The proposed structure and operation are illustrated in Fig. 1. Two perpendicularly magnetized pinning layers are separately placed beneath the ferromagnetic nanopillar. These pinning layers are magnetized in opposite directions. Although electrically isolated from each other, they are both electrically connected to the lower end of the pillar. Because the pillar is magnetized along its longitudinal axis, one of the pinning layers forms a continuous magnetic domain with the pillar, while a DW appears between the pillar and the other pinning layer. The MTJ includes an additional layer at the top of the pillar, though this layer is omitted in Fig. 1.

The structure allows SPC to selectively flow from the top of the pillar to either of the two pinning layers. By switching the current path, the magnetization configuration within the pillar can be manipulated. When the SPC flows through the side where a DW is present, the DW propagates into the pillar, creating a new magnetic domain at its bottom. Then, the DW splits into an upper and a lower part. The lower DW then moves toward the opposite pinning layer. Simultaneously, the upper DW moves upward. In contrast, when the SPC flows through the side without a DW, the magnetization at the pillar's bottom is preserved, while the DW within the pillar shift toward the top. This mechanism enables control of the magnetization pattern within the pillar via current path selection. The described behavior was validated through micromagnetic simulations.

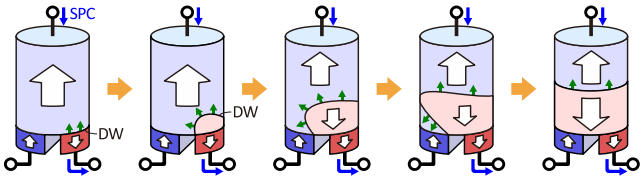

Fig. 1. Schematic of magnetization reversal process of the novel magnetic memory structure of ferromagnetic pillar on two perpendicularly magnetized thin layers. The large white arrows denote the magnetized directions. The direction of each blue arrow denotes the current direction of the SPC. The direction of each green small arrow denotes the direction of the DW motion.

III. Model and Methods

We considered a cylindrical ferromagnetic pillar measuring 50 nm in length along the z-direction and 20 nm in diameter. Two 5 nm thick perpendicularly magnetized pinning layers were attached beneath the pillar, as shown in Fig. 2(a). The pinning layers were modeled with semicircular cross-sections to match the pillar's geometry. The separation between the two

layers was set at 2 nm. The entire structure was discretized into cubic cells of 1.0 nm³. Magnetization dynamics in each cell were computed using the Landau–Lifshitz–Gilbert (LLG) equation, incorporating the STT term [2,3].

The pillar was assumed to have a saturation magnetization M_s of 100 kA/m, an exchange stiffness constant A of 1.0 pJ/m, and a perpendicular magnetic anisotropy energy density K_u of 0.1 MJ/m³ [3]. The pinning layers shared the same values for M_s and A but had a higher K_u of 2.0 MJ/m³ to stabilize their magnetization. The SPC was applied from the top of the pillar to the left pinning layer. Spin current conversion was modeled assuming a spin polarizability of P = 0.5 [3]. The initial magnetic states were set with magnetization along the $+z$-direction in both the pillar and right pinning layer, and along the $-z$-direction in the left pinning layer. The system was then allowed to relax (Fig. 2(b)).

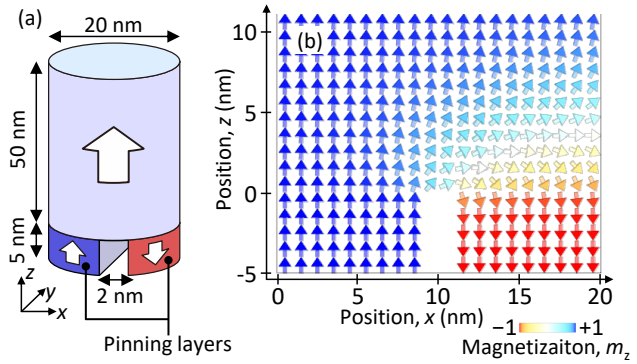

Fig. 2. (a) Structure and (b) initial magnetic state for the micromagnetic simulation. A magnified view of the lower part of the pillar is shown in (b). White arrows in (a) and small arrows in (b) indicate the magnetization direction.

IV. Results and Discussions

A micromagnetic simulation was performed to reverse the pillar's magnetization from the $+z$-direction to the $-z$-direction. A DW formed above the right pinning layer. Figure 3 shows the simulation results when a SPC was continuously applied from the top of the pillar through the right pinning layer. The current density of the SPC was of 5.0×10^{11} A/m² at the top of the pillar. As the SPC started flowing, the DW began moving upward, causing the $-z$-magnetized region to expand (Fig. 3(b)). One end of the DW was pinned at the branching point, where the pillar connected to the two pinning layers, and the DW expanded toward the left side of the pillar (Fig. 3(c)). Eventually, the expanding DW contacted the left surface of the pillar (Fig. 3(d)) and split into upper and lower parts (Fig. 3(e)). The lower part of the split DW stabilized near the right pinning layer, while the upper part continued to propagate upward toward the top of the pillar. Consequently, the entire magnetization of the pillar was reversed in the $-z$-direction (Fig. 3(f)).

When the pillar is magnetized in the $-z$-direction, applying the SPC from the pillar to the $+z$-magnetized left pinning layer causes a magnetization reversal to the $+z$-direction, following a process similar to that of the reversal to the $-z$-direction via the right pinning layer. During this process, the DW initially formed above the right pinning layer shifts above the left pinning layer.

As shown in Fig. 3(e), during the reversal process, the magnetization is vertically divided into upward and downward regions, corresponding to a two-bit intermediate state. Interpreting these magnetization configurations as two-bit states, four distinct states—"00," "01," "10," and "11"—can be realized. In this case, the pillar length was selected to allow the formation of a single DW. However, a longer pillar capable of supporting multiple DWs can store more information.

An example of a circuit comprising a multipillar structure is shown in Fig. 4. Because SPCs must be applied to both pinning layers, each pillar requires three terminals, and two interconnects must be provided at the bottom of each pillar. Additionally, because SPCs flow from the top to the bottom of the pillar, device selection can be achieved using both selector transistors and diodes.

In summary, a novel multi-bit memory structure utilizing a three-terminal pillar has been proposed. Its operations have been demonstrated through the micromagnetic simulations, underscoring its promise for the development of high-density multi-bit memory devices.

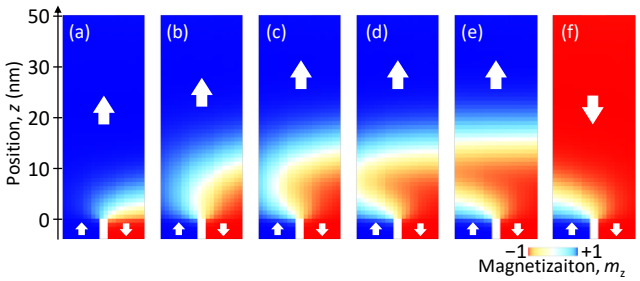

Fig. 3. Snapshots of the magnetic structure in the magnetization reversal prosses at time, t = (a) 0 ns, (b) 8 ns, (c) 16 ns, (d) 17 ns, (e) 18 ns, and (f) 24 ns. Each white arrow denotes the magnetization direction.

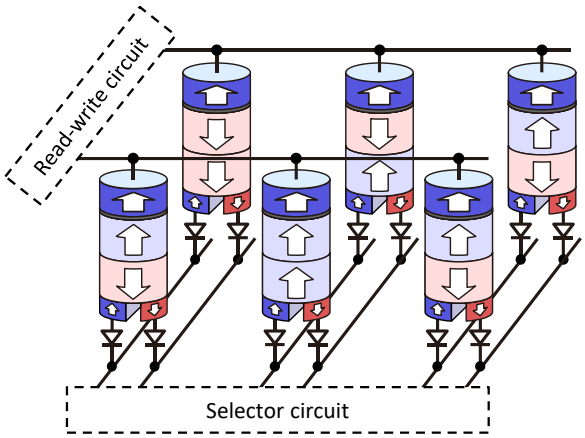

Fig. 4. Example circuit comprising six pillars with MTJ and individual diodes.

References

[1] Y. M. Hung, T. Li, R. Hisatomi, Y. Shiota, T. Moriyama, and T. Ono, "Low Current Driven Vertical Domain Wall Motion Memory with an Artificial Ferromagnet," *J. Magn. Soc. Jpn*., vol. 45, pp. 6, (2021).

[2] S. Honda and Y. Sonobe, "Single current control of magnetization in vertical high-aspect-ratio nanopillars on in-plane magnetization layers," *J. Phys. D: Appl. Phys*., vol. 57, pp.325002, (2024).

[3] S. Honda, Y. Sonobe, and S. J. Greaves, "Transforming domain motion for 3D racetrack memory with perpendicular magnetic anisotropy," *J. Phys. D: Appl. Phys*., vol. 54, pp.135002, (2021).

NIST SP 800-90B Compliant Perpendicular Magnetic Tunnel Junction Based True Random Number Generator

Qi Jia[1], Shannon Egan[2], Yang Lv[1] and Jian-Ping Wang[1*]

[1]Department of Electrical and Computer Engineering, University of Minnesota, Minneapolis, MN 55455, USA,
[2]Deep Science Ventures, London, UK

True random number generators (TRNGs) are essential for applications such as hardware security and cryptographic protocols. Stabilized spin-transfer torque-perpendicular magnetic tunnel junctions (STT-pMTJs) have emerged as a promising candidate for TRNGs due to their rapid switching speed and low energy consumption. The switching speed could be controlled by the voltage amplitude, enabling high quality bit generation with adjustable frequency. In previous studies, the quality of the generated bits is evaluated by NIST 800-22 standards, which are now considered outdated and insufficient for modern cryptographic requirements. In this work, we demonstrate a pMTJ-based TRNG with a low resistance-area (RA) product of 3.5 Ω·μm² and a tunnel magnetoresistance (TMR) ratio of 105%. The magnetization switching occurs in 2.70 ns with a probability of 50% at a current density of 3.38×10^7 A/cm². The generated bits achieve NIST SP 800-90B compliance with only a single XOR whitening step.

***Index Terms*—Spintronics, True random number generators, Magnetic tunnel junction**

I. Introduction

True Random Number Generators (TRNGs) are crucial for hardware security and cryptographic protocols. Conventional CMOS-based TRNGs face significant challenges due to poor power efficiency, hindering their scalability and reliability [1]. Spintronic devices, particularly magnetic tunnel junctions (MTJs), offer a promising alternative due to their low power consumption and rapid switching capabilities [2]-[11]. Recent studies have demonstrated that STT-pMTJ-based TRNGs can achieve randomness verified by the NIST 800-22 test suite [9]-[11]. However, this test suite is now considered outdated and insufficient for modern cryptographic requirements [12]. In contrast, NIST SP 800-90B defines stricter criteria for entropy sources [13], making it a critical standard for secure hardware applications.

In this work, we present a pMTJ-based TRNG that achieves NIST SP 800-90B compliance with only a single XOR whitening step. Voltage pulses induce probabilistic switching in the pMTJ, and the resulting bitstream is processed with XOR to enhance entropy. The processed output successfully passes all NIST SP 800-90B statistical tests, marking it as a promising candidate for next-generation secure random number generation.

II. TRNGs by STT-MTJ

The perpendicular MTJs used in this work are based on pMTJ of the core structure of CoFeB / MgO / CoFeB stack. The detailed structure is Ta(3) / CuN(40) / Ta(3) / CuN(40) / Ta(3) / Ru(10) / Ta(5) / CoFeB(1) / MgO / CoFeB(1) / $[Co(0.3)/Pd(1)]_{10}$ / Ta(5) / Cu(10) / Ru(5) / Ta(3), with all thickness in nanometers. Pillar-shaped devices with a diameter of 80 nm were fabricated using e-beam lithography and ion milling. The resulting MTJs exhibit a tunneling magnetoresistance (TMR) ratio of 105% and a resistance-area (RA) product of 3.5 Ω·μm². STT was employed to achieve deterministic switching between the parallel (P) and antiparallel (AP) states of the MTJ.

Two pulse generators were used to apply voltage pulses across the pMTJ. One generator produced a high-amplitude, long-duration pulse to reliably reset the MTJ to its initial state. The second pulse generator was then triggered to deliver a perturbation pulse with opposite polarity to attempt switching. The resistance state of the MTJ was measured after each perturbation pulse using a longer read-out voltage pulse to determine whether switching occurred. The overall cycle time is 100 μs (10 kbps).

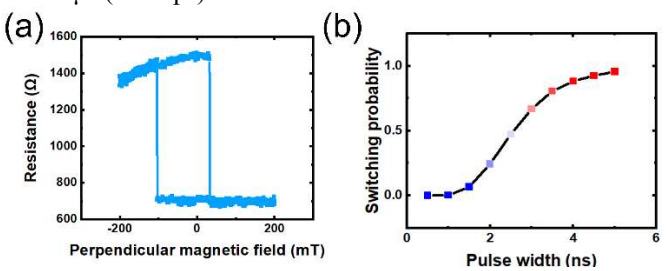

Fig. 1. (a) Resistance vs. perpendicular magnetic field, minor loop of the pMTJ. (b) Switching probability vs. perturbation pulse width of the pMTJ under fixed voltage of 1.19V. Test is at room temperature.

In the selected MTJ, whose R-H loop is shown in Fig. 1 (a), an out-of-plane magnetic field of -90 mT is applied to symmetrize the switching voltages for AP-to-P and P-to-AP transitions. In each trial, the MTJ was first reset to AP state using a -0.35 V, 500 ns pulse. The switching probability as a function of pulse width under a fixed pulse amplitude of 1.19 V is shown in Fig. 1(b). Each data point was obtained from 10,000 repeated trials. As the switching pulse width increases, the switching probability rises and approaches one, consistent with the nature of STT-induced switching. A 50% switching probability was achieved at a pulse width of 2.70 ns. To evaluate the randomness quality, we repeated the experiment under this condition and collected 10 million bits for statistical testing.

III. NIST Entropy Source Validation Testing

NIST SP 800-90B describes the validation process for entropy sources used in cryptographic random bit generation and is one of the key publications underpinning NIST's

Cryptographic Module Validation Program (CMVP) [13]. Under the SP 800-90B guidelines, random samples produced by a noise source may be evaluated according to the IID (independent and identically-distributed), or non-IID track. For the pMTJ-based TRNG, the binary outcome of each switching attempt (1 for a successful switch, 0 otherwise) is a Bernoulli random variable with switching probability p. Whether the IID assumption holds is primarily contingent on the stability of p across attempts (Fig. 2). If each switching attempt is an IID Bernoulli process, the number of successful switching events in n attempts should follow the binomial distribution with success probability p, i.e. X ~ B(n,p), where X is the observed number of AP-to-P switching events. XOR-whitened bitstreams using 2, 4, and 8 bits (abbreviated henceforth as XORk, where k is the number of bits) show excellent agreement with the statistics of a binomial distribution (Fig. 3), including the variance scaling as np(1-p) with the number of trials (Fig. 4), but raw bistreams do not. This simple analysis suggests that the IID assumption may be justified only for the XOR-whitened bitstreams.

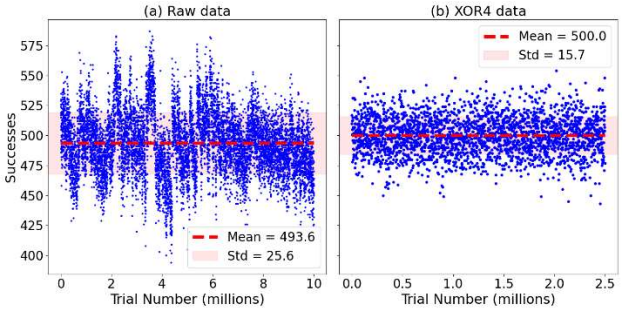

Fig. 2. (a) Number of successful switching attempts over 1000 trials for sequential samples of the raw bitstream. Visible clustering indicates that p is not constant for each set of switching attempts. (b) Number of 1's over 1000 values of the XOR4 bitstream.

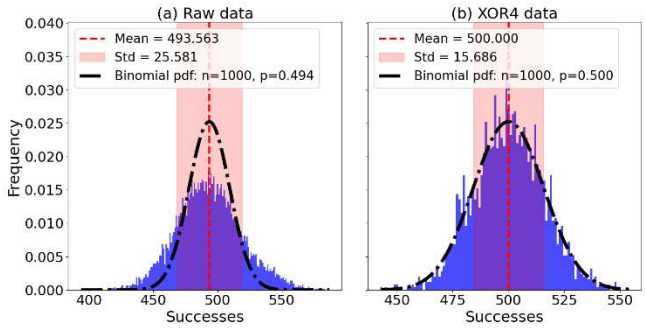

Fig. 3. Histogram of number of successful switching attempts over 1000 trials for sequential samples of the raw bitstream (a) and 4-bit XOR-whitened bitstream (b). In XOR4 data, the expected value and standard deviation of the sample mean show excellent agreement with a binomial distribution of $p = 0.5$ and $\sigma^2 = p(1-p)n = (15.811)^2$.

We ran all bitstreams through SP 800-90B IID track testing: the raw bitstream passes only 7/22 IID tests, while XOR2, XOR4, and XOR8 bitstreams pass all 22/22. This result forces us to reject the IID assumption in the raw bitstream but supports the IID assumption for XOR-whitened bitstreams. The final entropy estimated for each bitstream, each with different degrees of XOR whitening, is given in Table I.

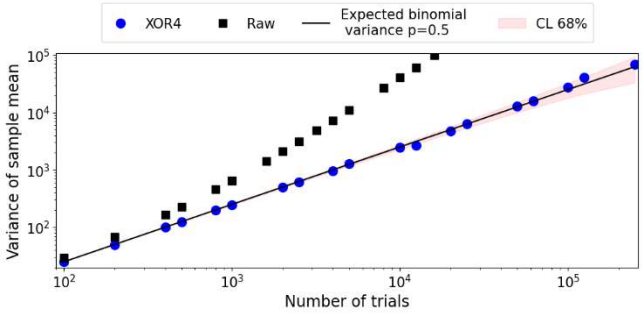

Fig. 4. Variance of the sample mean for sequential samples of XOR4 bitstreams. Each data point is extracted from the variance of the successful switching attempts histograms shown in Fig. 3.

TABLE I

Operation	Final entropy estimates (H)
Raw data	0.781805*
XOR2	0.981412
XOR4	0.995630
XOR8	0.995149

Final entropy estimates (H) from NIST entropy source validation, following the entropy estimation strategy from NIST SP 800-90B. *Raw data evaluated according to non-IID track.

REFERENCES

[1] K. Yang, et al. "16.3 A 23Mb/s 23pJ/b fully synthesized true-random-number generator in 28nm and 65nm CMOS," in 2014 IEEE International Solid-State Circuits Conference Digest of Technical Papers (ISSCC), Feb. 2014, pp. 280–281.

[2] W. H. Choi *et al.*, "A Magnetic Tunnel Junction based True Random Number Generator with conditional perturb and real-time output probability tracking," in *2014 IEEE International Electron Devices Meeting*, Dec. 2014, p. 12.5.1-12.5.4.

[3] A. Fukushima *et al.*, "Spin dice: A scalable truly random number generator based on spintronics," *Appl. Phys. Express*, vol. 7, no. 8, p. 083001, Jul. 2014.

[4] H. Lee, F. Ebrahimi, P. K. Amiri, and K. L. Wang, "Design of high-throughput and low-power true random number generator utilizing perpendicularly magnetized voltage-controlled magnetic tunnel junction," *AIP Adv.*, vol. 7, no. 5, p. 055934, Mar. 2017.

[5] L. Rehm *et al.*, "Temperature-resilient random number generation with stochastic actuated magnetic tunnel junction devices," *Appl. Phys. Lett.*, vol. 124, no. 5, p. 052401, Jan. 2024.

[6] Y. Wang, H. Cai, L. A. B. Naviner, J.-O. Klein, J. Yang, and W. Zhao, "A novel circuit design of true random number generator using magnetic tunnel junction," in *2016 IEEE/ACM International Symposium on Nanoscale Architectures (NANOARCH)*, Jul. 2016, pp. 123–128.

[7] Y. Q. Xu *et al.*, "Self-stabilized true random number generator based on spin–orbit torque magnetic tunnel junctions without calibration," *Appl. Phys. Lett.*, vol. 125, no. 13, p. 132403, Sep. 2024.

[8] X. Chen, J. Zhang, and J. Xiao, "Magnetic-Tunnel-Junction-Based True Random-Number Generator with Enhanced Generation Rate," *Phys. Rev. Appl.*, vol. 18, no. 2, p. L021002, Aug. 2022.

[9] H. J. Ng, S. Yang, et al. "Provably Secure Randomness Generation from Switching Probability of Magnetic Tunnel Junctions," Phys. Rev. Appl., vol. 19, no. 3, p. 034077, Mar. 2023.

[10] L. Rehm et al., "Stochastic Magnetic Actuated Random Transducer Devices Based on Perpendicular Magnetic Tunnel Junctions," Phys. Rev. Appl., vol. 19, no. 2, p. 024035, Feb. 2023.

[11] L. Schnitzspan, et al. "Nanosecond True-Random-Number Generation with Superparamagnetic Tunnel Junctions: Identification of Joule Heating and Spin-Transfer-Torque Effects," Phys. Rev. Applied, vol. 20, no. 2, p. 024002, Aug. 2023.

[12] I. T. L. Computer Security Division, "Decision to Revise NIST SP 800-22 Rev. 1a | CSRC," CSRC | NIST. Accessed: May 22, 2025. [Online].

[13] M. Sönmez Turan, et al. "Recommendation for the Entropy Sources Used for Random Bit Generation," National Institute of Standards and Technology, NIST Special Publication (SP) 800-90B, Jan. 2018.

Topological heterostructure engineering toward advanced read head technologies for hard disk drives

Zhenchao Wen[1], Talluri Manoj[1], Seiji Mitani[1], Hiroaki Sukegawa[1], Brian York[1], Xiaoyong Liu[2], Maki Maeda[2], and Quang Le[2]

[1]National Institute for Materials Science (NIMS), Tsukuba 305-0047, Japan, wen.zhenchao@nims.go.jp
[2]Western Digital, San Jose, California 95119, United States

The engineering of topological heterostructures is crucial for developing next-generation spintronic devices, including advanced read heads for ultrahigh-density hard disk drives. BiSb-based topological insulator (TI) systems are promising candidates for enhancing the spin Hall effect due to their unique surface states. However, interfacial issues with ferromagnetic (FM) layers can degrade device performance. In this work, we demonstrate that the strategic insertion of titanium (Ti)-based interlayers (ILs) in BiSb/FM heterostructures significantly improves spin Hall efficiency. Studies on BiSb/NiFe structures with a Ti interlayer show that the IL protects the topological surface states and suppresses interdiffusion, exhibiting both thermal and temporal robustness. These findings highlight how interface engineering can effectively manipulate spin Hall efficiency, offering a viable pathway for integrating topological materials into future advanced read head components.

Keywords: topological insulator BiSb, interface engineering, spin Hall efficiency, titanium-based interlayers

I. Introduction

The continuous demand for higher data storage densities in hard disk drives (HDDs) necessitates innovations in read head technologies. Topological insulators (TIs), such as BiSb, have emerged as promising materials due to their giant spin-charge conversion efficiency originating from topological surface states.[1], [2], [3] This unique property is highly relevant for developing advanced spintronic devices, including potentially novel read head sensors that could utilize spin Hall and inverse spin Hall effects.[4], [5], [6] However, challenges in fabricating high-quality TI thin films and managing interfacial effects with ferromagnetic (FM) layers can suppress these crucial surface states and hinder spin transport. An effective interlayer (IL) is essential to prevent interdiffusion and preserve the structural integrity of BiSb, thereby enhancing spin-charge conversion. This research focuses on engineering BiSb-based heterostructures with Ti-based ILs to optimize spin Hall efficiency, a key parameter for such advanced reader technology for ultrahigh-density HDDs.

II. Experimental Methodology

All thin films were deposited on single-crystalline c-plane sapphire [Al_2O_3 (0001)] substrates using a room-temperature DC magnetron sputtering system. To investigate thickness-dependent transport and structural properties, the BiSb layers' total thickness varied between 4 and 12 nm. In comparison, a nominal thickness of 10 nm was selected for optimal crystallinity and surface morphology in the heterostructure studies. Titanium-based interlayers, i.e., metallic Ti, TiN_x, and TiO_x, were introduced between BiSb and ferromagnetic layers (NiFe or CoFeB). Reactive sputtering was used for TiN_x and TiO_x depositions under controlled Ar/N_2 or Ar/O_2 gas environments.

The films' crystallographic texture and phase purity were examined by X-ray diffraction (XRD) using Cu-Kα radiation, and surface morphology was analyzed by atomic force microscopy (AFM). Reflection high-energy electron diffraction (RHEED) was also employed in situ to monitor surface crystallinity in the deposition chamber. Cross-sectional scanning transmission electron microscopy (STEM) was performed to evaluate the interfacial microstructure and elemental diffusion across layers. Magnetic properties, including magnetic moment and potential dead layer formation, were characterized using a vibrating-sample magnetometer (VSM). Device fabrication for spin-orbit torque (SOT) measurements was performed using conventional UV lithography and Ar ion milling to define bar-shaped devices integrated with a coplanar waveguide structure. Spin-torque ferromagnetic resonance (ST-FMR) measurements were then conducted at various frequencies and magnetic field angles to extract spin Hall efficiencies. Measurements were performed for both as-deposited and annealed samples (400 K, 1 h), as well as samples aged at room temperature for 45 days to evaluate thermal and temporal stability.

III. Results and Discussion

A. Structural and Morphological Analysis

XRD patterns confirmed that the BiSb films exhibited strong (0001)-textured growth, particularly for thicknesses above 8 nm, which is favorable for maintaining robust topological surface states. *In-situ* RHEED patterns after the deposition of BiSb showed polycrystalline features. At the same time, it became a highly textured structure after being post-annealed at 400 K. AFM images revealed smooth surface morphology, with average roughness below 0.7 nm, indicating high surface quality suitable for spin transport measurements. Thickness-dependent resistivity measurements for the BiSb thin films illustrated the emergence of topological surface states.

Cross-sectional STEM analysis indicated that the Ti-insertion after annealing improved crystallinity and that the Ti

layer acted as an effective barrier to suppress interdiffusion, which could preserve the topological properties of BiSb films.

B. Spin Hall Efficiency

We performed ST-FMR measurements to examine the spin Hall efficiency in the BiSb/IL/FM heterostructures, as shown in Figure 1. Applying an RF charge current in the BiSb layer generates an oscillating transverse spin current. This spin current transfers spin angular momentum to the FM layer through the IL, exciting FMR. The resulting FMR signal contains an anti-symmetric Lorentzian line shape (V_A) and a symmetric Lorentzian line shape (V_S). The V_A results from the Oersted field and the field-like torque, while the V_S is related to the damping-like torque from the spin current. All the samples show clear ST-FMR spectra.

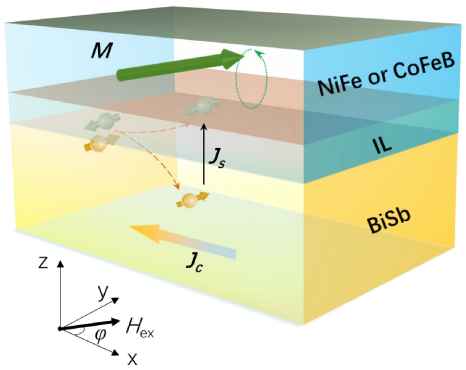

Fig. 1. Illustration of BiSb-based heterostructure and ST-FMR measurement.

Figure 2 shows representative ST-FMR spectra measured in the as-deposited samples of BiSb (10 nm)/NiFe (15 nm) and BiSb (10 nm)/Ti (2 nm)/NiFe (15 nm). A significantly large value of V_S/V_A was observed in the sample with Ti interlayer, indicating an enhancement of the spin Hall efficiency. After annealing at 400 K, the BiSb/NiFe sample without IL exhibited a spin Hall efficiency of ~0.3. The insertion of a Ti IL increased the spin Hall efficiency to ~1.2, indicating more than a fourfold improvement. This enhancement also persisted after 45-day ambient aging, demonstrating the thermal and temporal robustness of the Ti-inserted heterostructures. In the BiSb/IL/CoFeB systems, ST-FMR measurements showed that TiN_x as the IL yielded a relatively high spin Hall efficiency, while Ti and TiO_x showed moderate values. These differences suggest that a suitable IL can preserve the topological surface states of BiSb and suppress elemental interdiffusion, maintaining an effective large spin current across the interface.

IV. Conclusion

The engineering of topological heterostructures through the strategic use of interlayers demonstrates a significant enhancement in spin Hall efficiency for BiSb-based systems. The observed improvements, particularly with Ti and TiN_x interlayers, by protecting topological surface states and mitigating interdiffusion, are crucial for topological heterostructures. These findings highlight the potential of utilizing such interface-engineered TI/FM systems for developing advanced spintronic components, contributing towards next-generation read head technologies for HDDs where efficient spin-charge interconversion and robust material interfaces are imperative.

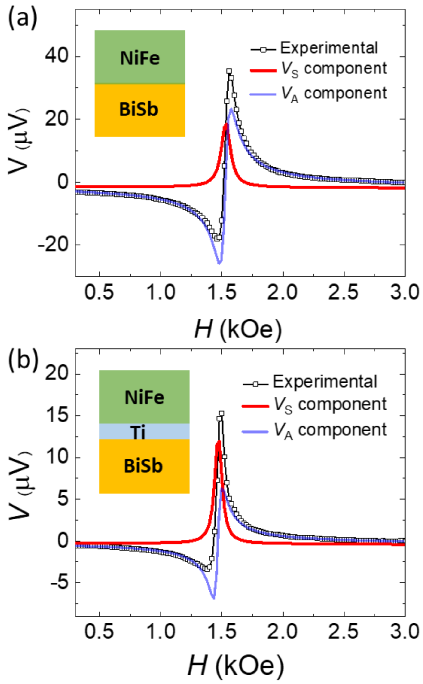

Fig. 2. Representative ST-FMR spectrum (f = 2 GHz, P = 15 dBm, and φ = 45°) in the samples of (a) BiSb (10 nm)/NiFe (15 nm) and (b) BiSb (10 nm)/Ti (2 nm)/NiFe (15 nm).

References

[1] N. H. D. Khang, Y. Ueda, and P. N. Hai, "A conductive topological insulator with large spin Hall effect for ultralow power spin–orbit torque switching," *Nat. Mater.*, vol. 17, pp. 808–813, Jul. 2018, doi: 10.1038/s41563-018-0137-y.

[2] T. Manoj *et al.*, "Spin–Orbit Torque Modulated by Interface Chemistry in Topological BiSb/NiFe Bilayers with Titanium Insertion," *ACS Appl. Electron. Mater.*, vol. 6, no. 6, pp. 4269–4276, Jun. 2024, doi: 10.1021/acsaelm.4c00357.

[3] X.-G. Zhu *et al.*, "Three Dirac points on the (110) surface of the topological insulator Bi1−xSbx," *New J. Phys.*, vol. 15, no. 10, p. 103011, Oct. 2013, doi: 10.1088/1367-2630/15/10/103011.

[4] V. T. Pham *et al.*, "Spin–orbit magnetic state readout in scaled ferromagnetic/heavy metal nanostructures," *Nat. Electron.*, vol. 3, no. 6, pp. 309–315, Jun. 2020, doi: 10.1038/s41928-020-0395-y.

[5] H. H. Huy *et al.*, "Large inverse spin Hall effect in BiSb topological insulator for 4 Tb/in2 magnetic recording technology," *Appl. Phys. Lett.*, vol. 122, no. 5, p. 052401, Jan. 2023, doi: 10.1063/5.0135831.

[6] M. Liu *et al.*, "Spin Hall magnetic field sensing device using topological insulator," *Appl. Phys. Lett.*, vol. 125, no. 24, p. 242401, Dec. 2024, doi: 10.1063/5.0233246.

Magnetization reversal cluster size under microwave field excitation

Nobuaki Kikuchi[1], Kota Sakunami[1], Takehito Shimatsu[2,3], and Satoshi Okamoto[4]

[1]Department of Mathematical Science and Electrical-Electronic-Computer Engineering, Graduate School of Engineering Science, Akita University, Akita 010-8502, Japan, kikuchin@gipc.akita-u.ac.jp
[2] Frontier Research Institute for Interdisciplinary Sciences, Tohoku University, Sendai 980-8578, Japan
[3]Research Institute of Electrical Communication, Tohoku University, Sendai, Miyagi 980-8577, Japan
[4]Institute of Multidisciplinary Research for Advanced Materials, Tohoku University, Sendai, 980-8577, Japan

We study the effect of microwave field applications on the cluster size of magnetization reversal by numerical calculation. Averaged grain diameter of 6 nm is assumed and the exchange interaction between grains is varied from 0 to 10 % of the bulk values. The exchange interaction between grains tends to increase the assistance effect, although the critical frequency significantly decreases. The analysis of the cluster size during magnetization reversal based on the autocorrelation function revealed that the microwave field reduces the cluster size of magnetization reversal, and the effect also vanishes at critical frequency. The result suggests that the both effect has to be considered for designing media.

***Index Terms*—Microwave assisted magnetic recording, microwave assisted switching, thermal activation, LLG equation.**

I. Introduction

MICROWAVE ASSISTED recording (MAMR) is one of the promising techniques to enhance magnetic recording densities [1]. By applying microwave field with GHz frequency, excited magnetization can be switched under reduced magnetic field. The switching behavior, so-called microwave assisted switching (MAS), allows us to employ magnetic media with higher magnetic anisotropy. Analytical and numerical calculations have predicted that the switching field decreases linearly with increasing microwave frequency. The ratio between the assistance effect (switching field reduction) and microwave frequency is given by $-2\pi/\gamma$ [2, 3], where γ is the gyromagnetic ratio. The reduction of switching field has been widely observed in experiments with various materials including granular media. It is widely known that exchange interaction between grains modifies the switching behavior of granular media [4-8]. In the previous studies, we have reported experimental results that the frequency dependence of the microwave assistance effect is strongly affected by introducing exchange interaction between grains in CoCrPt-SiO_2 granular films [6]. The introduced exchange interaction enhances assistance effect at low microwave frequency region, although the critical frequency moves toward lower frequency. It can be expected that the exchange interaction helps excitement of cooperative presession, while the reversal cluster size increases.

In this study, we have carried out quantitative evaluation of cluster size under microwave field by micromagnetics simulations.

II. Calculation method

Numerical calculations were carried out using a GPU-based micromagnetics software mumax3 [9]. In the calculation, a film of 512×512 nm^2 were divided into Voronoi cells with average grain size of 6 nm as shown in Fig. 1. The film thickness is set to be 12 nm. The saturation magnetization M_s and the uniaxial anisotropy constant K_u are M_s = 600 kA/m and 6×10^5 J/m^3, respectively. The exchange stiffness constant inside grain A_{bulk} is set to be 1×10^{-11} J/m, while the exchange stiffness constant between grains were varied between grains A_{ex} is varied from 0 to 1×10^{-12} J/m, corresponding to A_{ex}/A_{bulk} = 0 – 0.1. The temperature T is set as 300 K, to introduce the effect of thermal activation. The easy axis is along the film normal. Magnetization reversal behavior is calculated in an external dc magnetic field H_{dc} swept from $\mu_0 H_{dc}$ = 0 to 2 T. Microwave field H_{rf} is applied in-plane direction with the amplitude of $\mu_0 H_{rf}$ = 50 mT. The microwave frequency f_{rf} is varied from 0 to 32 GHz.

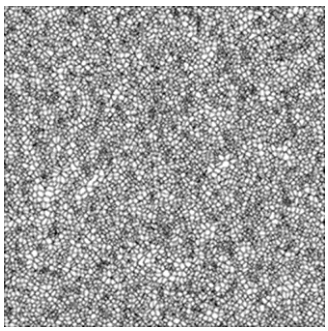

Fig. 1. Voronoi cells used for calculation. The total area is 512 × 512 nm^2 and the averaged grain diameter is 6 nm.

III. Results and Discussion

Figure 2 shows the magnetization configuration under external dc field around coercivity for f_{rf} = 0 and 14 GHz. The results for the exchange interaction between grains A_{ex}/A_{bulk} = 0, 0.02, 0.05 and 0.1 are shown. The bright area corresponds to the reversed region, while the dark area corresponds to the unreversed region. It is clearly seen that the increase of the exchange interaction causes the increase of the magnetic cluster size. The cluster size under microwave field application looks slightly smaller, but the difference is not significant. We evaluated the cluster size by calculating the spatial autocorrelation of the magnetization configuration. Figure 3 shows autocorrelation as a function of the radius r for f_{rf} = 14 GHz and A_{ex}/A_{bulk}= 0.05. We defined the autocorrelation length

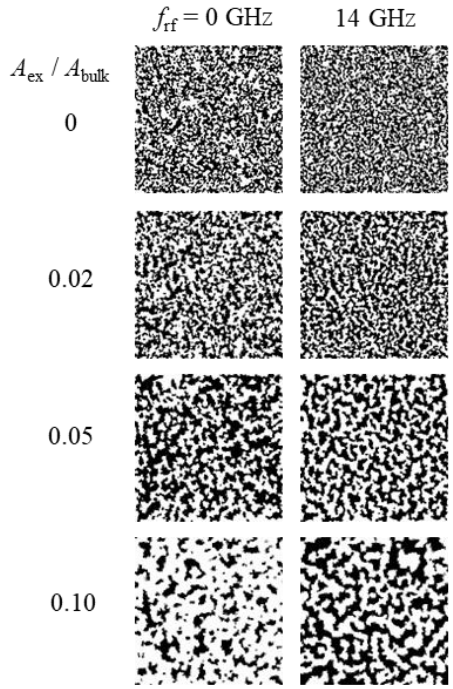

Fig. 2 Magnetization configuration under external dc field around coercivity. The microwave frequency f_{rf} = 0 and 14 GHz, and the ratio of exchange constant between grains and bulk are A_{ex}/A_{bulk} = 0 – 0.1, respectively. Each image corresponds to the area of 512×512 nm².

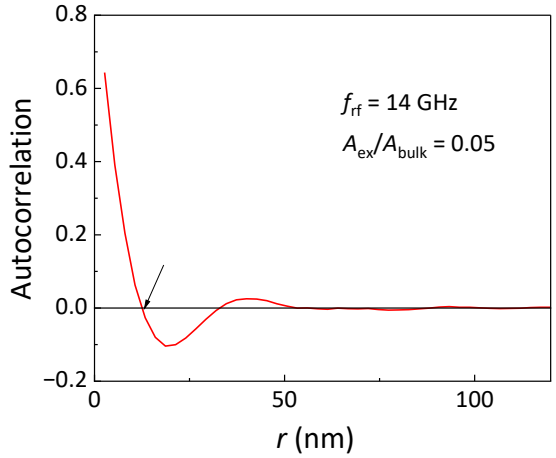

Fig. 3 Spatial autocorrelation as a function of radius r for f_{rf} = 14 GHz and A_{ex}/A_{bulk} = 0.05. The arrow indicates the autocorrelation length r_0 at which autocorrelation becomes zero.

r_0 at which the autocorrelation becomes zero, as indicated by the arrow in Fig. 3. The autocorrelation length r_0 is expected to reflect the magnetization cluster size. In Fig. 4 (a) and (b), coercivity and autocorrelation length are plotted as a function of microwave frequency for A_{ex}/A_{bulk}= 0 and 0.05. As shown in Fig. 4 (a), coercivity decreases with increasing the microwave frequency, and shows the rather clear critical frequency for both values of A_{ex}/A_{bulk}. The critical frequency becomes lower by the exchange interaction between grains. The cluster size also decreases with increasing the microwave frequency and returns to the value at f_{rf} = 0 GHz above the critical frequency. The two parameters, coercivity and autocorrelation length, show very similar frequency dependence. The results suggest that the

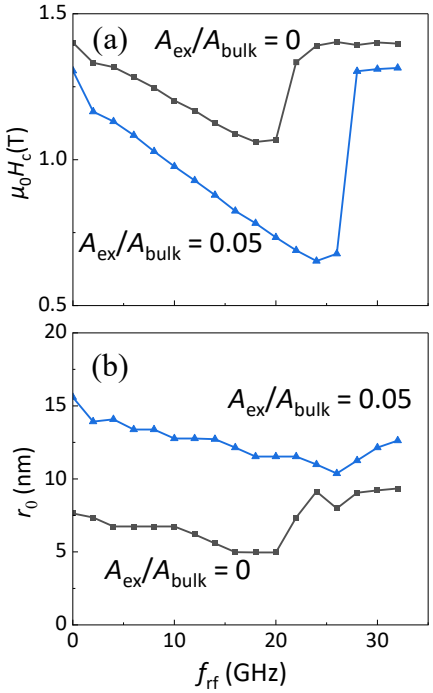

Fig. 4 (a) Coercivity and (b) autocorrelation length r_0 as a function of microwave frequency f_{rf} for A_{ex}/A_{bulk} = 0 and 0.05.

application of microwave field is effective not only for the reduction of switching field, but also for controlling the magnetic cluster size.

ACKNOWLEDGMENTS

This work was partly supported by ASRC and JSPS KAKENHI Grant Number JP25K07816.

REFERENCES

[1] J.-G. Zhu, X. Zhu, and Y. Tang, IEEE Trans. Magn., Vol. 44, pp. 125-131, 2008.
[2] G. Bertotti, I. D. Mayergoyz, C. Serpico, M. D'Aquino, and R. Bonin, J. Appl. Phys., Vol. 105, pp. 1-5, 2009.
[3] S. Okamoto, M. Igarashi, N. Kikuchi, and O. Kitakami, J. Appl. Phys., Vol. 107, p. 123914, 2010.
[4] S. Okamoto, N. Kikuchi, M. Furuta, O. Kitakami, and T. Shimatsu, Phys. Rev. Lett. Vol. 109, p. 237209, 2012
[5] H. Suto, T. Kanao, T. Nagasawa, K. Mizushima, and R. Sato, Sci. Rep. Vol. 7, p. 13804, 2017
[6] N. Kikuchi, K. Sato, S. Kikuchi, S. Okamoto, T. Shimatsu, O. Kitakami, H. Osawa, and M. Suzuki, J. Appl. Phys. Vol. 126, 083908, 2019.
[7] N. Kikuchi, K. Sato, S. Okamoto, O. Kitakami, T. Shimatsu, and H. Suto, Phys. Rev. B, Vol. 105, p. 054430, 2022.
[8] H. Suto, K. Kudo, T. Nagasawa, T. Kanao, K. Mizushima, R. Sato, S. Okamoto, N. Kikuchi, and O. Kitakami, Phys. Rev. B, vol. 91, p. 094401, 2015.
[9] A. Vansteenkiste, J. Leliaert, M. Dvornik, M. Helsen, F. Garcia-Sanchez B. Van Waeyenberge, AIP advances, Vol. 4, p. 107133, 2014

Impact of Metal, Oxide, and Hybrid Metal-Oxide Interlayers on Spin-Hall Effect in BiSb Topological Insulator and Magnetic Interfaces

Zhang Ruixian[1], Quang Le[2], XiaoYong Liu[2], Lei Xu[2], Brian R.York[1], Cherngye Hwang[1], Son Le[2], Maki Maeda[3], Tuo Fan[3], Yu Tao[3], Hisashi Takano[3], Min Liu[1], Shota Namba[1], Pham Nam Hai[1]

[1]Department of Electrical and Electronic Engineering, Institute of Science Tokyo, Tokyo 152-8552, Japan
[2]Western Digital Corp., Great Oaks site, San Jose, CA 95119, USA, quang.le@wdc.com
[3]Western Digital Corp., Fujisawa site, Kanagawa 252-0811, Japan
Email: zhang.r.an@m.titech.ac.jp

The charge-to-spin conversion efficiency at the interface between a topological insulator (TI) and a ferromagnetic (FM) layer can be enhanced by inserting an interlayer (ITL). However, the mechanism of this enhancement is unclear. In this work, we systematically investigate the ITL effects by introducing various metals, oxides, and hybrid metal/oxide ITL between a BiSb topological insulator and a CoFe ferromagnetic layer. Our findings revealed that using a metallic NiFeGe or insulating MgO ITL resulted in similarly high efficiencies, with the highest efficiency achieved when employing hybrid NiFeGe/MgO ITL. However, efficiency decreased when NiFeGe was combined with MgTiO with increasing TiO composition. Such behaviors can be qualitatively understood by considering the ITL intrinsic effect of enhancing the intrinsic spin Hall angle of BiSb via preventing Sb diffusion from BiSb and migration of the FM, and the extrinsic effect where the ITL spin transparency is determined by the spin tunneling/diffusion across the ITL and the spin-flip/spin-transfer at the ITL/FM interface. This study provides valuable insights and a framework for understanding and optimizing interlayer materials for ultralow power spin-orbit torque applications.

***Index Terms*—Topological insulator, spin Hall effect, spin-orbit torque, SOT-MRAM, interfacial effect, spin tunneling, spin diffusion.**

I. Introduction

Recently, several topological quantum materials with nontrivial band structures, such as Bi_2Se_3,[1] $(Bi,Sb)_2Te_3$,[2] and BiSb[3] topological insulators (TIs) and YPtBi topological semimetals (TSM)[4] have shown such a giant θ_{SH}. Among them, BiSb has attracted considerable attention as a promising SOT material candidate for future energy-efficient SOT device applications because it shows both giant room-temperature θ_{SH} and high electrical conductivity, and industrial tools can deposit it. However, the research on this BiSb material is still in its early stages, and the related physical, material, and device optimization remain to be addressed.

In this work, we aim to investigate and compare the effects of inserting metal, oxide, and hybrid metal-oxide interlayers between the BiSb and FM layer. We not only observe how effectively they can enhance the charge-to-spin conversion efficiency but also study the mechanism behind their effects. To determine the interlayers' relative efficiency, we evaluate their dampinglike SOT efficiency per unit current density, ξ^j_{DL}, or effective spin Hall angle θ^{eff}_{SH}, which is a function of the product of T_{IST}, the interfacial spin transparency, and θ_{SH}, the intrinsic spin Hall angle, as given by Eq. 1,[5]

$$\xi^j_{DL} \equiv \theta^{eff}_{SH} = T_{IST}\theta_{SH} \quad (1)$$

Then, we explain the impact of each type of interlayer on ξ^j_{DL}. Our study can provide a useful framework for understanding ultrahigh ξ^j_{DL} and guidance on increasing it by optimizing the TI's interlayer material for ultralow power SOT applications.

II. Experiment Procedure

The whole BiSb stack consists of a buffer, a 10 nm BiSb layer, a matrix of interlayers by wafer, a ferromagnetic (FM) 0.7 nm $Co_{40}Fe_{60}$ layer, and a capping layer that was deposited at room temperature on a silicon oxide substrate after a conventional cleaning process, followed by a light sputter etch inside a physical vapor deposition tool. The buffer and matrix of the interlayers are designed to promote BiSb (012) orientation, prevent migration and Sb diffusion, and offer greater resistivity than BiSb to minimize shunting. A series of interlayer materials, including metals, oxides, and hybrid metal/oxides such as NiFeGe, MgO, NiFeGe/MgO, and NiFeGe/MgTiO were incorporated into the BiSb stacks for a comparative analysis of their effectiveness on ξ^j_{DL} and impact on θ_{SH} and T_{IST}. Structural, thickness, composition, and orientation characterization of the BiSb stacks with a matrix of interlayers were confirmed by using XRR, XRF, and XRD data, and TEM image. Figure 1

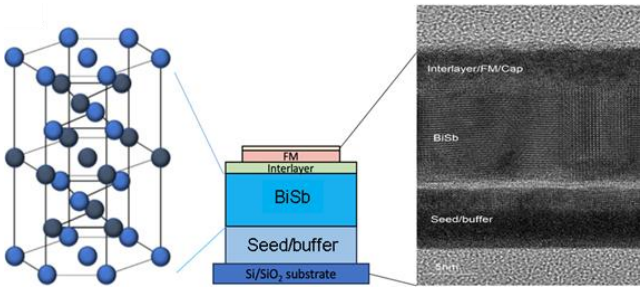

Figure 1. The representative BiSb stack consists of seed/buffer layers, a 10 nm BiSb layer, a matrix of interlayers by wafer, an FM layer, and a capping layer deposited at room temperature.

shows a typical stack structure and cross-section TEM.

In this work, ξ^j_{DL} is obtained by exploiting the second harmonics Hall technique. An AC is applied in-plane to the BiSb/FM Hall bar, generating an alternating pure spin current due to the spin Hall effect. This spin current diffuses to the adjacent FM layer across the interface, subsequently exerting an SOT on the FM layer. Consequently, the FM's oscillation as the result of the SOT gives rise to the second harmonic Hall voltage response, which is characterized by Eq. 2 for the case of in-plane magnetization,

$$R_H^{2\omega} = \frac{R_{AHE}}{2}\left(\frac{H_{AD}}{H_k + H_x}\right) + \alpha_{ONE} H_x + R_{ANE+SSE}, \qquad (2)$$

where $R_H^{2\omega}$ is the second harmonic Hall resistance, R_{AHE} is the anomalous Hall resistance, H_{AD} is the anti-damping like field, H_k is the effective magnetic anisotropy field, H_x is the in-plane applied magnetic field, α_{ONE} is the ordinary Nernst effect coefficient, and $R_{ANE+SSE}$ is a constant representing contribution of the anomalous Nernst effect and spin Seebeck effect.

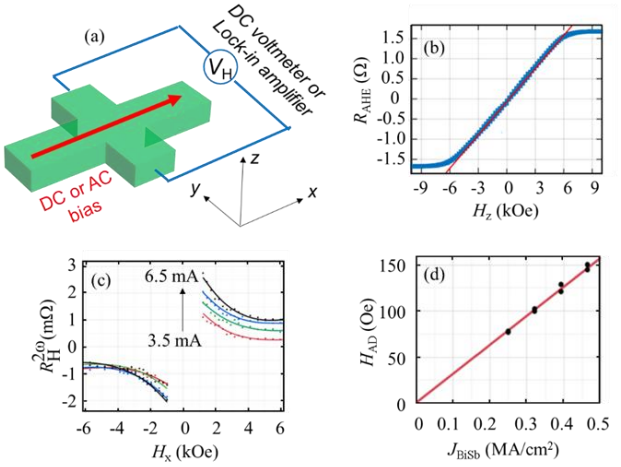

Figure 2. Representative measurement of a sample with a 10 nm-thick BiSb layer, a 1.2 nm MgO interlayer, a 0.7 nm-thick CoFe FM layer. **(a)** Illustration of the measurement circuit. **(b)** Anomalous Hall resistance measured with a perpendicular magnetic field.**(c)** Second harmonic Hall resistance (points) and the corresponding fitting (solid lines). **(d)** Damping-like field H_{AD} as a function of the current density J_{BiSb} in BiSb.

Figure 2(a) illustrates the measurement circuit using Hall bar devices. The fabricated Hall bar devices have four terminals and measures 10 × 25 μm². We first measured R_{AHE} and H_k with a DC bias and a perpendicular magnetic field. Then, we measure $R_H^{2\omega}$ while sweeping an in-plane magnetic field along the x direction. We then fit the $R_H^{2\omega}$ - H_x data into Eq. 2 to estimate H_{AD} and plot H_{AD} as a function of the current density inside BiSb, J_{BiSb}. Finally, we estimate ξ^j_{DL} from the slope of $\frac{H_{AD}}{J_{BiSb}}$ as shown in the following Eq. 3:

$$\xi^j_{DL} = (2e/\hbar) M_S\, t_{FM}\, \frac{H_{AD}}{J_{BiSb}}, \qquad (3)$$

where M_S is the measured saturation magnetization of the FMlayer, and t_{FM} = 0.7 nm is its thickness.

III. ξ^j_{DL} of Metals, Oxides, and Hybrid Metal-Oxides Interlayers

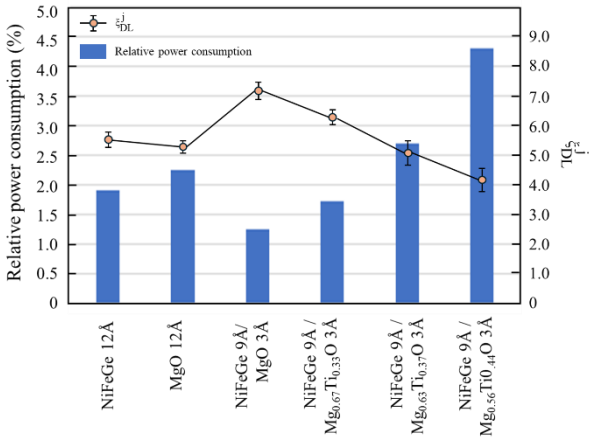

Figure 3. ξ^j_{DL} as the function of metal, oxide, and hybrid metal/oxide interlayers and power consumption as the function of interlayers, relative to that of Ta.

Figure 3 shows ξ^j_{DL} and relative power comsumption of sample A_1 with a NiFeGe (12 Å) ITL, sample A_2 with an MgO (12 Å) ITL, sample B with a hybrid NiFeGe (9 Å) /MgO (3 Å) ITL, and samples C_1-C_3 with a NiFeGe (9 Å) /$Mg_{1-x}Ti_xO$ (3 Å) ILT whose x was 0.33, 0.37, and 0.44, respectively. We normalized the power consumption by that of a reference sample with a 10 nm-thick Ta layer, which shows ξ^j_{DL} = 0.18. A closer examination of Fig. 3 reveals a large ξ^j_{DL}, small relative power consumption in the samples A_1 and A_2 with NiFeGe and MgO ITL, while the maximum ξ^j_{DL} and minimum relative power consumption is achieved in the sample B with the hybrid NiFeGe/MgO ITL, and it decreases in samples C_1-C_3 with the NiFeGe/MgTiO ITL whose TiO concentration gradually increases. In comparison, we only observed ξ^j_{DL} of 0.2 for the sample N without an ILT. This result clearly shows that selecting an optimal interlayer can effectively tune θ_{SH} and the spin transmission into the FM layer and hence ξ^j_{DL}.

We thoroughly studied the impact of different metal, oxide, and hybrid metal/oxide interlayers on the charge-to-spin conversion efficiency of BiSb thin films. Our findings revealed that utilizing a NiFeGe or MgO interlayer resulted in nearly the same high efficiency, with the highest efficiency achieved when using hybrid NiFeGe/MgO interlayers. However, efficiency decreased when NiFeGe was combined with MgTiO with increasing TiO composition. Such behaviors can be qualitatively understood by considering the ITL intrinsic effect of enhancing the intrinsic θ_{SH} via preventing Sb diffusion from BiSb and migration of the FM.

REFERENCES

[1] A. R. Melnik, et al. Nature 511, 449 (2014).
[2] H. Wu, P. Zhang, P. Deng, Q. Lan, Q. Pan, S. A. Razavi, X. Che, L. Huang, B. Dai, K. Wong, X. Han, K. L. Wang, Phys. Rev. Lett. 123, 207205 (2019)
[3] N. H. D. Khang, Y. Ueda, P. N. Hai, Nat. Mater. 17, 808 (2018).
[4] T. Shirokura, T. Fan, N.H.D. Khang, T. Kondo, P. N. Hai, Sci. Rep., 12, 2426 (2022).
[5] L. Zhu, D. C. Ralph, R. A. Buhrman, Phys. Rev. B 99, 180404(R) (2019)

Optical control of RKKY coupling and perpendicular magnetic anisotropy in a synthetic antiferromagnet

Meiyang Ma[1, 2], Jing Wu[3, 4, *], Bo Liu[1, 2, *], Lei Wang[5], Zhuoyi Li[1, 2], Xuezhong Ruan[1, 2], Zehua Hu[2], Fengqiu Wang[2], Xianyang Lu[1, 6], Tianyu Liu[7], Jun Du[7], Ke Xia[5], Yongbing Xu[1, 2, 4, 6, *]

[1] National Key Laboratory of Spintronics, Nanjing University, Suzhou 215163, China [2]School of Electronic Science and Engineering, Nanjing University, Nanjing 210093, China

[3]School of Integrated Circuits, Guangdong University of Technology, Guangzhou, 510006, China

[4]School of Physics, Electronics and Technology, University of York, York YO10 5DD, UK

[5]Key Laboratory of Quantum Materials and Devices of Ministry of Education, School of Physics, Southeast University, Nanjing 211189, China

[6]School of Integrated Circuits, Nanjing University, Suzhou 215163, China

[7]Department of Physics, Nanjing University, Nanjing 210093, China

Synthetic antiferromagnetics (SAF) provide an excellent platform for antiferromagnetic spintronics. Recently, the voltage-control of the Ruderman–Kittel– Kasuya–Yosida (RKKY) interaction in SAFs was studied experimentally. Optical control would offer unique opportunities for the ultrafast manipulation of spin states, however, it has yet to be demonstrated. Here, using femtosecond laser excitations in a [Co/Pt]-based perpendicular magnetic anisotropy (PMA) synthetic antiferromagnet (p-SAF), we drive a reduction of the RKKY coupling and the PMA. We attribute the reduced RKKY interaction to the optically smeared Fermi wave vector of the Ru layer, which mediates the exchange coupling between the constituent ferromagnetic layers. The PMA exhibits the same amplitude of decrease as the RKKY coupling, which we associate with electron redistributions in the 3d orbitals caused by the optically smeared Fermi level. While the pump excitation process is shown to have an influence on the modulations, thermal contributions are excluded. Our study establishes a link between the RKKY coupling and the PMA in a p-SAF structure and provides an approach to tune them in parallel.

***Index Terms*—Synthetic antiferromagnetics, RKKY interaction, Optical control**

I. Introduction

Antiferromagnetic (AF) spintronics has emerged as a major field in spintronics, fueled by its remarkable attributes of high magnetic field (H-field) stability and ultrafast operation speed[1]. However, this robustness also leads to a weak response to an external magnetic fields, which hampers conventional magnetic control methods[2]. Synthetic AF materials (SAF), however, offer great opportunities for AF devices due to their relatively weak exchange coupling. Recent experiments have demonstrated that an electric field can tailor the RKKY coupling and drive transitions between AF and FM[3]. These effective modulations typically rely on changes of the Fermi level influenced by charge accumulations at the surface or ion doping by applying a voltage[4]. Optical control of the RKKY coupling is therefore preferable for its advantages of simpler fabrication, inner-interface access[5] and flexibility[6]. Manipulating the interlayer coupling by femtosecond laser pulses is key for ultrafast spin dynamics such as all-optical switching (AOS) where the RKKY coupling is reported to mediate magnetization switching as little as a few picoseconds[7].

Here, we use antiferromagnetically coupled [Pt/Co]4/Ru/[Co/Pt]2 as a prototype system to investigate optical manipulations of the RKKY interaction and the interfacial PMA. We show by time-resolved magneto-optical Kerr effect (TR-MOKE) that a fs laser pulse can simultaneously and equally tune the RKKY coupling and the PMA in the [Pt/Co]4/Ru/[Co/Pt]2 system.

Our results provide insights into how a femtosecond laser pulse modulates the RKKY interaction and PMA, thereby enabling control of magnetization switching processes in a SAF system for applications in ultrafast magnetic data storage.

II. RESULTS

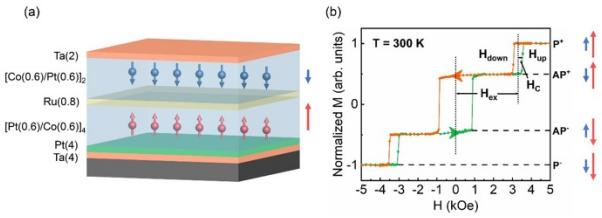

Figure 1 SAF-sample structure and the static magnetic properties. (a) SAF sample schematics. (b) Static out-of-plane hysteresis loop measured by VSM. The green and orange lines represent the process that sweeps the magnetic field from negative to positive and from positive to negative, respectively. The switching fields of the minor loop in two sweeping branches are defined as H_{up} and H_{down}, respectively.

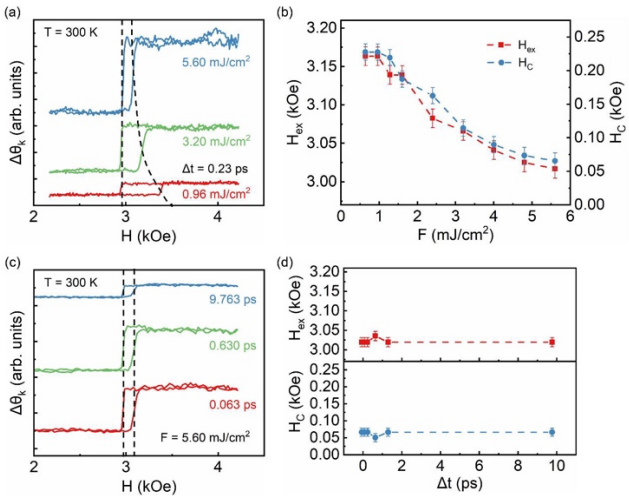

Figure 2 TR-MOKE measurements. (a) Transient minor hysteresis loops at selected pump fluences. As guided by the dashed lines, Hup shows an obvious reduction at high pump fluences while H_{down} remains unchanged. (b) Calculated Hex and HC values from the minor loops as a function of pump fluence F. Within experimental error bars they show the same trend after fs excitations. (c) Minor hysteresis loops probed at three different pump-probe delays under a fixed pump fluence of 5.60 mJ/cm2. (d) Extracted time-delayed Hex and HC from transient loops in (c), showing negligible variations within 10 ps. Error bars indicate the uncertainty in determining the displayed value from the experimentally measured data.

III. REFERENCES

1. Železný, J. et al. Relativistic N'eel-Order Fields Induced by Electrical Current in Antiferromagnets. Phys. Rev. Lett. 113, 157201 (2014).
2. Jungwirth, T. et al. Antiferromagnetic spintronics. Nat. Nanotechnol. 11,231-241 (2016).
3. Yang, Q. et al. Ionic liquid gating control of RKKY interaction in FeCoB/Ru/FeCoB and (Pt/Co)2/Ru/(Co/Pt)2 multilayers. Nat. Commun. 9, 991 (2018)
4. Fechner, M. et al. Switching Magnetization by 180° with an Electric Field. Phys. Rev. Lett.108, 197206 (2012).
5. Fan, Y. et al. Exchange bias of the interface spin system at the Fe/MgO interface. Nat. Nanotechnol. 8, 438-444 (2013).
6. Liu, B. et al. Light-Tunable Ferromagnetism in Atomically Thin Fe3GeTe2 Driven by Femtosecond Laser Pulse. Phys. Rev. Lett. 125, 267205 (2020).
7. Chatterjee, J. et al. RKKY Exchange Bias Mediated Ultrafast All-Optical Switching of a Ferromagnet. Adv. Funct. Mater. 32, 2107490 (2022)

Complex magnetism, Griffiths-like phase, Large Spontaneous and Conventional Exchange Bias Effect in Eu_2CoMnO_6

Abhijit Nayak[1], Nasiruddin Mondal[2], Devajyoti Mukherjee[2], Krishnamurthy Jyothinagaram[1]

[1]Department of Physics, National Institute of Technology, Andhra Pradesh, Tadepalligudem, abhijit.sclr@nitandhra.ac.in
[2]School of Physical Sciences, Indian Association for Cultivation of Science, Kolkata, West Bengal, psnm2251@iacs.res.in

Rapid quenching of the double perovskite Eu_2CoMnO_6 from high temperatures unveils a frozen B-site disordered state, giving rise to the coexistence of a low-temperature antiferromagnetic (AFM) phase (T_N =13K) and a high-temperature ferromagnetic (FM) phase (T_c = 114K). This magnetic phase separation drives the emergence of a large negative spontaneous exchange bias (SEB) of 1 T and a positive conventional exchange bias (CEB) of 1.5 T under a cooling field (H_{FC} = 7 T) at 2.5 K. Above T_C, persistent ferromagnetic correlations reveal a Griffiths-like phase (GP) with a Griffiths disorder parameter λ = 0.81. These findings demonstrate how quenched disorder and phase competition can be utilised to engineer robust exchange bias effects in complex oxide systems.

***Index Terms*— Complex magnetism, Griffiths-like phase, Large Exchange Bias Effect, Multiple valences of Co and Mn.**

I. Introduction

Exchange bias (EB) is pivotal in spintronic devices such as spin valves and magnetic tunnel junctions, where it provides magnetic layer stabilization and controlled spin polarization [1]. EB typically arises from the interfacial coupling between distinct magnetic phases, often requiring the coexistence of ferromagnetic (FM) and antiferromagnetic (AFM) order [2]. Double perovskites like Eu_2CoMnO_6 (ECMO) offer a natural platform for such phase coexistence. In the ordered structure, strong Co^{2+}–O–Mn^{4+} superexchange drives FM behavior, while B-site disorder introduces competing AFM interactions [3], [4]. In this study, rapid quenching of Eu_2CoMnO_6 enhanced B-site disorder, stabilizing a low-temperature AFM phase alongside the intrinsic FM phase. This phase coexistence resulted in the observation of a large negative spontaneous exchange bias (SEB) of 1 T and a positive conventional exchange bias (CEB) of 1.5 T under a cooling field of 7 T at 2.5 K. The simultaneous presence of SEB and CEB within a single material offers significant advantages for spintronic applications, enabling intrinsic magnetic pinning and tunable exchange coupling without the need for complex multilayer structures. High field measurements are being performed to further confirm the intrinsic exchange bias effect.

II. Synthesis Details

Polycrystalline Eu_2CoMnO_6 (ECMO) was synthesized via a conventional solid-state reaction. Stoichiometric amounts of Eu_2O_3 (preheated at 900 °C for 12 hours to remove moisture), Co_3O_4, and MnO_2 were thoroughly mixed, ground, and pressed into 15 mm diameter pellets under 10 MPa pressure. The pellets were sintered in a tubular furnace at temperatures between 900–1300 °C (in 100 °C increments) for 24 hours with intermediate grindings. Final sintering was performed at 1350 °C, followed by rapid quenching to room temperature.

III. PXRD Analysis

Room-temperature PXRD data were analyzed using Rietveld refinement, confirming that all reflections index to the monoclinic space group $P2_1/n$ (SG No. 15) without any impurity phases, as shown in Fig. 1.

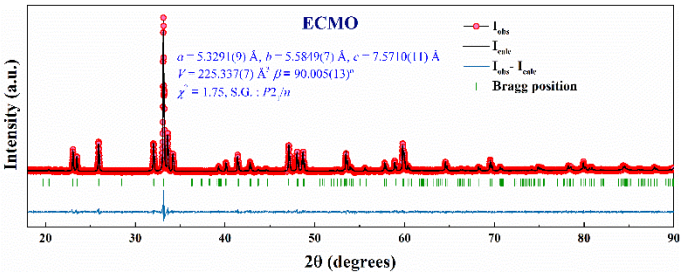

Fig. 1. PXRD pattern of ECMO along with the Rietveld refinement.

IV. XPS Analysis

XPS data were analyzed using XPSPEAK 4.1, and peak deconvolution revealed that Co exists in mixed valence states of Co^{2+} (68%) and Co^{3+} (32%), while Mn shows Mn^{3+} (45%) and Mn^{4+} (55%), as shown in Fig. 2.

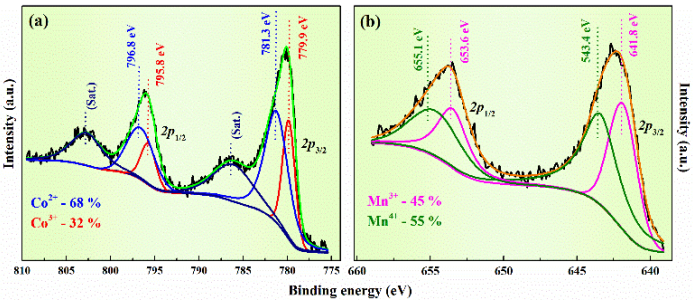

Fig. 2. XPS spectra of (a) Co and (b) Mn with the deconvoluted peaks.

V. Magnetic Measurements

A. Temperature-dependent magnetization M (T)

Fig. 3. (a) shows the *M*(T) behavior of ECMO under different

magnetic fields. At 100 Oe, the system exhibits conventional ferromagnetism with a transition at 114 K. Under higher fields, an additional AFM/SG-like transition emerges, which is more clearly visible in the d*M*/dT plot as shown in the inset. The magnetic complexity becomes evident in the χ^{-1} vs. T plot, where χ^{-1} follows a linear Curie–Weiss behavior up to 178 K, before showing a downturn and the onset of long-range order at 111 K. Curie–Weiss fitting yields an effective moment μ_{eff} of 7.79 μ_B/f.u. and a positive Weiss temperature θ of 50 K as shown in Fig. 3. (b). The elevated μ_{eff} and lowered θ indicate the presence of FM clusters above T_C and mixed FM–AFM correlations at low temperatures, respectively. The observed downturn behaviour was explained in terms of Griffiths' phase, and the fitting resulted in a disorder exponent (λ) of 0.81 as shown in Fig. 3.(c), further, with the cooling with the high fields the downturn behaviour disappears resulting in a C-W behaviour as shown in Fig. 3 (d) suggesting the presence of GP like phase.

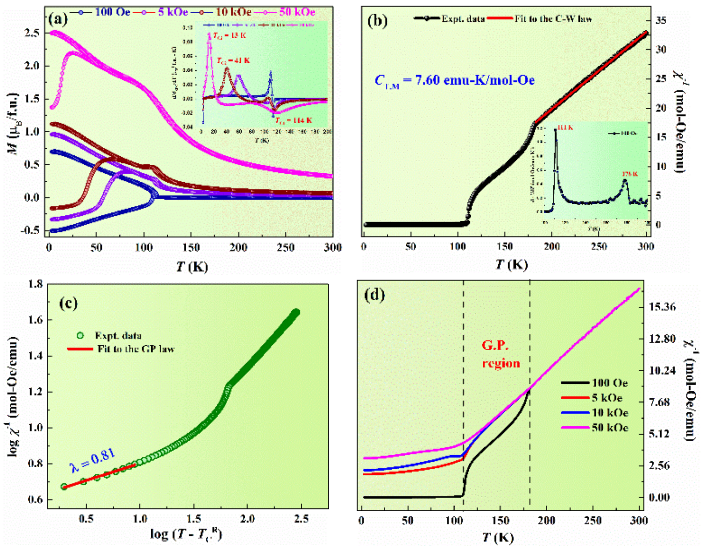

Fig. 3. (a) M (T) of ECMO with different fields, inset showing the dM_{ZFC}/dT, (b) C-W law fit in the high temperature region, (c) Griffith's phase analysis and (d) χ^{-1} with different cooling fields.

B. Field-dependent magnetization M (H)

Fig. 4(a) shows the ZFC *M (H)* loop of ECMO measured at 2.5 K, exhibiting a complete shift towards the positive field axis, characteristic of negative SEB. The loop shift, quantified as $H_{EB} = |H_{c1} + H_{c2}|/2$ (where H_{c1} and H_{c2} are left and right coercive fields, respectively), yielded a large H_{SEB} of 1 T at 2.5 K, persisting up to 20 K. To explore CEB, field-cooled *M (H)* measurements were performed after cooling the sample to 5 K under various H_{CF} as shown in Fig. 4(b). The highest negative H_{CEB} of 1.36 T was observed for H_{CF} = 1 T, followed by a decrease at higher fields, attributed to the enlargement of FM clusters and the inverse relation between magnetization and exchange bias, described by

$$H_{EX} = \frac{-J_{EX} \cdot S_{FM} \cdot S_{AFM}}{T_{FM} \cdot M_{FM}} \quad (1)$$

where J_{EX} is the interfacial exchange coupling, S_{FM} and S_{AFM} are the spins, T_{FM} is the FM layer thickness, and M_{FM} is the magnetization. Temperature-dependent CEB measurements as shown in Fig. 4(c) under H_{CF} = 7 T, reveal that EB emerges near 20 K, as shown in Fig. 4(d), coinciding with AFM/SG ordering, and increases with decreasing temperature, reaching a maximum of 1.5 T at 2.5 K. The onset of EB near the AFM transition suggests pinning of FM spins at the FM/AFM interfaces, requiring additional field for realignment, thus leading to loop shifts.

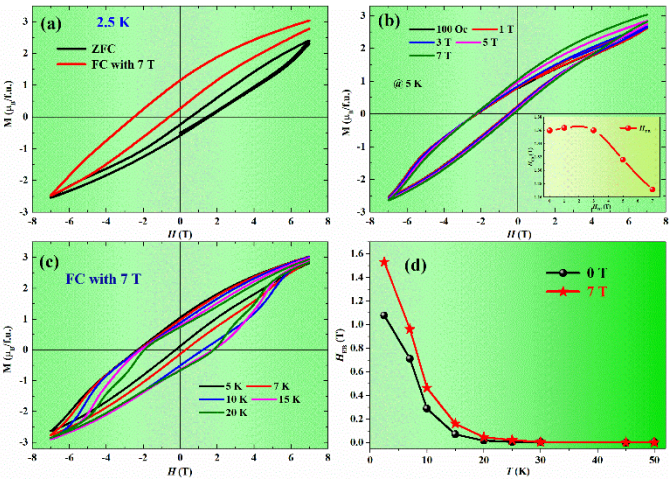

Fig. 4. *M* (H) of ECMO at (a) 2.5 K with ZFC and FC (with 7 T), (b) 5 K with different cooling fields, inset showing the variation of H_{EB} with H_{FC}, (C) with H_{FC} of 7 T at different temperatures and (d) variation of H_{SEB} and H_{CEB} with temperature.

REFERENCES

[1] R L Stamps, "Mechanisms for exchange bias," J. Phys. D: Appl. Phys. 33 R247, doi: 10.1088/0022-3727/33/23/201

[2] J Nogues and I. K. Schuller, "Exchange bias," J. Magn. Mag. Matr. 192 (1999) 203-232, doi:10.1016/S0304-8853(98)00266-2

[3] R. I. Dass and J. B. Goodenough, "Multiple magnetic phases of $La_2CoMnO_{6-\delta}$ ($0<\sim\delta<\sim0.05$)," *Phys. Rev. B*, vol. 67, no. 1, p. 014401, Jan. 2003, doi: 10.1103/PhysRevB.67.014401.

[4] A. Nayak *et al.*, "Effect of Co–Mn Ordering on Defect-Induced Modulation of Complex Magnetic, Metamagnetic, Griffiths Phase, and Exchange Bias-like Behavior of Eu_2CoMnO_6," *J. Phys. Chem. C*, vol. 129, no. 14, pp. 6976–6990, Apr. 2025, doi: 10.1021/acs.jpcc.4c07914.

Depinning of Domain Walls in a Notched Ferromagnetic Nanostrip: Role of Inertial and Nonlinear Damping Effects

Sarabindu Dolui[1], Sumit Maity[1], Sharad Dwivedi[1], and Giancarlo Consolo[2]
[1]Department of Mathematics, School of Sciences, National Institute of Technology Andhra Pradesh, Tadepalligudem, 534 101, India
[2]Department of Mathematics, Computer, Physical and Earth Sciences, University of Messina, 98166 Messina, Italy

In this work, we investigate theoretically the static and kinetic depinning field of a domain wall in a notched magnetic nanostrip under the generalized framework of the Landau–Lifshitz-Gilbert equation, which combines inertial and nonlinear viscous-dry friction damping effects.We assume a head-to-head transverse domain wall configuration and analyzed its motion subject to an external magnetic field. To deduce the equation ruling the spatio-temporal evoution of the magnetic domain wall, we adopt the Schryer and Walker trial function approach. The results show that static and kinetic depinning fields increase as the dry friction dissipation increases. Moreover, viscous dissipation exhibits a weak dependence on the kinetic depinning field and saturated domain wall velocity, while inertial damping due to the relaxation time of angular momentum significantly impacts the kinetic depinning field, depinning time, and breakdown velocity. Our numerical results are in good qualitative agreement with the recent observations reported in the literature.

***Index Terms*—Domain wall, Static depinning, Kinetic depinning, Viscous dissipation, Dry-friction dissipation, Inertial damping.**

I. Introduction

OVER the recent years, the ability to control the domain wall (DW) motion in ferromagnetic nanostructures has sparked a wide range of applications such as the next generation of memory state, magnetic sensors, logic devices, racetrack memories, etc. As these sophisticated applications continue to advance, there has been a need for DW-based, cost-effective electronic storage devices with less space consumption. As a result, ferromagnetic nanostructures (nanostrips/nanotubes) have emerged as a viable option for recording and storing data in these modern spintronic devices. In order to improve the performance of these devices and achieve higher processing speeds, it is necessary to gain a deep understanding of DW (the transition zone that separates the uniform magnetization regions, referred to as domains) motion in the presence of external sources. Specifically, the precise control over DW position.

In particular, a notch functions as a local pinning center for the magnetic walls, pivotal in controlling and modulating their behavior. The effective pinning field produced by the notch acts as an energetically significant potential well (or barrier) and represents an additive contribution to the overall effective field experienced by magnetic DWs. The specific zone around the notch wherein the DW is pinned or temporarily trapped is called the pinning field region. Motivated by the studies [1,2,3,4], the present work explores the combined action of an applied magnetic field, nonlinear dry friction-viscous dissipation, and inertial damping on DW depinning in a notched nanostructure. The main focus is to analyze two distinct scenarios of DW depinning: (i) static depinning, where the DW is initially pinned at the notch, and (ii) kinetic depinning, where a moving DW encounters the notch.

II. Micromagnetic Model

We consider a notched ferromagnetic nanostrip of length L_x, width L_y, and thickness L_z along the $\mathbf{e}_1, \mathbf{e}_2$ and $\mathbf{e}_3$ axes, respectively. As depicted in Fig. 1, a head-to-head TDW of width Δ is nucleated along the strip-axis ($\mathbf{e}_1$-direction), separating two faraway domains that point along $\pm\mathbf{e}_1$ directions.

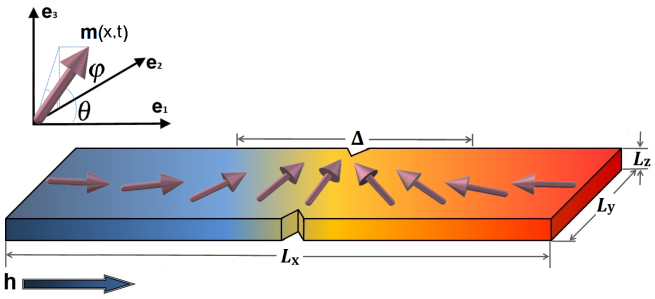

Fig. 1. Schematics of a ferromagnetic nanostrip with an artificial notch in the form of two symmetrical triangles and reference axes..

A. Governing Equation

The spatiotemporal evolution of the local magnetization vector $\mathbf{m}(x,t)$ within the ferromagnetic medium is governed by the inertial Landau-Lifshitz-Gilbert (iLLG) equation, which can be expressed as:

$$\frac{\partial \mathbf{m}}{\partial t} = -\gamma\left(\mathbf{m}\times\mathbf{h}_{\text{eff}}\right) + \mathbf{T}_{\text{damp}} + \mathbf{T}_{\text{inertia}}, \qquad (1)$$

where $\mathbf{m}(x,t) = \mathbf{M}(x,t)/M_s$ describes the normalized magnetization vector field $\mathbf{m} : \mathbb{R}\times\mathbb{R}^+ \to \mathbb{S}^2$, where $\mathbf{M}$ is magnetization vector field, M_s represents the saturation magnetization, '$\times$' denotes the vector product on $\mathbb{R}^3$, and $\mathbb{S}^2$ stands for a unit sphere in $\mathbb{R}^3$.

The total effective field, $\mathbf{h}_{\text{eff}}$ comprises contributions from the exchange $\mathbf{h}_{\text{ex}}$, anisotropy $\mathbf{h}_{\text{ani}}$, external $\mathbf{h}_{\text{ext}}$, demagnetization (stray) $\mathbf{h}_{\text{dmg}}$ and the pinning $\mathbf{h}_{\text{pin}}$.

The local pinning field $\mathbf{h}_{\text{pin}} = h_p(x)\mathbf{e}_1$ is induced by the notch located at $x = 0$, leading to a localized enhancement of the easy-axis anisotropy. Here, $h_p(x)$ defines the spatial variation of pinning field, which is given by:

$$h_p(x) = -\frac{1}{2\mu_0 M_s^2 L_y L_z}\frac{\partial V_{\text{pin}}(x)}{\partial x}, \tag{2}$$

where, $V_{\text{pin}}(x)$ is the space-dependent pinning potential of magnetostatic nature, which can be described by:

$$V_{\text{pin}}(x) = \begin{cases} \frac{1}{2}K_{\text{N}}\, x^2, & \text{for } |x| \le L_{\text{N}} \\ 0, & \text{otherwise.} \end{cases} \tag{3}$$

Here, K_N represents the elastic constant of the constriction.

The damping torque and inertial torque are defined as follows:

$$\mathbf{T}_{\text{damp}} = \left[\alpha_G\left(1 + \frac{\alpha_v}{\gamma^2}\left(\frac{\partial \mathbf{m}}{\partial t}\right)^2\right) + \gamma\alpha_d\left|\frac{\partial \mathbf{m}}{\partial t}\right|^{-1}\right]\left(\mathbf{m} \times \frac{\partial \mathbf{m}}{\partial t}\right), \tag{4}$$

$$\mathbf{T}_{\text{inertia}} = \alpha_G\tau\left[1 + \frac{\alpha_v}{\gamma^2}\left(\frac{\partial \mathbf{m}}{\partial t}\right)^2\right]\left(\mathbf{m} \times \frac{\partial^2 \mathbf{m}}{\partial t^2}\right), \tag{5}$$

where α_G and α_v are the linear Gilbert and nonlinear viscous damping coefficients, respectively. The parameter α_d is a positive phenomenological dry friction coefficient that captures the average effect of crystallographic defects in the material. The parameter τ denotes the relaxation time of angular momentum.

III. Numerical Results

In order to investigate the pinning and depinning of DWs, we consider a ferromagnetic nanostrip characterized by the material parameters of a cobalt-platinum-chromium (CoPtCr) alloy.

IV. Conclusion

Our results indicate that nonlinear viscous-dry friction and inertial damping play a vital role and yield an additional degree of freedom to control the DW position and its velocity precisely in a ferromagnetic nanostrip via geometrical notches. More precisely, ferromagnetic materials with low dry friction dissipation coefficients are more advantageous for developing energy-efficient high-speed devices. Moreover, our findings suggest that maintaining a lower relaxation time of angular momentum is favorable for achieving a low kinetic depinning field, which can enhance the performance of such devices.

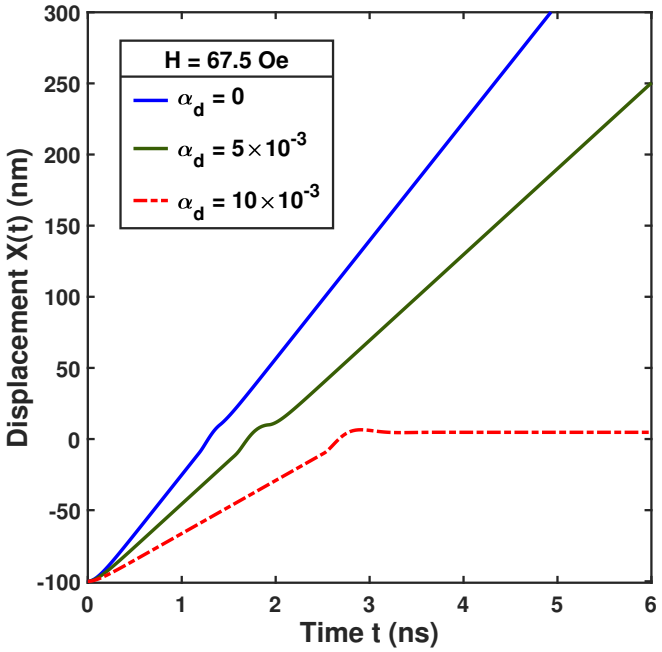

Fig. 2. The dependence of DW displacement $X(t)$ on time t, varying α_d.

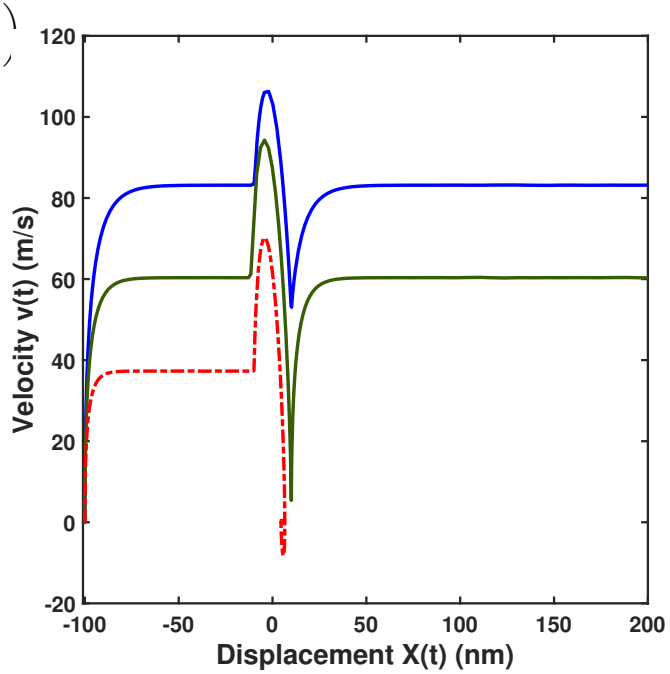

Fig. 3. The dependence of DW velocity $v(t)$ on DW displacement $X(t)$, varying α_d.

References

[1] S. S. Parkin, M. Hayashi, and L. Thomas, "Magnetic domain-wall racetrack memory," *science*, vol. 320, no. 5873, pp. 190–194, 2008.

[2] M. Kläui, H. Ehrke, U. Rüdiger, T. Kasama, R. E. Dunin-Borkowski, D. Backes, L. J. Heyderman, C. A. Vaz, J. A. C. Bland, G. Faini *et al.*, "Direct observation of domain-wall pinning at nanoscale constrictions," *Applied Physics Letters*, vol. 87, no. 10, 2005.

[3] K. Neeraj, M. Pancaldi, V. Scalera, S. Perna, M. d'Aquino, C. Serpico, and S. Bonetti, *Magnetization switching in the inertial regime*. APS, 2022, vol. 105, no. 5.

[4] S.-M. Ahn, K.-W. Moon, D.-H. Kim, and S.-B. Choe, "Detection of the static and kinetic pinning of domain walls in ferromagnetic nanowires," *Applied Physics Letters*, vol. 95, no. 15, 2009.

Damping modification in epitaxially grown continuous $L1_0$-FePt thin films with different substrates

Yuta Sasaki, Phillip David Bentley, Katsuaki Nakazawa, Takanobu Hiroto, Shinji Isogami, Hirofumi Suto, Yukiko K. Takahashi

[1]National Institute for Materials Science (NIMS), Tsukuba, 305-0047, Japan, SASAKI.Yuta@nims.go.jp

$L1_0$-ordered FePt has attracted interest for both magnetic recording and spintronic device applications due to its large perpendicular magnetic anisotropy and large magnetoresistance. However, its practical use in spintronic devices is limited because of its large Gilbert damping constant. In this study, we present a method to reduce the damping constant in $L1_0$-FePt thin films through microstructural engineering. Using time-resolved magneto-optical Kerr effect, we analyzed the magnetization dynamics of FePt films grown on MgO, $MgAl_2O_4$ and $SrTiO_3$ substrates. The FePt film grown on $SrTiO_3$ substrate has a smaller lattice mismatch than FePt grown on MgO and $MgAl_2O_4$ substrates, as well as a significantly lower damping constant of 0.030 compared to 0.059 for the MgO sample. These results highlight the possibility of substrate-induced nanostructure control of the magnetization dynamics toward. Our results show that $L1_0$-FePt is a promising material for spintronic applications which require both large perpendicular magnetic anisotropy and low damping.

All-optical method, L10-FePt, magnetization dyanmics. Time-resolved magneto-optical Kerr effect

I. Introduction

$L1_0$-ORDERED FePt has attracted significant interest as a magnetic recording material, owing to its large perpendicular magnetic anisotropy (PMA), large saturation magnetization, and chemical stability. Beyond recording media application, its large magnetoresistance and high spin injection efficiency make it a promising candidate for spintronic applications, [1,2] including a spin-Hall nano oscillator. [3,4] Theoretically, the large PMA field of $L1_0$-FePt allows for it to be used in spintronic device which can operate at precession frequencies above 100 GHz the point defined as the THz gap. However, despite these promising magnetic properties, the practical application of $L1_0$-FePt in spintronic devices has so far been limited primarily due to an insufficient understanding of its magnetization dynamics.

Only a few experimental studies have reported on the magnetization dynamics of $L1_0$-FePt [5,6], and those that do often cite relatively large Gilbert damping constants—ranging from 0.05 to 0.26. This relatively large damping constant is not suitable for the manipulation of magnetization precession in spintronic devices.

In our research group, we have established advanced measurement techniques to evaluate the fast magnetization dynamics of $L1_0$-FePt thin films. Using time-resolved magneto-optical Kerr effect (TRMOKE), we have explored the magnetization dynamics above 100 GHz in $L1_0$-FePt thin films to discuss the magnetic damping constant. [7,8] In order to get insight into the modification of the magnetic damping constant by controlling the microstructure, we have grown $L1_0$-FePt thin films on different substrates, MgO, $MgAl_2O_4$ (MAO) and $SrTiO_3$ (STO). We found that we could significantly reduce the damping constant of FePt by controlling the lattice mismatch between the $L1_0$-FePt thin film and the substrate. The film grown on the STO substrate had a smaller lattice mismatch and an improved microstructure, which correlated with a substantial reduction in the damping constant down to a value as low as 0.030.

II. Experimental procedure

$L1_0$-ordered FePt thin films with a thickness of 36 nm were fabricated via DC magnetron sputtering on single-crystalline MgO(001), MAO(001) and STO(001) substrates. Prior to deposition, the substrates were annealed at 650 °C for one hour in vacuum to eliminate surface contamination. Films were grown with a substrate temperature of 500 °C.

Structural characterization was performed using X-ray diffraction (XRD) with Cu $K\alpha_1$ radiation. Cross-sectional scanning transmission electron microscopy (STEM) imaging was carried out to characterize the microstructure. TRMOKE measurements were performed using an ultrafast laser system with a center wave length, pulse duration, and repetition rate of 1028 nm, 290 fs, and 10 kHz, respectively. A probe beam with a center wave length of 514 nm was generated using a BBO crystal, and the amplitude of a pump beam was modulated by a mechanical chopper operating at 870 Hz. The pump induced change in the Kerr rotation angle of the reflected probe beam was detected using a balanced photodiode detector and lock-in amplifier by varying the optical delay Δt between the pump and probe laser pulse. An external magnetic field up to 7.0 T was applied at 45° with respect to the film normal during measurements.

III. Results and discussion

As seen in Fig.1, XRD data of the FePt films grown on MgO, MAO and STO substrates showed well-defined superlattice peaks corresponding to the $L1_0$ phase.

TRMOKE data for all samples showed damped oscillational signal relating to the magnetization precession as shown in Figs. 2(a). By fitting these spectra using a damped sinusoidal function, we extracted the precession frequency f and effective damping constants α_{eff} as a function of magnetic field $\mu_0 H$. The

solid curves seen in Fig 2(b) represent the fitting of the precession frequency using Kittel's formula with a fixed *g*-factor of 2.002. PMA field for MgO, MAO and STO samples were evaluated to be 6.7, 6.5 and 8.4 T, respectively. In Fig.2(c), the STO sample showed a minimum damping value of 0.030, whereas the MgO and MAO samples exhibited a higher value of 0.059 and 0.037, respectively. Further detailed analysis and microstructure observation data will be discussed in the poster presentation.

Reducing the damping constant whilst maintaining a large PMA field is crucial for the development of high-frequency spintronic devices working in the THz gap. These findings highlight the importance of microstructure and engineering the interface to control the magnetization dynamics of ferromagnetic thin films. Our results provide a practical approach for optimizing $L1_0$-FePt for its use in high-frequency spintronic devices.[6]

This work was partially supported by the Japan Science and Technology Agency (JST) Core Research for Evolutional Science and Technology (CREST) (Grant No. JPMJC22C3), the Ministry of Education, Culture, Sports, Science and Technology (MEXT) Leading Initiative for Excellent Young Researchers (Grant No. JPMXS0320230032), and the Japan Society for the Promotion of Science (JSPS) KAKENHI (Grant Nos. JP21K14218 and JP18H03787).

References

[1] T. Seki, *et al*., Nat. Mater. **7** 125-129 (2008).
[2] K. M. Seeman, *et al*., Phys. Rev. Lett. **104**, 076402 (2010).
[3] L. Liu, *et al.*, Phys. Rev. Lett. 106, 036601 (2011).
[4] V. E. Demidov, *et al*., Appl. Phys. Lett. 105, 172410 (2014).
[3] X. Ma, *et al*., Phys. Rev. B **91**, 014438 (2015).
[4] J. Becker, *et al*., Appl. Phys. Lett. **104**, 152412 (2014).
[5] Y. Sasaki, et al., ACS Appl. Nano Mater. **6**, 5901-5908 (2023).
[6] P. D. Bentley, *et al*., Appl. Phys. Lett. **126**, 022404 (2025).

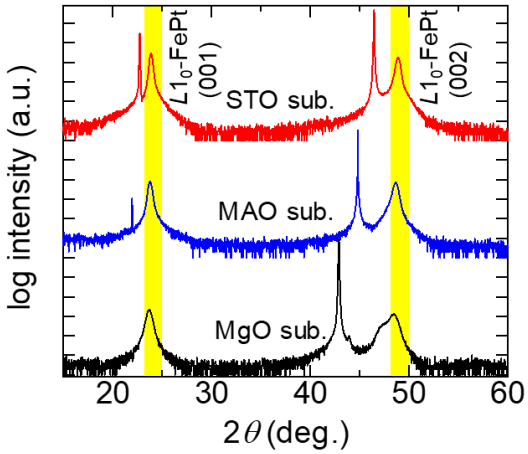

Fig. 1. XRD patterns of FePt thin films deposited on MgO, MAO and STO substrates.

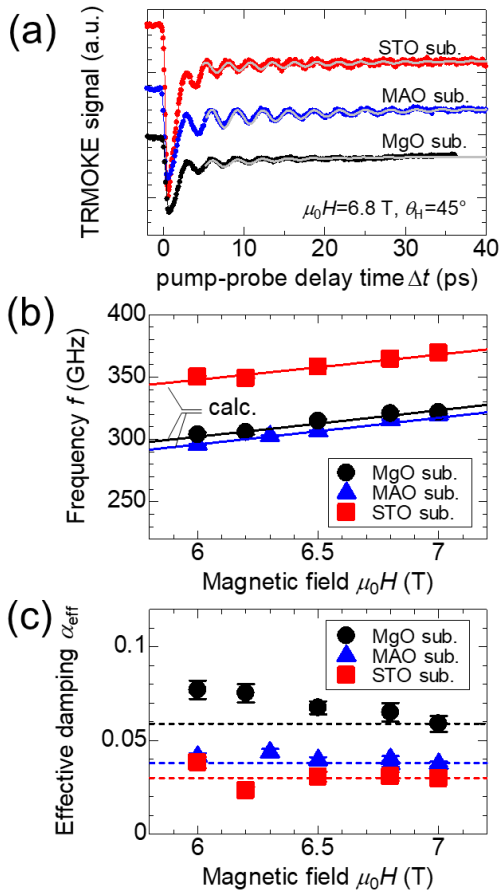

Fig. 2. (a)Typical wave forms of TRMOKE data for the films depositted on MgO, MAO, and STO substrates. Solid curves are the fitting results. (b)Precession frequency *f* and (c)effective damping constants α_{eff} of FePt thin films. Solid curves show the theoretical fitting results. Dashed lines show the minimum values of α_{eff} for each sample.

Giant bipolar unidirectional photomagnetoresistance

Yucheng Jiang[1]

[1]School of Physical Science and Technology, Suzhou University of Science and Technology, Suzhou 215009, China
jyc@usts.edu.cn

Positive magnetoresistance (PMR) and negative magnetoresistance (NMR) describe two opposite responses of resistance induced by a magnetic field. Materials with giant PMR are usually distinct from those with giant NMR due to different physical natures. Here, we report the unusual photomagnetoresistance in the van der Waals heterojunctions of WSe_2/quasi-two-dimensional electron gas, showing the coexistence of giant PMR and giant NMR. The PMR and NMR reach 1,007.5% at –9 T and –93.5% at 2.2 T in a single device, respectively. The magnetoresistance spans over two orders of magnitude on inversion of field direction, implying a giant unidirectional magnetoresistance (UMR). By adjusting the thickness of the WSe_2 layer, we achieve the maxima of PMR and NMR, which are 4,900,000% and –99.8%, respectively. The unique magnetooptical transport shows the unity of giant UMR, PMR, and NMR, referred to as giant bipolar unidirectional photomagnetoresistance. These features originate from strong out-of-plane spin splitting, magnetic field–enhanced recombination of photocarriers, and the Zeeman effect through our experimental and theoretical investigations. This work offers directions for high-performance light-tunable spintronic devices.NMR)

Index Terms*: *Photomagnetoresistance, Spin polarization, Two-dimensional electron gas, Van der Waals heterojunction, WSe_2

I. Introduction

Ordinary magnetoresistance (MR) is commonly found in conductive materials [1]. Most materials show the positive magnetoresistance (PMR) effect originating from the Lorentz force [2]-[3], which describes a magnetic field–induced increase of resistance. In contrast, the negative magneto-resistance (NMR) usually results from the spin-dependent scattering in the magnetic materials [4]-[5]. Large MR effects have attracted much interest for their valuable applications as spintronic sensors and memory devices [6]-[8]. Distinct in their physical mechanisms, PMR and NMR effects often counteract each other, inevitably rendering one dominant over the other in a single large-MR material. To the best of our knowledge, there has been no report of the systems with both giant PMR and giant NMR.

In this work, we fabricated lateral van der Waals (vdW) heterojunctions between WSe_2 and quasi-two-dimensional electron gas (WSe_2/Q2DEG) on $SrTiO_3$ (STO) substrates. Since the vdW heterojunctions are electrically insulating at low temperatures, we focus on the magnetic transport behavior of photocarriers : that is, photomagnetoresistance. In this system, we observe the giant bipolar unidirectional photomagneto-resistance (GBU-PhMR). With the definition of MR = $[R(B) / R(0) - 1] \times 100\%$, $R(B)$ and $R(0)$ represent the resistances under the magnetic field and the zero field respectively. the single device shows PMR of 1,007.5% at –9 T and NMR of -93.5% at 2.2 T, indicating the coexistence of giant PMR and giant NMR. The MR changes over two orders of magnitude upon reversing the magnetic field, displaying a giant unidirectional magneto-resistance (UMR) effect. By adjusting the thickness of the WSe_2 layer, we achieve the maxima of PMR and NMR that are 4,900,000% and –99.8%, comparable with the highest values reported so far [e.g., about 15,000,000% for PMR at 1.8 K in gray arsenic [9] and about –99% for NMR at 2 K in CrI_3 [10]]. Through theoretical and experimental studies, the GBU-PhMR can be attributed to the combined effect of strong out-of-plane spin splitting, magnetic field–enhanced recombination of photocarriers, and the Zeeman effect. This work explores the unique magnetic transport of photocarriers in a WSe_2/Q2DEG heterojunction and its potential applications in high-sensitivity spintronic devices.

II. Results

Fig. 1a shows a schematic of WSe_2/Q2DEG heterostructure. Based on our recent work, the Ar^+ ion bombardment assistant (AIBA) method is used to fabricate the device [11]. We used the WSe_2 crystals with a 2H phase and the (100) STO substrates with a perovskite structure. After the AIBA fabrication, a vdW contact can be achieved at the edges of WSe_2 and Q2DEG in Fig. 1b. Due to the intrinsic p-type conduction of WSe_2, a p–n junction is formed at the interface of WSe_2 and Q2DEG.

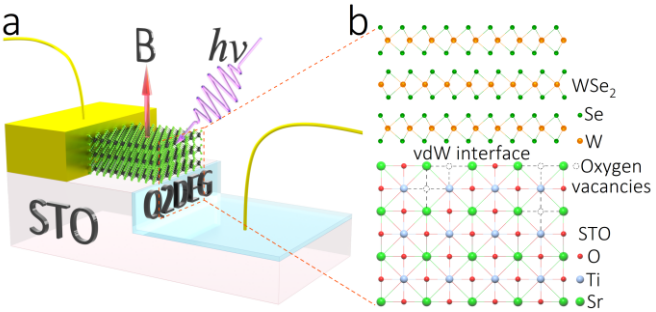

Fig. 1. Structure of the device. (a) Structural schematic of the WSe_2/Q2DEG heterostructure, showing the electric measurement under the magnetic field and light illumination. (b) Schematic diagram showing the vdW contact between WSe_2 and the oxygen-deficient STO surface.

Fig. 2a shows the MR as a function of the magnetic field, along the negative direction, the MR increases monotonously with the field, displaying giant PMR about 1,007.5%. However, the MR decreases greatly first and then, increases with the increase of the positive field. The largest NMR reaches –93.5% at 2.2 T). the device shows a coexistence of giant PMR and giant NMR accompanied by significant MR anisotropy depending on the sign of magnetic field, regarded as a GBU-PhMR effect. As is well known, the conventional MR materials usually exhibit the parity-symmetric field dependence of resistance. Distinctively, the GBU-PhMR device shows the

unidirectional dependence of MR on the magnetic field. The MR spans over two orders of magnitude on inversion of field direction, implying a giant UMR. We plotted the UMR vs. field curve in Fig. 2a, *Inset* with the definition of UMR = $[R(B) - R(-B)]/[R(B) + R(-B)] \times 100\%$. It is observed that the maximum UMR is over 95%, much higher than the other UMR materials reported recently.

Fig. 2b shows the *Resistance*$_j$ (R_j)–B curves with different thicknesses of WSe_2. Among them, the 11.3-nm device exhibits the largest PMR value and the approximate parity symmetry with respect to B = 0 T. The magnetic field induces an increase of R_j over four orders of magnitude, where MR = 4,900,000%. In the 40.3-nm sample, the NMR value reaches its maximum at 3.9 T, where MR = − 99.8%.

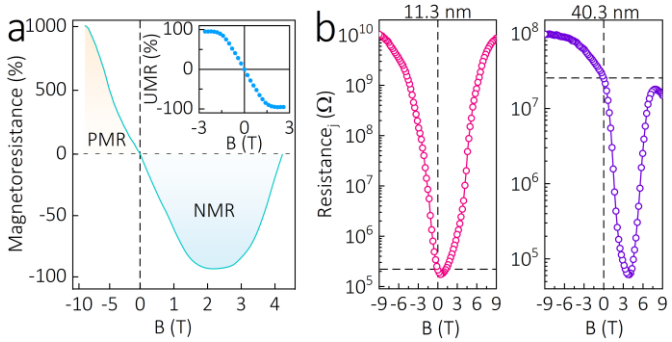

Fig. 2. GBU-PhMR. (a) Magnetic field dependence of magnetoresistance at continuous 405-nm optical illumination, where the different scales for positive and negative coordinates are used for a detailed description of giant PMR and NMR. (a, Inset) UMR vs. field. (b) *Resistance*$_j$–B curves at different WSe_2 thickness.

The definition of MR is usually used for measuring the large PMR effect. However, for large NMR, it is difficult to implement a detailed description of the resistance decrease induced by magnetic field if the resistance drops over two orders of magnitude. Thus, such a definition is not appropriate for the GBU-PhMR effect with both giant PMR and NMR. Here, we use MR_{GBU} defined as $MR_{GBU} = R(B)/R(0)$, to describe the giant PMR and NMR together. It is PMR if $MR_{GBU} > 1$ or NMR if $MR_{GBU} < 1$. In general, both PMR and NMR shown in the GBU-PhMR device are quite impressive, compared with other well-known materials with large PMR and NMR, it is in the most excellent category, as shown in Fig. 3.

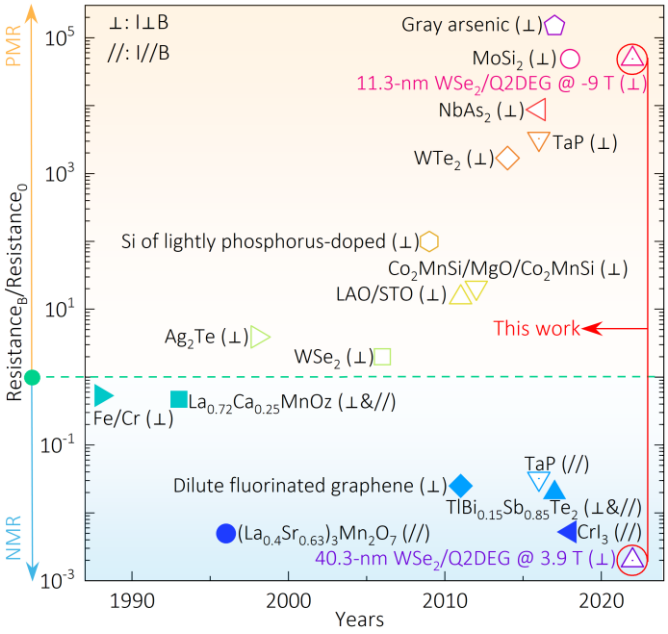

Fig. 3. A comparison of PMR and NMR of some well-known spintronic materials over four decades; 11.3- and 40.3-nm WSe_2/Q2DEG heterojunctions exhibit the giant PMR and NMR, respectively, comparable with those classic PMR and NMR materials. The symbols ⊥ and // show the current perpendicular and parallel to the magnetic fields, respectively.

REFERENCES

[1] A. B. Pippard, *Magnetoresistance in metals*, Cambridge university press, 1989.

[2] G. Giuliani, *A general law for electromagnetic induction*, *Europhys. Lett.* 2008, 81, 60002.

[3] N. W. Ashcroft, N. D. Mermin, *Solid State Physics,* Holt, Rinehart and Winston. New York, 1976.

[4] M. N. Baibich, J. M. Broto, and A. Fert et al., *Giant magnetoresistance of (001) Fe/(001) Cr magnetic superlattices, Phys. Rev. Lett.* 1988, 61, 2472-2475.

[5] B. Dieny, V. S. Speriosu, and S. S. P. Parkin et al., *Giant magnetoresistive in soft ferromagnetic multilayers, Phys. Rev. B* 1991, 43, 1297-1300.

[6] J. C. Rife, M. M. Miller, and P. E. Sheehan et al., *Design and performance of GMR sensors for the detection of magnetic microbeads in biosensors, Sens. Actuators A Phys.* 2003, 107, 209-218.

[7] R. S. Gaster, L. Xu, and S. J. Han et al., *Quantification of protein interactions and solution transport using high-density GMR sensor arrays, Nat. Nanotechnol.* 2011, 6, 314-320.

[8] B. Baek, W. H. Rippard, and S. P. Benz et al., *Hybrid superconducting-magnetic memory device using competing order parameters, Nat. Commun.* 2014, 5, 3888.

[9] M. Matin, R. Mondal, N. Barman et al., *Extremely large magnetoresistance induced by Zeeman effect-driven electron-hole compensation and topological protection in $MoSi_2$, Phys. Rev. B* 2018, 97, 205130.

[10] T. Song, X. Cai, and M. W. Y. Tu et al. *Giant tunneling magnetoresistance in spin-filter van der Waals heterostructures, Science* 2018, 360, 1214-1218.

[11] Y. Chen, A. He, and G. Liu et al., *A universal method to fabricate p-n or Schottky heterojunctions based on two-dimensional electron gas*, *Appl. Phys. Lett.* 2019, 115, 241603.

Interface Design for Concurrent Realization of High Perpendicular Magnetic Anisotropy and Low Magnetic Damping in Fe/MgO

Yosephine Novita Apriati[1], Masato Tsuchida[1], Muhammad Arifin[1,2], and Kohji Nakamura[1]

[1]Graduate School of Engineering, Mie University, Tsu, Mie 514-8507, Japan
[2]Department of Physics, Gadjah Mada University, Yogyakarta 55281, Indonesia

In spin transfer torque magnetoresistive random-access memory (STT-MRAM) the problem in writing mechanism arises mainly due to the need of large current to switch magnetization direction of the free ferromagnet layer. As the device development of 1x nm cell diameter is preferable, keeping thermal stability to suppress data retention failures while maintaining fast switching mechanism become challenging as trade-off relationship between magnetic anisotropy and damping constant is ongoing. The Fe/MgO system reported as superior structure for magnetic tunnel junctions owing to the high perpendicular magnetic anisotropy (PMA) originated from $\boldsymbol{p-d}$ coupling at interface. Modifying Fe/MgO interface offers prospect of achieving high PMA and low magnetic damping simultaneously. This work focusses in exploring interface modification effect, specifically by using nitride and fluoride compounds, i.e., having one less/more electron than oxide of MgO for high PMA and low magnetic damping from first principles. The result signifies that the LiF/MgO, BN/MgO, and MgN/MgO modifications achieve high PMA enhancement up to 600% while reducing magnetic damping about 75% lower than those in the pristine Fe/MgO model. The origins majorly driven by the band realignment of minority spin from interfacial Fe $\boldsymbol{d}$-orbital at around Fermi level.

***Index Terms*—perpendicular magnetic anisotropy, damping, magnetic tunnel junctions.**

I. Introduction

The current read-write mechanism in spin transfer torque magneto-resistive random-access memory (STT-MRAM) demands advance technologies, specifically for retention failures suppression in small size devices of 1x nm. It remains important to keep a sufficient perpendicular magnetic anisotropy (PMA) for thermal stability of the system while maintaining minimal magnetic damping, i.e., holding the long memory retention without losing switching efficiency. The Fe/MgO system, widely known as one promising magnetic tunnel junction (MTJ) design owing to the high interfacial PMA (iPMA) that majorly accounts to the *p-d* coupling at the interface [1]. Having high PMA and low magnetic damping become critical to achieve a refined MTJ, however the attempts via heavy metal modification, which successfully gives strong iPMA due to strong spin-orbit parameter is also followed by the increase in magnetic damping [2]. This is because the two features share same origin of the spin-orbit coupling. Replacing MgO tunnel barrier with spinel $MgAl_2O_4$ lower a significant magnetic damping due to the small lattice mismatch <1%, however the Fe/$MgAl_2O_4$ model fails to achieve higher iPMA compared to those in Fe/MgO [3]. The exploration of MTJ design with a trade-off relationship between iPMA and magnetic damping is ongoing, e.g., by interface engineering, capping layer modification, and tuning the dielectric constant of the insulator. This work focus is to explore various interface modification in Fe/MgO system, specifically considering the anions with one less/more electron from the MgO oxide, i.e., the nitride and fluoride compounds to achieve MTJ design with high iPMA and low magnetic damping simultaneously.

II. Computational Details and Method

The magnetic tunnel junction is modelled by considering a pristine Fe/MgO system in ten atomic monolayers (ML) of Fe(001) and five ML MgO(001). The interface modification model is constructed by replacing one ML of MgO at the interface with *PX*, i.e., the Fe/*PX*(1 ML)/MgO(4 ML) models. The *PX* is a combination between atomic compounds with a cation site (*P*) and an anion site (*X*). In this work, *PX* modification is divided into two groups, i.e., Group I for nitride anion i.e., BN/MgO, AlN/MgO, GaN/MgO, and MgN/MgO. Group II for fluoride anion i.e., LiF/MgO, and MgF/MgO. In-plane lattice constants are set to the optimized bcc-Fe (2.83 Å). Density-functional theory calculations carried out by full-potential linearized augmented plane wave method [4] within generalized gradient approximation. For anisotropy energy and magnetic damping calculations, a 110×110 $\boldsymbol{k}$-point is implemented. The magnetocrystalline anisotropy energy (E_{MCA}) is determined based on Force theorem, i.e., sum of energy eigenvalue difference between the bands for magnetization oriented along in-plane ($\varepsilon_b^{\rightarrow}(\boldsymbol{k})$) and out-of-plane ($\varepsilon_b^{\uparrow}(\boldsymbol{k})$), with positive E_{MCA} assigned for PMA [5,6], as follows,

$$E_{MCA} = \frac{1}{a^2}\sum_k\left\{\sum_b \varepsilon_b^{\rightarrow}(k) - \sum_b \varepsilon_b^{\uparrow}(k)\right\}, \qquad (1)$$

where a is the lattice constant. Magnetic damping constant, α is estimated following the Landau-Lifshitz-Gilbert equation by Kamberský torque correlation model [7,8], as in,

$$\alpha = \frac{\pi}{M}\sum_{\boldsymbol{k}}\sum_{b,b'}|\Gamma^{-}{}_{bb'}(\boldsymbol{k})^{-}|^2 W_{bb'}(\delta). \qquad (2)$$

where M is the magnetization, b and b' are band indices, $\Gamma^{-}{}_{bb'}(\boldsymbol{k})$ is the matrix element of the spin–orbit torque operator, and $W_{bb'}(\delta)$ is the energy factor with two Lorentz functions scattered at energies ε_b and $\varepsilon_{b'}$ with a scattering rate δ.

III. RESULT AND DISCUSSION

The calculated result for PMA and magnetic damping constant for all models are shown in Fig. 1(a). The red cross shows result for the pristine Fe/MgO model, and the blue dots for the Fe/*PX*/MgO models with the legends indicate insulating barrier interface modification. The pristine Fe/MgO model exhibits PMA of 0.3 mJ/m^2 and α is 0.02. The magnitude agrees with previous experimental and first-principles studies [9,10]. The offset may arise due to different lattice constants and/or number of Fe layers. The MgN/MgO and BN/MgO modifications from Group I, also the LiF/MgO modification from Group II, show significant improvement in both PMA and α, i.e., achieving a high PMA with low α simultaneously. Meanwhile, the other modifications, i.e., GaN/MgO, AlN/MgO, and MgF/MgO, alters PMA and α within a close range as of those in the pristine Fe/MgO model.

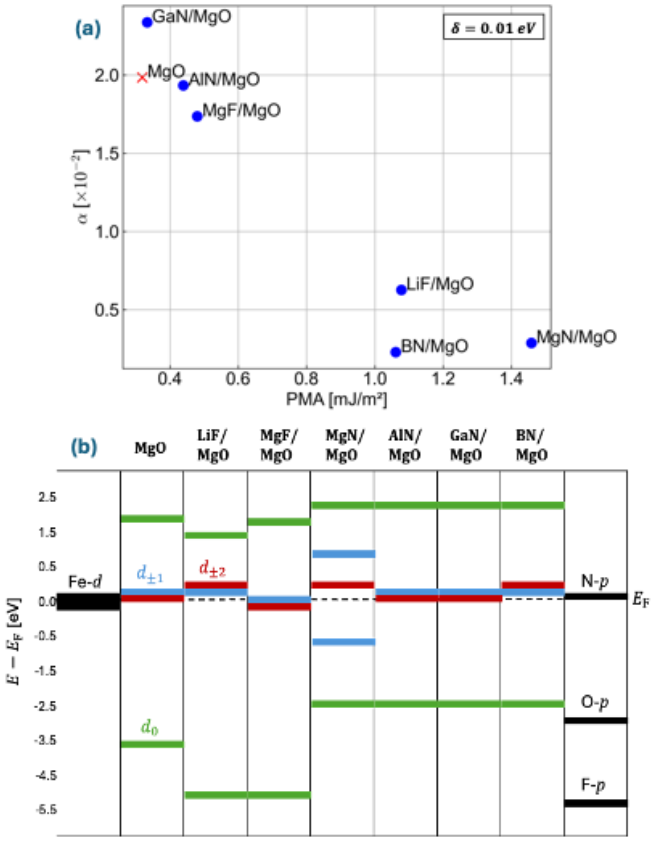

Fig. 1.(a). Relationship between PMA and α for the pristine Fe/MgO and the interface modified model, Fe/MX/MgO. (b). Minority-spin *d*-orbital configuration by *p-d* hybridization between the interfacial Fe and the adjacent anion (N, O, and F), for all models. Green, blue, and red represent d_0 (d_{z^2}), $d_{\pm1}$ ($d_{xz,yz}$), and $d_{\pm2}$(d_{xy,x^2-y^2}), respectively.

The majority-spin of interfacial Fe d-orbital, being fully occupied and located at energy range between 1.0 to 4.0 eV, gives the major role to drive anisotropy and magnetic damping only arises from the minority-spin. Fig. 1(b) illustrates the energy diagram of minority-spin d-orbital by $p-d$ orbitals hybridization between the interfacial Fe and the adjacent anion, (N, O, and F) in all models. For all models, p_0-d_0 coupling is observed, creating bonding and anti-bonding states at energy around 2.0 eV and -2.5 to -5.0 eV, respectively. While $d_{\pm1}$ and $d_{\pm2}$ orbitals are degenerated at around E_F. A special exception observed in the MgN/MgO modification as the coupling between $p_{\pm1}-d_{\pm1}$ orbitals creating additional bonding and anti-bonding states around 1.0 eV and -1.0 eV, respectively.

Anisotropy energy calculated by perturbative theory considering that the spin conserving terms from minority spin at around E_F gives main contribution to E_{MCA} is as follows,

$$E_{\mathrm{MCA}}^{\downarrow\downarrow}=\xi^2 \sum_{\boldsymbol{k}} \sum_{m,m'} \frac{\left|\langle m,\boldsymbol{k}|L_z|m',\boldsymbol{k}\rangle\right|^2-\left|\langle m,\boldsymbol{k}|L_x|m',\boldsymbol{k}\rangle\right|^2}{\varepsilon_{m'}-\varepsilon_m}, \quad (3)$$

where ζ is SOC strength and $\varepsilon_m(|m,\boldsymbol{k}\rangle)$ is the energy eigenvalue (eigenfunction) for m, i.e., m and m' are for occupied and unoccupied state, respectively. The angular momentum L_a has weight depending to the pair of m, i.e., $m=m'$ gives positive contribution to E_{MCA} while it is the opposite for $m\neq m'$. In the LiF/MgO and BN/MgO modifications, $d_{\pm2}$ state is pushed above E_F while the rest of d-states are at E_F, reducing the second term of Eq. (3), resulting a 400% PMA enhancement from pristine Fe/MgO model. For the MgN/MgO modification, $d_{\pm1}$ state completely removed from E_F leaves only $d_{\pm2}$ states at E_F, consequently the first term in Eq. (3) is raised while the second term become insignificant [11], and E_{MCA} is 600% higher than the pristine Fe/MgO model.

In Eq. (2), Lorentz function of energy attributes to the states closest to E_F, and the non-zero matrix element of $\Gamma^{-}_{bb'}(\boldsymbol{k})$ governs only by d −orbitals from minority spin at E_F since the spin-lowering operator may vanishes due to the large exchange splitting, consequently a clean E_F gives lower α. Here, δ is set empirically to 0.01 eV for a typical bulk Fe [12] in all models as α mainly accounts for the interfacial Fe. This is true for the LiF/MgO, BN/MgO, and MgN/MgO modifications, as the d-states which are pushed above and/or below E_F, gives significant reduced α, around 75% lower than those of the pristine Fe/MgO model.

In summary, achieving high PMA and low α simultaneously in Fe/MgO system by interface engineering is observed from first principles. The result signifies that the interfacial Fe d-orbitals configuration at around E_F plays an important role for the generation of high PMA and low α simultaneously. Specifically, the LiF/MgO, BN/MgO, and MgN/MgO [11] modifications exhibit nearly a 600% enhancement in PMA and a 75% reduction in α compared to those in the pristine Fe/MgO model.

References

[1] R. Shimabukuro, K. Nakamura, T. Akiyama, and T. Ito, Phys. E: Low Dimens. Syst. Nanostructures 42, 1014 (2010).
[2] S. Hashimoto, Y. Ochiai, and K. Aso, J. Appl. Phys. 66, 4909 (1989).
[3] K. Masuda and Y. Miura, Phys. Rev. B 98, 224421 (2018).
[4] K. Nakamura, T. Ito, A. J. Freeman, L. Zhong, and J. Fernandez-de Castro, Phys. Rev. B 67, 014420 (2003).
[5] M. Weinert, R. E. Watson, and J. W. Davenport, Phys. Rev. B 32, 2115 (1985).
[6] G. H. O. Daalderop, P. J. Kelly, and M. F. H. Schuurmans, Phys. Rev. B 41, 11919 (1990).
[7] K. Gilmore, Y. U. Idzerda, and M. D. Stiles, Phys. Rev. Lett. 99, 027204 (2007).
[8] V. Kamberský, Phys. Rev. B 76, 134416 (2007)
[9] B.-H. Huang, Y.-H. Fu, C.-C. Kaun, and Y.-H. Tang, J. Magn. Magn. Mater. 585, 171098 (2023).
[10] A. Hallal, H. X. Yang, B. Dieny, and M. Chshiev, Phys. Rev. B 88, 184423 (2013).
[11] Y.N. Apriati, K. Nawa, K. Nakamura, Appl. Phys. Lett. 126, 082403 (2025)
[12] E. Barati, M. Cinal, D. M. Edwards, and A. Umerski, Phys. Rev. B 90, 014420 (2014).

Effect of Excimer Laser Annealing on Crystallization and Atomic Ordering of $Co_2Mn_{0.5}Fe_{0.5}Ge$ Heusler Alloy Thin Films toward Spintronic Applications

Hirofumi Suto[1]*, Keita Katayama[2], Yohei Tanaka[3], Dolly Taparia[1], Tomoya Nakatani[1], Hisato Yabuta[2], and Yuya Sakuraba[1]

1. Research Center for Magnetic and Spintronic Materials, National Institute for Materials Science (NIMS), Tsukuba, Japan
2. Graduate School and Faculty of information Science and Electrical Engineering, Kyushu University, Fukuoka, Japan
3. Department of Gigaphoton Next GLP, Kyushu University, Fukuoka, Japan

E-mail: suto.hirofumi@nims.go.jp

Heusler alloys exhibit intriguing material properties, including high spin polarization, large anomalous Hall effect and low damping, making them highly attractive for spintronic applications. One major challenge in the fabrication of Heusler-alloy-based thin film devices is high-temperature treatment required to promote the atomic ordering to obtain the full potential, which is often incompatible with the temperature restriction of the practical device fabrication. In this study, we explore excimer laser annealing (ELA) as an alternative annealing method to address the above temperature constraint. By conducting ELA right after the deposition of Heusler-alloy-based film, steep temperature gradient along the depth direction can allow the film to reach sufficient temperature, keeping the underlying structures within the temperature limitation. We apply ELA to $Co_2Mn_{0.5}Fe_{0.5}Ge$ (CMFG) Heusler alloy thin films and found that crystallization and atomic ordering of the CMFG films were induced similar to the conventional furnace annealing, without interdiffusion or roughness increase. These results demonstrate the potential of ELA as a viable annealing technique, thereby expanding the application of Heusler alloys.

Index Terms—**Excimer laser annealing, Heusler alloys, Spintronics, Magnetic recording**

I. Introduction

Heusler alloys exhibit unique properties such as high spin polarization, large anomalous Hall effect and low damping. These properties are expected to greatly enhance the device performance in spintronic application. In current-perpendicular-to-plane giant magnetoresistance (CPP-GMR) read heads [1], and anomalous Hall effect read heads [2], studied for next-generation hard-disk-drives (HDDs), high spin polarization and large anomalous Hall effect are crucial for enhancing the output. Low damping can improve the efficiency of magnetization oscillation and magnetization switching in microwave-assisted writing devices [3,4] and magnetoresistive-random-access-memory (MRAM) cells. To fully realize the potential of the Heusler alloys, heat treatment is usually conducted to promote atomic ordering. However, device fabrication in practical applications imposes temperature limitations. In the case of HDD read heads, process temperature is limited to 300°C due to the temperature tolerance of the soft magnetic shield layers. In the case of MRAM, the process temperature of memory cells fabricated in the back-end-of-line process is limited to 400°C.

Here, we explore excimer laser annealing (ELA) [5] as an alternative annealing method for Heusler alloys to address the above conflicting temperature requirements. By applying a pulse laser after the deposition of a Heusler-alloy-based device film, steep temperature gradient along the depth direction is induced as laser absorption and subsequent heat generation occurs at the surface. This temperature gradient can allow the film near the surface to reach the required temperature, while keeping the underlying structures within the temperature limitation. Although ELA has already found large-scale practical use such as in fabrication of poly-crystalline Si on glass or flexible substrates, where amorphous Si layers are rapidly heated to the melting point for crystallization before heat diffusion into the substrate causes damage, its application to spintronic Heusler alloys remains unexplored.

II. Experimental

The samples consisting of Ta(2 nm) / CoFeBTa(1.5 nm) / CMFG(50 nm) / Ru(2 nm) were prepared by sputter deposition on thermally oxidized Si substrates. The composition of CMFG was estimated by X-ray fluorescence (XRF) to be $Co_{1.992}Mn_{0.712}Fe_{0.372}Ge_{0.928}$. Pulsed KrF excimer laser with a wavelength of 248 nm, a pulse duration of 83 ns was introduced to the homogenizing optics to form uniform rectangular fluence profile and applied to the sample surface. The irradiated area was 0.369 mm × 1.198 mm. A series of 1000 laser pulses was applied at a repetition rate of 10 Hz. Crystallization and atomic ordering of the samples were examined using X-ray diffraction (XRD). Surface morphology was measured using atomic force microscopy (AFM). Anisotropic magnetoresistance (AMR) and resistivity measurements were conducted by applying a current of 1 mA to the strips with a width of 40 μm and length of 170 μm and measure the resistance by the four-terminal method.

III. Results and Discussions

Figure 1(a) shows the photo image of the ELA sample for various fluence levels from 40 to 300 mJ/cm^2. The position marks, denoted by the red box, were made by damaging the film with high fluence laser, and the 2 mm wide area next to the position guide, denoted by the blue box, is the ELA area made by sweeping the laser spot. Noticeable degradation of Surface specularity occurred when the fluence is 160 mJ/cm^2 or more, suggesting a change in surface morphology. Figures 1(b) shows the corresponding out-of-plane XRD profiles. For fluence below 100 mJ/cm^2, the profiles show no peaks, indicating the amorphous structure. However, from 100 mJ/cm^2, 004, 220 fundamental peaks, and 002 superlattice peaks appear,

demonstrating that the crystallization and *B*2 atomic ordering of the CMFG layers were successfully induced by ELA. At 200 mJ/cm^2, the peaks become sharp and intense, presumably due to growth of larger grains by agglomeration.

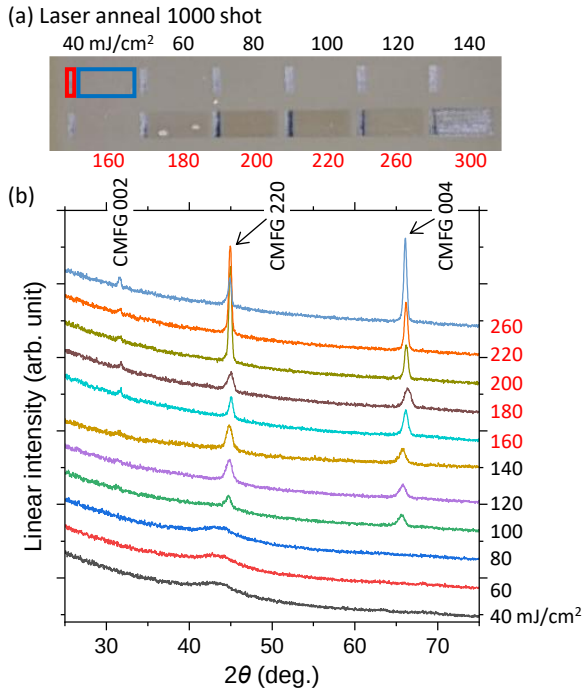

FIG.1. (a) Photo image of the ELA sample. (b) Out-of-plane XRD profiles obtained for the ELA samples for various fluence values.

Figure 2 shows the fluence dependence of average roughness (R_a). In the as-deposited state, the sample surface is very flat with R_a of approximately 0.15 nm. The roughness remains unchanged up to 140 mJ/cm^2 and starts to increase monotonically with fluence. Such increased roughness due to excess fluence is detrimental in device fabrication in practical applications. The ELA conditions with increased roughness shows overall agreement with the specularity degradation.

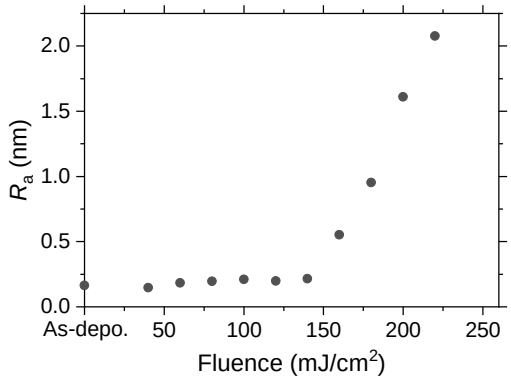

FIG. 2. R_a of the as-deposited and ELA samples as a function of fluence.

Figure 3 shows resistivity and AMR ratio as a function of fluence. The resistivity decreased from 120 mJ/cm^2 and shows a large drop at 140 mJ/cm^2 followed by continuous decrease to a minimum at 180 mJ/cm^2. This resistivity change is attributed to the improved atomic ordering and growth of the crystal. Beyond this fluence, the resistivity shows an upturn, presumably reflecting the increased roughness and interdiffusion due to excessive fluence. The AMR ratio is almost zero in the as-deposited state, and becomes negative after ELA, showing similar trend to that of the resistivity. The negative AMR is associated with the half-metallicity as discussed in Ref. [6]. Notably, at fluence of 140 mJ/cm^2, crystallization and atomic ordering of CMFG with relatively large negative AMR was obtained with no roughness increase, revealing the optimal ELA condition and demonstrating the applicability of ELA to the fabrication of Heusler-alloy-based spintronic devices.

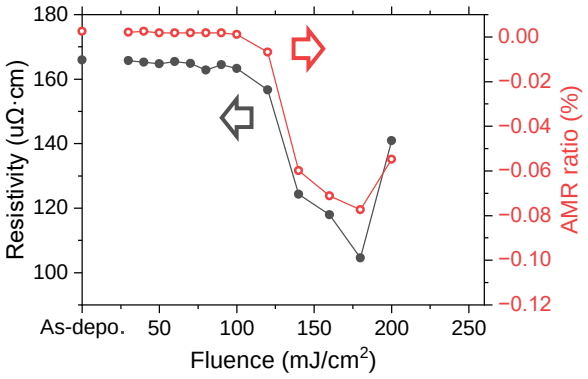

FIG. 3. Resistivity and AMR of the as-deposited and ELA samples as a function of fluence.

ACKNOWLEDGEMENT

KrF excimer laser annealing in this work was conducted by a courtesy of Gigaphoton. Inc. This work is partially supported by Advanced Storage Research Consortium (ASRC), JSPS KAKENHI (grant numbers 23K03934).

REFERENCES

[1] T. Nakatani, et al., "Advanced CPP-GMR spin-valve sensors for narrow reader applications," IEEE trans. Magn. **54**, 3300211 (2018).

[2] T. Nakatani, et al., "Perspective on nanoscale magnetic sensors using giant anomalous Hall effect in topological magnetic materials for read head application in magnetic recording," Appl. Phys. Lett. **124**, 070501 (2024).

[3] J. -G. Zhu, et al., "Microwave assisted magnetic recording," IEEE Trans. Magn. **44**, 125 (2008).

[4] V. Barwal, et al., "Reducing critical current for spin-transfer-torque-induced magnetization reversal in current-perpendicular-to-plane giant magnetoresistance devices: effect of low damping and enhanced spin scattering asymmetry in $Co_2FeGa_{0.5}Ge_{0.5}$ Heusler alloy," in preparation.

[5] M. Beppu, et al., "Sn doping into β-Ga_2O_3 by a KrF excimer laser," Appl. Phys. A **131**, 441 (2025).

[6] V.K. Kushwaha, et al., "Prediction of half-metallic gap formation and Fermi level position in Co-based Heusler alloy epitaxial thin films through anisotropic magnetoresistance effect," Phys. Rev. Mater. **6**, 064411 (2022).

Proposal and Micromagnetic Validation of Bipolar Switching in Voltage-Controlled MRAM Devices

Muftah Al-Mahdawi[1], *Senior Member, IEEE*, and Mikihiko Oogane[2,3]
[1]Program of Mechatronics Engineering, Libyan International University, Benghazi, Libya, mahdawi@ieee.org.
[2]Center for Science and Innovation in Spintronics (Core Research Cluster), Tohoku University, Sendai 980-8577, Japan.
[3]Department of Applied Physics, Tohoku University, Sendai 980-8579, Japan

We propose a voltage-controlled MRAM structure with bipolar switching, where opposite voltage polarities write different bit states. A synthetic antiferromagnet (SAF) free layer has the same symmetry as the simultaneous application of electric and magnetic fields. Micromagnetic simulations validate the proposal, and show self-limiting switching.

***Index Terms*—MRAM, voltage-controlled magnetic anisotropy, bipolar switching, micromagnetic simulation, magnetoelectric effect.**

I. Introduction

MAGNETIC random access memory (MRAM) with voltage-control of magnetic anisotropy (VCMA) is promising for higher-level cache and main memory applications [1]. It offers high density and low-energy writing. In the V-MRAM, a voltage pulse lowers the magnetic anisotropy energy of the storage layer momentarily, which drives the magnetization in a precessional trajectory [2], [3]. However, there are multiple challenges with the writing process: for low-energy writing, a large change of magnetic anisotropy by electric field is needed, an in-plane external field is required to break the symmetry and set the precession axis, tight control over the pulse width and shape is needed to achieve a low writing error rate [4]. One major challenge is that the writing process is unipolar, the same writing pulse toggles the bit state. Therefore, a read-then-write sequence is needed to store the proper bit state. In this work, we propose a V-MRAM design that enables bipolar writing using opposite voltage polarities. The switching is self-limiting, and tolerant to pulse width variation.

II. Proposed Bipolar V-MRAM

We base our proposal on symmetry considerations, mainly the space-inversion symmetry (I), time-reversal symmetry (R), and the combined time-space inversion symmetry (IR). Bipolar switching is switching to a '1' or '0' bit state by changing the polarity of the applied electric field. This is similar to the linear magnetoelectric (ME) effect, which requires a spin structure breaking the single I and R symmetries, while keeping the IR symmetry [5]. The reason for unipolar switching in V-MRAM is that all three symmetries are broken. We propose to use a synthetic antiferromagnet (SAF) structure in the free layer of the V-MRAM [Fig. 1]. The SAF with perpendicular magnetic anisotropy breaks the single I and R symmetries, but retains the combined IR symmetry [Fig. 1(a)]. Therefore, a linear ME effect is allowed, a simultaneous application of collinear electric and magnetic fields controls the spin state. The direction of the electric field (E) is opposite on each interface of the free layer. On one side, E increases

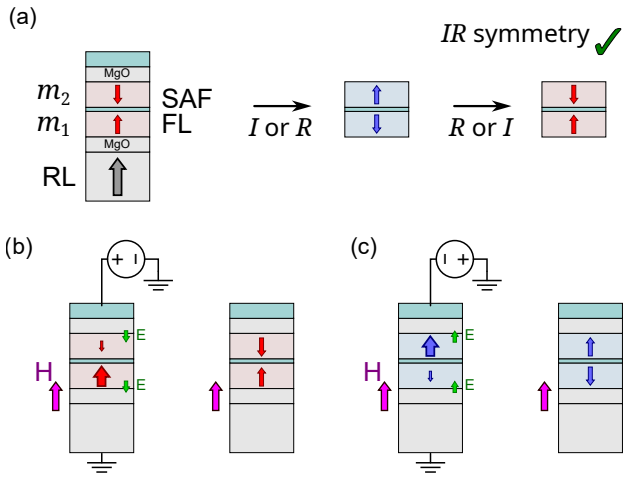

Fig. 1. (a) Schematic of the bipolar V-MRAM with SAF free layer. The SAF is symmetric under IR operation. The writing of bit state by applying a postive writing voltage (b), and a negative writing voltage (c).

the magnetic anisotropy energy, while decreasing it on the other. This is illustrated by the arrow size in Fig. 1(b). The stable sublayer magnetization interacts with the stray magnetic field from the reference layer (RL). Depending on E polarity [Figs. 1(b,c)], we can choose either of the stable spin configurations, which is retained after the removal of the voltage. The resistance readout is from the tunneling current in the bottom side between the free sublayer and the reference layer. Thus, we can select the final bit state by the polarity of the writing voltage. Two switching meachnisms are possible: thermally activated and dynamic. In this work, we investigate the dynamic response, and leave the probabilistic (thermal) switching for a future report.

III. Micromagnetic Simulation

For verification, we simulate the dynamical switching using the micromagnetics simulation package MuMax3 [6]. We use typical parameters for a $Co_{40}Fe_{40}B_{20}$/MgO interface: saturation magnetization $M_s = 1600$ kA/m, interfacial perpendicular

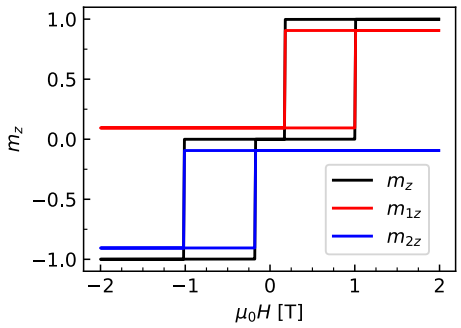

Fig. 2. The hysteresis loop in a magnetic field applied out-of-plane. The sublayer loops are vertically-shifted and scaled for clarity.

anisotropy $K_i = 1.6$ mJ/m^2 [7], Gilbert damping parameter $\alpha = 0.02$, exchange stiffness $A_{\text{ex}} = 15$ pJ/m. We simulate an antiferrmagnetically coupled bilayer system of CoFeB (1 nm) / CoFeB (1 nm). The interlayer exchange stiffness $A_{\text{int}} = -0.5$ pJ/m, which is equivalent to an interlayer exchange coupling energy $J_{\text{int}} = -1.0$ mJ/m^2. We simulate the voltage effect by changing K_i for each sublayer, during time evolution simulations. We introduce a change of ± 1.44 mJ/m^2, corresponding to a VCMA coefficient of 720 fJ/Vm at an $E = 2$ V/nm, which are consistent with reported values [8]. The voltage and VCMA polarities are defined in Fig. 1 The simulation geometry is a cylindrical disk 10 nanometer in diameter, with a discretization cell size of $1.25 \times 1.25 \times 1\text{nm}^3$, representing a 1X MRAM memory element.

IV. Results and Discussion

We show the hysteresis loop simulation result in Fig. 2 in a perpendicular magnetic field. We plot the out-of-plane magnetization component of the normalized magnetization (m_z). The square loops indicate spin-flip switching.

Figure 3 (a) shows the time evolution of sublayer magnetizations under consecutive voltage pulses, highlighted by the shaded spans. We determine the bit state after pulse removal. For an out-of-plane magnetic field $\mu_0 H = +0.2$ T (green-shaded spans), a positive E pulse writes a '1' bit; and a negative E writes '0'. For $\mu_0 H = -0.2$ T (magenta-shaded spans), the relation is reveresed. The pattern is repeatable, and independent of the initial state.

In Fig. 3(b), we show the dynamics near the edges of a voltage pulse. After the onset of the negative voltage pulse, anisotropy of layer 1 is reduced, and enhanced on layer 2. During the voltage application ($t > 30$ ns), layer 1 magnetization tilts towards the inplane direction. Now, two fields are acting on layer 2, the stray out-plane-field, and the larger inplane exchange field from layer 1. After the voltage is removed ($t > 40$ ns), the layer 2 magnetization precesses a half cycle to $+z$ direction. At the same time, the anisotropy of layer 1 returns back, and m_1 is pushed to $-z$ direction. Now, the precession axis becomes the z axis, and the magnetizations quickly damp towards their final position. Notably, the switching is self-limiting and completes without the need for precise timing of pulse width, or an external inplane field.

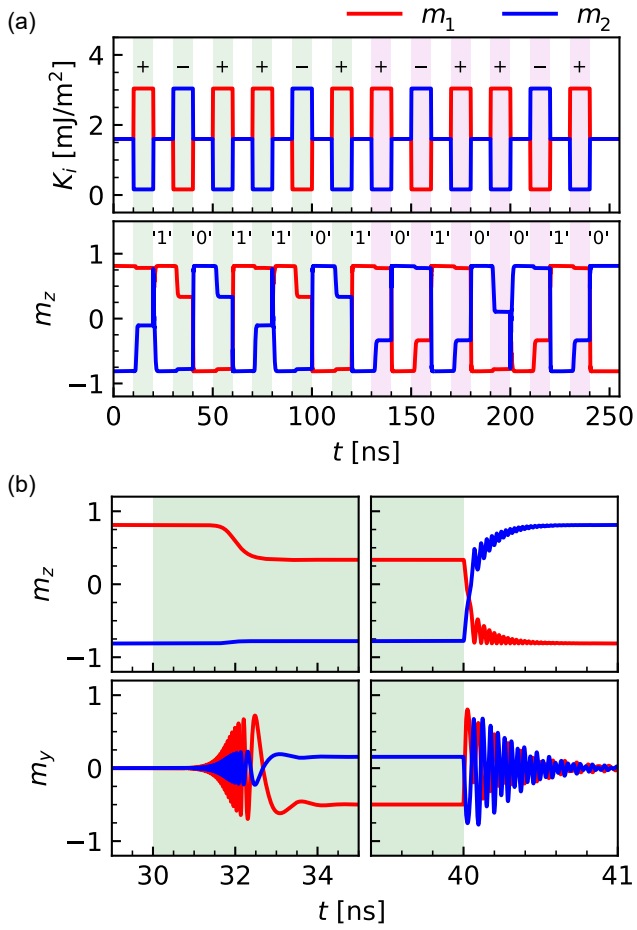

Fig. 3. (a) Bipolar magnetization switching after consecutive voltage pulses, under a positive magnetic field (green-shaded areas), or a negative magnetic field (magneta-shaded). (b) The switching dynamics near the edges of a voltage pulse.

V. Conclusions

We proposed a voltage-controlled MRAM structure based on a SAF free layer, to enable bipolar switching. Guided by symmetry considerations and verified by micromagnetic simulations, the design offers robust and self-limiting switching without precise pulse control or external inplane fields. This proposal offeres a path towards field-free error-tolerant MRAM devices. Furthermore, the use of a SAF free layer is promising for immunity to external field disturbances.

References

[1] H. Yoda *et al.*, "Voltage-control spintronics memory (VoCSM) having potentials of ultra-low energy-consumption and high-density," in *2016 IEEE International Electron Devices Meeting (IEDM)*. IEEE, Dec. 2016, pp. 27.6.1–27.6.4.
[2] Y. Shiota *et al.*, *Nature Materials*, vol. 11, no. 1, pp. 39–43, Nov. 2011.
[3] S. Kanai *et al.*, *Applied Physics Letters*, vol. 101, no. 12, p. 122403, Sep. 2012.
[4] T. Yamamoto *et al.*, *Phys. Rev. Appl.*, vol. 11, p. 014013, Jan 2019.
[5] M. Al-Mahdawi *et al.*, *Physical Review Materials*, vol. 5, no. 9, p. 094406, Sep. 2021.
[6] A. Vansteenkiste *et al.*, *AIP Advances*, vol. 4, no. 10, p. 107133, 2014.
[7] T. Ogasawara *et al.*, *AIP Advances*, vol. 9, no. 12, p. 125053, Dec. 2019.
[8] T. Nozaki *et al.*, *APL Materials*, vol. 10, no. 8, p. 081103, 08 2022.

Exploring Skyrmion Deformation in Antiferromagnetic Systems: A Pathway to Next-Generation Memory Devices

Xiuzhu Wang[1], Zehan Chen[1], and Qiming Shao[1,2], *Member, IEEE*
[1]Department of Electronic and Computer Engineering, The Hong Kong University of Science and Technology, Hong Kong SAR, China
[2]Department of Physics, The Hong Kong University of Science and Technology, Hong Kong SAR, China

Magnetic skyrmions possess a unique topological protection property, making them highly promising candidates as information carriers in advanced recording and memory technologies. However, these carriers can experience deformation when subjected to high current densities, potentially disrupting stable data transmission. In this study, we investigate skyrmion deformation across various magnetic systems, including ferromagnetic (FM), ferrimagnetic (FiM), and antiferromagnetic (AFM) systems, to assess their viability in memory applications. Through micromagnetic simulations and theoretical analysis, we focus on AFM skyrmions, which show the least susceptibility to deformation. Our analysis involves deriving a canting term from the Thiele equation, highlighting a critical factor that accounts for the reduced deformation observed in AFM systems. This insight underscores the superior stability of AFM skyrmions, positioning them as an optimal choice for skyrmion-based memory devices. The findings suggest that AFM systems can enhance the reliability and efficiency of skyrmion-driven information storage and transmission, advancing the fundamentals of recording and memory technologies.

***Index Terms*—Skyrmion, antiferromagnetic system, information storage, memory**

I. Introduction

THIS document is a template for Latex. The electronic version can be downloaded from the conference website.

The magnetic skyrmion presents a transformative potential for advanced recording and memory applications, such as racetrack memory devices, [1]–[5] transistor-like devices, [6], [7] and neuromorphic computing systems. [6] Key attributes of skyrmions that make them suitable for these applications include their topological stability, [8]–[11] nanoscale dimensions, [8], [12]–[14] and the ability to be manipulated by lower current densities compared to domain walls. [15]–[17]

Several control mechanisms are available for skyrmions, including spin current, [18], [19] magnetic field gradients, [20] spin waves, [21] and temperature variations. [22] Among these, current-driven manipulation is prevalent due to its high efficiency and technological compatibility.

In ferromagnetic (FM) systems, skyrmions tend to deform and disintegrate under high current densities, [1], [12], [15], [23] limiting their effectiveness in memory devices. Antiferromagnetic (AFM) systems offer promising alternatives, characterized by weak stray fields [24], [25] and terahertz spin dynamics, [26], [27] which can mitigate skyrmion deformation. [28]–[33] A schematic illustrating AFM skyrmion deformation is presented in Fig. 1(a). The commensurate spins in AFM eliminate skyrmion Hall effect (SkHE), [34], [35] which leads to the deflection of the skyrmion's trajectory and a higher risk of boundary annihilation. We use Mumax3 [36], [37] to simulate the FM, FiM, and AFM systems. The simulation results indicate that increasing the applied current density causes a skyrmion to gradually deform from a circular shape to an elliptical shape, expanding until it ultimately breaks down, as shown in Fig. 1(b). Our simulations reveal that AFM skyrmions possess larger stiffness, meaning that they are more resistant to current-induced deformation.

This study investigates skyrmion deformation across FM, FiM, and AFM systems using micromagnetic simulations, highlighting transitions from strong to negligible Magnus forces. Our findings reveal that AFM skyrmions exhibit minimal deformation. Theoretically, we examine skyrmion deformation through force balance analysis, identifying magnetic canting as a crucial factor enhancing AFM skyrmion stability. We quantify skyrmion deformation in terms of stress, size, shape, and orientation, [28], [29], [31], [38] comparing AFM and FM skyrmions. Our numerical simulations closely align with analytical solutions, underscoring AFM systems' potential in revolutionizing recording and memory technologies. And we could use the δ term to define the skyrmion deformation:

$$\delta = \frac{1}{(2D/w + 2A/R^2)} \left(\frac{A\boldsymbol{\delta}_0}{w^2} + \alpha \frac{M_S}{\gamma} \frac{\boldsymbol{v}}{R} \right) \cdot \hat{\boldsymbol{\varphi}}. \quad (1)$$

where $\boldsymbol{\delta}_0 = \tau_{\mathrm{ad}} M_S \hat{\boldsymbol{i}} / 2K\gamma$, refers to the AFM domain canting far from the skyrmion, $\boldsymbol{v}$ is the moving speed of skyrmion caused by the current. Normally the relation between skyrmion radius and domain wall width is $R \gg w$, and under such condition δ can be approximated as $\delta \approx (A/2Dw)\boldsymbol{\delta}_0 \cdot \hat{\boldsymbol{\varphi}}$. On the contrary, the canting in FM skyrmion is given by $\delta_{\mathrm{FM}} = -v_r M_S / 2D\gamma$. Comparing the canting between AFM and FM systems provides a clearer insight into why the deformation in AFM is considerably smaller:

$$\begin{aligned} \delta_{\mathrm{AFM,max}} &\approx \frac{A|\boldsymbol{\delta}_0|}{2Dw} \approx \frac{1}{2} \cdot \left(\frac{w\tau_{\mathrm{ad}} M_S}{2D\gamma} \right), \\ \delta_{\mathrm{FM,max}} &\approx \left(\frac{\pi}{\alpha} \right) \cdot \delta_{\mathrm{AFM,max}}. \end{aligned} \quad (2)$$

where $\delta_{\mathrm{AFM,max}} \ll \delta_{\mathrm{FM,max}}$ as the damping $\alpha < 1$.

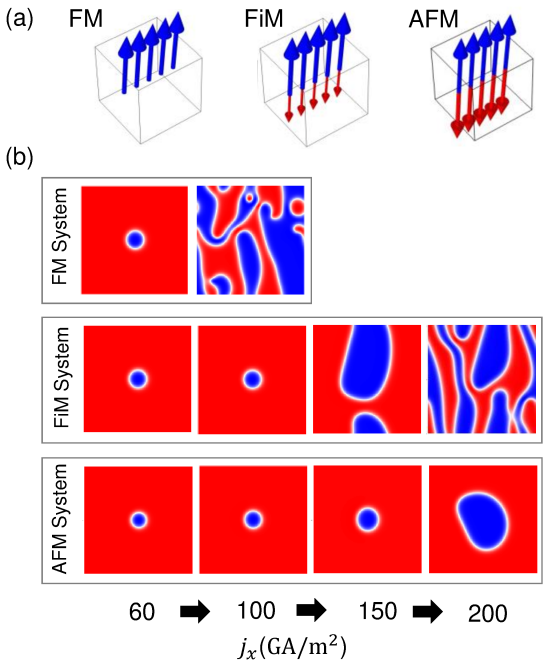

Fig. 1. (a) Schematic structure of the AFM skyrmion deformation. (b) The skyrmion deformation under different applied current densities in different systems. The skyrmion breaks down at 60 $\mathrm{GA/m^2}$ and 150 $\mathrm{GA/m^2}$ in the FM and FiM system respectively, but it still remains stable at 200 $\mathrm{GA/m^2}$ in the AFM system.

References

[1] A. Fert, N. Reyren, and V. Cros, "Magnetic skyrmions: advances in physics and potential applications," *Nat. Rev. Mater.*, vol. 2, no. 7, pp. 1–15, 2017.

[2] R. Tomasello, E. Martinez, R. Zivieri, L. Torres, M. Carpentieri, and G. Finocchio, "A strategy for the design of skyrmion racetrack memories," *Sci. Rep.*, vol. 4, no. 1, pp. 1–7, 2014.

[3] S.-G. Je, D. Thian, X. Chen, L. Huang, D.-H. Jung, W. Chao, K.-S. Lee, J.-I. Hong, A. Soumyanarayanan, and M.-Y. Im, "Targeted writing and deleting of magnetic skyrmions in two-terminal nanowire devices," *Nano Lett.*, vol. 21, no. 3, pp. 1253–1259, 2021.

[4] S. S. Parkin, M. Hayashi, and L. Thomas, "Magnetic domain-wall racetrack memory," *Science*, vol. 320, no. 5873, pp. 190–194, 2008.

[5] A. Fert, V. Cros, and J. Sampaio, "Skyrmions on the track," *Nat. Nanotechnol.*, vol. 8, no. 3, pp. 152–156, 2013.

[6] X. Zhang, Y. Zhou, K. M. Song, T.-E. Park, J. Xia, M. Ezawa, X. Liu, W. Zhao, G. Zhao, and S. Woo, "Skyrmion-electronics: writing, deleting, reading and processing magnetic skyrmions toward spintronic applications," *J. Phys. Condens. Matter*, vol. 32, no. 14, p. 143001, 2020.

[7] S. Luo and L. You, "Skyrmion devices for memory and logic applications," *APL Mater.*, vol. 9, no. 5, 2021.

[8] T. H. R. Skyrme, "A unified field theory of mesons and baryons," *Nucl. Phys.*, vol. 31, pp. 556–569, 1962.

[9] Y. Zhou, E. Iacocca, A. A. Awad, R. K. Dumas, F. Zhang, H. B. Braun, and J. Åkerman, "Dynamically stabilized magnetic skyrmions," *Nat. Commun.*, vol. 6, no. 1, p. 8193, 2015.

[10] X. Yu, Y. Onose, N. Kanazawa, J. H. Park, J. Han, Y. Matsui, N. Nagaosa, and Y. Tokura, "Real-space observation of a two-dimensional skyrmion crystal," *Nature*, vol. 465, no. 7300, pp. 901–904, 2010.

[11] C. Felser and S. Parkin, "Topology, skyrmions, and heusler compounds," *MRS Bull.*, vol. 47, no. 6, pp. 600–608, 2022.

[12] J. Iwasaki, M. Mochizuki, and N. Nagaosa, "Universal current-velocity relation of skyrmion motion in chiral magnets," *Nat. Commun.*, vol. 4, no. 1, p. 1463, 2013.

[13] J. M. Coey, *Magnetism and magnetic materials*. Cambridge university press, 2010.

[14] N. Manton and P. Sutcliffe, *Topological solitons*. Cambridge University Press, 2004.

[15] R. Tomasello, V. Puliafito, E. Martinez, A. Manchon, M. Ricci, M. Carpentieri, and G. Finocchio, "Performance of synthetic antiferromagnetic racetrack memory: domain wall versus skyrmion," *J. Phys. D: Appl. Phys.*, vol. 50, no. 32, p. 325302, 2017.

[16] A. Goussev, J. Robbins, and V. Slastikov, "Domain-wall motion in ferromagnetic nanowires driven by arbitrary time-dependent fields: an exact result," *Phys. Rev. Lett.*, vol. 104, no. 14, p. 147202, 2010.

[17] L. Caretta, M. Mann, F. Büttner, K. Ueda, B. Pfau, C. M. Günther, P. Hessing, A. Churikova, C. Klose, M. Schneider *et al.*, "Fast current-driven domain walls and small skyrmions in a compensated ferrimagnet," *Nat. Nanotechnol.*, vol. 13, no. 12, pp. 1154–1160, 2018.

[18] J. Sampaio, V. Cros, S. Rohart, A. Thiaville, and A. Fert, "Nucleation, stability and current-induced motion of isolated magnetic skyrmions in nanostructures," *Nat. Nanotechnol.*, vol. 8, no. 11, pp. 839–844, 2013.

[19] A. Hrabec, J. Sampaio, M. Belmeguenai, I. Gross, R. Weil, S. M. Chérif, A. Stashkevich, V. Jacques, A. Thiaville, and S. Rohart, "Current-induced skyrmion generation and dynamics in symmetric bilayers," *Nat. Commun.*, vol. 8, no. 1, p. 15765, 2017.

[20] A. Casiraghi, H. Corte-León, M. Vafaee, F. Garcia-Sanchez, G. Durin, M. Pasquale, G. Jakob, M. Kläui, and O. Kazakova, "Individual skyrmion manipulation by local magnetic field gradients," *Commun. Phys.*, vol. 2, no. 1, p. 145, 2019.

[21] Y. Liu, G. Yin, J. Zang, J. Shi, and R. K. Lake, "Skyrmion creation and annihilation by spin waves," *Appl. Phys. Lett.*, vol. 107, no. 15, 2015.

[22] Z. Wang, M. Guo, H.-A. Zhou, L. Zhao, T. Xu, R. Tomasello, H. Bai, Y. Dong, S.-G. Je, W. Chao *et al.*, "Thermal generation, manipulation and thermoelectric detection of skyrmions," *Nat. Electron.*, vol. 3, no. 11, pp. 672–679, 2020.

[23] Y. Tchoe and J. H. Han, "Skyrmion generation by current," *Phys. Rev. B*, vol. 85, no. 17, p. 174416, 2012.

[24] T. Jungwirth, X. Marti, P. Wadley, and J. Wunderlich, "Antiferromagnetic spintronics," *Nat. Nanotechnol.*, vol. 11, no. 3, pp. 231–241, 2016.

[25] V. Baltz, A. Manchon, M. Tsoi, T. Moriyama, T. Ono, and Y. Tserkovnyak, "Antiferromagnetic spintronics," *Rev. Mod. Phys.*, vol. 90, no. 1, p. 015005, 2018.

[26] H. Qiu, T. S. Seifert, L. Huang, Y. Zhou, Z. Kašpar, C. Zhang, J. Wu, K. Fan, Q. Zhang, D. Wu *et al.*, "Terahertz spin current dynamics in antiferromagnetic hematite," *Adv. Sci.*, vol. 10, no. 18, p. 2300512, 2023.

[27] B. Ivanov, "Spin dynamics for antiferromagnets and ultrafast spintronics," *J. Exp. Theor. Phys.*, vol. 131, pp. 95–112, 2020.

[28] S. Perrard, A. Rivière, W. Mostert, and L. Deike, "Bubble deformation by a turbulent flow," *J. Fluid Mech.*, vol. 920, p. A15, 2021.

[29] A. Fujiwara, Y. Danmoto, K. Hishida, and M. Maeda, "Bubble deformation and flow structure measured by double shadow images and piv/lif," *Exp. Fluids*, vol. 36, pp. 157–165, 2004.

[30] S. J. Poulos, "The steady state of deformation," *J. Geotech. Eng.*, vol. 107, no. 5, pp. 553–562, 1981.

[31] B. Bunner and G. Tryggvason, "Effect of bubble deformation on the properties of bubbly flows," *J. Fluid Mech.*, vol. 495, pp. 77–118, 2003.

[32] G.-h. Shi, "Discontinuous deformation analysis: a new numerical model for the statics and dynamics of deformable block structures," *Eng. Comput.*, vol. 9, no. 2, pp. 157–168, 1992.

[33] S. Vélez, S. Ruiz-Gómez, J. Schaab, E. Gradauskaite, M. S. Wörnle, P. Welter, B. J. Jacot, C. L. Degen, M. Trassin, M. Fiebig *et al.*, "Current-driven dynamics and ratchet effect of skyrmion bubbles in a ferrimagnetic insulator," *Nat. Nanotechnol.*, vol. 17, no. 8, pp. 834–841, 2022.

[34] R. Juge, S.-G. Je, D. d. S. Chaves, L. D. Buda-Prejbeanu, J. Peña-Garcia, J. Nath, I. M. Miron, K. G. Rana, L. Aballe, M. Foerster *et al.*, "Current-driven skyrmion dynamics and drive-dependent skyrmion hall effect in an ultrathin film," *Phys. Rev. Appl.*, vol. 12, no. 4, p. 044007, 2019.

[35] X. Zhang, Y. Zhou, and M. Ezawa, "Magnetic bilayer-skyrmions without skyrmion hall effect," *Nat. Commun.*, vol. 7, no. 1, p. 10293, 2016.

[36] A. Vansteenkiste, J. Leliaert, M. Dvornik, M. Helsen, F. Garcia-Sanchez, and B. Van Waeyenberge, "The design and verification of mumax3," *AIP Adv.*, vol. 4, no. 10, 2014.

[37] J. Leliaert and J. Mulkers, "Tomorrow's micromagnetic simulations," *J. Appl. Phys.*, vol. 125, no. 18, 2019.

[38] H. Koibuchi, S. E. Hog, V. Egorov, F. Kato, and H. T. Diep, "Mathematical modeling of skyrmion shape deformation under uni-axial stresses," in *J. Phys. Conf. Ser.*, vol. 1391, no. 1. IOP Publishing, 2019, p. 012013.